University of Texas at Arlington

# MavMatrix

2023

# Estimation of Suspended Sediment Concentration along the Lower Brazos River using Satellite Imagery and Machine Learning

Trevor Stull

# ESTIMATION OF SUSPENDED SEDIMENT CONCENTRATION ALONG THE LOWER

# BRAZOS RIVER USING SATELLITE IMAGERY AND MACHINE LEARNING

By

Trevor Ernest-Paul Stull

Thesis

Presented to the Faculty of the Graduate School of

The University of Texas at Arlington in Partial Fulfillment

of the Requirements for the Degree of

MASTER OF SCIENCE IN CIVIL ENGINEERING

The University of Texas at Arlington

August 2023

Supervising Committee:

Habib Ahmari, Supervising Professor

Yu Zhang

Jessica Eisma

# Abstract

Suspended sediment transport in river basins is important for many water management planning activities to maintain safe drinking water for the community and maintenance of water quality and waterways for the ecosystem. Currently, the traditional way to measure suspended sediment effectively and reliably is by collecting field samples in the river body, which is very time consuming and only provide a point value of suspended sediment within the waterbody at the instant the sample was taken. This thesis focuses on developing models that estimate suspended sediment concentrations for the lower Brazos River using satellite imagery from publicly available data and machine learning methods. The use of optical properties such as satellite imagery and turbidity measurements have been gaining support recently and provide a more continuous record of suspended sediment concentrations and in the case of satellite imagery a spatial relationship once a model is developed. Historical samples of suspended sediment concentrations from the United States Geological Survey and Texas Commission on Environmental Quality and satellite imagery from Landsat Missions and Sentinel Mission 2 were utilized to develop models to estimate suspended sediment concentrations for the lower Brazos River. Models used in this thesis to accomplish this goal include support vector machines, artificial neural networks, extreme learning machines, and exponential relationships. In addition, flow and depth measurements from the United States Geological Survey were used to develop rating curves to estimate suspended sediment concentrations for the Brazos River as a baseline comparison of the models that used satellite imagery to estimate suspended sediment concentrations. Models were evaluated using the Taylor Diagram analysis on the test data set developed for the Brazos River data. Sixteen of the models using satellite imagery as inputs that were developed for this thesis performed with a coefficient of determination $R^2$ above 0.69 with the three best performing models having an $R^2$ of 0.83 to 0.85. One of the best performing models was then applied estimate suspended sediment concentrations before, during, and after Hurricane Harvey to evaluate Hurricane Harvey's impact to the sediment dynamics along the lower Brazos River and the model's ability to achieve this goal. The models that used satellite imagery developed for this thesis were also evaluated on the San Bernard River to test their ability outside of the Brazos River; however, all models achieved an $R^2$ below 0.04. In addition, the importance

of input variable to estimate suspended sediment concentrations were evaluated using the principal component analysis which determined that the NIR, red, and green bands were significant to achieve this goal. This was confirmed with the best performing models developed incorporating the Red-Green Ratio as an input.

## Acknowledgement

I would like to thank my supervising professor Dr. Habib Ahmari for providing guidance and support to me throughout the journey to complete this thesis. I would also like to thank my parents Ernest and Leslie Stull who taught me the importance of education, hard work, and perseverance to accomplish any goal I set my mind to. A special thanks goes to my wife Vaishanavi Mirapurkar who has been my biggest supporter throughout this journey. I cannot express enough how without this core group of advocates in my corner, I would not have been able to accomplish this journey.

I would also like to take a moment to recognize those that were not able to witness me finish this goal but supported me during the time that they were still on this Earth and I am sure are continuing to root for me wherever they are now.

**Table of Contents**

## List of Figures

## List of Tables

# 1.0    Introduction

## 1.1    Background and Motivation

Suspended sediment transport in river basins is important for many water management planning activities including estimation of useful life of reservoirs, evaluation of land use impacts, and quantifying sediment-associated nutrient and contaminant amounts. In general, increased amounts of suspended sediment can lead to increased amounts of contaminants in water because many contaminants can be attached to suspended sediment particles or are suspended sediment particles. This increased level of contamination can affect treatment processes. Also, increased suspended sediment can lead to increased sedimentation within reservoirs that reduces their overall capacity, which could cause future water capacity shortages. Furthermore, increased suspended sediment can adversely affect native aquatic life. Thus, it can be very valuable to accurately estimate suspended sediment concentrations in waterbodies.

Currently, the traditional way to measure suspended sediment effectively and reliably is by collecting field samples in the river body. This method is very time consuming and can be extremely dangerous for field staff following severe flooding events. These field samples also only provide a point value of suspended sediment within the waterbody at the instant the sample was taken.

Efforts have been made to use less labor-intensive methods to estimate suspended sediment concentration, including use of turbidity measurements and satellite imagery data. Turbidity measurement, as a surrogate for suspended sediment, can provide a continuous measure of suspended sediment in a waterbody but also only provides a point estimate provided that a relationship between suspended sediment concentration and turbidity is established for the monitoring site. On the other hand, satellite imagery can provide a spatial measure of suspended sediment that field data cannot produce without significant efforts. It can also potentially provide a more continuous record than field measurements. The timing of satellite imagery data is at best daily to every other day with newer technologies, thus making suspended sediment estimates using satellite imagery not as continuous a record as turbidity measurements.

Given these are both optical measurements of a waterbody, the relationship of turbidity and satellite imagery data to suspended sediment concentrations can be very complex. Researchers have begun to use more complex modeling algorithms to accurately predict these relationships. In recent years, machine learning algorithms such as decision trees, and artificial neural networks have been utilized to simulate these relationships. The research presented in this thesis focuses on using machine learning algorithms and satellite imagery data to estimate suspended sediment concentrations in river bodies.

## 1.2    Research Objective and Plan

The main objective of this study was to develop models that estimate suspended sediment concentration along the lower Brazos River near the Gulf of Mexico and evaluate their performance. This is accomplished by performing the following tasks.

1.  Processing publicly available river flow and gauge depth data for the Brazos River, suspended sediment concentration data for the Brazos River and San Bernard River, and satellite imagery from Landsat Missions and Sentinel Mission 2.

2.  Completing an analysis of the importance of the input variables used in the study to estimate suspended sediment concentrations using the principal component analysis and canonical correlation analysis.

3.  Developing models that estimate suspended sediment concentrations for the Brazos River using a variety of methods including rating curves, support vector machines, artificial neural networks, extreme learning machines, and exponential relationships.

4.  Evaluating model performance using the Taylor Diagram analysis on the Brazos River and the San Bernard River.

5.  Appling a model developed to estimate suspended sediment concentrations to evaluate the model's ability and to analyze the sediment dynamics before, during, and after Hurricane Harvey.

### 1.3    Thesis Organization

This thesis is organized as follows: Chapter 1 consists of the motivation, background, and objective of this research. Chapter 2 discusses the relevant literature on sediment dynamics in rivers, the historical methods and limitations of estimating suspended sediment concentrations in rivers, and the historical methods and limitations of using satellite imagery for estimating properties in water bodies. Chapter 3 presents the methods and procedures of processing the data collected for this study, the development of models to estimate suspended sediment concentrations, and how the models were evaluated. Chapter 4 contains the results and discussion of the input variable analysis, model development, and model applications. The summary and conclusion of this research along with the limitations of the work completed and recommendations for future work regarding this topic are presented in Chapter 5.

## 2.0    Literature Review

### 2.1    Suspended Sediment Processes

Sediment yield/load and suspended sediment concentration are typical values that are estimated during studies involving sediment in river bodies. Sediment yield/load is the amount of sediment passed through a unit area over a unit time and depends on the suspended sediment concentration and the flow in a river. Sediment yield/load provides a long-term metric for sediment in a river body. Conversely, suspended sediment concentration is the amount of sediment present in a volume of water and is a metric that represents the sediment at a certain time and location in a river body. As discussed previously, this research focuses on improving suspended sediment concentration estimate methods because it can improve sediment yield/load estimates.

A typical method to estimate suspended sediment is to use a rating curve between flow measurements and suspended sediment measurements from the river. A typical equation for flow-suspended sediment relationship is shown below in Equation (2.1).

$$SSC = a * Q^b$$ 
<div align="right">Equation (2.1)</div>

where $a$ and $b$ are coefficients that are calibrated for the site, *SSC* is the suspended sediment concentration, and *Q* is the stream flow.

In general, this method can be very effective at estimating suspended sediment concentration at a given site. The underlying assumption with this method is that as flow increases, the suspended sediment concentration also increases. The reasoning is that higher flows lead to more available energy in the river to dislodge and transport more particles. This additional energy also allows for the transport of larger particles in the water. While in general, this assumption holds true for most sites and situations, due to the complex dynamics of the suspended sediment process, there are cases where this assumption is not true or where this relationship can be affected. Figure 2-1 shows the daily flow vs. average daily suspended sediment concentration for the Lavaca River near Edna, Texas from 1945-1989. As shown, increasing flows in the Lavaca River did lead to increased suspended sediment concentrations up to a flow of approximately 1,000 cfs, then it shows a reverse trend between flow and suspended sediment concentration.
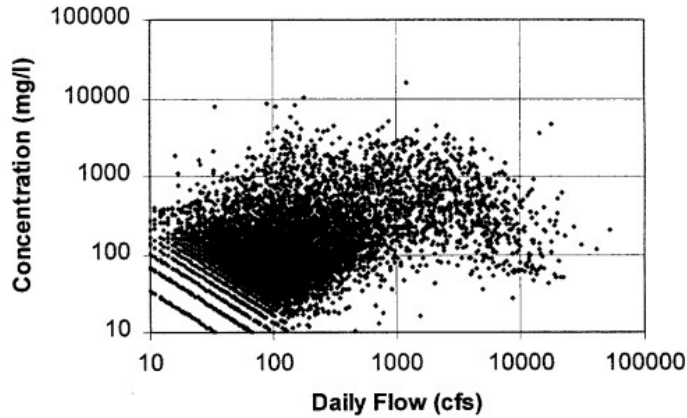
**Figure 2-1:** Daily Flow vs. Suspended Sediment Concentration in the Lavaca River near Edna, Texas from 1945-1989 (Coonrod,1998)

The rating curve does not always hold for every river basin because suspended sediment concentration in a river is affected by more than just the flow in the river. Figure 2-2 shows variables that affect sediment yield, which is the multiplication of flow and suspended sediment concentration. The precipitation relates to the flow of the river, but the flow fails to account for the sediment availability of the river basin or the complete sediment carrying capacity of the river in certain situations. The sediment availability and sediment carrying capacity depend on watershed characteristics, channel properties, and water properties (e.g., viscosity). The following sections discuss these characteristics in more detail and their effect on suspended sediment concentration estimates.
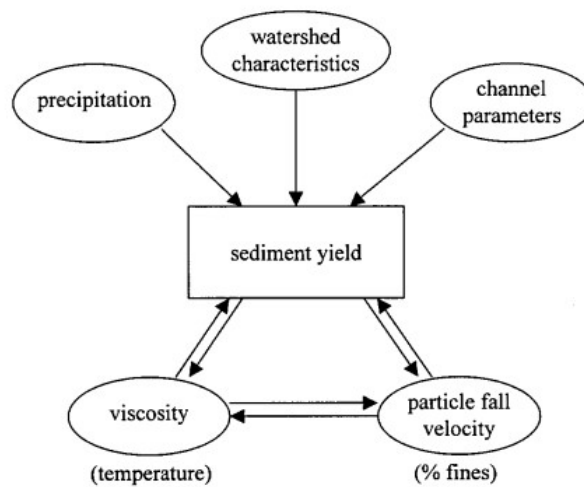


**Figure 2-2:** Variables that Affect Sediment Yield (Coonrod,1998)

2.1.1    Climatic Effects on Suspended Sediment Processes

Research has shown that suspended sediment processes follow a climatic pattern like the seasonal variability. Seasonal variability affects the temperature, land cover, and storm event patterns of a river basin. Temperature effects the viscosity of water such that increasing temperature leads to lower water viscosity. Lower viscosity increases the settling velocity of particles which is likely to lower suspended sediment concentrations. These affects are likely negligible compared to the climatic impacts to land cover and storm event patterns.

In many North American watersheds, the decreased temperatures and precipitation during the winter season leads to a reduced vegetation cover in the watershed. Furthermore, in agricultural lands, variation of the seasons leads to variation of commercial crop being cultivated and thus the density and presence of vegetation for these areas. Poesen (1996) observed variations in ephemeral gully and interrill/rill erosion contributions to the total suspended sediment between seasons at the Central Belgium site investigated in his study. A large portion of this variability was caused by variable vegetation cover due to seasonal crop rotations. In general, when a watershed has a reduced vegetation cover, the suspended sediment concentration is larger. The effects of land cover and land uses on suspended sediment processes is discussed further in Section 2.1.2.3.

Storm patterns are also affected by the seasonal variability of the river basin. For example, Coonrod (1998) reported that in the Lavaca River near Edna, Texas, spring months (April through June) produced storms with the most intense rainfall and were the wettest time periods. These frequent and more intense events led to the highest suspended sediment concentrations in the Lavaca River. In general, more intense rainfall events result in higher suspended sediment concentrations because more sediment can be dislodged and conveyed due to the high intensity and higher flows caused by the event. Thus, if a river basin experiences seasons where more intense storm events are more likely to occur, then these time periods also likely have higher suspended sediment concentrations.

The global climatic pattern of the river basin also affects the suspended sediment processes. For example, Coonrod (1998) observed some rivers in more arid climates experienced higher suspended sediment concentrations. In general, areas with lower annual rainfall have lower vegetation which

increases the likelihood of sediment being dislodged by rainfall and thus increasing suspended sediment concentrations. Conversely, areas with higher annual rainfall have denser vegetation which lowers the likelihood of sediment being dislodged by rainfall leading to lower suspended sediment concentrations. These global climatic trends can be affected by the soil properties of the river basin as well, which is discussed in more detail in Section 2.1.2.2.

## 2.1.2 Watershed Characteristics Effects on Suspended Sediment Processes

Watershed characteristics are another major factor that affect suspended sediment concentrations. This section discusses how different watershed characteristics affect suspended sediment concentrations.

### 2.1.2.1 Dam/Reservoir Presence Effects

One such watershed characteristic is the presence of a dam/reservoir. Dams commonly trap sediment in the upstream reservoir which can potentially decrease downstream suspended sediment concentration. However, dams can also scouring immediately downstream of the dam/reservoir due to reduction in sediment load in the water released from the reservoir. Coonrod (1998) observed watersheds with dams had lower suspended sediment concentration averages over an annual period than watersheds without dams. He also observed that the presence of dams/reservoirs impacted the suspended sediment concentration in arid areas more than in more temperate areas. However, this general trend was not true in all situations in the watersheds in the Coonrod (1998) study.

### 2.1.2.2 Soil Properties/Type Effects

As mentioned previously, part of the underlying assumption of the rating curve method is that increasing flows lead to increasing sediment concentrations because more larger sediment particles can be conveyed by the flows. However, several researchers have shown situations where increases in flows in a river did not lead to an increase in suspended sediment particle size or suspended sediment concentration over an extended time. For example, Walling (1989) showed several different flow-particle size relationships for several sites in the River Exe basin in Devon, UK. Several sites did show an increase in particle size with increased flows in this study, but many other sites did not. Figure 2-3

illustrates some of the sites in the River Exe basin that contradicted the typical flow and particle size relationship (increasing flow leads to increased suspended sediment particle size). These relationships were explained by the characteristics of the parent soil in the upstream basins of these sites and the preferential delivery mechanics at these sites. Walling (1989) reasoned that these sites likely had parent soils that were composed with higher percentages of fine-grained particles or were in areas with reduced delivery efficiency caused by, for example, flood inundation. This observation highlights the impact that the parent soil and river dynamics can have on the suspended sediment process showing that increases in river flows do not always lead to an increased suspended sediment particle size.
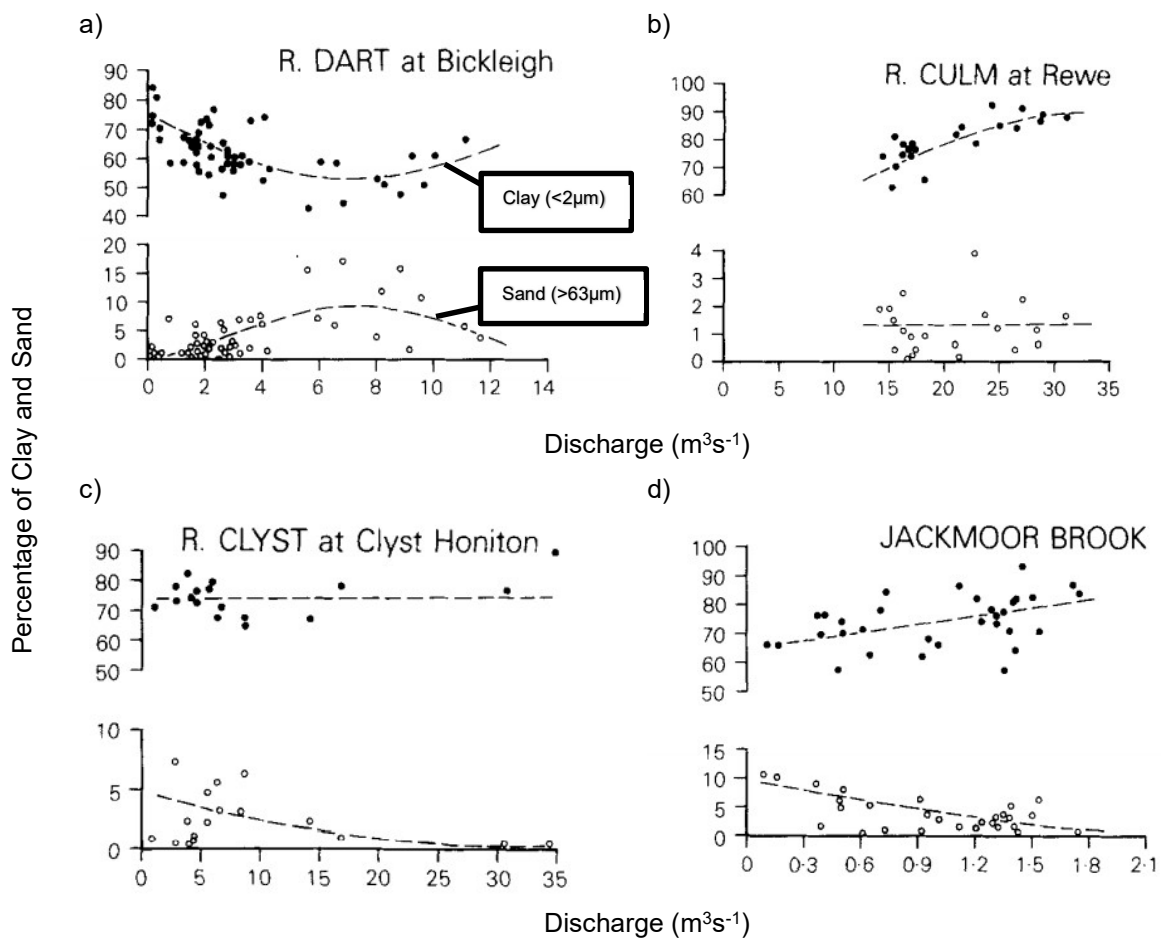
**Figure 2-3:** Particle Size and Flow Relationships at (a) Bickleigh Station at River Dart, (b) Rewe Station at River Culm, (c) Clyst Honiton at River Clyst, and (d) Jackmoor Brook (Walling, 1989)

Poesen (1996) also showed how differences in soil types of the parent soil can affect suspended sediment interactions by evaluating the contribution of total suspended sediment from rill/interril and ephemeral gulley erosion at a given site. The site located in Portugal in the Alentejo region, 5 km east of Mertola in this study showed higher contributions of suspended sediment from ephemeral gully erosion than rill and interrill erosion compared to other two sites investigated. Poesen (1996) hypothesized that this was because the Portugal site had soil with fairly high rock fragments which reduced interrill and rill erosion due to its resistance to be dislodged by rain impacting it. The other two sites investigated in this study were either sandy loam in texture or high in silt and clay content, which both are more prone to interril and rill erosion because they are less resistant to being dislodged by rain impacting it. This shows the impact the physical characteristics of different soil types have on the ability of the parent soil to become suspended sediment.

### 2.1.2.3 Land Use and Land Cover Effects

In addition to the parent soil characteristics affecting the typical flow and suspended sediment relationship, the land use within the basin can affect this relationship. Lefrancois (2007) showed that average suspended sediment concentrations and storm related sediment totals over a monthly period increased when monthly average flows were not increasing. Lefrancois (2007) reasoned these abnormal trends were due to the variability in availability of sediment for transport caused by cattle activity in the river basins investigated. Average suspended sediment concentrations and storm related sediment totals were highest when cattle activity on the land was highest, and it was reasoned that the cattle dislodged more soil making it available for sediment transport processes. Cattle activity affecting suspended sediment highlights the effect that differing land uses have on suspended sediment processes.

Along the same vein as land use affecting suspended sediment, the land cover, which is tied to the land use, can play a large role in suspended sediment transport dynamics in a river basin. For example, Poesen (1996) saw variations in ephemeral gully and interrill/rill erosion contributions to the total suspended sediment between seasons at the Central Belgium site investigated in this study. Part of this variation was caused by the variable rain regime for this site throughout the season, but a large portion of this variability was also caused by variable vegetation cover due to seasonal crop rotations. For

example, two rain events with similar rain intensities that occurred in early summer and early fall (26 mm in 30 min and 20 mm in 20 min, respectively) had contributions from ephemeral gully and interrill/rill erosion that were drastically different between the events because of the crops cultivated during the different seasons were so different. For the early summer event, ephemeral gully erosion contributed 24% of the total suspended sediment while the early fall event led to high ephemeral gully erosion contributions to the total suspended sediment. During early summer, the crops did not provide as much vegetation cover on the hillsides of the Central Belgium site leading to the reduced ephemeral gully erosion contribution to total suspended sediment because interill/rill erosion on the uncovered hillside dominated.

### 2.1.3    In-river Processes Effects

Not only are there complexities in the upstream basins of rivers caused by soil characteristics and land uses that affect suspended sediment transport, processes in the river itself affect the suspended sediment process. Within the river, complex interactions between the suspended sediment particles, the flow regime of the river, the organics in the river, and the surficial fine-grained laminae can affect suspended sediment processes. Due to these complexities, it is very common for flocculation to occur in rivers forming larger, more irregularly shaped suspended sediment particles than expected based on the native or parent soil. Droppo (2005) investigated the difference of several physical properties between soil aggregate, surficial fine-grained laminae, and suspended sediment particles showing that suspended sediment and surficial fine-grained laminae particles had very complex shapes likely because they are a conglomeration of different particles. These complex shapes caused suspended sediment and surficial fine-grained laminae particles to have higher porosities, lower densities, and lower settling velocities than the more uniform and spherical soil aggregates. Droppo (2005) also hypothesized that once soil aggregate entered the river or stream that these particles either settled to the surficial fine-grained laminae or were combined with other particles that allows the soil aggregate to remain suspended longer.

Processes within the bed material/surficial fine-grained laminae also lead to interesting effects on suspended sediment processes. The surficial fine-grained laminae is typically defined as the topmost layer of the bed material in a river that is a stationary fluid. This layer is composed of the most recently

deposited material in the riverbed. The surficial fine-grained laminae is very unique from site to site because of its dependance on the flow dynamics in the river and organic material in the river bed. Depending on the properties of the surficial fine-grained laminae, it can greatly impact how the river suspended sediment behaves. For example, the surficial fine-grained laminae in Lake Ontario showed that organic activity in this layer led to higher friction coefficients of the soil than expected (Droppo, 2001). This biostabilization likely leads to combinations of particles that would not occur if this organic activity were not present. These organic processes can affect how the riverbed interact with the flow regime in the river and lead to variable suspended sediment responses between sites and storm events.

### 2.1.4    General Heuristics of Suspended Sediment

All the complex interactions mentioned above can affect the sediment processes between different sites in two separate river basins and even different sites in the same river basin. These complex sediment processes lead to general heuristics, making the estimation of suspended sediment much more difficult than the general flow rating curve method. Lefrancois (2007) used three classes of suspended sediment responses to flows to help classify storm events and explain some of the general heuristics occurring due to the complex interactions related to the suspended sediment processes in the river basin. Figure 2-4 depicts these three classes: Class A responses are defined as events with suspended sediment concentration and discharge peak simultaneously; Class B responses are defined as events with suspended sediment concentration peaks occurring before discharge peak; and , Class C responses are defined as events with discharge peaks occurring before suspended sediment concentration peaks. In general, suspended sediment concentrations will follow Class A or B responses because usually more sediment is available for transport on the rising limb of the flow hydrograph. Class C responses can occur in situations where distant sediment particles arrive in the river body at the monitoring site.
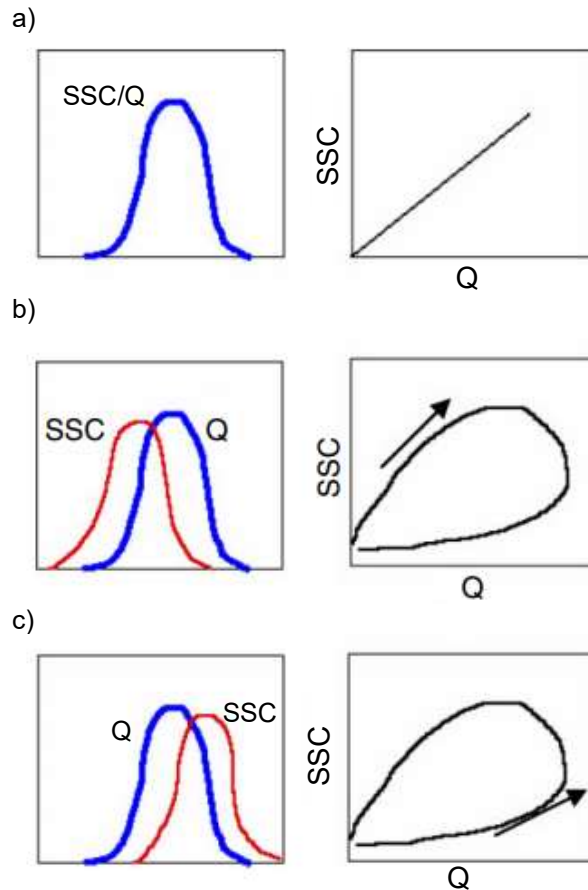
**Figure 2-4:** Classification of Suspended Sediment Concentration (SSC) Response to Discharge (Q): a) Class A: Simultaneous SSC and Q, b) Class B: SSC Peak before Q Peak, and c) Class C: SSC Peak after Q Peak (Lefrancois, 2007)

## 2.2    Typical Suspended Sediment Measurement Techniques

Typical field measurements of suspended sediment concentration within a river are taken at a single point within a river channel. These samples are then sent to a laboratory to measure suspended sediment concentrations amongst other water quality metrics. This typical method of field measurement of suspended sediment concentration is a very time-consuming process and lends itself to providing only a single data point of water quality at the instant of time the sample was collected in the field. The United States Geological Survey (USGS) maintains and operates many surface water gages, including stream gages where water quality data, such as suspended sediment concentrations, is periodically collected. However, because of the intensive effort to collect and measure water quality data, these parameters are

not collected frequently, if collected at all. Efforts to use alternative methods to estimate water quality data, specifically suspended sediment concentrations, have been made in recent years to fill in gaps in field measurements.

2.2.1    Turbidity Measurements

Turbidity, the optical property of a waterbody, which measures the degree to which a beam of light passing through the water is absorbed or scattered, has been used in multiple locations as a surrogate for suspended sediment, and in many cases has proven more accurate than using flow as a surrogate to estimate suspended sediment. The reasoning to use turbidity as a surrogate is that as more particles are present in the water column, the higher the turbidity reading will be, helping to eliminate some of the general heuristics present between the flow and suspended sediment. Foster (1992) showed that turbidity and suspended sediment measurements tracked well together through a qualitative analysis by plotting these two variables on the same graph. Minella (2008) also showed a similar agreement between turbidity and suspended sediment measurements with these variables on the same graph for their study area.

*2.2.1.1  Turbidity Measurement Limitations as an Estimator for Suspended Sediment*

Despite the benefits of using turbidity measurements as a surrogate for suspend sediment estimation, turbidity measurements also face their limitations as an estimation tool.  Three properties of water and suspended sediment that affect turbidity measurement's ability to estimate suspended sediment are the size and shape of the sediment particles, organic matter in the suspended sediment, and color of the water and suspended sediment. These properties of the water and suspended sediment affect light reflectivity off the sediment particles and thus light absorption by the turbidity meters. For example, Foster (1992) showed that smaller particle sizes of sieved suspended sediment samples from rivers they investigated lead to higher turbidity measurements.

As discussed previously, the particle size and shape, organic matter in the suspended sediment, and color of the water and suspended sediment can be very unique to a specific site due to the complex interactions of the river basin and river processes that affect suspended sediment concentrations. A

common way to combat the effect of these properties on the turbidity measurements is to use in-situ suspended sediment samples collected from the river to calibrate turbidity meters instead of using laboratory prepared suspended sediment samples. Minella (2008) showed that the calibration of the turbidity meter with in-situ suspended sediment samples predicted the river's suspended sediment concentrations more accurately than the turbidity meter that was calibrated using the laboratory prepared suspended sediment concentrations.

Another common approach to improve the ability of the turbidity measurement's accuracy of estimating suspended sediment is to include the particle size and shape of the sediment particles, organic matter in the suspended sediment, and/or color of the water and suspended sediment in the empirical model being developed. For example, Jastram (2010) showed that the inclusion of any physical property (organic carbon percentage, specific surface area, and various particle size percentages) of the suspended sediment alongside turbidity improved the model's accuracy to estimate suspended sediment concentration compared to model performance using just turbidity measurements. The physical parameter that improved the model the most was the percentage of particles finer than 0.054 mm. Since measuring the physical parameters of suspended sediment can be very time consuming and costly, Jastram (2010) tried to use hydrologic parameters as a surrogate for the physical properties. All combinations of the hydrologic measurements were not able to predict any of the physical properties that accurately ($R^2 < 0.45$), but the natural logarithm of stage performed the best and was used as a physical property surrogate. The model that used turbidity and the natural logarithm of stage showed better performance than the model with just turbidity but worse performance than the model using sediment physical properties with turbidity measurements.

Suspended sediment estimation is not only affected by the physical properties of the suspended sediment and water interactions with turbidity measurements but is also highly dependent on the collection of storm event suspended sediment responses. Even if flow were being used to try and estimate suspended sediment, collection of suspended sediment during storm events would be crucial to model development to estimate suspended sediment concentrations. Much of a system's total suspended sediment load can be attributed to large storm events that lead to drastic increases in suspended

sediment concentrations, so without the measurement of these events, a model developed for a site may severely underestimate suspended sediment concentrations. Jastram (2010), Foster (1992), Sari (2017), and Minella (2008) used methods to ensure the collection of data during storm/flood events to try and capture peak suspended sediment concentrations to improve model estimation efforts.

Once a turbidity-suspended sediment concentration relationship is established in a river, the turbidity readings can provide near real-time suspended sediment estimates. This continuous estimate of suspended sediment concentrations fills in gaps in data and reduces efforts in field sample collection. However, these estimates provide only a single point of information within the river body. Also, the estimate of suspended sediment concentration using turbidity would be prone to error caused by the characteristics of suspended sediment mentioned above.

## 2.2.2 Remote Sensing in Waterbodies

Another optical measure that has been used for suspended sediment concentration estimation since the 1970s is satellite reflectance readings. Satellites can measure the reflectance of the sun's radiation from the earth's surface and have increased resolution and reduced error of measurement devices since the 1970s allowing for applications of such data in more areas such as in-land river bodies. These reflectance values being used for suspended sediment estimation in in-land river bodies have a similar logic as using turbidity measurements where waterbodies with higher satellite reflectance values generally indicates higher suspended sediment concentrations.

Unlike turbidity measurements, satellite reflectance readings can provide a spatial distribution of suspended sediment concentration in a river body allowing for a regional assessment of suspended sediment concentration. However, this improvement in spatial information comes at a cost of temporal information. Currently, satellites collect, at best, reflectance readings every other day. Table 2-1 summarizes satellites that collect reflectance values that have been used in the literature reviewed. Some of these satellite reflectance products have only been used in ocean water quality applications given their large pixel size and could not be used in some in-land river applications. Aircraft readings of surface reflectance could also be used to provide even higher resolution readings than those listed.

**Table 2-1:** Summary of Satellites Recording Reflectance

| Satellite | Pixel Resolution (m) | Period Between Readings (days) | Data Record |
|---|---|---|---|
| Landsat | 30 x 30 | 16 | 1972-Present |
| Sentinel | Down to 5 x 5 | 2-10 | 2016-Present |
| MODIS | 250 x 250, 500 x 500, and 1,000 x 1,000 | 1-2 | 1999-Present |
| SeaWIFS | 1,000 x 1,000 and 4,000 x 4,000 | 1 | 1997-2010 |
| SPOT | Down to 1.5 x 1.5 | 1-3 | 1986-Present |

In the literature reviewed that used satellite reflectance values to estimate suspended sediment, a buffer region was considered surrounding the sample site to develop a relationship for the estimate. The buffer region was used to determine representative satellite reflectance readings for the suspended sediment concentration recorded at the sample site. Both daily suspended sediment concentration and instantaneous suspended sediment concentration readings over at least a year long period were used to develop this relationship and was dependent on the availability of data at the site analyzed in the study. Peterson (2018) and Pereira (2018) used a rectangular region of 3 pixels wide by 11 pixels long placed 3 pixels upstream of the sample site if the sample site was at a bridge structure. These studies were used in the Mississippi River. Sobel (2020) used a 2-pixel buffer surrounding the sample site while Park (2014) used a 5-pixel by 5-pixel square surrounding the sample site. Both the Sobel (2020) and Park (2014) studies were completed on large waterbodies (Galveston Bay and Amazon River, respectively). These buffers were also used to ensure pure water pixels were used during model development.

Once a relationship was developed using the regional satellite reflectance values of the buffer zone and suspended sediment concentrations, the relationship was applied to pixels throughout the study's analysis extent to develop spatial suspended sediment concentration maps. The river bodies these relationships were applied to were defined by several means. Pereira (2018) used navigation charts provided by the US Army Corps of Engineers (USACE) to delineate the low-water boundaries and channel centerlines near the gauge location to define the river body. Park (2014) defined the river body as pure water pixels by using linear spectral mixing and a filter constraint. Linear spectral mixing assumes a pixel of reflectance readings is a linear combination of radiances of all materials in the pixel (Shimabukuro, 1991). The proportion of each material's reflectance to the pixel's reflectance must sum to

one for this method. In addition, the number of materials used must be, at most, one less than the number of bands recorded in the data.

Several limitations using satellite reflectance values to estimate suspended sediment were cited including sunglint, cloud cover, boat navigations, satellite image timing, and presence of organic material/chlorophyll-α according (e.g., Sobel (2020) and Reisinger (2017)). Sunglint is a phenomenon that causes areas of very high surface reflectance values compared to surrounding values. This phenomenon is caused by several factors including the surface roughness of the water, wind speed and direction, solar sensor viewing geometries, and the water refractive index. Reisinger (2017) accounted for satellite images with sunglint by removing data marked with cloud interference by the data provider, had a normalized sunglint radiance greater than 0.001, and sensor zenith angles were greater than 60.

Cloud cover and boat navigation also affected satellite reflectance values and were filtered out like sunglint affects. For example, Peterson (2018) used the Landsat pixel quality filter to ensure water pixels with low cloud confidence remained then used thresholds of 6.5% for Landsat 4-5 and 7 and 4.5% Landsat 8 for the blue band filter to filter cirrus clouds and cloud shadows. In addition, Peterson (2018) used a surface reflectance standard deviation filter of 0.5% to filter out river vessel traffic. Similarly, Zhang (2010) used the cloud masking technique proposed by Wang (2006) that used MODIS surface wave infrared (SWIR) thresholds of 2.35% and 2.15% for top-of-the-atmosphere reflectance in the 1240 and 1640 nm bands to filter clear images in open ocean applications.

The lag time between satellite data records can lead to mismatch of the reflectance values and the suspended sediment sample taken and reduce the available data for calibration. To combat this issue and increase their dataset for the model, Sobel (2020) used satellite data recorded up to two days before the sample site's collection and up to three days if no rain was recorded for a five-day period before the recorded satellite data.

As stated above, chlorophyll-α was cited to affect satellite reflectance's relationship to suspended sediment concentrations when concentrations were greater than 30 µg/L. Sobel (2020) filtered out samples with concentrations of chlorophyll-α greater than this threshold to remove these interferences. Other researchers accepted the potential effect Chlorophyll-α and organic matter had on poor model

performance because removing the samples reduced the dataset too much. An example of this issue is the work by Reisinger (2017).

### 2.2.2.1  Physical Based Model for Remote Sensing Techniques

Several researchers have used the underlying physics of satellite reflectance values to develop assumptions and models to predict water quantities. For example, Legleiter (2009) used these physics-based models to estimate the depth of the waterbody using satellite reflectance values. This physics-based approach builds on the concept that the total reflectance/radiance reading at a satellite sensor is the sum of bottom reflectance from bottom of a stream or waterbody ($L_B$), reflectance from scattering of light in the water column ($L_C$), reflectance from the water surface ($L_s$), and reflectance from atmospheric scattering or path radiance ($L_p$) and is given by Equation (2.2). Figure 2-5 provides a visual representation of this general equation.

$$L(\lambda) = L_B(\lambda) + L_C(\lambda) + L_S(\lambda) + L_P(\lambda)$$
<div align="right">Equation (2.2)</div>
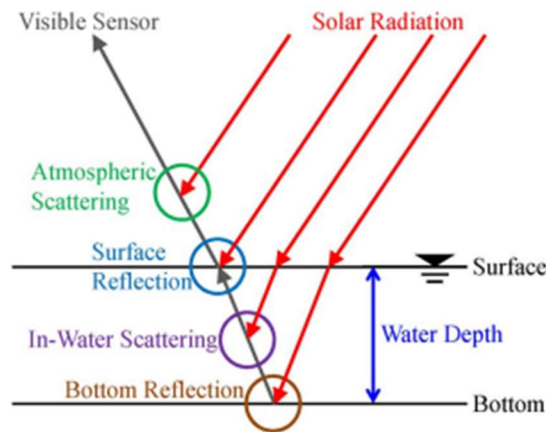


**Figure 2-5:** Total Reflectance at Satellite Sensor (Kanno, 2012)

Ideally bottom reflectance should be the dominant component to allow for the best estimate of water depth when applying this physics-based background to depth estimation of waterbodies. This would be the case in waters with small depth, low suspended sediment concentrations that minimize water column reflectance/scattering, and low surface reflectance and atmospheric scattering. These conditions

rarely occur in ocean applications, and bottom reflectance is usually a small component of the total reflectance, accounting for 8-10% of the total reflectance (Mishra, 2005).

In the application of this physics-based approach for suspended sediment estimation, it would be ideal if the total reflectance was dominated by the water column scattering. The water column scattering component should be highest in waters with high suspended sediment concentrations/high turbidity and with deep depth. In these situations, the water is optically deep and has bottom reflectance values that are negligible compared to the water column reflectance values. Sobel (2020) assumed areas with suspended sediment concentrations greater than 50 mg/L were dominated by water column reflectance even if the water depth was less than 3 m. Legleiter (2011) stated a general maximum detectable depth in highly turbid waters was 0.5 m, meaning waters deeper than 0.5 m would be relatively unaffected by bottom reflectance values. The Legleiter (2011) study evaluated the feasibility of depth estimation in river bodies with suspended sediment concentrations ranging from 96 mg/L to 214 mg/L and stated the actual maximum depth of a river body was dependent on the specific suspended sediment concentrations and sensor resolution. In general, the maximum detectable depth is determined when the difference of radiance at a depth and the radiance of an infinite water column is no longer greater than the noise or resolution of the sensor. Legleiter (2011) used water column reflectance with zero bottom reflectance as an analogy for water column reflectance with an infinite depth. Conversely, Mishra (2005) assumed the maximum detectable depth was the inverse of the attenuation coefficient, which is discussed in more detail below.

General trends of the water column reflectance are commonly developed using the attenuation coefficient of the water. The attenuation coefficient is an apparent measure of the physical properties of the waterbody but has been proven to be highly related to the absorption and backscattering of water. This coefficient was estimated by measuring downwelling spectral irradiance in the water at different depths within the waterbody in Legleiter (2011) and Mishra (2005). These researchers used the Beer-Lambert Law to develop a relationship between downwelling spectral irradiance at different depths ($E_d$) and the attenuation coefficient ($K_d$) which assumes the downwelling spectral irradiance has an exponential relationship with water depth (Equation (2.3)) . In Equation (2.3), $z$ is a reference depth just

below the water surface and $z_m$ are the different depths where downwelling spectral irradiance was measured. With this formulation, the estimated attenuation coefficient is determined by the slope of the natural logarithm of downwelling spectral irradiance values vs. water depth. Legleiter (2011) and Mishra (2005) stated that the actual attenuation coefficient or effective attenuation coefficient is twice the estimated values using Equation (2.3).

$$-K_d(z_m - z, \lambda) = \ln\left[\frac{E_d(z_m, \lambda)}{E_d(z, \lambda)}\right]$$
Equation (2.3)

Mishra (2005) assumed the attenuation coefficient was constant horizontally and vertically in the waterbody. However, this is not necessarily true because suspended sediment concentrations affect attenuation coefficients of the waterbody. Suspended sediment concentrations can vary spatially in a river body, meaning the attenuation coefficient can also vary spatially. Furthermore, the attenuation coefficient can be affected by the cloud cover over the waterbody and the angle of the sun's radiance which affects the amount of radiance that reaches the river body. Mishra (2005) corrected for the effects of varying solar radiance angles by normalizing radiance readings taken throughout the day by initial radiance readings and used Gordon normalization to account for cloud cover affects.

As shown in Equation (2.3), different wavelengths of radiance have different attenuation coefficients. This is because different wavelengths are affected by the medium differently. For example, in waterbodies, red and near-infrared (NIR) wavelengths of light are absorbed the most while blue and green wavelengths are scattered the most. This means that increases in attenuation coefficients of the medium affects wavelengths differently but in general increasing attenuation coefficients magnify these different relationships. So, for example, higher attenuation coefficients in waterbodies lead to larger scattering of blue and green wavelengths. Due to these varying relationships for different wavelengths, it was very common for researchers to use band ratios or specific bands to explain the physical phenomena of the waterbody. For example, a ratio of green to blue bands greater than one was stated to generally represent the presence of chlorophyll-α or organic matter in the water (Lyzenga ,2006). Reisinger (2017) stated the red band of wavelengths were optimal for measuring suspended sediment concentration because its reflectance in the water column is around the red portion and has little impact from

phytoplankton pigments in low concentrations. Legleiter (2009) used optimal band ratio analysis to select the best band ratios to estimate water depth.

Other researchers have also utilized more complex methods that use all the bands measured instead of two bands determined from optimal band ratio analysis. One such method is the modified Lyzenga's method presented in Kanno (2012). The modified Lyzenga's method is shown by Equation (2.4), which is a modification of the general physics-based method of satellite reflectance values. In this equation, $V$ is the in water scattering at an infinite depth, $B$ is the bottom reflectance, $k$ is the attenuation coefficient, $h$ is the water depth, $T$ is the round-trip transmittance through the atmosphere and the water, $E$ is the downwelling radiance at the top of the atmosphere, $S$ is the surface reflection, and $A$ is the path radiance.

$$L(\lambda) = \{V(\lambda) + [B(\lambda) - V(\lambda)]\exp(-k(\lambda)h)\}T(\lambda)E(\lambda) + S(\lambda) + A(\lambda) \qquad \text{Equation (2.4)}$$

Equation (2.4) can be simplified further to Equation (2.5) after introducing the variable $X$ that is linearly related to the depth of the water and assuming the total reflectance at infinite depth is a linear relationship to the NIR band reflection.

$$X(\lambda) = -k(\lambda)h + \log\left[\left(B(\lambda) - V(\lambda)\right)T(\lambda)E(\lambda)\right] \qquad \text{Equation (2.5)}$$

If Equation (2.5) is represented in terms of all bands from 1 to m, it takes the form of Equation (2.6) where $X$, $k$, and $C$ are matrices of size 1 by m.

$$X = -kh + C \qquad \text{Equation (2.6)}$$

In the Lyzenga method, Equation (2.6) is converted to Equation (2.7) with the constraints listed below. This equation is solved using least squares regression to find appropriate values of β. In this equation, β is affected by the round-trip transmittance through the atmosphere and the downwelling radiance at the top of the atmosphere. Equation (2.7) shows the correction for the effective attenuation coefficient where $\theta_s$ is the solar zenith angle and $\theta_v$ is nadir viewing angle.

$$h = X/[\sec\theta_s + \sec\theta_v]\beta$$
$$\begin{cases} k\beta = -1 \\ C\beta = 0 \end{cases} \qquad \text{Equation (2.7)}$$

The modification proposed by Zanno (2012) changes Equation (**2.5**) to Equation (2.8), which allows for the introduction of an additional β coefficient for each image being trained, allowing for β

coefficients for bands 1 to m to remain constant. This requires the addition of a variable function that is one for a specific image and zero otherwise in the *X* matrix.

$$X(\lambda) = -k(\lambda)h + \log\big[\big(B(\lambda) - V(\lambda)\big)\big] + \log[T(\lambda)E(\lambda)] \qquad \text{Equation (2.8)}$$

**2.3      Machine Learning Techniques used in Suspended Sediment Concentration Estimation**

Machine learning techniques have been used in a growing number of fields to develop models with high predictive power in situations that have very complex relationships. This trend has also been observed in hydrologic arenas, especially for sediment estimation. For sediment estimation, supervised learning techniques have been implemented the most. Supervised learning techniques include those that use an algorithm to model relationships of labeled data.

An important component of machine learning techniques is how the data is partitioned. It is common to split data into three sets when implementing a machine learning technique. These sets include the training set, validation/holdout set, and the test set. The training set is typically the largest set and is used to train the machine learning algorithm directly. The validation/holdout set is similar to the test set but is used to tune hyperparameters of the machine learning algorithm. Finally, the test set is the set of data used for reporting model performance and has not been seen by the model prior to reporting. In older research, it was very common to use a 70%/15%/15% or 80%/10%/10% data split (Burkov, 2019). With larger datasets, smaller percentages can be used for validation and test sets because there are still sizeable amounts of data in each set. Conversely, in cases with small amounts of data, cross validation of the training data can be used instead of using a holdout set.

Once the data has been split appropriately, the data is processed and then input into a machine learning algorithm. Different data processing techniques and machine learning algorithms used in this research are discussed in subsequent sections.

2.3.1    Data Processing Techniques

Data used for a machine learning algorithm is typically processed before training the algorithm. This type of preprocessing is typically called feature engineering in the machine learning community. The goal of feature engineering is to create or reduce features to those that have high predictive power for the

model, can be computed quickly, are reliable, and are uncorrelated between themselves. It is also very important that data used to train machine learning models has similar distribution to the test data and the data the model will see in deployment. So, it is common to use the same techniques on both the training data and testing data to maintain the same distributions.

Normalization or standardization of features is common practice to reduce the risk of numerical overflow and assure no individual feature dominates. Normalization typically transforms the data into a range of [-1,1] or [0,1] while standardization is the z-score calculation to rescale data to have properties of a standard normal distribution.

It is also very common to combine features through simple arithmetic as a form of dimensional reduction. There are also more complex dimensional reduction techniques that are more statistically based. This research focuses on two such techniques called *principal component analysis* and *canonical correlation analysis*. Both techniques have been commonly used in machine learning algorithms to improve model performance.

### 2.3.1.1 Principal Component Analysis

Principal component analysis is concerned with explaining the variance-covariance structure of a set of variables and is used for data reduction and interpretation. Dimension reduction is achieved because principal components can explain most of the variability with fewer components or variables than the original number of variables. Easier interpretation of data is achieved using principal components by revealing relationships that were not evident in the original variables. Principal components are a linear combination of the original variables to transform the original coordinate system to one that maximizes variability of the data. This means that the principal components only depend on the covariance matrix of the data.

Johnson and Wichern (2007) used Equation (2.9) for linear combinations of the variables where matrices $Y$, $X$, and $a$ are of size $p$ by n where $p$ is the number of principal component or features, and $n$ is the number of samples.

$$Y_1 = a'_1 X = a_{11}X_1 + a_{12}X_2 + \cdots + a_{1p}X_p$$
$$\vdots$$
$$Y_p = a'_p X = a_{p1}X_1 + a_{p2}X_2 + \cdots + a_{pp}X_p$$

Equation (2.9)

Principal components are the uncorrelated linear combinations whose variances are as large as possible. Equation (2.10) and Equation (2.11) give the variance and covariance for the above linear combinations where $\Sigma$ is the covariance matrix. For this formulation the matrix of principal components, $\lambda$, is limited to a unit vector given the constraint $a'_i a_i = 1$. In this formulation, $\lambda$ can be seen as the eigenvector for $\Sigma$. This results in the variance of the linear combinations equaling the eigenvalues of $\Sigma$ where $\lambda_1 \geq \lambda_2 \geq \cdots \geq \lambda_p \geq 0$. As a result, the principal components are ordered from highest variance to lowest variance.

$$Var(Y_i) = a'_i \Sigma a_i = \lambda_i$$

Equation (2.10)

$$Cov(Y_i, Y_k) = a'_i \Sigma a_k$$

Equation (2.11)

As a result of Equation (2.10), the total population variance is given by Equation (2.12) . This allows the analyst to determine the percent of the total population variance explained by the principal components. It is common to use only the principal components that result in 80-90% of the population variance. In addition, the eigen vectors allow the analyst to measure the importance of the variable to the associated principal component.

$$\text{Total population variance} = \sigma_{11} + \sigma_{22} + \cdots + \sigma_{pp}$$
$$= \lambda_1 + \lambda_2 + \cdots + \lambda_p$$

Equation (2.12)

### 2.3.1.2 Canonical Correlation Analysis

Another feature reduction method that has been used in recent years is canonical correlation analysis. This analysis uses correlation features between two groups of feature vectors to not only fuse information but also eliminate redundant information within the features. This analysis works by taking two zero-mean random vectors $X$ and $Y$ and finds a pair of directions $\alpha$ and $\beta$ that maximize the correlation between projections $a_1 = \alpha^T X$ and $b_1 = \beta^T Y$ called the first pair of canonical variates. Additional pairs of canonical variates are found that are uncorrelated with each other until all correlation features of $X$ and $Y$ are extracted. The maximum number of pairs of canonical variates is limited by the lowest number of features of the two datasets. The size of $X$, or the number of features, is given by $p$, while the size of $Y$, or

the number of features, is given by q. Sun (2005) used Equation (2.13) and Equation (2.14) to describe

the pairs of canonical variates.

$$X^* = (\alpha_1, \alpha_2, \dots, \alpha_d)^T x = W_x^T x$$ Equation (2.13)

$$Y^* = (\beta_1, \beta_2, \dots, \beta_d)^T y = W_y^T y$$ Equation (2.14)

The following two linear transformations (Equation (2.15) and Equation (2.16)) are also used as

part of this analysis as the combinational feature projection. These two equations are the canonical

correlation discriminant features and are one of the final outputs of the canonical correlation analysis.

$$Z_1 = \begin{pmatrix} X^* \\ Y^* \end{pmatrix} = \begin{pmatrix} W_x^T x \\ W_y^T y \end{pmatrix} = \begin{pmatrix} W_x & 0 \\ 0 & W_y \end{pmatrix}^T \begin{pmatrix} x \\ y \end{pmatrix}$$ Equation (2.15)

$$Z_2 = X^* + Y^* = W_x^T x + W_y^T y = \begin{pmatrix} W_x \\ W_y \end{pmatrix}^T \begin{pmatrix} x \\ y \end{pmatrix}$$ Equation (2.16)

The transformation matrices called canonical projective matrices are given by Equation (2.17),

and the criterion function used to solve the analysis is given by Equation (2.18).

$$W_1 = \begin{pmatrix} W_x & 0 \\ 0 & W_y \end{pmatrix} \ and \ W_2 = \begin{pmatrix} W_x \\ W_y \end{pmatrix}$$ Equation (2.17)

$$corr(X^*, Y^*) = \frac{cov(X^*, Y^*)}{var(X^*)var(Y^*)} = \frac{\alpha^T S_{xy} \beta}{\left(\alpha^T S_{xx} \alpha \beta^T S_{yy} \beta\right)^{1/2}}$$ Equation (2.18)

In Equation (2.18), $S_{xx}$ and $S_{yy}$ are the in-sample variance matrices of data sets $X$ and $Y$,

respectively, and $S_{xy}$ is the covariance matrix of data sets $X$ and $Y$. $S_{xx}$ is of size $p$ by $p$, $S_{yy}$ is of size $q$ by

$q$, and $S_{xy}$ is of size $p$ by $q$.

The following constraints are used to complete the canonical correlation analysis.

$$\begin{cases} \max\bigl(corr(X^*, Y^*)\bigr) \\ \alpha^T S_{xx} \alpha = \beta^T S_{yy} & \beta = 1 \\ \alpha_i^T S_{xx} \alpha = \beta_i^T S_{yy} & \beta = 0 \quad (i = 1, 2, \dots, k-1) \\ \alpha \in \mathbb{R}^p, & \beta \in \mathbb{R}^q \end{cases}$$ Equation (2.19)

The following steps are used to find the canonical correlation discriminant features.

1. Compute the in-sample variance matrices of data sets $X$ and $Y$ ($S_{xx}$ and $S_{yy}$) and the between set

    covariance matrix $S_{xy}$.

2. Compute $G_1$ and $G_2$ by from Equation (2.20) and Equation (2.21) then find their non-zero eigenvalues that correspond to orthonormal eigenvectors $u_i$ and $v_i$ using singular value decomposition.

$$G_1 = S_{xx}^{-1/2} S_{xy} S_{yy}^{-1} S_{yx} S_{xx}^{-1/2}$$ <div align="right">Equation (2.20)</div>

$$G_2 = S_{yy}^{-1/2} S_{yx} S_{xx}^{-1} S_{xy} S_{yy}^{-1/2}$$ <div align="right">Equation (2.21)</div>

Single value decomposition for $G_1$ and $G_2$ are given by Equation (2.22) through Equation (2.24) where $\lambda$ are non-zero eigenvalues and $r$ is the rank of $S_{xy}$.

$$G_1 = HH^T$$ <div align="right">Equation (2.22)</div>

$$G_2 = H^T H$$ <div align="right">Equation (2.23)</div>

$$H = \sum_{i=1}^{r} \lambda_i u_i v_i^T$$ <div align="right">Equation (2.24)</div>

3. Calculate the canonical projective vectors $\alpha$ and $\beta$ using Equation (2.25) and Equation (2.26).

$$\alpha_i = S_{xx}^{-1/2} u_i$$ <div align="right">Equation (2.25)</div>

$$\beta_i = S_{yy}^{-1/2} v_i$$ <div align="right">Equation (2.26)</div>

4. Use either $Z_1$ or $Z_2$ to find the canonical correlation discriminant features.

In addition to the canonical correlation discriminant features, this analysis provides statistical insight of how features between two sets relate to each other (Sherry, 2005). Canonical projective vectors can be used to interpret the contribution of the original variables to the projected variates in the analysis. The standardized canonical projective vectors are generally used to compare variables between each other. Also, the different dimensions' canonical coefficients can be used to interpret the resulting dimension's explanatory power is for the two sets. This can provide similar information that a principal component analysis can provide by supplying which features are the most important.

### 2.3.2 Machine Learning Modeling Algorithms

Many artificial intelligence/machine learning algorithms have been deployed in hydrological applications in recent years. Afan (2016) and Rajee (2020) provided a review and summary of past research using artificial intelligence models for sediment prediction. Both studies cite that recent research has heavily used artificial neural networks in sediment prediction applications. Other algorithms cited in

these two studies that have been applied for sediment prediction include support vector machines, decision trees, genetic algorithms, and adaptive nero-fuzzy interference system. This research focuses on three algorithms, *support vector machine*, *artificial neural network*, and *extreme learning machine*. The extreme learning machine algorithm is a simpler version of the artificial neural network algorithm that has been shown to perform well in sediment prediction using satellite imagery according to Peterson (2018).

### 2.3.2.1 Support Vector Machine

Support vector machines were originally created for classification applications. The original version of the algorithm creates a linear decision boundary using Equation (2.27). In this equation, *W* is a matrix of weights, *x* is a matrix of inputs, and *b* is a vector of coefficients.

$$W \times x - b = 0 \hspace{4cm} \text{Equation (2.27)}$$

The classes are separated by setting Equation (2.27) to -/+ 1 to place members of one class above +1 when Equation (2.27) is positive and members of the other class below -1 when it is negative. Figure 2-6 illustrates this decision boundary and class separation. The goal of the classification version of the support vector machine is to maximize the distance between the two classes and the decision boundary. This is done by minimizing the Euclidean norm of matrix W ($\|W\|$) given by $\sqrt{\Sigma_{j-1}^{D}(W^{(j)})^2}$. Thus, in cases with easily separable classes, the following cost function (Equation (2.28)) is used to develop values for W and b. $y_i$ is a way to simplify the constraints of $W \times x - b \geq +1$ if $y_i = +1$ and $W \times x - b \leq -1$ if $y_i = -1$ and produces a value of 1 when the constraints are met and 0, otherwise.

$$\min\left(\frac{1}{2}\|W\|^2\right), \text{such that } y_i(W \times x - b) - 1 \geq 0 \hspace{1cm} i = 1, \dots, N \hspace{0.5cm} \text{Equation (2.28)}$$
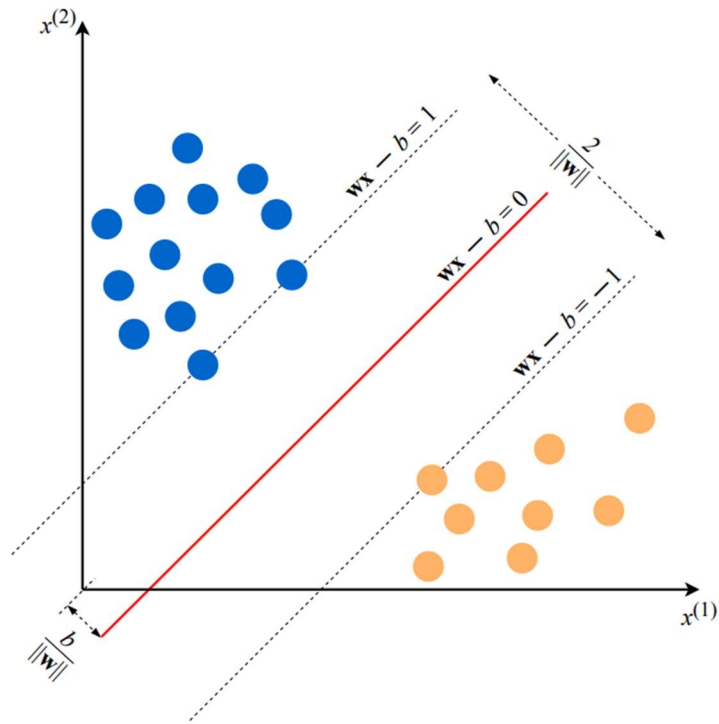
**Figure 2-6:** Example of Support Vector Machine Decision Boundary (Burkov, 2019)

In most cases, however, classes are not easily separable as the example given above. In these situations, the cost function is modified to expand the distance of the decision boundary to include some points within each class. A hinge loss function is introduced that produces a value of zero if the input is on the correct side of the decision boundary or the distance the point is from the decision boundary. The cost function below (Equation (2.29)) is ultimately minimized following the addition of this hinge loss function, where $C$ determines the tradeoff between increasing the size of the decision boundary and ensuring each data point lies on the correct side of the decision boundary. The $C$ value is determined through trial and error. This cost function is solved using Lagrange multipliers, thus finding an optimal solution for the problem.

$$C\|W\|^2 + \frac{1}{N}\sum_{i=1}^{N} \max\big(0, 1 - y_i(W \times x - b)\big) \qquad \text{Equation (2.29)}$$

The support vector machine algorithm can be modified for non-linear applications by introducing a kernel function that transforms the input data into a non-linear space of higher dimension. The function

used for such transformation is typically denoted using the symbol, φ. This results in the cost function

given by Equation (2.30). Kernel functions that have been successfully implemented into the support

vector algorithm include linear, polynomial, gaussian, radial basis function, sigmoid, and exponential. The

appropriate kernel can be selected either through database knowledge or trial and error.

$$C\|W\|^2 + \frac{1}{N}\sum_{i=1}^{N}\max\left(0, 1 - y_i(W \times \varphi(x) - b)\right) \qquad \text{Equation (2.30)}$$

The support vector machine algorithm can also be modified to apply to regression applications by

introducing an error term, $\varepsilon$. This error term expands the decision boundaries to include the input data. In

the case of regression applications, the decision boundary is a function that fits the input data the best.

The cost function is thus modified to Equation (2.31), penalizing points outside the bounds of $\varepsilon$. So, the

constraints of $y_i$ become set to $\varepsilon$.

$$C\|W\|^2 + \frac{1}{N}\sum_{i=1}^{N}\max\left(0, \varepsilon - y_i(W \times \varphi(x) - b)\right) \qquad \text{Equation (2.31)}$$

### 2.3.2.2  Artificial Neural Network

As stated earlier, artificial neural networks have been more frequently used in sediment prediction

and hydrological systems. This algorithm is often used in situations with very complicated interactions and

large amounts of data. An artificial neural network is composed of nodes that use outputs from nodes in

previous layers of the neural network, weighted by values that are calibrated, to produce the desired

output. Each node in the neural network uses Equation (2.32), where g() is called the activation function,

W is a matrix of weights, z is a vector of either outputs from the previous layer or a matrix of the inputs,

and b is a vector of coefficients.

$$\text{Node output} = g(W \times z + b) \qquad \text{Equation (2.32)}$$

The typical activation function used is the *sigmoid function*, but the activation function can take

different forms. Other common activation functions that have been used in recent years include the

*hyperbolic tangent* (TanH) *function* and the *rectified linear unit* (ReLU) *function*. All three activation

functions are provided in Equation (2.33) through Equation (2.35).

$$\text{Sigmoid} = \frac{1}{1 + e^{-x}}, \qquad\qquad \text{Equation (2.33)}$$

$$TanH = \frac{e^x - e^{-x}}{e^x + e^{-x}}, \qquad\qquad \text{Equation (2.34)}$$

$$ReLU = \begin{cases} 0 & \text{if } x < 0 \\ x & \text{otherwise} \end{cases} \qquad\qquad \text{Equation (2.35)}$$

Figure 2-7 illustrates an example of an artificial neural network algorithm construction. This figure shows an artificial neural network with four total layers where the first layer is the input data/input layer, and the following three layers are computation layers. Depending on the literature, a layer in an artificial neural network could include the input data, or input layer. The first and second computation layers both include four nodes while the third and final computation layer, often referred as the output layer, has one node that produces the final prediction of the model. The number of computation layers and nodes required is different from problem to problem.
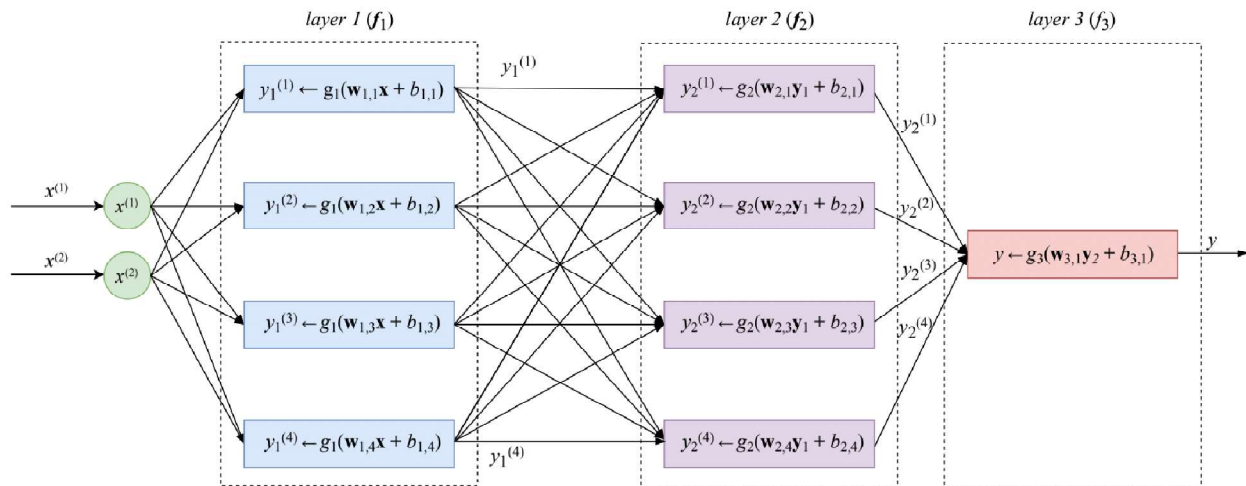


**Figure 2-7:** Example of Artificial Neural Network (Burkov, 2019)

The weights, W, and coefficients, b, for each node are typically calibrated using the backward propagation algorithm that uses gradient decent to converge to the optimal calibration. The backward propagation algorithm begins the gradient calculations starting in the last layer and incrementally calculates the gradient of each layer until the first layer is reached. This gradient is then used to adjust the weights using Equation (2.36) and Equation (2.37), where $\alpha$ is the learning rate that controls the size of the update and $\frac{\partial y}{\partial w}$ and $\frac{\partial y}{\partial b}$ are the partial derivatives of the neural network with respect to W and b. These

updates continue until the gradient does not exceed some threshold, or a certain number of iterations are reached. Each time the algorithm updates the weights through an entire set of data it is called an epoch. In situations where the input data is very large, only part of an epoch is used to update weights to allow the model to converge to a solution quicker. This method is called minibatch stochastic gradient descent.

$$W \leftarrow W - \alpha \frac{\partial y}{\partial w},$$  Equation (2.36)

$$b \leftarrow b - \alpha \frac{\partial y}{\partial b},$$  Equation (2.37)

Another common approach recently deployed in artificial neural networks is referred as a momentum term in the update equation. This momentum term scales the learning rate based on the previous update's gradient. An example of a momentum term is given by Equation (2.38) and Equation (2.39), where $\beta$ is the momentum term that adjusts the updates. This momentum term improves the performance of the model by reducing the number of iterations required for convergence in some cases.

$$W \leftarrow W - (1 - \beta)\alpha \frac{\partial y}{\partial w} - \beta \frac{\partial y}{\partial w}^{t-1}$$  Equation (2.38)

$$b \leftarrow b - (1 - \beta)\alpha \frac{\partial y}{\partial b} - \beta \frac{\partial y}{\partial b}^{t-1},$$  Equation (2.39)

In general, as the number of epochs increase, the performance of artificial neural networks increases. However, this reduction in bias on the input data can increase the model's error to other input data, or variance. Figure 2-8 illustrates this tradeoff between the reduced bias and increased variance of an artificial neural network. As Figure 2-8 shows, artificial neural networks initially reduce the error for both the training set and holdout set with increasing epochs until a point where the model begins to have increased errors in the holdout data while experiencing reduced errors in the training set. The artificial neural network should be set to stop training before this occurs to improve its theoretical performance on unseen datasets.
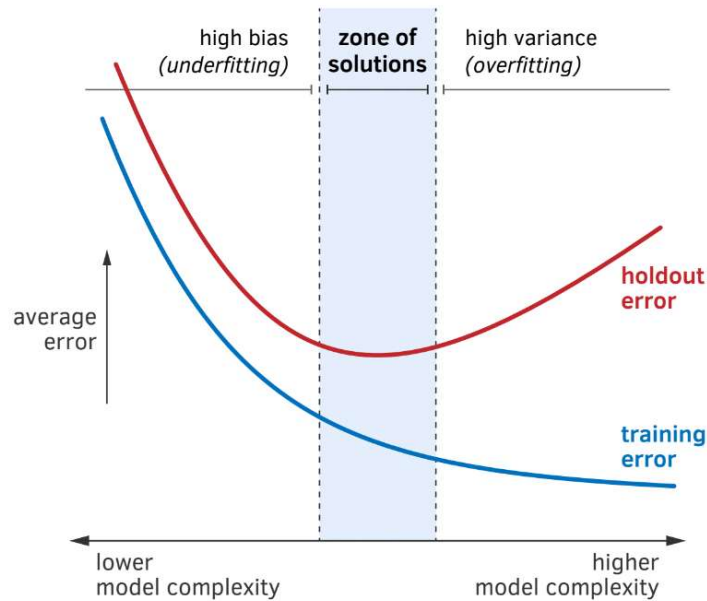
**Figure 2-8:** Example of General Bias and Variance Tradeoff versus Model Complexity (Burkov, 2020)

Another way to combat overfitting with artificial neural networks is to introduce regularization to the algorithm. Regularization forces the algorithm to produce a less complex model that, as a result, is less prone to overfitting. The two most common regularization methods are L1 (lasso) and L2 (ridge) regularization (Burkov, 2019). Both methods introduce an additional term in the cost function that multiples a hyperparameter, $C$, by the weights of the artificial neural network. For L1 regularization, $C$ is multiplied by the sum of the weights while in L2 regularization, $C$ is multiplied by the Euclidean norm of the weights. L2 regularization results in a similar cost function as Equation (2.29) for support vector machines. Larger values of $C$ result in a model that is less complex and less prone to overfitting.

In the research for sediment prediction reviewed, artificial neural networks with three layers were used where the first layer was the input data to the model, the second layer, often called the hidden layer, contained the nodes with activation functions, g(x), and the third layer was the output layer. The number of nodes was determined by the researcher and varied from study to study. However, Olyaie (2015) suggested the range of nodes in the hidden layer should be between $(2n^{1/2} + m)$ and $(2n + 1)$ where n is the number of input variables and m is the number of outputs. The third layer consisted of the output variable, in this case suspended sediment. Olyaie (2015) showed that the implementation of this three-

layer artificial neural network outperformed the standard rating curve method for certain combinations of current and previous flow and suspended sediment measurements that were used as the input data for the artificial neural network. Sari (2017) developed an artificial neural network with three layers that used turbidity and water level measurements to estimate suspended sediment in their study area that had a Nash-Sutcliffe efficiency coefficient of 0.953, showing the potential effectiveness of this algorithm's ability of sediment prediction in river basins.

*2.3.2.3 Extreme Learning Machine*

An algorithm with a similar form as artificial neural networks, called extreme learning machine, has been sited by Peterson (2018) to show superior performance over other algorithms. An extreme learning machine has an input layer, a hidden layer, and an output layer. Unlike a neural network algorithm, the extreme learning machine uses an optimization approach to solve for weights. The cost function in Equation (2.40) is used to solve the optimization problem of the extreme learning machine algorithm, where *x* is the input data, *y* is the actual output, w is the weight vector and *b* is the bias vector of hidden node *j*, and *g()* is a nonlinear activation function. The output weight vector is denoted by $\beta_j$ and links the hidden node and the output node.

$$min\|y_i - \widehat{y_i}\|_{i=1}^N = \min \sqrt{\left(\sum_{i=1}^N (y_i - \sum_{j=1}^L \beta_j g_j(w_j x_j + b_j))\right)^2} \qquad \text{Equation (2.40)}$$

When the above cost function is minimized, it is set equal to zero. In this case, Equation (2.40) can be rewritten as Equation (2.41). In this simplified form, *T* is a matrix of true outputs, *H* is a matrix of the hidden layer where each column is a node, and $\hat{\beta}$ is a matrix of the output weights.

$$H\hat{\beta} = T \qquad \text{Equation (2.41)}$$

In this algorithm, the weights and bias values in the hidden layer are initially assigned randomly and are unadjusted throughout the training process. Only output weights are adjusted through the training process. Thus, the above equation is solved similarly to a least squares solution for $\hat{\beta}$. Huang (2006) proved this solution is valid for activation functions that are infinitely differentiable, and the number of hidden nodes is less than or equal to the number of sample data points. If the number of hidden nodes

equals the number of samples, H is a square matrix and is easily invertible to solve for output weights. In cases where this is not true, Equation (2.42) is used to determine the output weights

$$\hat{\beta} = H^+T \qquad\qquad \text{Equation (2.42)}$$

$H^+$ in Equation (2.42) is the Moore-Penrose generalized inverse of matrix H. The Moore-Penrose generalized inverse must satisfy the following conditions in Equation (2.43) where A is a matrix of size m by n and G is the Moore-Penrose generalized inverse matrix of size n by m.

$$AGA = A, GAG = G, (AG)^T = AG, (GA)^T = GA \qquad\qquad \text{Equation (2.43)}$$

### 2.3.3    Model Performance Measures

Several different evaluation metrics have been used to evaluate the model performance of artificial intelligence algorithms. According to Rajaee (2020) some of the most common evaluation metrics of sediment prediction using artificial intelligence algorithms include the *mean squared error* (MSE), *root mean square error* (RMSE), and the *coefficient of determination* ($R^2$). The coefficient of determination is the square of the *correlation coefficient* (R). Equation (2.44) through Equation (2.46) show the formula for these common metrics where $y_n$ is the observed value, $\overline{y_n}$ is the average of the observed values, $\sigma_{y_n}$ is the standard deviation of the observed values, $\widehat{y_n}$ is the predicted value, $\overline{\widehat{y_n}}$ is the average of the predicted values, and $\sigma_{\widehat{y_n}}$ is the standard deviation of the predicted values.

$$RMSE = [\frac{1}{N}\sum_{n=1}^{N}(y_n - \widehat{y_n})^2]^{1/2} \qquad\qquad \text{Equation (2.44)}$$

$$MSE = (RMSE)^2 \qquad\qquad \text{Equation (2.45)}$$

$$R = \frac{\frac{1}{N}\sum_{n=1}^{N}(y_n - \overline{y_n})(\widehat{y_n} - \overline{\widehat{y_n}})}{\sigma_{y_n}\sigma_{\widehat{y_n}}} \qquad\qquad \text{Equation (2.46)}$$

A method to present a concise statistical summary was presented in Taylor (2001). The method is a diagram that summarizes the correlation coefficient, root mean square error, and ratio of variances. This diagram presented in Taylor (2001) can be used to compare different models or to track changes in performance of a model as it is modified. Equation (2.47) is used to develop the Taylor diagram. In this

equation the RMSE is the centered version, which subtracts the average values of the observed and predicted values.

$$RMSE'^2 = \sigma_{y_n}^2 + \sigma_{\widehat{y}_n}^2 - 2\sigma_{y_n}\sigma_{\widehat{y}_n} * R \qquad \text{Equation (2.47)}$$

Equation (2.47) was related to the law of cosines to develop a geometric relationship between all these statistics. The law of cosines is provided in Equation (2.48), and the geometric representation of the statistical version is presented in Figure 2-9.

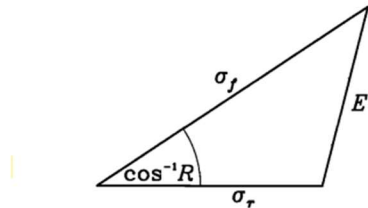$$c^2 = a^2 + b^2 - 2ab * \cos(\theta) \qquad \text{Equation (2.48)}$$



**Figure 2-9:** Geometric Relationship between Common Statistics (Taylor, 2001)

Figure 2-10 shows the final form of the proposed Taylor diagram. The standard deviations are represented by the radial distances from the origin, so the reference field standard deviation is ~5.5, while the test field has a standard deviation of ~6.5 in the example presented. The correlation coefficient is represented as the azimuthal distance and are labeled according to the relationship in Figure 2-9. Thus, the test field and reference field have a correlation coefficient of 0.7 in this example. The RMSE between the two fields is represented by the dashed lines, so the test field and reference field have a RMSE of ~5 in this example. The reference field point is plotted along the abscissa in these diagrams.
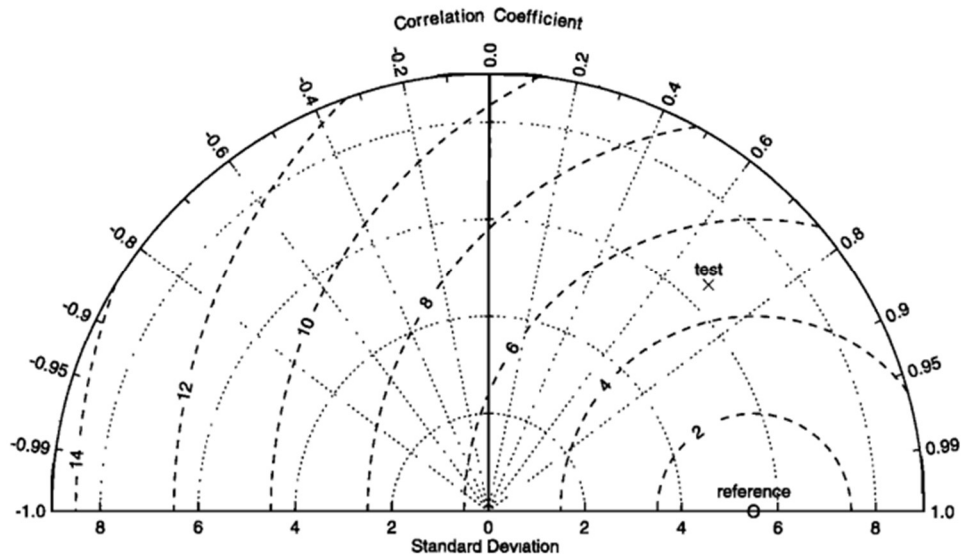
**Figure 2-10:** Taylor Diagram (Adopted from Taylor, 2001)

The Taylor diagram provides a representation of model performance where the closest test field to the reference preforms the best. A different standard deviation represents the model not matching the observed variations and a decreasing correlation coefficient represents the model not matching the phasing of the observed data. This diagram can be used to compare different model performances and track changes in model performance of different fields. However, this diagram does not provide a measure of statistical significance between different models. Also, it does not incorporate the variability of the observations or their uncertainty.

## 3.0    Research Materials and Methods

### 3.1    Project Area and Background

The focus of this study is to estimate the suspended sediment concentration within the Brazos River near the outfall to the Gulf of Mexico. The Brazos River watershed is one of the largest in Texas with a total land surface area of approximately 44,620 square miles originating in New Mexico and terminating in Brazoria County near Freeport, Texas. The watershed for the Brazos River is shown in Figure 3-1. As a result of the size of the Brazos River watershed, the river conveys a large sediment load that has been leading to net deposition in the Gulf of Mexico near the mouth of the river according to Philips (2006). This has led to issues with the nearby San Bernard River mouth closing and requiring frequent dredging. The San Bernard River is directly south of the Brazos River watershed and directly north of the Colorado River watershed. The San Bernard watershed is shown in Figure 3-2 and is approximately 900 square miles. Developing accurate suspended sediment concentration estimates will help future researchers and engineers evaluate the sediment characteristics of the Brazos River to combat the issues it is causing to the San Bernard River.
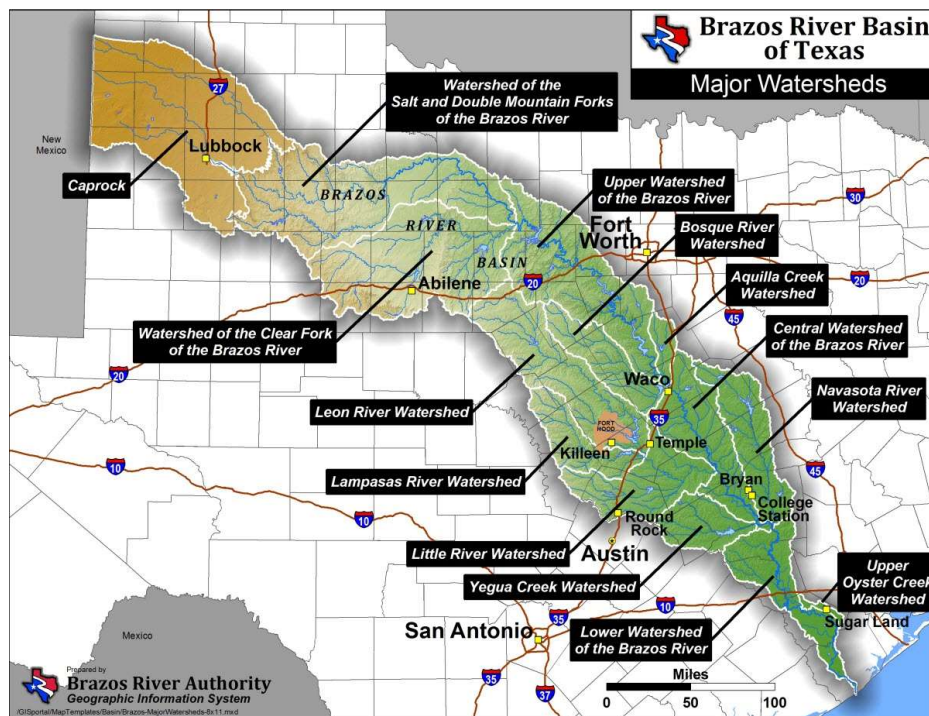


**Figure 3-1:** Brazos River Watershed (Brazos River Authority)
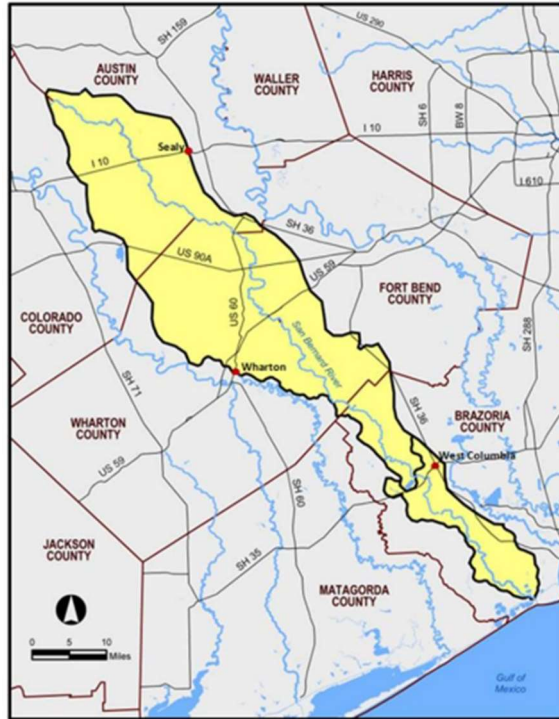
**Figure 3-2:** San Bernard River Watershed (Houston-Galveston Area Council, 2017)

Past research by Storm (2013) and Philips (2006) have been conducted along the Brazos River to evaluate and document the sediment and hydraulic characteristics of the river because of its importance to the state of Texas. This past research provides a general context to the historic sediment transport and hydraulic characteristics for area of this study. Philips (2006) reviewed research along the lower reaches of the Brazos River near the Gulf of Mexico and had the following major conclusions or findings about these sections of the Brazos River:

- Backwater effects occur in downstream reaches and flow diversions to Oyster Creek and other streams cause a reduction in flow as flow goes to the mouth of the river.

- Reservoirs in upstream reaches have not been observed to have led to major changes in river discharge or sand transport. The minor changes in sediment transport have shown a general reduction in sediment regime if changes have been observed.

- There has been no evidence of general channel widening, and tidal river reaches have not seen much lateral channel change and migration.

- The river is transport-limited instead of supply-limited from a sediment transport perspective.

- Erosion of the river is dominated by incision where it exists. This is speculated to be partially caused by an increase in slope to the mouth of the river caused by avulsion.

- The river is wave-dominated at the delta except for high river flow events, which can be a sign of low sand contents in the river delta.

Storm (2013) conducted analysis of six USGS gages from Waco to Rosharon to use USGS and field collected data to develop sediment rating curves to determine the general sediment transport of the Brazos River. This research noted that the primary sediment material observed within the Brazos River was silt and clay. Furthermore, it was observed that increasing flows in the Brazos River lead to an increase in fines material and a decrease in sand load. The increase in fines material was speculated to be a result of greater loading of fines during the observed flow events. Finally, this research concluded that there were two major classes of sediment transport for the Brazos River, one for low flows that are less than 20,000 cfs and one for relatively high flows that are greater than the 1.5-year return period.

## 3.2    Sampling Data

Two sampling locations with publicly available suspended sediment concentration data from the National Water Quality Monitoring Council (NWQMC) and data collected by Storm (2013) along the Brazos River were used for this study. These sampling locations included three unique numbered gauging locations owned and maintained by two different agencies. The northernmost location near Rosharon has two gauges owned by USGS and Texas Commission on Environmental Quality (TCEQ) (USGS 08116650 and TCEQMAIN-16355) while the southernmost location near Freeport has one gauging location owned by TCEQ (TCEQMAIN-11843). One gauging location between these areas (TCEQMAIN-16878) also had a single suspended sediment concentration data point. The TCEQMAIN-16878 gauging location was not included as part of this study because the other three gauging locations were deemed to have an adequate amount of data for the study. In addition, publicly available data of suspended sediment concentration for the San Bernard River was gathered at TCEQMAIN-12146 to evaluate the ability of the Brazos River suspended sediment concentration estimator developed for this

study to be applied to different areas. The locations of these gauges and a summary of the suspended sediment concentration data from these gauges used in this study are shown in Figure 3-3 and Figure 3-4, respectively. Table 3-1 documents some important summary statistics for each of the gauging locations. In general, the Brazos River has higher suspended sediment concentrations that the San Bernard River.

**Table 3-1:** Gage Suspended Sediment Concentration Sample Summary

| Gage | Count | Minimum SSC (mg/L) | Maximum SSC (mg/L) | Mean SSC (mg/L) |
|------|-------|--------------------|--------------------|-----------------|
| USGS-08116650 | 329 | 2 | 4,740 | 438 |
| TCEQMAIN-16355 | 141 | 4 | 1,520 | 324 |
| TCEQMAIN-11843 | 208 | 1 | 4,650 | 196 |
| TCEQMAIN-12146 | 213 | 2 | 493 | 39 |
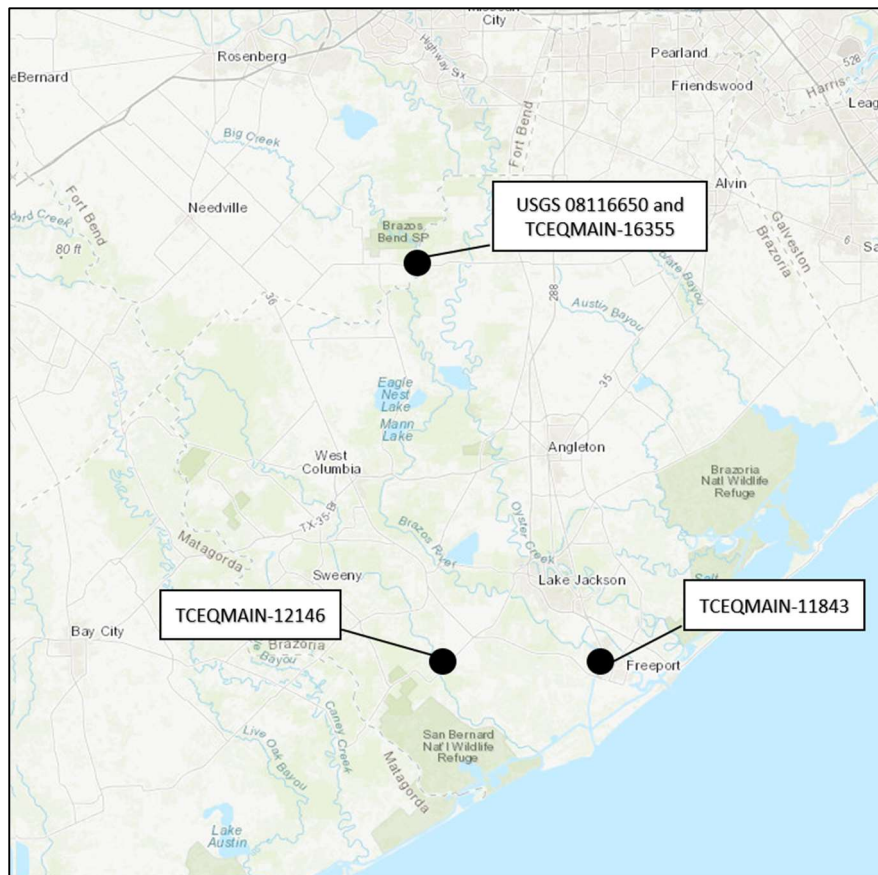


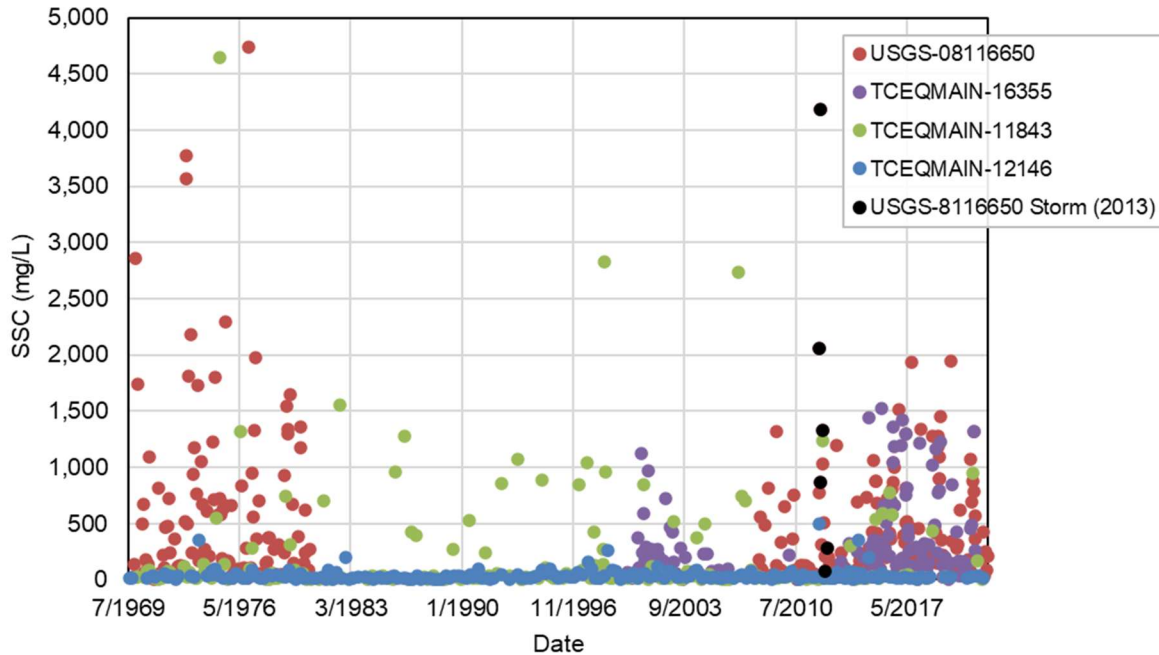**Figure 3-3:** Suspended Sediment Sampling Locations in Study Area

**Figure 3-4:** Suspended Sediment Concentration Data for Brazos and San Bernard Rivers in the Study Area

The USGS and TCEQ both measure suspended sediment concentration but use slightly different laboratory testing procedures to determine these measurements. The USGS primarily uses a suspended sediment concentration (SSC) testing procedure that uses the entire sample collected for the measurement as stipulated by the American Society for Testing and Materials (ASTM) while the TCEQ uses a total suspended solids testing procedure that uses a subsample of the sample collected for the measurement. There are two main testing procedures for the total suspended solids (TSS) testing procedure as outlined below.

- Environmental Protection Agency (EPA) Method – This method stirs the sample collected and then collects a sub-sample by pouring directly from the sample container.

- Standard Method – This method stirs the sample collected and then collects a sub-sample using a pipette to draw a portion of the sample from the entire sample container.

It must also be noted that the USGS gauging site used for this study (USGS-08116650) was observed to use both the ASTM procedure and the TSS procedure.

The ASTM and both TSS procedures lead to different measurements because of the different procedures they employ. Past research by Gray (2000) and Guo (2006) have indicated that TSS and ASTM procedures generally underestimate true suspended solid concentrations, but that the total suspended solid procedures tend to lead to more erroneous measurements than ASTM procedures. The errors that result from the total suspended solids procedures have been observed to be heavily dependent on the particle size distribution of the sample. The following observations from Guo (2006) and Gray (2000) were made regarding particle size distribution influence on errors of suspended sediment concentration/total suspended solids measurements.

- Guo (2006):
  - There were minimal errors in total suspended solids measurements for samples with most solid particle sizes up to 53 μm.
  - Total suspended solids measurement procedures were not able to detect any solids concentration for samples with most solid particle sizes greater than 106 μm.

- Gray (2000):
  - There were minimal errors in total suspended solids measurements with most solid particles finer than 0.062 mm.
  - Samples with sand proportions larger than 33% lead to bigger discrepancies in total suspended solids measurements.

The Storm (2013) study field data collected for suspended solids at USGS-08116650 is shown in Figure 3-5 and Table 3-2. Lines are added to Figure 3-5 to identify sand particle sizes (0.06 mm and greater) and percent finer of 70% because of Gray (2000) and Guo (2006) findings. As shown in Figure 3-5, only the sample taken on 5/17/2012 during a low flow condition had sand proportions greater than 70%. This indicates that at the upstream sampling location near Rosharon (gauging sites USGS 08116650 and TCEQMAIN-16355), there could be errors in suspended sediment concentration measurements for total suspended solids samples. These samples could have significantly lower suspended sediment concentrations than true values because of larger solid particles. These effects were assumed to not occur in a large enough percentage of the historical samples at the upstream location

near Rosharon to correct for in this study. It was anticipated that the downstream sampling location near

Freeport would have smaller particle size distributions for suspended solids because flows were noted to

decrease moving downstream the river (Phillips, 2006). As a result, it was assumed that there would be

limited error in suspended sediment concentrations measurements at the downstream location near
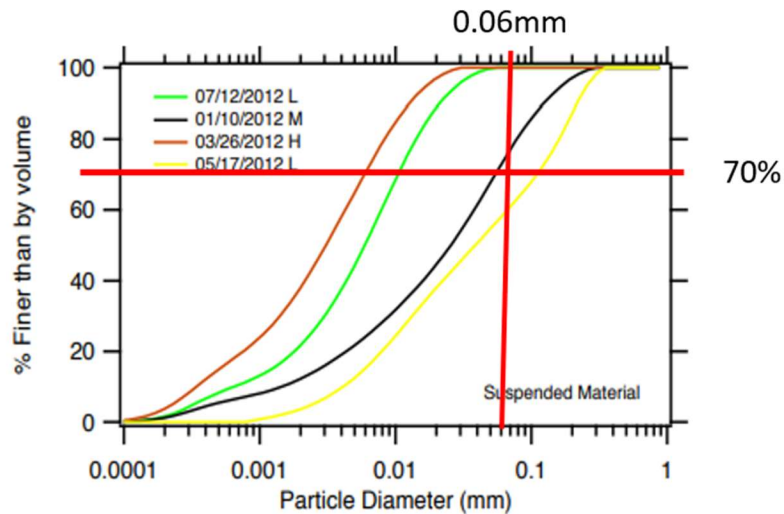
Freeport introduced by samples that used total suspended solids procedures.



**Figure 3-5:** Particle Size Distribution for Suspended Sediment Samples at USGS 08116650 from Storm (2013). (L: low flow, M: moderate flow, H: high flow, see Table 3-2)

**Table 3-2:** Field Data Collected at USGS 081106650 from Storm (2013) (Portion of Table 4-1 from Storm (2013))

| Site | Date | Condition | Location on Hydrograph | SS Sample Method | Bed Size Measured? (Used) | SS Size Measured? (Used) | $Q$ [cfs] | $R_h$ [ft] | $U$ [ft/s] | $d_{16}$ [mm] | $d_{50}$ [mm] | $d_{84}$ [mm] | $d_{90}$ [mm] | Wash Load [%] | Total SSC [mg/l] |
|------|------|-----------|------------------------|------------------|---------------------------|--------------------------|-----------|-----------|------------|--------------|--------------|--------------|--------------|---------------|------------------|
| Rosharon | 01/10/12 | Moderate | Peak | DIS | yes | Yes | 10,500 | 13.0 | 3.4 | 0.29 | 0.38 | 0.55 | 0.61 | 71 | 2,062 |
| Rosharon | 01/28/12 | Moderate | Rising | DIS | yes | No (01/10/12) | 4,400 | 8.1 | 3.1 | 0.31 | 0.46 | 0.72 | 1.00 | 71 | 863 |
| Rosharon | 01/30/12 | High | Peak | DIS | yes | No | 15,700 | 15.5 | 4.0 | 0.25 | 0.38 | 0.77 | 1.00 | 100 | 4,185 |
| Rosharon | 03/26/12 | High | Peak | DIS | No (1/30/12) | Yes | 47,600 | 27.3 | 5.7 | 0.25 | 0.38 | 0.77 | 1.00 | 71* | 1,325 |
| Rosharon | 05/17/12 | Low | Falling | Bucket | No (7/12/12) | Yes | 2,100 | 6.6 | 1.9 | 0.12 | 0.23 | 0.90 | 1.30 | 57 | 81 |
| Rosharon | 07/12/12 | Low | Rising | Bucket | yes | Yes | 1,500 | 6.2 | 1.5 | 0.12 | 0.23 | 0.90 | 1.30 | 100 | 282 |

## 3.3    Flow and Depth Data

Flow and depth data from the USGS 08116650 was collected for this study to compare models

generated using satellite data to the standard suspended sediment concentration estimation methods of

a flow rating curve. In practice, a flow rating curve is either used to estimate suspended sediment

concentration or sediment load. For this study, both methods were investigated to compare models

developed using satellite data. Furthermore, sediment load for this study only includes suspended sediment load and does not account for bed load contributions. Average daily flow readings at USGS 08116650 were linked to suspended sediment concentration data collected on the same day, resulting in a total of 470 pairs of flow and sediment data. Figure 3-6 and Figure 3-7 show the data pairs at USGS 08116650 for flow and sediment. Log-scales were used for both the x and y axis because this is a common practice for the flow rating curve method. This data is provided in Appendix D.
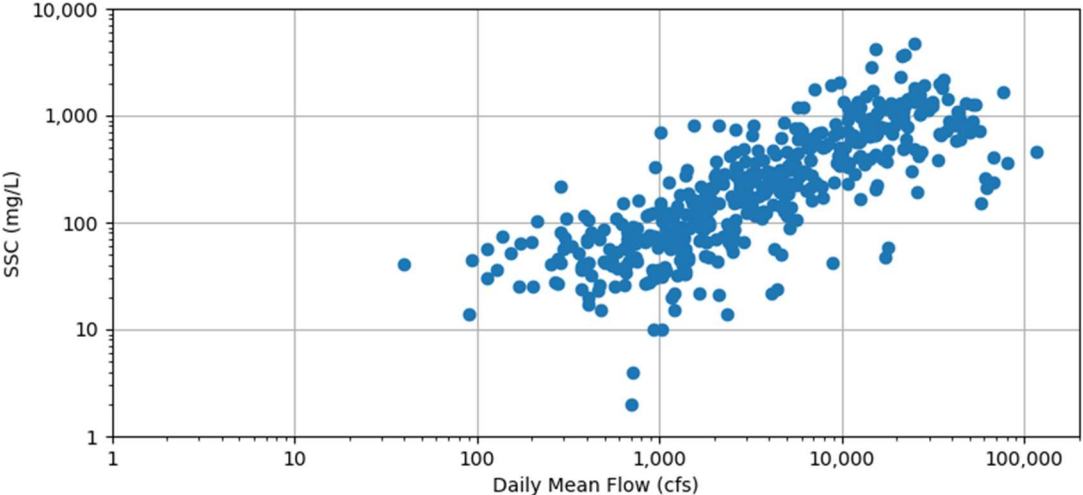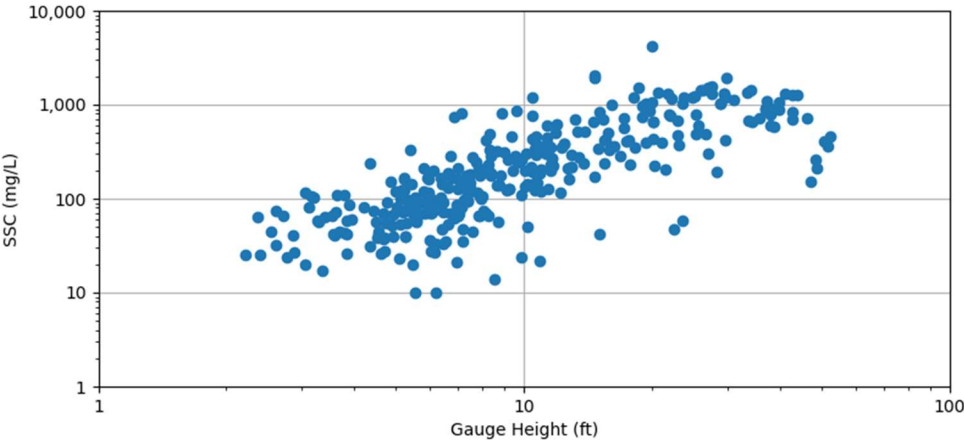


**Figure 3-6:** Mean Flow vs. Suspended Sediment Concentration for Brazos River at the USGS 08116650 station
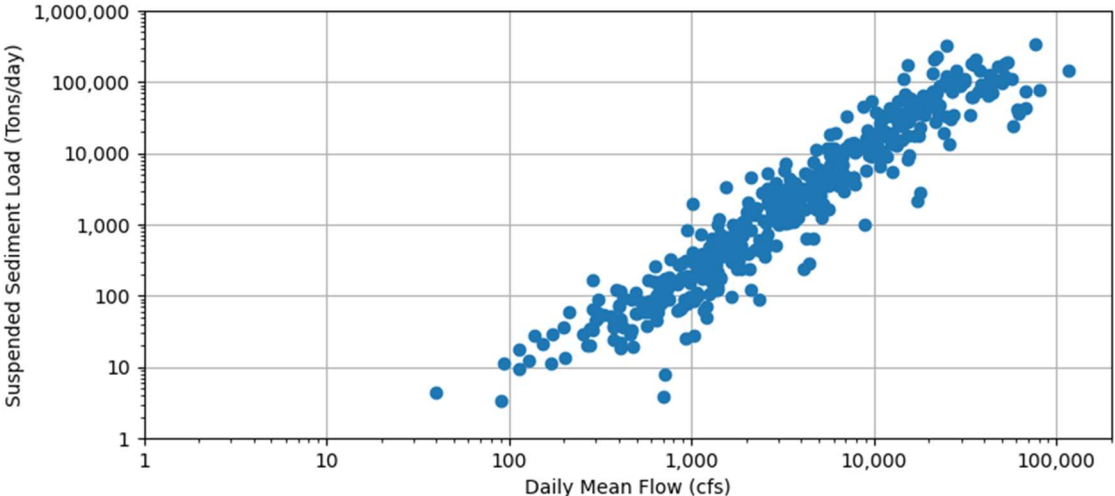


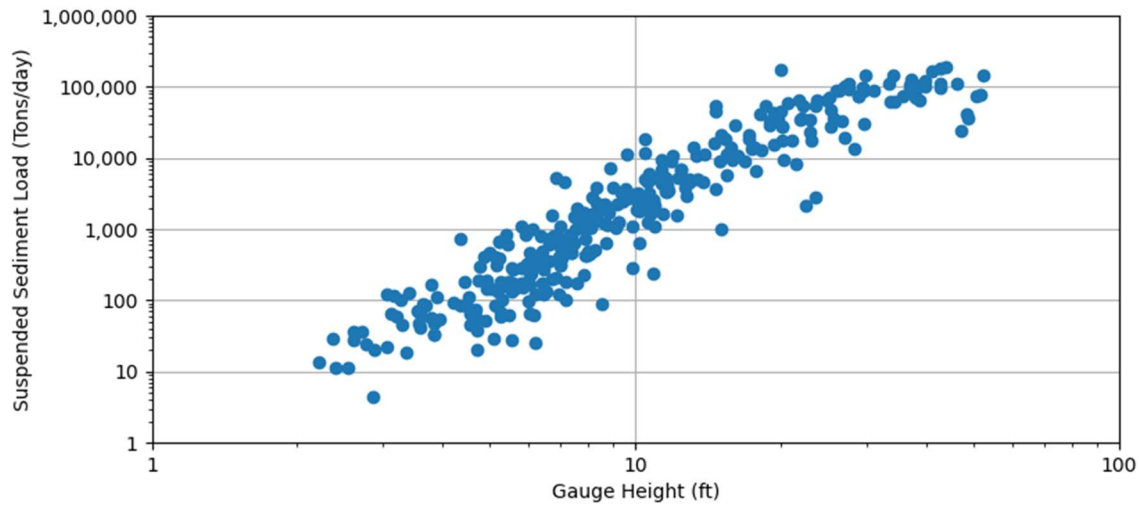**Figure 3-7:** Mean Flow vs. Suspended Sediment Load for Brazos River at the USGS 08116650 station

This study also used a non-standard rating curve with the depth measurements at USGS 08116650. For this depth rating curve, depth replaced the flow term in the standard rating curve. Depth was also used because, as shown in Figure 3-8, flow and depth have a very strong relationship to each other. Daily depth readings were linked to the suspended sediment concentration data collected on the same day, resulting in a total of 331 pairs of depth and sediment data. Figure 3-9 and Figure 3-10 show the data pairs at USGS 08116650 for depth and sediment. This data is provided in Appendix D.
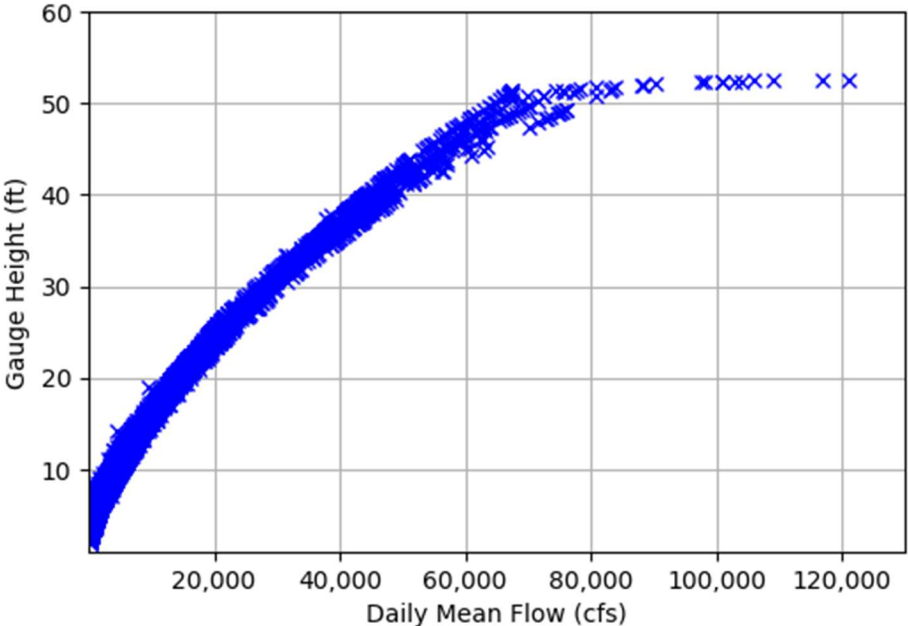


**Figure 3-8:** Mean Flow vs. River Depth for Brazos River at the USGS 08116650 station



**Figure 3-9:** River Depth vs. Suspended Sediment Concentration for Brazos River at the USGS 08116650 station

**Figure 3-10:** River Depth vs. Suspended Sediment Load for Brazos River at the USGS 08116650 station

### 3.4    Satellite Data

Two sources of publicly available optical image satellite data were used for this study: Landsat and Sentinel satellite missions. Landsat satellite data is collected, processed, and provided by the USGS with satellite data going back to July 1972 with nine total missions. A summary of the timeline of the nine missions is shown in Figure 3-11. The Landsat images for missions 1–3 were collected at a 60 m (196.8 ft) resolution while images for missions 4 and onwards were/are collected at a 30 m (98.4 ft) resolution. Because of the narrow width of the Brazos River at the upstream sample location near Rosharon (approximately 170 ft wide channel based on aerial imagery), Landsat Missions 1–3 were not used for this study.
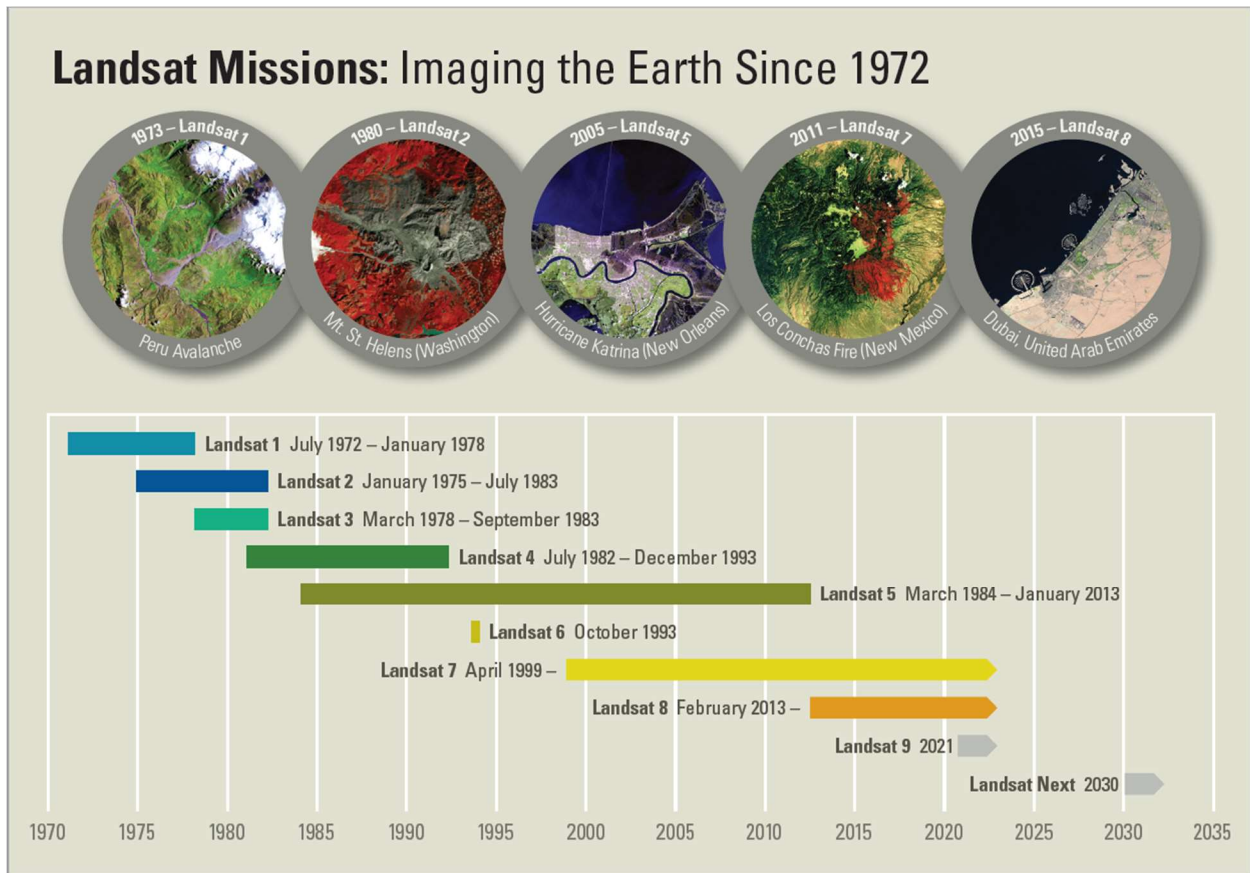
**Figure 3-11:** Landsat Missions Timeline (United States Geological Survey)

Sentinel satellite data is collected, processed, and provided by the European Space Agency (ESA). Sentinel missions include six different missions that each collect specific data such as air quality tracers or optical imagery. Sentinel Mission 2 is the mission that collects optical imagery and was used for this study. Two satellites (A and B) are actively measuring optical imagery for Sentinel Mission 2. Satellite A was launched in 2016 while satellite B was launched in 2018. The resolution of data collected for Sentinel Mission 2 are either 10 m, 20 m, or 60 m. As mentioned above, narrow river widths at the upstream sample location near Rosharon prevent the use of images that are 60 m in resolution from this data source.

Figure 3-12 summarizes the different bands of data collected by all the satellite data used in this study (Landsat Missions 4–9 and Sentinel Mission 2). Landsat Mission 9 collects the same bands as Landsat Mission 8. Likewise, Landsat Missions 4 and 5 collected the same bands as Landsat Mission 7.

As shown in Figure 3-12, many of the bands are collected over the exact same or a very similar range of wavelengths across all missions. The following bands were used from the different missions for this study.

- Landsat Missions 4–7: Bands 1–5 and 7

- Landsat Missions 8–9: Bands 2–7

- Sentinel Mission 2: Bands 2–4, 8, and 11–12

For the Sentinel Mission 2 bands used in this study, bands 2–4 and 8 have a resolution of 10 m, and bands 11–12 have a resolution of 20 m. Bands with similar ranges of wavelength ranges were grouped together for this study. The band groups used for this study are shown in Table 3-3.
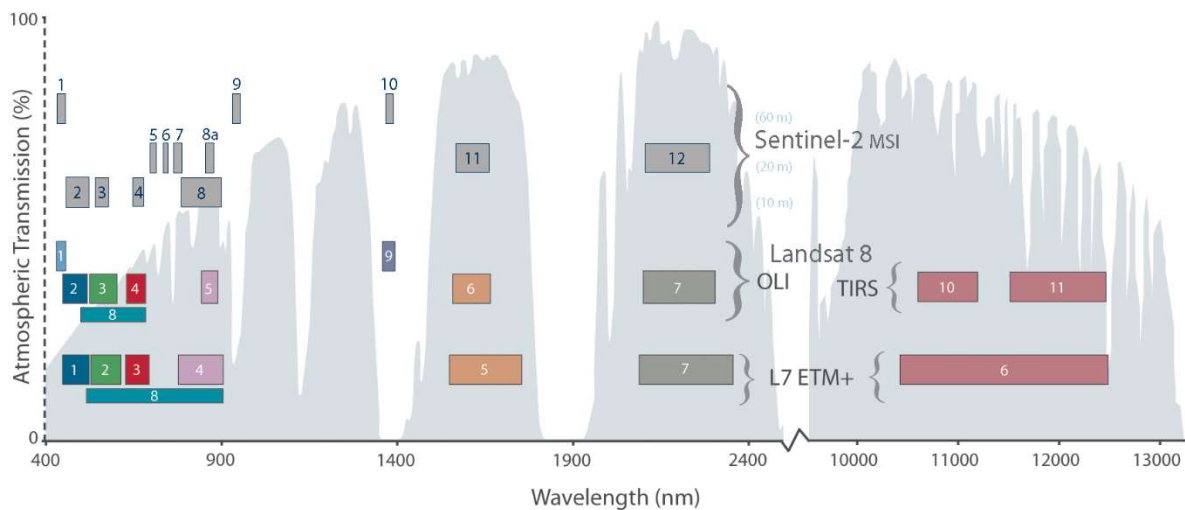


**Figure 3-12:** Comparison of Landsat Mission and Sentinel Mission 2 Bands Collected (United States Geological Survey)

**Table 3-3:** Band Groups used in the Study

| Band Group | Landsat Missions 4–7 Band | Landsat Missions 8–9 Band | Sentinel Mission 2 Band |
|---|---|---|---|
| Blue | 1 | 2 | 2 |
| Green | 2 | 3 | 3 |
| Red | 3 | 4 | 4 |
| Near Infrared (NIR) | 4 | 5 | 8 |
| ~1500 nm | 5 | 6 | 11 |
| ~2100 nm | 7 | 7 | 12 |

Landsat missions and Sentinel Mission 2 have different levels of processed data that are available. Table 3-4 summarizes the different levels of processed data for the Landsat missions and

Sentinel Mission 2. For this study, Level 2 data products were used because this level of product is the highest for both Landsat and Sentinel images that is provided. More importantly, this level of product is a measure of surface reflectance values that are atmospherically corrected by processing algorithms developed by the space agencies to correct for potential errors in satellite measurements, such as the sun angle and angle of instrument measurement. The surface reflectance values from these data sources are anticipated to include components from bottom reflectance, water column reflectance, and surface reflectance from the water based on Equation (**2**.**2**). The atmospheric reflectance component from Equation (**2**.**2**) is not desired because varying suspended sediment concentrations should affect water column reflectance and surface reflectance from the waterbody the most, making these components the most important for this study. Bottom reflectance could potentially interfere with the models developed if there are shallow water depths and/or low suspended sediment concentrations.

**Table 3-4:** Landsat and Sentinel Mission 2 Processing Levels

| Processing Level | Landsat Missions | Sentinel Mission 2 |
|---|---|---|
| Level 1 | Real time data that represents reflectance values at the satellite, or top of atmosphere readings. | B:Top of atmosphere radiances in sensor geometry.<br>C: Top of atmosphere reflectances in cartographic geometry. |
| Level 2 | Processed Level 1 data and is generation of atmospherically corrected geophysical retrievals of Earth's surface, or bottom of atmosphere/surface reflectance readings. | Processed Level 1 data that is bottom of atmosphere reflectances in cartographic geometry. |
| Level 3 | Processed Level 2 data that has burned area, dynamic surface water extent, and fractional snow-covered area. | Not provided. |
| Analysis Read Data | Processed Level 2 data that is tiled, georegistered, top of atmosphere and atmospherically corrected geophysical product in common equal area projection. | Not provided. |

Landsat missions provide Level 2 processed data for all missions used in this study (Missions 4–9) and have valid reflectance value ranges from 7,273 – 43,636. Sentinel Mission 2 data only started providing Level 2 products following December 2018. For images before December 2018 for Sentinel

Mission 2 data, ESA provided data processing tools were used to create Level 2 products from Level 1C

data collected. Sentinel Mission 2 data have valid reflectance value ranges from 1–10,000. A total of

1,312 Landsat images were collected using EarthExplorer tools provided by USGS and a total of 912

Sentinel Mission 2 images were collected using Sentinel Application Programming Interface (API) calls.

Both Landsat and Sentinel Mission 2 Level 2 products are provided with quality pixels that

label/classify the pixels in categories such as water or land based on algorithms developed by USGS and

ESA, respectively. The meanings for these pixels for all the data used in this study are shown in Table

3-5 through Table 3-7. These meanings are from USGS and ESA product documentation. The use of

these values is discussed further in the following section.

**Table 3-5:** Landsat Missions 4–7 Quality Pixel Value Meanings

| Pixel Value | Fill | Dilated Cloud | Cirrus | Cloud | Cloud Shadow | Snow | Clear | Water | Cloud Conf. | Cloud Shadow Conf. | Snow/ Ice Conf. | Cirrus Conf. | Pixel Description |
|---|---|---|---|---|---|---|---|---|---|---|---|---|---|
| 1 | Yes | No | N/A | No | No | No | No | No | None | None | None | None | Fill |
| 5440 | No | No | N/A | No | No | No | Yes | No | Low | Low | Low | None | Clear with low sets |
| 5442 | No | Yes | N/A | No | No | No | Yes | No | Low | Low | Low | None | Dilated cloud over land |
| 5504 | No | No | N/A | No | No | No | No | Yes | Low | Low | Low | None | Water with low sets |
| 5506 | No | Yes | N/A | No | No | No | No | Yes | Low | Low | Low | None | Dilated cloud over water |
| 5696 | No | No | N/A | No | No | No | Yes | No | Mid | Low | Low | None | Mid conf. cloud |
| 5760 | No | No | N/A | No | No | No | No | Yes | Mid | Low | Low | None | Med conf. cloud over water |
| 5896 | No | No | N/A | Yes | No | No | No | No | High | Low | Low | None | High conf. cloud |
| 7440 | No | No | N/A | No | Yes | No | No | No | Low | High | Low | None | High conf. cloud shadow |
| 7568 | No | No | N/A | No | Yes | No | No | Yes | Low | High | Low | None | Water with cloud shadow |
| 7696 | No | No | N/A | No | Yes | No | No | No | Mid | High | Low | None | Mid conf. cloud with shadow |
| 7824 | No | No | N/A | No | Yes | No | No | Yes | Mid | High | Low | None | Mid conf. cloud with shadow over water |
| 7960 | No | No | N/A | Yes | Yes | No | No | No | High | High | Low | None | High conf. cloud with shadow |
| 8088 | No | No | N/A | Yes | Yes | No | No | Yes | High | High | Low | None | High conf. cloud with shadow over water |
| 13664 | No | No | N/A | No | No | Yes | Yes | No | Low | Low | High | None | High conf. snow/ice |

**Table 3-6:** Landsat Missions 8–9 Quality Pixel Value Meanings

| Pixel Value | Fill | Dilated Cloud | Cirrus | Cloud | Cloud Shadow | Snow | Clear | Water | Cloud Conf. | Cloud Shadow Conf. | Snow/ Ice Conf. | Cirrus Conf. | Pixel Description |
|---|---|---|---|---|---|---|---|---|---|---|---|---|---|
| 1 | Yes | No | No | No | No | No | No | No | None | None | None | None | Fill |
| 21824 | No | No | No | No | No | No | Yes | No | Low | Low | Low | Low | Clear with low sets |
| 21826 | No | Yes | No | No | No | No | Yes | No | Low | Low | Low | Low | Dilated cloud over land |
| 21888 | No | No | No | No | No | No | No | Yes | Low | Low | Low | Low | Water with low sets |
| 21890 | No | Yes | No | No | No | No | No | Yes | Low | Low | Low | Low | Dilated cloud over water |
| 22080 | No | No | No | No | No | No | Yes | No | Mid | Low | Low | Low | Mid conf. cloud |
| 22144 | No | No | No | No | No | No | No | Yes | Mid | Low | Low | Low | Med conf. cloud over water |
| 22280 | No | No | No | Yes | No | No | No | No | High | Low | Low | Low | High conf. cloud |
| 23888 | No | No | No | No | Yes | No | Yes | No | Low | High | Low | Low | High conf. cloud shadow |
| 23952 | No | No | No | No | Yes | No | No | Yes | Low | High | Low | Low | Water with cloud shadow |
| 24088 | No | No | No | Yes | Yes | No | No | No | Mid | High | Low | Low | Mid conf. cloud with shadow |
| 24216 | No | No | No | Yes | Yes | No | No | Yes | Mid | High | Low | Low | Mid conf. cloud with shadow over water |
| 24344 | No | No | No | Yes | Yes | No | No | No | High | High | Low | Low | High conf. cloud with shadow |
| 24472 | No | No | No | Yes | Yes | No | No | Yes | High | High | Low | Low | High conf. cloud with shadow over water |
| 30048 | No | No | No | No | No | Yes | Yes | No | Low | Low | High | Low | High conf. snow/ice |
| 54596 | No | No | Yes | No | No | No | Yes | No | Low | Low | Low | High | High conf. cirrus |
| 54852 | No | No | Yes | No | No | No | Yes | No | Mid | Low | Low | High | Cirrus, mid cloud |
| 55052 | No | No | Yes | Yes | No | No | No | No | High | Low | Low | High | Cirrus, high cloud |
| 56856 | No | No | No | Yes | Yes | No | No | No | Mid | High | Low | High | Cirrus, mid cloud, shadow |
| 56984 | No | No | No | Yes | Yes | No | No | Yes | Mid | High | Low | High | Cirrus, mid cloud, shadow, over water |
| 57240 | No | No | No | Yes | Yes | No | No | Yes | High | High | Low | High | Cirrus, high cloud, shadow |

**Table 3-7:** Sentinel Mission 2 Quality Pixel (Scene Classification) Value Meanings

| Bit Value | Classification |
|-----------|----------------|
| 0 | No data |
| 1 | Saturated or defective |
| 2 | Dark area pixels |
| 3 | Cloud shadows |
| 4 | Vegetation |
| 5 | Bare soils |
| 6 | Water |
| 7 | Unclassified |
| 8 | Cloud medium probability |
| 9 | Cloud high probability |
| 10 | Thin cirrus |
| 11 | Snow or ice |

### 3.4.1   Satellite Data Preparation

Buffer areas near the three sampling locations were created to determine a representative pixel value for the sampling sites. The average of the pixel values in the buffer area was used for this representative value. Buffer areas were created upstream of the sampling locations to incorporate pixels that only contained water based on a combination of aerial imagery and quality pixel values. It was observed that the stream path of the Brazos and San Bernard Rivers did not change at the sample locations in this study over the period of satellite data collected based on the historical aerial images and quality pixels. Thus, static buffer areas were created for this study. The buffer areas were created based on the 30 m by 30 m pixels from Landsat and are shown in Figure 3-13 through Figure 3-15. The Brazos River buffer areas did not require any updates to be used for Sentinel Mission 2 bands 11–12 that have a resolution of 20 m by 20 m. These buffer areas were observed to not capture any non-water 20 m by 20 m pixels. However, the buffer area on the San Bernard River required minor updates to be used for the 20 m by 20 m pixels of Sentinel Mission 2 bands 11–12 to prevent the capture of non-water pixels. This updated buffer area is shown in Figure 3-16. Thus, for the San Bernard River, the two buffer areas shown were used in this study.

**Figure 3-13:** A 90 m by 30 m Buffer at the Upstream Sampling Location near Rosharon on the Brazos River



**Figure 3-14:** A 90 m by 90 m Buffer at the Downstream Sampling Location Near Freeport on the Brazos River

**Figure 3-15:** A 4,500 m² (Five  30 m by 30 m Pixels) Buffer for the San Bernard River Sampling Location



**Figure 3-16:** A 4,400 m² (Eleven 20 m by 20 m Pixels) Buffer for the San Bernard River Sample Location

The quality pixels were used to remove average pixel values from the buffer areas to prevent the interference of clouds on surface reflectance values. More specifically, any of the quality pixels with values that indicate any cloud cover, saturation, or snow/ice in the buffer area resulted in removal of that

scene for use at that sample location. It was observed that pixel values on the Brazos River and San Bernard River were not always labeled as water pixels based on the quality pixels and could have been labeled bare soils/land, cloud shadow, or dark areas. It was hypothesized this occurred because of the general nature of the quality labeling algorithms used by the USGS and ESA. Thus, scenes with these non-water labels were not removed for this study.

The satellite data that was collected for this study was linked to the closest suspended sediment concentration sample data by date of their acquisition. This means that satellite images could be linked to suspended sediment concentrations that were before, on the same day, or after the date of acquisition of the satellite images. For this study, only pairs of satellite and suspended sediment concentration data with up to a 3-day difference in the acquisition dates were used to be consistent with the maximum day difference used by Sobel (2020). The resulting relationship between the six satellite bands and suspended sediment concentration are shown in Figure 3-17 through Figure 3-28. The valid data range for Landsat missions and Sentinel Mission 2 were used to convert raw surface reflectance values to percentages to allow use of both sources for suspended sediment concentration estimation. This data is provided in Appendix D.
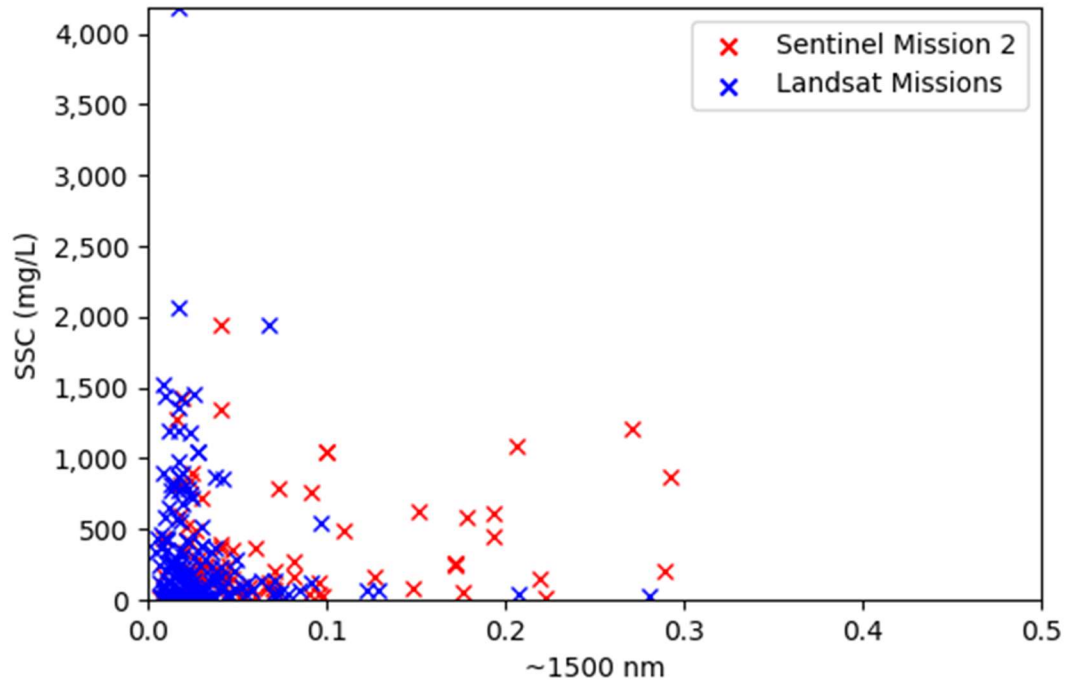
**Figure 3-17:** The 1500 nm Band vs. Suspended Sediment Concentration along Brazos River with up to a 3-Day Difference in Acquisition Dates
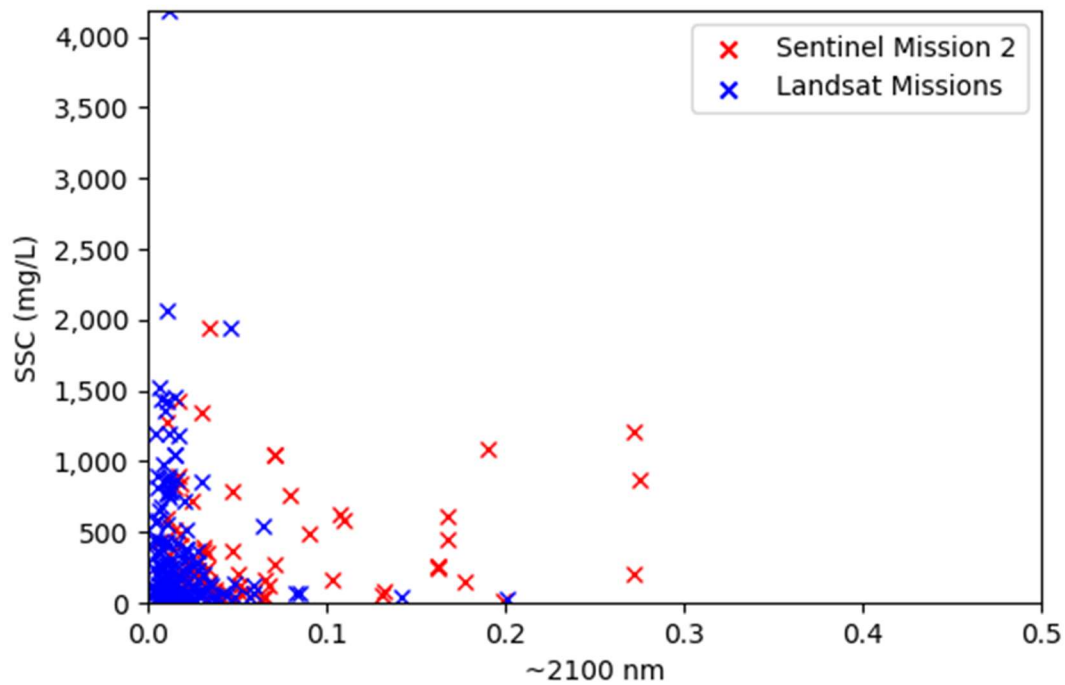


**Figure 3-18:** The 2100 nm Band vs. Suspended Sediment Concentration along Brazos River with up to a 3-Day Difference in Acquisition Dates
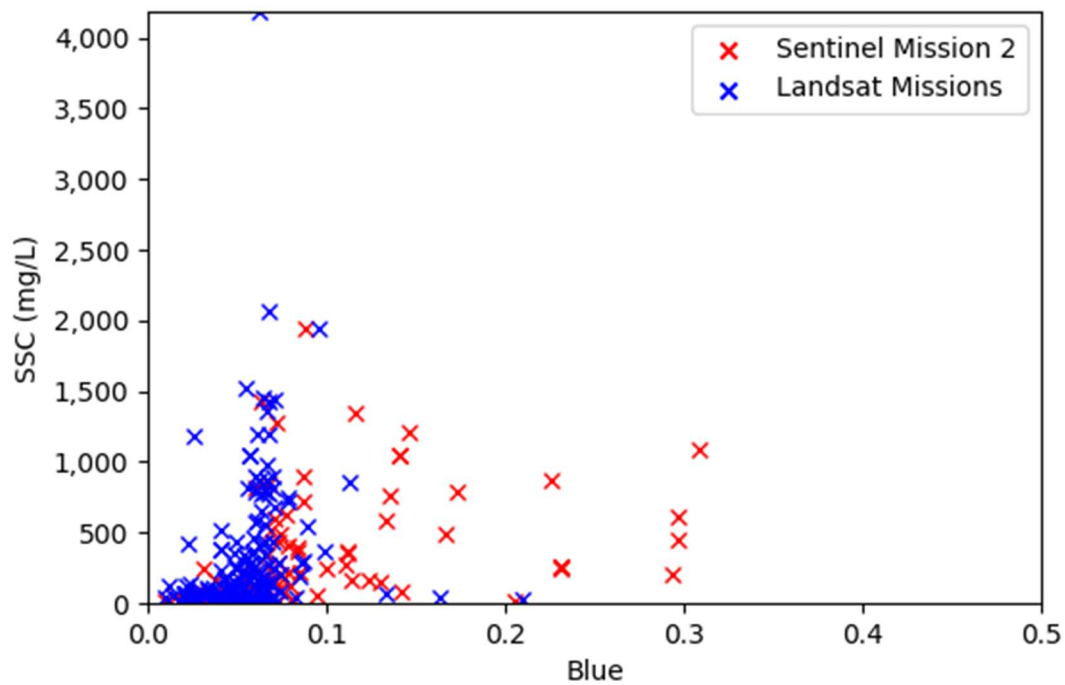
**Figure 3-19:** The Blue Band vs. Suspended Sediment Concentration along Brazos River with up to a 3-Day Difference in Acquisition Dates
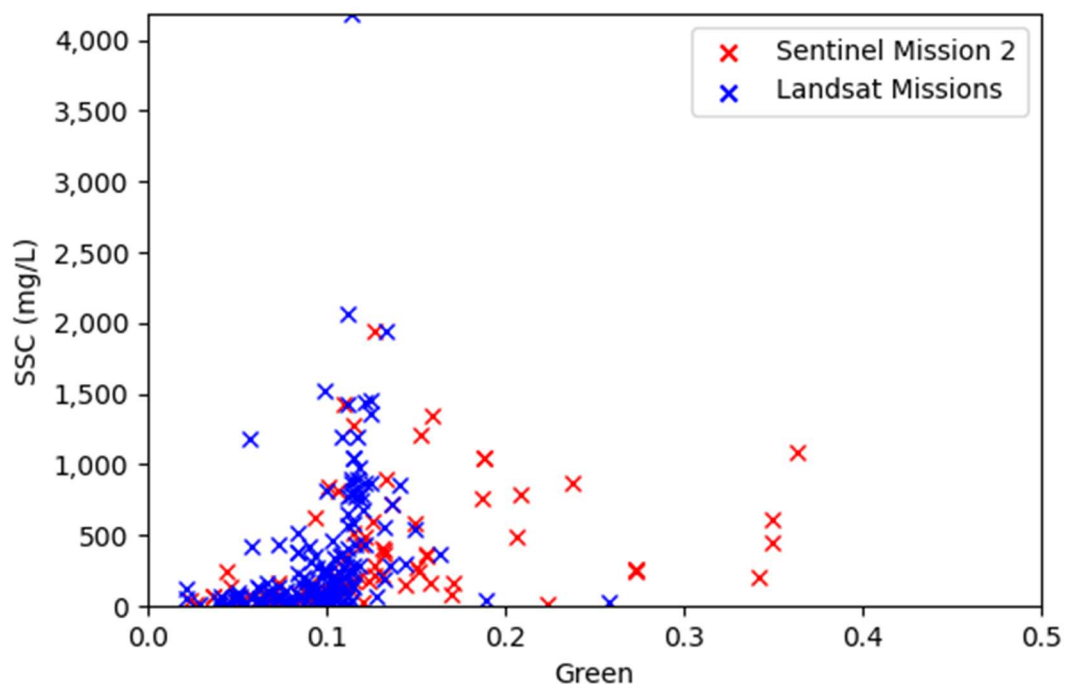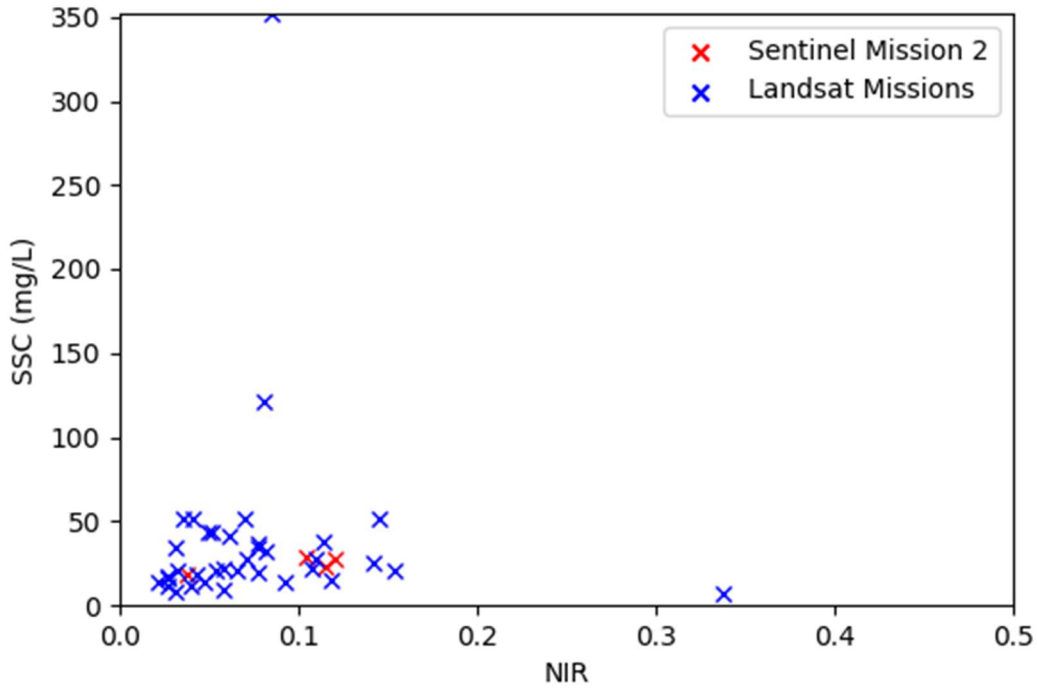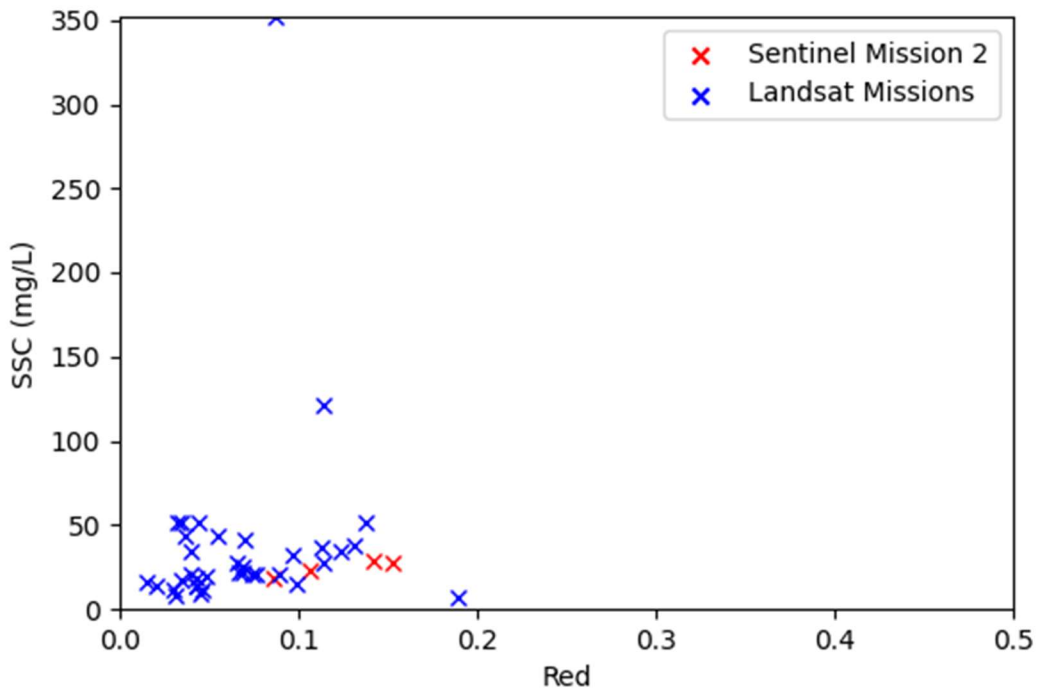


**Figure 3-20:** The Green Band vs. Suspended Sediment Concentration along Brazos River with up to a 3-Day Difference in Acquisition Dates
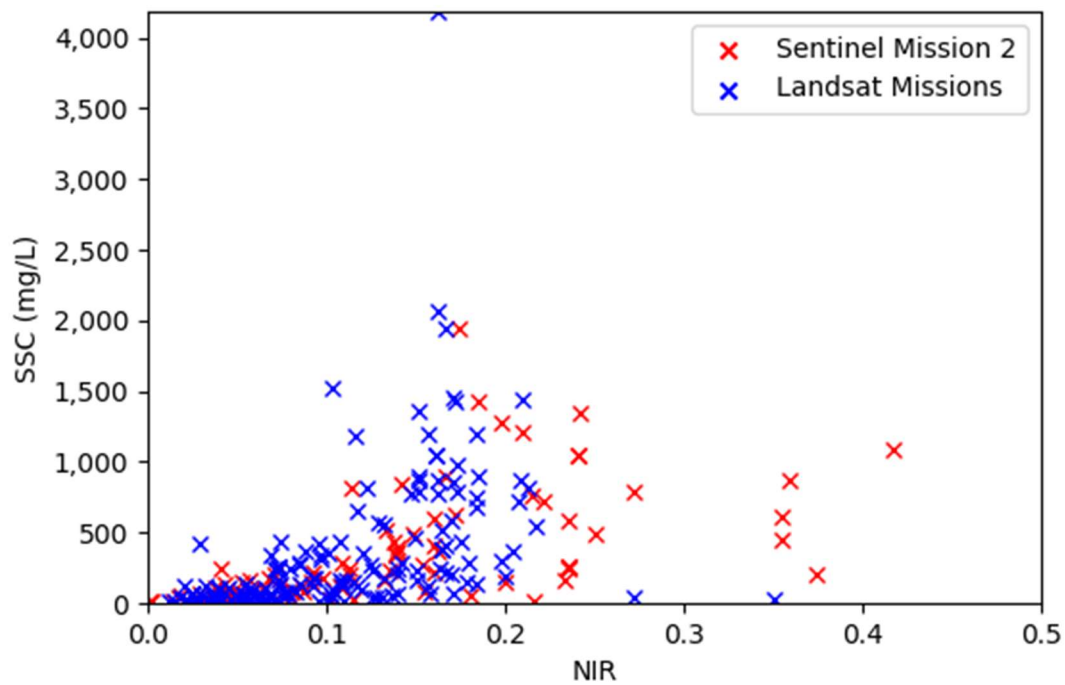
**Figure 3-21:** The NIR Band vs. Suspended Sediment Concentration along Brazos River with up to a 3-Day Difference in Acquisition Dates
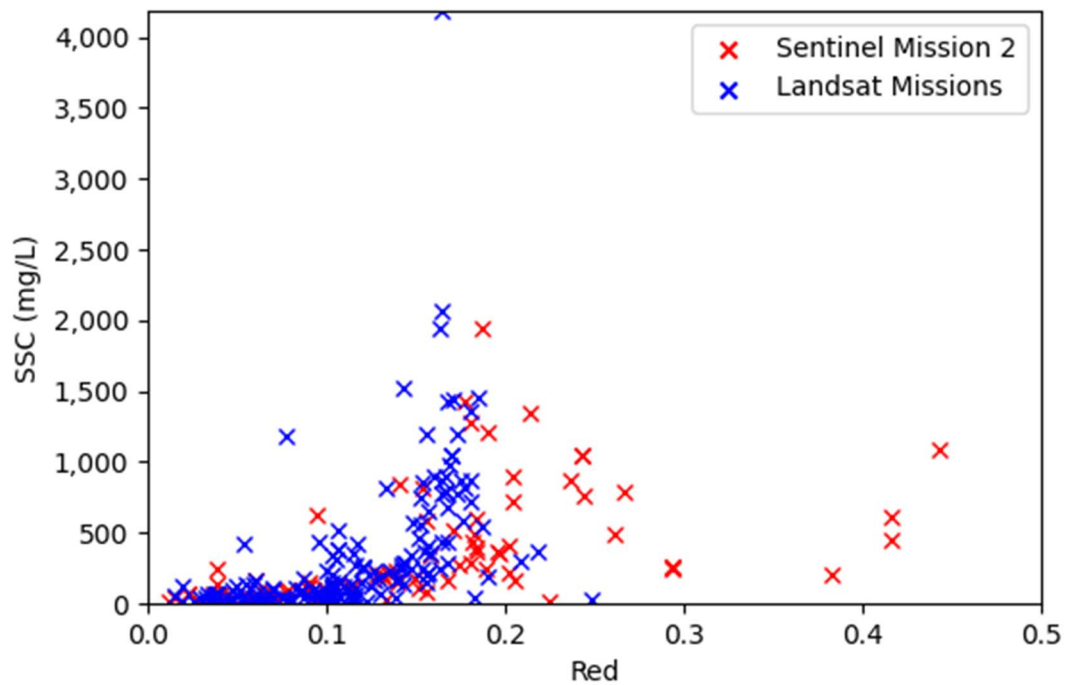


**Figure 3-22:** The Red Band vs. Suspended Sediment Concentration along Brazos River with up to a 3-Day Difference in Acquisition Dates
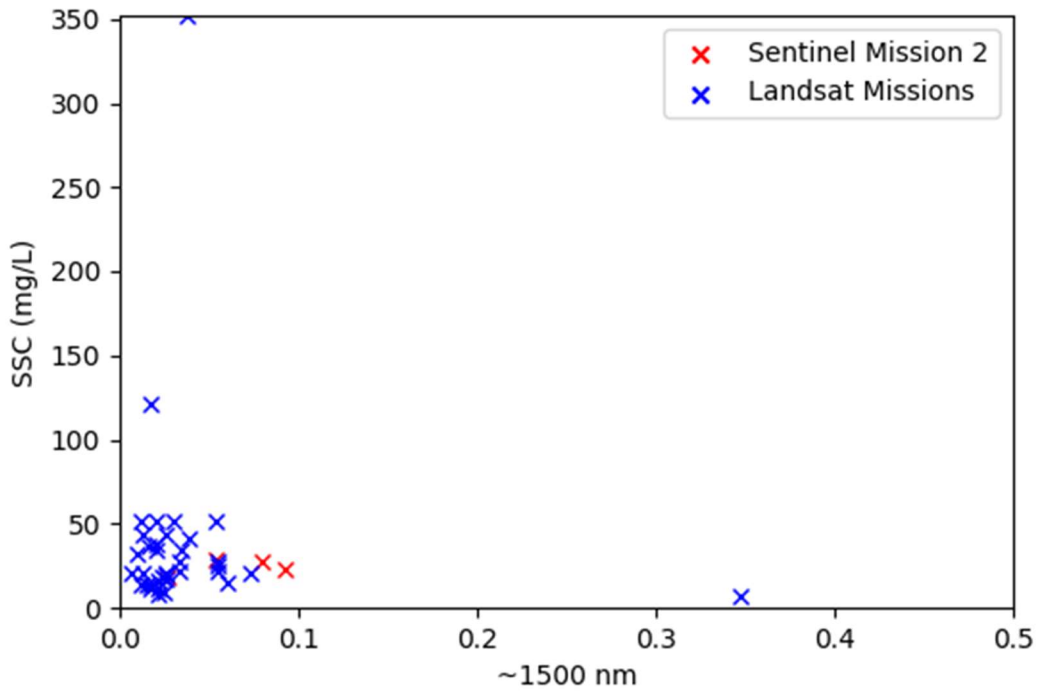
**Figure 3-23:** The 1500 nm Band vs. Suspended Sediment Concentration along San Bernard River with up to a 3-Day Difference in Acquisition Dates
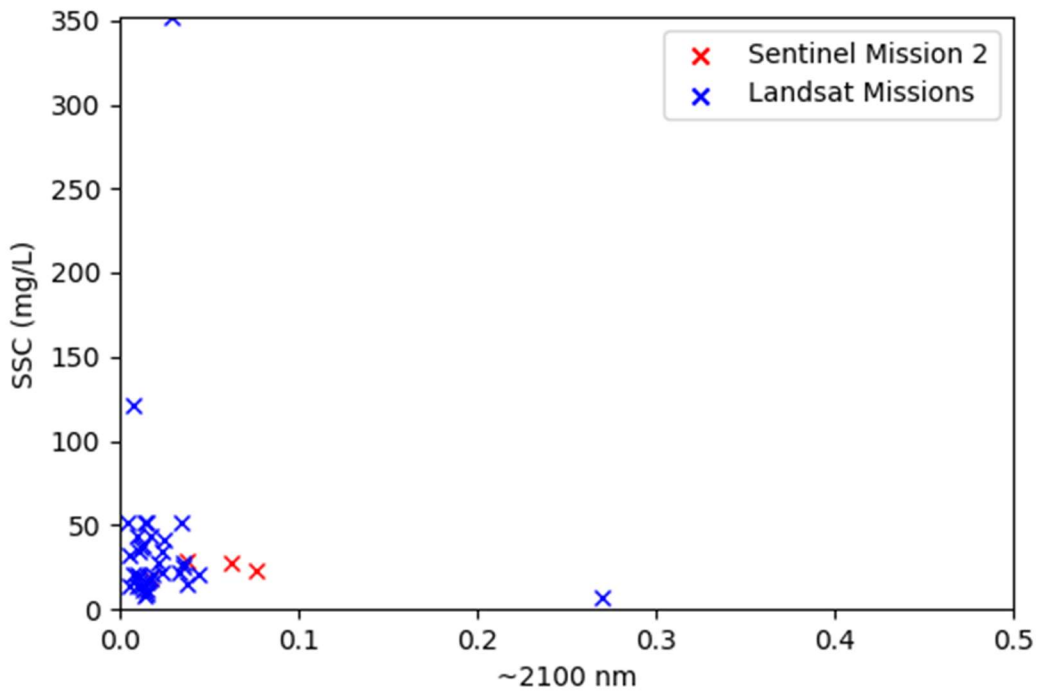


**Figure 3-24:** The 2100 nm Band vs. Suspended Sediment Concentration along San Bernard River with up to a 3-Day Difference in Acquisition Dates
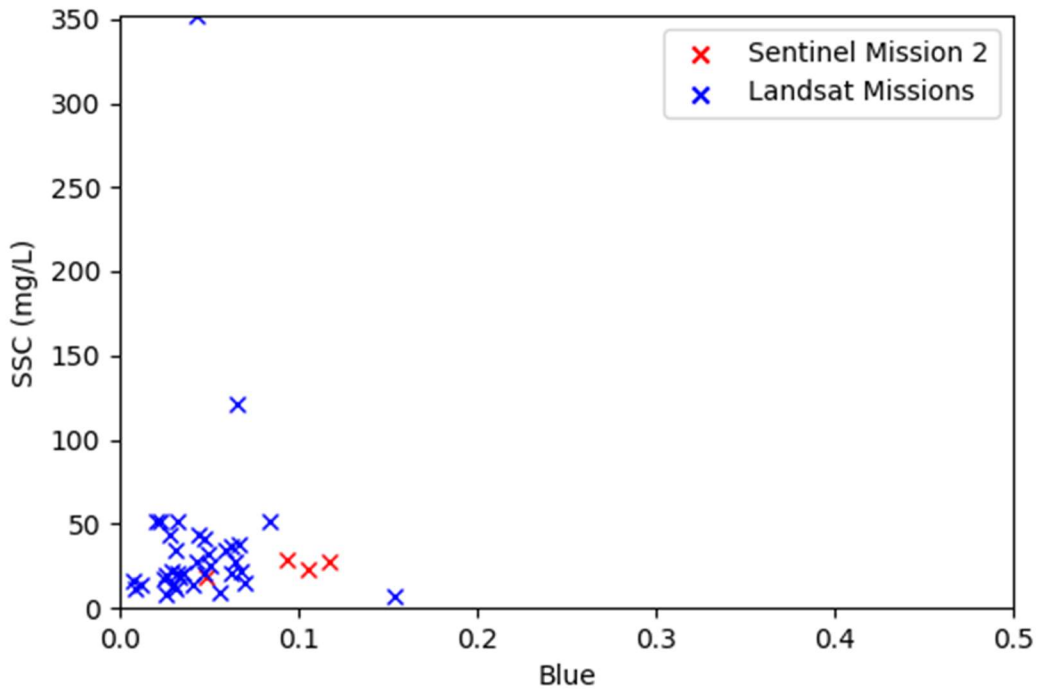
**Figure 3-25:** The Blue Band vs. Suspended Sediment Concentration along San Bernard River with up to a 3-Day Difference in Acquisition Dates
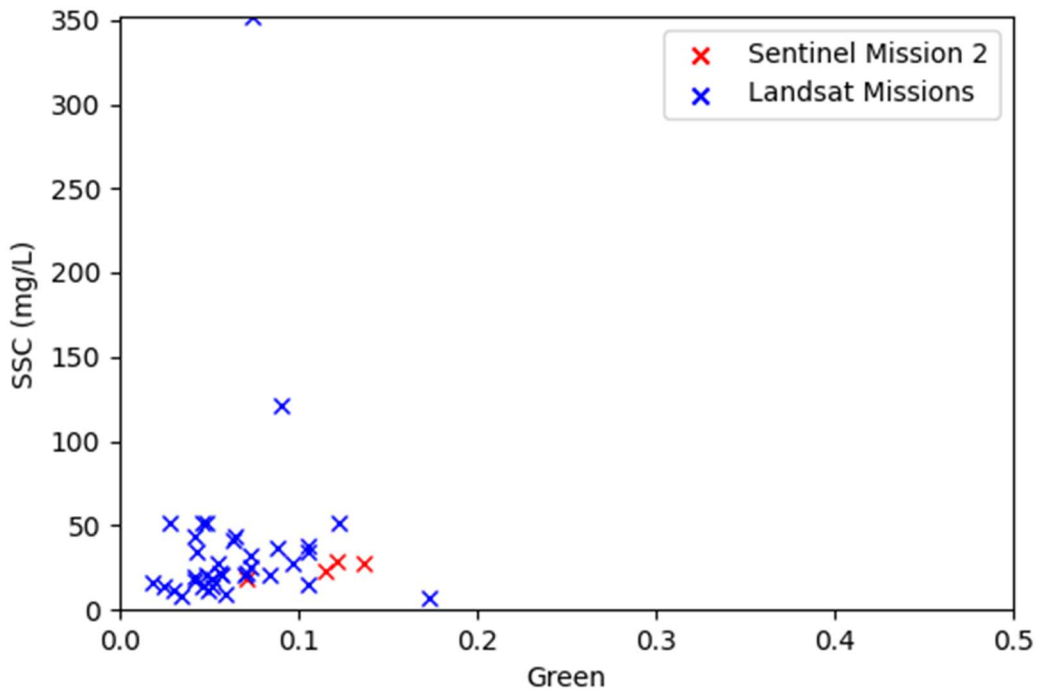


**Figure 3-26:** The Green Band vs. Suspended Sediment Concentration along San Bernard River with up to a 3-Day Difference in Acquisition Dates

**Figure 3-27:** The NIR Band vs. Suspended Sediment Concentration along San Bernard River with up to a 3-Day Difference in Acquisition Dates



**Figure 3-28:** The Red Band vs. Suspended Sediment Concentration along San Bernard River with up to a 3-Day Difference in Acquisition Dates

Sobel (2020) used rainfall totals of nearby rain gauges in their study in the previous five days of a suspended sediment sample to remove satellite image and suspended sediment concentration pairs that were not acquired on the same date. This was done because suspended sediment concentration is likely to change the most during rainfall/flood events and satellite images not taken on the same day during these events would potentially miss these changes. Nearby rain gauges did not appear to be strongly correlated to the suspended sediment concentration samples or flows collected for the work completed for this thesis. It was hypothesized that this was the case because the sample sites used in this thesis are near the mouth of the Brazos River and the flow and sediment load at these locations were influenced more by the upstream watershed of the Brazos River. Instead, daily mean flow data at USGS 08116650 (near Rosharon) was used to evaluate if a large change in flow occurred between satellite image and suspended sediment concentration acquisition. In Figure 3-29, an example of data points that were excluded because of the daily mean flow data is shown. As shown in this figure, the satellite image for sample points on 1/28/12 and 1/30/12 were taken 1 and 3 days before the suspended sediment concentration sample just before a major flood event. Thus, both sample points on 1/28/12 and 1/30/12 were removed from the dataset. In addition to removing points based on proximity to flood events, any satellite images that were linked to multiple suspended sediment concentration samples were only retained as a data pair for the closest sample date. An example of this is shown in Figure 3-29 for the sample points on 1/10/12 and 1/11/12 where the data pair for the sample on 1/10/12 was excluded from the final data set. This same methodology was used for suspended sediment concentration samples at TCEQMAIN-11843. Since no flow data was available near that sample site, it was assumed that the upstream gauge could be a good indication of flood events downstream. No flow data was available for the San Bernard River, so the flow removal technique was not used on that data set. All the flow, suspended sediment concentration, and acquisition lag figures developed for the Brazos River are provided in Appendices A and B.
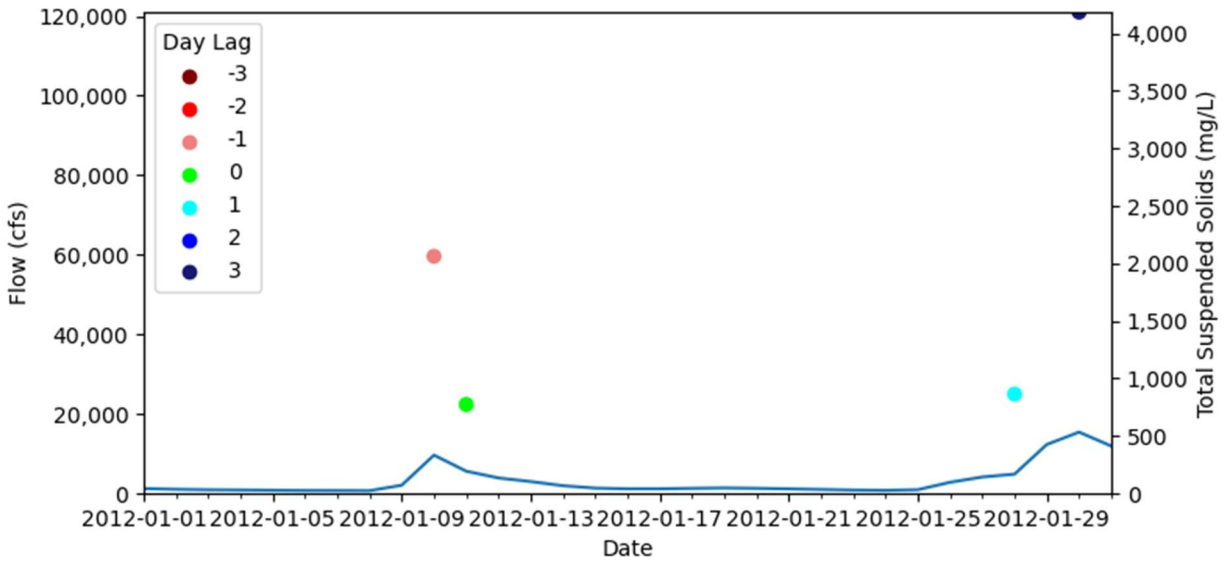
**Figure 3-29:** Example of Flow, Suspended Sediment Concentration, and Acquisition Lag

The resulting relationship between the six satellite bands and suspended sediment concentration following this removal technique are shown in Figure 3-30 through Figure 3-35. This data refinement resulted in a total of 210 (138 for Landsat missions and 72 for Sentinel Mission 2) satellite and suspended sediment concentration sample pairs for the Brazos River that were used for this study.
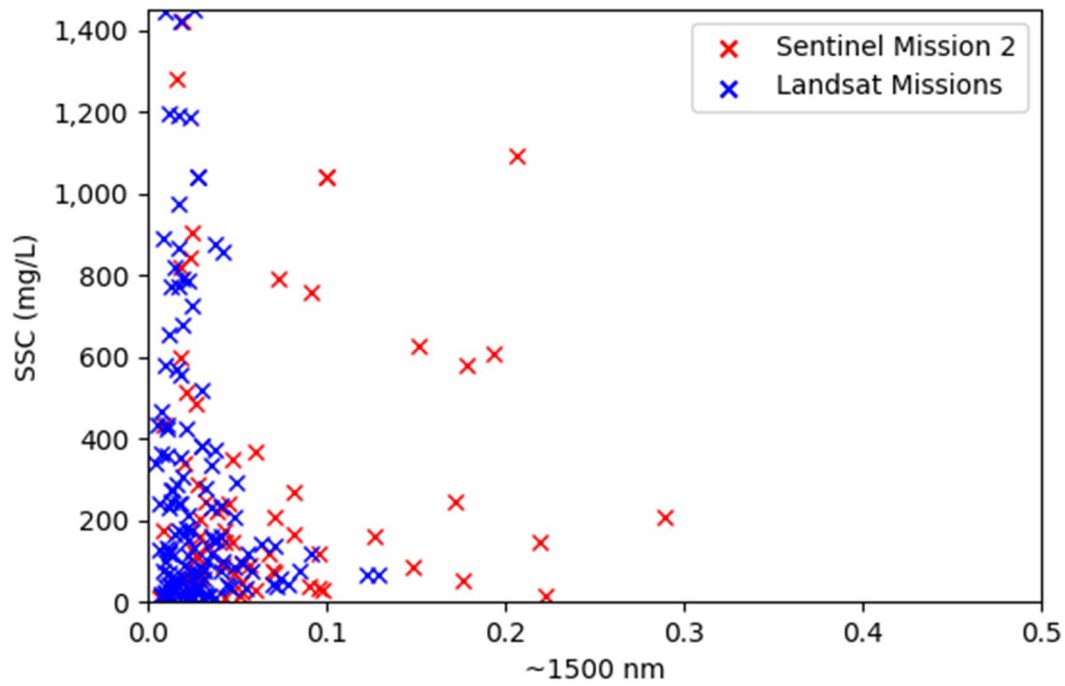
**Figure 3-30:** The 1500 nm Band vs. Suspended Sediment Concentration along Brazos River Following all Data Removal
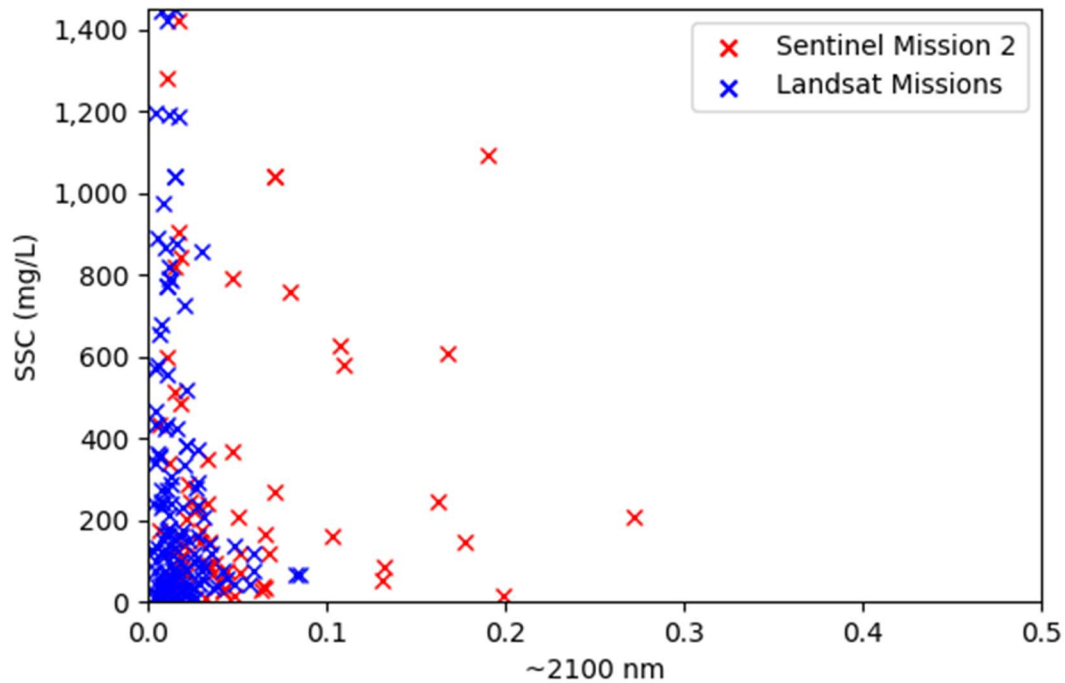


**Figure 3-31:** The 2100 nm Band vs. Suspended Sediment Concentration along Brazos River Following all Data Removal
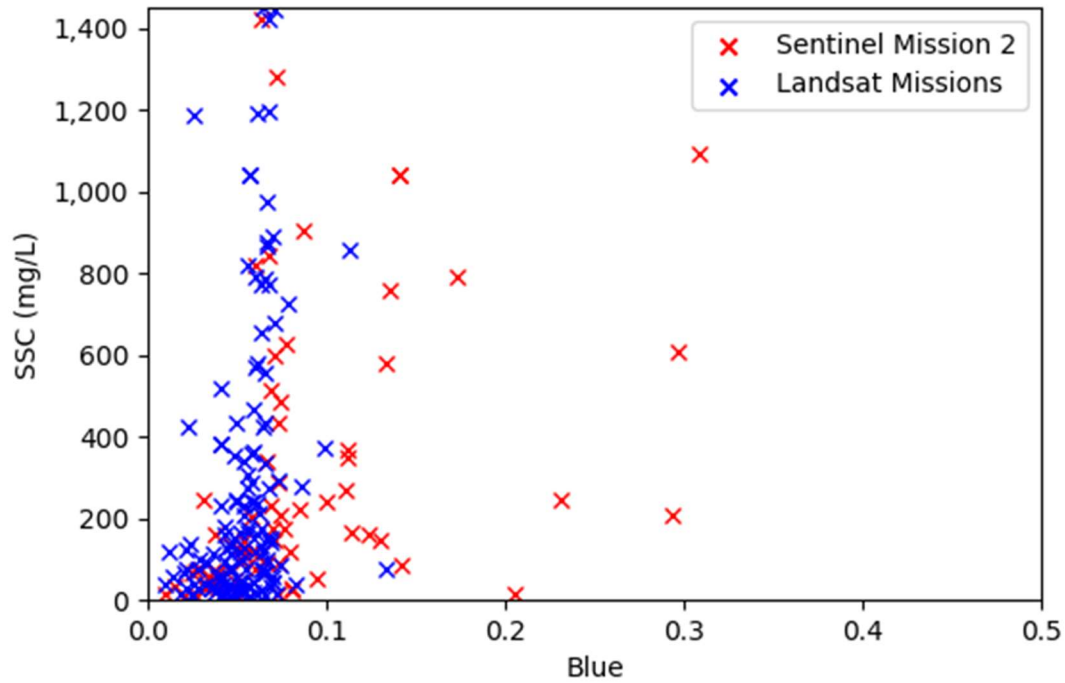
**Figure 3-32:** The Blue Band vs. Suspended Sediment Concentration along Brazos River Following all Data Removal
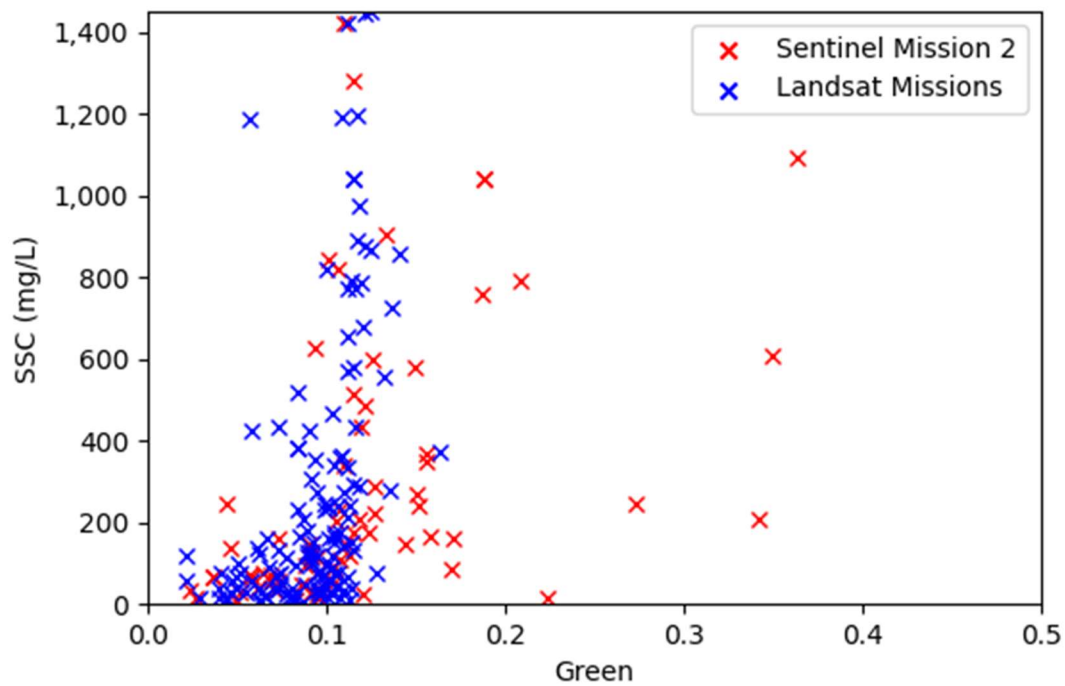


**Figure 3-33:** The Green Band vs. Suspended Sediment Concentration along Brazos River Following all Data Removal
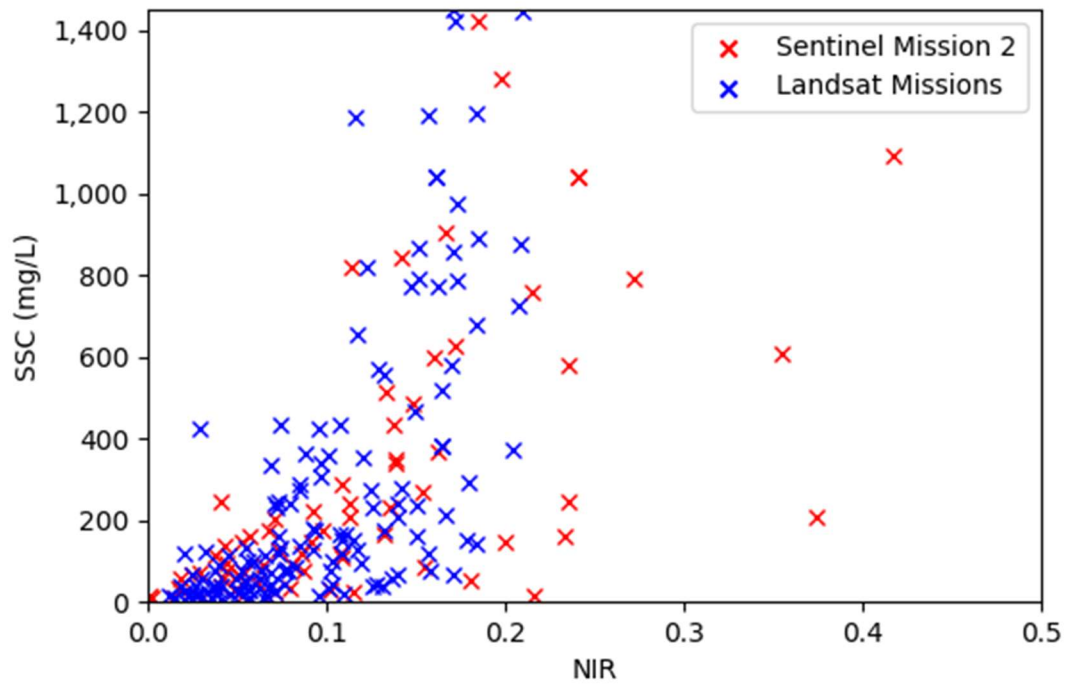
**Figure 3-34:** The NIR Band vs. Suspended Sediment Concentration along Brazos River Following all Data Removal
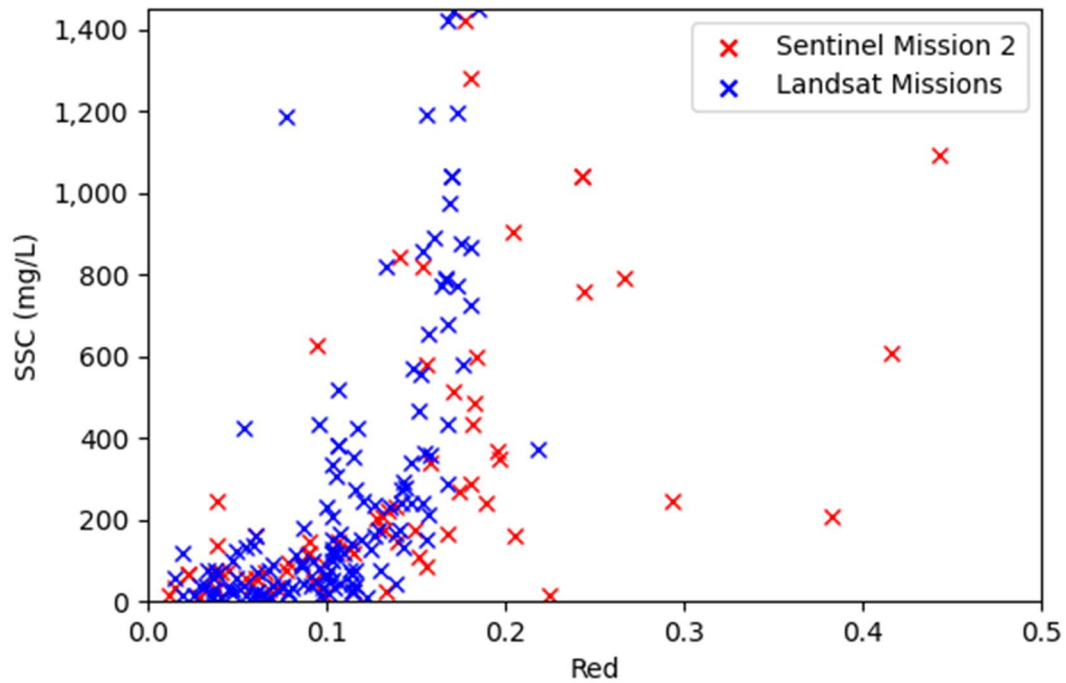


**Figure** 3-35: Red Band vs. Suspended Sediment Concentration along Brazos River Following all Data Removal

### 3.5    Modeling Techniques

The models evaluated in this study to estimate suspended sediment concentrations are listed below. The rating curve methods were also used to estimate the suspended sediment load, which is common practice for the flow rating curve method. The rating curve methods and exponential relationship were developed using the least squared regression technique. The methods used for the machine learning algorithms are discussed in more detail throughout this section.

- Rating Curve with Flow

- Rating Curve with Depth

- Exponential relationship with Satellite Data

- Support Vector Machine

- Artificial Neural Network

- Extreme Learning Machine

The exponential relationship was included because it is loosely related to the Lyzenga method used to estimate water depths and the propensity of optical water properties to follow the Beer-Lambert law. Equation (3.1) shows the general exponential relationship used to estimate suspended sediment concentrations where $a$ and $b$ are matrices of coefficients of size n by 1 where n is the number of satellite bands or band ratios used and $L(\lambda)$ are the surface reflectance bands or band ratios used to estimate suspended sediment concentrations. The equation is evaluated in such a way that each band or band ratio is evaluated by Equation (3.1) then added together to estimate suspended sediment concentrations. Also, the equation was limited to allow only positive values for components of $a$ to prevent the equation from returning negative values.

$$SSC = a * e^{b*L(\lambda)}$$
<div align="right">Equation (3.1)</div>

For the three machine learning algorithms used in this study (support vector machine, artificial neural network, and extreme learning machine), the algorithms were trained to estimate the natural logarithm of suspended sediment concentrations. These natural logarithm estimates were converted to true suspended sediment concentration estimates by using the exponential function before evaluating the average RSME. This extra conversion prevented the machine learning algorithms from producing

negative values. No data or function manipulations were used to force the rating curve methods to produce positive values.

Principal component analysis and canonical correlation analysis were used to evaluate the importance of variables to estimate suspended sediment concentrations and suspended sediment loads in the Brazos River. For these analyses, only data pairs at the upstream location near Rosharon were used where flow, depth, satellite data, and suspended sediment concentrations were available. All data variables were standardized for these analyses by subtracting each data variable point by the mean of the data variable and then dividing by the standard deviation of the data variable. This allowed for a direct comparison of data variable significance based on the analyses output. For the principal component analysis, the eigenvalues, proportions, and principal variates were used to evaluate the significance of data variables. For the canonical correlation analysis, only the canonical variates were used to evaluate the significance of data variables.

Past research has shown that certain bands, band ratios, and band combinations are more important to suspended sediment estimation than others when using surface reflectances. Sobel (2020) used red, NIR, and the square of NIR bands in various combinations to estimate suspended sediment concentration in Galveston Bay using Sentinel Mission 2 satellite data. Reisinger (2017) used the ratio between red and green bands to estimate total suspended solids within the Corpus Christi Bay using MODIS data. Chen (2015) used red, NIR, the difference of bands (red-NIR), sediment index ((red-NIR)/(red+NIR)), the ratio of NIR and red bands, and the log-ratio of NIR and red bands (log(NIR)/log(red)) to estimate total suspended solids for an estuary of Yangtze River and the Xuwen Coral Reef Protection Zone off the coast of China using MODIS data. Pereira (2018) used band ratios between red and green bands for Landsat Mission 8, and ratios between NIR and red, blue, and green bands for Landsat Missions 4-7 to estimate suspended sediment concentration and turbidity along the Mississippi and Missouri Rivers. All these different bands, band ratios, and band combinations were investigated in this study and included in the models evaluated. Table 3-8 summarizes the band combinations used for the models developed in this study.

**Table 3-8:** Band Combinations used for Models

| Name of Band Combination | Band Combinations |
|---|---|
| All Six Bands | ~2,100 nm, ~1,500 nm, Red, NIR, Green, Blue |
| Four Major Bands | Red, NIR, Green, Blue |
| Red | Red |
| NIR | NIR |
| Red Difference | Red-NIR |
| Sediment Index | (red-NIR)/(red+NIR) |
| NIR-Red Ratio | NIR/Red |
| NIR-Red log-Ratio | log(NIR)/log(Red) |
| Red Squared | $Red^2$ |
| NIR Squared | $NIR^2$ |
| Red-Green Ratio | Red/Green |
| NIR Ratios | NIR/Blue, NIR/Green, NIR/Red |

A training/test dataset split of 85%/15% was used for this study on the final satellite and suspended sediment concentration pairs discussed in the previous section resulting in a 179/31 split. Normally, machine learning approaches split the data into three sets, a training set, validation set, and test set with a 70%/15%/15% (Burkov 2019). This study instead used five-fold cross validation of the training set, which is a common practice according to Burkov (2020). The five-fold cross validation was used for hyperparameter tuning by evaluating the average RSME across the five folds. Following hyperparameter tunning, the hyperparameters with the lowest average RSME were selected to be trained on the entire training set.

The resulting distribution of the training/test data split is critical to the success of any machine learning algorithm. Both sets should be representative of the distribution that is expected to be experienced by the machine learning algorithm. Figure 3-36 illustrates the histogram of suspended sediment concentrations from the final satellite and suspended sediment concentration pairs used in this study for the Brazos River. As shown, the suspended sediment concentrations have a major class imbalance that would affect the training/test data distributions if a truly random data split approach were used. Thus, for this study, the final data pairs were split into the five classes listed below where each class was split into training/test data randomly to maintain a similar distribution between both sets.

- Suspended sediment concentrations less than 200 mg/L.

- Suspended sediment concentrations between 200 mg/L and 400 mg/L.

- Suspended sediment concentrations between 400 mg/L and 600 mg/L.

- Suspended sediment concentrations between 600 mg/L and 1,000 mg/L.

- Suspended sediment concentrations greater than 1,000 mg/L.
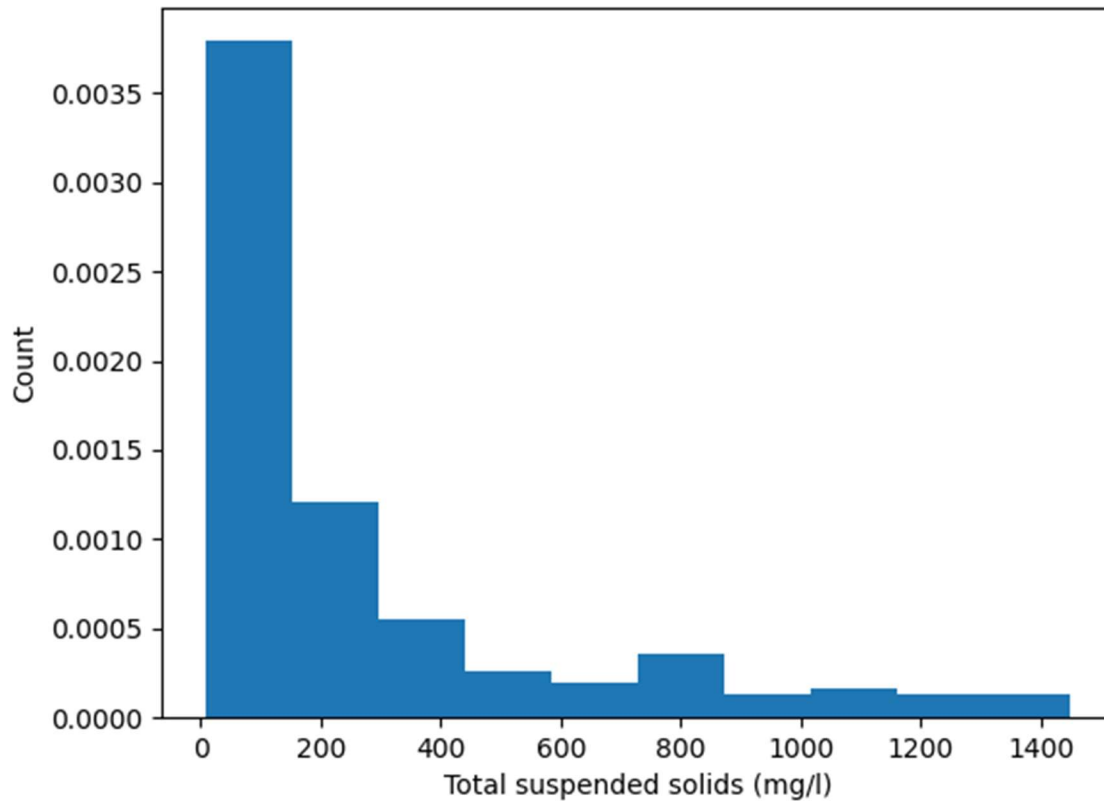


**Figure 3-36:** Histogram of Final Satellite and Suspended Sediment Concentrations Pairs for the Brazos River

The data points split into the test set were used to create test sets of the flow and depth suspended sediment concentration pairs to allow for more direct comparisons of the different model approaches using the Taylor diagram. The remaining data not selected in the test sets was used to train the flow and depth rating curves developed in this study. This resulted in a training/test data split of 470/29 for the flow and suspended sediment concentration pairs and 331/28 for the depth and suspended sediment concentration pairs. The test sets for these pairs of data are smaller than the satellite and suspended sediment concentration test set because there are some sample points represented by both Landsat and Sentinel satellite images.

The hyperparameter tuning approach used in this study was a grid search approach. The range of hyperparameters tuned for each of the three machine learning algorithms used in this study are listed in Table 3-9. The C, epsilon, alpha, and learning rate hyperparameters were evaluated in factors of ten, meaning the epsilon hyperparameters evaluated in the grid search were 0.1, 1, 10, 100, and 1000. The range of neurons in the hidden layer for the artificial neural network and extreme learning machine were based on Olyaie (2015) suggestions that the range of nodes in the hidden layer should be between $(2n^{1/2} + m)$ and $(2n + 1)$ where n is the number of input variables and m is the number of outputs. For band and band ratio combinations with only one input, the hidden layer ranges used for hyperparameter tuning could potentially lead to a more complicated model than required and was considered during evaluation of the models developed. Following the selection of the best performing hyperparameters, the tuned models were evaluated on the test datasets and graphed in the Taylor diagram for evaluation and comparison of model performances.

**Table 3-9:** Hyperparameter Tuning Grid Search Ranges

| Machine Learning Algorithm | Hyperparameters Tuned | Range of Hyperparameters Investigated |
|---|---|---|
| Support Vector Machine | Kernel | Linear, RBF, Sigmoid, Polynomial |
| | Degree[1] | 2, 3, 4, 5 |
| | Gamma[2] | 10/6, 1/6, 1/60, 1/600, 1/6000 |
| | C | $10^{-7}$ to $10^2$ |
| | Epsilon | $10^{-1}$ to $10^3$ |
| Artificial Neural Network[3] | Hidden Layer Size | 6 to 13 |
| | Activation Function | Relu, Sigmoid, Tanh |
| | Alpha | $10^{-7}$ to $10^3$ |
| | Learning Rate | $10^{-5}$ to $10^{-3}$ |
| | Momentum | 0.1, 0.3, 0.5, 0.7, 0.9 |
| Extreme Learning Machine | Alpha | $10^{-7}$ to $10^7$ |
| | Number of Neurons | 6 to 13 |
| | Activation Function | Relu, Sigmoid, Tanh |

[1]Degree inputs are only applicable for a polynomial kernel function.
[2]Gamma inputs are not applicable to the linear kernel function but are used for all other kernel functions investigated in this study.
[3]Artificial neural networks used stochastic gradient descent for weight optimization with a single hidden layer.

In addition to evaluating the performance of the models on the data pairs for the Brazos River, the satellite and suspended sediment concentration data pairs prepared for the San Bernard River were used to evaluate the models developed in this study. This means that the San Bernard River data was effectively used like an additional test set. Models developed for a river to estimate suspended sediment concentrations have historically only been applied to the river in which the data was collected from. Neither of the rating curve methods could be applied to the San Bernard River because flow and depth measurements have not been historically collected for this river by the USGS. Furthermore, rating curves are very specific to a given river and the rating curves on the Brazos River would likely not be able to successfully estimate the San Bernard River suspended sediment concentration even if flow and depth measurements were historically collected for the river. The performance of the models on the San Bernard River data were evaluated using the Taylor diagram.

## 4.0 Results and Discussion

### 4.1 Principal Component Analysis and Canonical Correlation Analysis

The principal component analysis results for the eigenvalues and proportions of variance are summarized in Table 4-1. This shows that the first three principal components created from this analysis account for just over 90% (90.2%) of the population's variance in explaining suspended sediment concentration and sediment load. Thus, to analyze the principal component weights, only these first three principal components were used.

**Table 4-1:** Principal Component Analysis Eigenvalue and Proportion of Variance

| Principal Component | Eigenvalue | Proportion of Variance (%) |
|---|---|---|
| 1 | 7.25 | 42.4 |
| 2 | 5.11 | 29.9 |
| 3 | 3.06 | 17.9 |
| 4 | 0.785 | 4.59 |
| 5 | 0.376 | 2.20 |
| 6 | 0.219 | 1.28 |
| 7 | 0.151 | 0.884 |
| 8 | 0.0642 | 0.376 |
| 9 | 0.0389 | 0.228 |
| 10 | 0.0155 | 0.0904 |
| 11 | 0.0125 | 0.0733 |
| 12 | 7.26E-03 | 0.0425 |
| 13 | 5.45E-03 | 0.0319 |
| 14 | 1.81E-03 | 0.0106 |
| 15 | 1.37E-03 | 8.03E-03 |
| 16 | 7.53E-04 | 4.40E-03 |
| 17 | 2.95E-32 | 1.73E-31 |

Table 4-2 summarizes the principal component vectors for the first three components and the rankings developed based on these vectors. Ranks were assigned to each variable in a principal component by the absolute value of the variable's vector component. Overall rank scores were developed by using the weighted average of the rank and proportion of variance of the principial component. The top six variables based on the overall rank score developed from this analysis are the following: Blue, NIR-Blue Ratio, Sediment Index, NIR-Red log-Ratio, Red-Green Ratio, and NIR Squared. It is surprising that the overall rank score resulted in the blue band being the best because it is more common the NIR and/or red bands are more important for estimating suspended sediment concentration and sediment load. The five other variables in the top six are consistent with this expectation as they are various combinations of

the NIR and/or red bands. It is also surprising that daily mean flow did not rank higher in this analysis given the rating curve is commonly applied in river applications to estimate suspended sediment concentration and/or sediment load.

**Table 4-2:** Principal Component Vectors and Ranks

| Component/ Variable | Principal Component 1 | | Principal Component 2 | | Principal Component 3 | | Overall Rank Score |
|---|---|---|---|---|---|---|---|
| | Vector | Rank | Vector | Rank | Vector | Rank | |
| Blue | 0.344 | 3 | 0.353 | 3 | 0.352 | 3 | 3.00 |
| Green | 0.070 | 13 | 0.107 | 9 | 0.105 | 11 | 11.28 |
| Red | 0.173 | 9 | 0.077 | 13 | -0.079 | 14 | 11.32 |
| NIR | 0.026 | 16 | -0.084 | 12 | -0.144 | 8 | 13.09 |
| ~1500 nm | -0.174 | 8 | -0.094 | 11 | -0.126 | 9 | 9.19 |
| ~2100 nm | -0.138 | 10 | -0.027 | 16 | -0.106 | 10 | 11.99 |
| Red Difference | -0.072 | 12 | -0.123 | 7 | 0.002 | 17 | 11.33 |
| Sediment Index | 0.273 | 4 | 0.434 | 2 | 0.169 | 5 | 3.54 |
| NIR-Red Ratio | 0.205 | 7 | 0.230 | 4 | -0.007 | 16 | 7.79 |
| NIR-Red log-Ratio | 0.644 | 1 | -0.104 | 10 | -0.345 | 4 | 4.58 |
| Red Squared | 0.054 | 15 | 0.033 | 15 | -0.081 | 13 | 14.60 |
| NIR Squared | -0.223 | 6 | 0.109 | 8 | 0.145 | 7 | 6.86 |
| Red-Green Ratio | 0.383 | 2 | -0.174 | 6 | -0.085 | 12 | 5.31 |
| NIR-Blue Ratio | 0.229 | 5 | -0.701 | 1 | 0.372 | 2 | 3.08 |
| NIR-Green Ratio | 0.073 | 11 | -0.196 | 5 | 0.149 | 6 | 8.02 |
| Daily Mean Flow | -0.055 | 14 | 0.035 | 14 | -0.063 | 15 | 14.20 |
| Gauge Height | -6.77E-16 | 17 | 4.05E-16 | 17 | -0.680 | 1 | 13.83 |

Table 4-3 summarizes the canonical coefficients and rankings developed based on these coefficients. The canonical coefficients are the weights of the different variables assigned to estimate the respective canonical prediction. Ranks were assigned based on the absolute value of these canonical coefficients. The overall rank score was taken as the average of the two ranks for the two canonical predictions. The top six variables based on the overall rank score developed from this analysis are the following: Sediment Index, NIR-Red log-Ratio, Green, Red, Daily Mean Flow, and Red Difference. The red band and daily mean flow had the exact same overall rank score and were tied for the fourth best overall rank. The results from this analysis are more consistent with what is to be expected as different combinations of the NIR and Red bands and the daily mean flow had five of the top six overall rank scores. The green band is a little surprising as this is not a band that is commonly used to estimate suspended sediment concentration and sediment load. The green band has commonly been used to signify the presence of organic material such as chlorophyll-α.

**Table 4-3:** Canonical Correlation Analysis Coefficients and Ranks

| Component/ Variable | Canonical 1 | | Canonical 2 | | Overall Rank Score |
|---|---|---|---|---|---|
| | Coefficient | Rank | Coefficient | Rank | |
| Blue | 0.080 | 14 | 0.037 | 12 | 13.0 |
| Green | -0.634 | 2 | -0.313 | 3 | 2.5 |
| Red | 0.469 | 6 | 0.231 | 5 | 5.5 |
| NIR | 0.381 | 7 | 0.092 | 11 | 9.0 |
| ~1500 nm | -0.073 | 15 | 0.034 | 14 | 14.5 |
| ~2100 nm | 0.030 | 16 | -0.026 | 16 | 16.0 |
| Red Difference | 0.214 | 10 | 0.304 | 4 | 7.0 |
| Sediment Index | 0.666 | 1 | 0.352 | 2 | 1.5 |
| NIR-Red Ratio | 0.084 | 13 | 0.034 | 13 | 13.0 |
| NIR-Red log-Ratio | -0.571 | 3 | -0.402 | 1 | 2.0 |
| Red Squared | 0.169 | 12 | -0.169 | 8 | 10.0 |
| NIR Squared | -0.232 | 9 | 0.180 | 7 | 8.0 |
| Red-Green Ratio | -0.234 | 8 | -0.154 | 9 | 8.5 |
| NIR-Blue Ratio | -0.002 | 17 | 0.008 | 17 | 17.0 |
| NIR-Green Ratio | 0.188 | 11 | 0.115 | 10 | 10.5 |
| Daily Mean Flow | -0.511 | 5 | 0.192 | 6 | 5.5 |
| Gauge Height | 0.527 | 4 | -0.032 | 15 | 9.5 |

Based on the principal component analysis and canonical correlation analysis overall ranks, the NIR, red, and green bands were suspected to be the most important for estimating the suspended sediment concentration for the Brazos River. Commonly, the principal component vectors and/or the canonical coefficients are used as inputs for machine learning algorithms. This was not employed in this study because the resulting principal component vectors and canonical coefficients are very dependent on the data used to develop them, which could cause the machine learning algorithms to experience high variance by performing well on the training data but poorly on the test data. Thus, the results of these two analyses were only used to help identify variables that could be important for estimating suspended sediment concentrations for within this study.

## 4.2 Model Development

### 4.2.1 Rating Curve Model Development

Table 4-4 summarizes the resulting models for the rating curves developed for this study. The rating curves summarized in Table 4-4 are a power function with the form outlined by Equation (2.1). The sediment load mentioned in Table 4-4 is only for suspended sediments and replaces SSC in the power function. Coefficients *a* and *b* are based on the result of the least squares regression on the training data

set while the RSME, R, and $\sigma_{\widehat{y_n}}$ are based on the model predictions for the test data set. RSME and $\sigma_{\widehat{y_n}}$ were not calculated for the rating curves used to estimate sediment load because they were not compared to the other models using the Taylor Diagram. The units of coefficient $a$ are such that the model return the units of the variable it is trying to predict. For example, the $a$ coefficient for the flow vs. SSC rating curve has units of mg/L×(cfs)$^{-b}$. All of the rating curves result in relatively good performance of predicting the test data set with $R^2$ above 0.75. The rating curves developed to estimate sediment load perform better than their counterparts developed to estimate suspended sediment concentration resulting in $R^2$ above 0.95 for the test data set.

Storm (2013) developed a flow rating curve to estimate suspended sediment load that resulted in coefficients of $a$ and $b$ of 0.002 and 1.737, respectively. These coefficients are based on the model developed for the historical and field data collected during the Storm (2013) study. The Storm (2013) model for flow vs. sediment load is slightly different than the flow vs. sediment load model summarized in Table 4-4. The difference in the model from Storm (2013) results in higher sediment load estimates for higher flows than the model summarized in Table 4-4. This difference is likely a result of the use of TCEQMAIN-16355 total suspended sediment data and the inclusion of historical data beyond 2010. Most of the time, suspended sediment concentration samples are expected to be relatively low compared to those collected during flood events just following a storm. Most of the samples collected by USGS and TCEQ at the Rosharon gauge are likely during non-flood events which result in the model summarized in Table 4-4 to lead to lower sediment load predictions than the model developed in Storm (2013). This fact of the data could also lead to models not performing well for higher suspended sediment concentrations and will be discussed further for the models that use satellite image data inputs.

**Table 4-4:** Rating Curve Methods' Results

| Model | $a^1$ | $b$ | RSME (mg/L) | R | $\sigma_{\hat{y}_n}$ (mg/L) |
|---|---|---|---|---|---|
| SSC vs. Flow | 8.80 | 0.455 | 158 | 0.87 | 324 |
| Sediment Load vs. Flow | 11.5 | 0.848 | N/A$^2$ | 0.98 | N/A$^2$ |
| SSC vs. Flow Depth | 54.0 | 0.782 | 176 | 0.86 | 221 |
| Sediment Load vs. Flow Depth | 335 | 1.52 | N/A$^2$ | 0.98 | N/A$^2$ |

[1]Coefficient *a* has units that result in the units of the variable being predicted by the model. SSC is in units of mg/L and sediment load is in units of Tons/day.
[2]The two rating curves developed to estimate sediment load were not evaluated using the Taylor Diagram method.

### 4.2.2 Exponential Relationship Model Development

Table 4-5 summarizes the resulting models for the exponential relationship developed for this study. Coefficients *a* and *b* are based on the result of the least squares regression on the training data set while the RSME, R, and $\sigma_{\hat{y}_n}$ are based on the model predictions for the test data set. Only the model that used the Red-Green Ratio as an input variable performed well with a $R^2$ of above 0.75 (0.83). All other models performed significantly worse than this model. It is surprising that the models that used the Sediment Index and NIR-Red log-Ratio performed the worst given how well they ranked in the principal component analysis and canonical correlations analysis.

**Table 4-5:** Exponential Model Results

| Band Combination | $a$ | $b$ | RSME (mg/L) | R | $\sigma_{\hat{y}_n}$ (mg/L) |
|---|---|---|---|---|---|
| All Six Bands | [1.36e-05, 6.38, 38.2, 61.8, 79.0, 97.3] | [-11.5, 1.04, 4.58, 6.82, -41.2, -45.3] | 278 | 0.70 | 65 |
| Four Major Bands | [3.91e-05, 6.58, 58.0, 89.4] | [-4.71, -1.54, 4.49, 5.66] | 27* | 0.58 | 84 |
| Red | [162] | [4.60] | 277 | 0.57 | 93 |
| NIR | [159] | [5.12] | 280 | 0.59 | 80 |
| Red Difference | [289] | [-5.06] | 331 | -0.30 | 35 |
| Sediment Index | [298] | [-1.02] | 328 | -0.07 | 54 |
| NIR-Red Ratio | [202] | [0.342] | 327 | -0.15 | 40 |
| NIR-Red log-Ratio | [1123] | [-1.32] | 329 | -0.12 | 51 |
| Red Squared | [241] | [7.97] | 301 | 0.46 | 46 |
| NIR Squared | [239] | [9.65] | 303 | 0.52 | 34 |
| Red-Green Ratio | [2.85] | [3.78] | 133 | 0.91 | 277 |
| NIR Ratios | [66.4, 5.71e-06, 51.4] | [-1.21, 0.292, 1.45] | 284 | 0.47 | 109 |

4.2.3    Machine Learning Algorithm Model Development

Table 4-6 through Table 4-8 summarize the best performing hyperparameters following the grid search conducted in this study. The average RSME is the average of the RSME for the five folds of data used during the five-fold cross-validation. No single hyperparameter was consistent for a given algorithm, except the learning rate for the artificial neural network. This can be expected given that the best performing hyperparameter for a given algorithm can vary drastically with a minor change in the input variables. Based on the average RSME from the hyperparameter tuning process, the best performing input variables across the different models are the following (order does not signify anything): All Six Bands, Four Major Bands, Red-Green Ratio, and NIR Ratios.

**Table 4-6:** Support Vector Machine Hyperparameter Tuning Results

| Band Combination | Kernel | Degree | Gamma | C | Epsilon | Average RSME (mg/L) |
|---|---|---|---|---|---|---|
| All Six Bands | Radial Basis Function (RBF) | N/A | 1/6 | 1,000 | 0.1 | 193 |
| Four Major Bands | RBF | N/A | 1/6 | 1,000 | 0.1 | 191 |
| Red | Sigmoid | N/A | 10/6 | 1,000 | 0.1 | 275 |
| NIR | RBF | N/A | 10/6 | 1,000 | 0.1 | 278 |
| Red Difference | RBF | N/A | 10/6 | 100 | 1.0 | 363 |
| Sediment Index | RBF | N/A | 10/6 | 1,000 | 1.0 | 339 |
| NIR-Red Ratio | RBF | N/A | 10/6 | 1,000 | 1.0 | 338 |
| NIR-Red log-Ratio | RBF | N/A | 10/6 | 100 | 1.0 | 348 |
| Red Squared | Sigmoid | N/A | 1/60 | 1,000 | 0.1 | 347 |
| NIR Squared | Sigmoid | N/A | 1/60 | 1,000 | 0.1 | 343 |
| Red-Green Ratio | Polynomial | 2 | 1/6 | 1,000 | 1.0 | 247 |
| NIR Ratios | RBF | N/A | 1/60 | 1,000 | 0.1 | 200 |

**Table 4-7:** Artificial Neural Network Hyperparameter Tuning Results

| Band Combination | Hidden Layer Size | Activation Function | Alpha | Learning Rate | Momentum | Average RSME (mg/L) |
|---|---|---|---|---|---|---|
| All Six Bands | 12 | Relu | $10^{-7}$ | 0.01 | 0.9 | 240 |
| Four Major Bands | 6 | Relu | $10^{-7}$ | 0.01 | 0.9 | 265 |
| Red | 9 | Tanh | $10^{-7}$ | 0.01 | 0.7 | 333 |
| NIR | 11 | Relu | $10^{-7}$ | 0.01 | 0.5 | 324 |

| | | | | | | |
|---|---|---|---|---|---|---|
| Red Difference | 8 | Logistic | $10^{-7}$ | 0.01 | 0.9 | 338 |
| Sediment Index | 8 | Logistic | $10^{-7}$ | 0.01 | 0.9 | 336 |
| NIR-Red Ratio | 6 | Logistic | 10 | 0.01 | 0.9 | 338 |
| NIR-Red log-Ratio | 7 | Logistic | $10^{-7}$ | 0.01 | 0.9 | 338 |
| Red Squared | 9 | Logistic | 1 | 0.01 | 0.9 | 339 |
| NIR Squared | 9 | Logistic | 1 | 0.01 | 0.9 | 339 |
| Red-Green Ratio | 10 | Relu | $10^{-7}$ | 0.001 | 0.9 | 251 |
| NIR Ratios | 9 | Relu | $10^{-3}$ | 0.01 | 0.9 | 214 |

**Table 4-8:** Extreme Learning Machine Hyperparameter Tuning Results

| Band Combination | Alpha | Number of Neurons | Activation Function | Average RSME (mg/L) |
|---|---|---|---|---|
| All Six Bands | $10^{-6}$ | 12 | Tanh | 193 |
| Four Major Bands | $10^{-5}$ | 8 | Tanh | 190 |
| Red | $10^{-7}$ | 6 | Tanh | 301 |
| NIR | $10^{-7}$ | 6 | Tanh | 284 |
| Red Difference | $10^{-7}$ | 6 | Tanh | 366 |
| Sediment Index | $10^{-7}$ | 7 | Relu | 346 |
| NIR-Red Ratio | $10^{-7}$ | 13 | Tanh | 348 |
| NIR-Red log-Ratio | $10^{-7}$ | 6 | Tanh | 357 |
| Red Squared | 0.1 | 8 | Tanh | 353 |
| NIR Squared | 0.1 | 8 | Tanh | 351 |
| Red-Green Ratio | $10^{-4}$ | 6 | Tanh | 251 |
| NIR Ratios | $10^{-6}$ | 7 | Sigmoid | 211 |

Table 4-9 summarizes the RSME, R, and $\sigma_{\hat{y}_n}$ based on the model predictions for the test data set for all the machine learning algorithm and input combinations used in this study. The best performing hyperparameters from the hyperparameter tuning process were used to train each model to the entire training set. The trained models were then used to create predictions for the test set to create the RSME, R, and $\sigma_{\hat{y}_n}$ values. Just like during the hyperparameter tuning process, the best performing machine learning algorithms had the four following inputs: All Six Bands, Four Major Bands, Red-Green Ratio, and NIR Ratios. All of the models that used these inputs had $R^2$ of above 0.75. The support vector machine that used the red band as an input also performed reasonably well with a $R^2$ of 0.69. All other models performed significantly worse than this. Also, in general, it appears that the Red-Green Ratio was the most influential input variable as the R value for the NIR Ratios, Four Major Bands, and All Six Bands models were only slightly better than or the same as those achieved with the Red-Green Ratio models. Again, it is surprising that the models that used the NIR-Red log-Ratio performed the worst given how

well they ranked in the principal component analysis and canonical correlations analysis. This could indicate there could be a flaw in using the absolute value of principal component vector weights and canonical coefficients to rank the importance of input variables instead of using a more statistically rooted method to determine statistical significance.

**Table 4-9:** Machine Learning Algorithm Results

| Machine Learning Algorithm | Band Combination | RSME (mg/L) | R | $\sigma_{\widehat{y_n}}$ (mg/L) |
|---|---|---|---|---|
| Support Vector Machine | All Six Bands | 142 | 0.91 | 243 |
| | Four Major Bands | 131 | 0.92 | 265 |
| | Red | 200 | 0.83 | 174 |
| | NIR | 255 | 0.60 | 176 |
| | Red Difference | 324 | -0.30 | 16 |
| | Sediment Index | 300 | 0.40 | 59 |
| | NIR-Red Ratio | 293 | 0.45 | 74 |
| | NIR-Red log-Ratio | 312 | 0.25 | 37 |
| | Red Squared | 305 | 0.41 | 40 |
| | NIR Squared | 307 | 0.50 | 25 |
| | Red-Green Ratio | 138 | 0.90 | 270 |
| | NIR Ratios | 140 | 0.92 | 236 |
| Artificial Neural Network | All Six Bands | 179 | 0.91 | 170 |
| | Four Major Bands | 180 | 0.92 | 163 |
| | Red | 286 | 0.44 | 140 |
| | NIR | 284 | 0.52 | 84 |
| | Red Difference | 319 | -0.29 | 1 |
| | Sediment Index | 319 | -0.02 | 10 |
| | NIR-Red Ratio | 320 | -0.12 | 5 |
| | NIR-Red log-Ratio | 319 | -0.06 | 1 |
| | Red Squared | 319 | -0.54 | 1 |
| | NIR Squared | 319 | -0.57 | 0 |
| | Red-Green Ratio | 172 | 0.90 | 186 |
| | NIR Ratios | 178 | 0.90 | 176 |
| Extreme Learning Machine | All Six Bands | 138 | 0.92 | 242 |
| | Four Major Bands | 133 | 0.92 | 254 |
| | Red | 280 | 0.51 | 220 |
| | NIR | 268 | 0.55 | 151 |
| | Red Difference | 325 | -0.30 | 18 |
| | Sediment Index | 300 | 0.41 | 58 |
| | NIR-Red Ratio | 304 | 0.37 | 53 |
| | NIR-Red log-Ratio | 314 | 0.20 | 31 |
| | Red Squared | 306 | 0.42 | 34 |
| | NIR Squared | 309 | 0.50 | 21 |
| | Red-Green Ratio | 142 | 0.91 | 248 |
| | NIR Ratios | 143 | 0.92 | 221 |

**4.3     Model Performance**

4.3.1    Taylor Diagram Analysis for the Brazos River

Figure 4-1 illustrates the Taylor Diagram for the models developed for the Brazos River in this study. All RSME, R, and standard deviations are based on model performance to the test data sets. For the flow and depth rating curves, the test data sets had a slightly different size than the test data set for the satellite data. As a result, the flow and depth test data sets have a slightly different standard deviation than the test data set for the satellite data. For the purposes of this study and the Taylor Diagram analysis, it was assumed this difference was negligible. The difference between the standard deviations in the test sets was also deemed acceptable because the flow and depth rating curves were indented to primarily be a baseline comparison to the models developed using the satellite data since they could not be applied outside of the Brazos River. For the Taylor Diagram analysis, the goal of the models is to be as close to the reference data set (test data set in this study) as possible. This usually results in a high correlation coefficient, a low RSME, and a standard deviation produced by the model predictions that is the same as the standard deviation of the reference data set (test data set in this study). As noted by Taylor (2001) the Taylor Diagram does not provide a statistically significant measure of model performance, and it was thus used to help visualize and generally compare the model performance between the different models.

As shown in Figure 4-1, there is a cluster of sixteen (16) models that perform significantly better than the remaining models based on their correlation coefficients. These models include the depth and flow rating curves, the exponential relationship with the Red-Green Ratio input, the support vector machine with Red Band input, and the twelve (12) machine learning algorithms with All Six Bands, Four Major Bands, Red-Green Ratio, and NIR Ratios as inputs. All these models perform in a relatively tight region of R and RSME values and are probably all reasonable to be deployed for the Brazos River. The three models that result in predictions with a standard deviation closest to the standard deviation of the test data set are the flow rating curve, the exponential relationship with the Red-Green Ratio as an input, and the support vector machine with the Red-Green Ratio as an input. In general, the four extreme learning machine and support vector machine models with All Six Bands, Four Major Bands, Red-Green

Ratio, and NIR Ratios as inputs have the lowest average RSME compared to other algorithms. The one-to-one comparison for all of the models to the training and test data sets are provided in Appendix C.
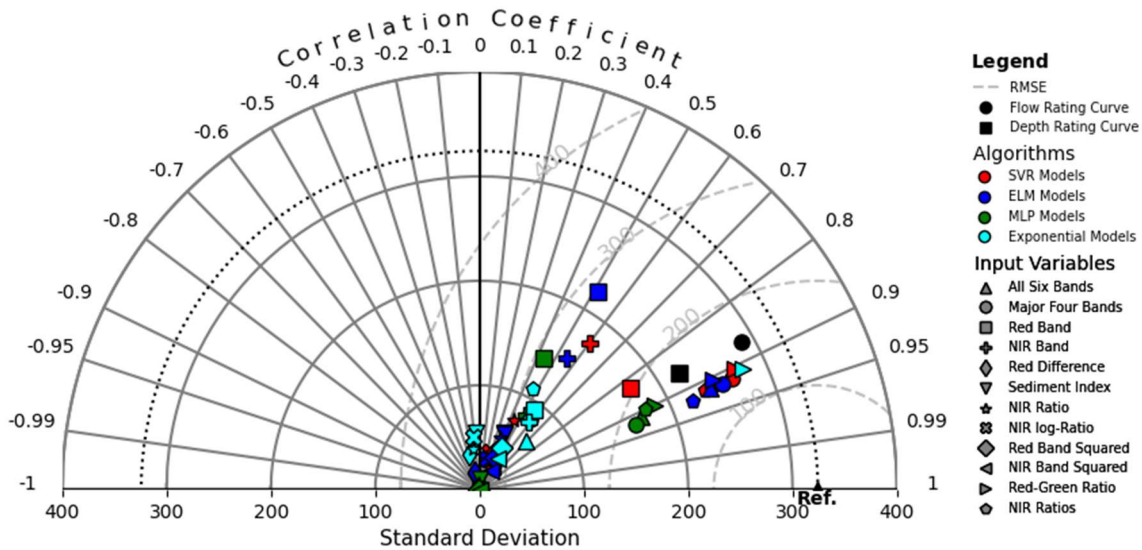


**Figure 4-1:** Taylor Diagram for Brazos River Data

### 4.3.2 Performance of Models on San Bernard River

Table 4-10 summarizes the RSME, R, and $\sigma_{\widehat{y}_n}$ based on the model predictions for the San Bernard River data. All models are those that were developed using the Brazos River training data set. Only the models developed using the satellite data were evaluated on the San Bernard River. These results are also illustrated in Figure 4-2 as a Taylor Diagram. The reference data depicted in this figure is the San Benard River data collected for this study. In general, all the models developed for the Brazos River perform very poorly based on the RSME and R calculated. None of the models developed for the Brazos River result in a $R^2$ greater than 0.04 on the San Bernard River data. The one-to-one comparison for all of the models to the San Bernard River data are provided in Appendix C. In general, the San Bernard River data has significantly lower suspended sediment concentrations than the Brazos River. All the best performing models on the San Bernard River data according to the RSME and R values generally overestimate the suspended sediment concentrations for the San Bernard River. This could indicate that the reflectance values for the San Bernard River data could be influenced by the river bottom reflectance component or different sediment type carried by this river. The sediment carried by these two

rivers might be optically different. The poor performance of the models on the San Bernard River data could also indicate that the models should not be applied outside of the Brazos River.



**Figure 4-2:** Taylor Diagram for San Bernard River Data

**Table 4-10:** Model Results on San Bernard River

| Model Algorithm | Band Combination | RSME (mg/L) | R | $\sigma_{\widehat{y_n}}$ (mg/L) |
|---|---|---|---|---|
| Support Vector Machine | All Six Bands | 62 | 0.20 | 134 |
| | Four Major Bands | 116 | 0.01 | 33 |
| | Red | 125 | 0.04 | 40 |
| | NIR | 146 | -0.04 | 61 |
| | Red Difference | 67 | -0.13 | 27 |
| | Sediment Index | 62 | 0.15 | 13 |
| | NIR-Red Ratio | 74 | 0.16 | 65 |
| | NIR-Red log-Ratio | 58 | 0.11 | 84 |
| | Red Squared | 55 | 0.04 | 105 |
| | NIR Squared | 87 | -0.08 | 134 |
| | Red-Green Ratio | 92 | 0.18 | 33 |
| | NIR Ratios | 109 | 0.17 | 40 |
| Artificial Neural Network | All Six Bands | 64 | 0.15 | 42 |
| | Four Major Bands | 166 | -0.04 | 154 |
| | Red | 71 | 0.05 | 49 |
| | NIR | 151 | -0.07 | 137 |
| | Red Difference | 54 | -0.13 | 2 |
| | Sediment Index | 56 | -0.10 | 9 |
| | NIR-Red Ratio | 55 | -0.12 | 6 |
| | NIR-Red log-Ratio | 54 | -0.10 | 1 |
| | Red Squared | 54 | -0.05 | 0 |
| | NIR Squared | 54 | 0.07 | 0 |
| | Red-Green Ratio | 96 | 0.21 | 91 |
| | NIR Ratios | 106 | 0.13 | 98 |
| Extreme Learning Machine | All Six Bands | 66 | 0.13 | 45 |
| | Four Major Bands | 123 | -0.00 | 110 |
| | Red | 98 | 0.02 | 83 |
| | NIR | 147 | -0.06 | 134 |
| | Red Difference | 67 | -0.13 | 33 |
| | Sediment Index | 66 | 0.21 | 53 |
| | NIR-Red Ratio | 66 | 0.16 | 48 |
| | NIR-Red log-Ratio | 57 | 0.12 | 27 |
| | Red Squared | 55 | 0.04 | 11 |
| | NIR Squared | 78 | -0.08 | 53 |
| | Red-Green Ratio | 86 | 0.18 | 78 |
| | NIR Ratios | 116 | 0.11 | 109 |
| Exponential | All Six Bands | 100 | -0.07 | 80 |
| | Four Major Bands | 107 | -0.03 | 90 |
| | Red | 68 | 0.09 | 47 |
| | NIR | 127 | -0.05 | 112 |
| | Red Difference | 90 | -0.13 | 66 |
| | Sediment Index | 81 | -0.11 | 55 |
| | NIR-Red Ratio | 75 | -0.12 | 45 |
| | NIR-Red log-Ratio | 84 | -0.12 | 59 |
| | Red Squared | 56 | 0.04 | 16 |
| | NIR Squared | 95 | -0.08 | 74 |
| | Red-Green Ratio | 114 | 0.19 | 112 |
| | NIR Ratios | 204 | -0.08 | 193 |

### 4.3.3 Summary of Model Performance

Based on the work completed in this study, sixteen (16) models as listed below were developed that can be reasonably applied to the Brazos River.

- Depth Rating Curve

- Flow Rating Curve

- Exponential Relationship with the Red-Green Ratio as an input

- Support Vector Machine with the Red Band as an input

- Support Vector Machines, Artificial Neural Networks, and Extreme Learning Machines with the following inputs:
  - All Six Bands
  - Four Major Bands
  - Red-Green Ratio
  - NIR-Ratios

All sixteen of the models developed performed similar on the test data sets based on RSME and R values with the extreme learning machine and support vector machine with the four major bands as an input performing the best. The $R^2$ for all of these models range from approximately 0.69 to 0.85. The fourteen (14) models developed using satellite data inputs can be reasonably applied from the mouth of the river to northernmost gauging location near Rosharon, Texas used in this study.

The Red-Green Ratio appeared to be the most influential to estimating suspended sediment concentration based on the best performing models according to the Taylor Diagram analysis and the results of the principal component and canonical correlation analyses. This band ratio as an input into the exponential relationship model was the simplest model outside of the rating curve methods developed for this study. This simplicity makes this model slightly more preferable over the others because it can be easily understood, applied, and modified to similar areas in the future. Furthermore, the exponential model with the Red-Green Ratio input had an $R^2$ of 0.83 and an RSME of 133 mg/L on the test data which are only slightly worse than the best performing models which had an $R^2$ of 0.85 and an RSME of 131 mg/L on the test data.

Despite the development of numerous models that performed well on the Brazos River, none of these models performed well when applied to the San Bernard River data. In general, the San Bernard River data has significantly lower suspended sediment concentrations than the Brazos River. All the best performing models on the San Bernard River data according to the RSME and R values generally overestimate the suspended sediment concentrations for the San Bernard River. This could indicate that the reflectance values for the San Bernard River data could be influenced by the bottom reflectance component and suspended sediment that is optically different from the Brazos River sediment. The poor performance of the models on the San Bernard River data could also indicate that the models should not be applied outside of the Brazos River.

## 4.4    Case Study

One of the best performing models developed during this study was applied to the Brazos River and a portion of its estuary to estimate suspended sediment concentrations before, during, and after Hurricane Harvey. Hurricane Harvey was a catastrophic hurricane that lasted from August 17, 2017 to September 3, 2017 that made landfall on Texas near Houston on August 30, 2017. This hurricane resulted in some of the highest, if not the highest, rainfall totals on record in the area and resulted in the highest daily mean flow rate over the data recorded for USGS-08116650 near Rosharon, Texas used in this thesis. For this case study, the model used to estimate suspended sediment concentrations based on satellite images before, during, and after Hurricane Harvey was the exponential model with the Red-Green Ratio as an input. Since Hurricane Harvey lasted so long, images for the months of August and September of 2017 were collected and processed.

Table 4-11 summarizes the satellite images collected and processed for this case study. The satellite images were clipped to the Brazos River and a portion of its estuary using aerial imagery. This assumed that the width of the river did not vary significantly during Hurricane Harvey and that the river has not changed course since 2017. Pixels labelled as medium or high confidence clouds, cloud shadows, ice, and snow based on the quality pixels provided by the satellite image's source were removed. This resulted in a total of 28 images with estimates of suspended sediment concentrations. The satellite image collected as part of Sentinel Mission 2 on August 7th, 2017 was completely removed

because of the filtering used for the case study. Landsat Mission 9 was not included because it was not

launched until 2021.

**Table 4-11:** Satellite Images Processed for Case Study

| Date | Landsat Mission 7 | Landsat Mission 8 | Sentinel Mission 2 |
|------|-------------------|-------------------|--------------------|
| 8/2/2017 | N/A | N/A | Yes |
| 8/4/2017 | Yes | N/A | N/A |
| 8/5/2017 | N/A | N/A | Yes |
| 8/7/2017 | N/A | N/A | Yes |
| 8/10/2017 | N/A | N/A | Yes |
| 8/12/2017 | N/A | Yes | Yes |
| 8/15/2017 | N/A | N/A | Yes |
| 8/17/2017 | N/A | N/A | Yes |
| 8/20/2017 | Yes | N/A | Yes |
| 8/22/2017 | N/A | N/A | Yes |
| 8/25/2017 | N/A | N/A | Yes |
| 8/27/2017 | N/A | N/A | Yes |
| 8/28/2017 | N/A | Yes | N/A |
| 8/30/2017 | N/A | N/A | Yes |
| 9/1/2017 | N/A | N/A | Yes |
| 9/4/2017 | N/A | N/A | Yes |
| 9/5/2017 | Yes | N/A | N/A |
| 9/6/2017 | N/A | N/A | Yes |
| 9/9/2017 | N/A | N/A | Yes |
| 9/11/2017 | N/A | N/A | Yes |
| 9/13/2017 | N/A | Yes | N/A |
| 9/14/2017 | N/A | N/A | Yes |
| 9/16/2017 | N/A | N/A | Yes |
| 9/19/2017 | N/A | N/A | Yes |
| 9/21/2017 | Yes | N/A | Yes |
| 9/24/2017 | N/A | N/A | Yes |
| 9/26/2017 | N/A | N/A | Yes |
| 9/29/2017 | N/A | Yes | Yes |

Some of the processed images did not result in many pixels with estimated suspended sediment

concentrations following the filtering process. Thus, a general area just upstream (Area 1) and two miles

downstream (Area 2) of USGS-08116650 were used to estimate the average suspended sediment

concentration estimated by the model to evaluate the model's performance to field measurements over

the case study area. The two general areas used to estimate the average suspended sediment

concentration near the USGS-08116650 gauge are shown in Figure 4-3. The estimated suspended

sediment concentration for pixels in these areas are shown in Figure 4-4 and Figure 4-5. Only images

where a majority of the pixels were not filtered out are shown within these figures. The image on August

12th, 2017 for Area 1 is from Landsat Mission 8 while the images on August 12th, 2017 for Area 2 and

September 29th, 2017 for Area 1 and 2 are from Sentinel Mission 2. The images for the two areas show that the average estimated suspended sediment concentrations for these general areas are roughly the same for almost all the scenes. Only the scene on September 6th, 2017 shows a noticeable difference in average estimated suspended sediment concentration between the two areas where Area 1 has a value of 879 mg/L while Area 2 has a value of 742 mg/L.

In general, these images show a decrease in estimated suspended sediment concentrations from August 10th, 2017 to August 15th, 2017 where suspended sediment concentrations are then consistent through August 28th, 2017. Following this period of consistent suspended sediment concentration, estimated suspended sediment concentrations are elevated from August 30th, 2017 to September 19th, 2017 with maximum values occurring on August 30th, 2017, September 6th, 2017, and September 9th, 2017. Following September 19th, 2017, estimated suspended sediment concentrations are assumed to decrease as estimated suspended sediment concentrations on September 26th, 2017 returned to levels seen from August 15th, 2017 to August 28th, 2017.

The images also show that the model can result in a wide range of estimated suspended sediment concentration values for a given satellite image in an area. This is more evident for higher suspended sediment concentration estimates. For example, the suspended sediment concentration estimates for Area 2 on August 30th, 2017 range from approximately 650 to 1000 mg/L. This could indicate that the model should not be used for inter-pixel relationships and should be used to estimate suspended sediment concentrations for a general area. Also, this inter-pixel variance is less prominent for lower suspended sediment concentrations as shown by the estimates from August 15th, 2017 to August 28th, 2017 and estimates after September 26th, 2017.
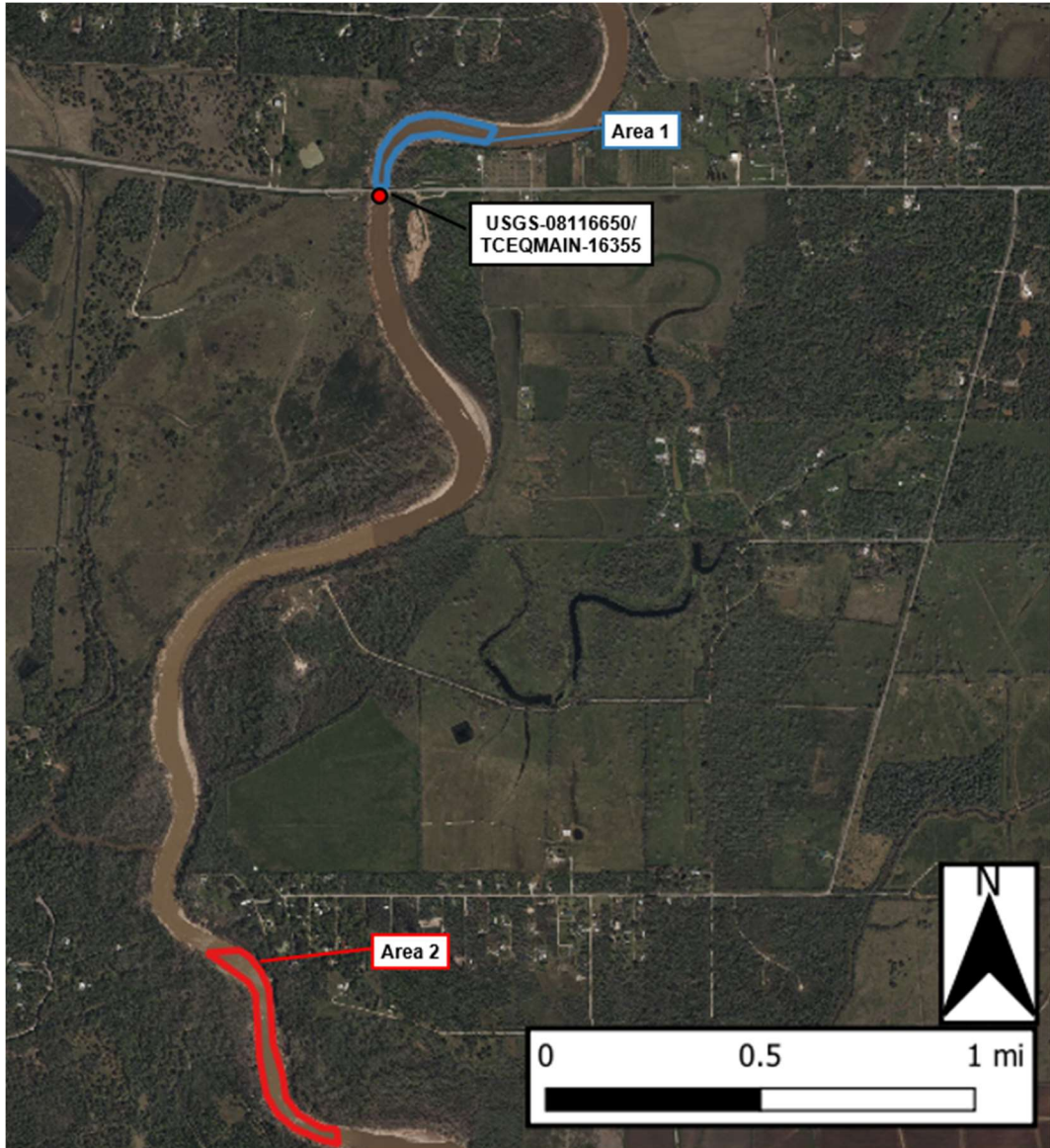
**Figure 4-3:** Upstream Areas of Model Application
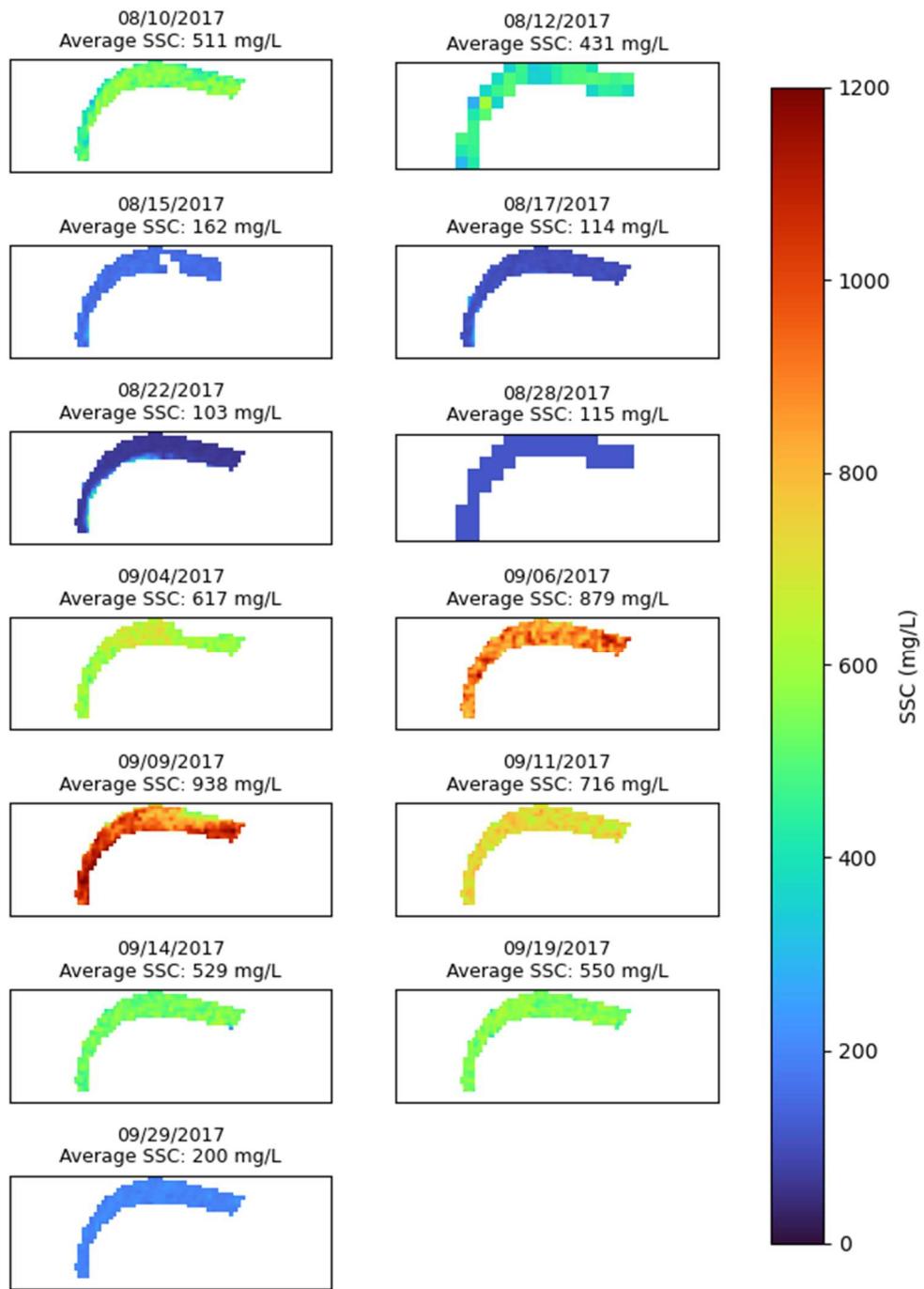
**Figure 4-4:** Estimated Suspended Sediment Concentration – Area 1
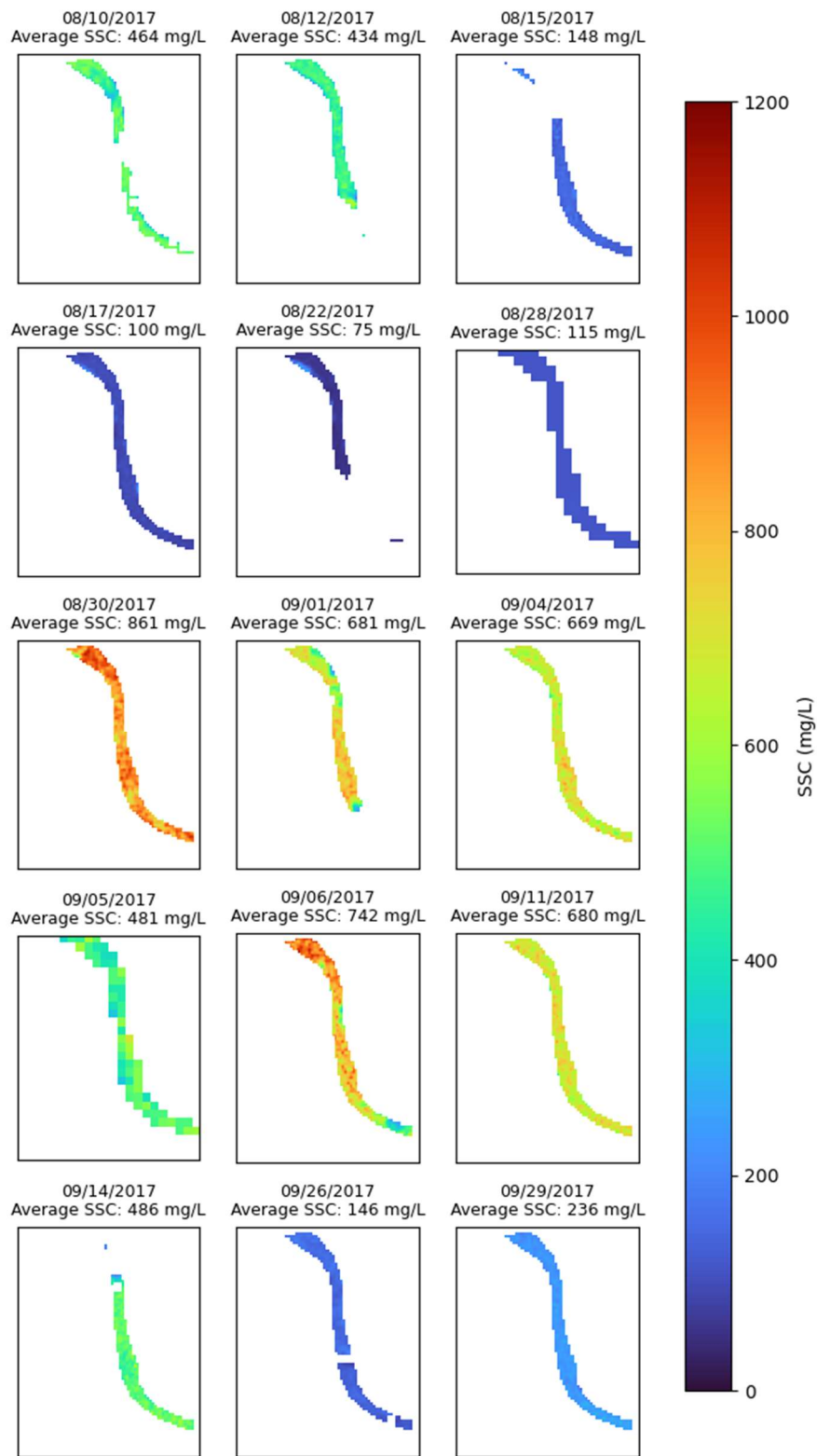
**Figure 4-5:** Estimated Suspended Sediment Concentration – Area 2

The average estimated suspended sediment concentrations shown in Figure 4-4 and Figure 4-5 developed for the Areas 1 and 2 were compared to the daily mean flow and recorded suspended sediment concentrations at USGS-08116650. Figure 4-6 shows this comparison. The recorded suspended sediment concentrations on August 22nd, 2017, and September 27th, 2017 were collected at TCEQMAIN-16355, which is approximately the same location as the USGS-08116650 gauge. The estimated suspended sediment concentrations are nearly identical to field measurements before and after the large daily mean flow spike caused by Hurricane Harvey. Also, the estimated suspended sediment concentrations show a similar lag in response relative to the daily mean flow that is observed in the field data. However, the estimates suspended sediment concentration on August 30th, 2017 is about twice the field measurement. This vast difference could be a result of a difference in timing of the satellite image and the collected field measurement because during flood events suspended sediment concentrations can vary dramatically. The estimated suspended sediment concentrations also show that the Brazos River continued to have elevated suspended sediment concentrations weeks after the flow spike caused by Hurricane Harvey. This delay in suspended sediment concentration reduction because of Hurricane Harvey is a similar response that is seen in the estimated suspended sediment concentration for the small flow spike on August 9th, 2017. During this smaller event, estimated suspended sediment concentrations took up to a week to return to lower levels.
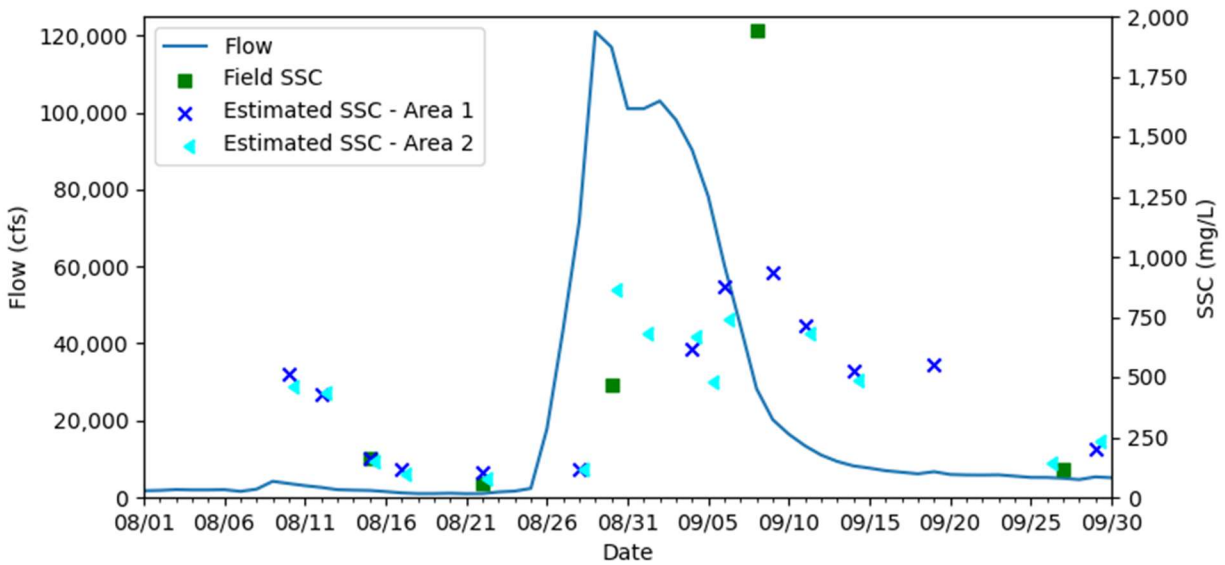
**Figure 4-6:** Flow and Suspended Sediment Concentration in the Case Study area in 2017

The model was also used to estimate suspended sediment concentrations in the Brazos River mouth and estuary. The area where the model was implemented is shown in Figure 4-7. This figure also shows where the average of the estimated suspended sediment concentrations was taken for this area. The area of average estimated suspended sediment concentrations is just downstream of the flood gates and just before the river discharges to the estuary. The model was only used for the estuary of the Brazos River on satellite images that are shown in Figure 4-4 and Figure 4-5 where a majority of pixels were not filtered out. Figure 4-8 illustrates the estimated suspended sediment concentration developed for the estuary of the Brazos River.

In general, the estimated suspended sediment concentration in the estuary and at the mouth of the Brazos River are lower than the suspended sediment concentrations estimated in upstream portions of the Brazos River. The comparison of average estimated suspended sediment concentrations in the case study area are summarized in Table 4-12. The reduction in average estimates suspended sediment concentrations from upstream to downstream could be a result of sediment deposition between these locations. This is most evident for the images on August 12th, 2017 and September 19th, 2017 which experienced a reduction in average estimated suspended sediment concentrations of 365 mg/L and 427

mg/L, respectively. Both days had relatively low daily mean flows, which is an indication of lower carrying capacity of a river. On September 11th, 2017, the average estimated suspended sediment concentration at the mouth of the Brazos River is only 58 mg/L lower than the average estimated suspended sediment concentration on the same day at the upstream locations. Also, on September 11th, 2017, the estimated suspended sediment concentration in the estuary indicates there was a plume of sediment leaving the Brazos River that was traveling west along the coast. On this day, the daily mean flow was significantly higher than the daily mean flows for all other images of the mouth and estuary developed. This higher flow can explain why for this day the estimated suspended sediment concentrations show a plume of sediment at the mouth of the Brazos and a small reduction in estimated suspended sediment concentration from upstream area to the mouth.

**Table 4-12:** Estimates Average Suspended Sediment Concentration Along the Brazos River

| Date | Average Upstream SSC (mg/L) | Average Mouth SSC (mg/L) |
|---|---|---|
| 8/12/2017 | 431 | 66 |
| 8/17/2017 | 114 | 56 |
| 8/22/2017 | 103 | 42 |
| 9/11/2017 | 716 | 658 |
| 9/19/2017 | 550 | 123 |
| 9/26/2017 | 146 | 57 |
| 9/29/2017 | 200 | 76 |

Again, images in this area indicate that the model can lead to a wide variation of estimated suspended sediment concentrations between pixels. For example, images from August 12th, 2017 to August 22nd, 2017, and the image on September 29th, 2017, the estimated suspended sediment concentrations show areas of low suspended sediment below 70 mg/L to areas of higher suspended sediment concentrations above 100 mg/L. This type of relationship is not expected unless sediment is introduced into the system and is likely a result of interference of bottom reflectance from low water depth in estuary caused by sand bars. In the image on September 11th, 2017, there are some dots of very low estimated suspended sediment which are not realistic and could be a result of unfiltered cloud shadows as a result of mislabeled quality pixels. At a more zoomed in scale, the estimated suspended sediment concentrations for some images produced with Sentinel Mission 2 show areas of lower suspended sediment in lines that resemble waves along the coast.
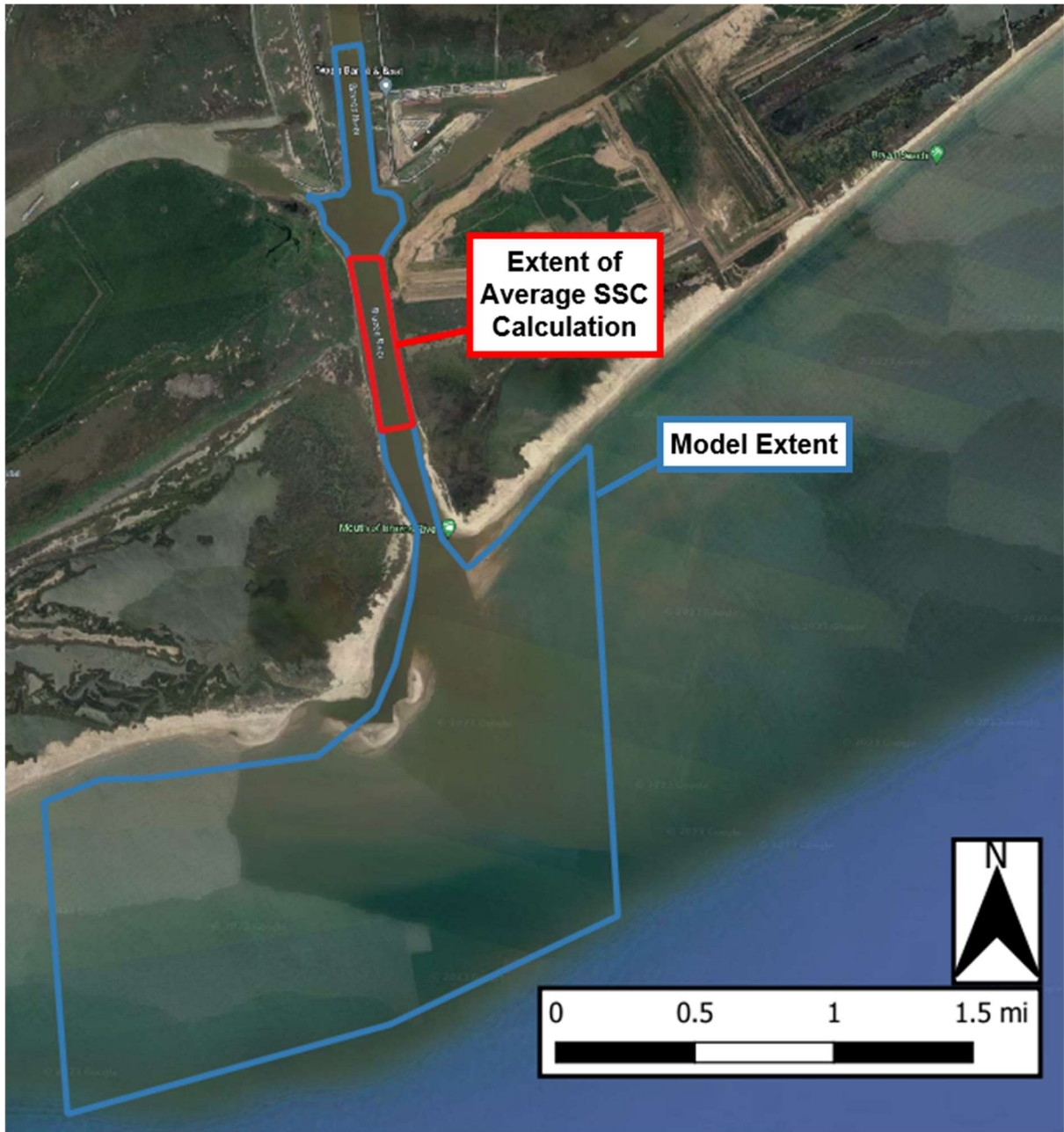
**Figure 4-7:** Bay Area Model Application
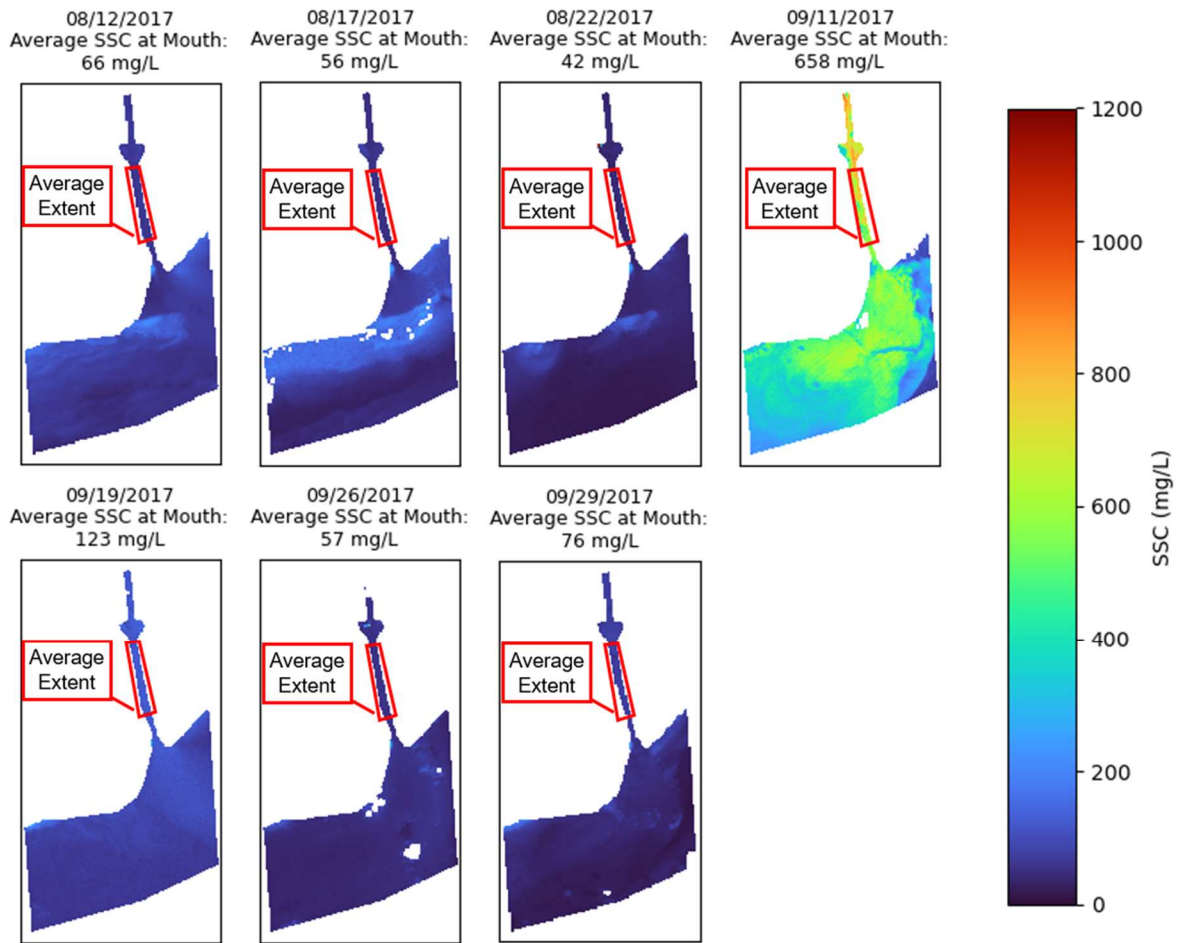
**Figure 4-8:** Estimated Suspended Sediment Concentrations at the Brazos River Mouth

## 5.0    Conclusion

Suspended sediment transport in river basins is important for many water management planning activities including estimation of useful life of reservoirs, evaluation of land use impacts, and quantifying sediment-associated nutrient and contaminant amounts. In general, increased amounts of suspended sediment can lead to increased amounts of contaminants in water because many contaminants can be attached to suspended sediment particles or are suspended sediment particles. This increased level of contamination can affect treatment processes. Also, increased suspended sediment can lead to increased sedimentation within reservoirs that reduces their overall capacity, which could cause future water capacity shortages. Furthermore, increased suspended sediment can adversely affect native aquatic life. Thus, it can be very valuable to accurately estimate suspended sediment concentrations in waterbodies.

This thesis evaluated several methods to estimate suspended sediment concentrations in the Brazos River including rating curves that used flow or depth as inputs, machine learning algorithms that included support vector machines, artificial neural networks, and extreme learning machines which used satellite images as inputs, and an exponential algorithm that used satellite images as inputs. The rating curve methods were used as baseline models as they are the standard approach to estimate suspended sediment concentrations in rivers. Also, rating curves were developed to estimate sediment load to compare to previous studies. Rating curve models were developed using data from USGS-08116650 and TCEQMAIN-16355. Models that used satellite images also included data from TCEQMAIN-11843. Satellite images from Landsat Missions 4, 5, 7, 8, and 9 and Sentinel Mission 2 were collected and processed to remove pixels that included cloud cover, saturation, or snow/ice from satellite image data. Different combinations of bands were created from this processed satellite image data to be used as input variables. Pairs of satellite images and suspended sediment data with up to a three-day lag were created from this data. These data pairs were filtered further by reviewing the daily mean flows of USGS-08116650 and removing pairs near flood events or multiple pairs with the same suspended sediment concentration data point.

A principal component analysis and canonical correlation analysis was conducted on the flow, depth, and satellite image input variables to evaluate which inputs could be the most influential to estimating suspended sediment concentration and sediment load. Based on the overall rankings of these two analyses, the NIR, red, and green bands were suspected to be the most important for estimating the suspended sediment concentration in the Brazos River.

All the data sets were split into a training and test set where the test set. After completing hyperparameter tuning using five-fold cross validation for the machine learning models, a Taylor Diagram analysis was used to help compare performance between models on the test data set. Both rating curve models that estimated suspended sediment concentrations had an $R^2$ of approximately 0.75 with RSME of 158 mg/L and 176 mg/L. The rating curves that estimated sediment load performed significantly better with an $R^2$ of approximately 0.96. The rating curves developed that estimated sediment load for this thesis generally underpredicted sediment load compared to the same rating curve developed by Storm (2013). This difference is likely a result of the use of TCEQMAIN-16355 total suspended sediment concentration data and the inclusion of historical data beyond 2010. Most of the time, suspended sediment concentration samples are expected to be relatively low compared to those collected during flood events just following a storm.

Fourteen of the models that were developed using satellite image data performed similar or better than both rating curve methods that estimate suspended sediment concentration based on the $R^2$ and RSME values. These models include the following:

- Exponential Relationship with the Red-Green Ratio as an input

- Support Vector Machine with the Red Band as an input

- Support Vector Machines, Artificial Neural Networks, and Extreme Learning Machines with the following inputs:

    o All Six Bands

    o Four Major Bands

    o Red-Green Ratio

    o NIR-Ratios

The three best performing models that used satellite image data based on the Taylor Diagram analysis were the support vector machine and extreme learning machine that used the Four Major Bands as input variables and the exponential relationship that used the Red-Green Ratio as an input. All three models had $R^2$ and RSME values ranging from 0.83 to 0.85 and 131 to 133 mg/L, respectively. This means all three of these models performed better than the rating curve methods on the test data set and all these models performed roughly the same. Also, based on these results it was concluded that the Red-Green Ratio is important to estimating the suspended sediment concentration of the Brazos River. This lines up with the results of the overall rankings following the principal component analysis and canonical correlation analysis where Red, and Greens ranked the highest.

All the models that used satellite image data that were developed for the Brazos River were deployed on the San Bernard River to evaluate the models' ability to be applied to other rivers. San Bernard River suspended sediment concentration data used for this analysis was from TCEQMAIN-12146. Data pairs were created in a similar process as the Brazos River, but these pairs did not remove pairs that could have been influenced by flood events because no extensive daily mean flow record was available at the time of this analysis for the San Bernard River. The Taylor Diagram analysis was used on the entire San Bernard River data pairs. Based on this analysis, all the models developed for the Brazos River perform very poorly on the San Bernard River based on the RSME and R calculated. None of the models developed for the Brazos River result in a $R^2$ greater than 0.04 on the San Bernard River data. This poor performance could indicate that the reflectance values for the San Bernard River data could be influenced by the river bottom reflectance component or different sediment type carried by this river. The sediment carried by these two rivers might be optically different. The poor performance of the models on the San Bernard River data could also indicate that the models should not be applied outside of the Brazos River. In general, the San Bernard River data has significantly lower suspended sediment concentrations than the Brazos River. All the best performing models on the San Bernard River data according to the RSME and R values generally overestimate the suspended sediment concentrations for the San Bernard River.

The exponential relationship with the Red-Green Ration as an input was used to create estimated suspended sediment concentration images for the Brazos River and a portion of the bay that the Brazos River discharges to before, during, and after Hurricane Harvey. In general, the model matched general trends in average estimated suspended sediment concentrations that were expected by daily mean flows and general trends of suspended sediment concentration observed in field measurements at USGS-08116650. More specifically, an increase in flow at USGS-08116650 resulted in a similar magnitude increase in estimated suspended sediment concentrations that lagged the changes in flows. Also, for lower flow events, the model predicted sediment deposition between USGS-08116650 and the mouth of the river, while during higher flow events, the model predicted little to no sediment deposition in the river resulting in a sediment plume propagating south and west from the Brazos River in the bay. Despite this good general performance, the model exhibited high inter-pixel variance for higher estimated suspended sediment concentrations and lower suspended sediment concentrations where depth varied significantly.

## 5.1    Limitation of Study and Applications

This study developed models that performed reasonably well at predicting suspended sediment concentrations in the Brazos River. However, the models developed for this study had the following limitations.

- The models developed for this study exhibited large inter-pixel variance when deployed to satellite image scenes along the Brazos River. Part of this variance was due to mislabeled quality pixels, boats navigating the river, and waves in the bay. However, in areas without these anomalies, the model showed high inter-pixel for areas where estimated suspended sediment concentrations for pixel values exceeded 1,000 mg/L and areas of lower depth below estimated suspended sediment concentrations for pixel values of 100 mg/L. In general, the models developed underpredicted suspended sediment concentrations above 1,000 mg/L, Furthermore, for low suspended concentration and low depth areas, the bottom reflectance could be saturating surface reflectance. This indicates that the models should be applied to evaluate suspended sediment concentrations in general areas and not evaluate relationships as fine as pixel to pixel. Furthermore, the model can be reasonably applied when estimated suspended sediment

concentrations range from 0-1,000 mg/L except for areas of low flow depth below suspended sediment concentration of 100 mg/L.

- In general, anomalies such as boats, clouds, and waves in the bay were observed to interfere with optical relationship being developed to estimate suspended sediment concentration. This study tried to handle clouds by using quality pixels from the space agencies, but this was not a perfect filtering method. Other anomalies were not directly handled in this study. Furthermore, cloud cover limits the application of models developed for this study in areas that experience many days of cloud cover or during prolonged storm events. These models would also not be applicable in areas with prolonged ice cover on the river.

- The models developed for this study that used satellite image data that ranged from 10 m to 30 m in pixel resolution. This limits the ability to apply the models developed in further upstream portions of the river. Assuming a pixel encompasses only the river, the models could be deployed for rivers as narrow as 33 ft if 10 m pixel resolution images are available or as narrow as 99 ft if 30 m pixel resolution images are available. This is rarely the case, and it is generally accepted that satellite images should be used on rivers that are at least three times the width of the pixel resolution to guarantee at least one pure water pixel. For these models that results in rivers as narrow as 99 ft if 10 m pixel resolution images are available or as narrow as 296 ft if 30 m pixel resolution images are available,

- None of the models developed for the Brazos River performed well at estimating suspended sediment concentrations in the San Bernard River and generally overestimated suspended sediment concentrations in the San Bernard River. This could indicate that the reflectance values for the San Bernard River data could be influenced by the bottom reflectance component and suspended sediment that is optically different from the Brazos River sediment. This indicates that the models developed could only be applicable to rivers with similar sediment type as the Brazos River.

## 5.2     Future Research

The following are recommended for future studies.

---

- Using satellite image and suspended sediment concentration pairs that are only collected on the same date, preferably the same time. This could include the redevelopment of the models in this study with this restriction to see if performance improves.

- Application of models developed in this study to more similar rivers to the Brazos River that experience similar flow, suspended sediment concentration ranges, and sediment type to further evaluate their ability to be applied to areas outside the Brazos River.

- Use of higher resolution satellite image data to allow for use of the models developed further upstream in the Brazos River. This could also include an evaluation to see if this higher resolution is comparable to the data used in this study to allow for a larger data set for model development.

- Development of a physically/mathematically derived relationship between satellite image reflectance values and suspended sediment concentrations. Such types of relationships have been developed for depth estimation in water bodies.

## References

Alissa Sherry & Robin K. Henson (2005) Conducting and Interpreting Canonical Correlation Analysis in Personality Research: A User-Friendly Primer, Journal of Personality Assessment, 84:1, 37-48, DOI: 10.1207/s15327752jpa8401_09.

Brazos River Authority. *Brazos River Watershed*. *https://brazos.org/About-Us/Environmental/Brazos-River-Watershed*. June 25, 2023.

Burkov, Andriy. *Machine learning engineering*. Vol. 1. True Positive Incorporated, 2020.

Burkov, Andriy. *The hundred-page machine learning book*. Vol. 1. Quebec City, QC, Canada: Andriy Burkov, 2019.

Coonrod, Julia Ellen Allred. *Suspended sediment yield in Texas watersheds*. The University of Texas at Austin, 1998.

Foster IDL, Millington R, Grew RG. 1992. The impact of particle size controls on stream turbidity measurement; some implications for suspend sediment yield estimation. In Erosion and Sediment Transport Monitoring Programmes in River Basins, Bogen J, Walling DE, Day TJ (eds). IAHS Publication No. 210. IAHS Press: Wallingford; 51–62.

Haitham Abdulmohsin Afan, Ahmed El-shafie, Wan Hanna Melini Wan Mohtar, Zaher Mundher Yaseen. Past, present and prospect of an Artificial Intelligence (AI) based model for sediment transport prediction. Journal of Hydrology. Volume 541, Part B, 2016. Pages 902-913. ISSN 0022-1694. *https://doi.org/10.1016/j.jhydrol.2016.07.048*.

Houston-Galveston Area Council. San Bernard River Watershed Protection Plan - H-GAC. 2017. www.h-gac.com/getmedia/07925d0e-b82b-4b40-8735-6cbc12f53122/San-Bernard-WPP.

Huang, G.B.; Zhu, Q.Y.; Siew, C.K. Extreme learning machine: Theory and 641 applications. Neurocomputing 2006, 70, 489–501.

Gray, John R. *Comparability of suspended-sediment concentration and total suspended solids data*. No. 4191. US Department of the interior, US Geological Survey, 2000.

Guo, Qizhong. *Correlation of total suspended solids (TSS) and suspended sediment concentration (SSC) test methods*. Rutgers University, Department of Civil and Environmental Engineering, 2006.

I.G. Droppo, K. Nackaerts, D.E. Walling, N. Williams. Can flocs and water stable soil aggregates be differentiated within fluvial systems? CATENA. Volume 60, Issue 1. 2005. Pages 1-18. ISSN 0341-8162. *https://doi.org/10.1016/j.catena.2004.11.002*

Ian G. Droppo, Carl L. Amos; Structure, Stability, and Transformation of Contaminated Lacustrine Surface Fine-Grained Laminae. *Journal of Sedimentary Research* 2001; 71 (5): 717–726. doi: *https://doi.org/10.1306/2DC40963-0E47-11D7-8643000102C1865D*

Jastram JD, Zipper CE, Zelazny LW, Hyer KE. Increasing precision of turbidity-based suspended sediment concentration and load estimates. J Environ Qual. 2010 Jul-Aug;39(4):1306-16. doi: 10.2134/jeq2009.0280. PMID: 20830919.

Johnson, Richard and Wichern, Dean. *Applied Multivariate Statistical Analysis*. Pearson Education, 2007.

Kanno, A., & Tanaka, Y., 2012. Modified Lyzenga's method for estimating generalized coefficients of satellite-based predictor of shallow water depth. IEEE Geoscience and Remote Sensing Letters, 9(4), 715-719.

Lefrancois J, Grimaldi C, Gascuel-Odoux C, Gilliet N (2007) Suspended sediment and discharge relationships to identify bank degradation as a main sediment source on small agricultural catchments. Hydrol Process 21(21):2923–2933

Legleiter, C. J., and D. A. Roberts (2009), A forward image model for passive optical remote sensing of river bathymetry, Remote Sens. Environ., 113(5), 1025–1045.

Legleiter, C. J., Kinzel, P. J., and Overstreet, B. T. (2011), Evaluating the potential for remote bathymetric mapping of a turbid, sand-bed river: 1. Field spectroscopy and radiative transfer modeling, *Water Resour. Res.*, 47, W09531, doi:*10.1029/2011WR010591*.

Lyzenga, David R., Norman P. Malinas, and Fred J. Tanis. "Multispectral bathymetry using a simple physically based algorithm." *IEEE Transactions on Geoscience and Remote Sensing* 44.8 (2006): 2251-2259.

Minella, J.P.G., Merten, G.H., Reichert, J.M. and Clarke, R.T. (2008), Estimating suspended sediment concentrations from turbidity measurements and the calibration problem. Hydrol. Process., 22: 1819-1830. *https://doi.org/10.1002/hyp.6763*

Mishra, D. R., S. Narumalani, D. Rundquist, and M. Lawson (2005), Characterizing the vertical diffuse

attenuation coefficient for downwelling irradiance in coastal waters: Implications for water

penetration by high resolution satellite data, ISPRS J. Photogramm. Remote Sens., 60(1), 48–64

Olyaie, Ehsan, et al. "A Comparison of Various Artificial Intelligence Approaches Performance for

Estimating Suspended Sediment Load of River Systems: a Case Study in United States."

Environmental Monitoring and Assessment, vol. 187, no. 4, 2015, doi:10.1007/s10661-015-4381-

1.

Park, E., Latrubesse, E.M., 2014. Modeling suspended sediment distribution patterns of the Amazon

River using MODIS data. Remote Sens. Environ. 147, 232–242.

https://doi.org/10.1016/j.rse.2014.03.013. *https://www.frontiersin.org/article/10.3389*

*/fmars.2017.00233. Accessed 20 Oct 2017*.

Pereira, L.S.F.; Andes, L.C.; Cox, A.L.; Ghulam, A. Measuring suspended-sediment concentration and

turbidity in the middle Mississippi and lower Missouri Rivers using Landsat data. J. Am. Water

Resour. Assoc. 2018, 54, 440–450.

Peterson, Kyle T., Vasit Sagan, Paheding Sidike, Amanda L. Cox, and Megan Martinez. 2018.

"Suspended Sediment Concentration Estimation from Landsat Imagery along the Lower Missouri

and Middle Mississippi Rivers Using an Extreme Learning Machine" Remote Sensing 10, no. 10:

1503. *https://doi.org/10.3390/rs10101503*

Philips, Jonathan D. (2006). "Geomorphic Context, Constraints, and Change in the lower Brazos and

Navasota Rivers, Texas". University of Kentucky, Department of Geography.

Poesen, J. W., Vandaele, K., & Van Wesemael, B. (1996). Contribution of gully erosion to sediment

production on cultivated lands and rangelands. IAHS Publications-Series of Proceedings and

Reports-Intern Assoc Hydrological Sciences, 236, 251-266.

Reisinger, A., Gibeaut, J. C., & Tissot, P. E. (2017). Estuarine suspended sediment dynamics:

observations derived from over a decade of satellite data. Frontiers in Marine Science

Sari, V., dos Reis Castro, N.M. & Pedrollo, O.C. Estimate of Suspended Sediment Concentration from

      Monitored Data of Turbidity and Water Level Using Artificial Neural Networks. Water Resour

      Manage 31, 4909–4923 (2017). https://doi.org/10.1007/s11269-017-1785-4

Shimabukuro, Y. E., & Smith, J. A. (1991). The least-squares mixing models to generate fraction images

      derived from remote-sensing multispectral data. IEEE Transactions on Geoscience and Remote

      Sensing, 29, 16–20.

Sobel, R.S., Kiaghadi, A. & Rifai, H.S. Modeling water quality impacts from hurricanes and extreme

      weather events in urban coastal systems using Sentinel-2 spectral data. Environ Monit Assess

      192, 307 (2020). *https://doi.org/10.1007/s10661-020-08291-5*.

Storm, Kyle. (2013). "Suspended Sediment Sampling and Annual Sediment Yield on the Lower Brazos

      River". University of Houston, Department of Civil and Environmental Engineering.

Sun, Q.S.; Zeng, S.G.; Liu, Y.; Heng, P.A.; Xia, D.S. A new method of feature fusion and its application in

      image recognition. Pattern Recognit. 2005, 38, 2437–2448.

Taher Rajaee, Hamideh Jafari. Two decades on the artificial intelligence models advancement for

      modeling river sediment concentration: State-of-the-art. Journal of Hydrology. Volume 588, 2020.

      125011. ISSN 0022-1694. *https://doi.org/10.1016/j.jhydrol.2020.125011*.

Taylor, K. E. 2001. Summarizing multiple aspects of model performance in a single diagram. Journal of

      Geophysical Research: Atmospheres, 106(D7), 7183–7192.

United States Geological Survey. *Landsat Missions Timeline*.

      *https://www.usgs.gov/media/images/landsat-missions-timeline*. June 28, 2023.

United States Geological Survey. *USGS EROS Archive - Sentinel-2 - Comparison of Sentinel-2 and*

      *Landsat*. *https://www.usgs.gov/centers/eros/science/usgs-eros-archive-sentinel-2-comparison-*

      *sentinel-2-and-landsat*. June 28, 2023.

Walling, D.E., Moorehead, P.W. The particle size characteristics of fluvial suspended sediment: an

      overview. Hydrobiologia 176, 125–149 (1989). *https://doi.org/10.1007/BF00026549*

Wang M, Shi W. Cloud masking for ocean color data processing in the coastal regions. IEEE Trans

      Geosci Remote Sensing 2006; 44:3196–205.

Zhang, H., and Wang, M. (2010). Evaluation of sun glint models using MODIS measurements. J. Quant. Spectrosc. Radiat. Transf. 111, 492–506. doi: 10.1016/j.jqsrt.2009.10.001

## Appendix A – Landsat Flow vs. TSS
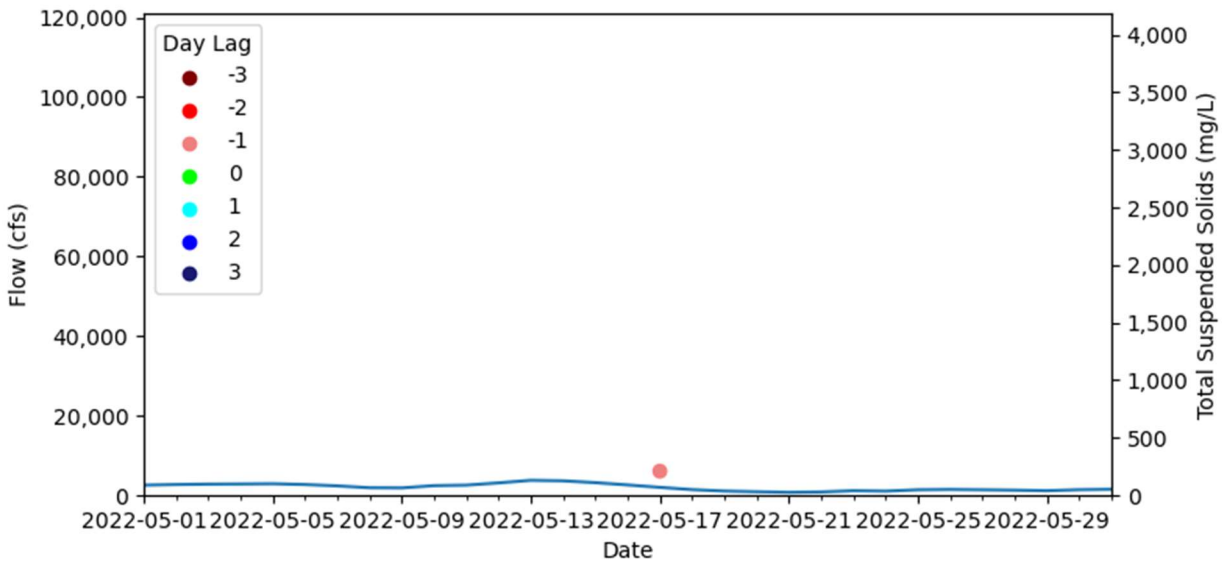


**Figure A-1:** May 2022 Flow and Total Suspended Solids Graph for Landsat Data
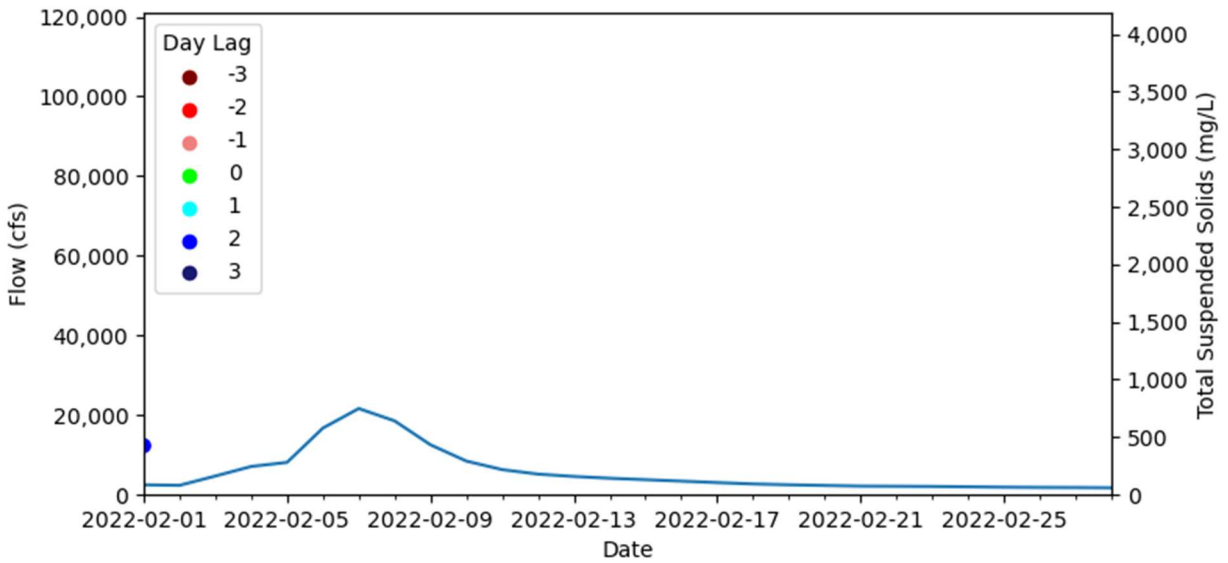


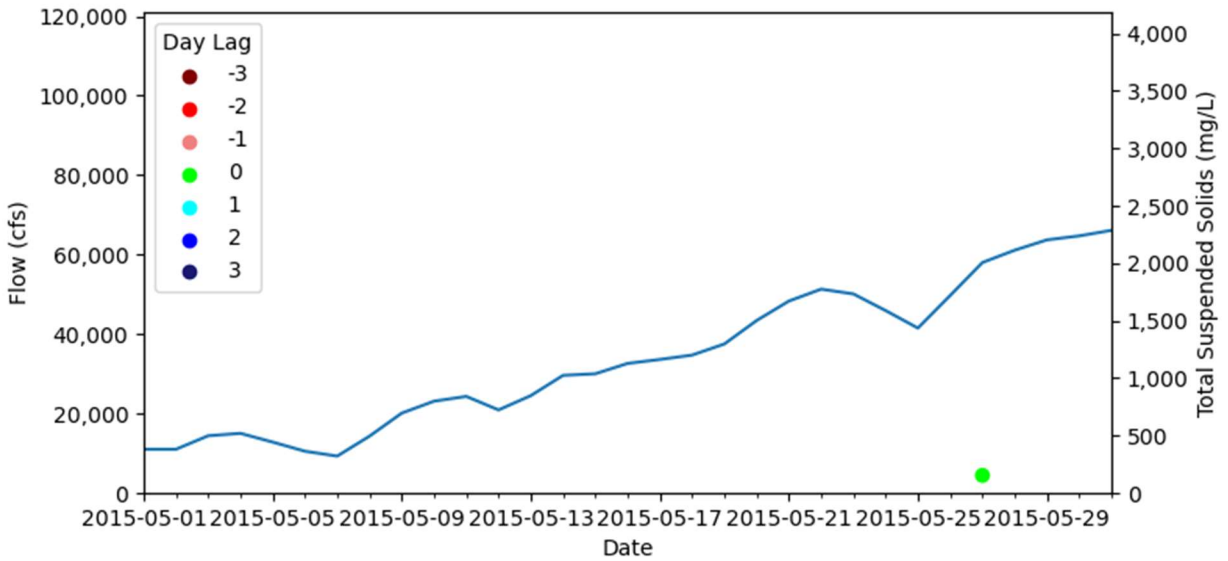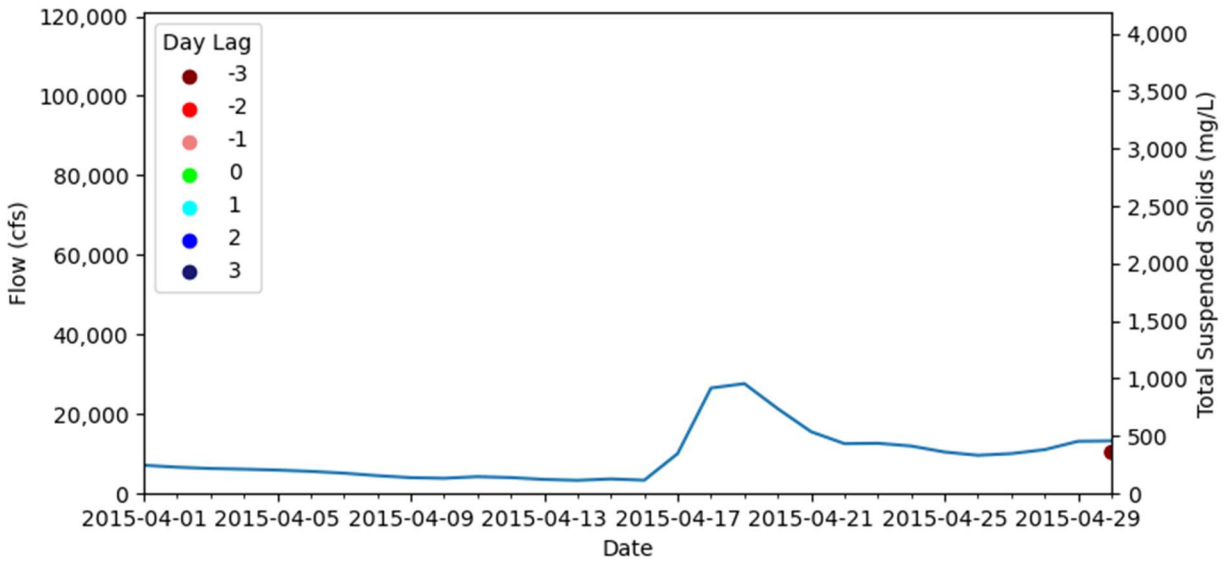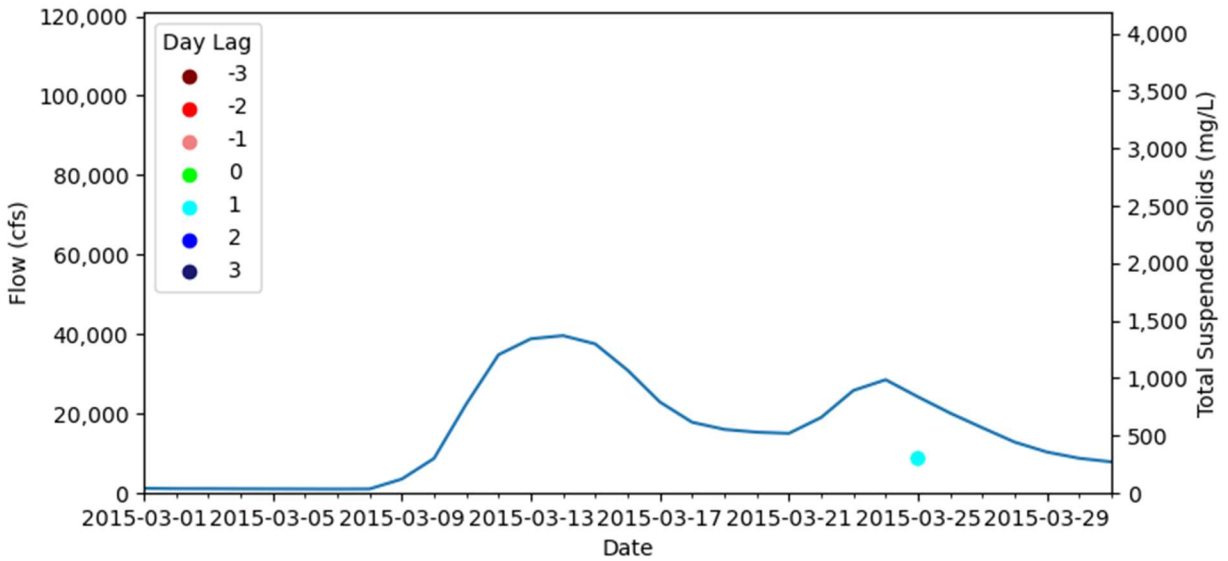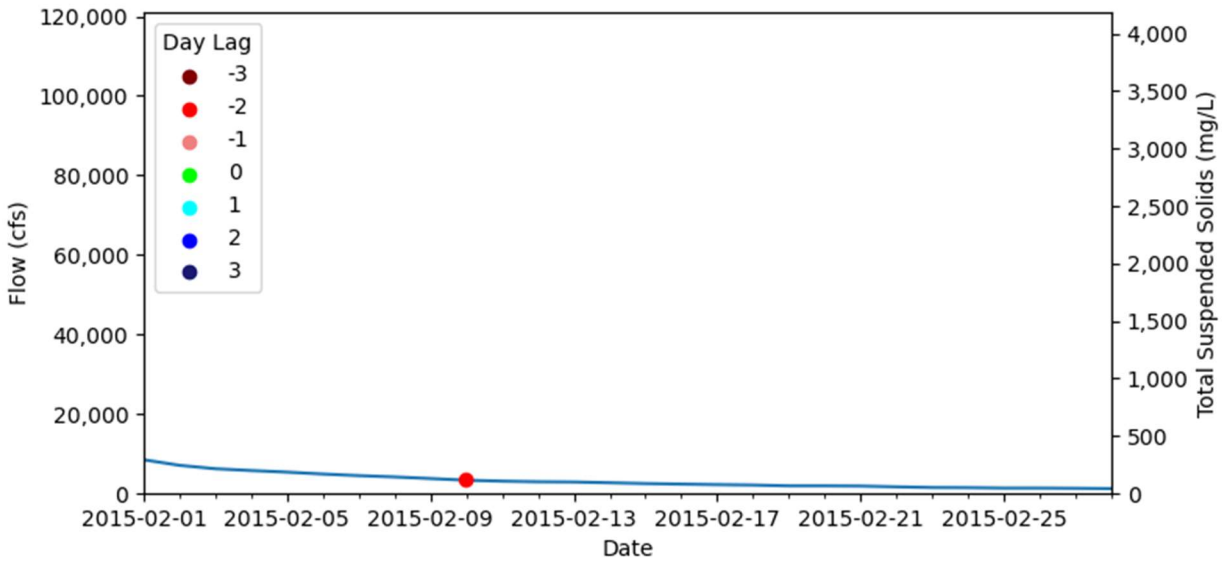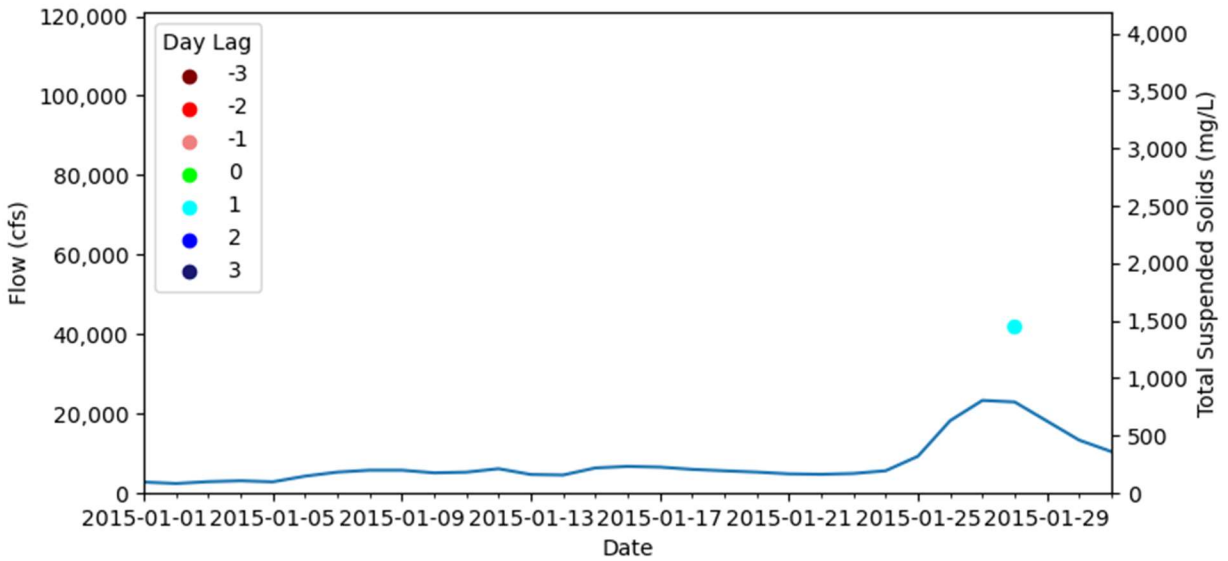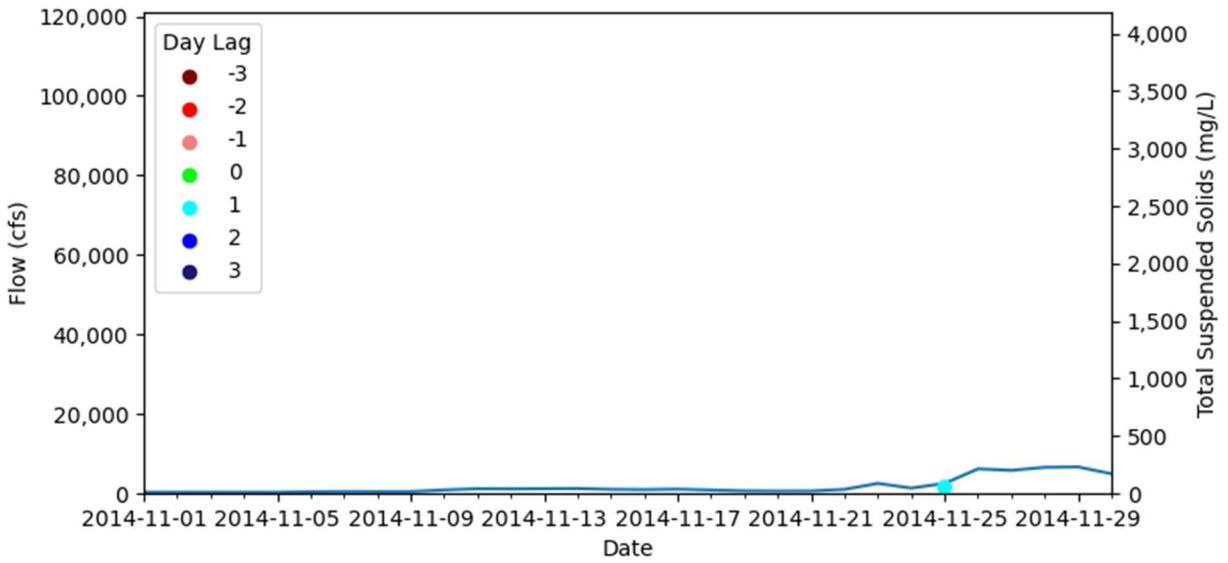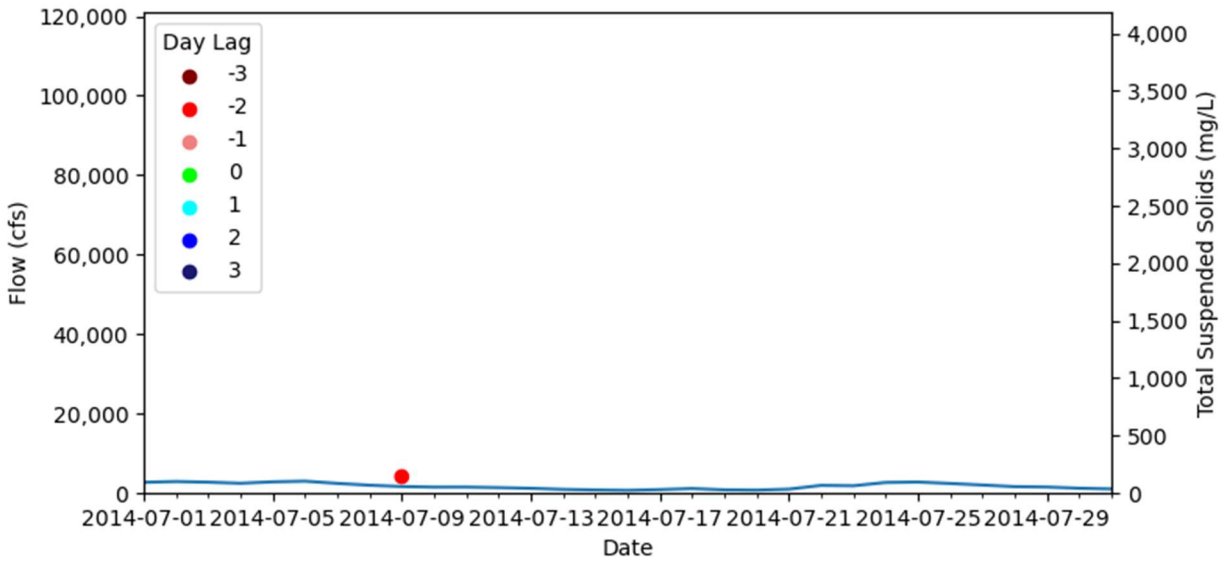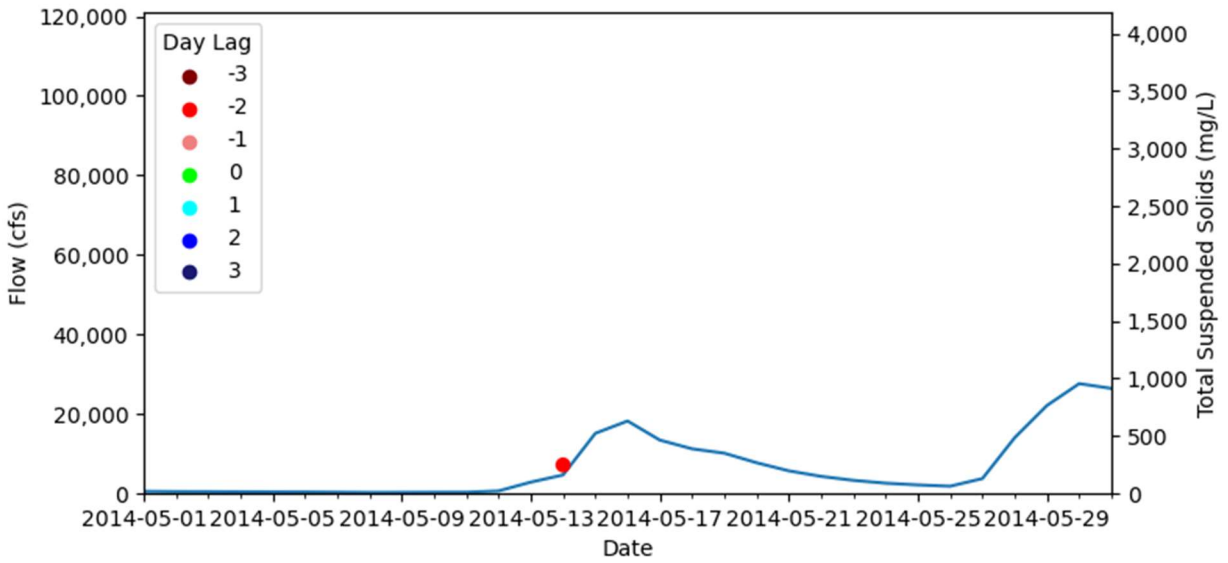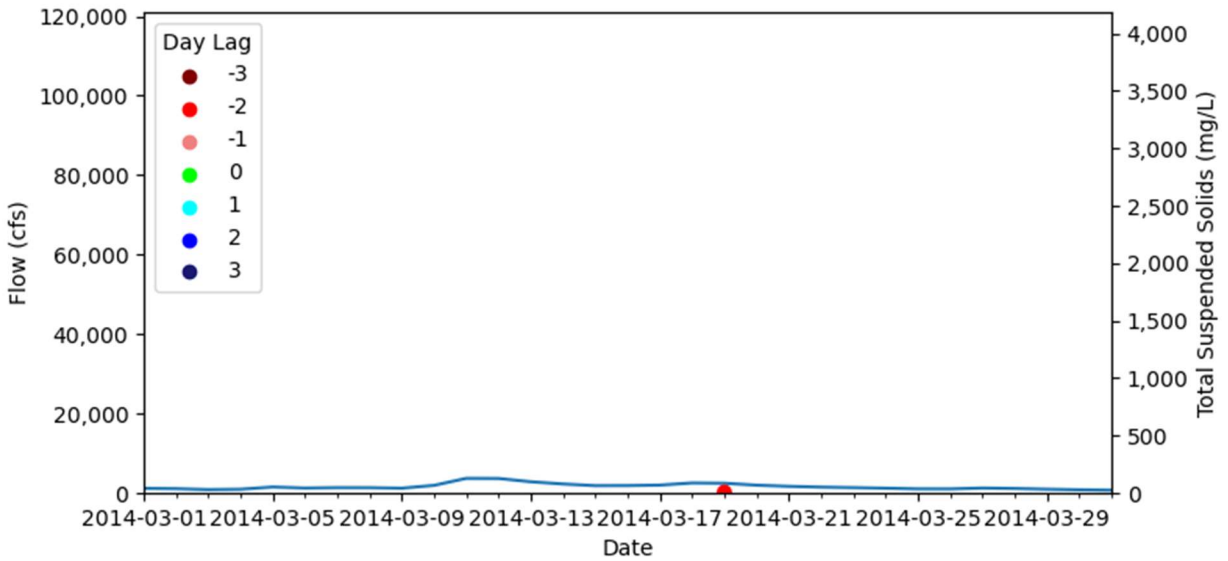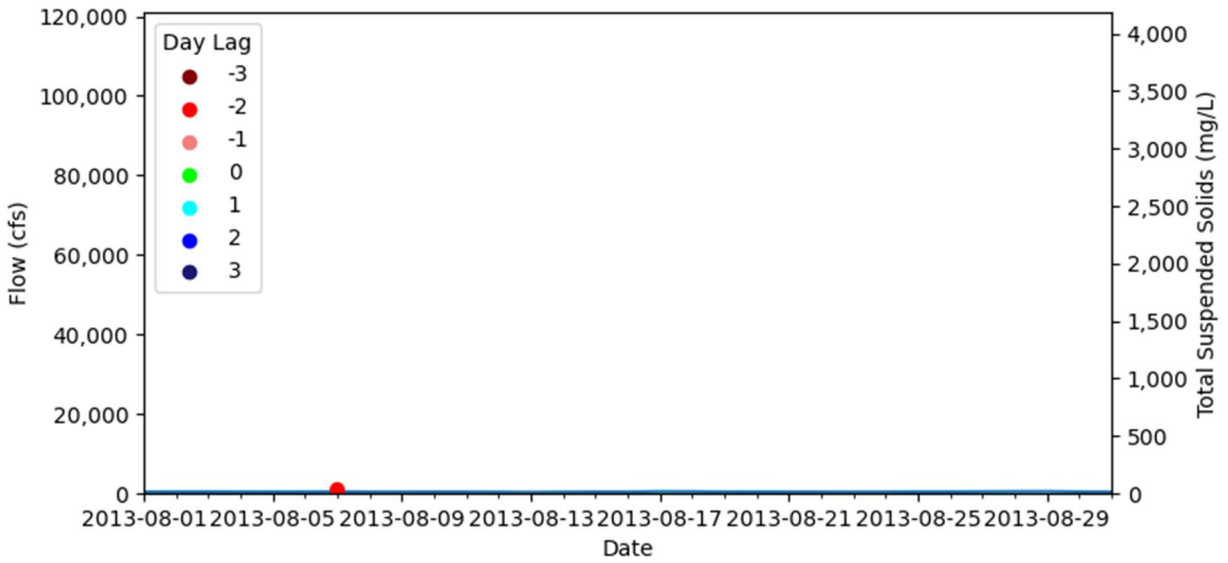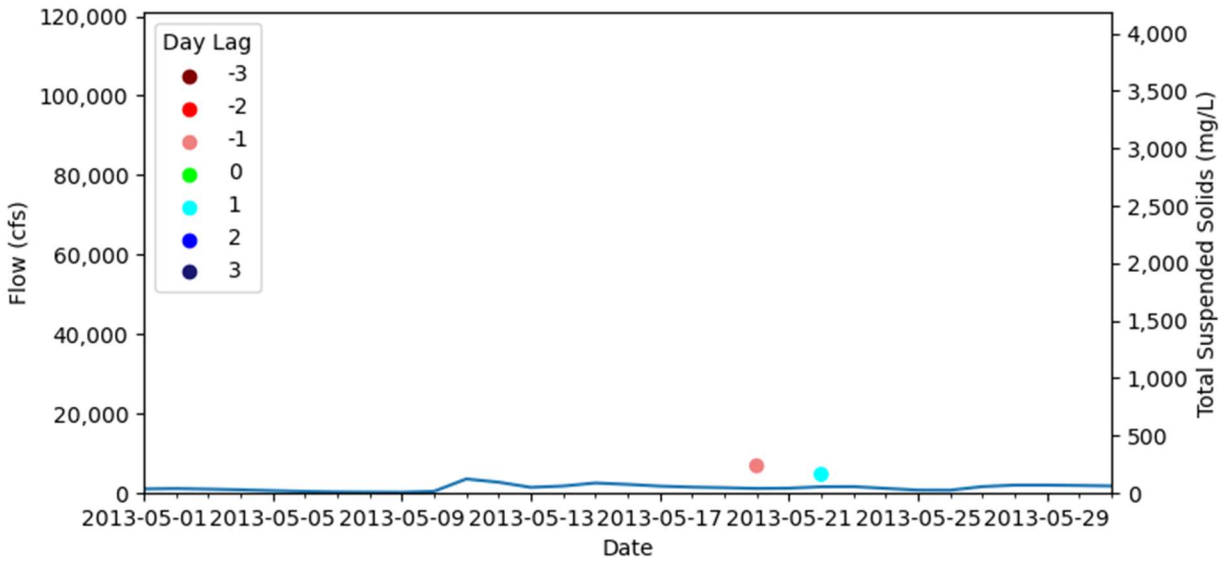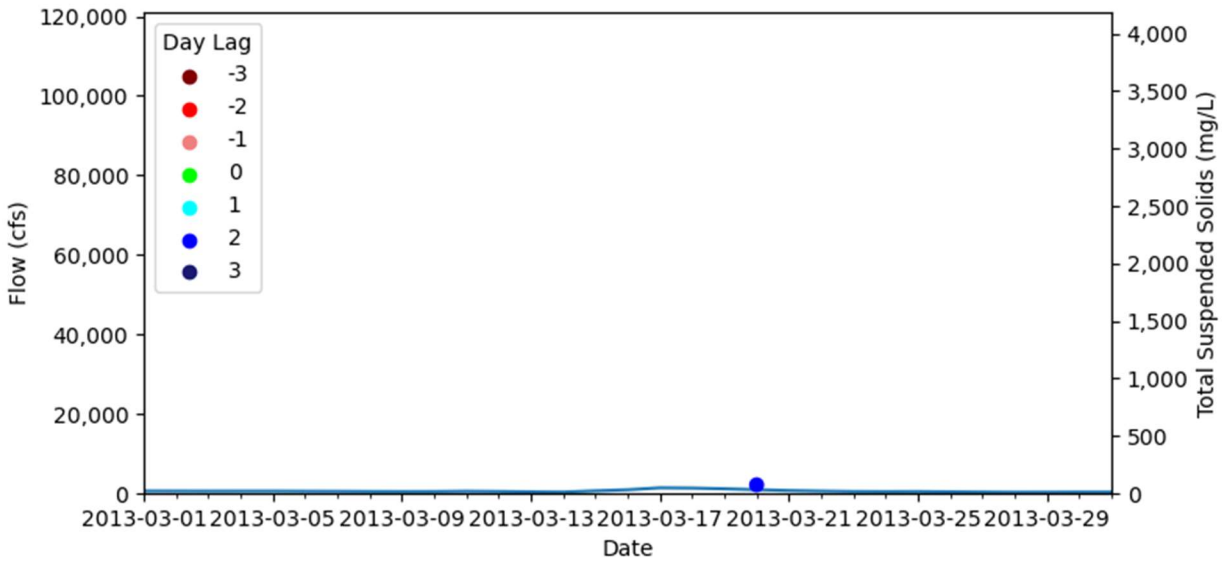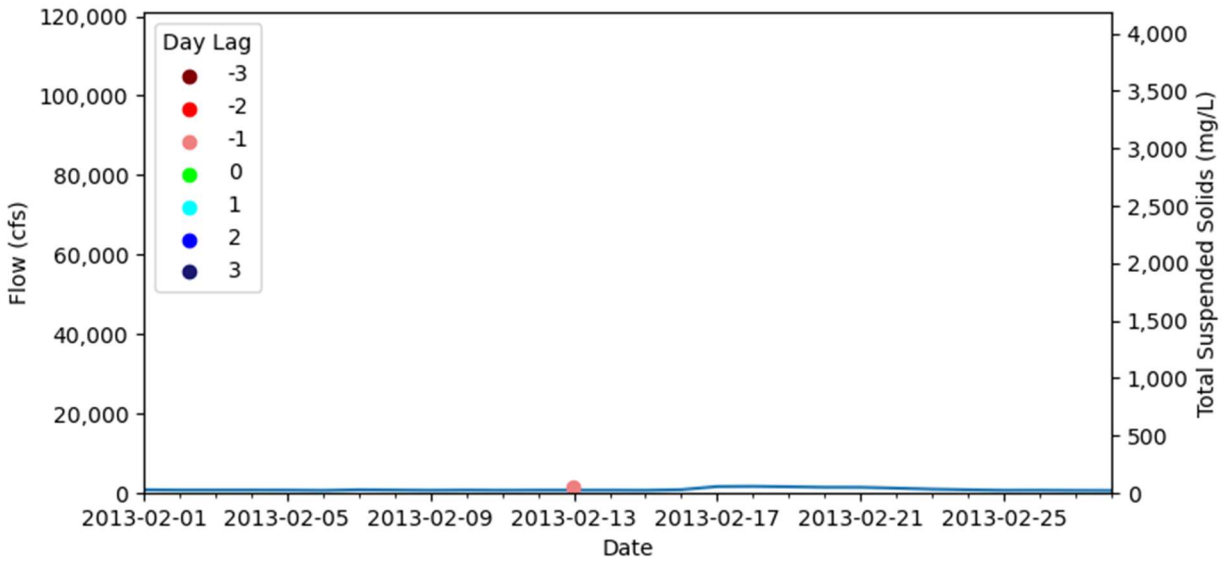**Figure A-2:** February 2022 Flow and Total Suspended Solids Graph for Landsat Data
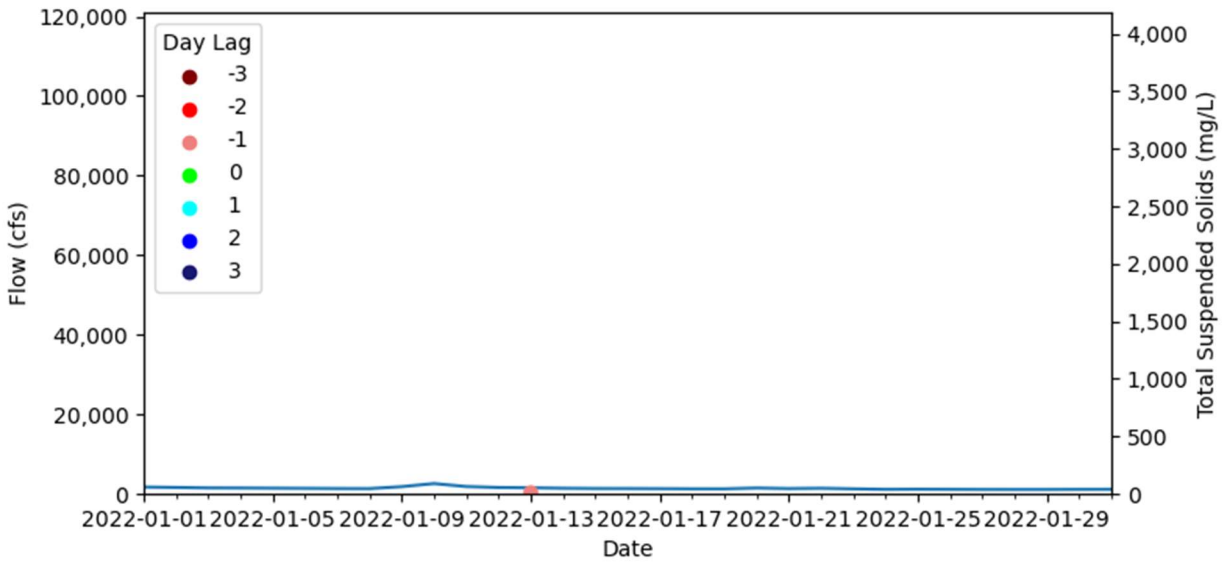
**Figure A-3:** January 2022 Flow and Total Suspended Solids Graph for Landsat Data
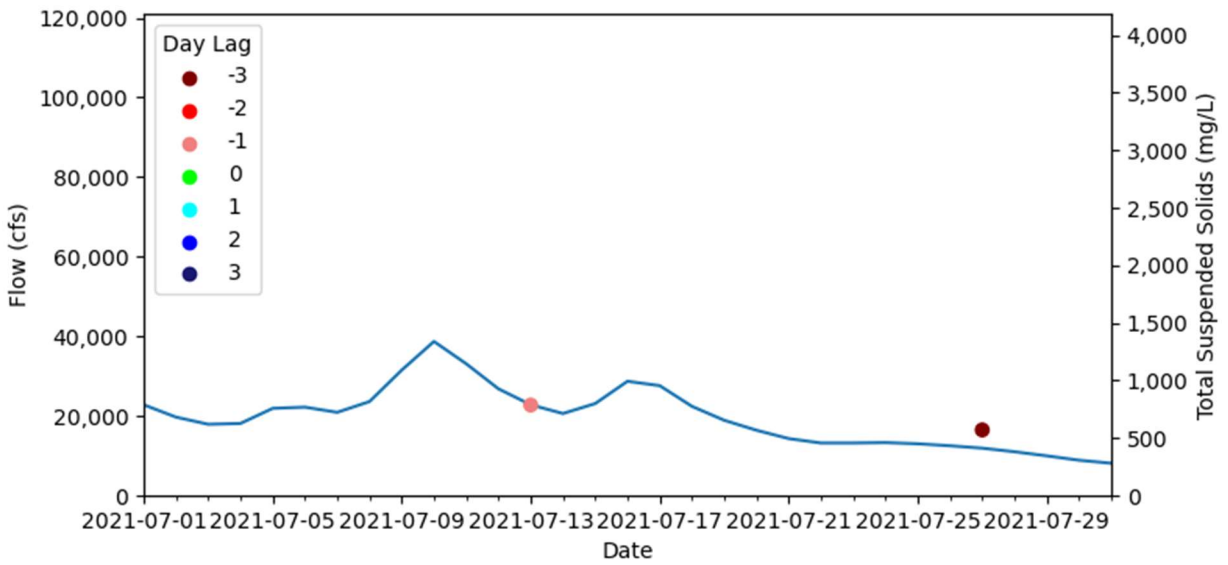


**Figure A-4:** July 2021 Flow and Total Suspended Solids Graph for Landsat Data
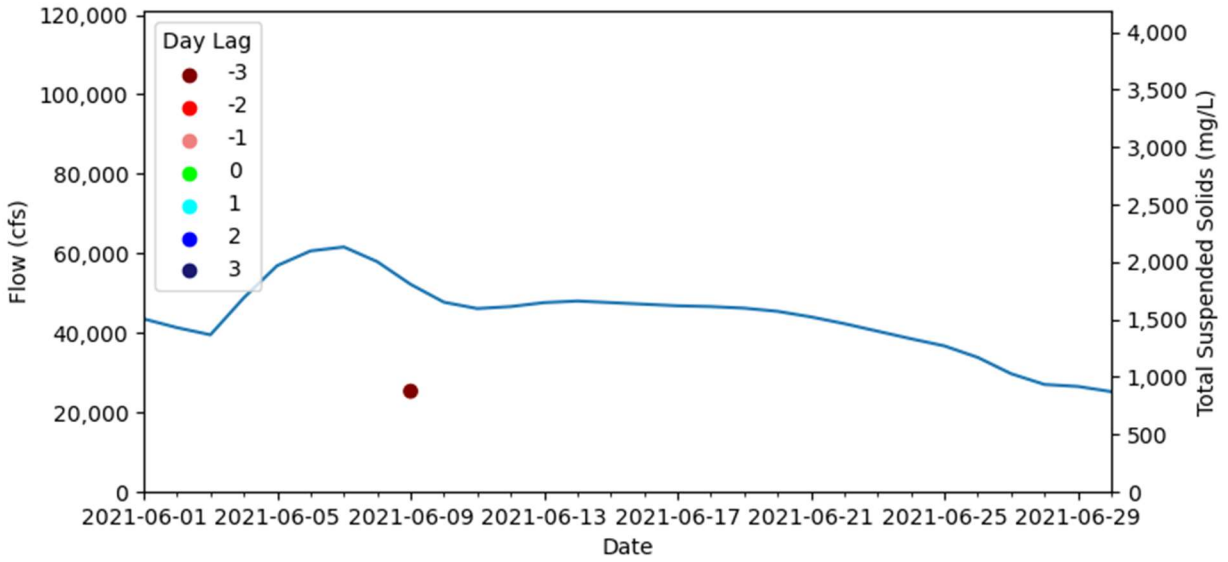
**Figure A-5:** June 2021 Flow and Total Suspended Solids Graph for Landsat Data
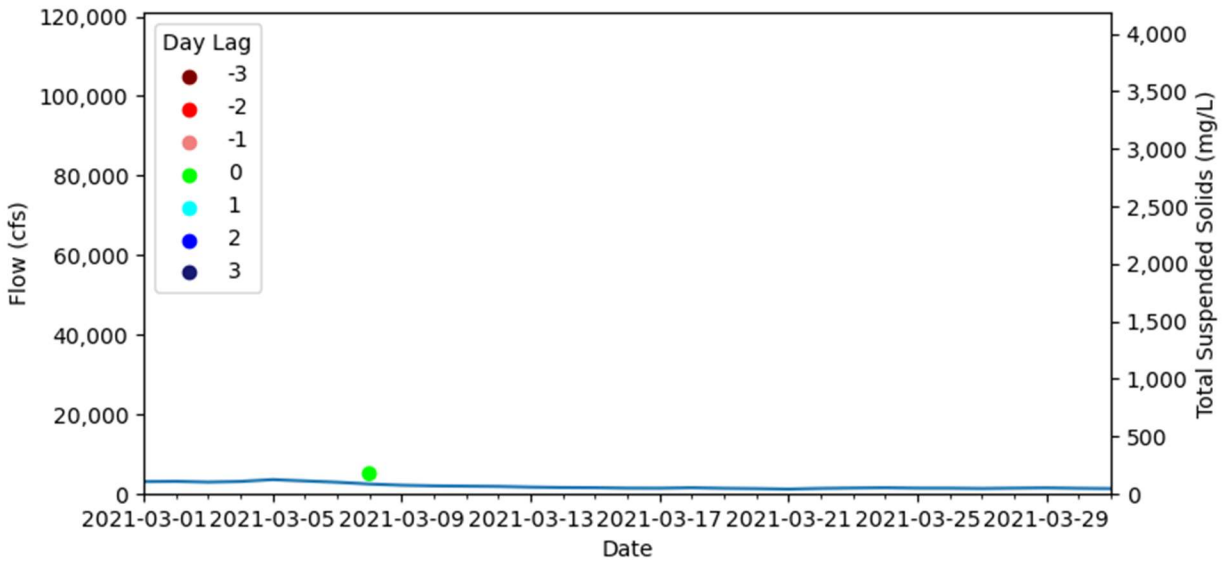


**Figure A-6:** March 2021 Flow and Total Suspended Solids Graph for Landsat Data
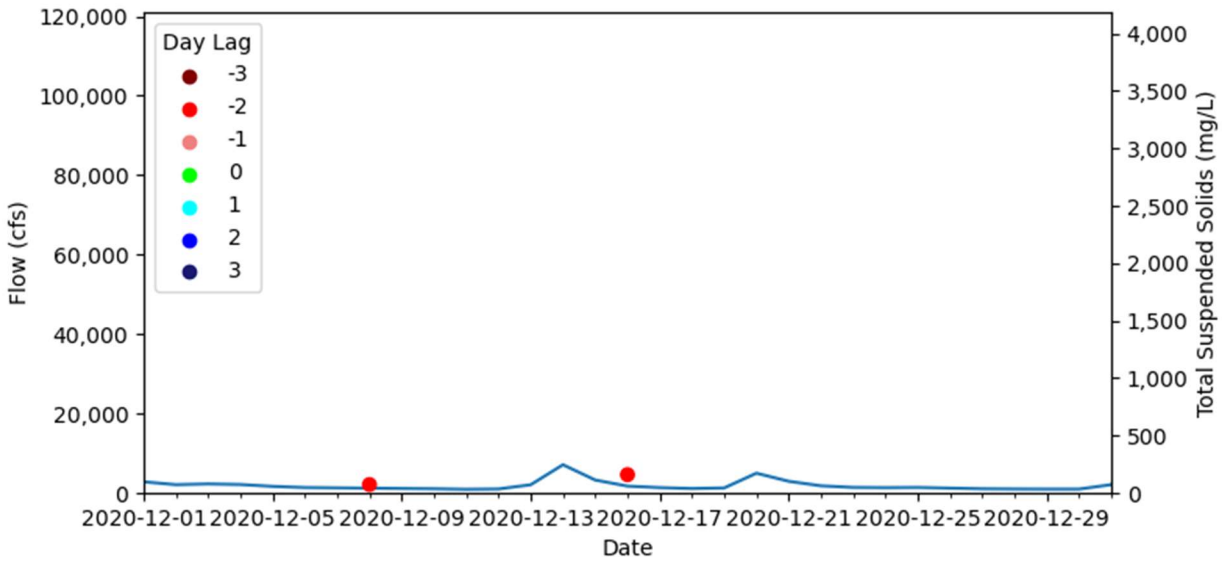
**Figure A-7:** December 2020 Flow and Total Suspended Solids Graph for Landsat Data
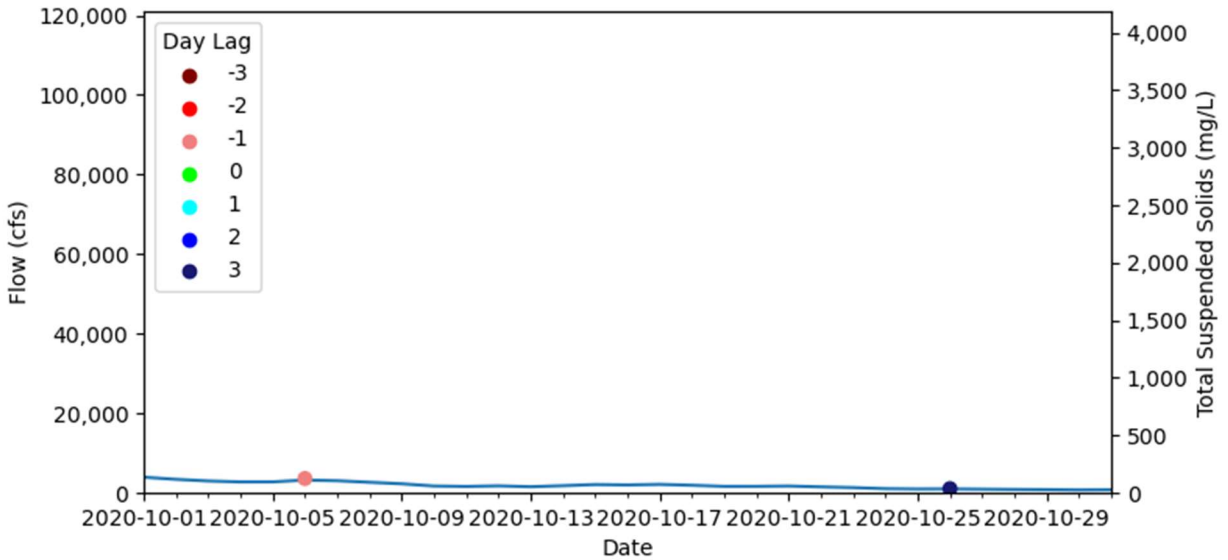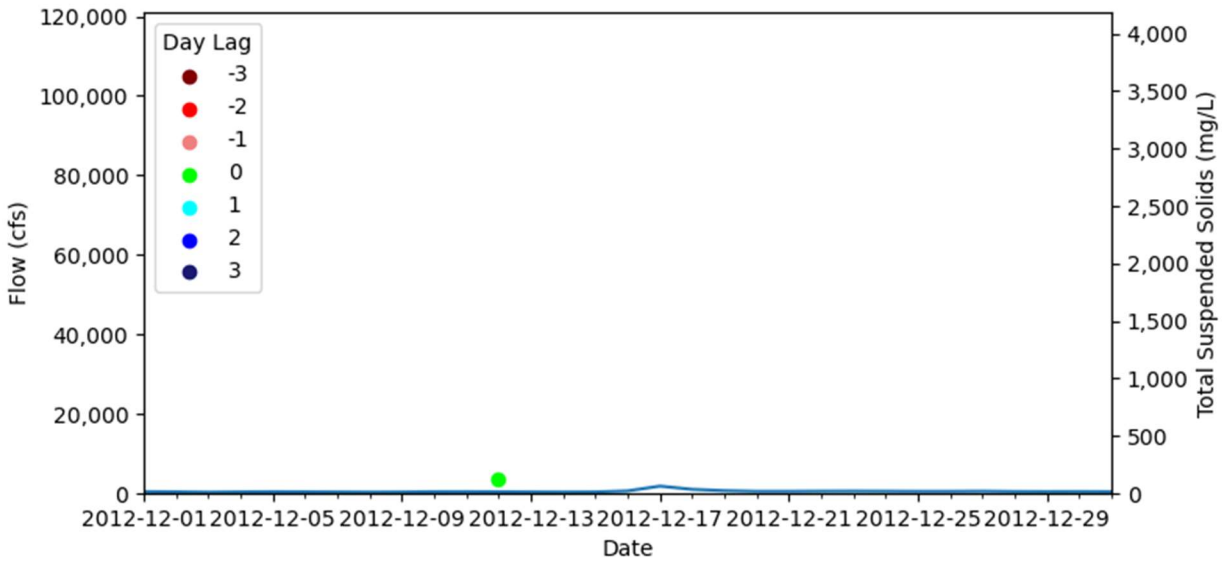


**Figure A-8:** October 2020 Flow and Total Suspended Solids Graph for Landsat Data
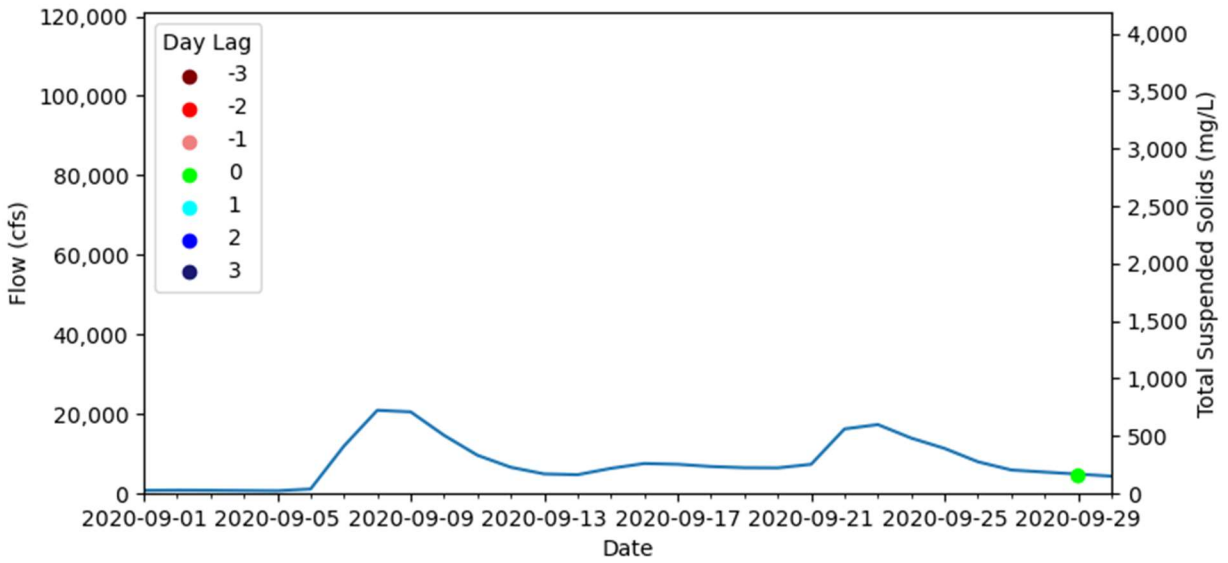
**Figure A-9:** September 2020 Flow and Total Suspended Solids Graph for Landsat Data
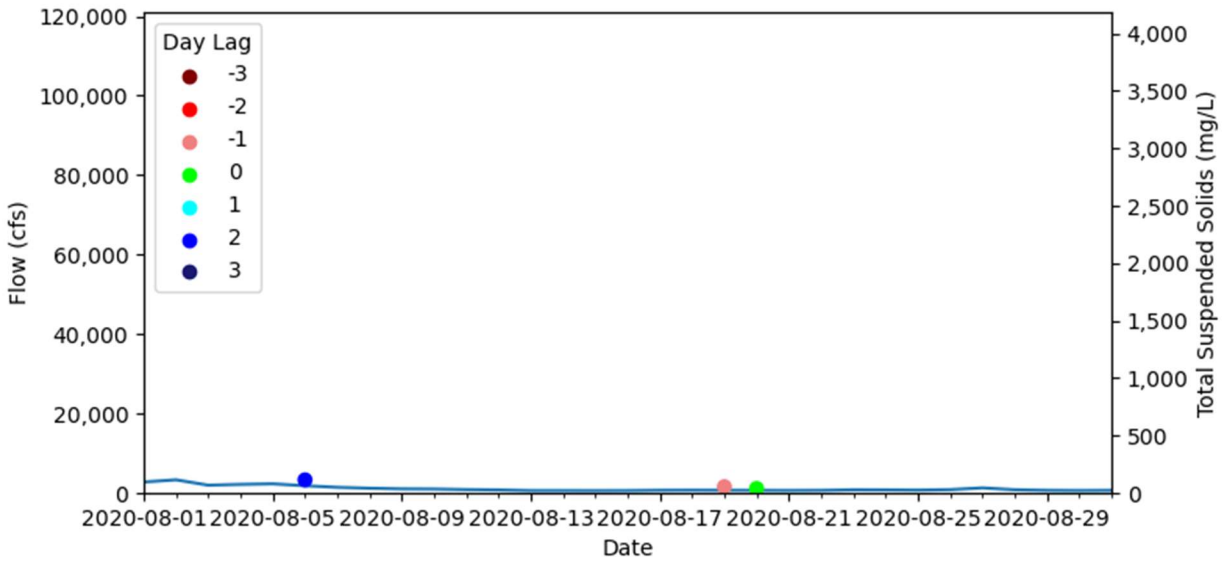
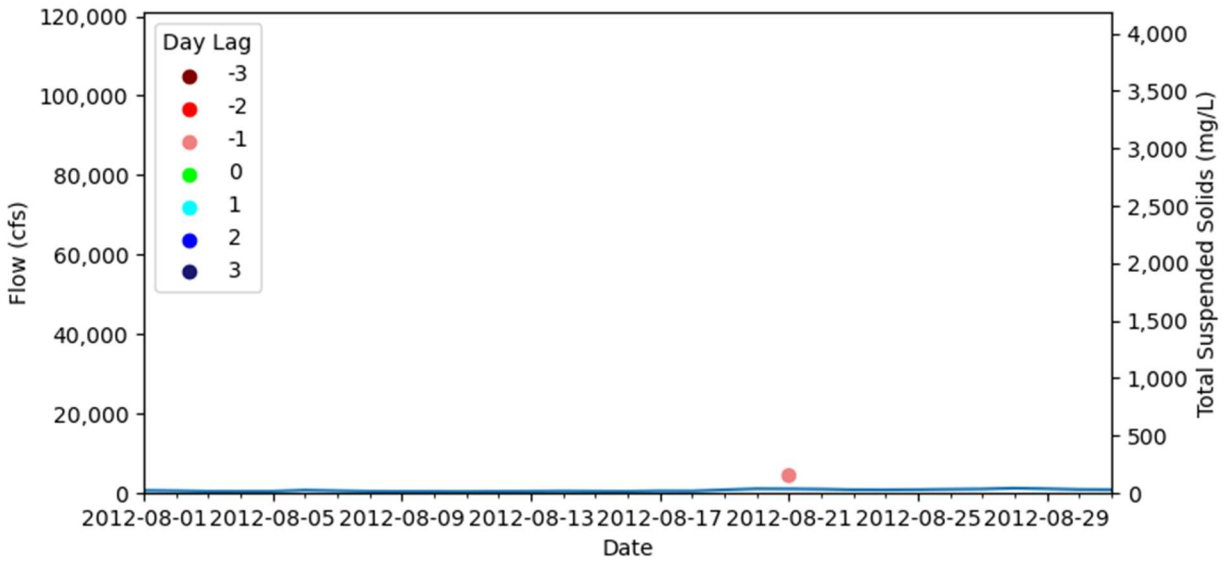

**Figure A-10:** August 2020 Flow and Total Suspended Solids Graph for Landsat Data
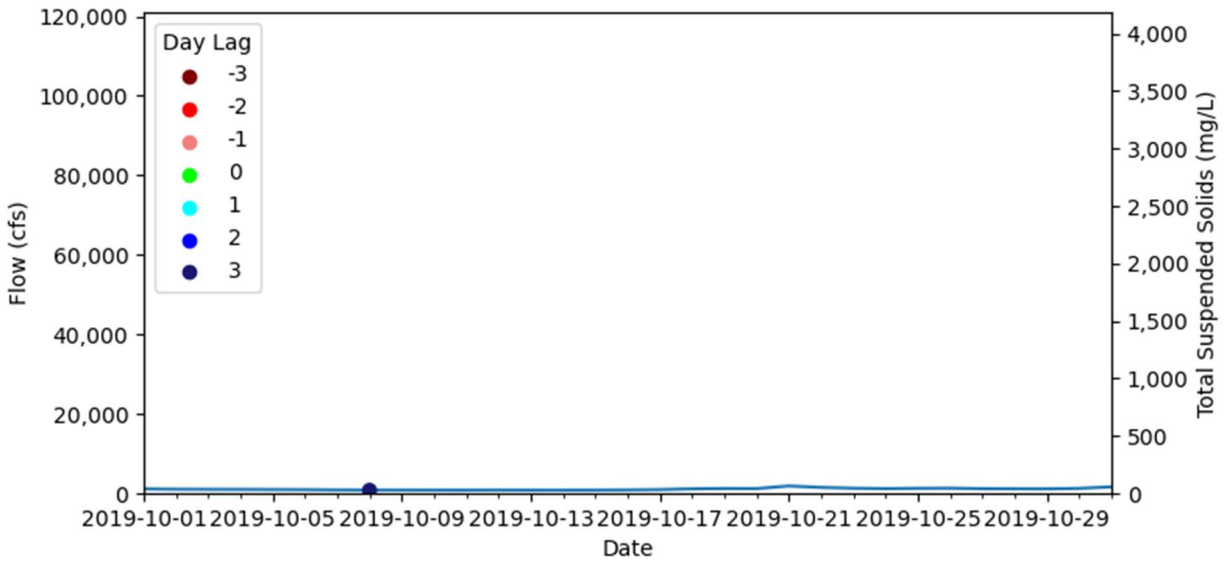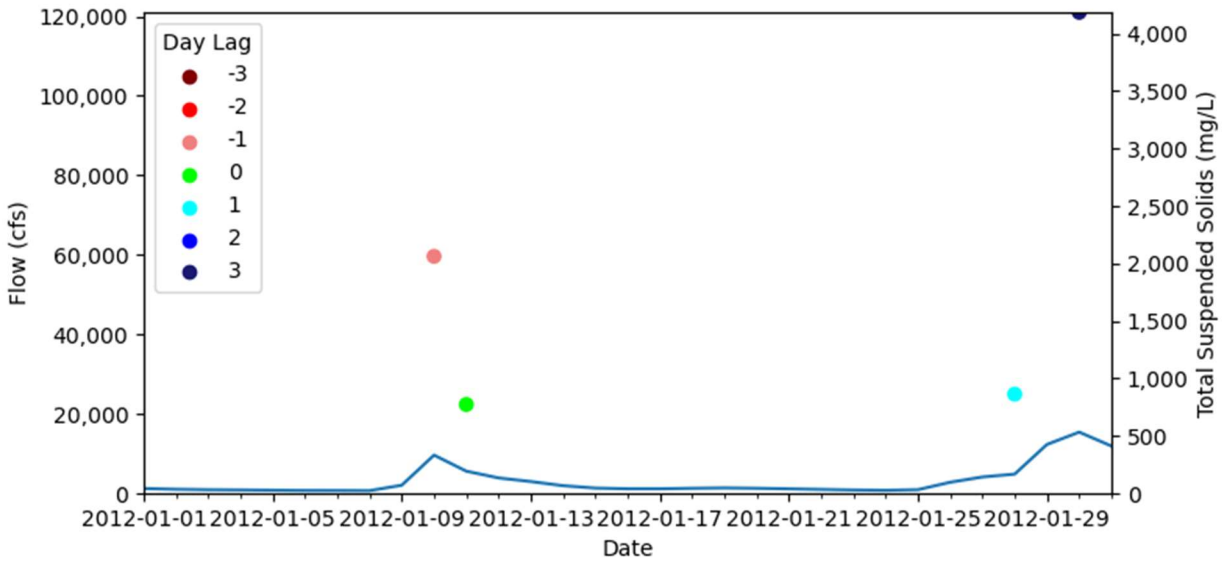
**Figure A-11:** October 2019 Flow and Total Suspended Solids Graph for Landsat Data
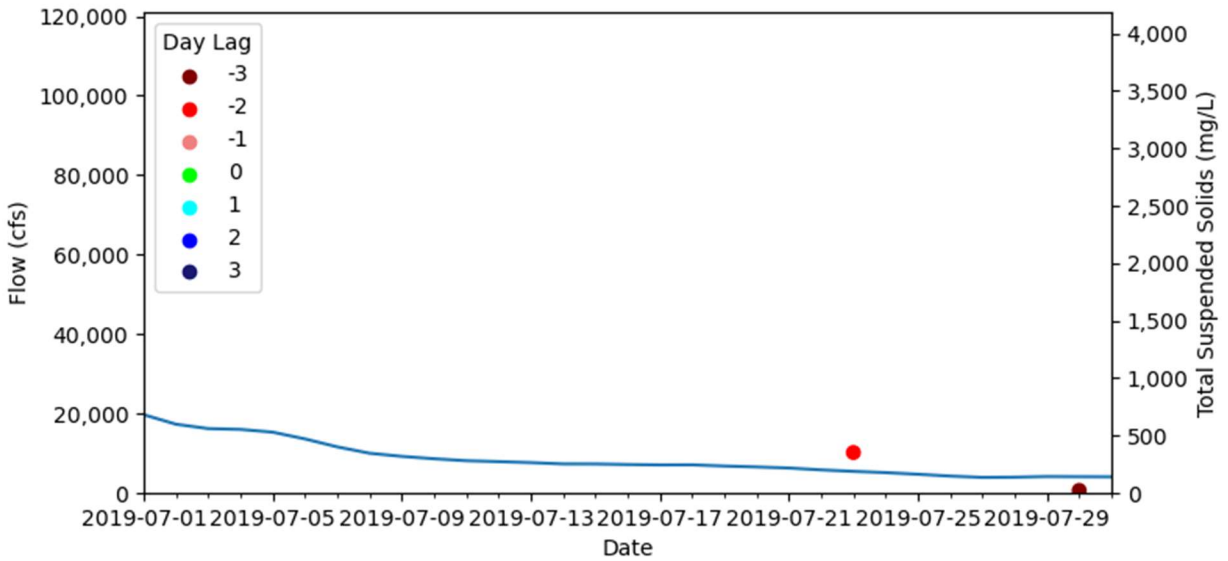


**Figure A-12:** July 2019 Flow and Total Suspended Solids Graph for Landsat Data
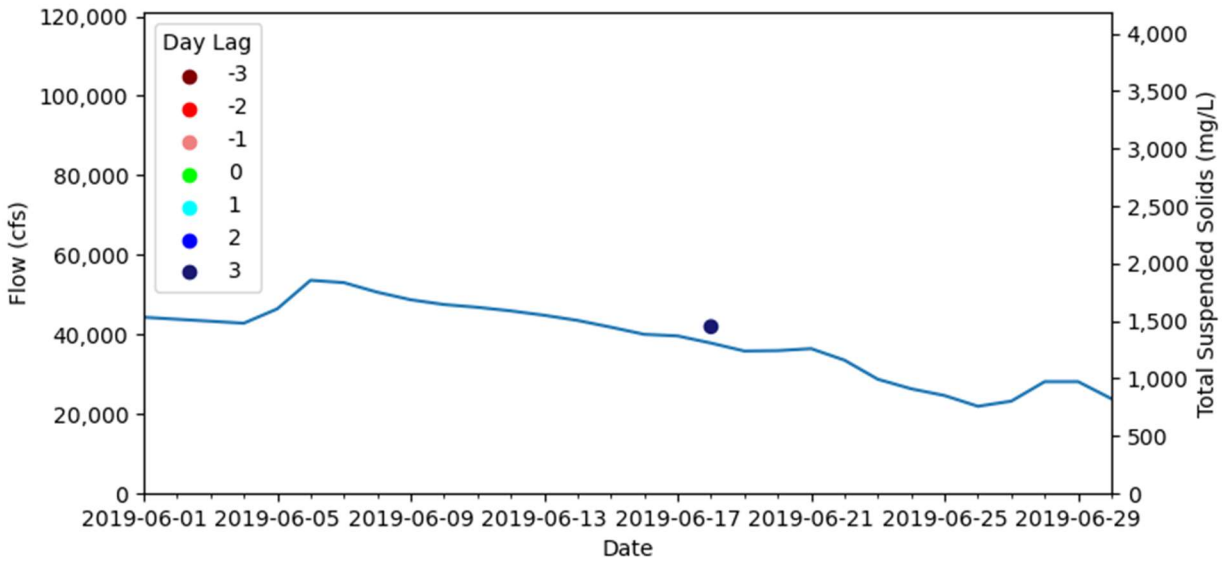
**Figure A-13:** June 2019 Flow and Total Suspended Solids Graph for Landsat Data
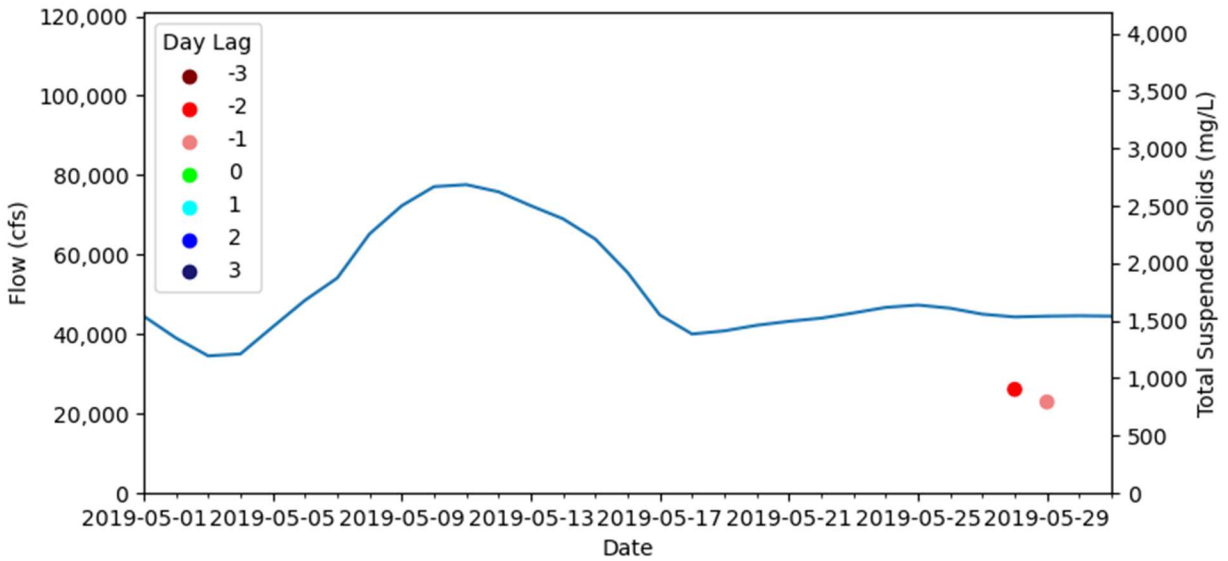


**Figure A-14:** May 2019 Flow and Total Suspended Solids Graph for Landsat Data
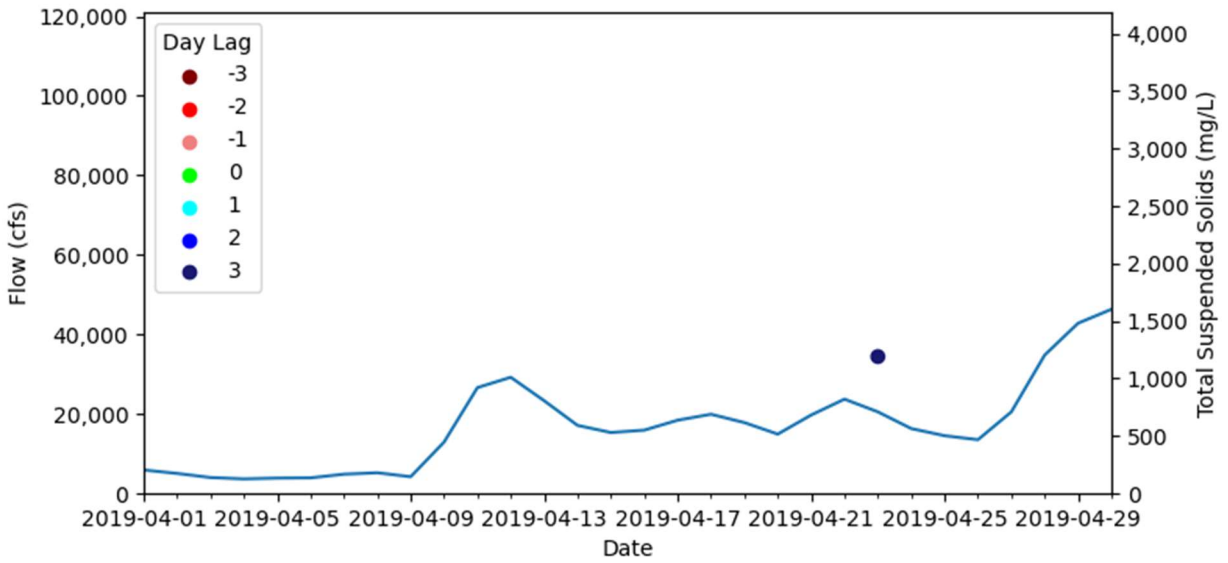
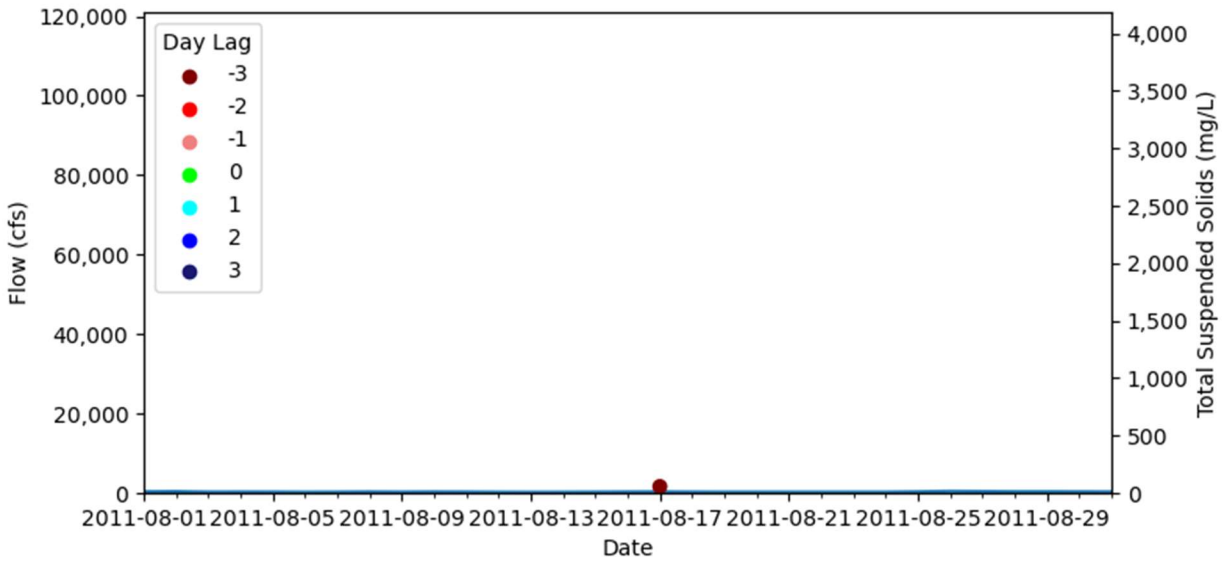**Figure A-15:** April 2019 Flow and Total Suspended Solids Graph for Landsat Data
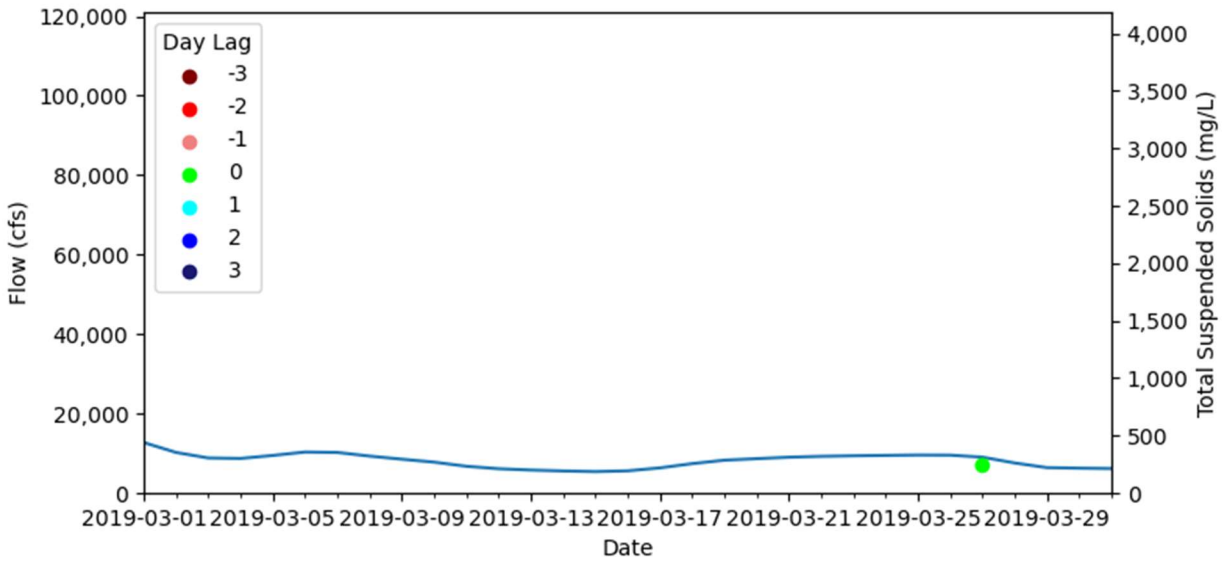


**Figure A-16:** March 2019 Flow and Total Suspended Solids Graph for Landsat Data
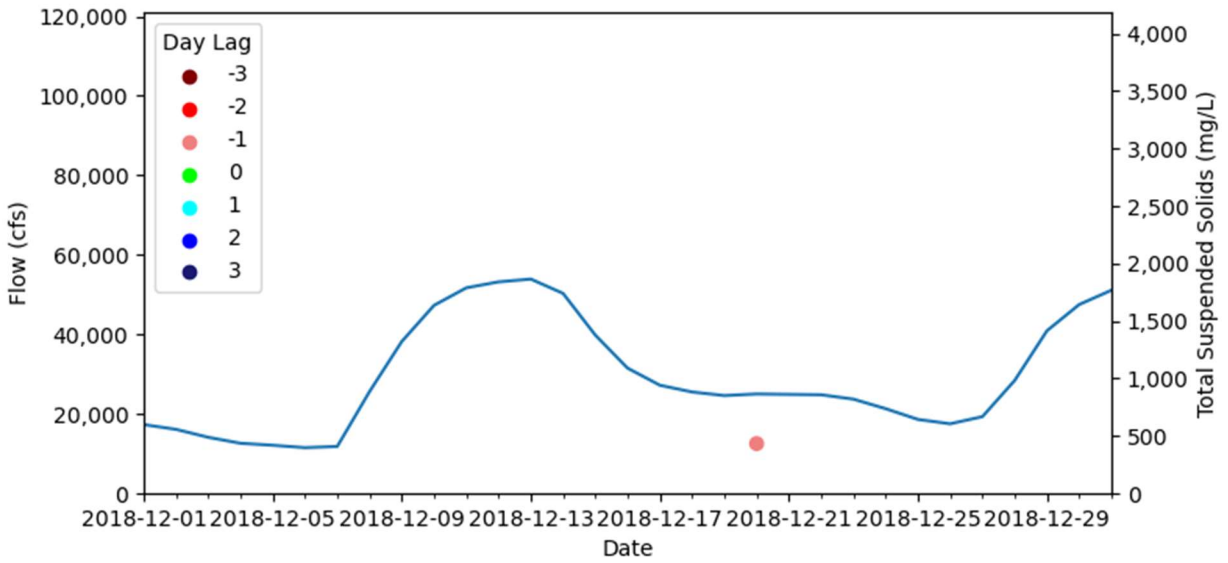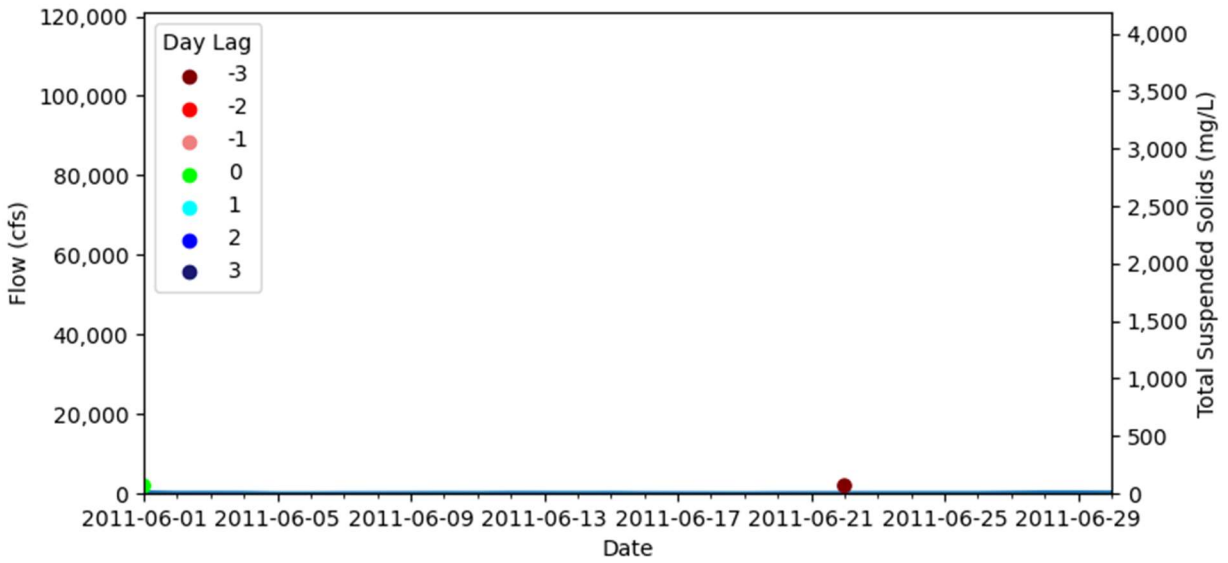
**Figure A-17:** December 2018 Flow and Total Suspended Solids Graph for Landsat Data
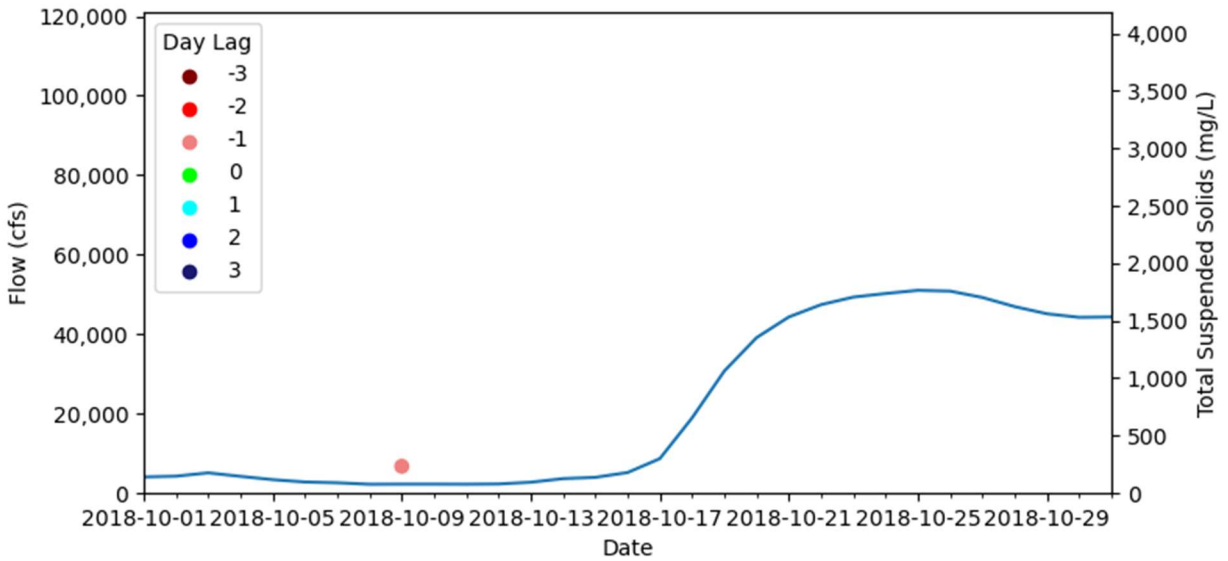


**Figure A-18:** October 2018 Flow and Total Suspended Solids Graph for Landsat Data
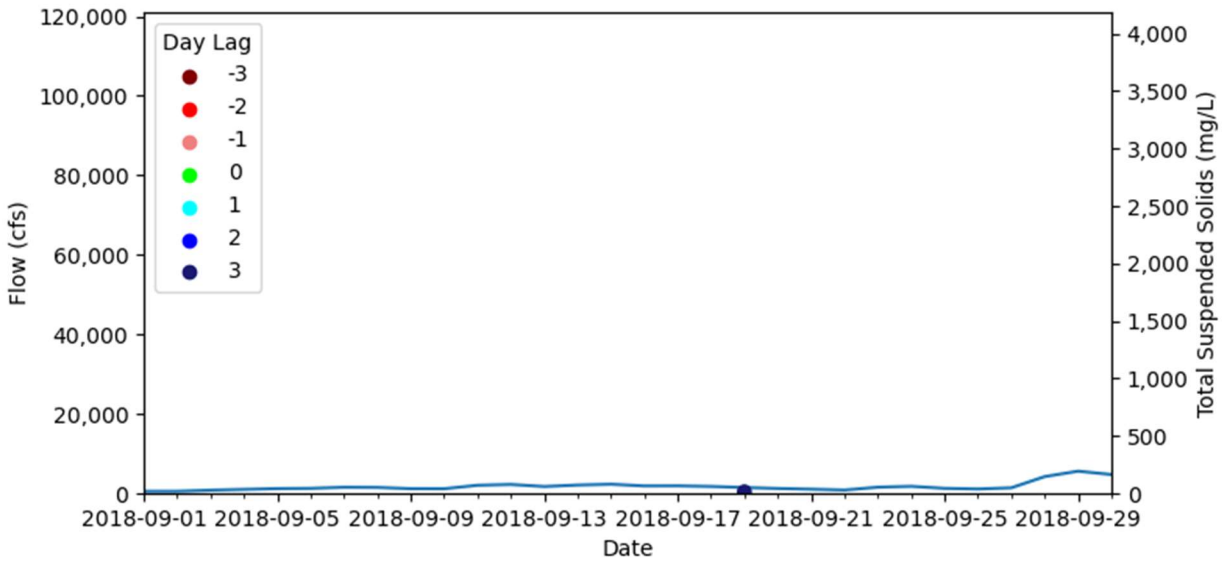
**Figure A-19:** September 2018 Flow and Total Suspended Solids Graph for Landsat Data
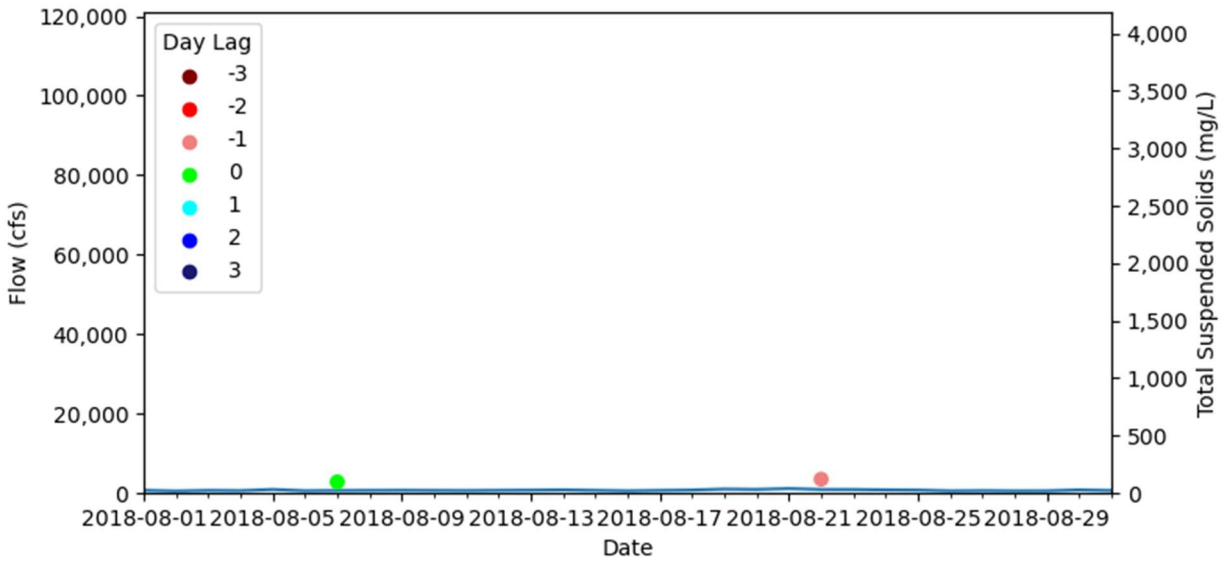


**Figure A-20:** August 2018 Flow and Total Suspended Solids Graph for Landsat Data
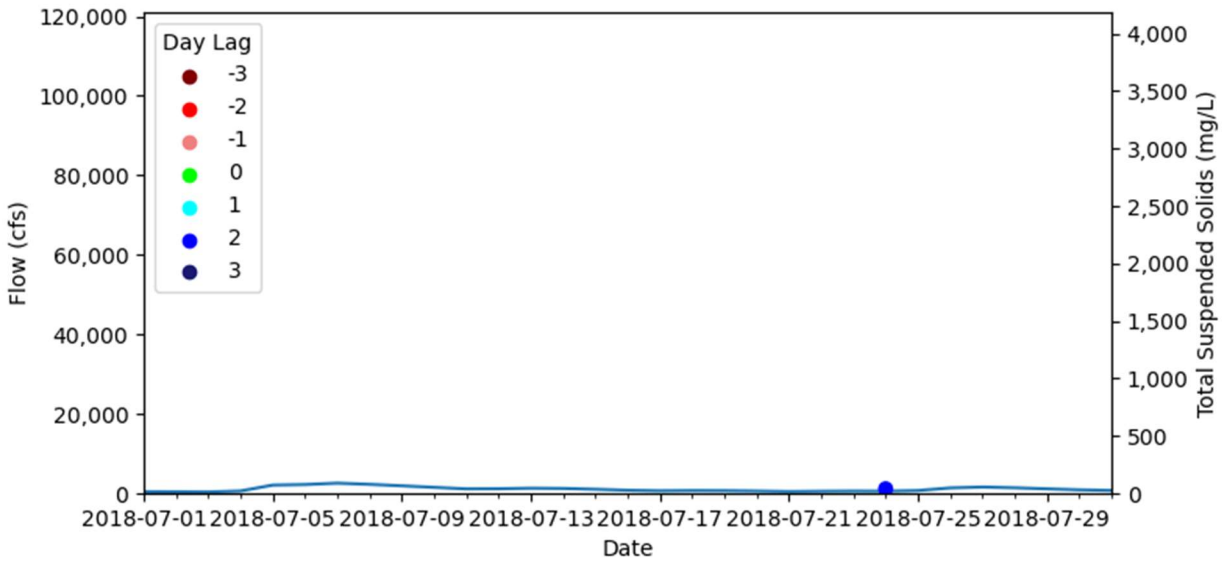
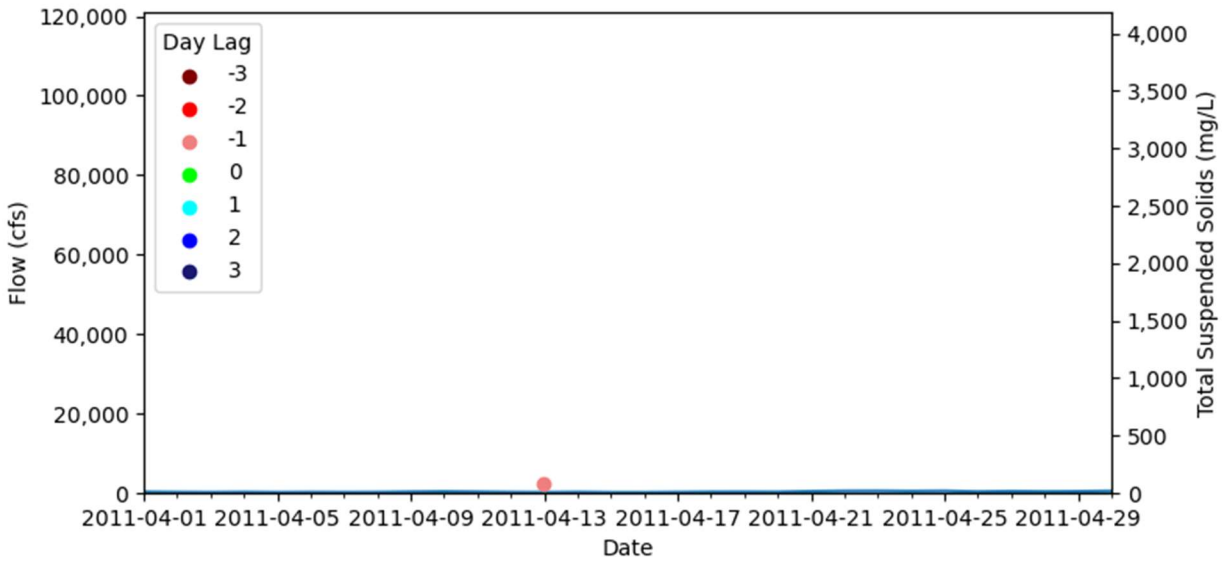**Figure A-21:** July 2018 Flow and Total Suspended Solids Graph for Landsat Data
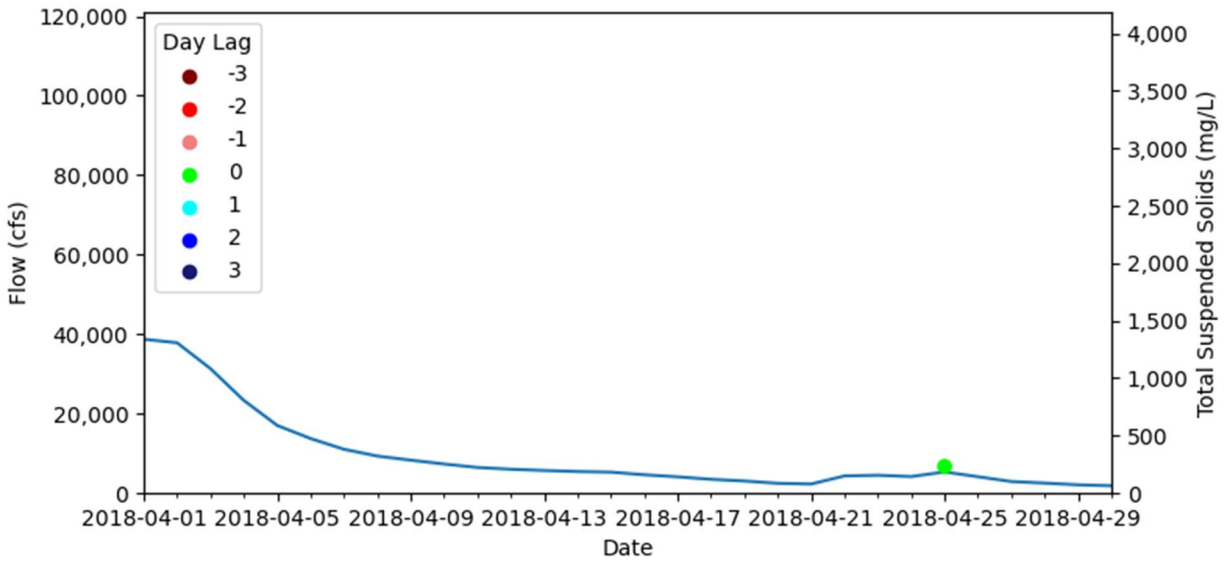


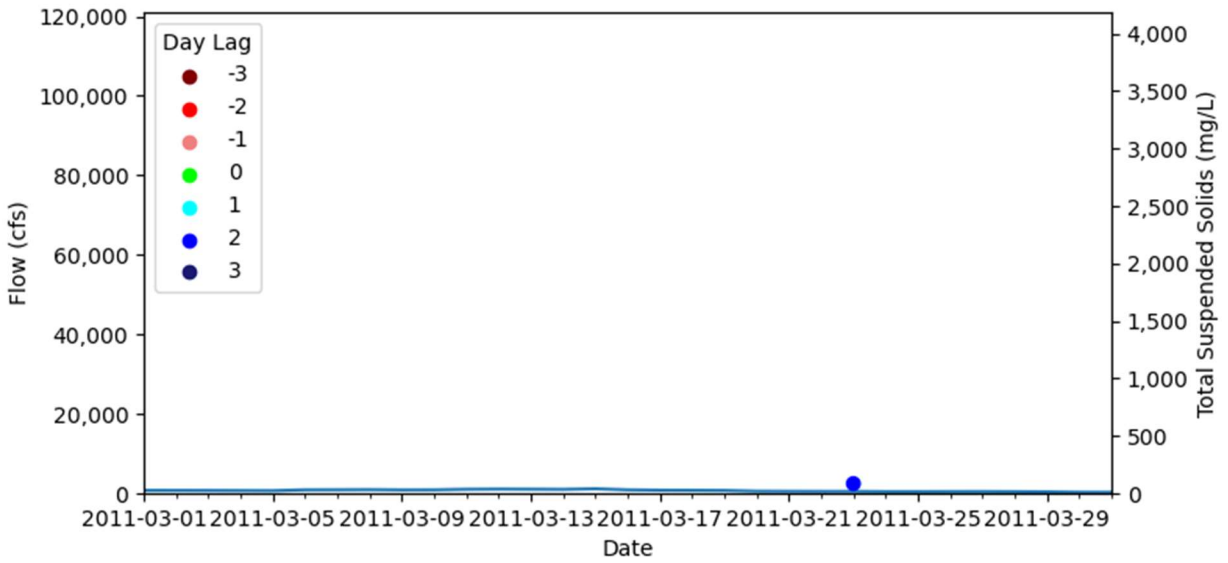**Figure A-22:** April 2018 Flow and Total Suspended Solids Graph for Landsat Data
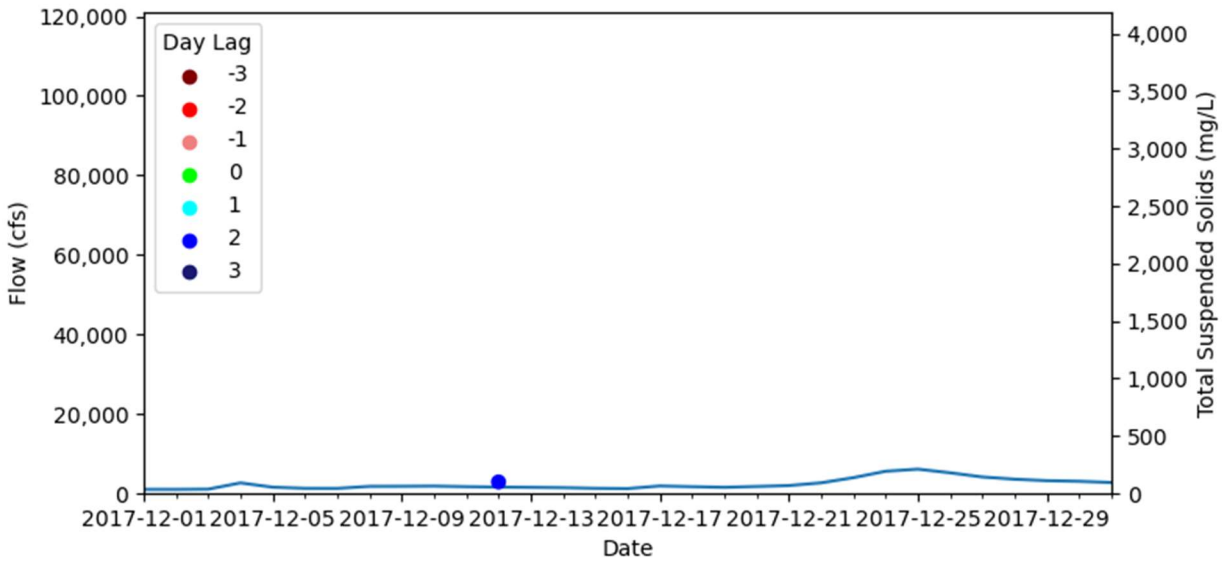
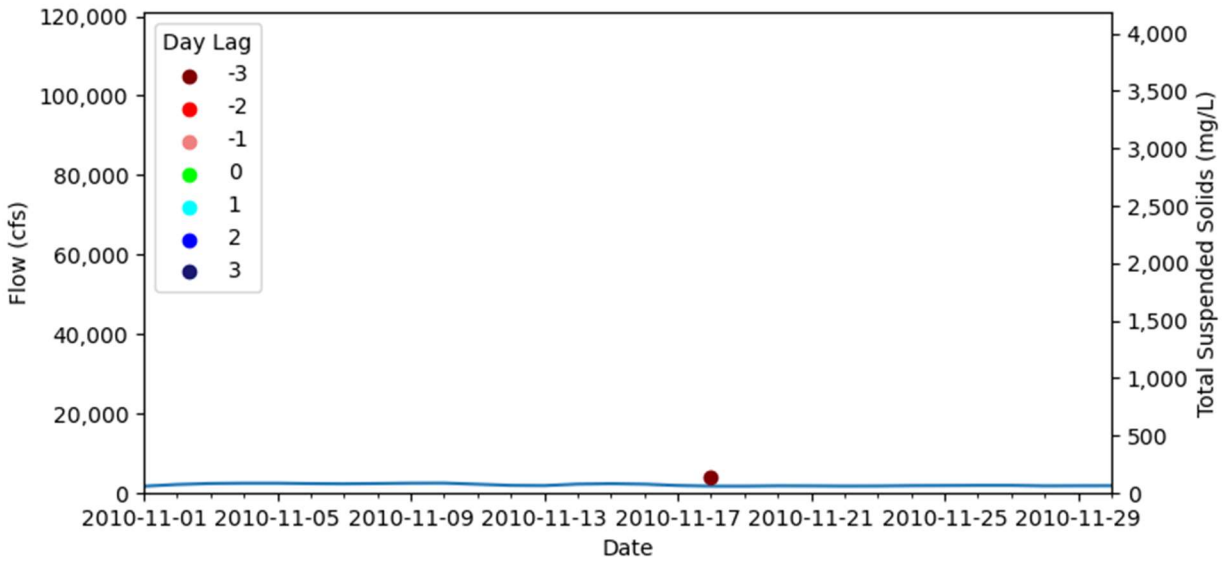**Figure A-23:** December 2017 Flow and Total Suspended Solids Graph for Landsat Data
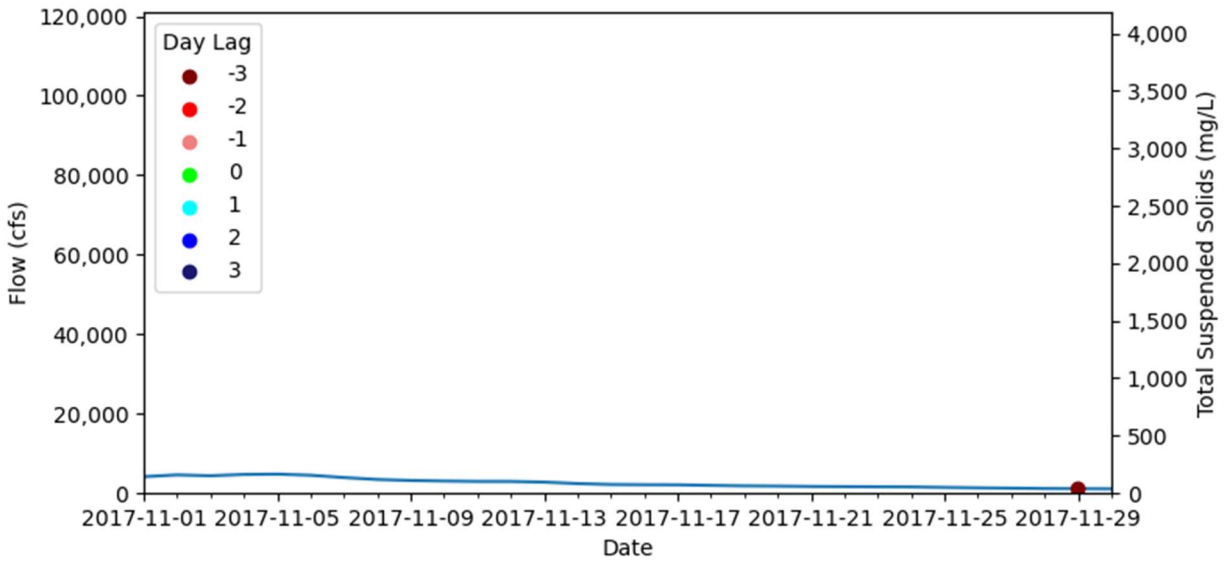


**Figure A-24:** November 2017 Flow and Total Suspended Solids Graph for Landsat Data
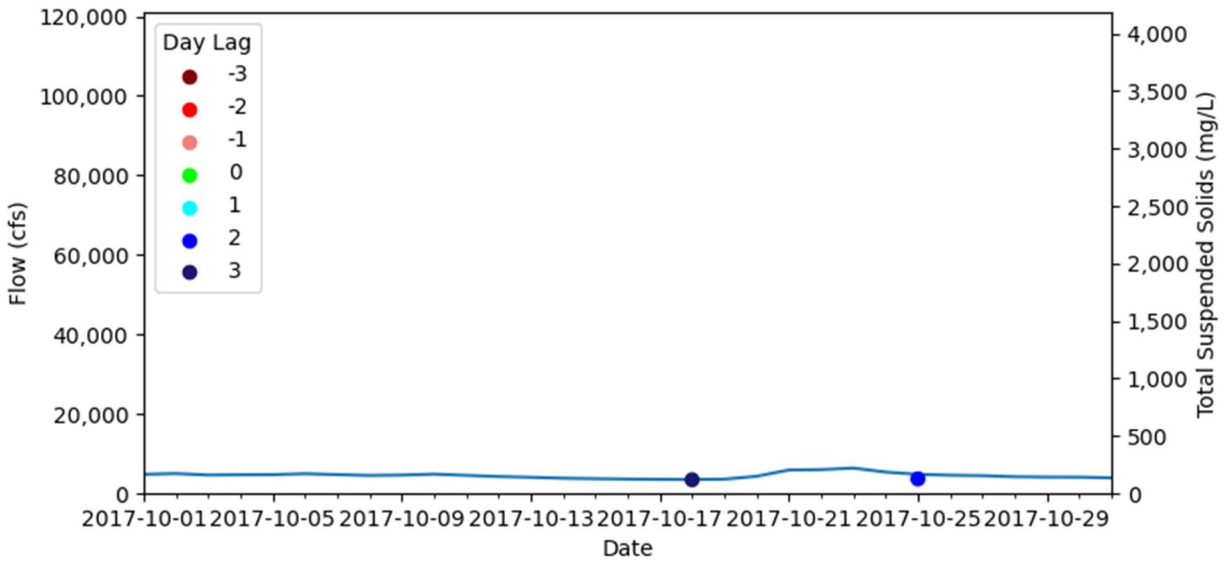
**Figure A-25:** October 2017 Flow and Total Suspended Solids Graph for Landsat Data
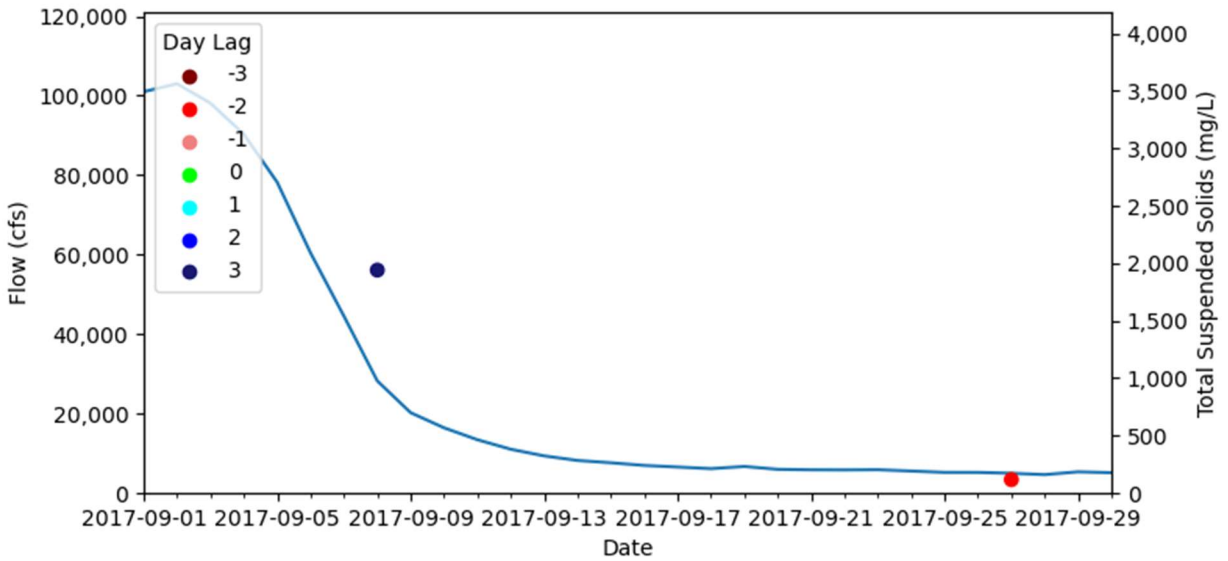


**Figure A-26:** September 2017 Flow and Total Suspended Solids Graph for Landsat Data
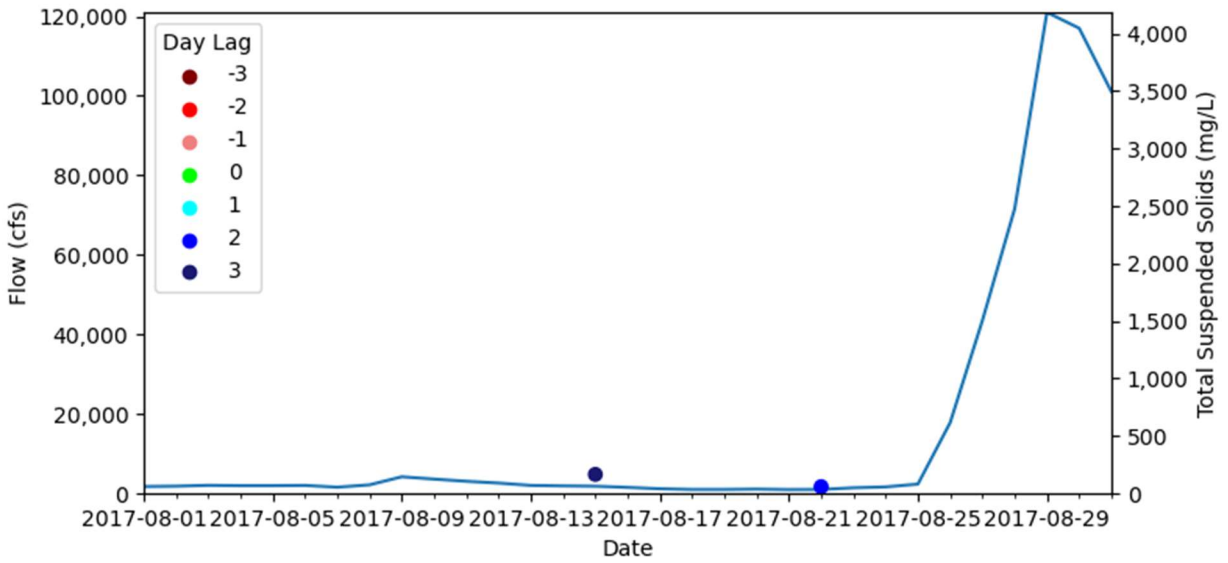
**Figure A-27:** August 2017 Flow and Total Suspended Solids Graph for Landsat Data
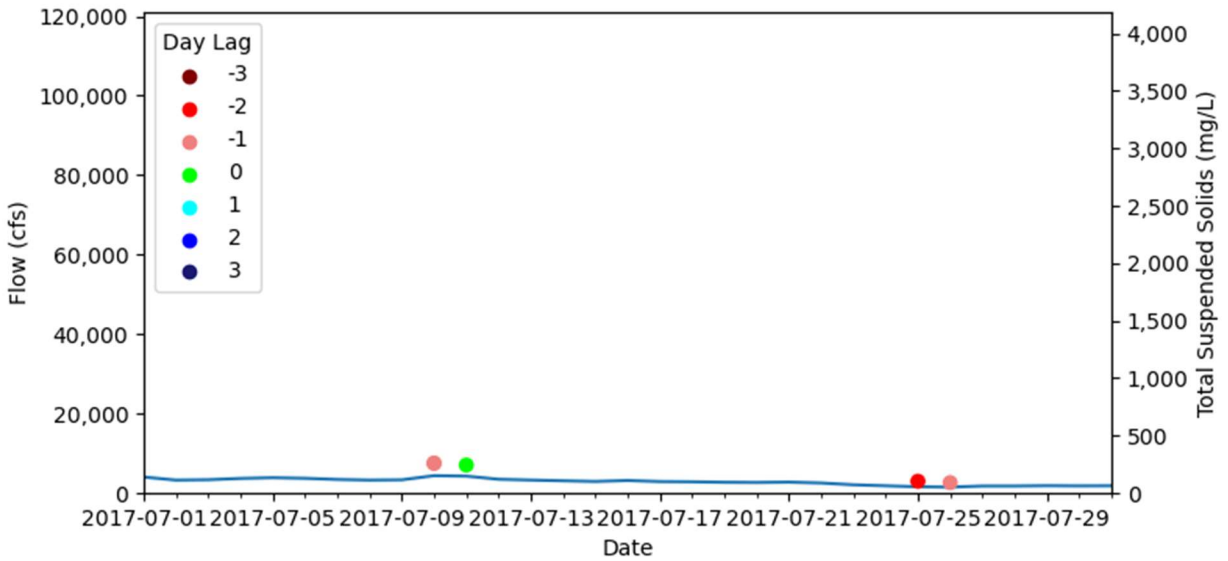


**Figure A-28:** July 2017 Flow and Total Suspended Solids Graph for Landsat Data
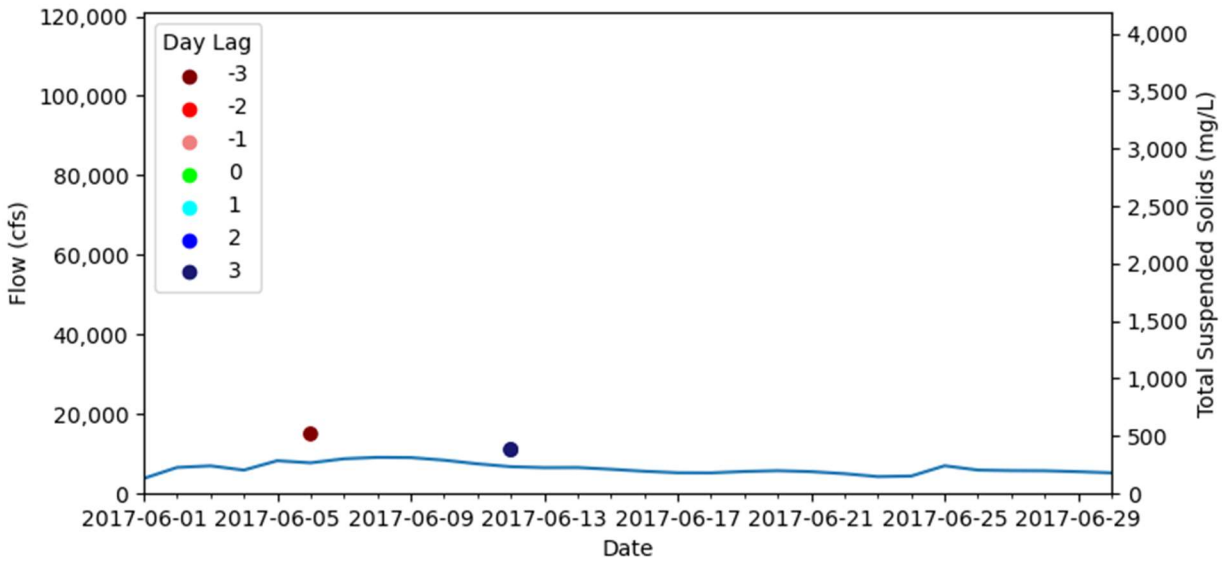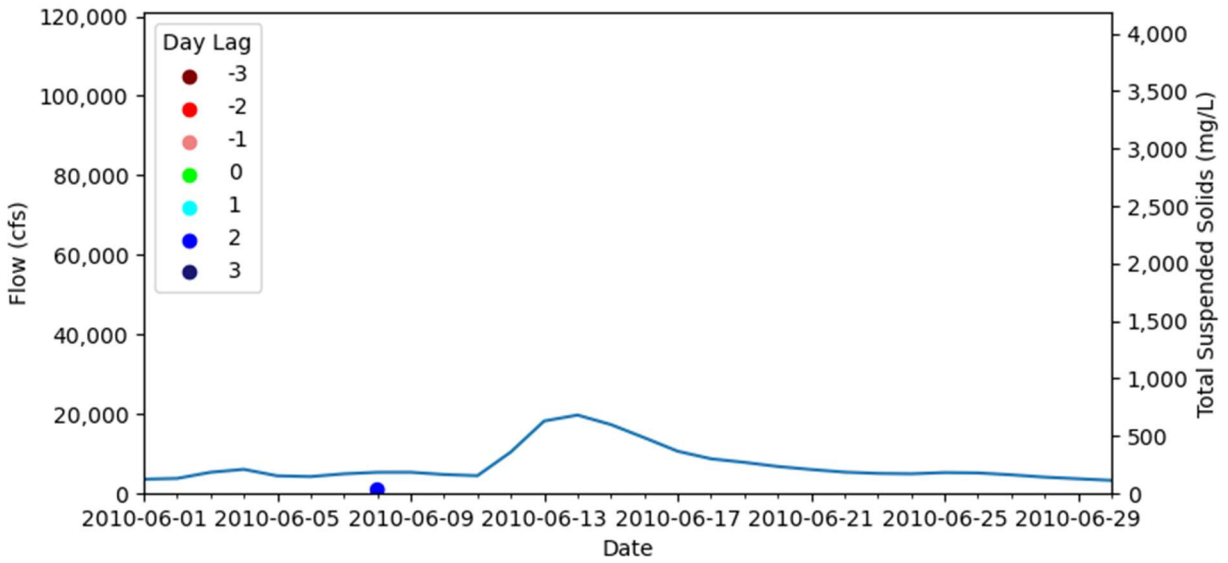
**Figure A-29:** June 2017 Flow and Total Suspended Solids Graph for Landsat Data
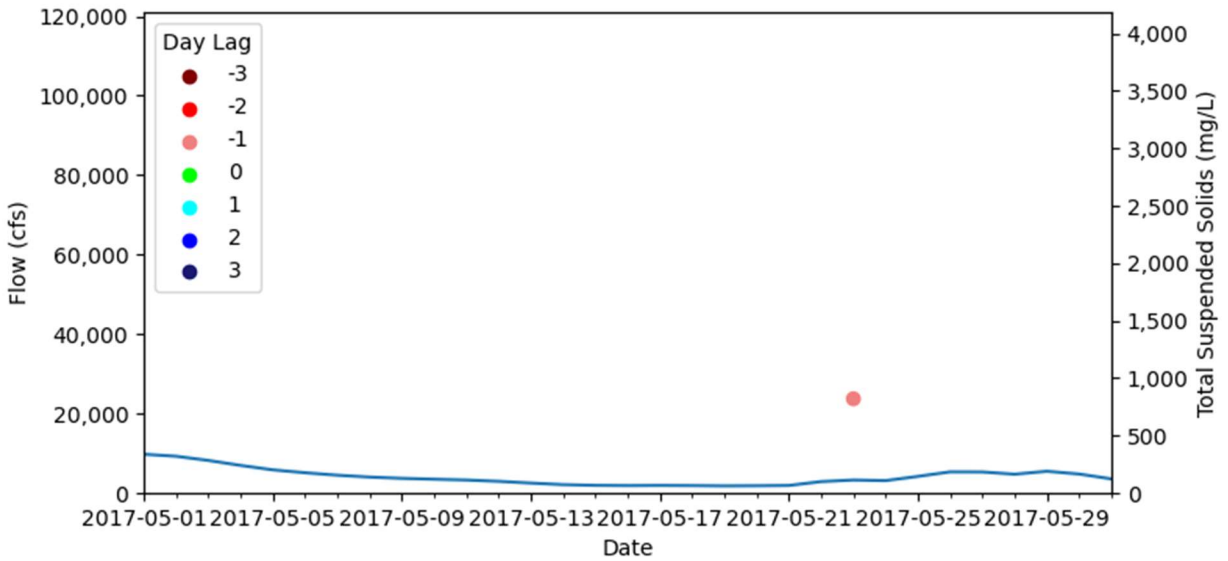


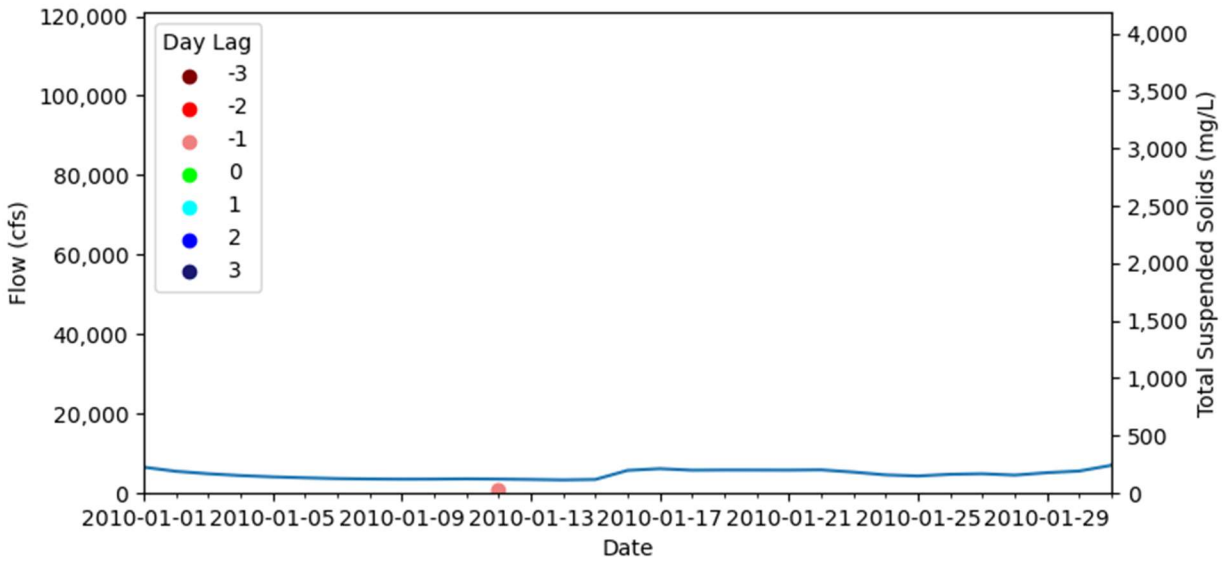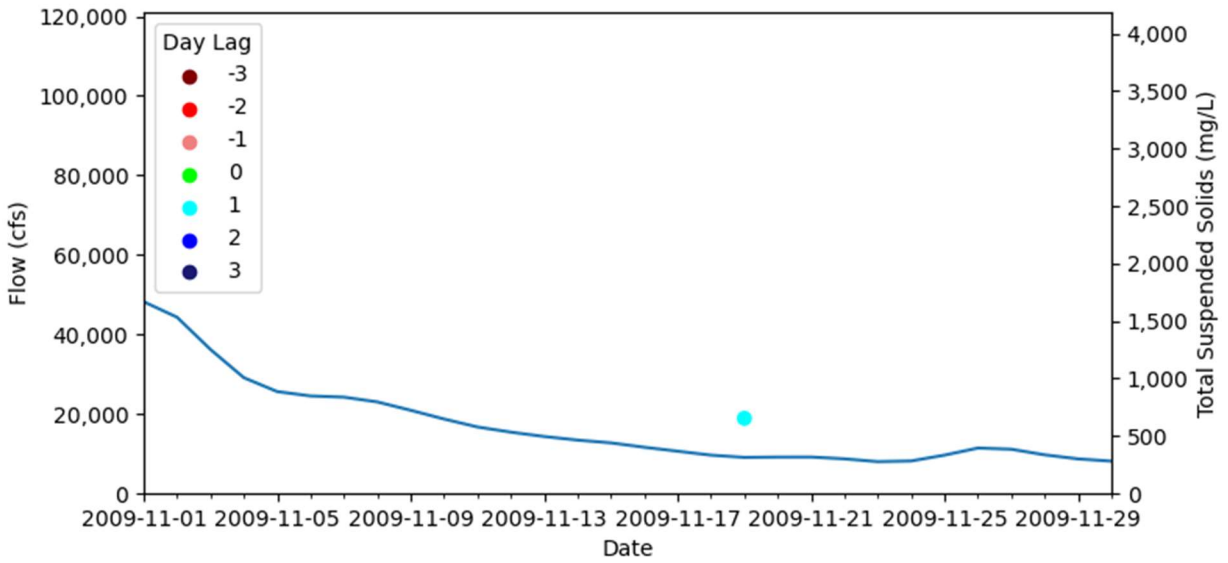**Figure A-30:** May 2017 Flow and Total Suspended Solids Graph for Landsat Data
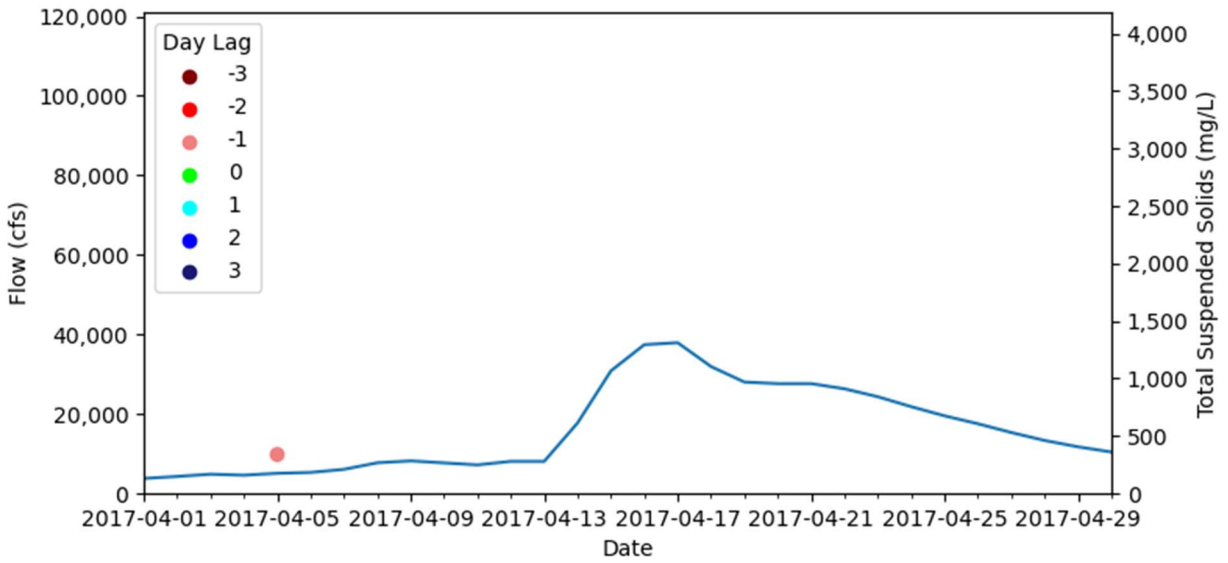
**Figure A-31:** April 2017 Flow and Total Suspended Solids Graph for Landsat Data
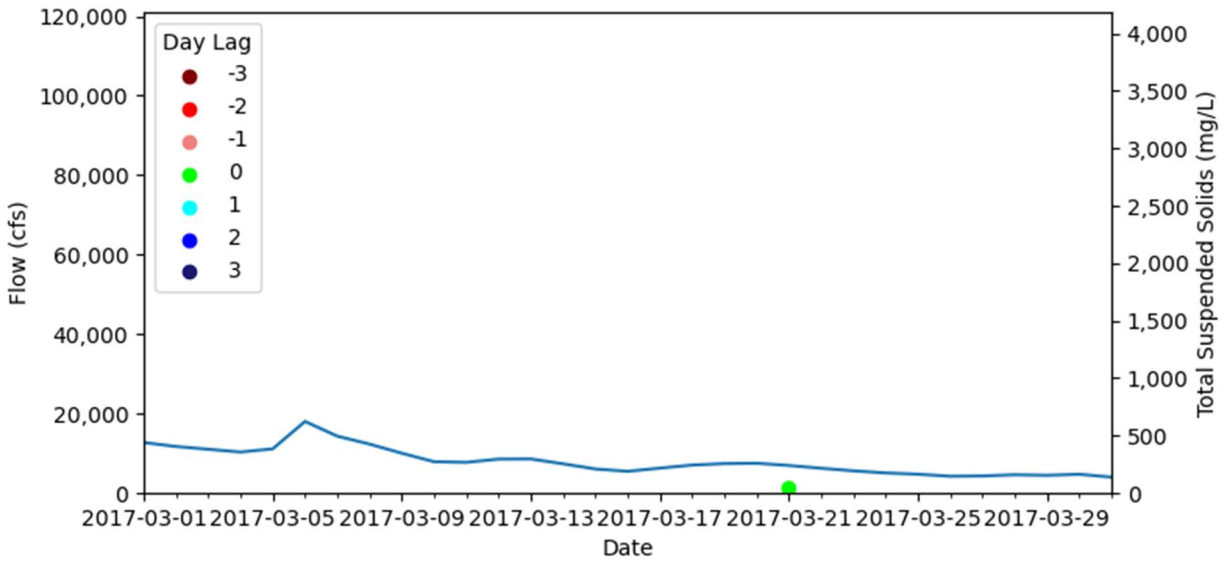


**Figure A-32:** March 2017 Flow and Total Suspended Solids Graph for Landsat Data
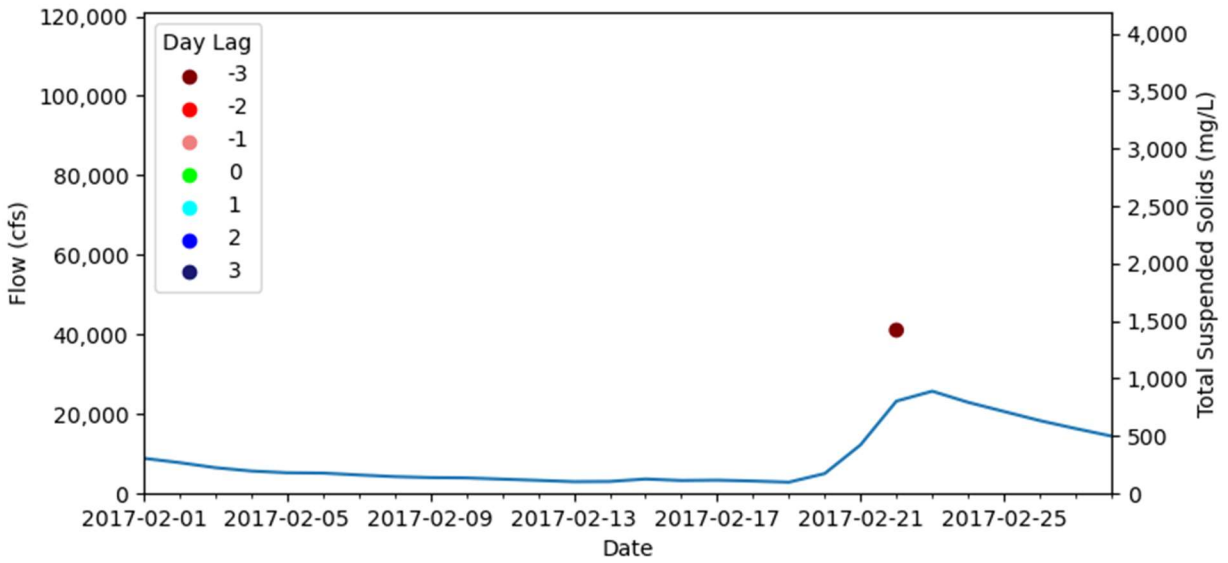
**Figure A-33:** February 2017 Flow and Total Suspended Solids Graph for Landsat Data
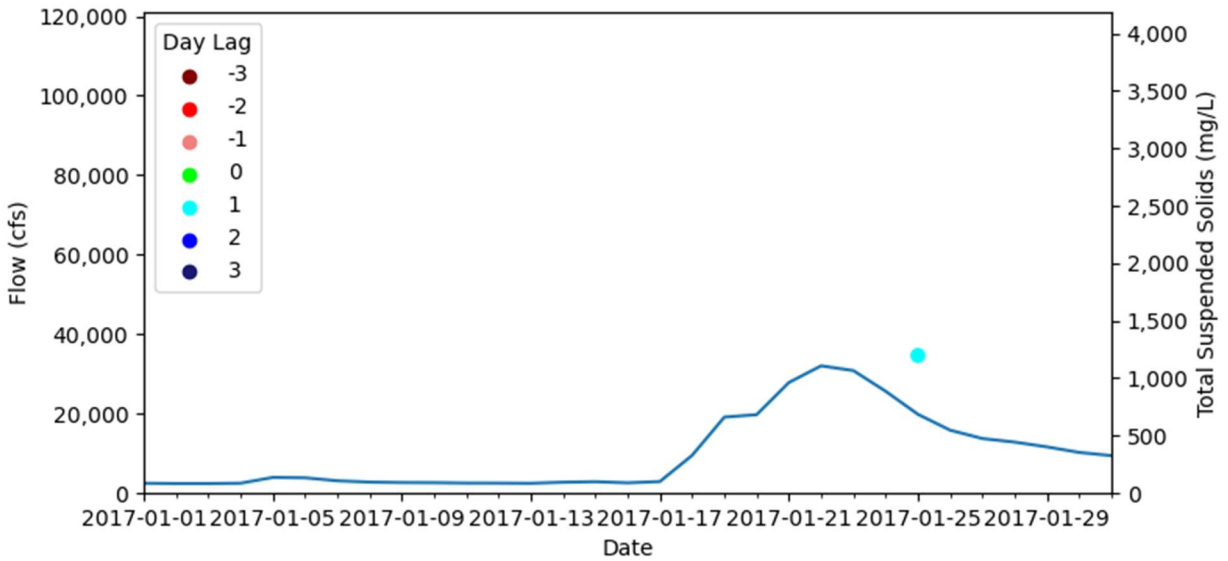


**Figure A-34:** January 2017 Flow and Total Suspended Solids Graph for Landsat Data
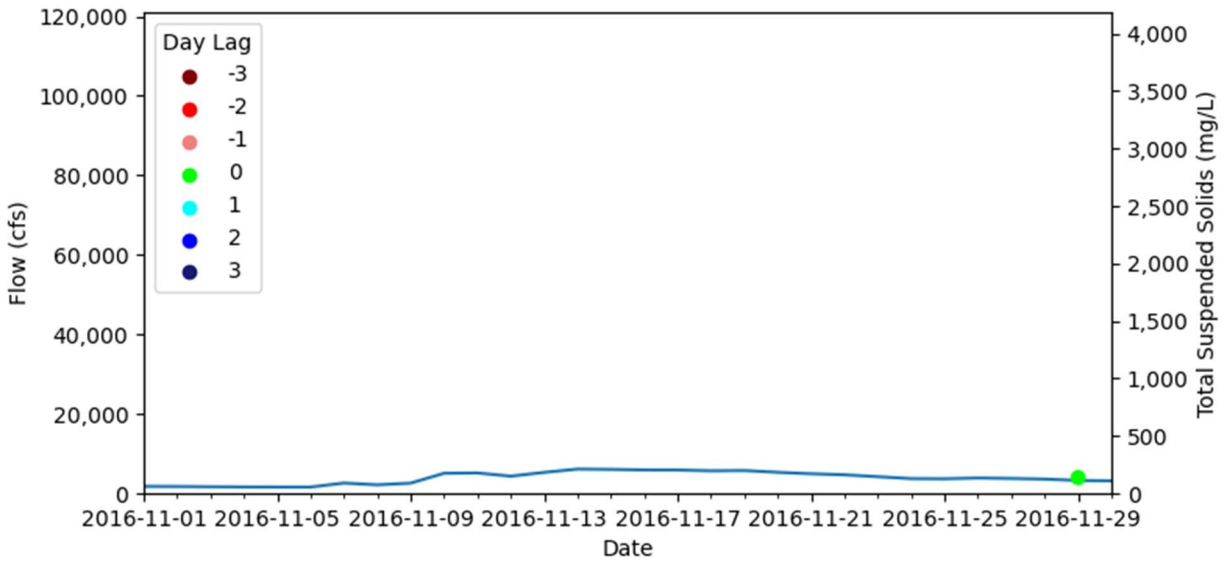
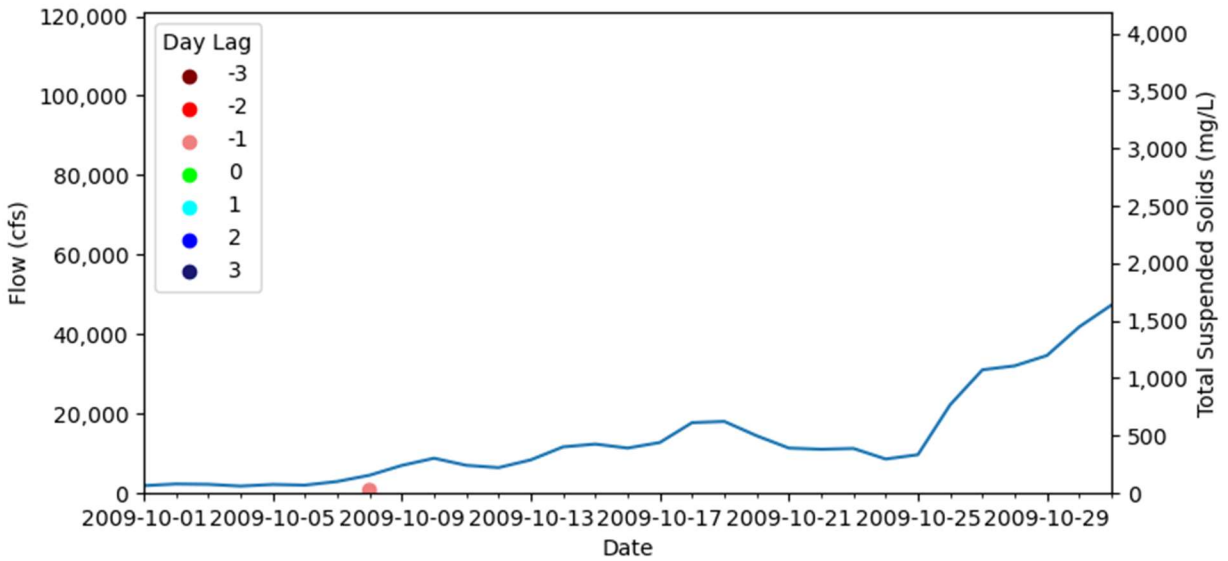**Figure A-35:** November 2016 Flow and Total Suspended Solids Graph for Landsat Data
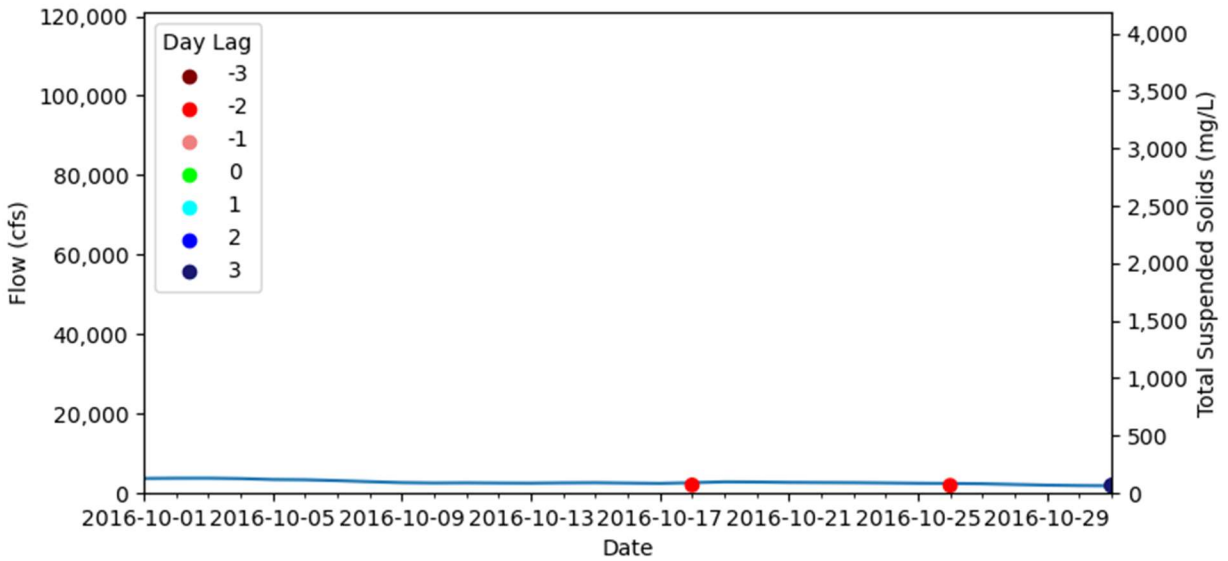


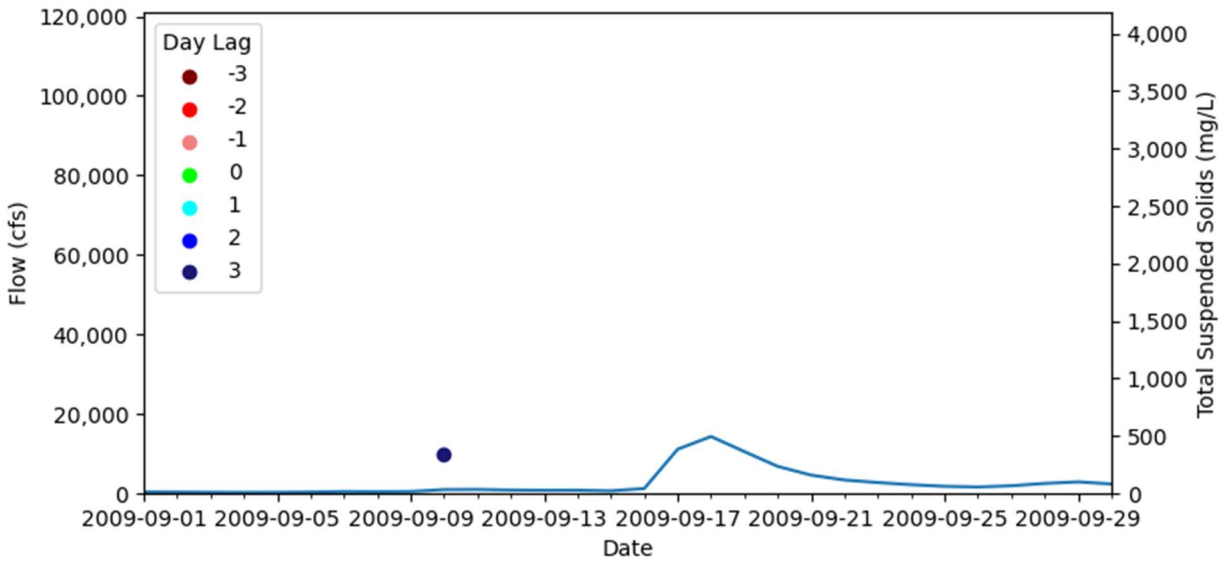**Figure A-36:** October 2016 Flow and Total Suspended Solids Graph for Landsat Data
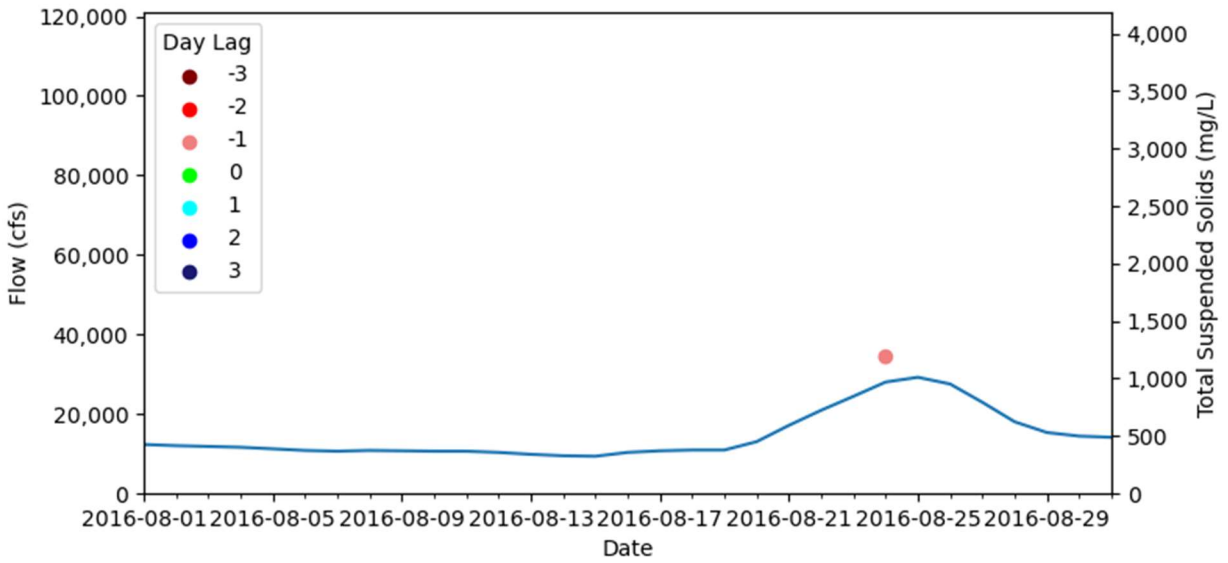
**Figure A-37:** August 2016 Flow and Total Suspended Solids Graph for Landsat Data
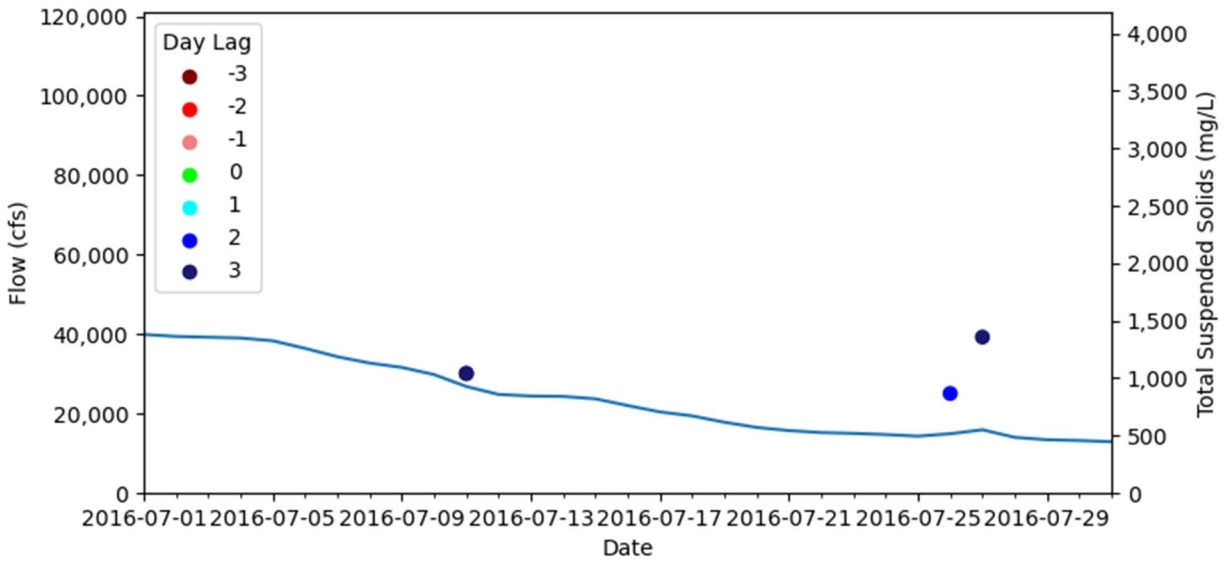


**Figure A-38:** July 2016 Flow and Total Suspended Solids Graph for Landsat Data
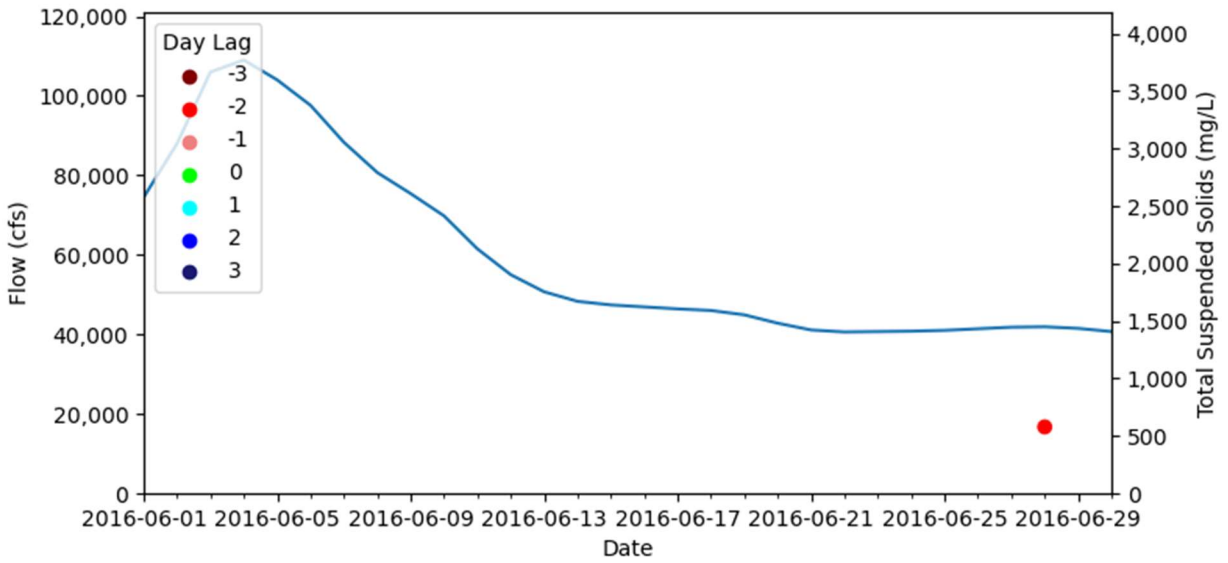
**Figure A-39:** June 2016 Flow and Total Suspended Solids Graph for Landsat Data
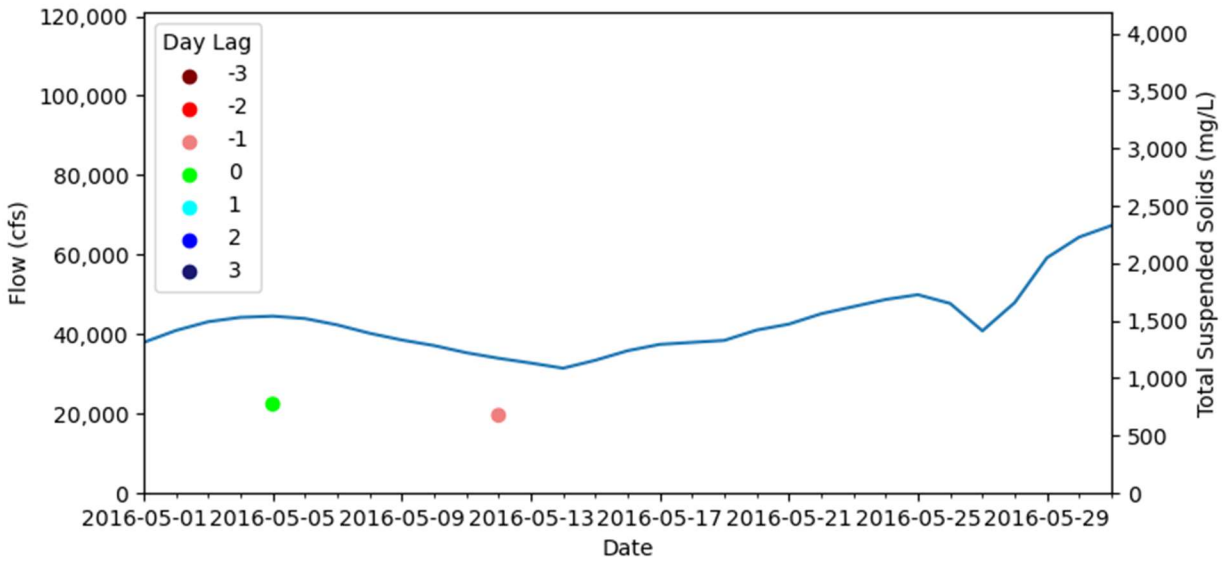


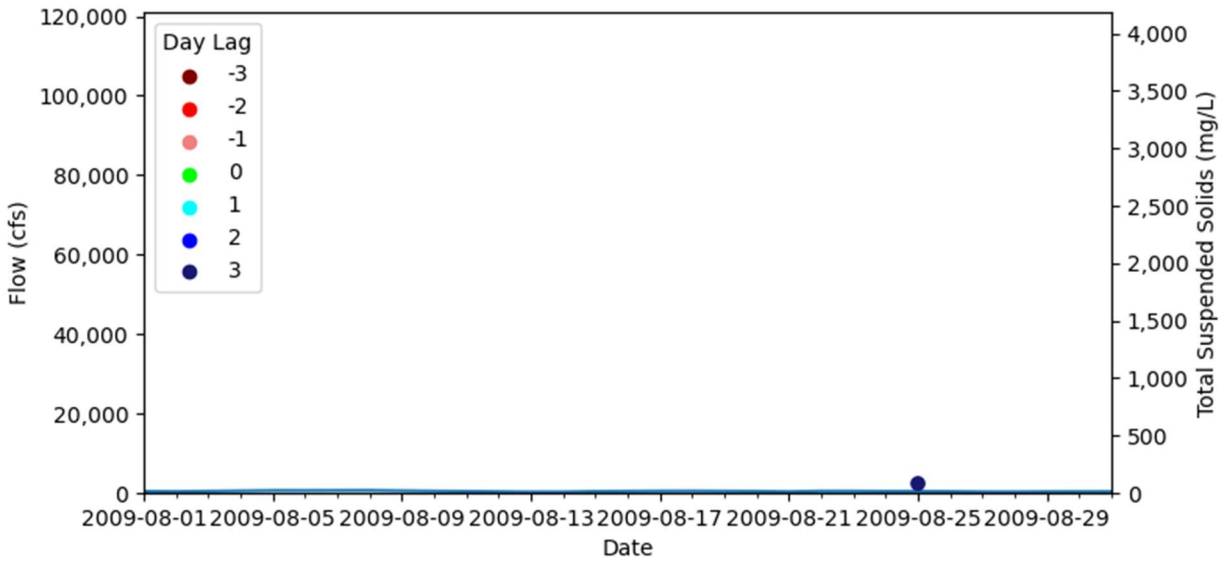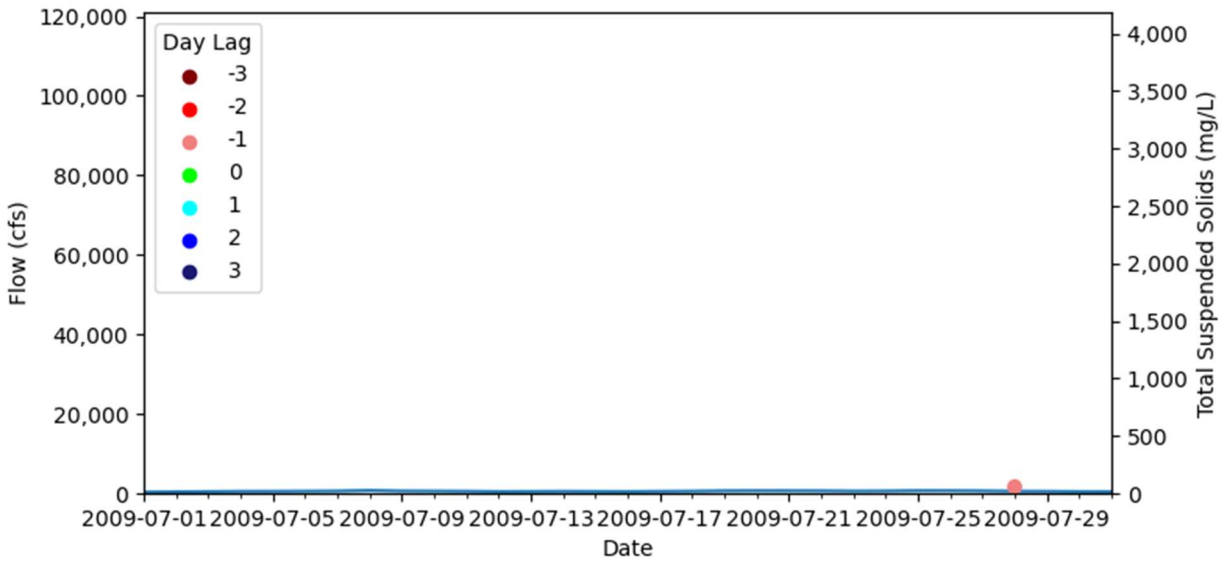**Figure A-40:** May 2016 Flow and Total Suspended Solids Graph for Landsat Data
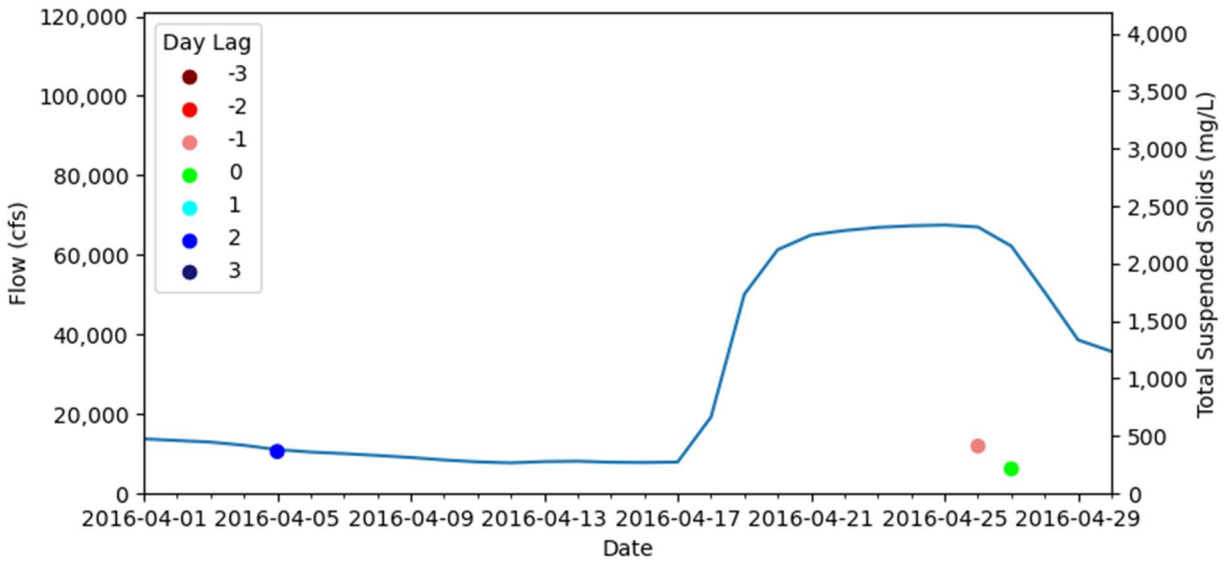
**Figure A-41:** April 2016 Flow and Total Suspended Solids Graph for Landsat Data
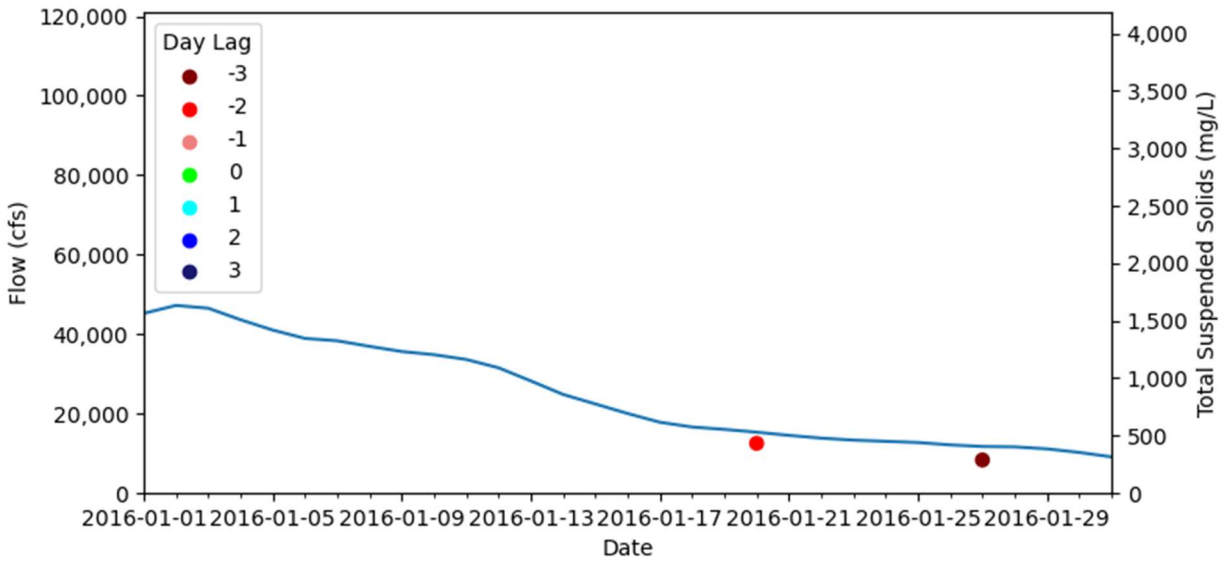


**Figure A-42:** January 2016 Flow and Total Suspended Solids Graph for Landsat Data
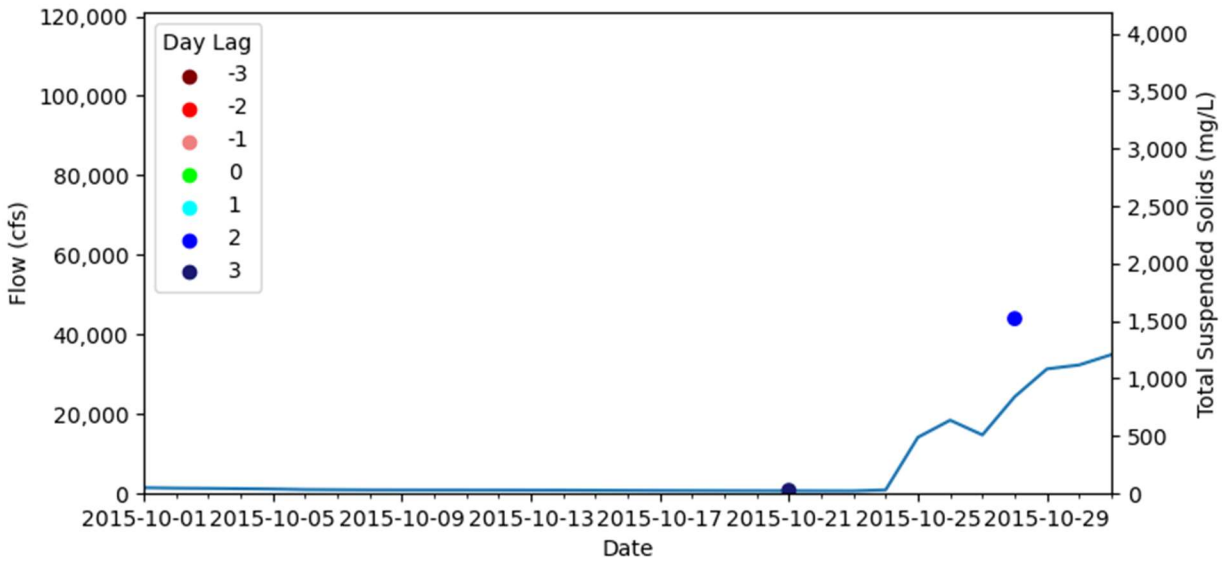
**Figure A-43:** October 2015 Flow and Total Suspended Solids Graph for Landsat Data
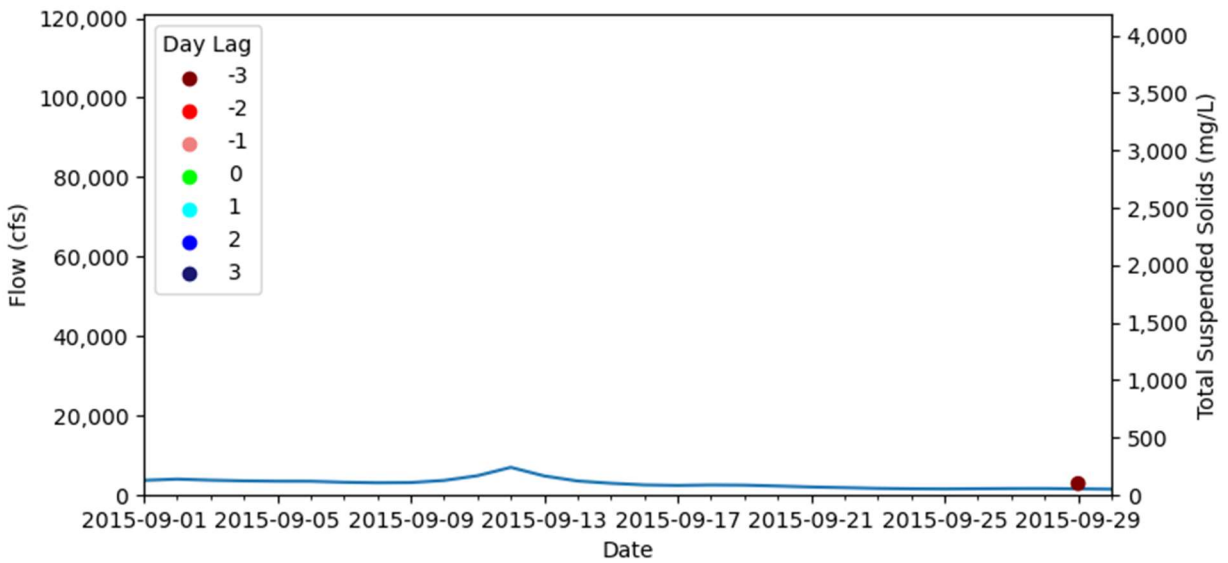


**Figure A-44:** September 2015 Flow and Total Suspended Solids Graph for Landsat Data
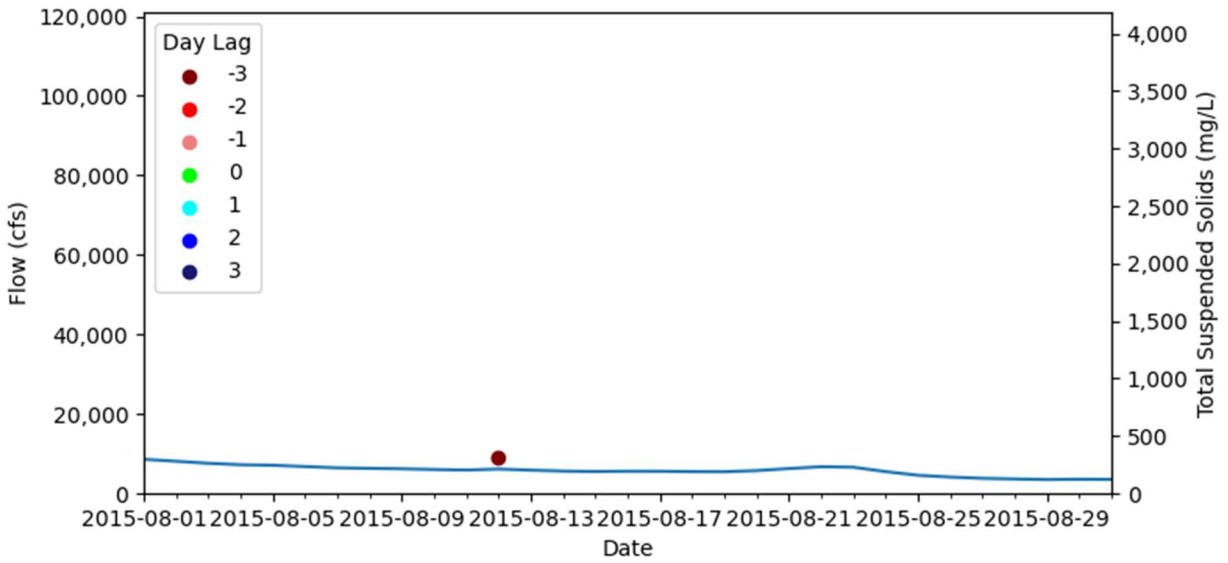
**Figure A-45:** August 2015 Flow and Total Suspended Solids Graph for Landsat Data
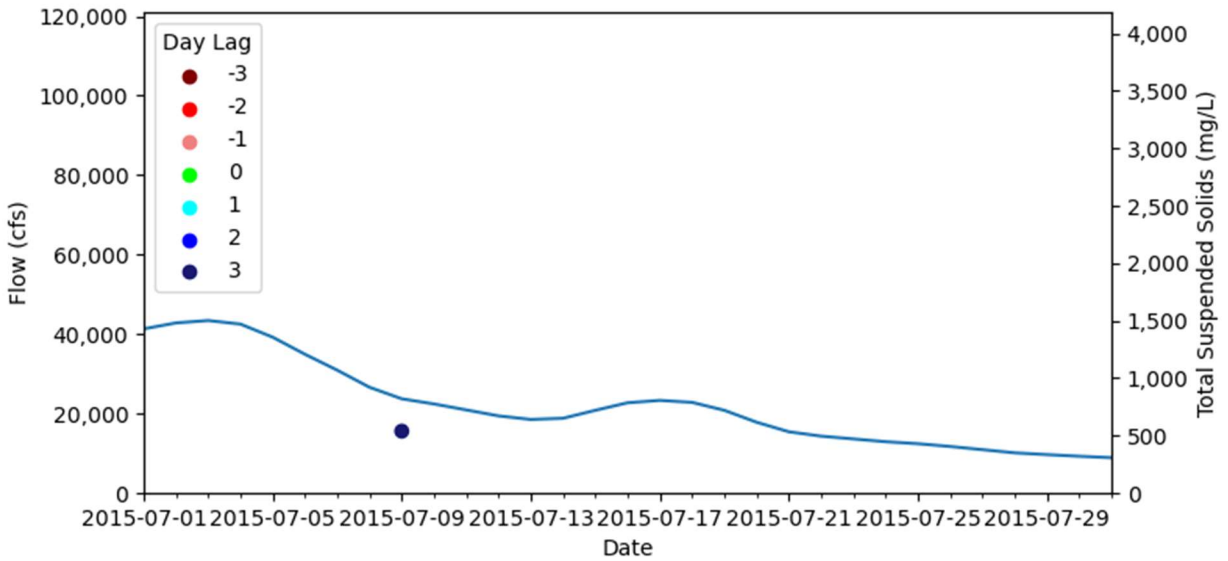


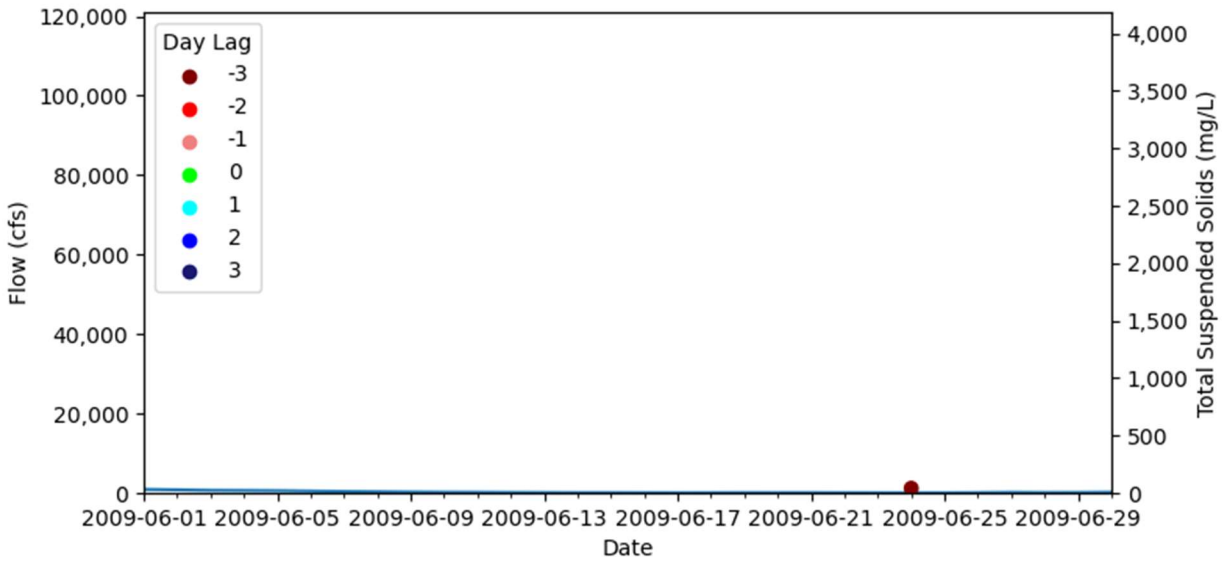**Figure A-46:** July 2015 Flow and Total Suspended Solids Graph for Landsat Data
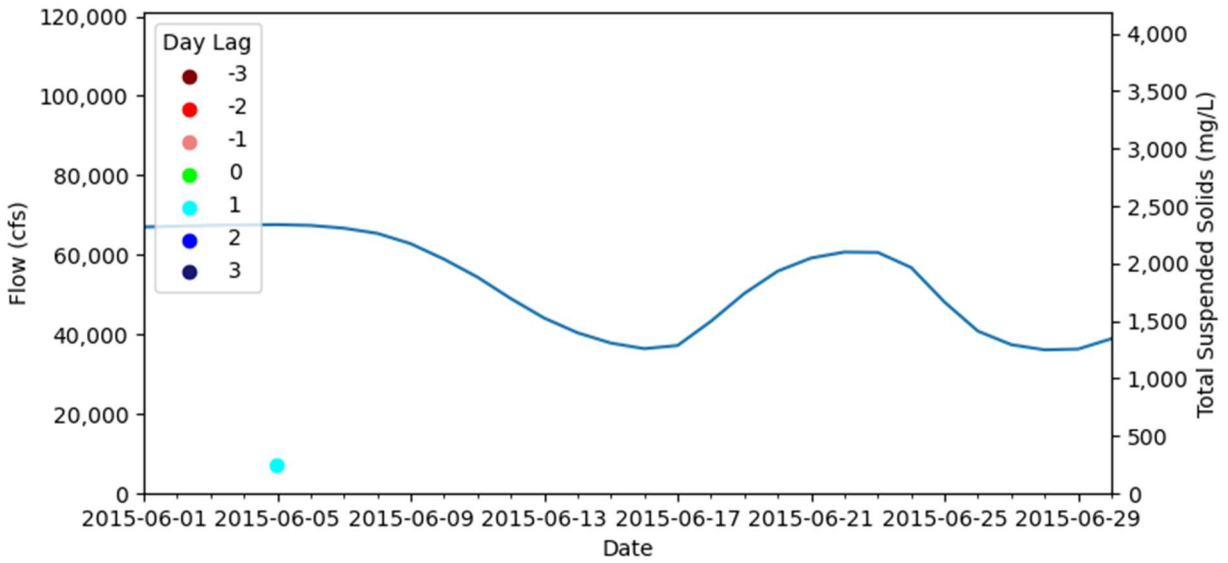
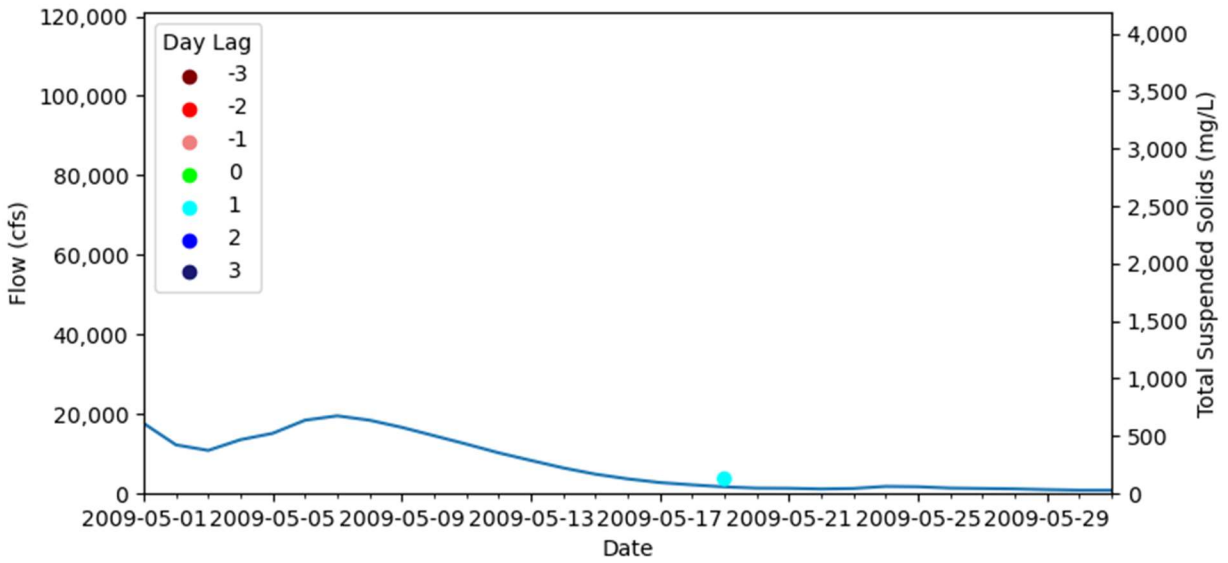**Figure A-47:** June 2015 Flow and Total Suspended Solids Graph for Landsat Data



**Figure A-48:** May 2015 Flow and Total Suspended Solids Graph for Landsat Data

**Figure A-49:** April 2015 Flow and Total Suspended Solids Graph for Landsat Data



**Figure A-50:** March 2015 Flow and Total Suspended Solids Graph for Landsat Data

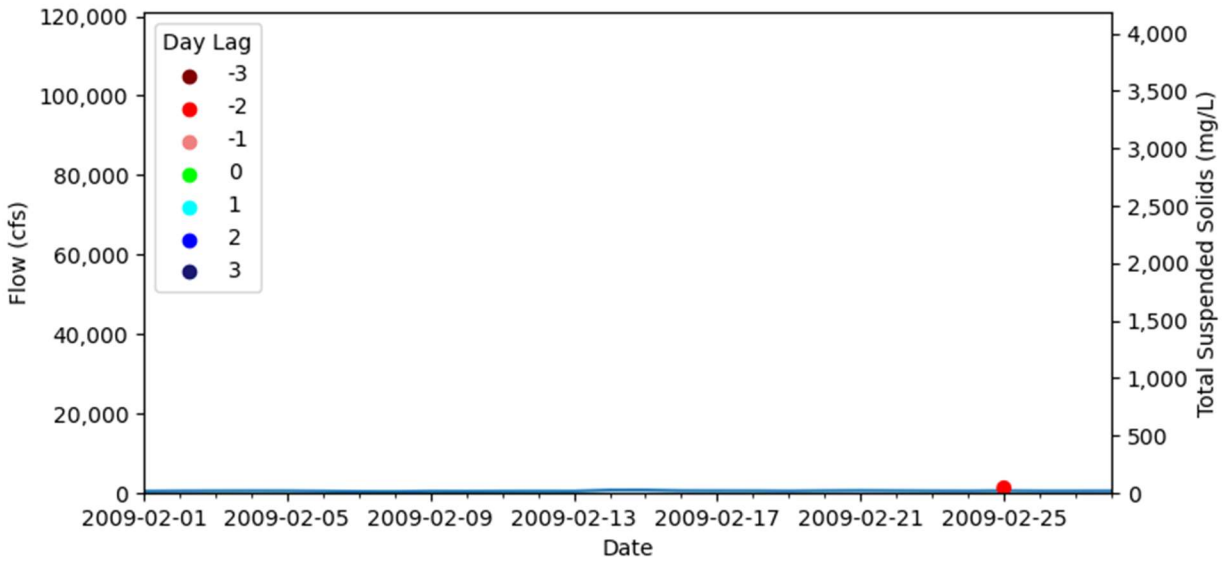**Figure A-51:** February 2015 Flow and Total Suspended Solids Graph for Landsat Data



**Figure A-52:** January 2015 Flow and Total Suspended Solids Graph for Landsat Data
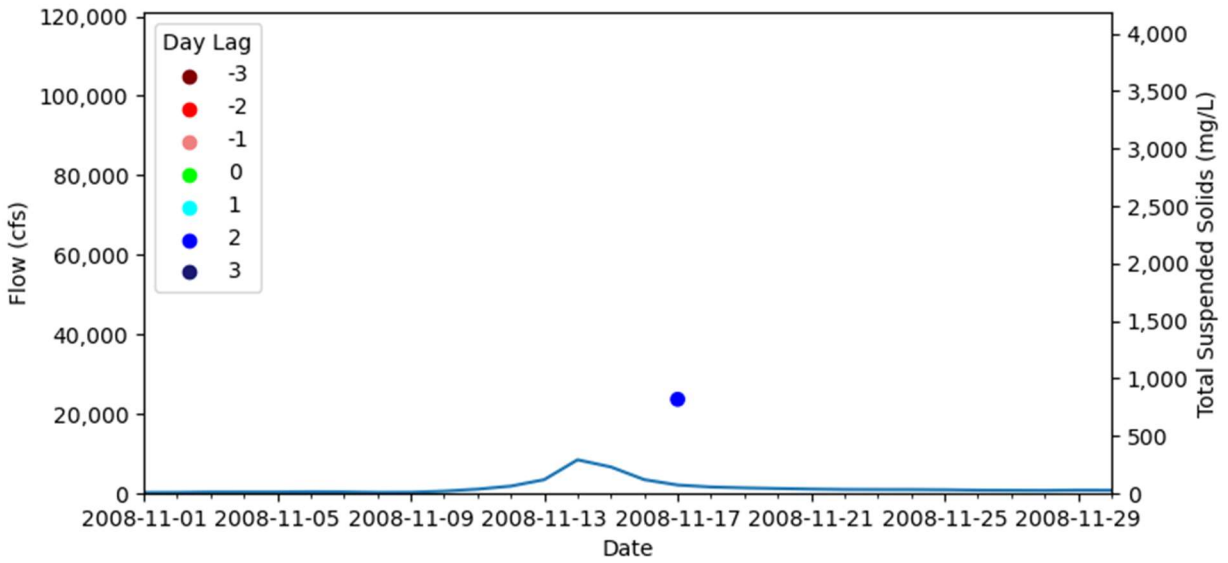
**Figure A-53:** November 2014 Flow and Total Suspended Solids Graph for Landsat Data
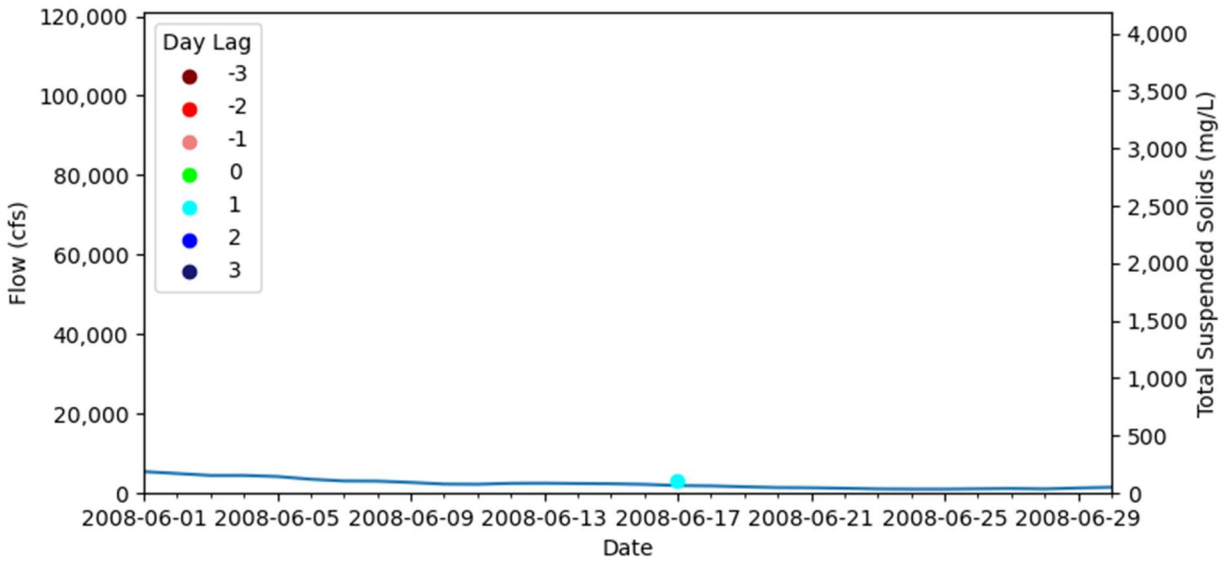


**Figure A-54:** July 2014 Flow and Total Suspended Solids Graph for Landsat Data

**Figure A-55:** May 2014 Flow and Total Suspended Solids Graph for Landsat Data



**Figure A-56:** March 2014 Flow and Total Suspended Solids Graph for Landsat Data

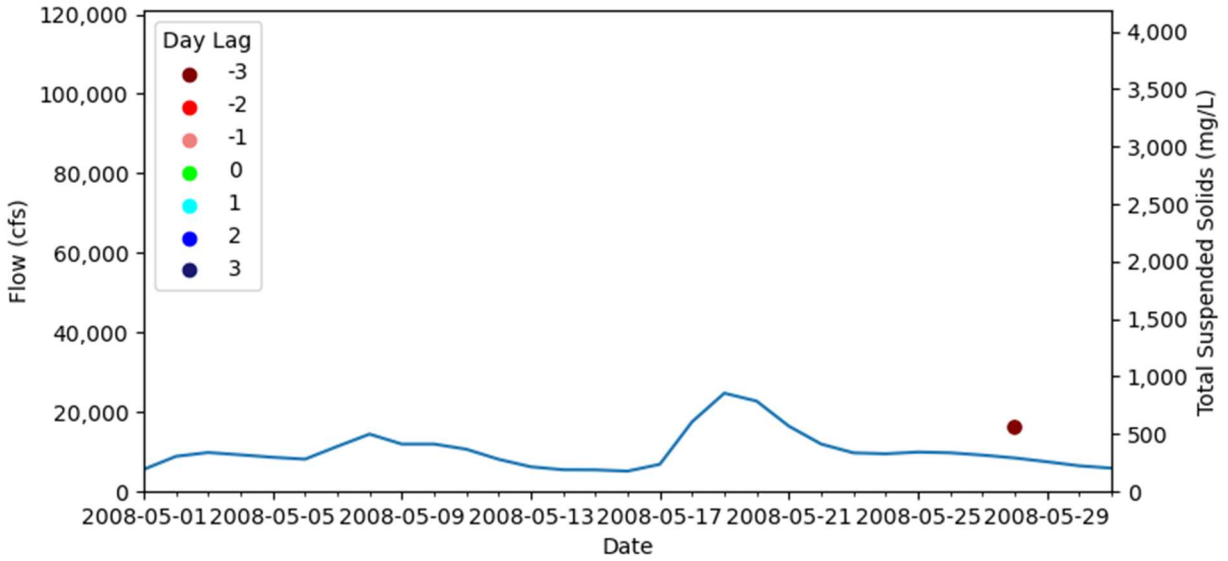**Figure A-57:** August 2013 Flow and Total Suspended Solids Graph for Landsat Data
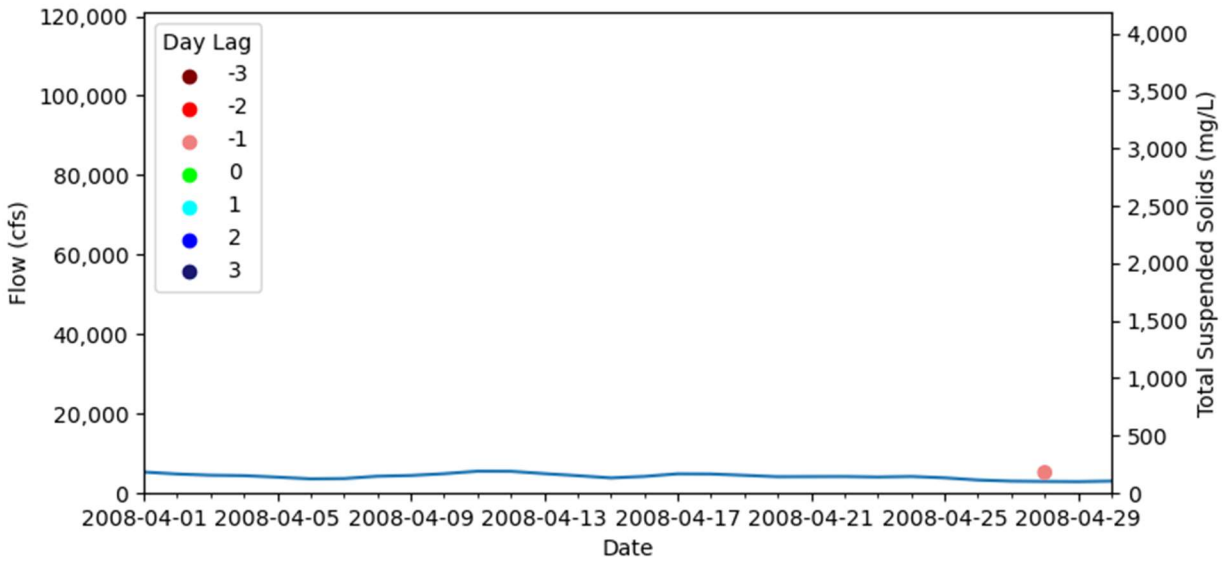


**Figure A-58:** May 2013 Flow and Total Suspended Solids Graph for Landsat Data

**Figure A-59:** March 2013 Flow and Total Suspended Solids Graph for Landsat Data



**Figure A-60:** February 2013 Flow and Total Suspended Solids Graph for Landsat Data

**Figure A-61:** December 2012 Flow and Total Suspended Solids Graph for Landsat Data



**Figure A-62:** August 2012 Flow and Total Suspended Solids Graph for Landsat Data

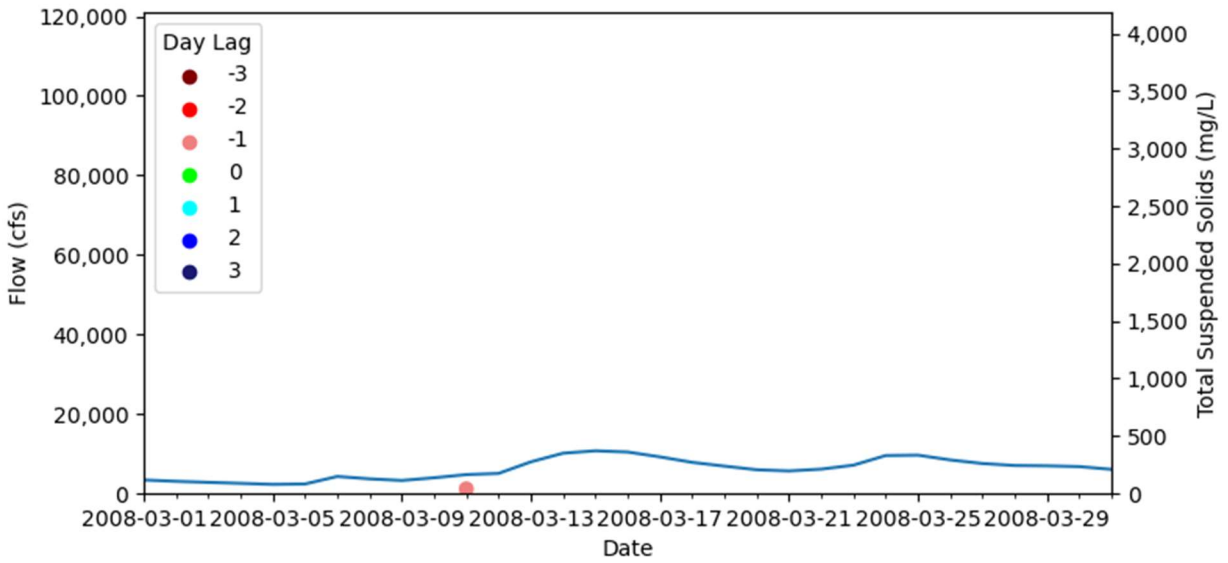**Figure A-63:** January 2012 Flow and Total Suspended Solids Graph for Landsat Data



**Figure A-64:** August 2011 Flow and Total Suspended Solids Graph for Landsat Data

**Figure A-65:** June 2011 Flow and Total Suspended Solids Graph for Landsat Data



**Figure A-66:** April 2011 Flow and Total Suspended Solids Graph for Landsat Data

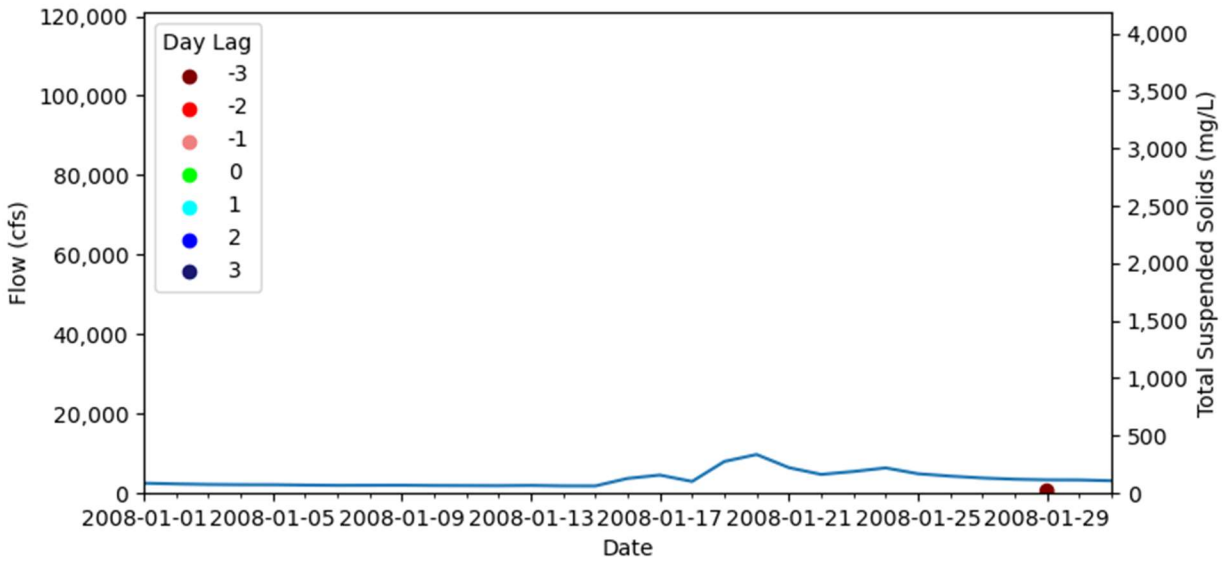**Figure A-67:** March 2011 Flow and Total Suspended Solids Graph for Landsat Data



**Figure A-68:** November 2010 Flow and Total Suspended Solids Graph for Landsat Data

**Figure A-69:** June 2010 Flow and Total Suspended Solids Graph for Landsat Data



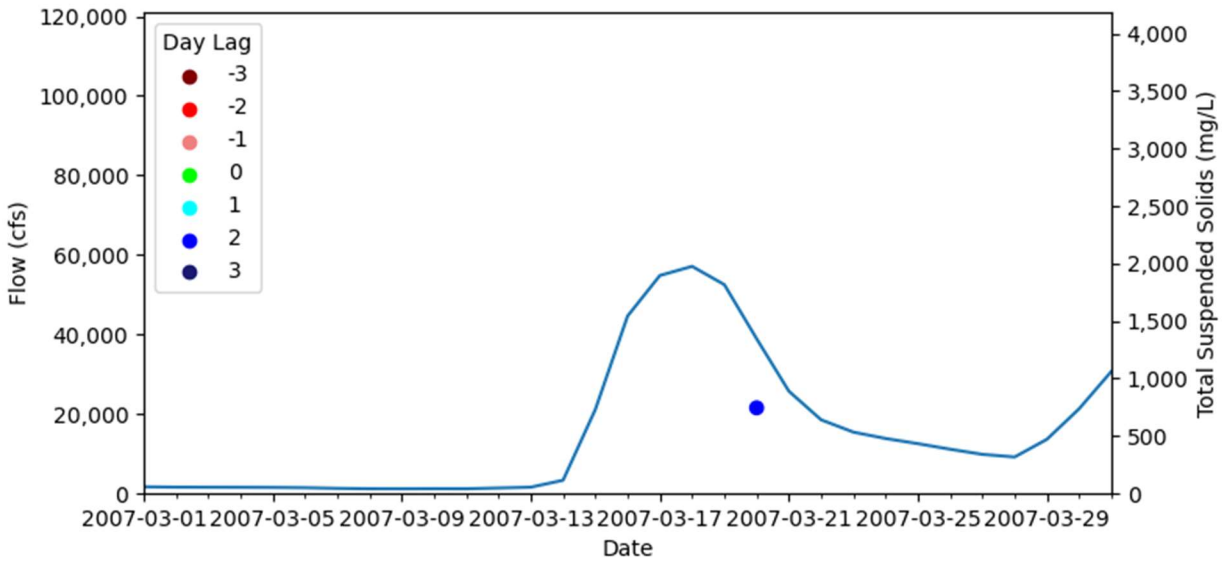**Figure A-70:** January 2010 Flow and Total Suspended Solids Graph for Landsat Data

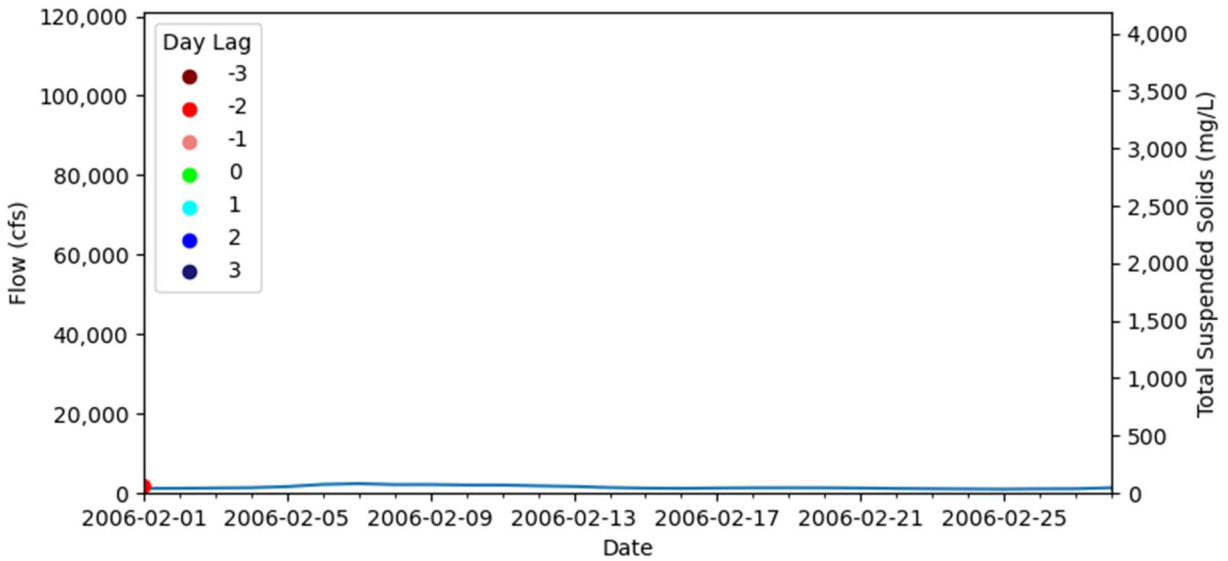**Figure A-71:** November 2009 Flow and Total Suspended Solids Graph for Landsat Data



**Figure A-72:** October 2009 Flow and Total Suspended Solids Graph for Landsat Data

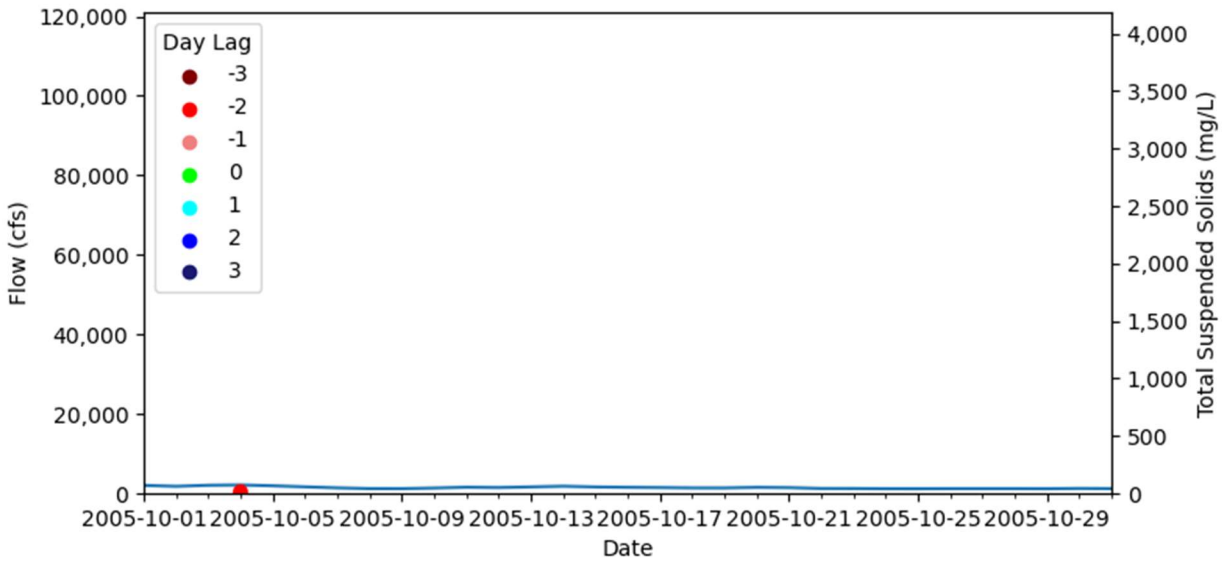**Figure A-73:** September 2009 Flow and Total Suspended Solids Graph for Landsat Data



**Figure A-74:** August 2009 Flow and Total Suspended Solids Graph for Landsat Data

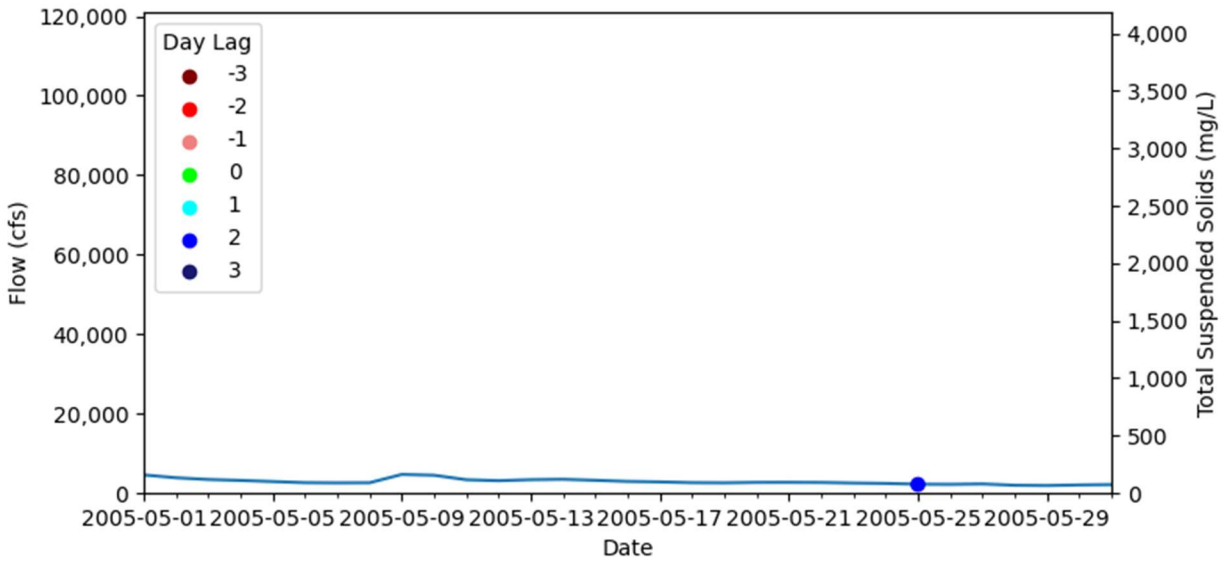**Figure A-75:** July 2009 Flow and Total Suspended Solids Graph for Landsat Data



**Figure A-76:** June 2009 Flow and Total Suspended Solids Graph for Landsat Data

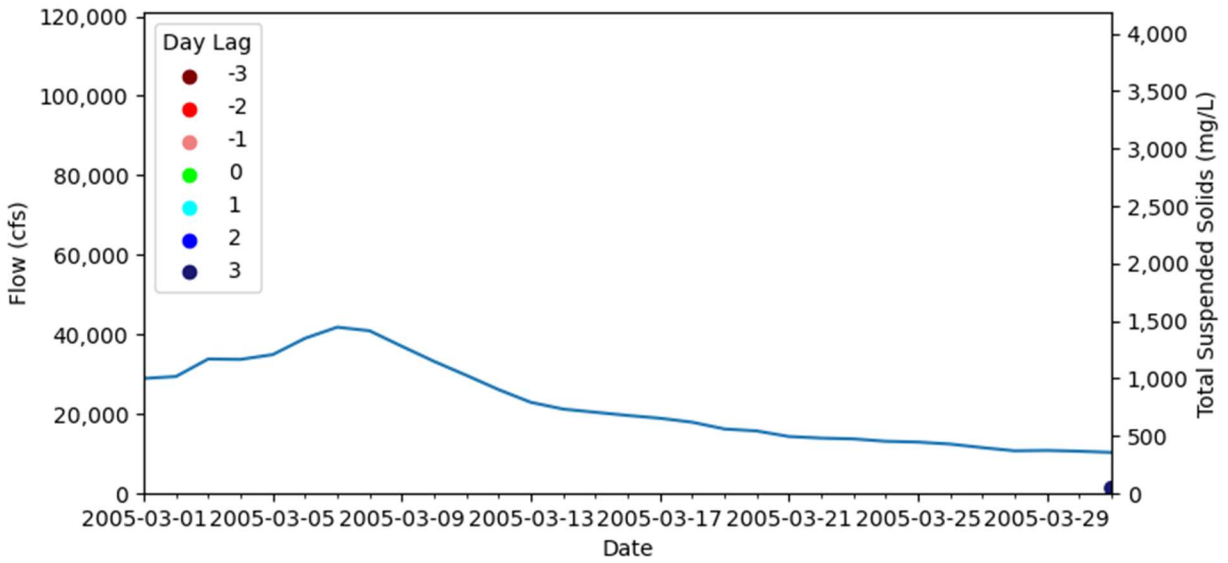**Figure A-77:** May 2009 Flow and Total Suspended Solids Graph for Landsat Data



**Figure A-78:** February 2009 Flow and Total Suspended Solids Graph for Landsat Data

**Figure A-79:** November 2008 Flow and Total Suspended Solids Graph for Landsat Data



**Figure A-80:** June 2008 Flow and Total Suspended Solids Graph for Landsat Data

**Figure A-81:** May 2008 Flow and Total Suspended Solids Graph for Landsat Data



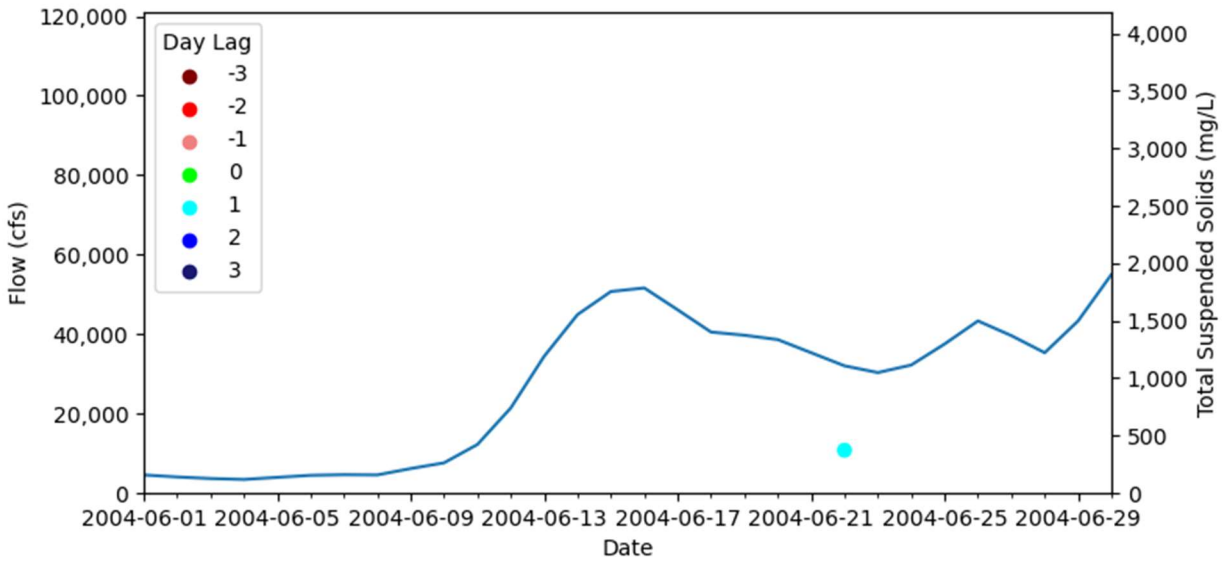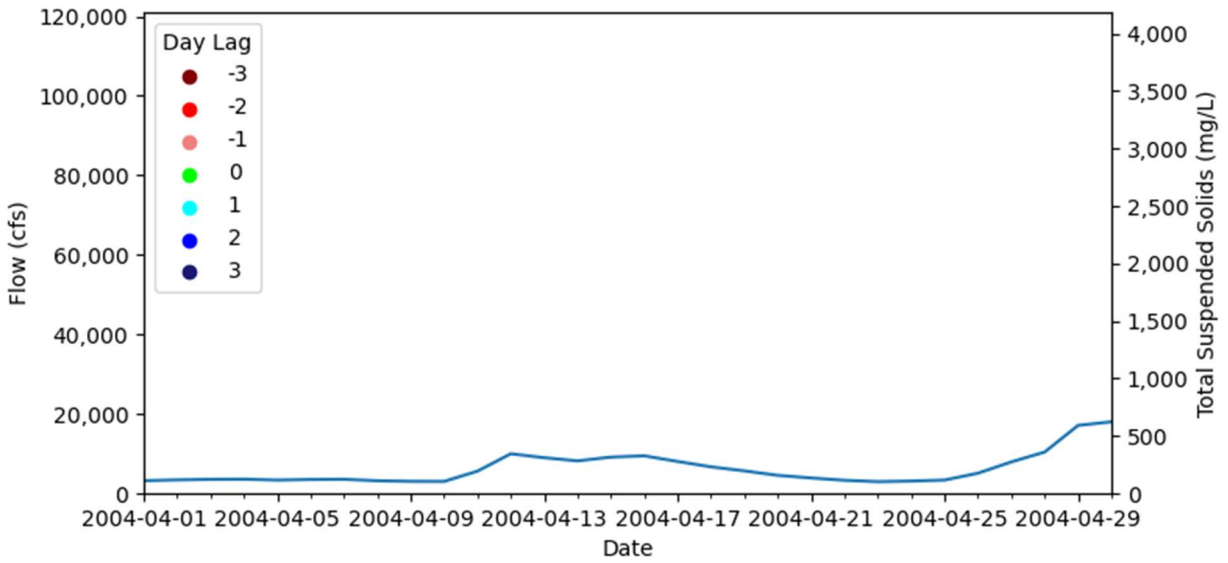**Figure A-82:** April 2008 Flow and Total Suspended Solids Graph for Landsat Data

**Figure A-83:** March 2008 Flow and Total Suspended Solids Graph for Landsat Data



**Figure A-84:** January 2008 Flow and Total Suspended Solids Graph for Landsat Data

**Figure A-85:** March 2007 Flow and Total Suspended Solids Graph for Landsat Data



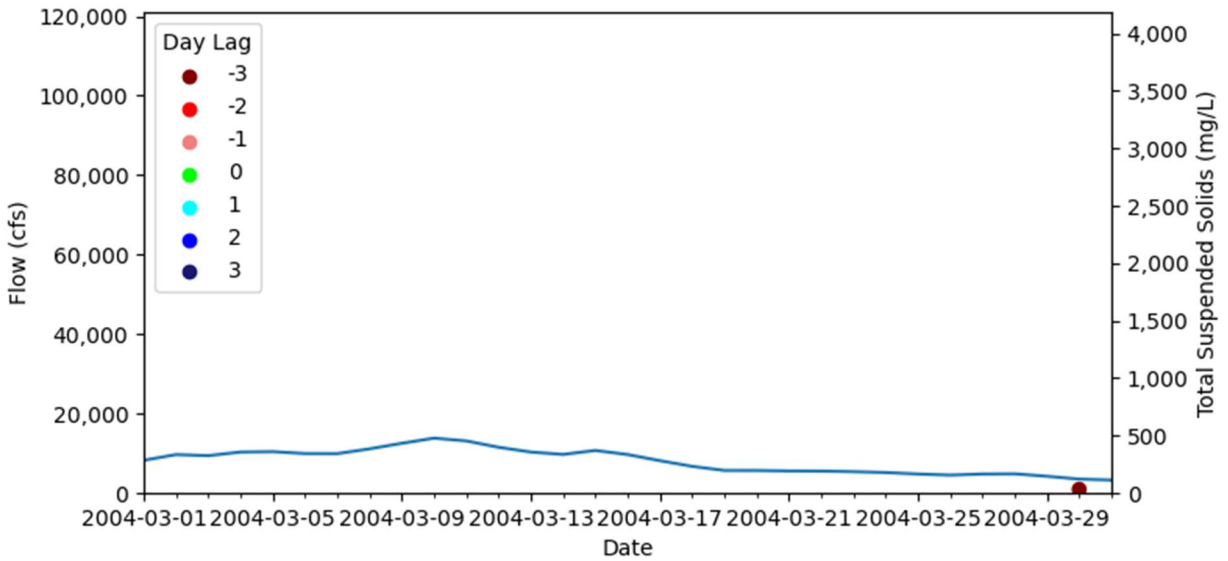**Figure A-86:** February 2006 Flow and Total Suspended Solids Graph for Landsat Data

**Figure A-87:** October 2005 Flow and Total Suspended Solids Graph for Landsat Data



**Figure A-88:** May 2005 Flow and Total Suspended Solids Graph for Landsat Data

**Figure A-89:** March 2005 Flow and Total Suspended Solids Graph for Landsat Data



**Figure A-90:** June 2004 Flow and Total Suspended Solids Graph for Landsat Data

**Figure A-91:** April 2004 Flow and Total Suspended Solids Graph for Landsat Data



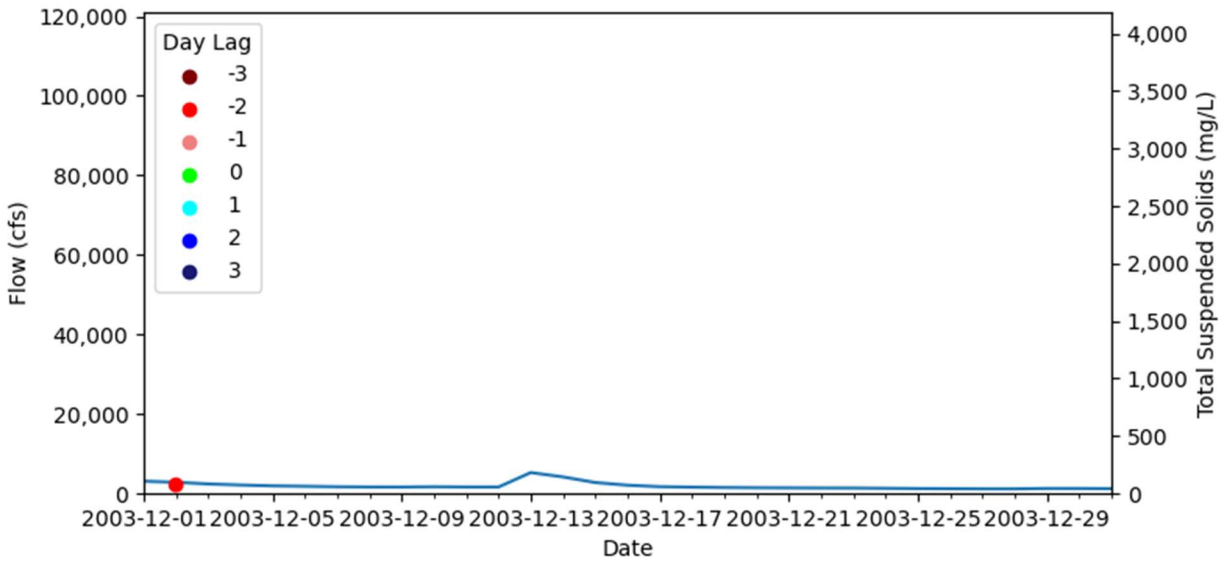**Figure A-92:** March 2004 Flow and Total Suspended Solids Graph for Landsat Data

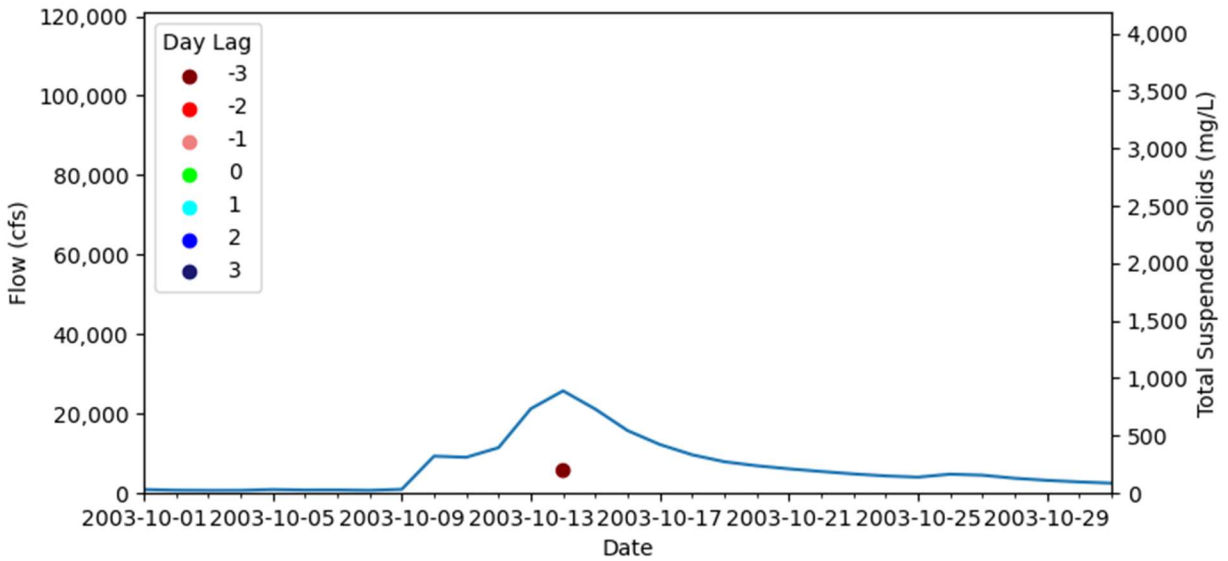**Figure A-93:** December 2003 Flow and Total Suspended Solids Graph for Landsat Data



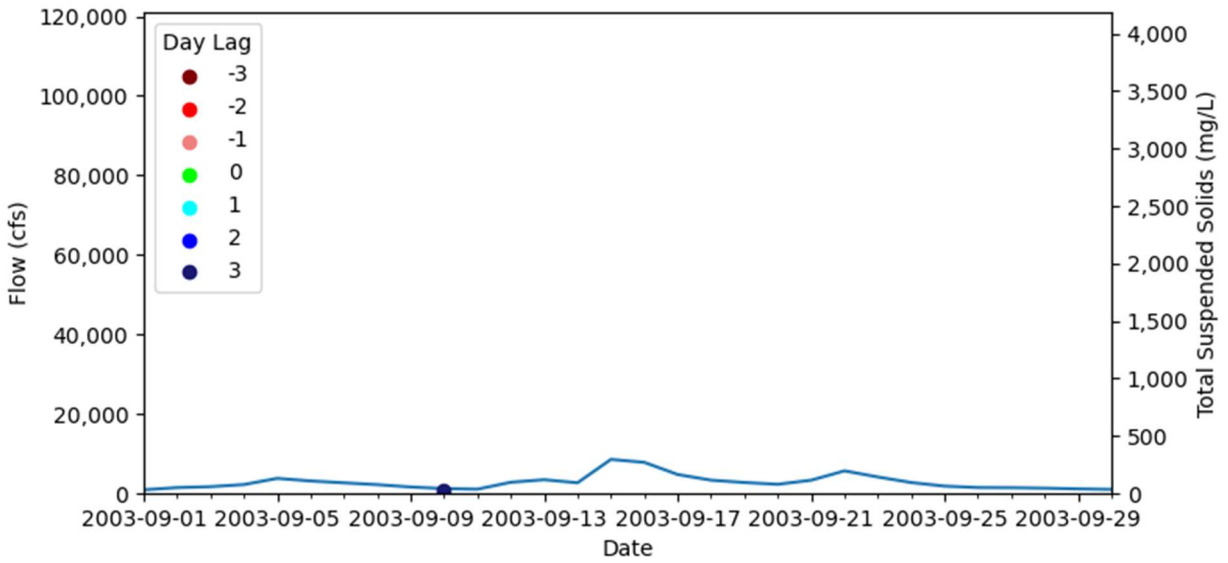**Figure A-94:** October 2003 Flow and Total Suspended Solids Graph for Landsat Data

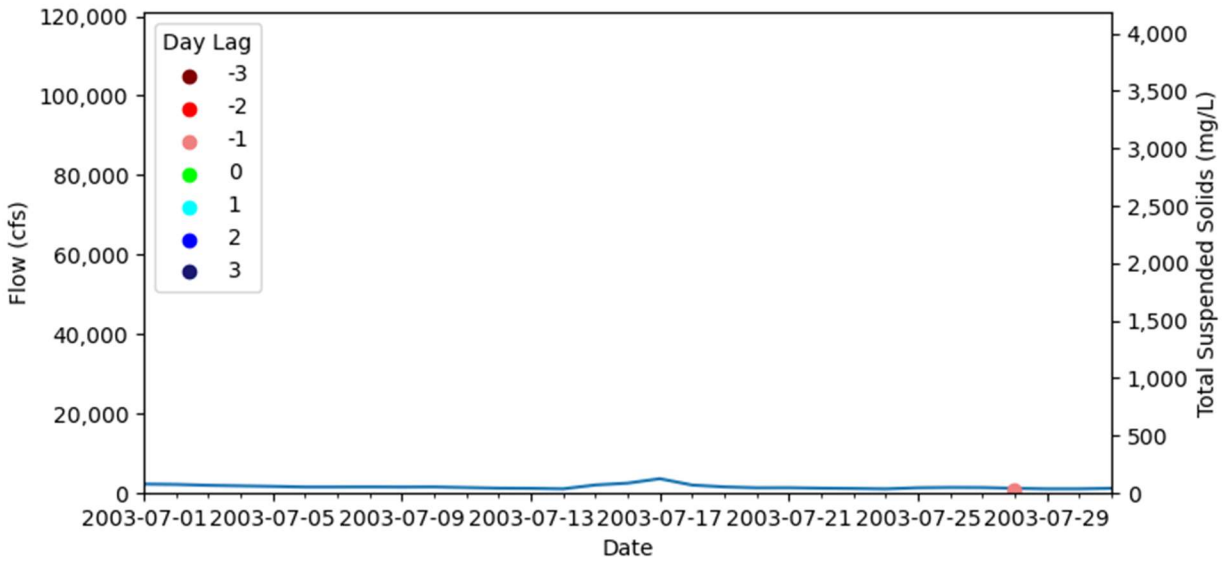**Figure A-95:** September 2003 Flow and Total Suspended Solids Graph for Landsat Data



**Figure A-96:** July 2003 Flow and Total Suspended Solids Graph for Landsat Data
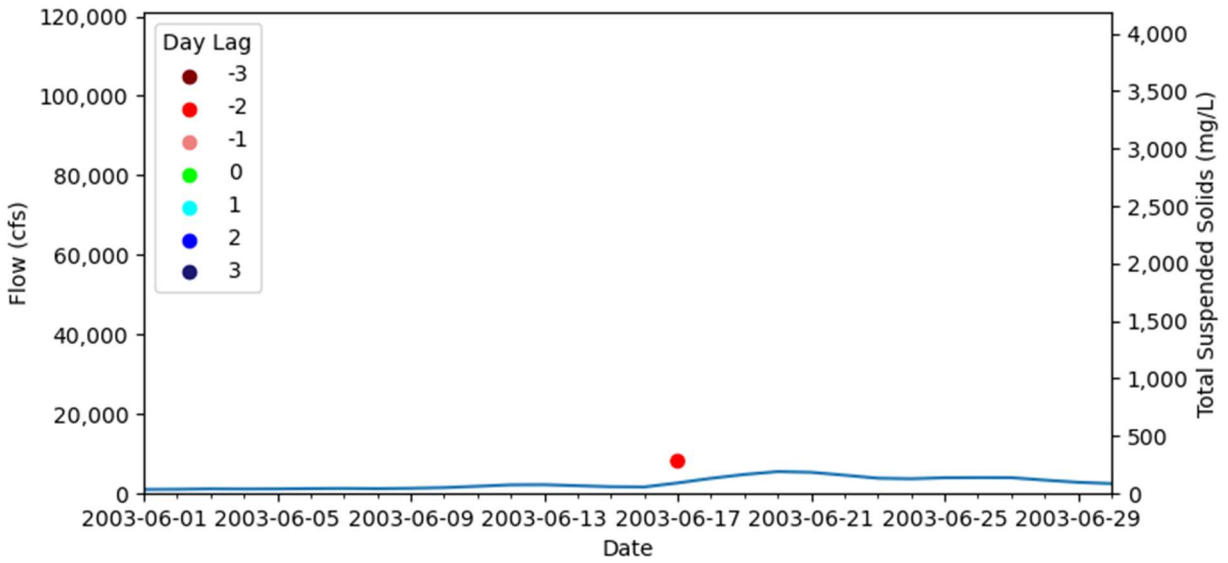
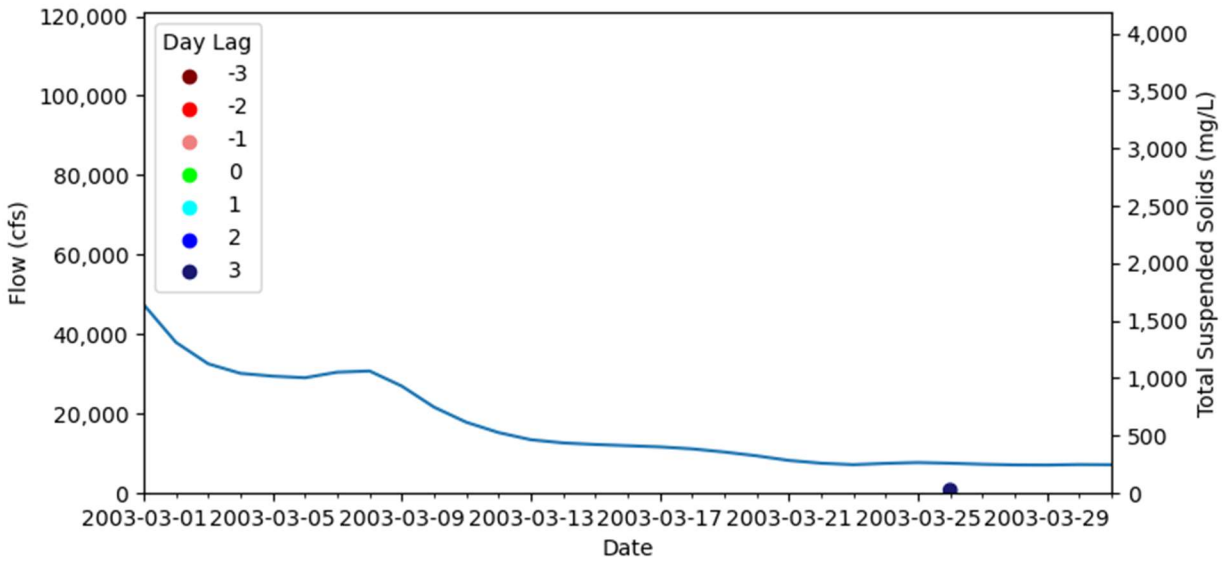**Figure A-97:** June 2003 Flow and Total Suspended Solids Graph for Landsat Data



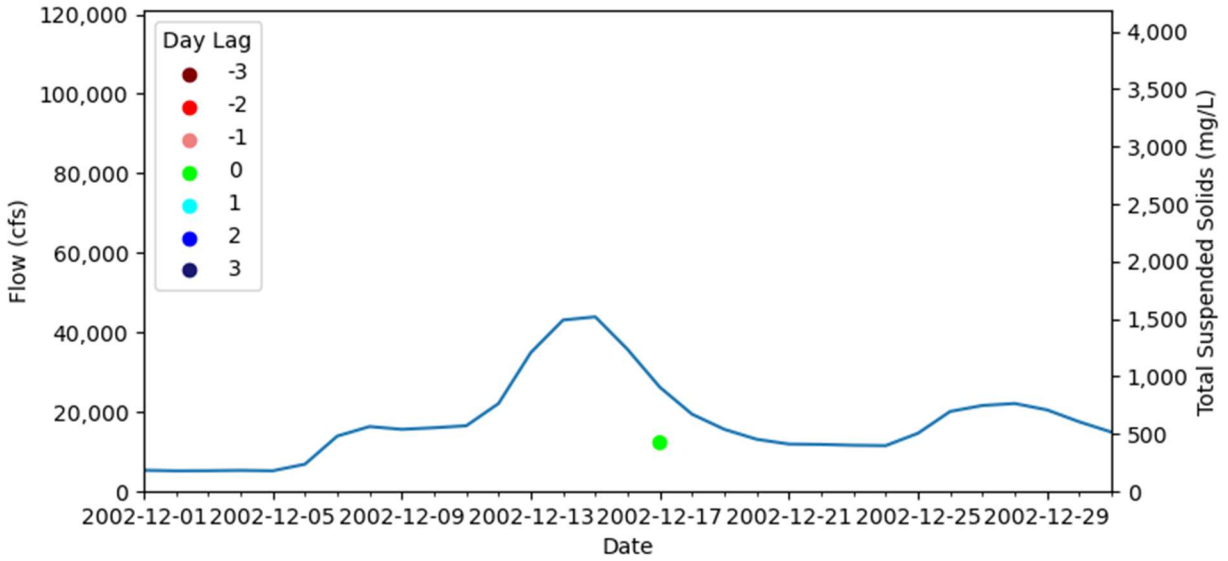**Figure A-98:** March 2003 Flow and Total Suspended Solids Graph for Landsat Data

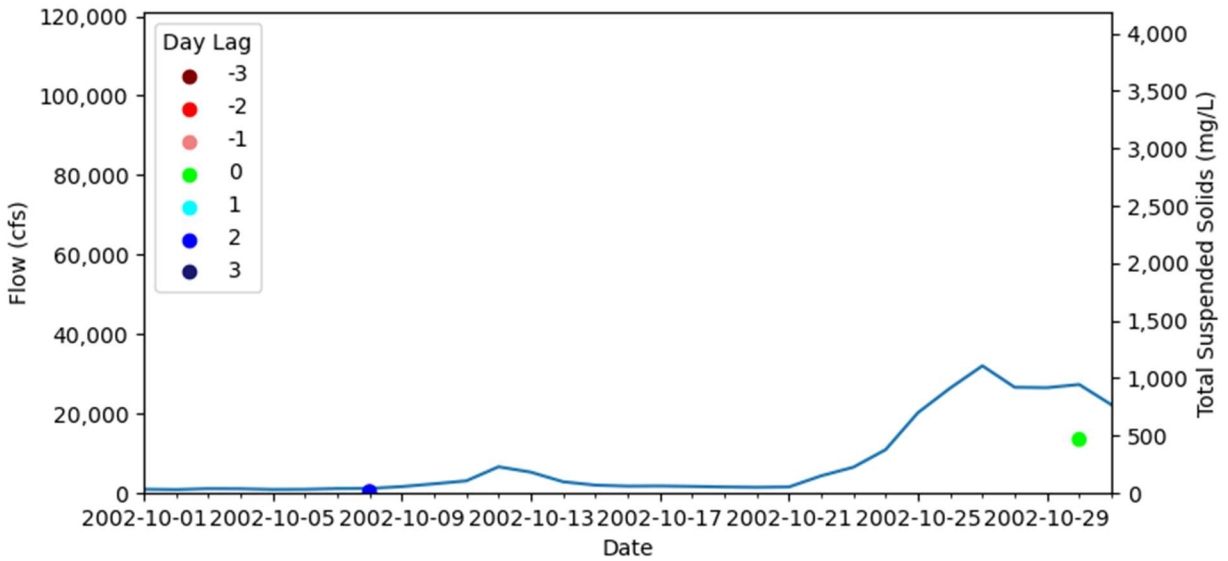**Figure A-99:** December 2002 Flow and Total Suspended Solids Graph for Landsat Data



**Figure A-100:** October 2002 Flow and Total Suspended Solids Graph for Landsat Data

**Figure A-101:** July 2002 Flow and Total Suspended Solids Graph for Landsat Data



**Figure A-102:** June 2002 Flow and Total Suspended Solids Graph for Landsat Data

**Figure A-103:** January 2002 Flow and Total Suspended Solids Graph for Landsat Data



**Figure A-104:** December 2001 Flow and Total Suspended Solids Graph for Landsat Data

**Figure A-105:** September 2001 Flow and Total Suspended Solids Graph for Landsat Data



**Figure A-106:** August 2001 Flow and Total Suspended Solids Graph for Landsat Data

**Figure A-107:** June 2001 Flow and Total Suspended Solids Graph for Landsat Data



**Figure A-108:** July 2001 Flow and Total Suspended Solids Graph for Landsat Data
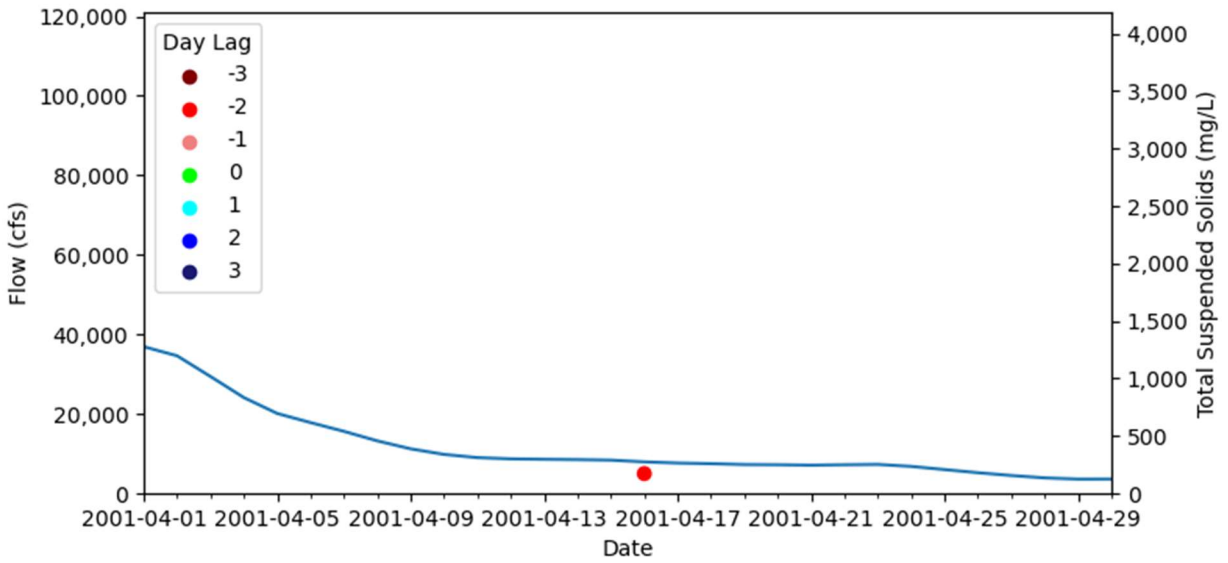
**Figure A-109:** April 2001 Flow and Total Suspended Solids Graph for Landsat Data



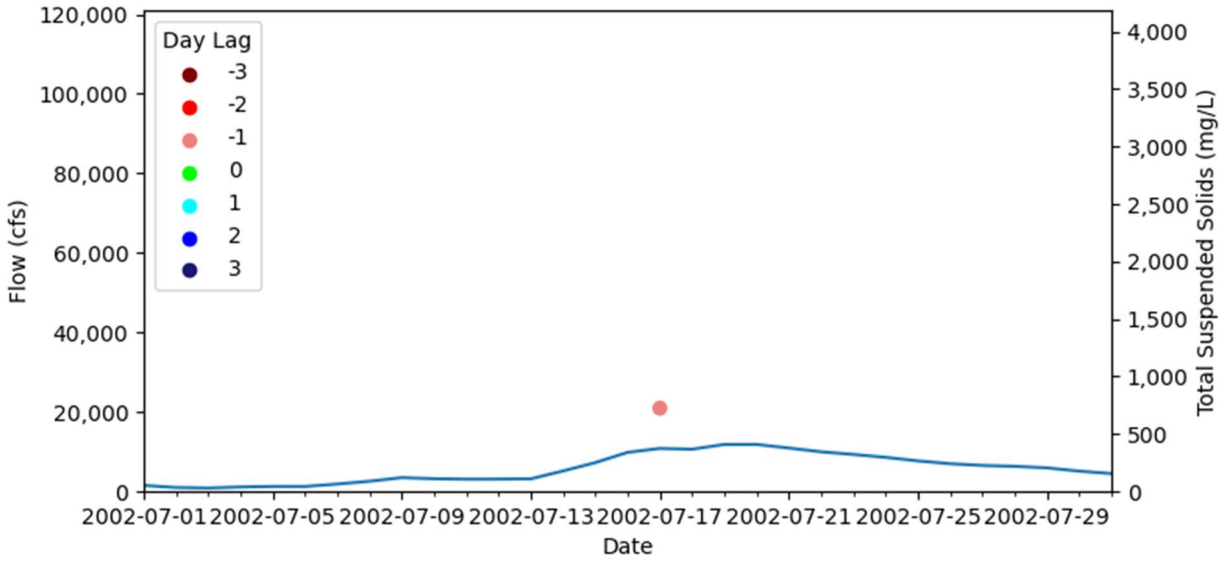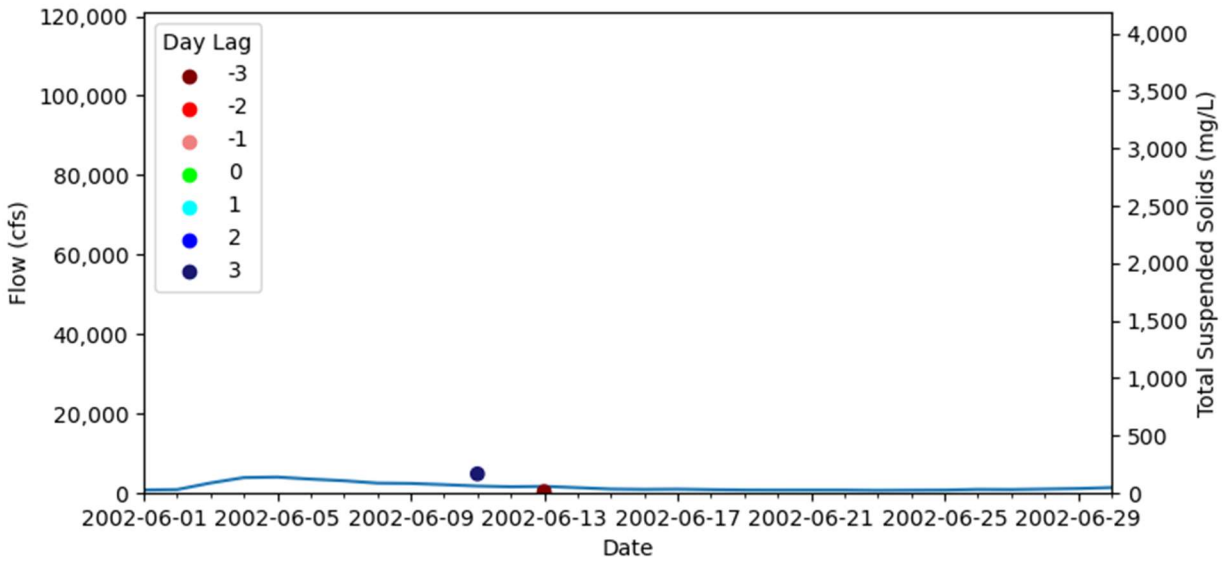**Figure A-110:** October 2000 Flow and Total Suspended Solids Graph for Landsat Data
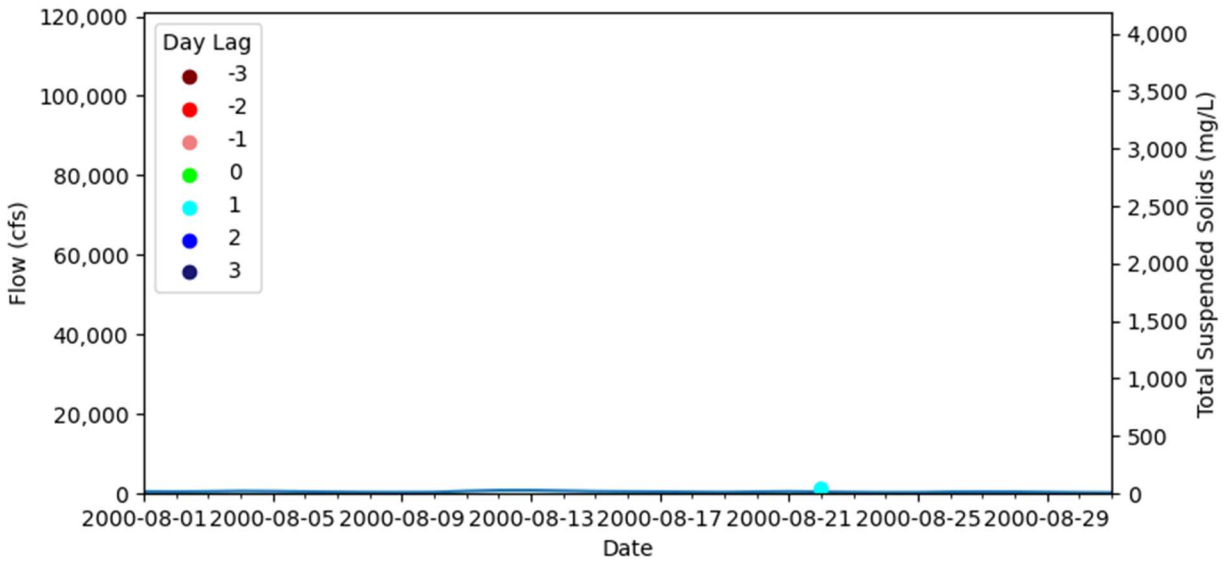
**Figure A-111:** August 2000 Flow and Total Suspended Solids Graph for Landsat Data
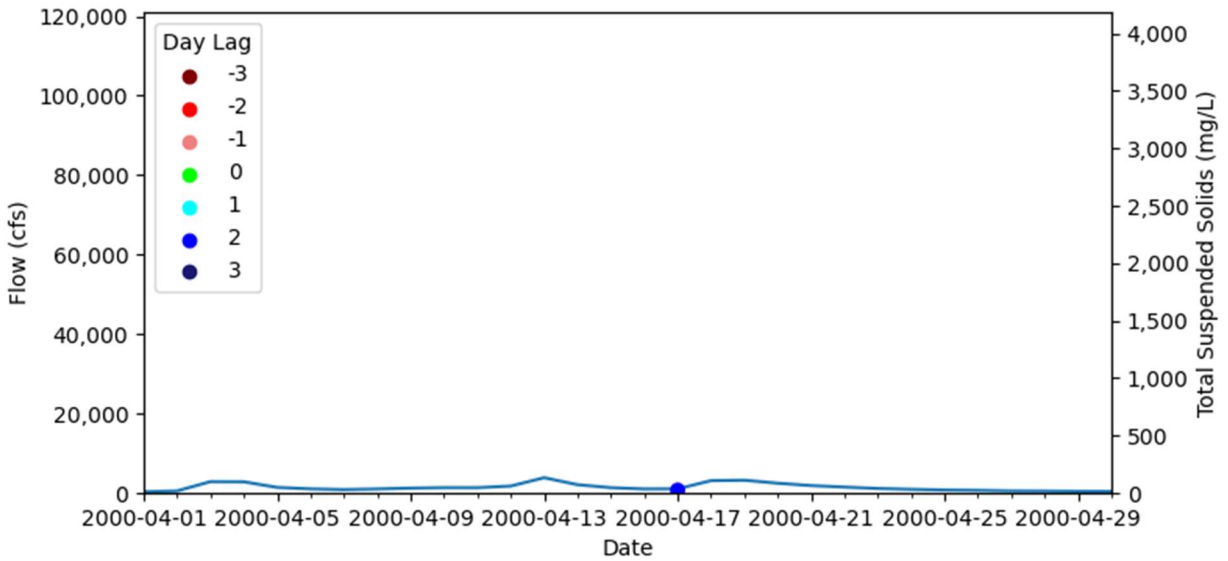


**Figure A-112:** April 2000 Flow and Total Suspended Solids Graph for Landsat Data
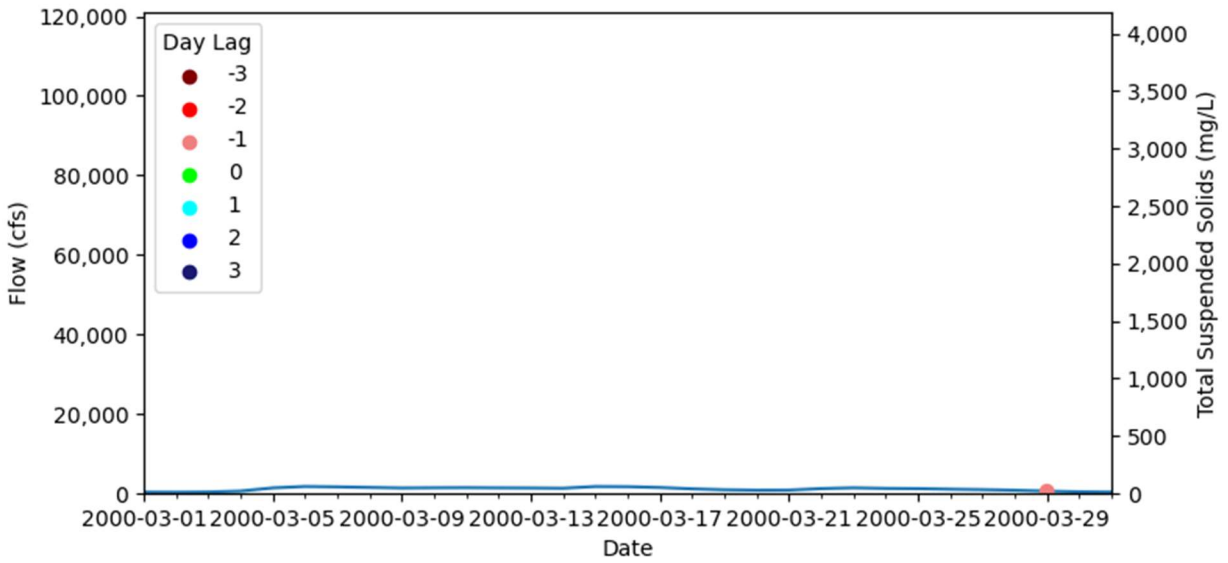
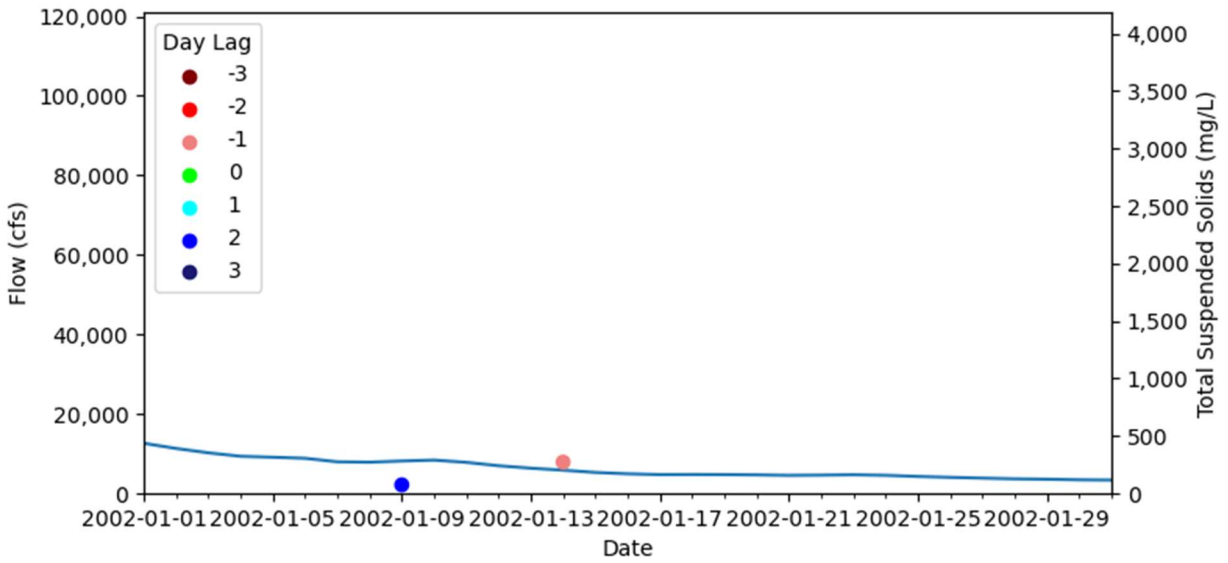**Figure A-113:** March 2000 Flow and Total Suspended Solids Graph for Landsat Data
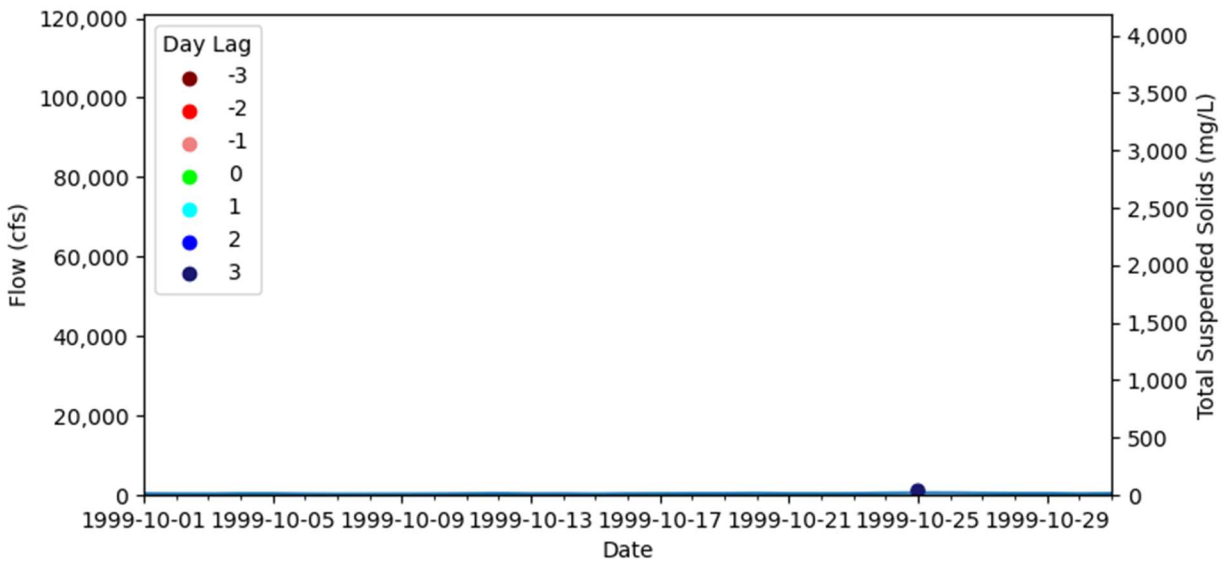


**Figure A-114:** October 1999 Flow and Total Suspended Solids Graph for Landsat Data
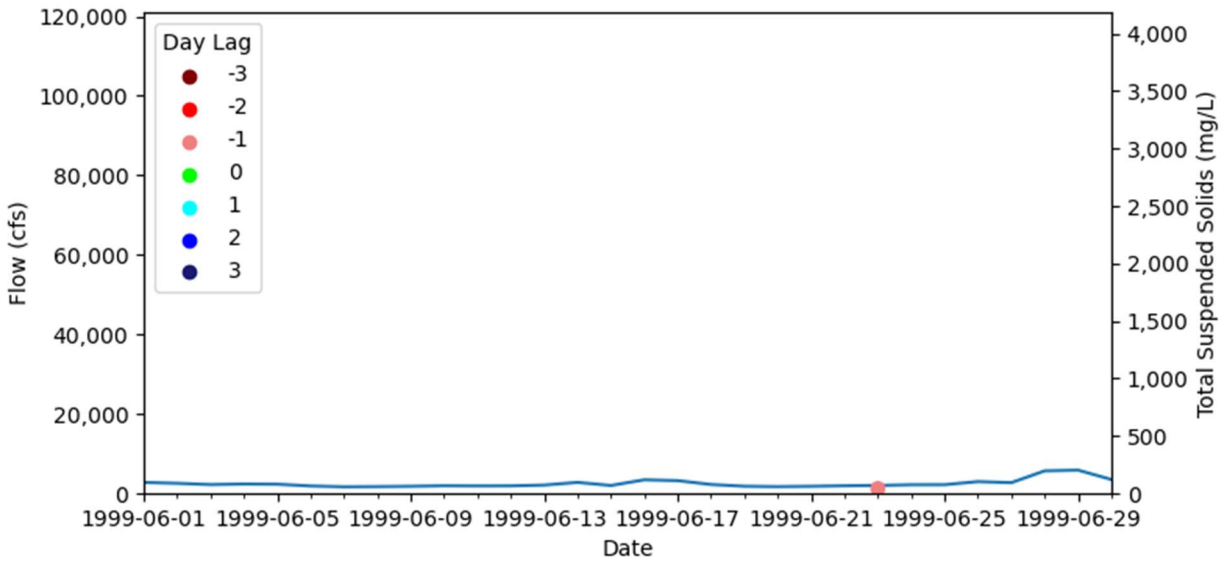
**Figure A-115:** June 1999 Flow and Total Suspended Solids Graph for Landsat Data
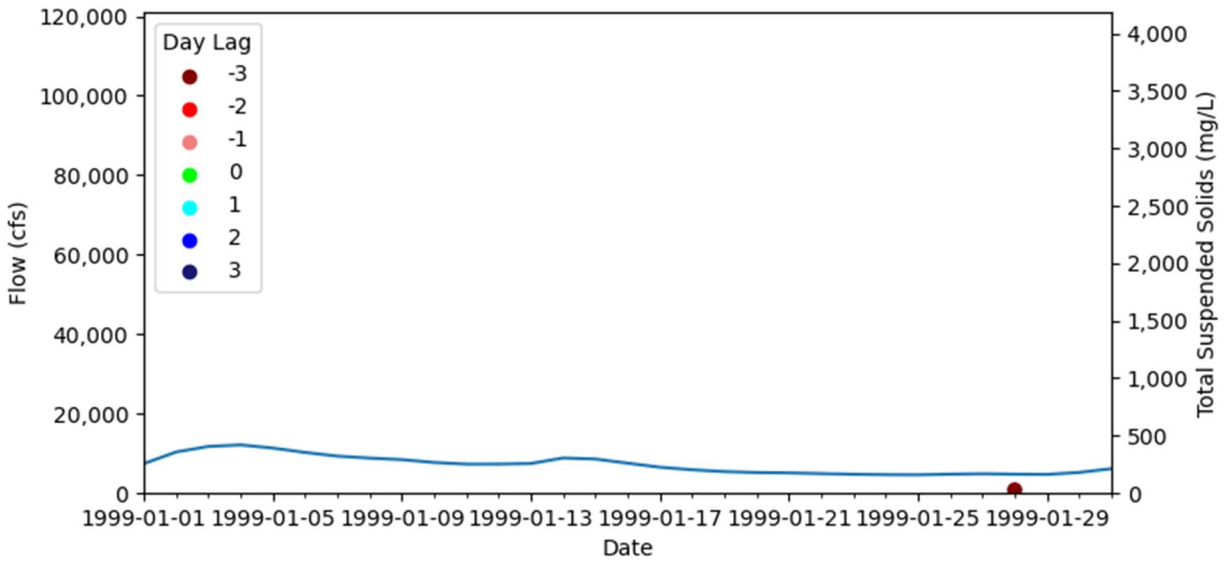


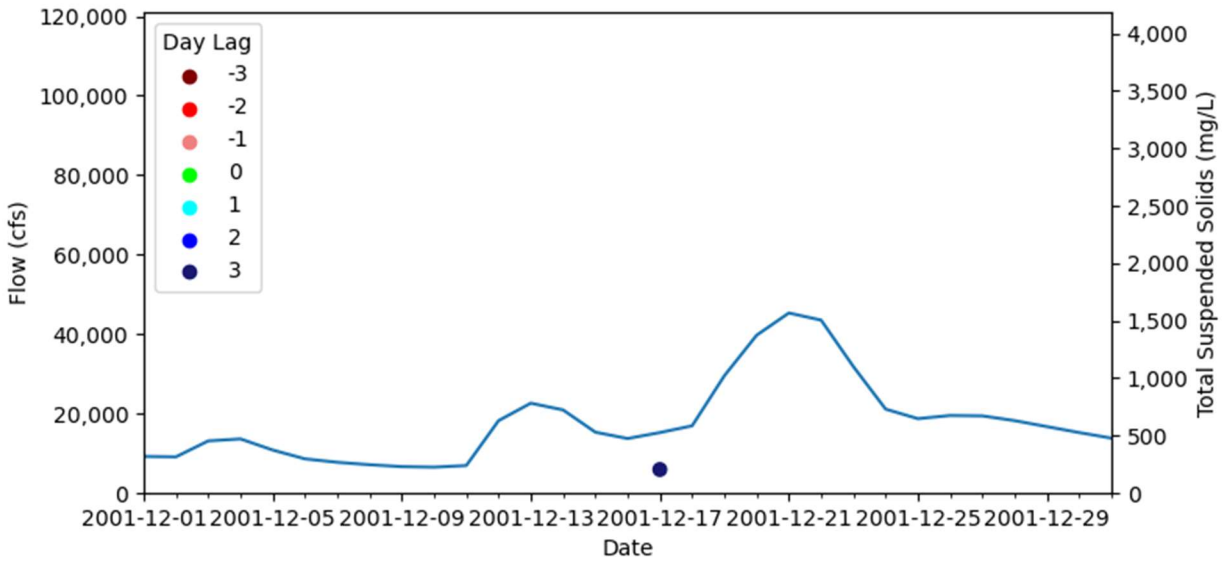**Figure A-116:** January 1999 Flow and Total Suspended Solids Graph for Landsat Data
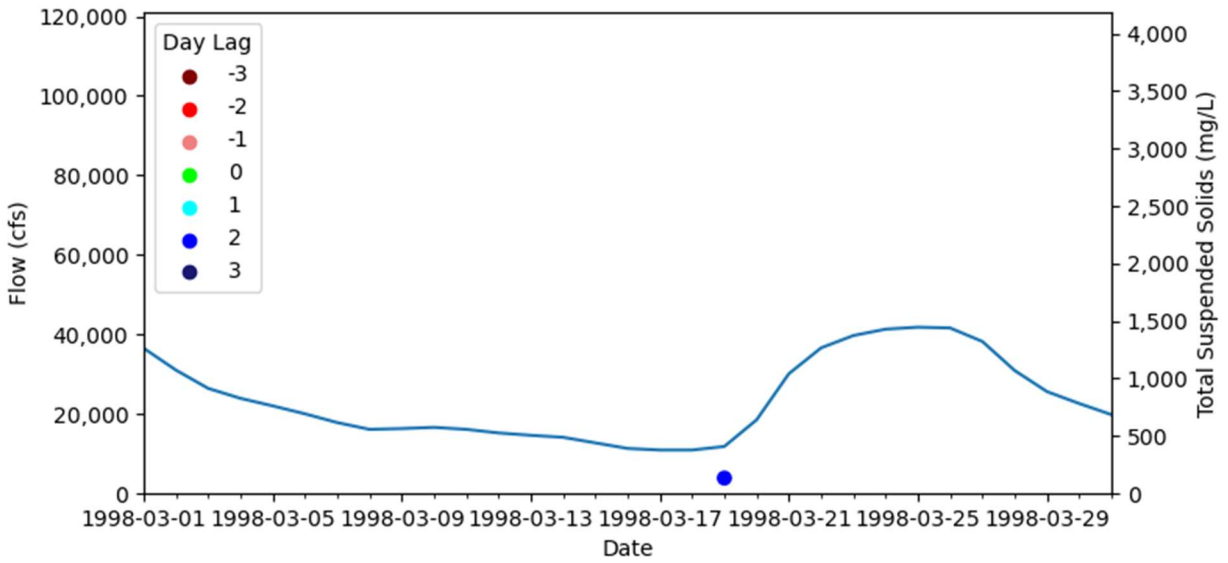
**Figure A-117:** March 1998 Flow and Total Suspended Solids Graph for Landsat Data
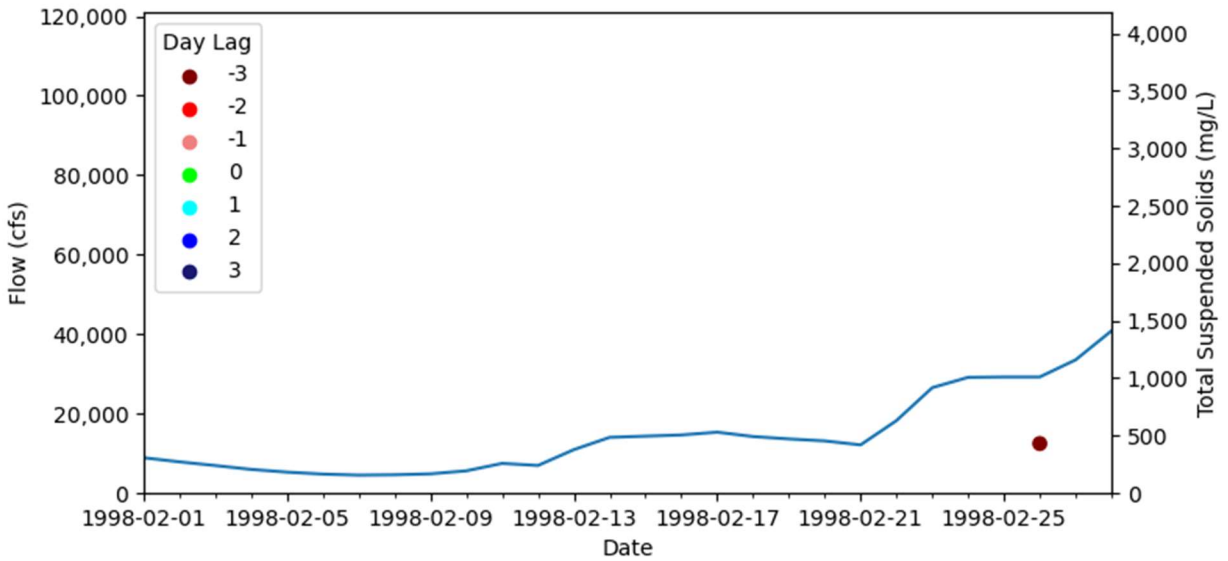


**Figure A-118:** February 1998 Flow and Total Suspended Solids Graph for Landsat Data
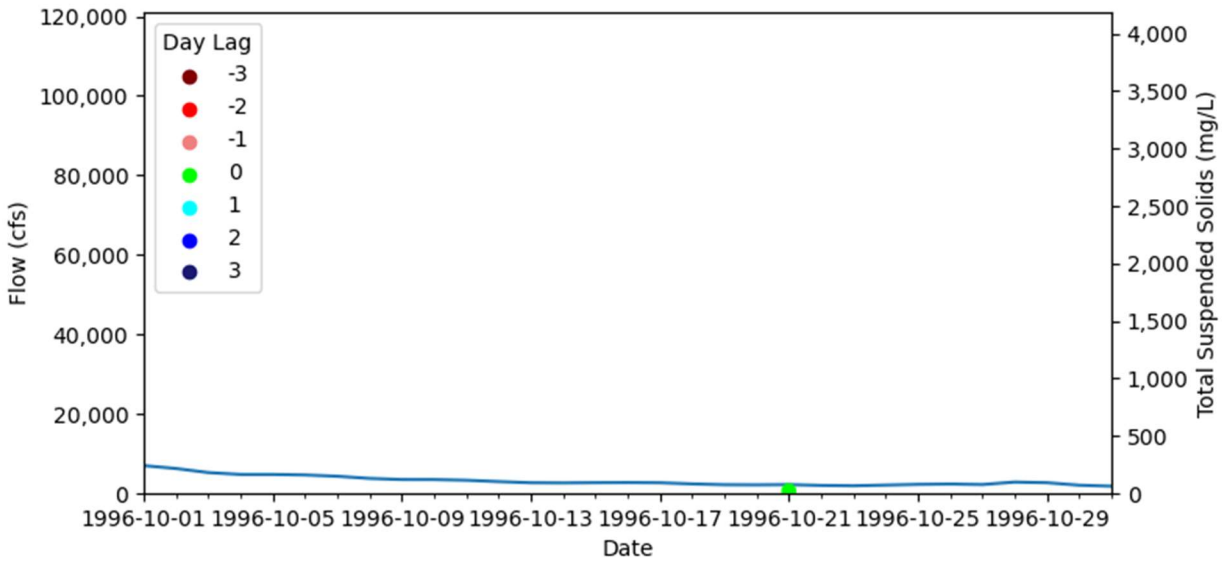
**Figure A-119:** October 1996 Flow and Total Suspended Solids Graph for Landsat Data
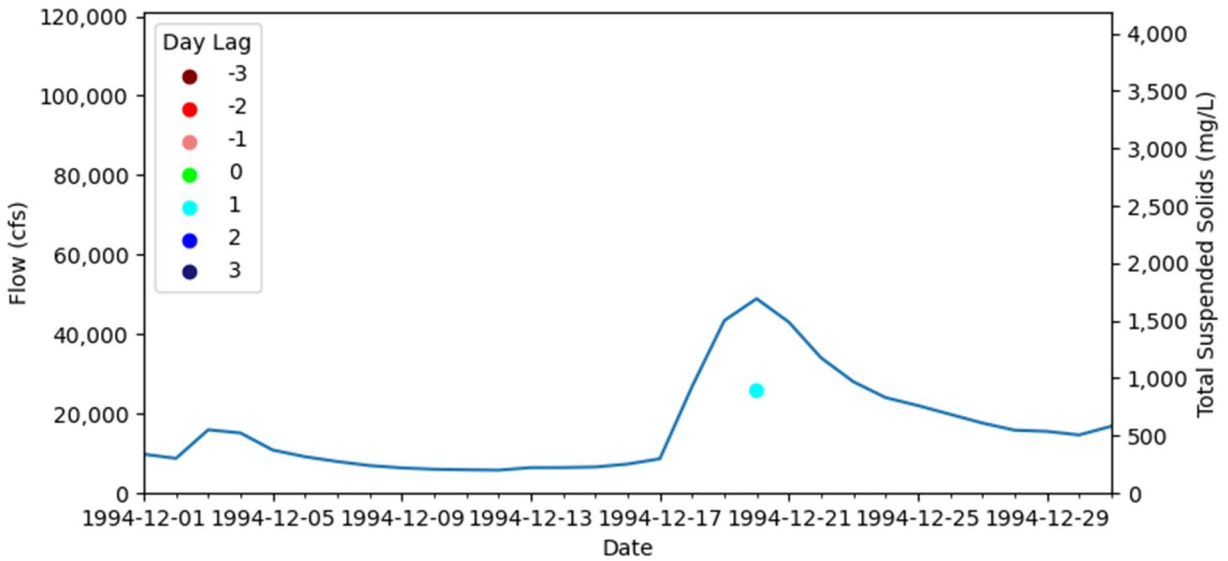


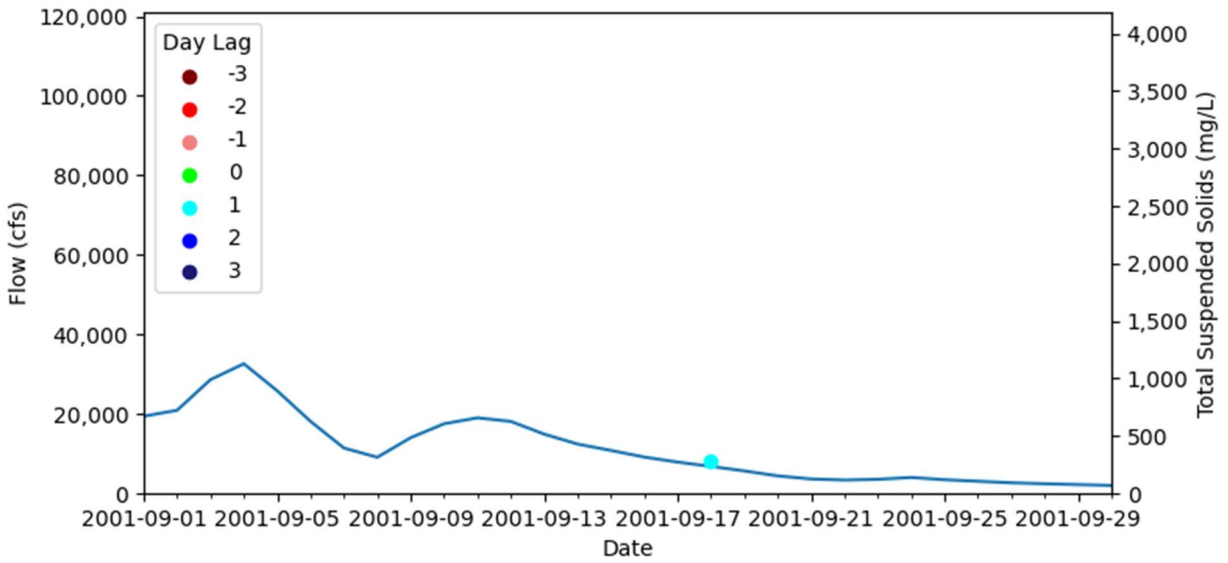**Figure A-120:** December 1994 Flow and Total Suspended Solids Graph for Landsat Data
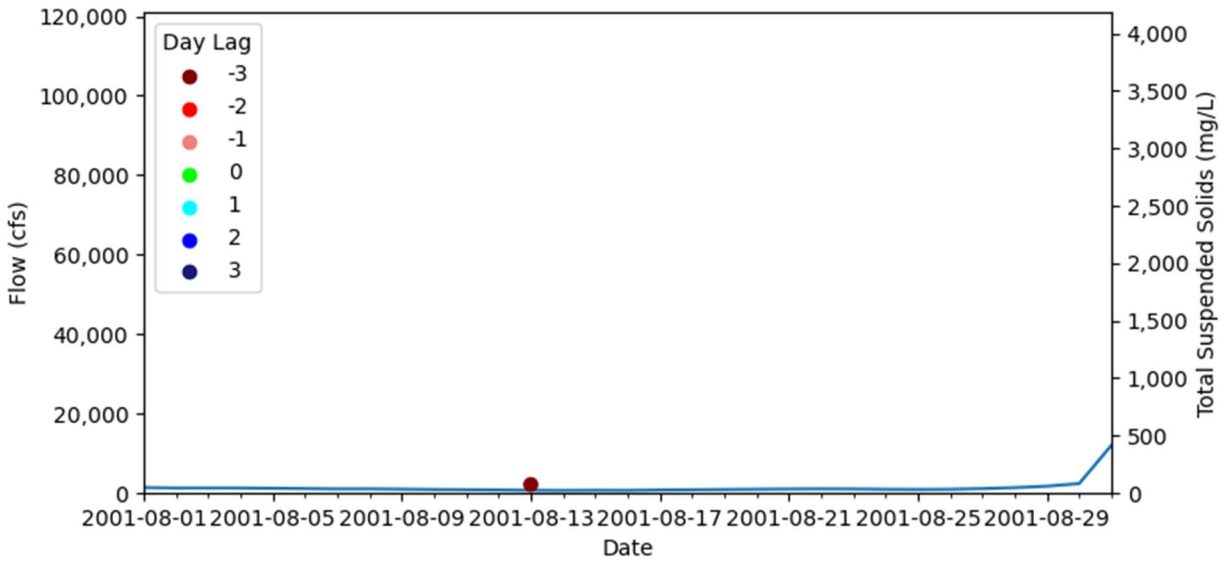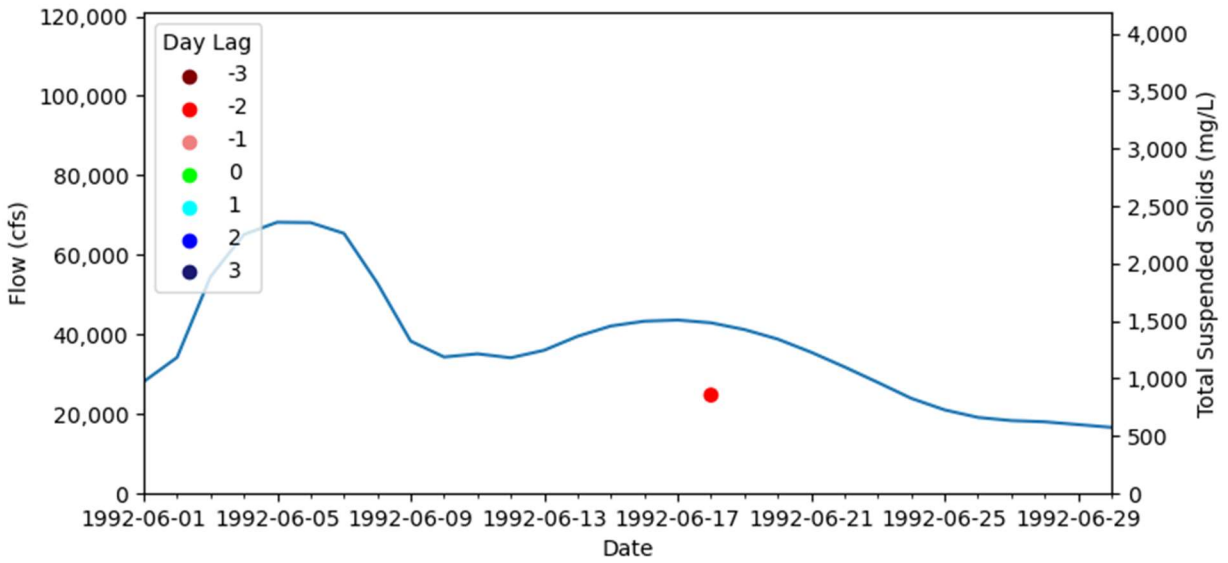
**Figure A-121:** June 1992 Flow and Total Suspended Solids Graph for Landsat Data
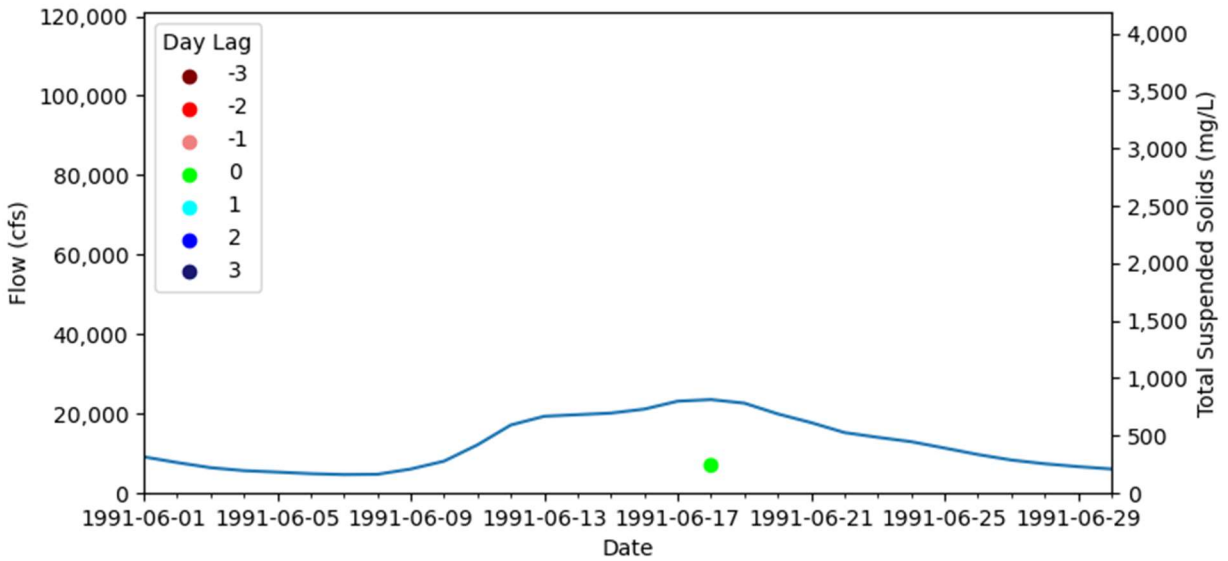


**Figure A-122:** June 1991 Flow and Total Suspended Solids Graph for Landsat Data
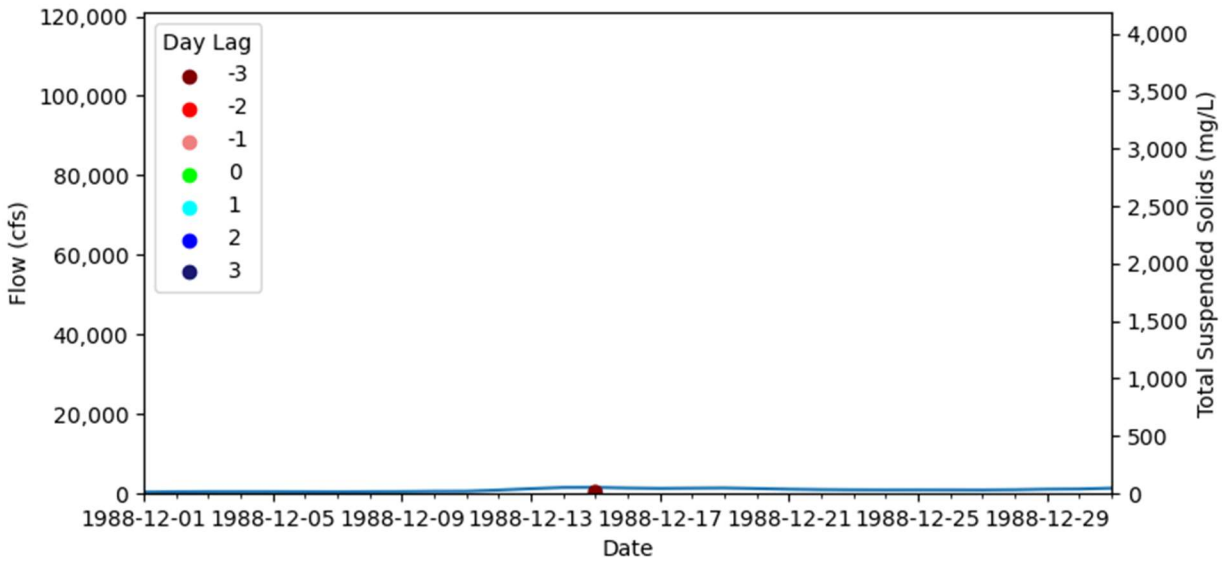
**Figure A-123:** December 1988 Flow and Total Suspended Solids Graph for Landsat Data
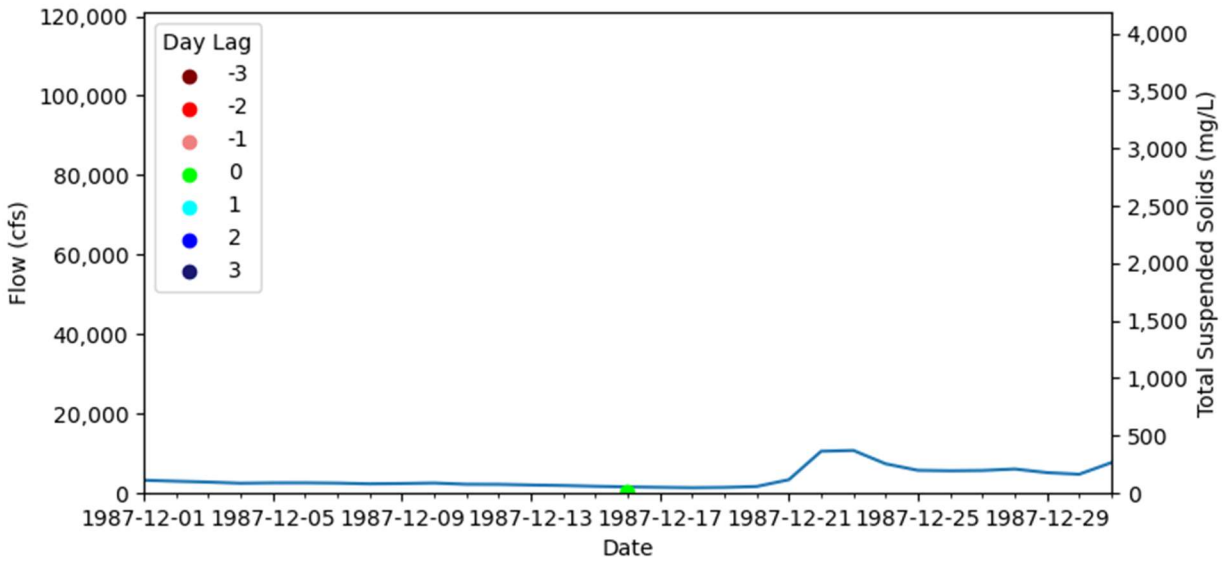


**Figure A-124:** December 1987 Flow and Total Suspended Solids Graph for Landsat Data
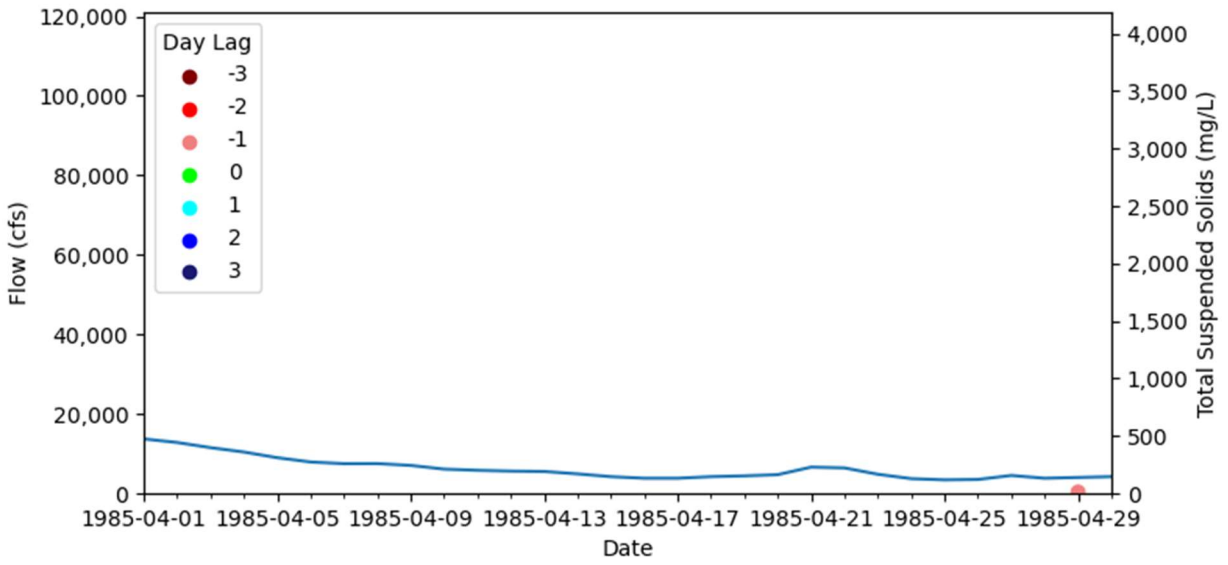
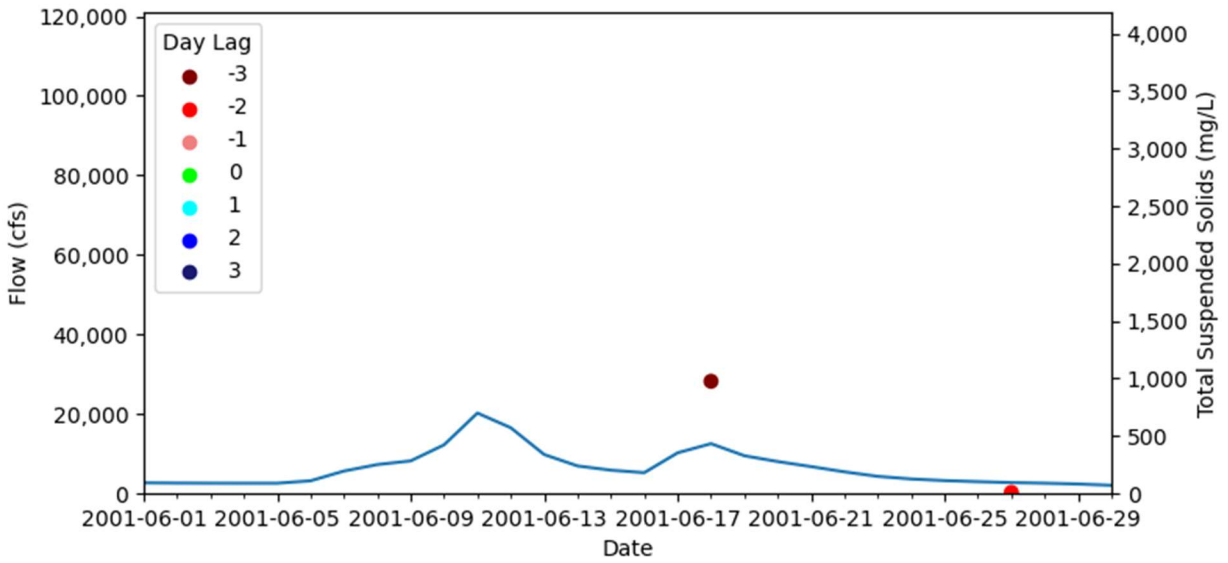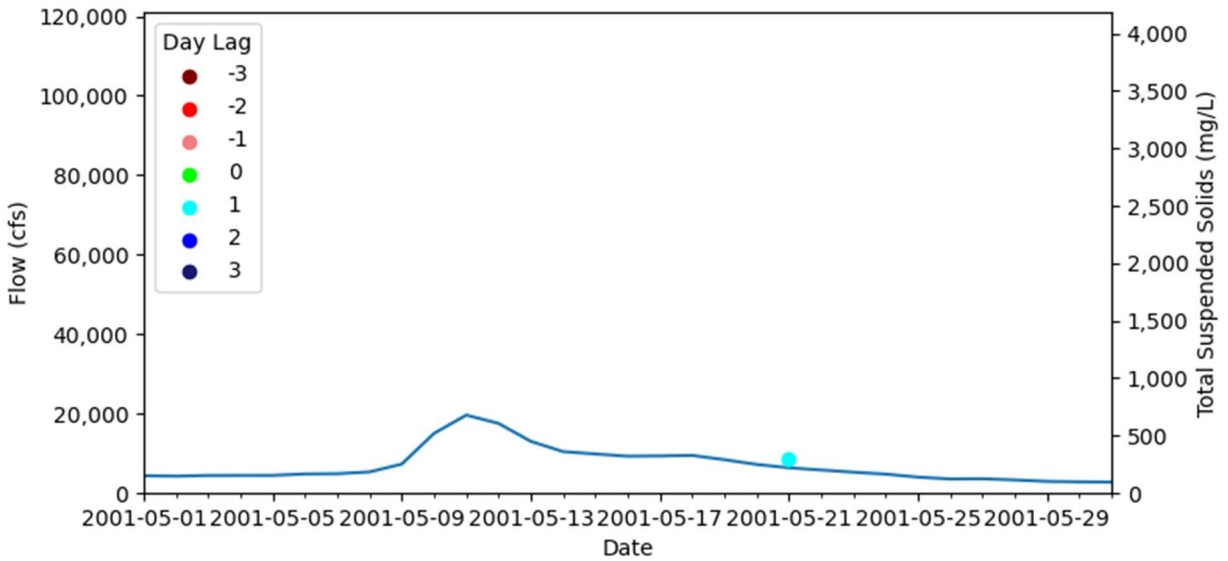**Figure A-125:** April 1985 Flow and Total Suspended Solids Graph for Landsat Data

## Appendix B – Sentinel Flow vs. TSS



**Figure B-1**: May 2022 Flow and Total Suspended Solids Graph for Sentinel Data



**Figure B-2**: April 2022 Flow and Total Suspended Solids Graph for Sentinel Data

**Figure B-3**: January 2022 Flow and Total Suspended Solids Graph for Sentinel Data



**Figure B-4**: December 2021 Flow and Total Suspended Solids Graph for Sentinel Data
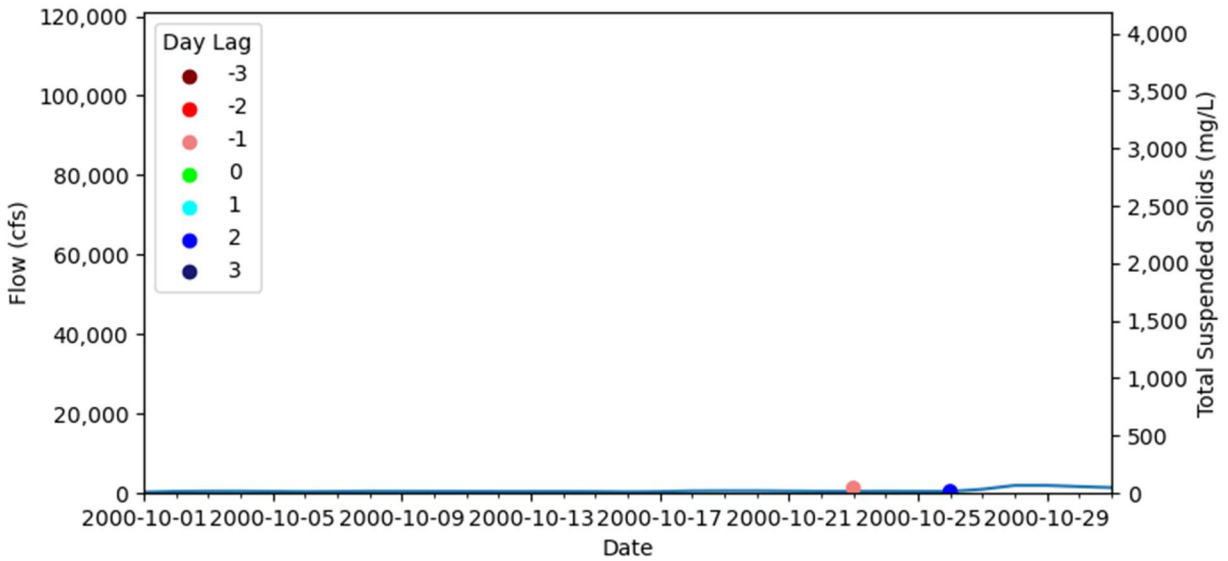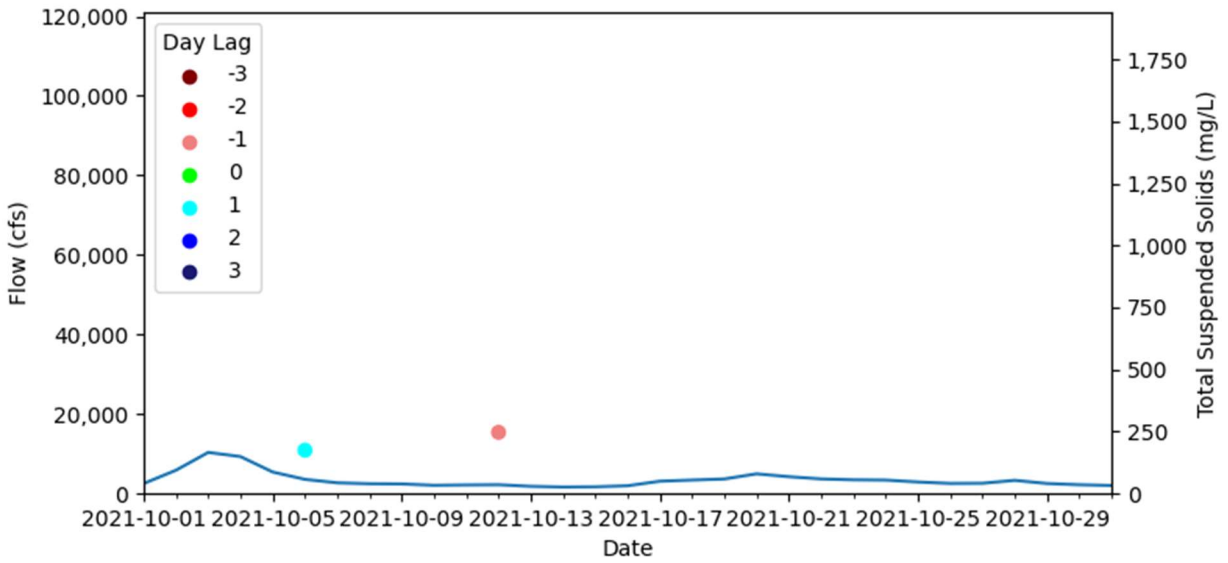
**Figure B-5**: October 2021 Flow and Total Suspended Solids Graph for Sentinel Data
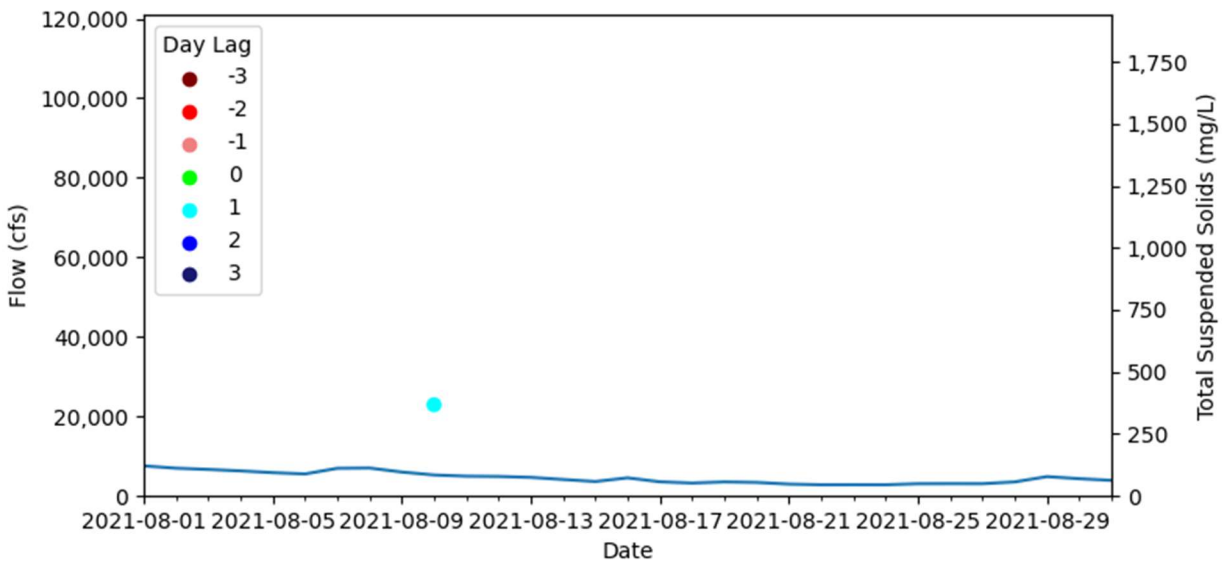


**Figure B-6**: August 2021 Flow and Total Suspended Solids Graph for Sentinel Data
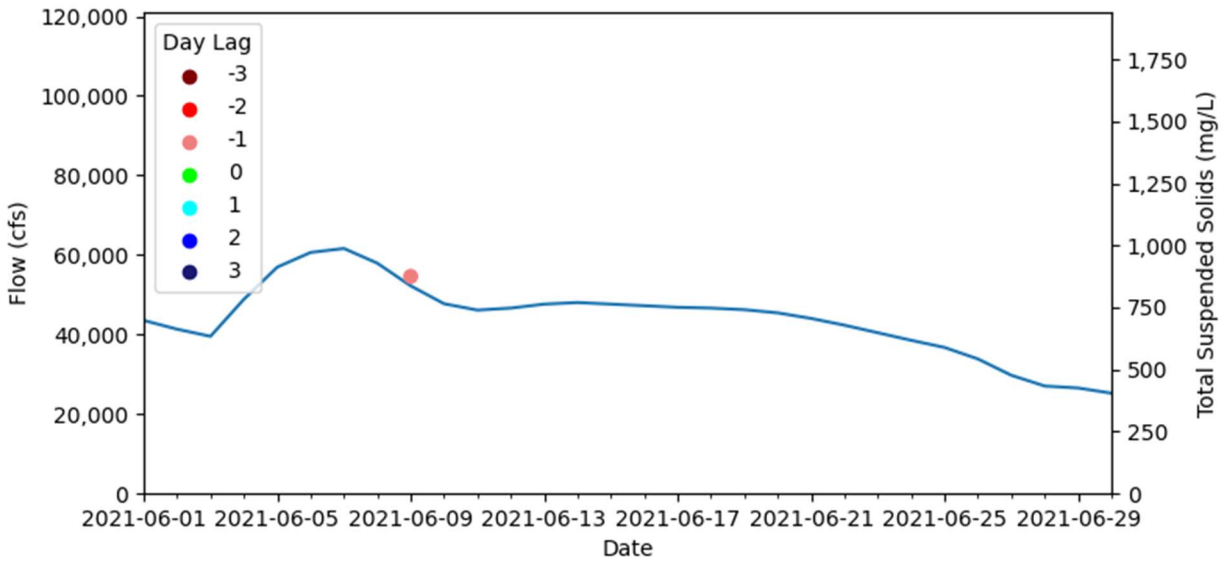
**Figure B-7**: June 2021 Flow and Total Suspended Solids Graph for Sentinel Data
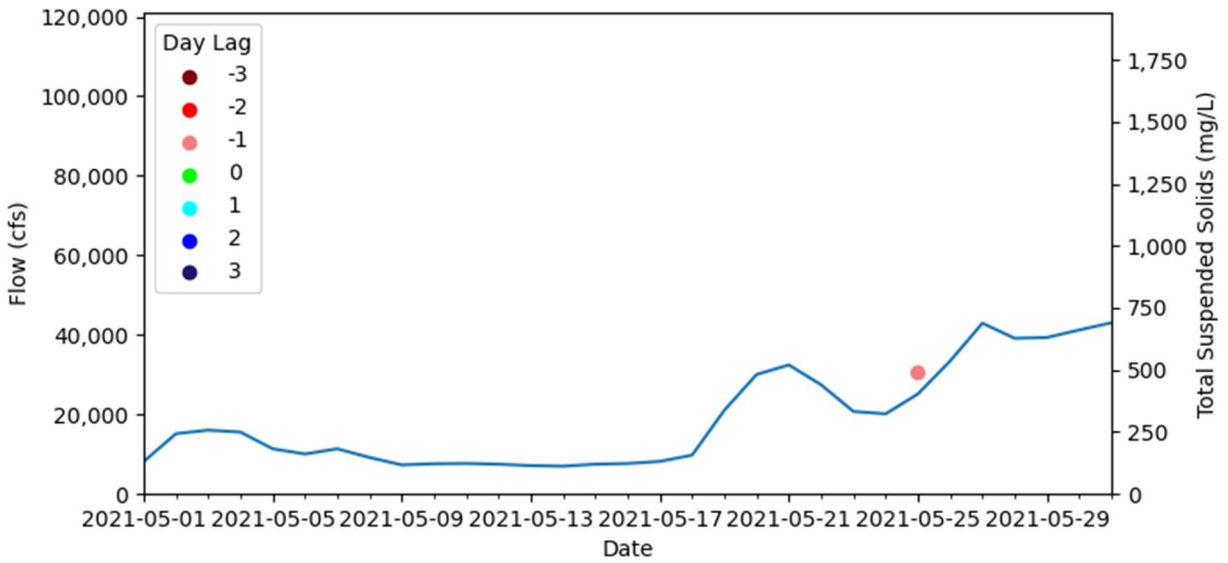


**Figure B-8**: May 2021 Flow and Total Suspended Solids Graph for Sentinel Data
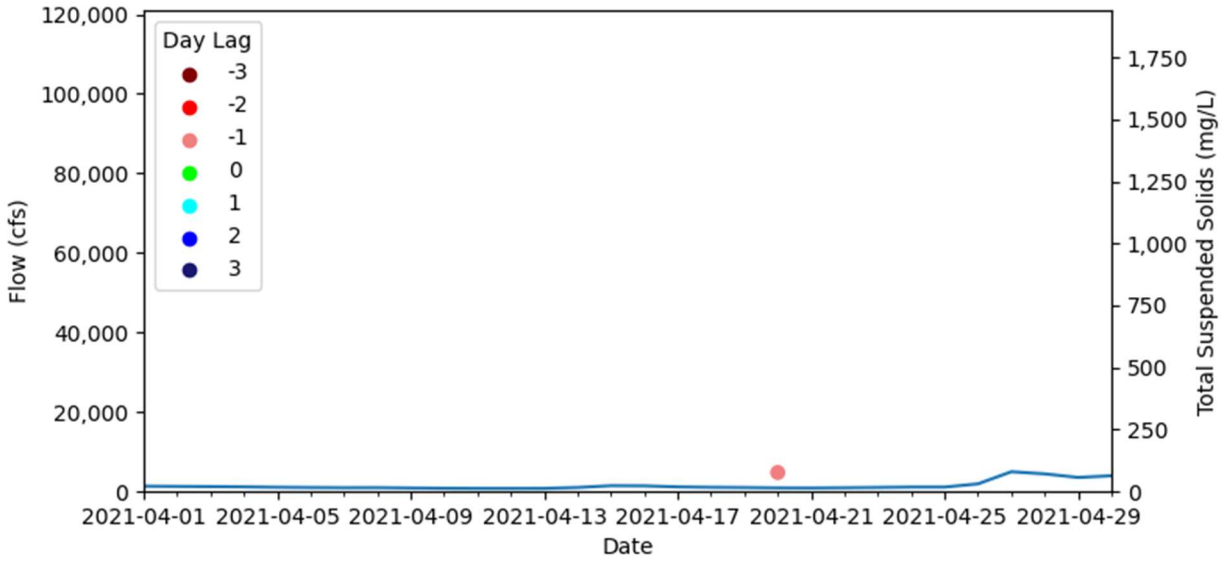
**Figure B-9**: April 2021 Flow and Total Suspended Solids Graph for Sentinel Data
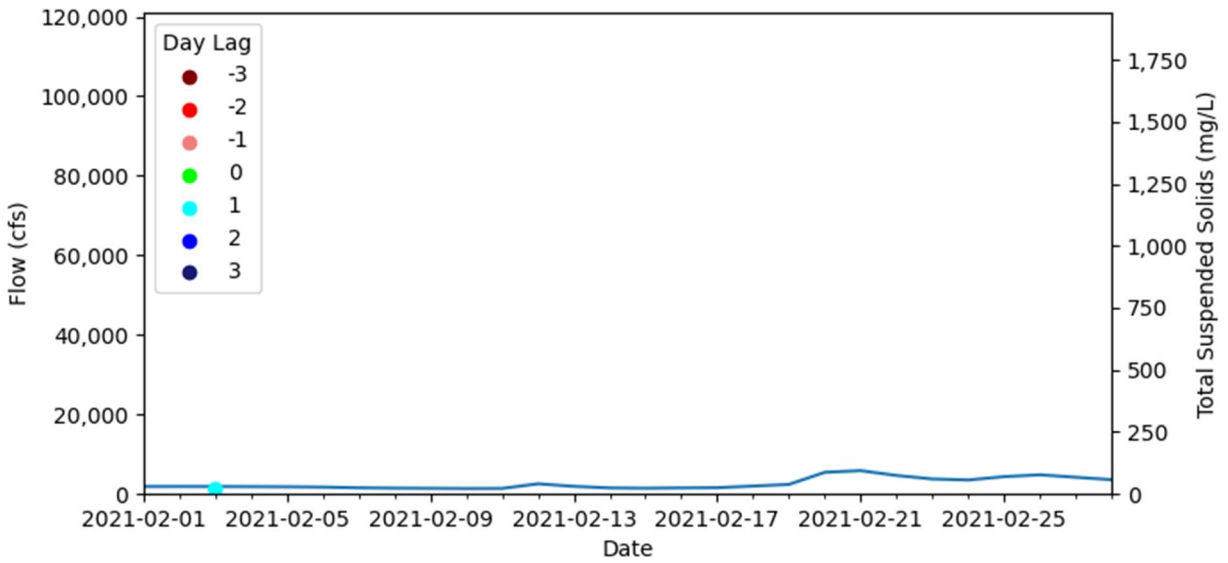


**Figure B-10**: February 2021 Flow and Total Suspended Solids Graph for Sentinel Data
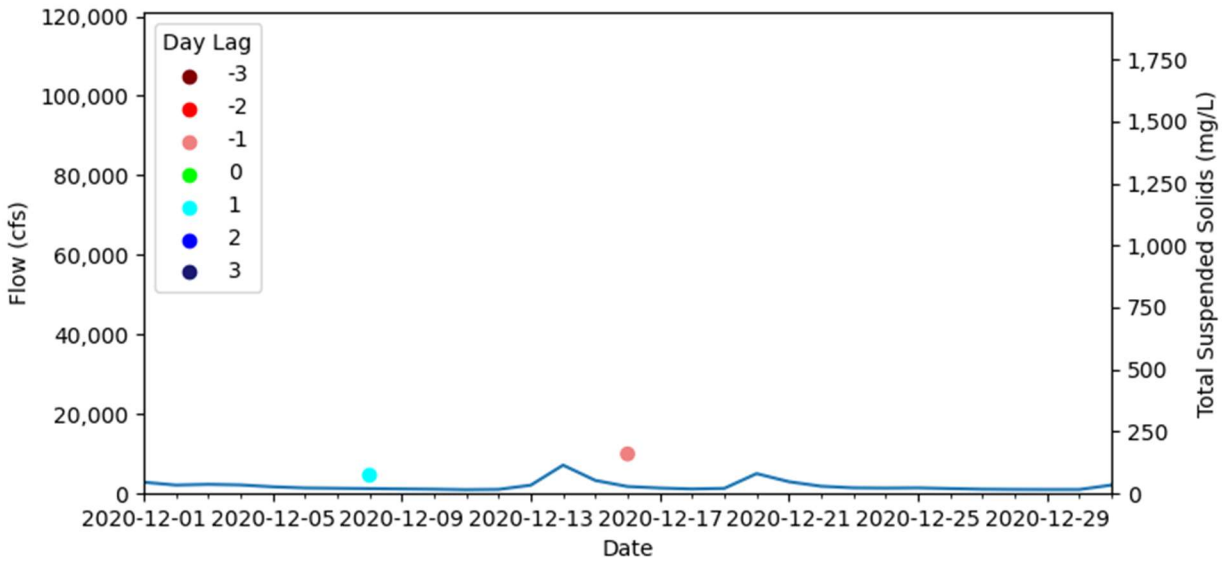
**Figure B-11**: December 2020 Flow and Total Suspended Solids Graph for Sentinel Data
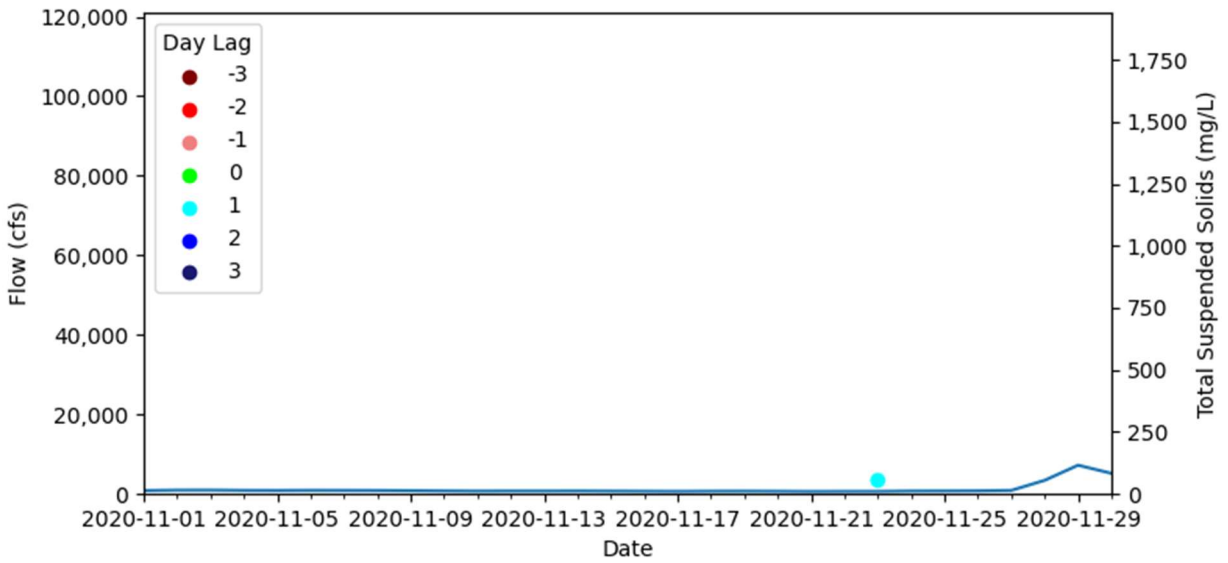


**Figure B-12**: November 2020 Flow and Total Suspended Solids Graph for Sentinel Data
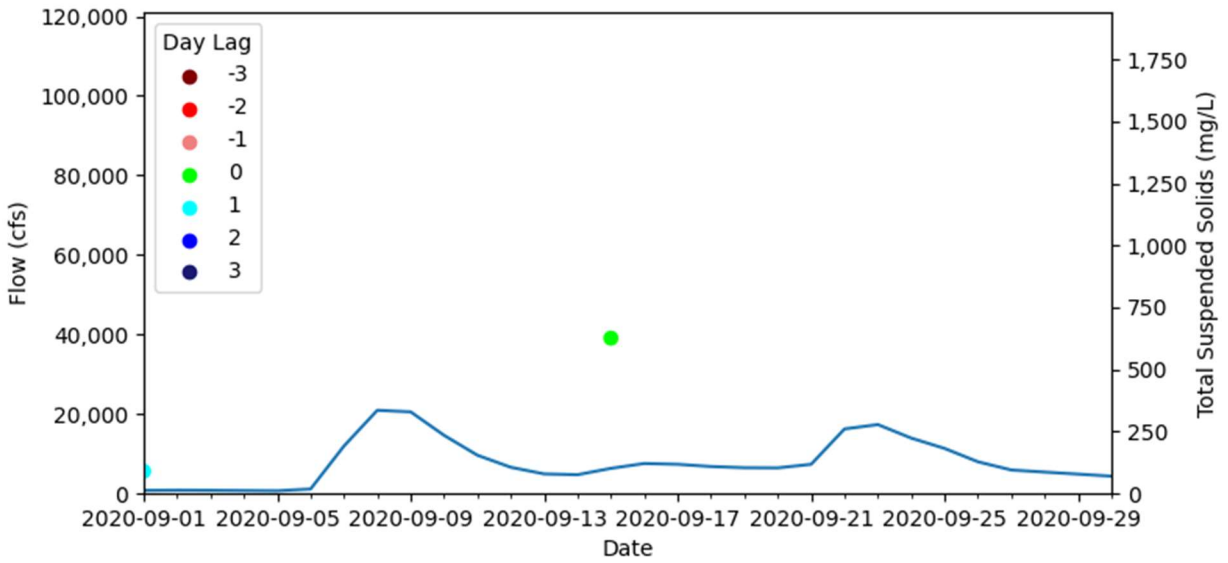
**Figure B-13**: September 2020 Flow and Total Suspended Solids Graph for Sentinel Data
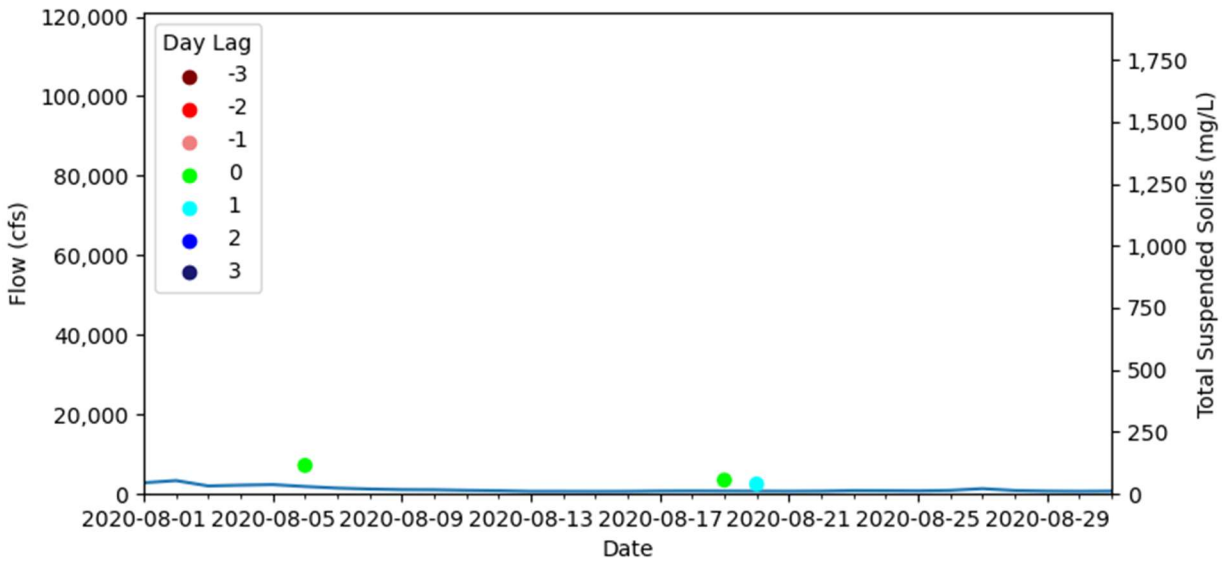


**Figure B-14**: August 2020 Flow and Total Suspended Solids Graph for Sentinel Data
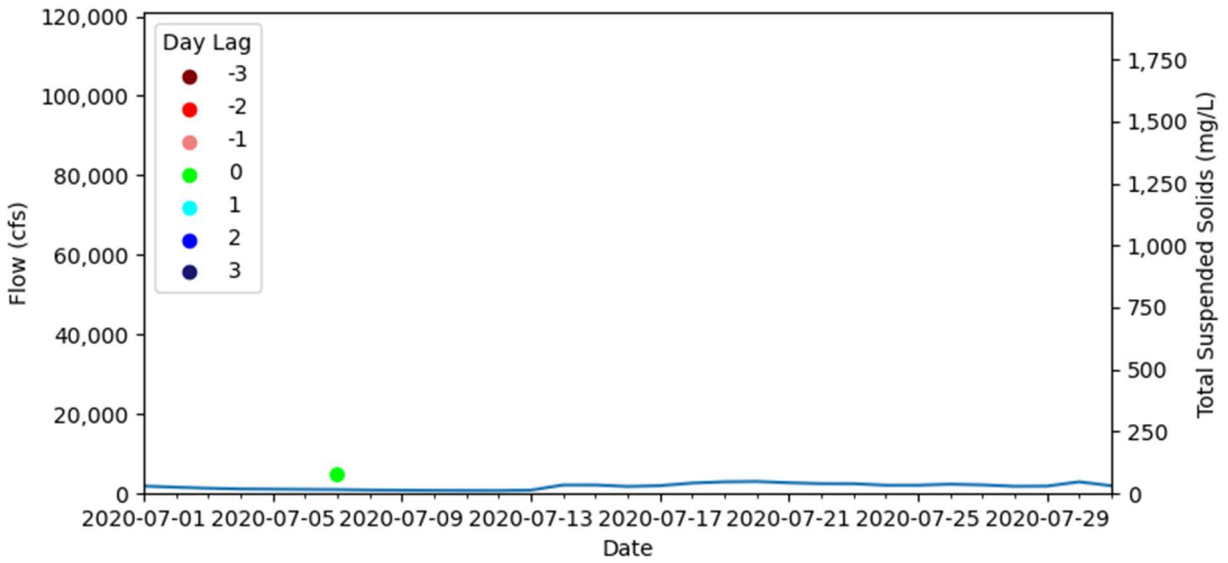
**Figure B-15**: July 2020 Flow and Total Suspended Solids Graph for Sentinel Data
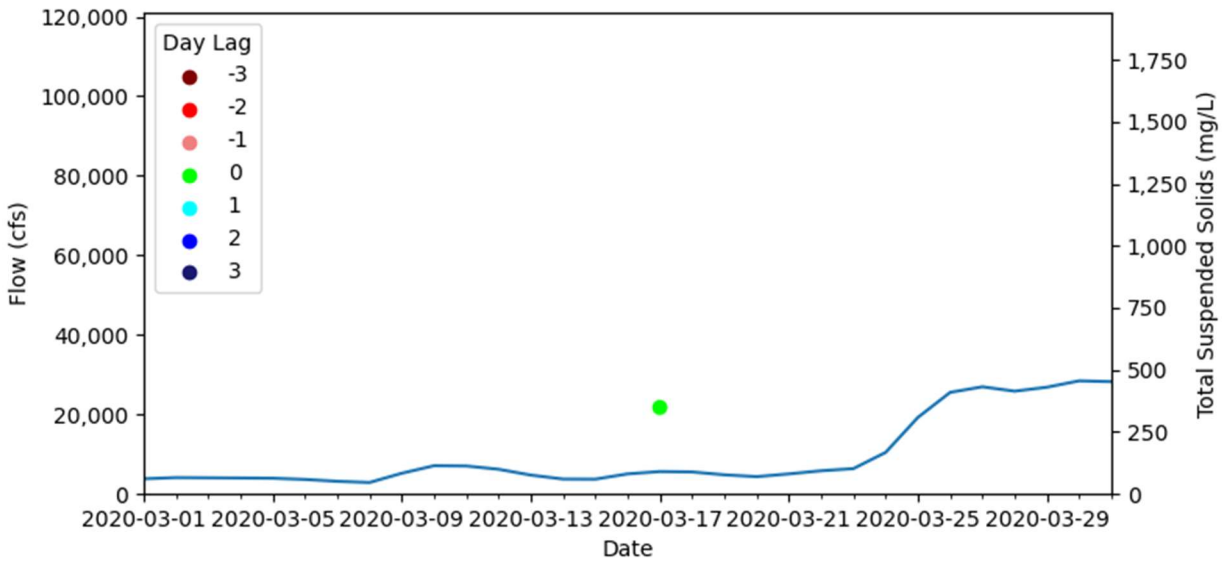


**Figure B-16**: March 2020 Flow and Total Suspended Solids Graph for Sentinel Data
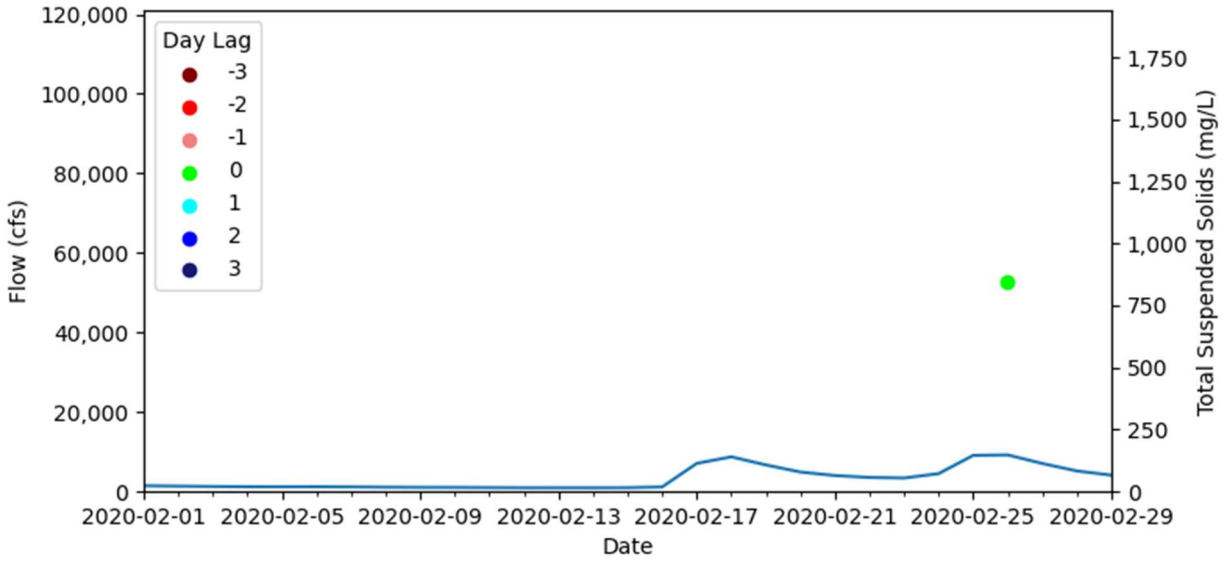
**Figure B-17**: February 2020 Flow and Total Suspended Solids Graph for Sentinel Data
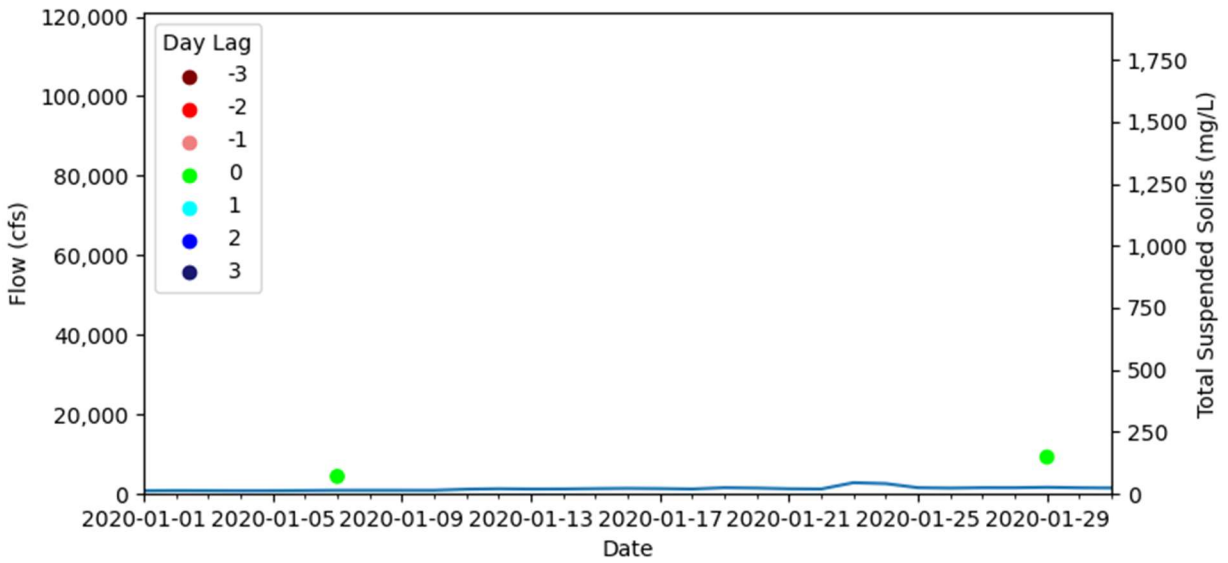


**Figure B-18**: January 2020 Flow and Total Suspended Solids Graph for Sentinel Data
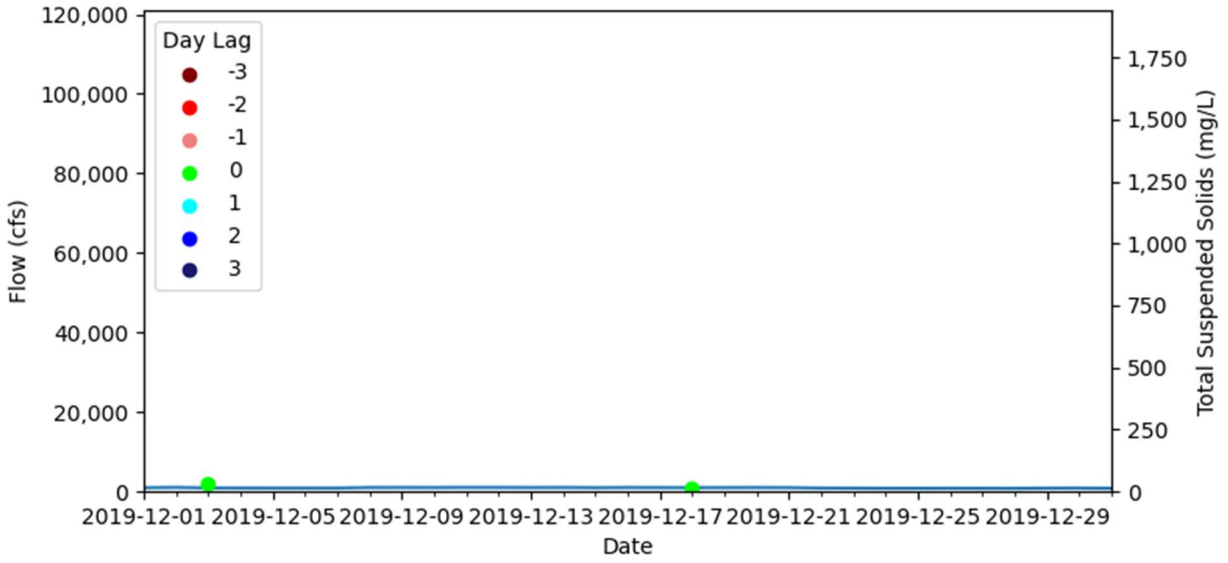
**Figure B-19**: December 2019 Flow and Total Suspended Solids Graph for Sentinel Data
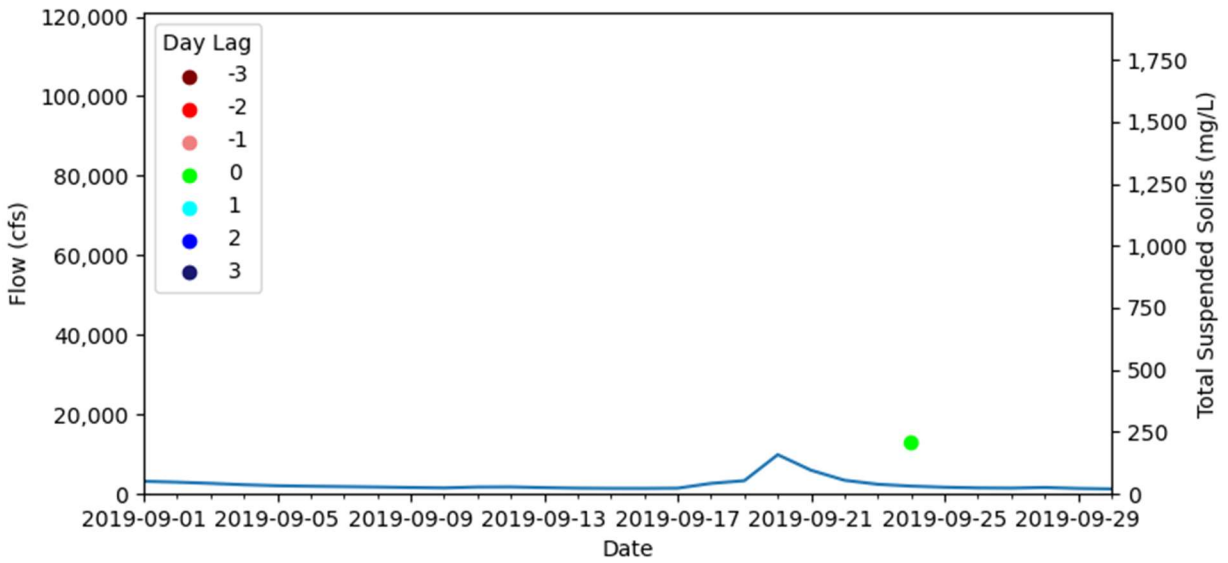


**Figure B-20**: September 2019 Flow and Total Suspended Solids Graph for Sentinel Data
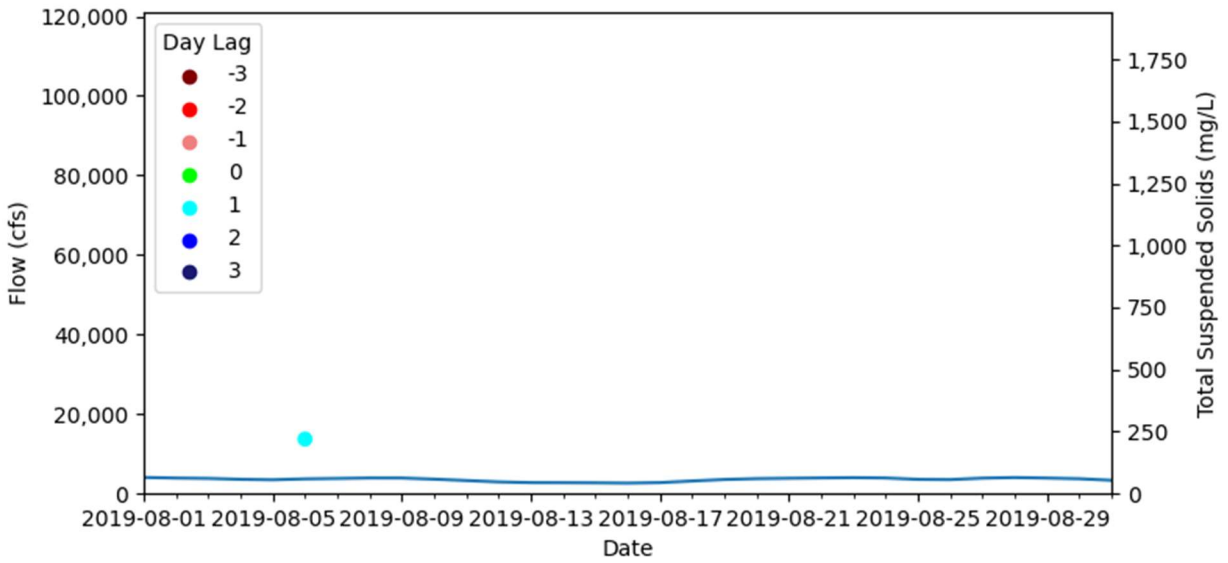
**Figure B-21**: August 2019 Flow and Total Suspended Solids Graph for Sentinel Data
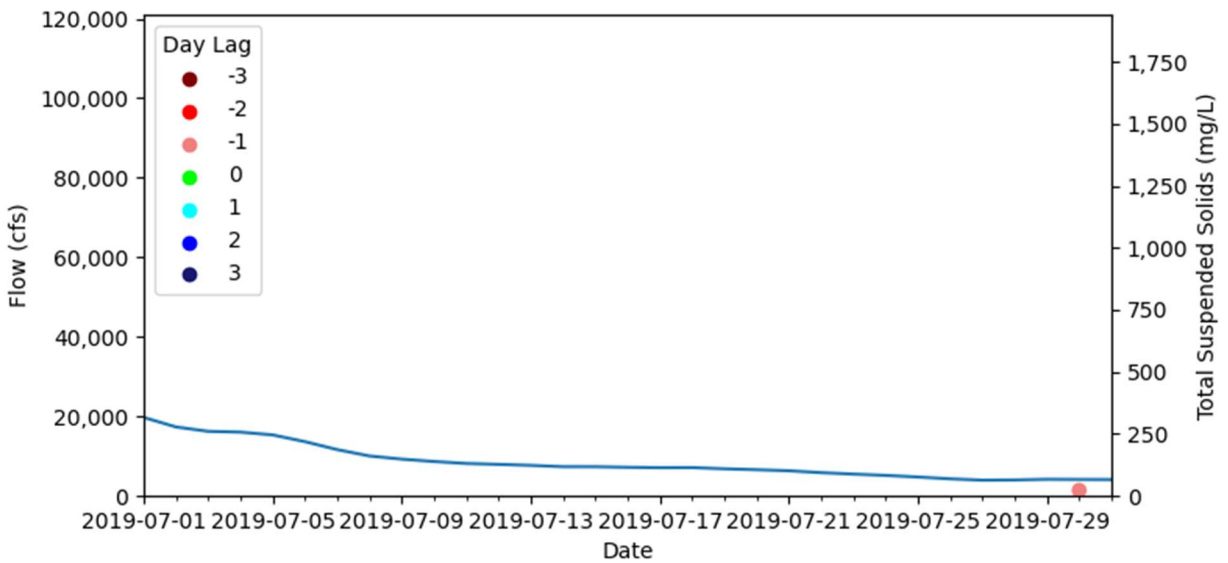


**Figure B-22**: July 2019 Flow and Total Suspended Solids Graph for Sentinel Data
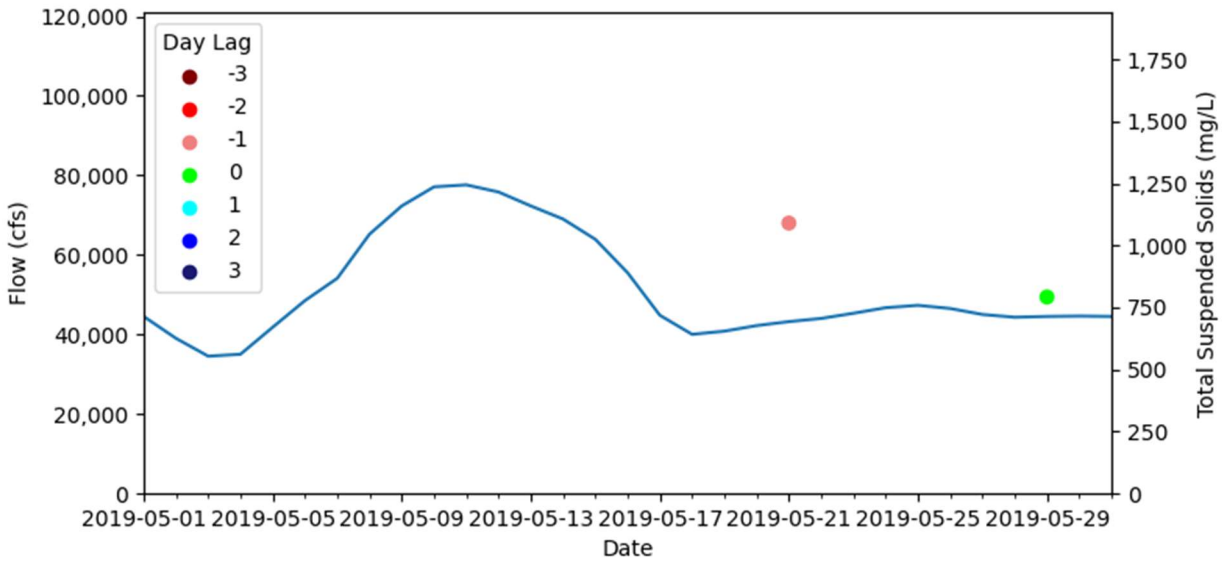
**Figure B-23**: May 2019 Flow and Total Suspended Solids Graph for Sentinel Data
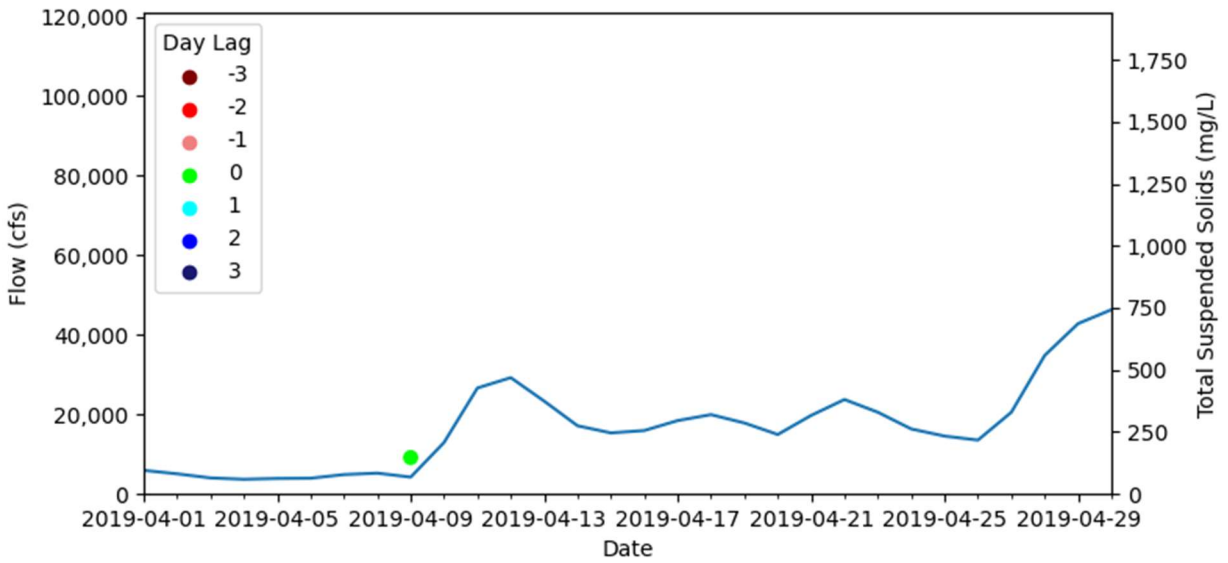


**Figure B-24**: April 2019 Flow and Total Suspended Solids Graph for Sentinel Data
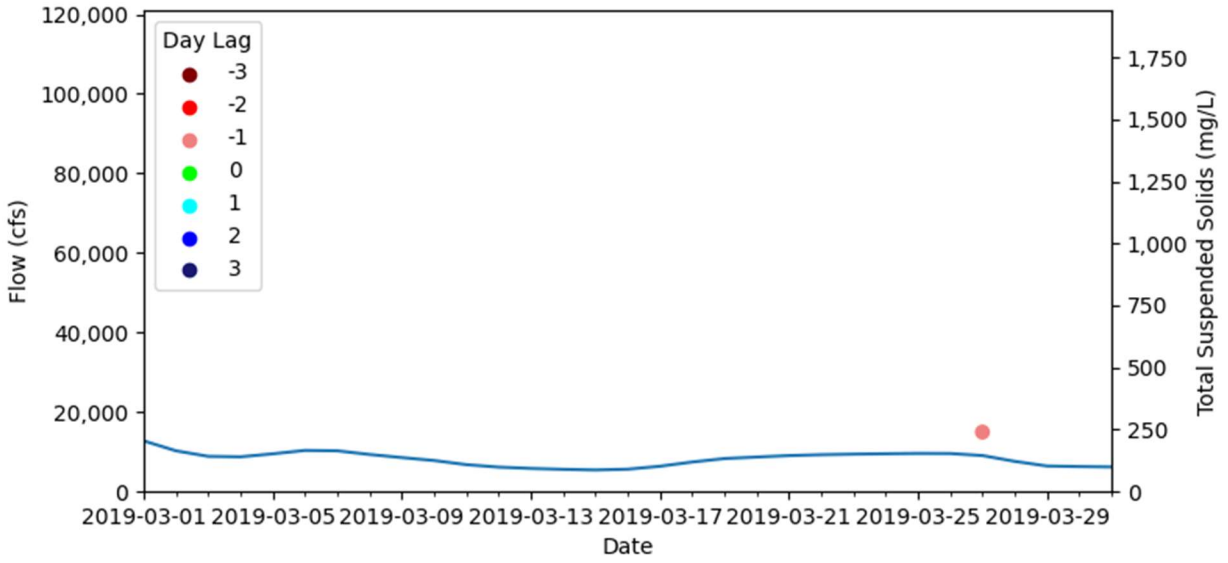
**Figure B-25**: March 2019 Flow and Total Suspended Solids Graph for Sentinel Data
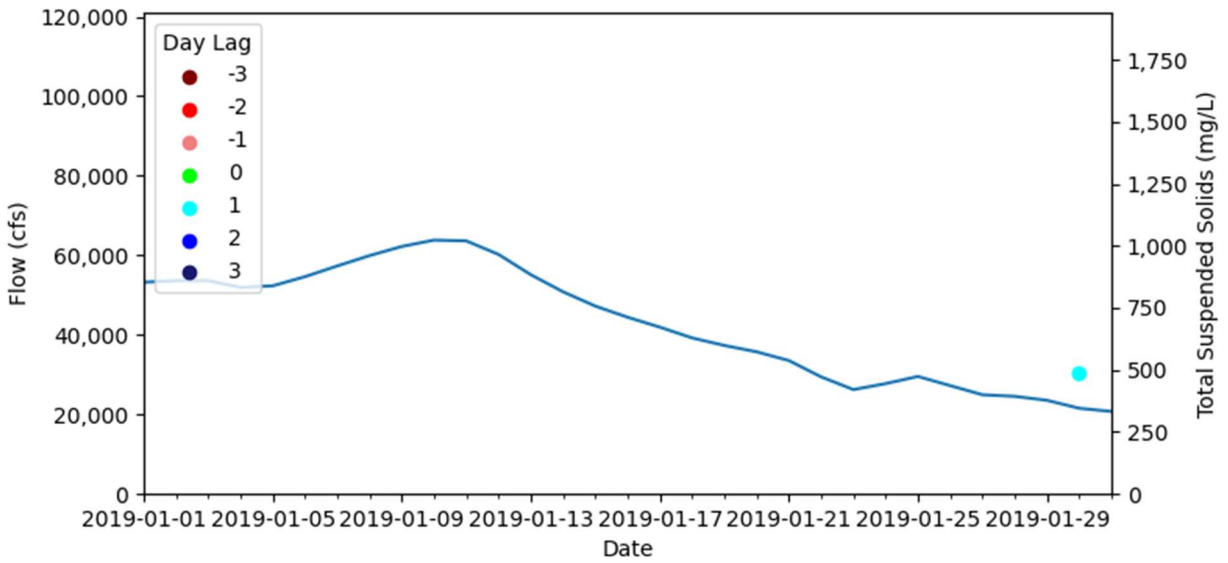


**Figure B-26**: January 2019 Flow and Total Suspended Solids Graph for Sentinel Data
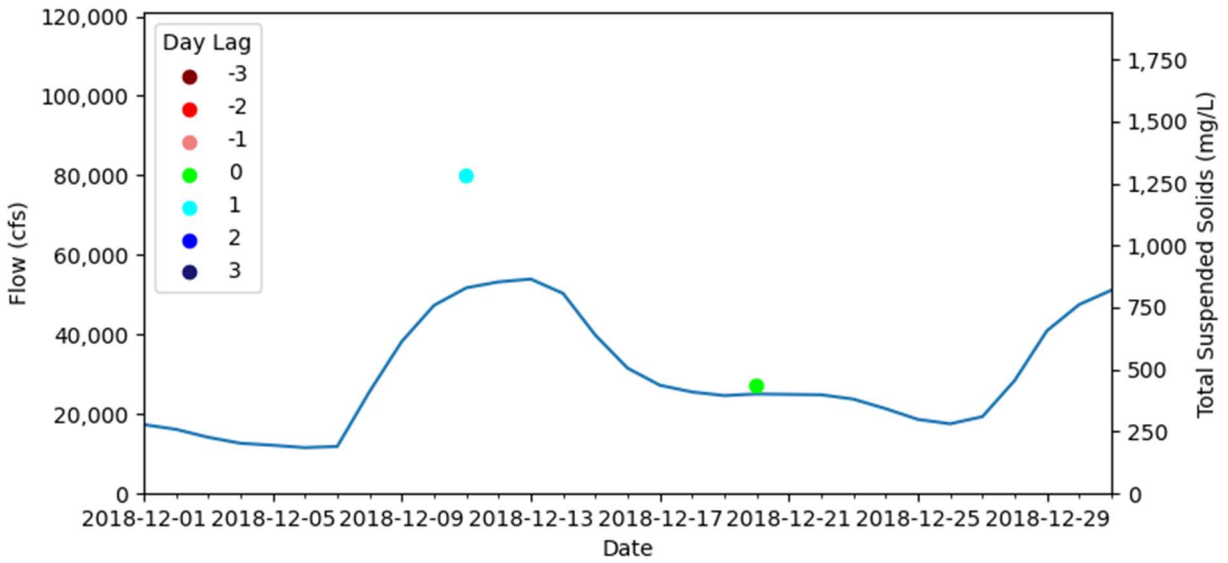
**Figure B-27**: December 2018 Flow and Total Suspended Solids Graph for Sentinel Data
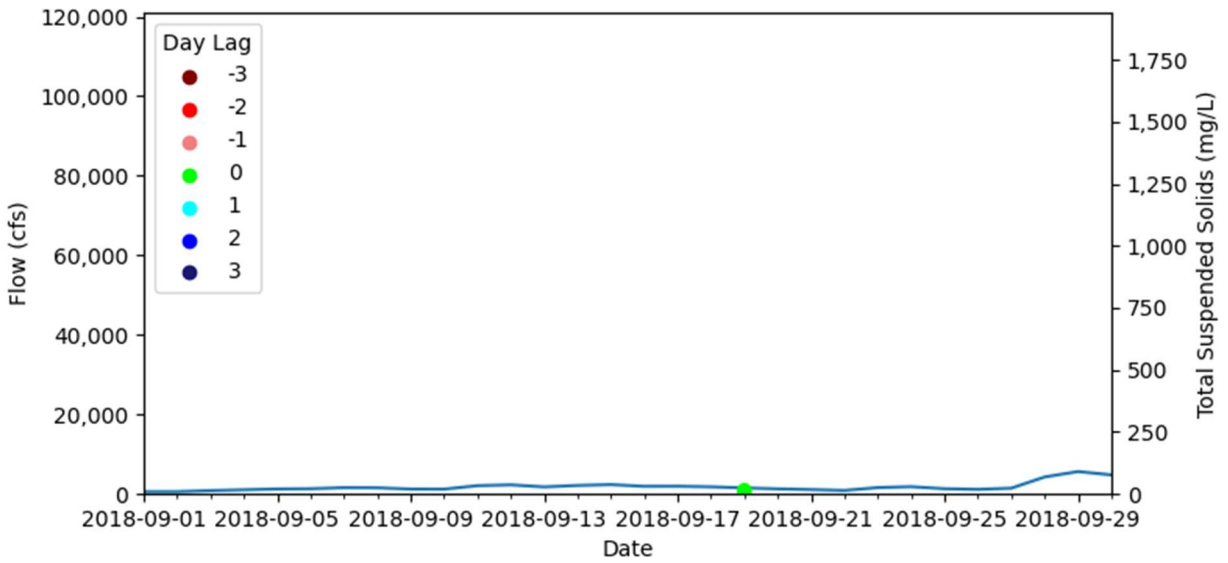


**Figure B-28**: September 2018 Flow and Total Suspended Solids Graph for Sentinel Data
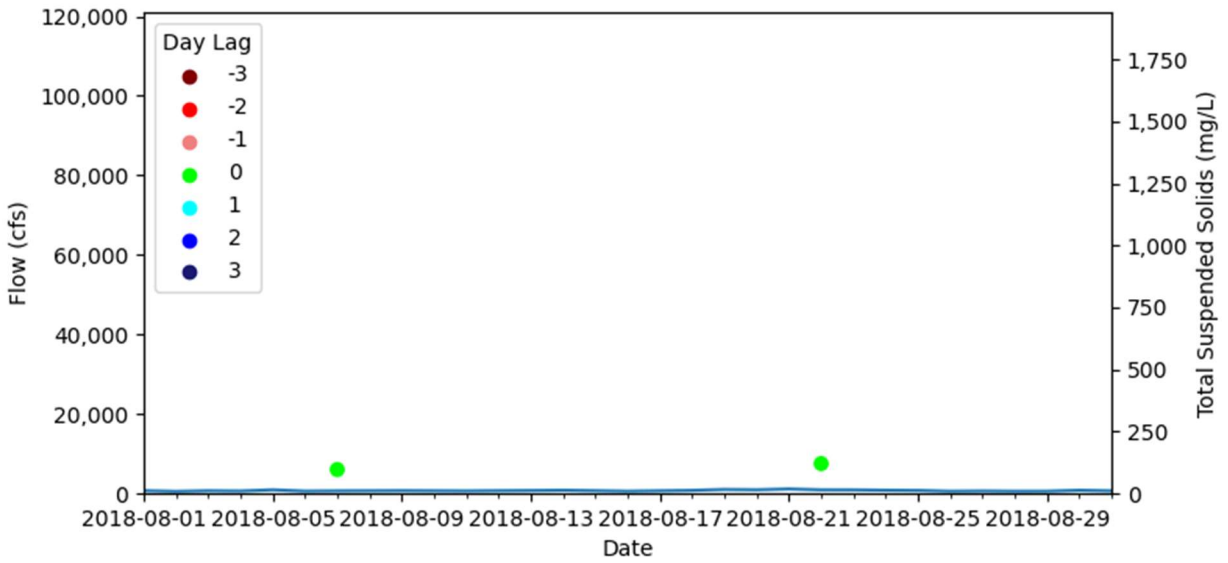
**Figure B-29**: August 2018 Flow and Total Suspended Solids Graph for Sentinel Data
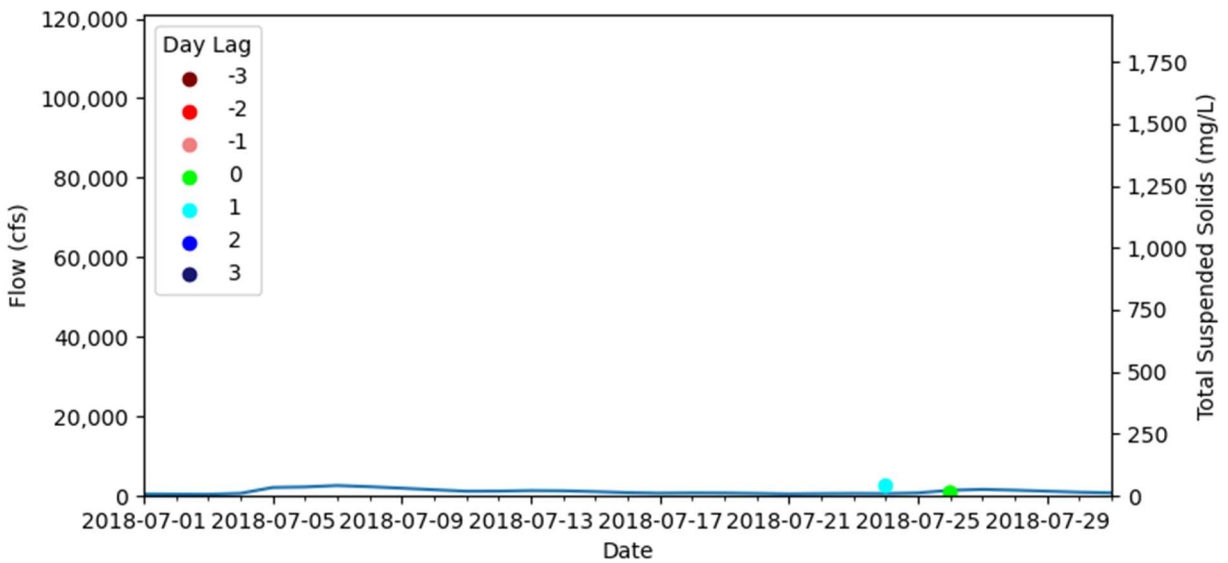


**Figure B-30**: July 2018 Flow and Total Suspended Solids Graph for Sentinel Data
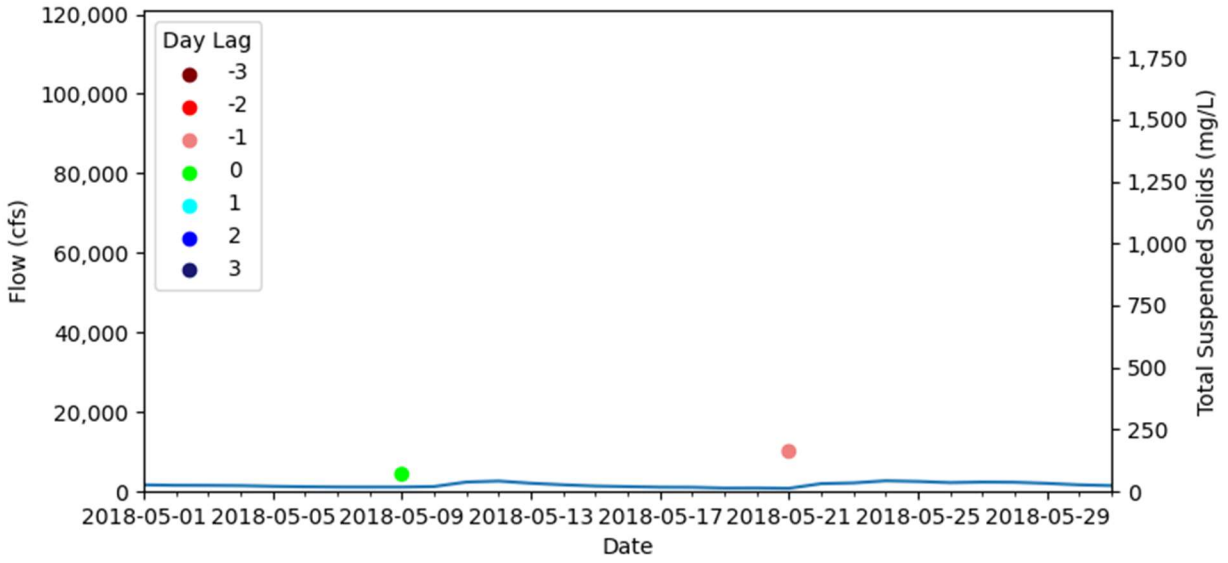
**Figure B-31**: May 2018 Flow and Total Suspended Solids Graph for Sentinel Data
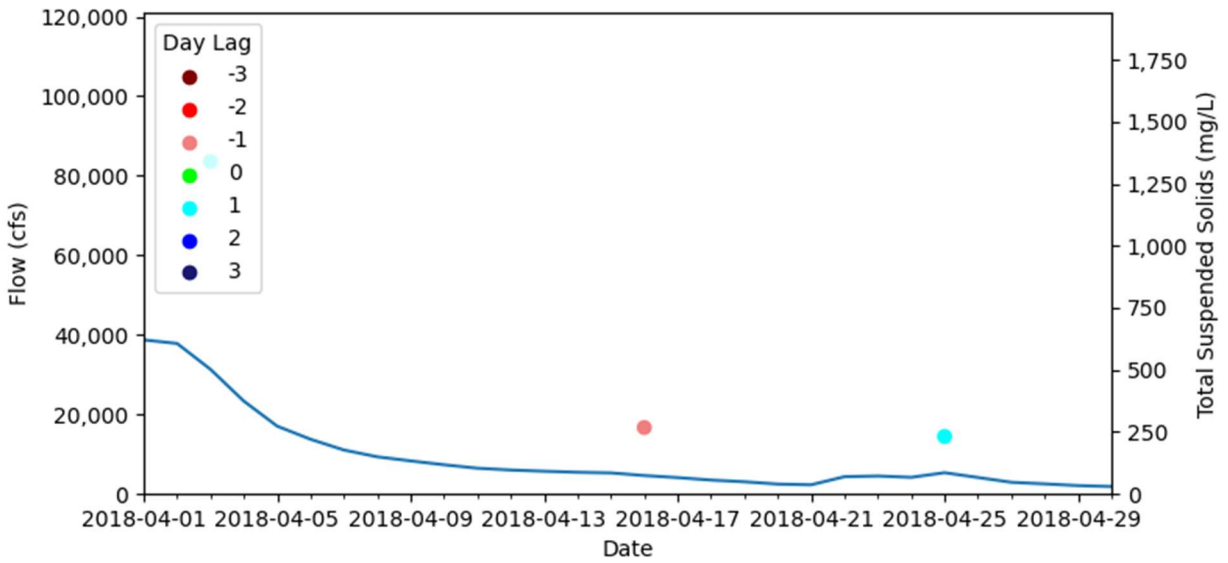


**Figure B-32**: April 2018 Flow and Total Suspended Solids Graph for Sentinel Data
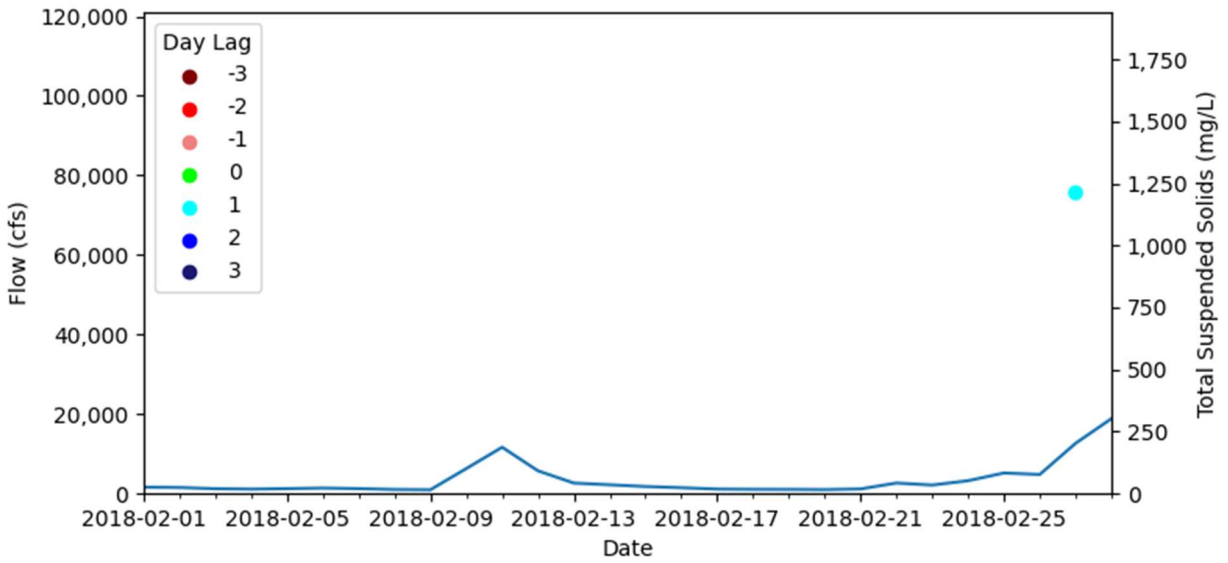
**Figure B-33**: February 2018 Flow and Total Suspended Solids Graph for Sentinel Data
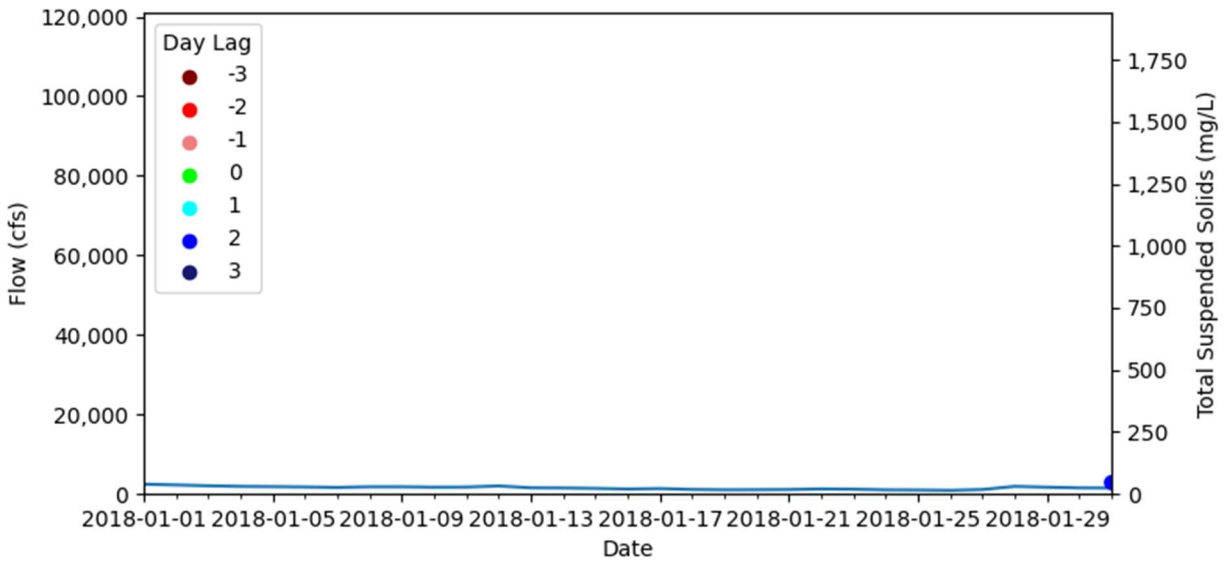


**Figure B-34**: January 2018 Flow and Total Suspended Solids Graph for Sentinel Data
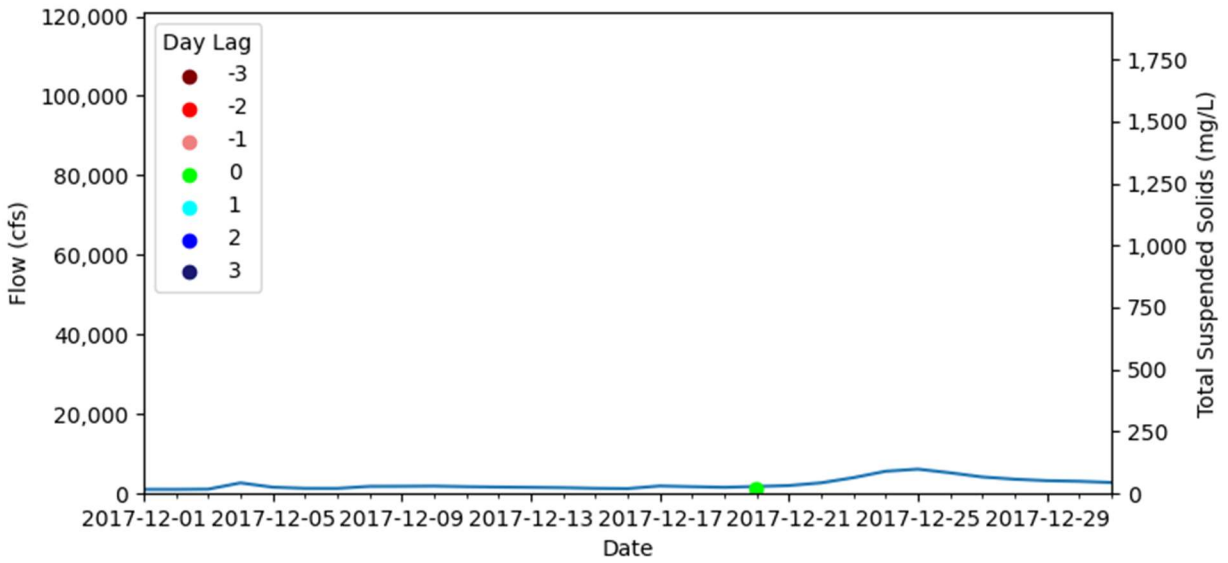
**Figure B-35**: December 2017 Flow and Total Suspended Solids Graph for Sentinel Data
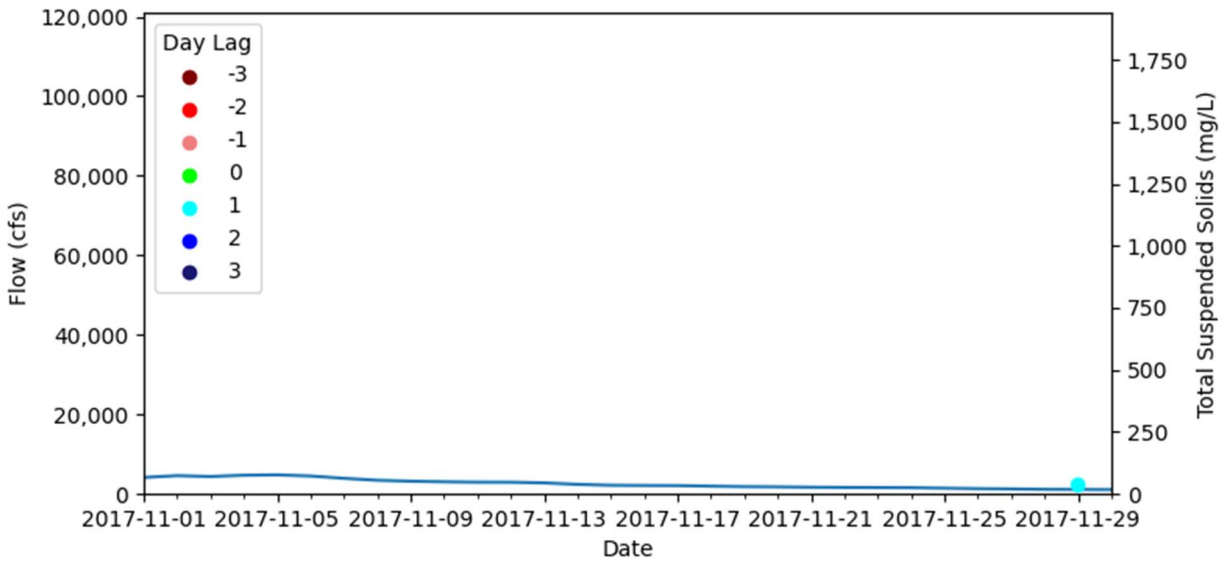


**Figure B-36**: November 2017 Flow and Total Suspended Solids Graph for Sentinel Data
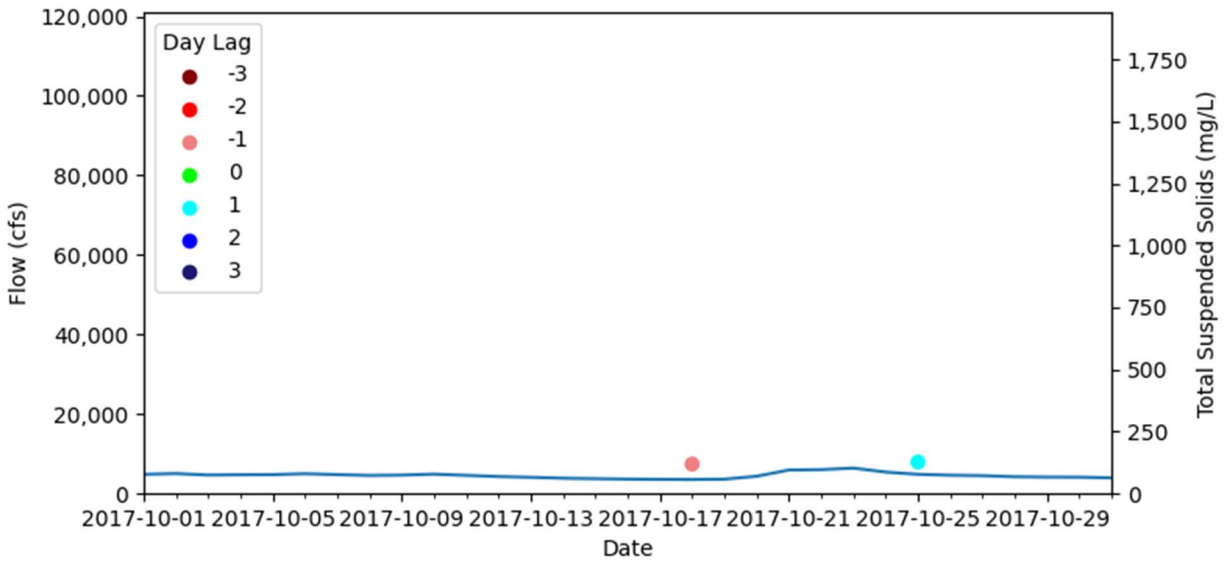
**Figure B-37**: October 2017 Flow and Total Suspended Solids Graph for Sentinel Data
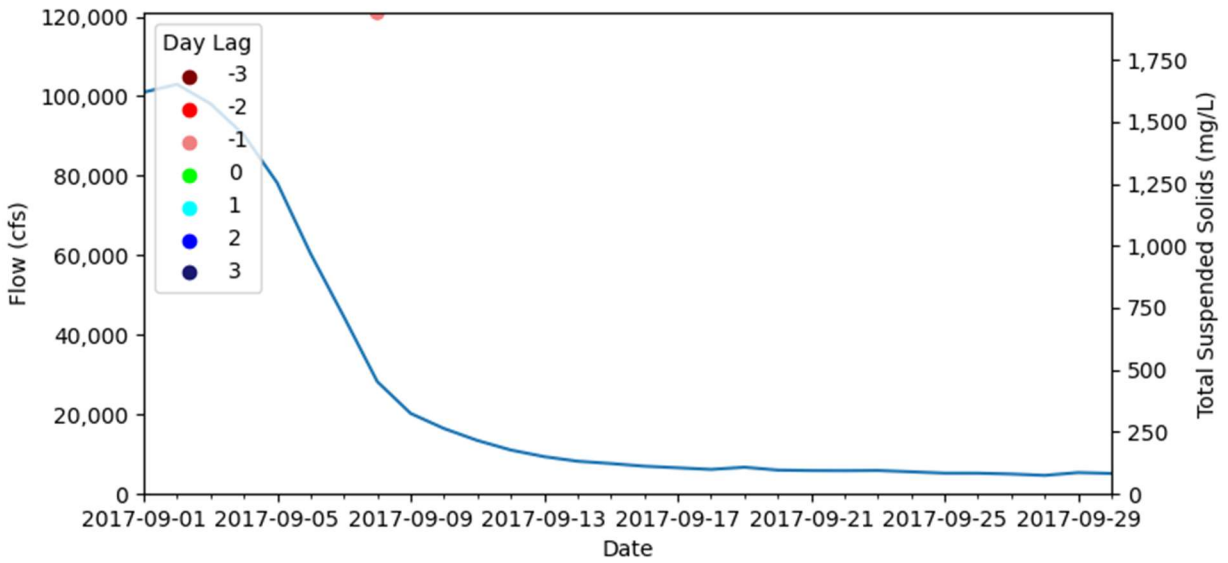


**Figure B-38**: September 2017 Flow and Total Suspended Solids Graph for Sentinel Data
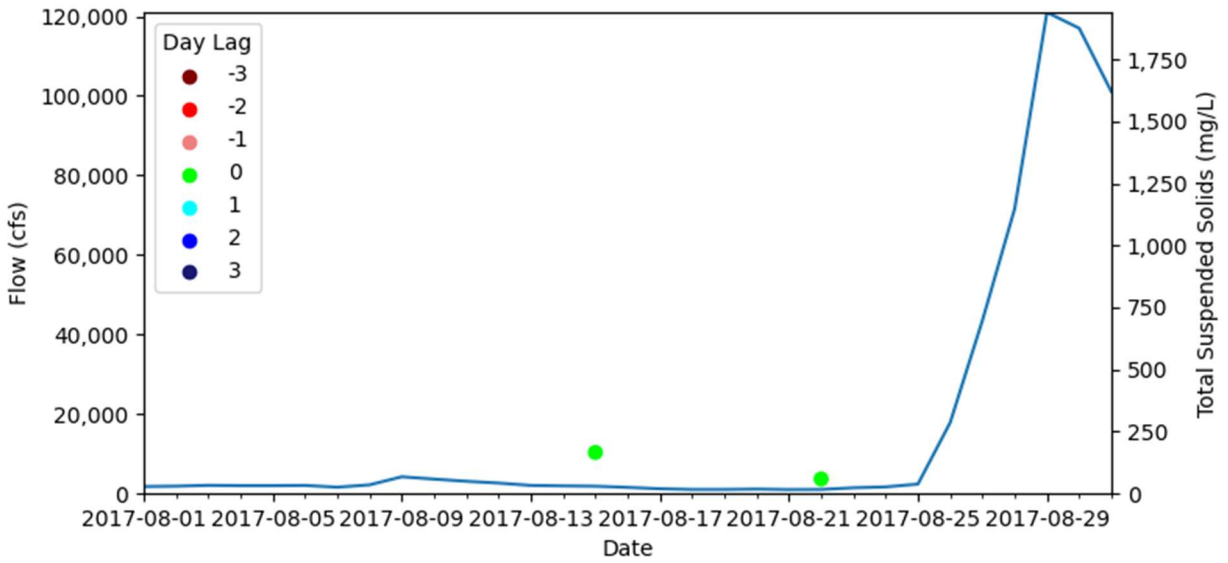
**Figure B-39**: August 2017 Flow and Total Suspended Solids Graph for Sentinel Data
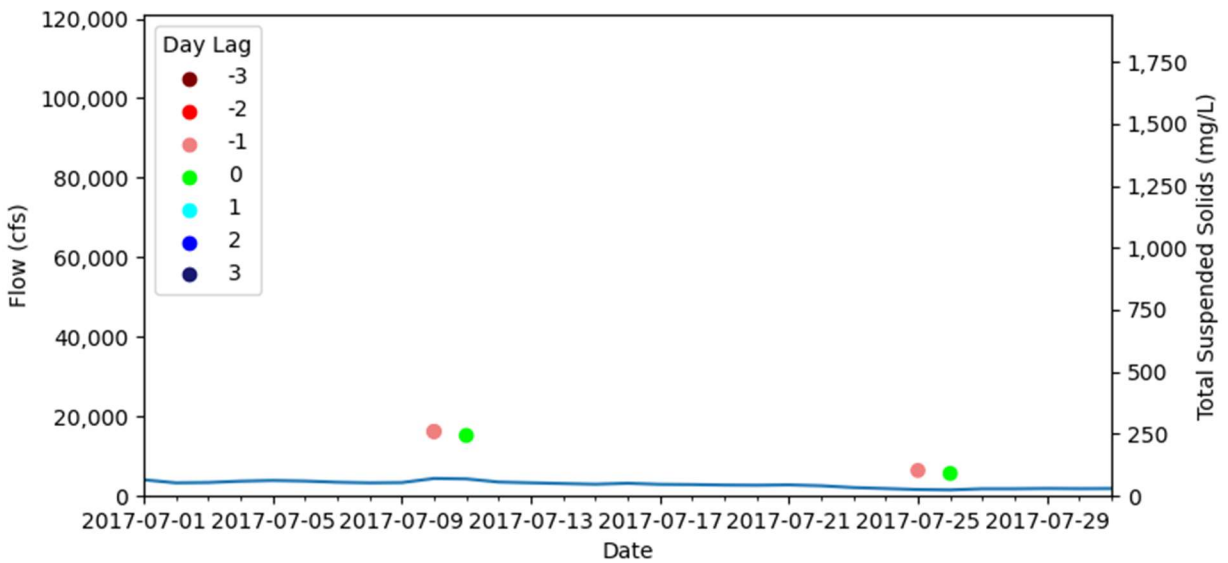


**Figure B-40**: July 2017 Flow and Total Suspended Solids Graph for Sentinel Data
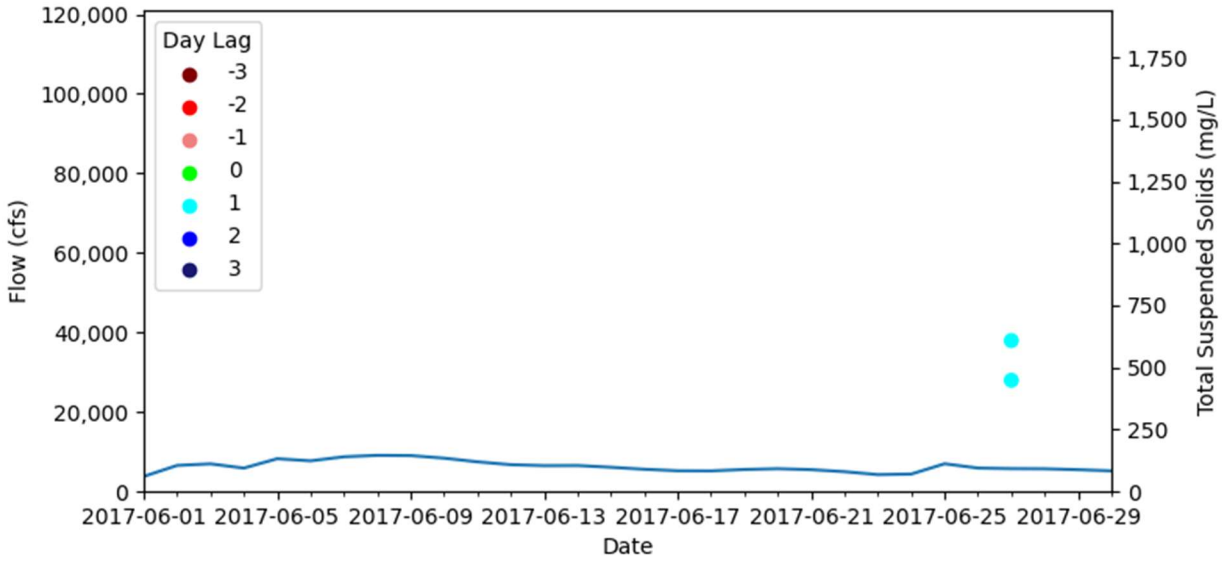
**Figure B-41**: June 2017 Flow and Total Suspended Solids Graph for Sentinel Data
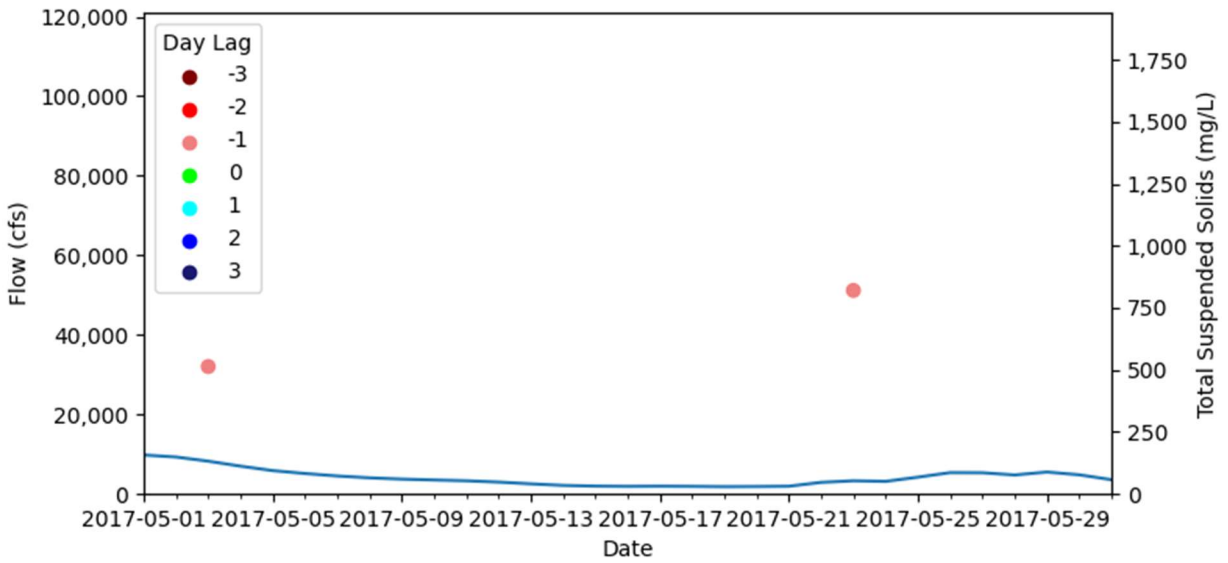


**Figure B-42**: May 2017 Flow and Total Suspended Solids Graph for Sentinel Data
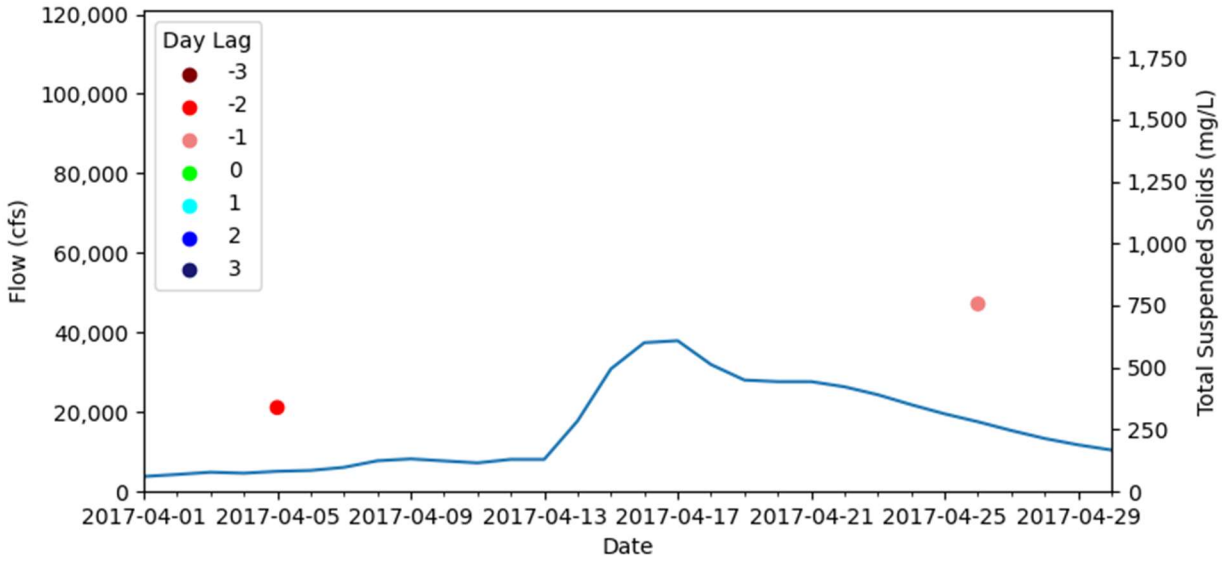
**Figure B-43**: April 2017 Flow and Total Suspended Solids Graph for Sentinel Data
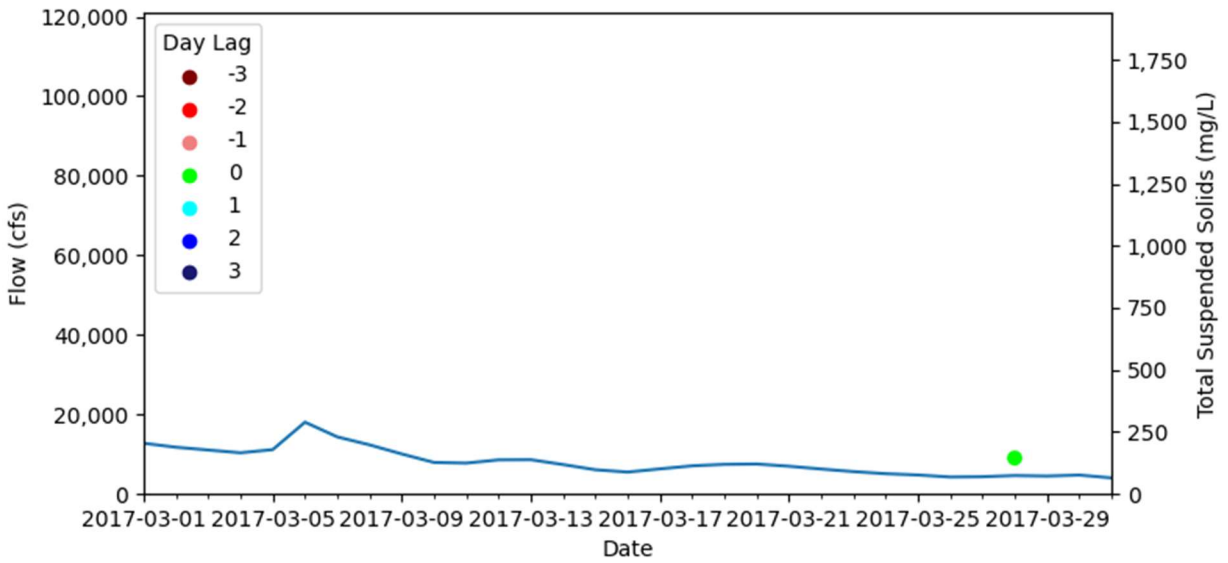


**Figure B-44**: March 2017 Flow and Total Suspended Solids Graph for Sentinel Data
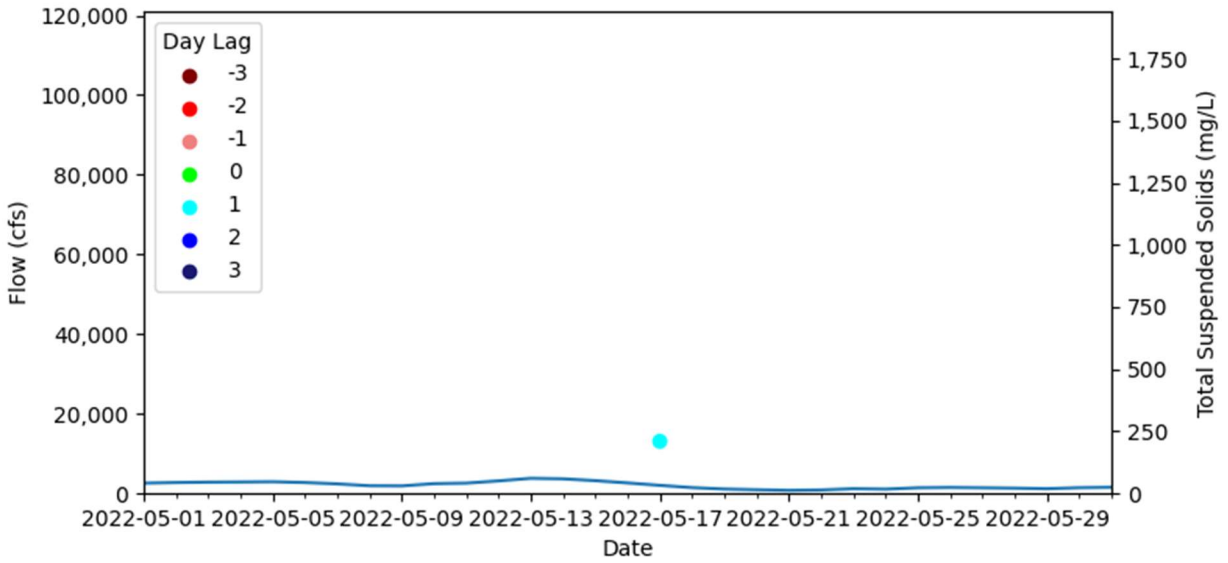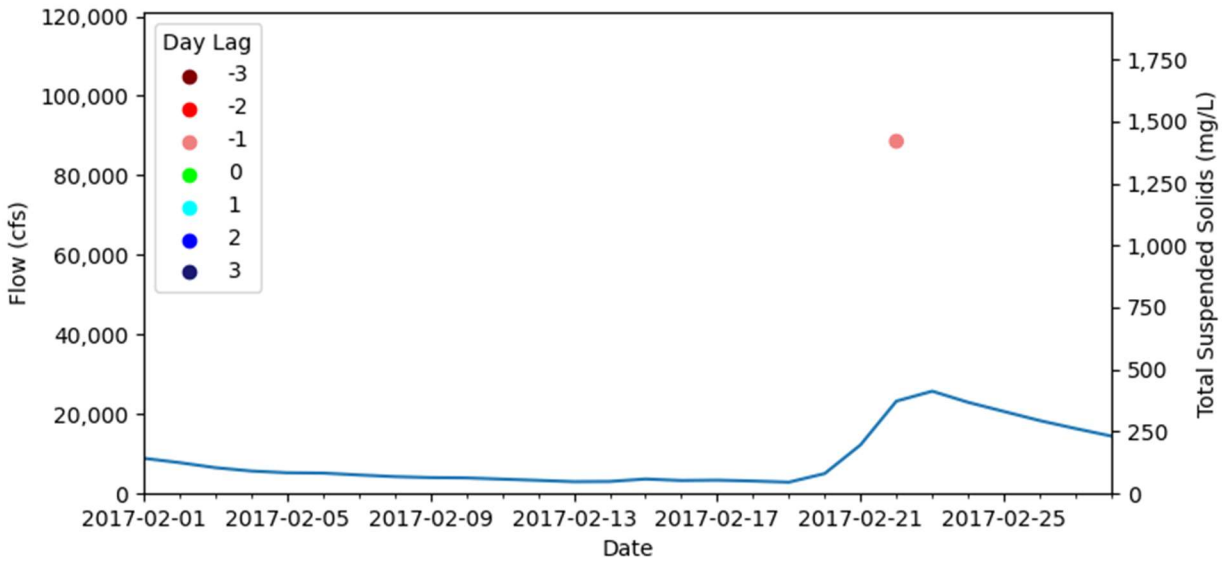
**Figure B-45**: February 2017 Flow and Total Suspended Solids Graph for Sentinel Data
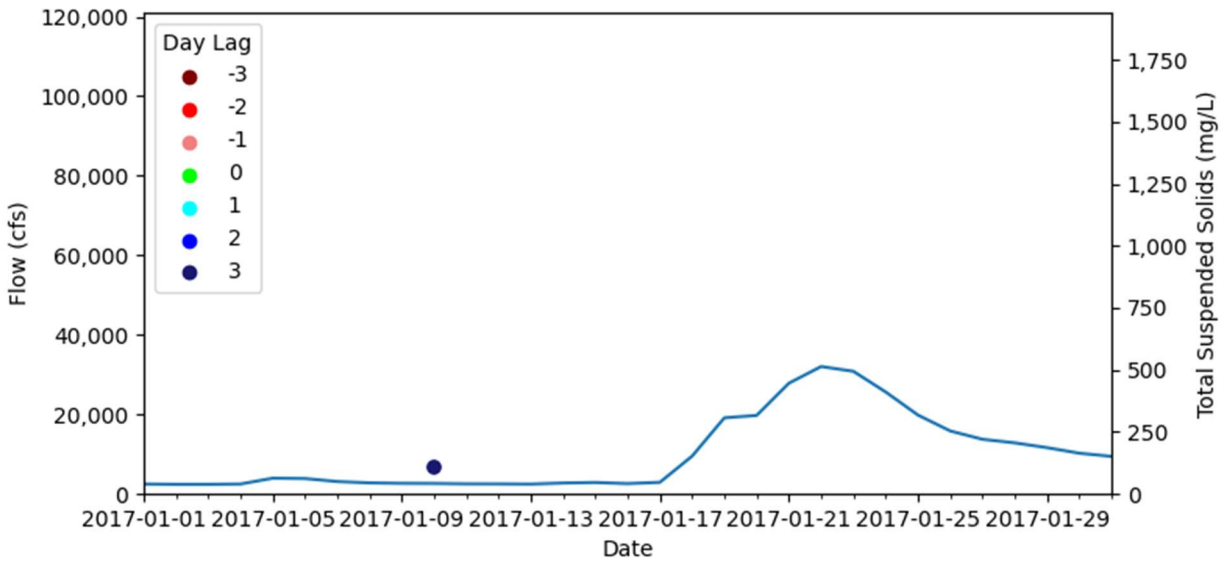


**Figure B-46**: January 2017 Flow and Total Suspended Solids Graph for Sentinel Data
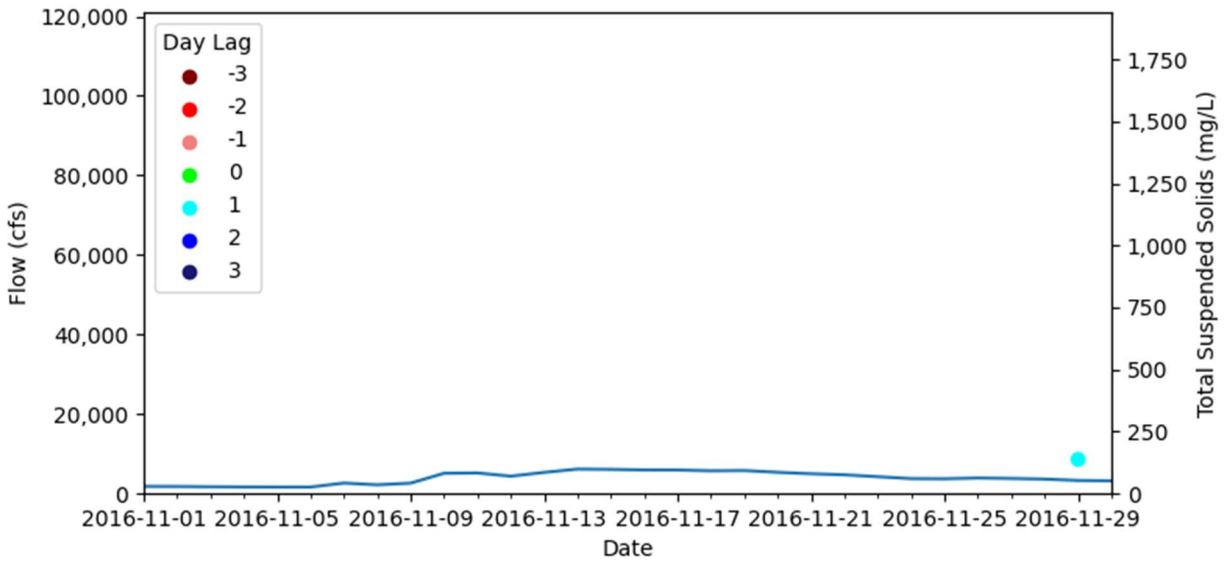
**Figure B-47**: November 2016 Flow and Total Suspended Solids Graph for Sentinel Data
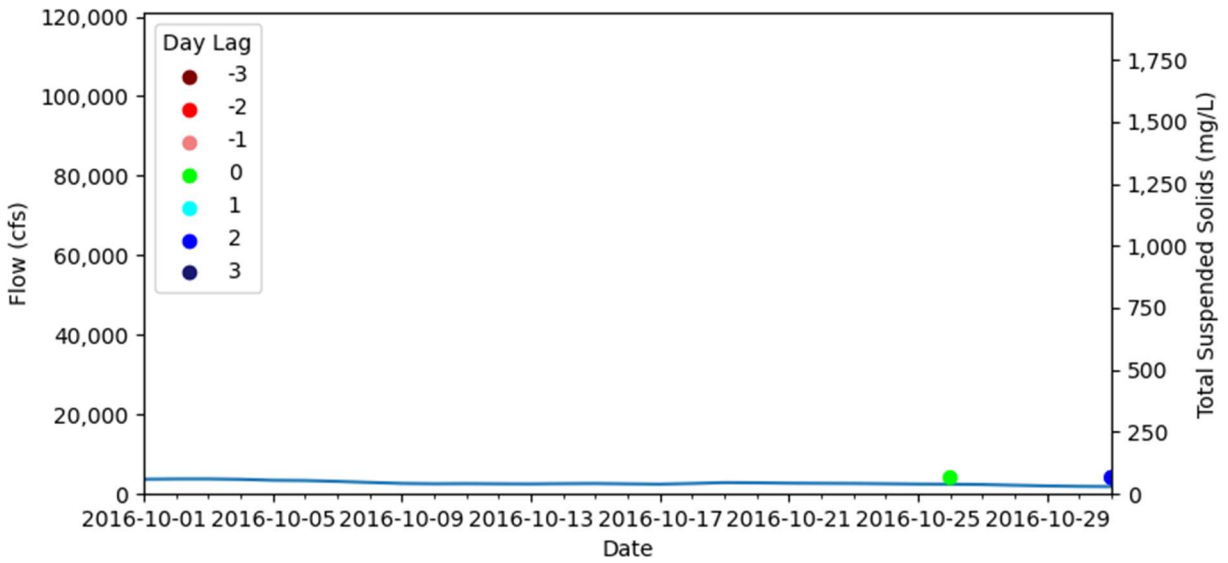


**Figure B-48**: October 2016 Flow and Total Suspended Solids Graph for Sentinel Data
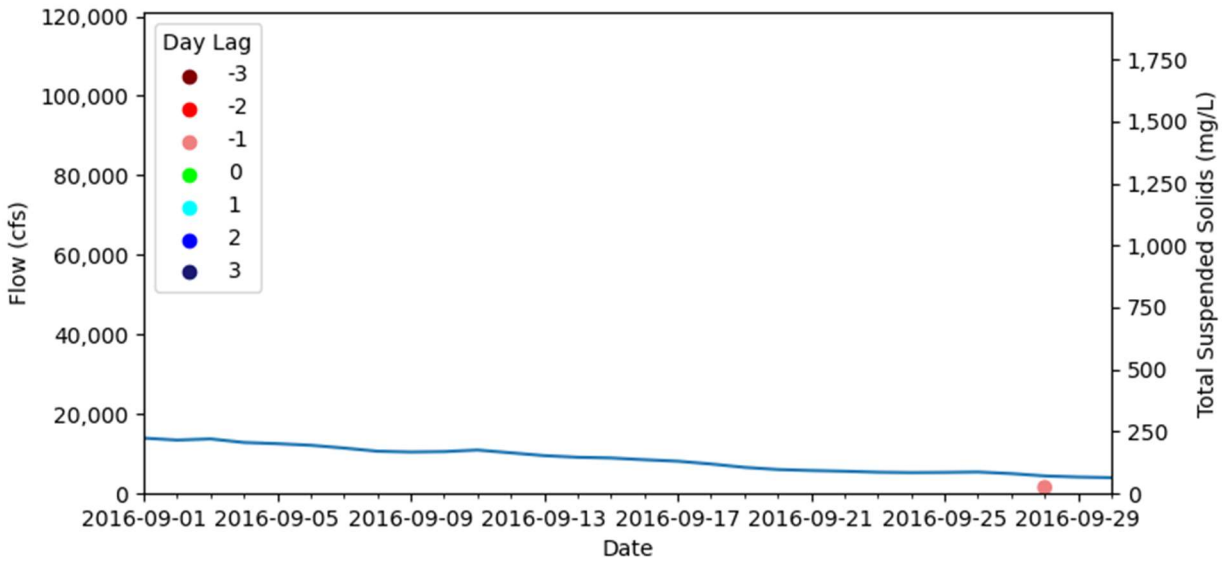
**Figure B-49**: September 2016 Flow and Total Suspended Solids Graph for Sentinel Data
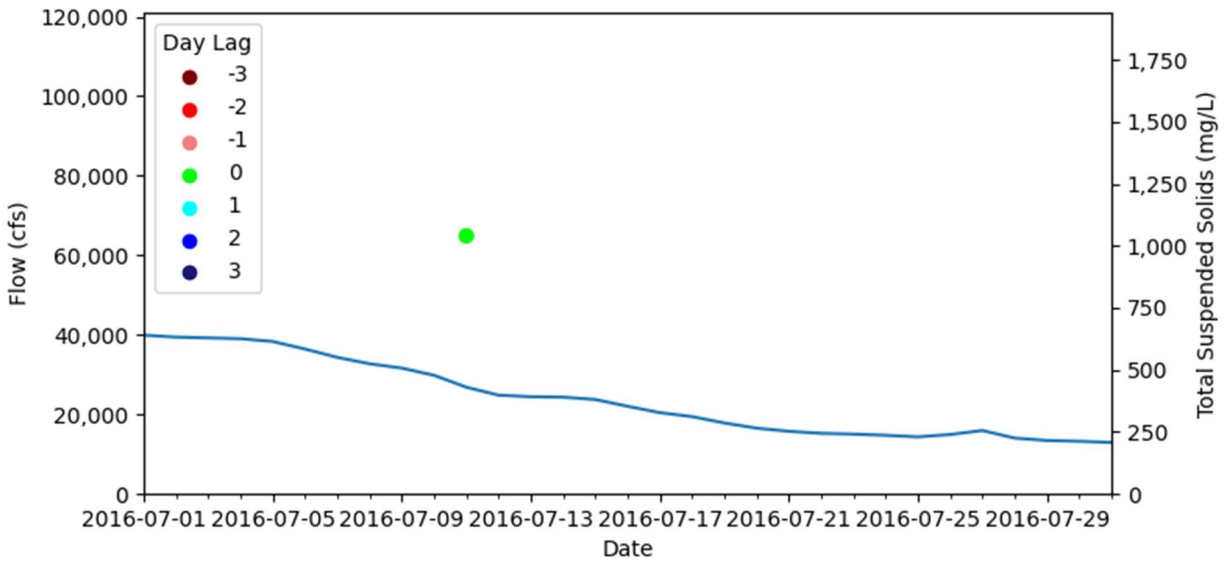


**Figure B-50**: July 2016 Flow and Total Suspended Solids Graph for Sentinel Data
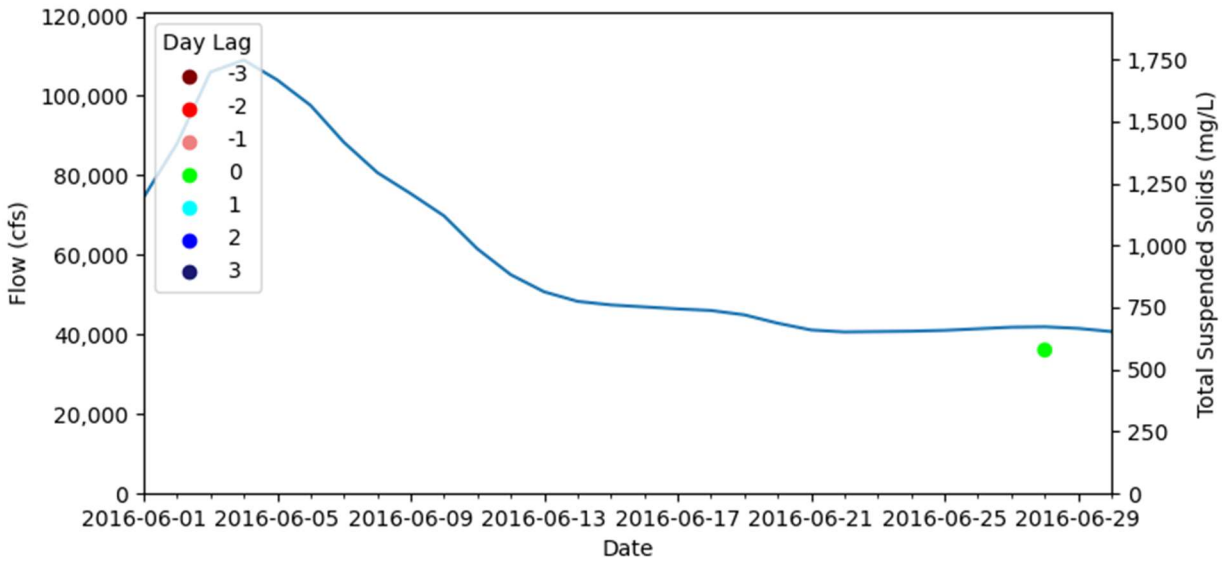
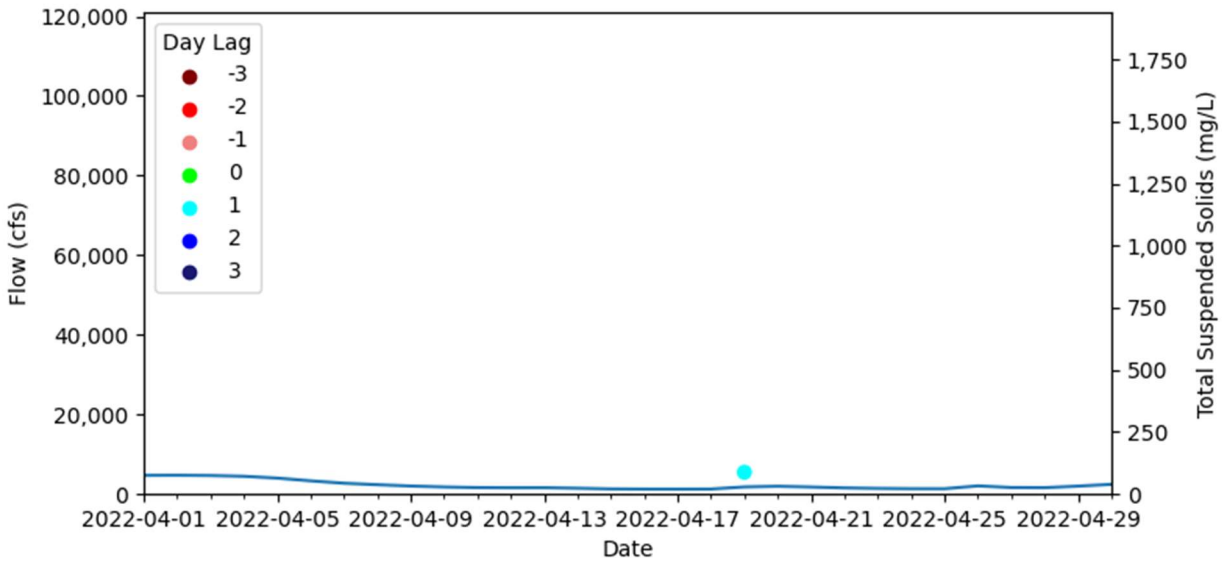**Figure B-51**: May 2016 Flow and Total Suspended Solids Graph for Sentinel Data
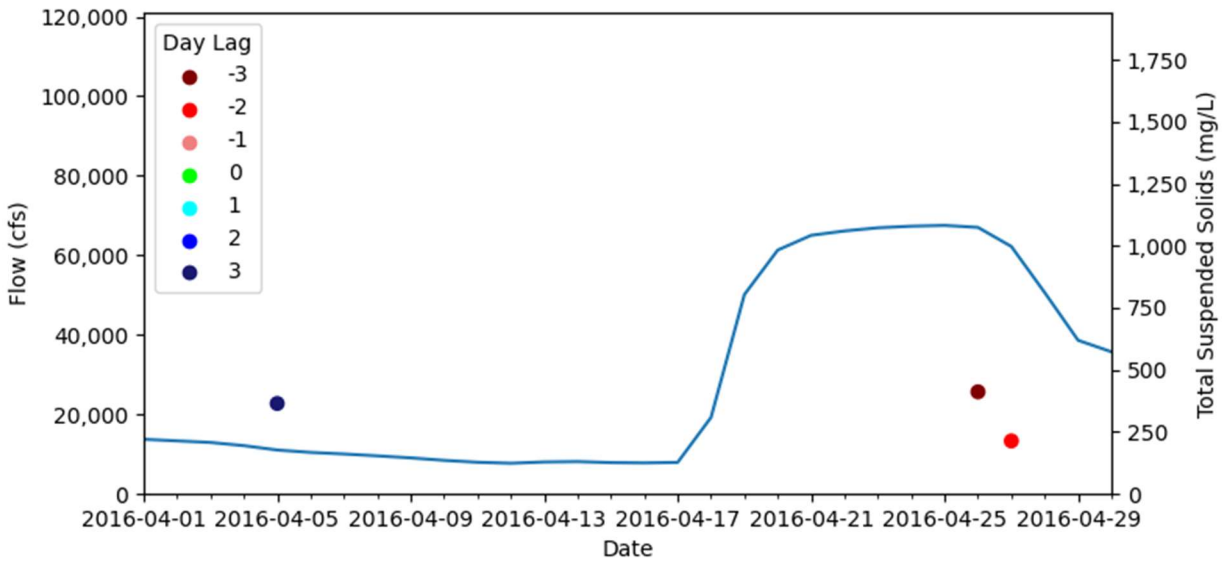


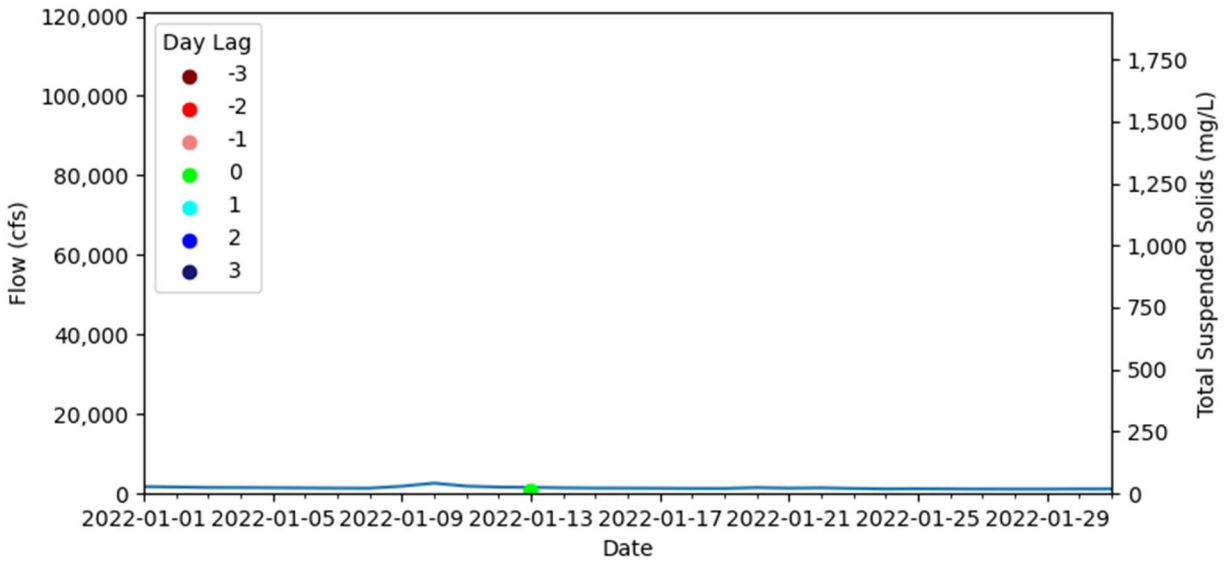**Figure B-52**: April 2016 Flow and Total Suspended Solids Graph for Sentinel Data
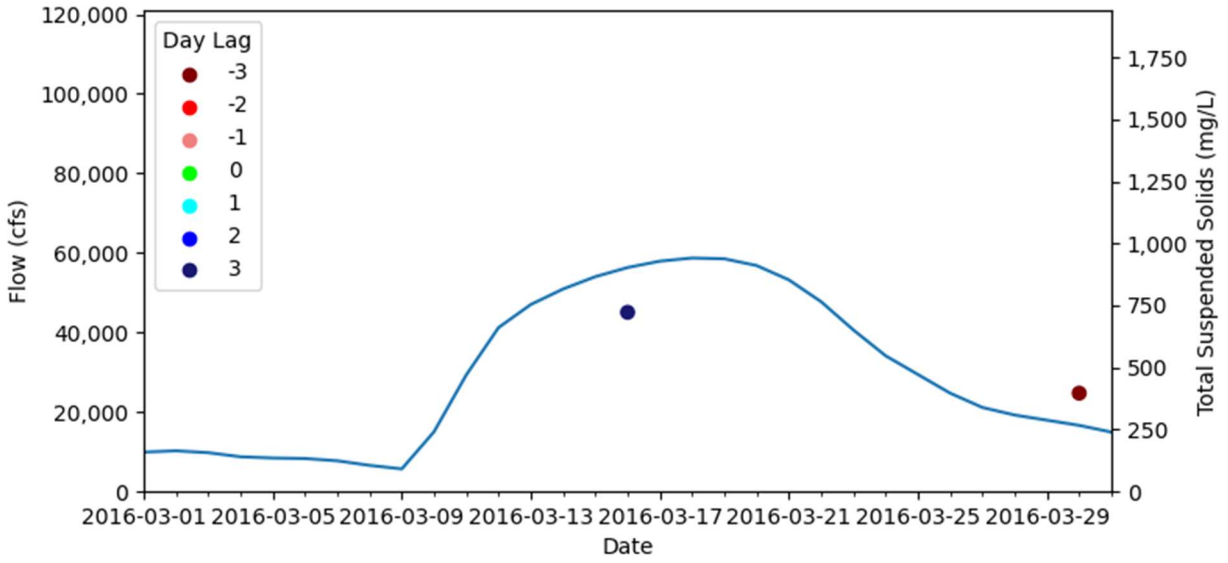
**Figure B-53**: March 2016 Flow and Total Suspended Solids Graph for Sentinel Data
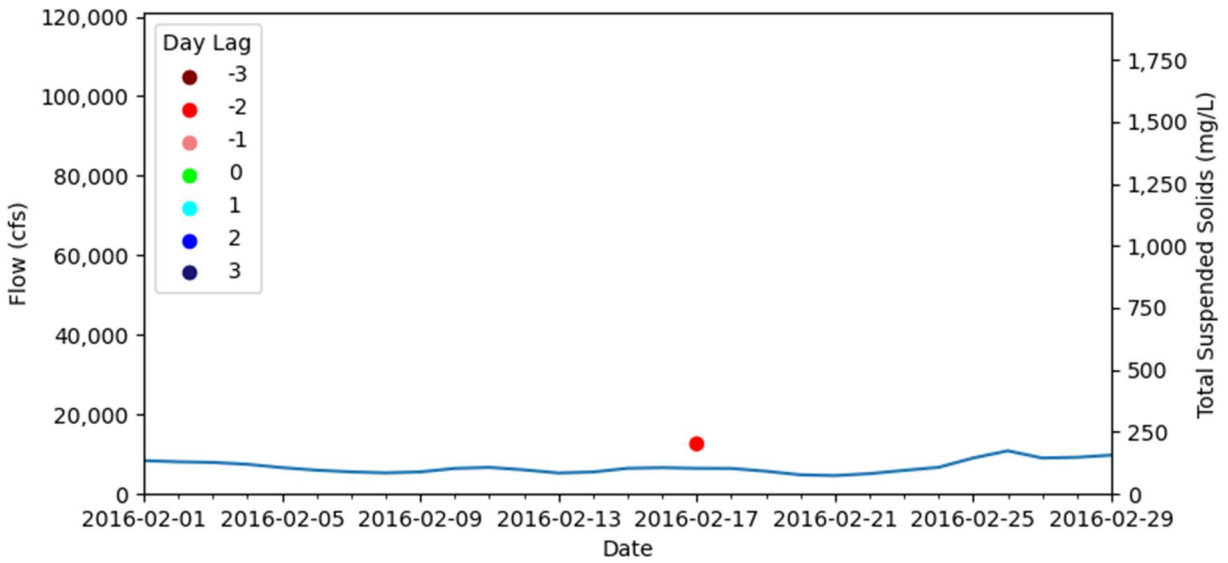


**Figure B-54**: February 2016 Flow and Total Suspended Solids Graph for Sentinel Data
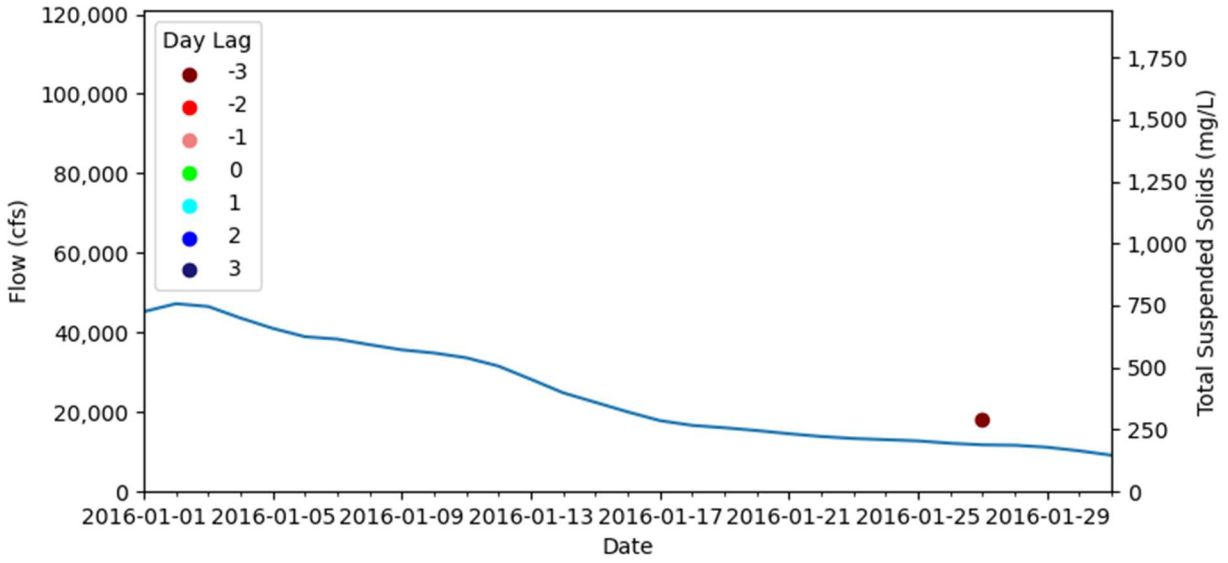
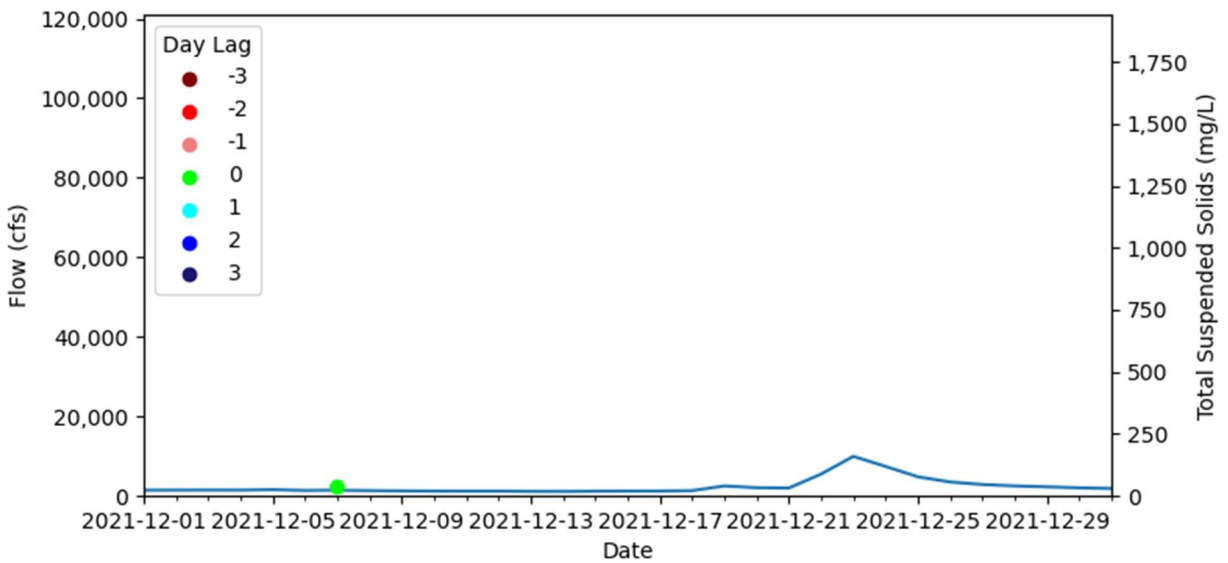**Figure B-55**: January 2016 Flow and Total Suspended Solids Graph for Sentinel Data
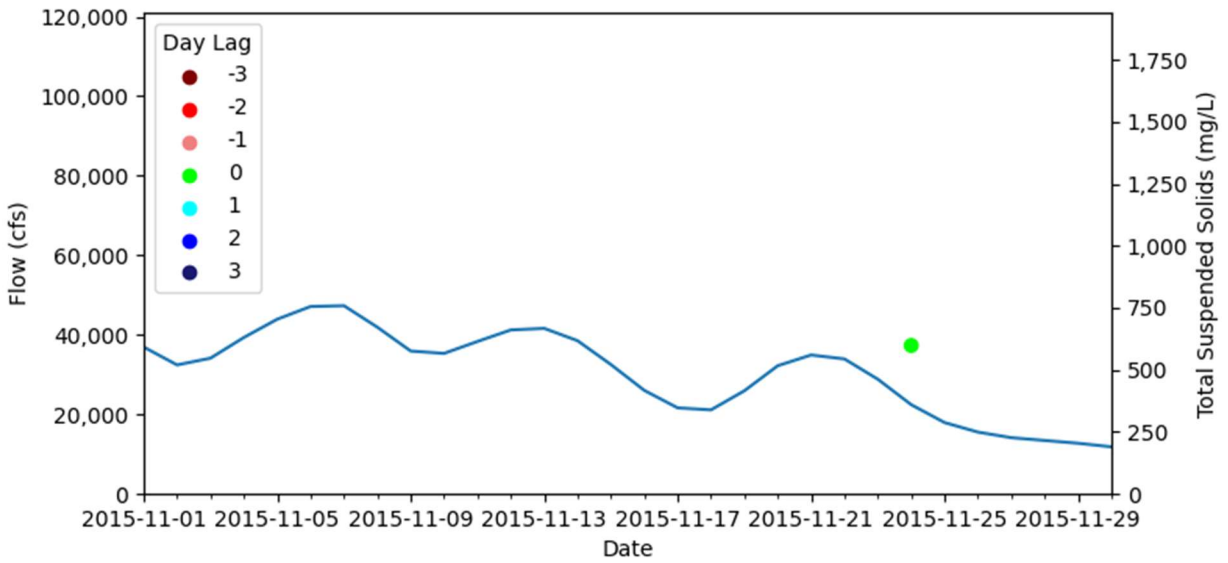


**Figure B-56**: November 2015 Flow and Total Suspended Solids Graph for Sentinel Data
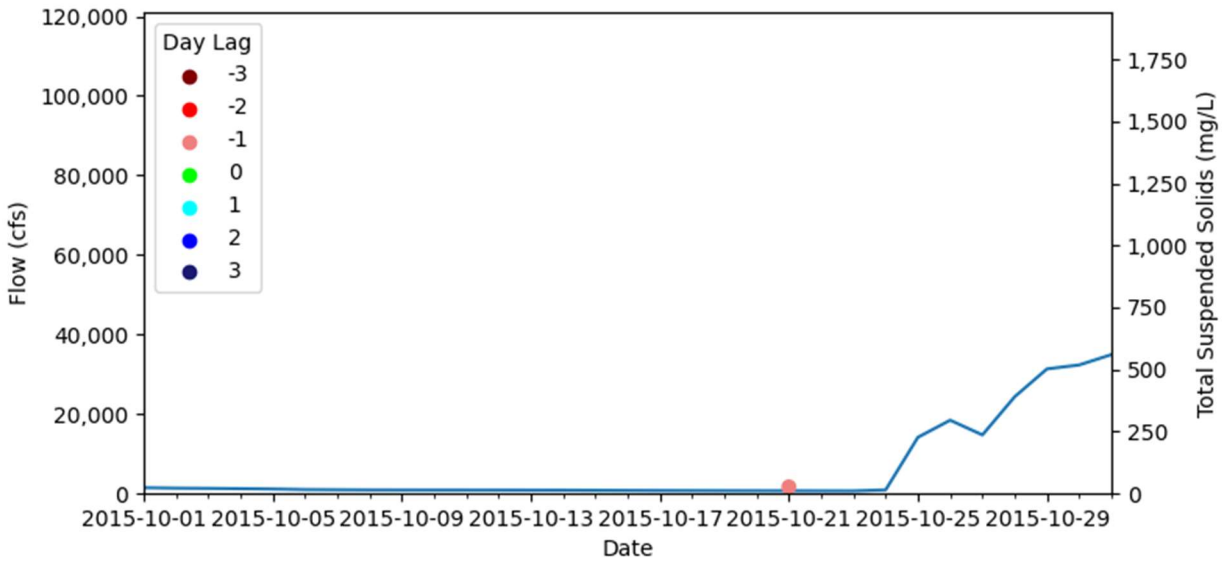
**Figure B-57**: October 2015 Flow and Total Suspended Solids Graph for Sentinel Data
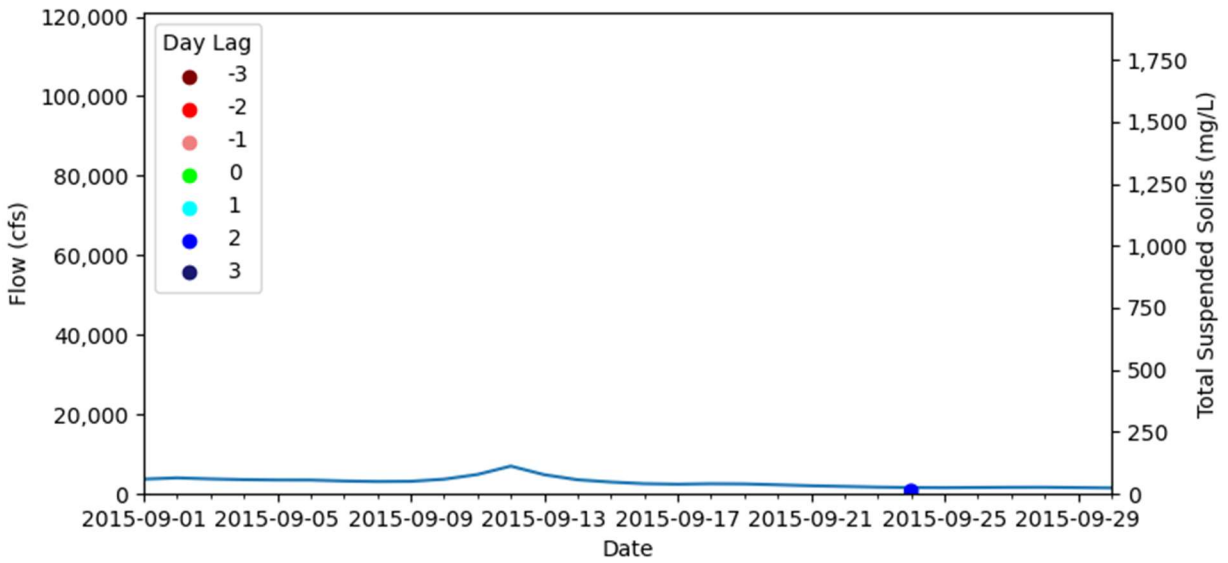


**Figure B-58**: September 2015 Flow and Total Suspended Solids Graph for Sentinel Data

# Appendix C – Model Result Comparisons

a)



b)



c)
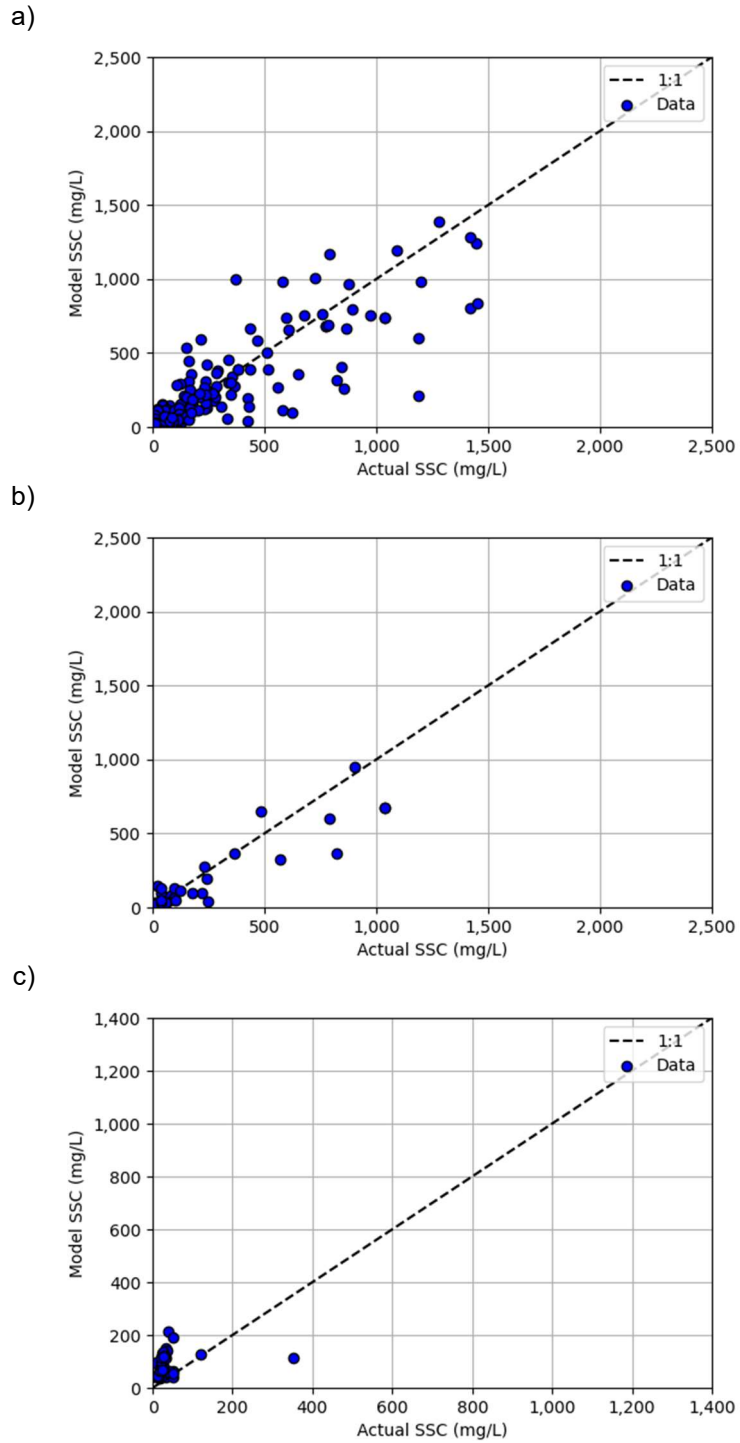


**Figure C-1:** Support Vector Machine Performance with All Six Bands for the (a) Training Data Set, (b) Test Data Set, and (c) San Bernard Data

a)
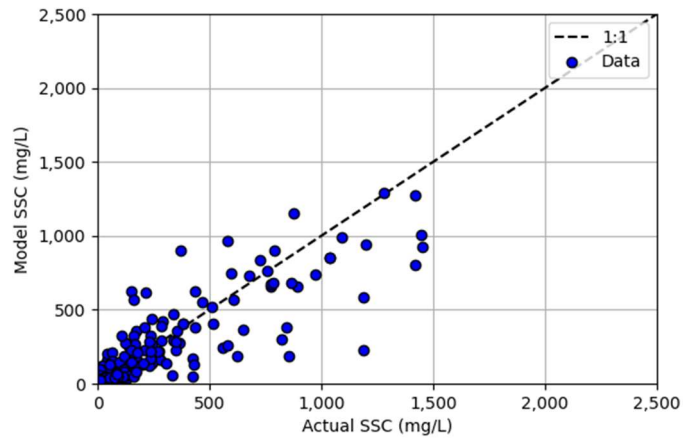
b)
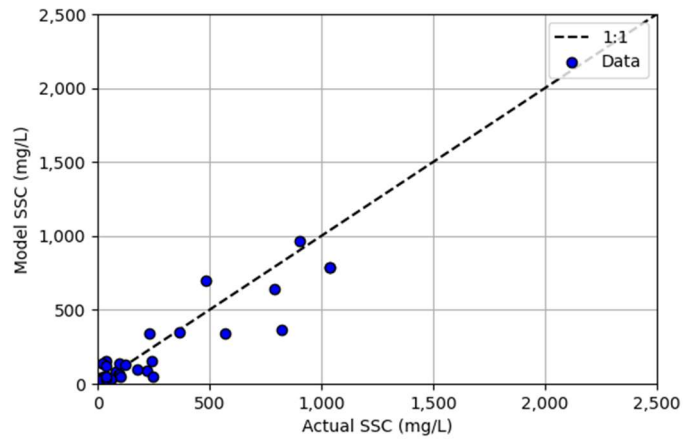
c)
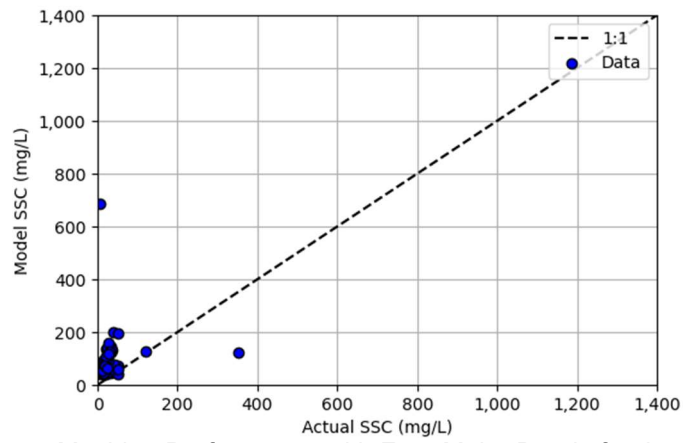
**Figure C-2:** Support Vector Machine Performance with Four Major Bands for the (a) Training Data Set, (b) Test Data Set, and (c) San Bernard Data

a)



b)



c)
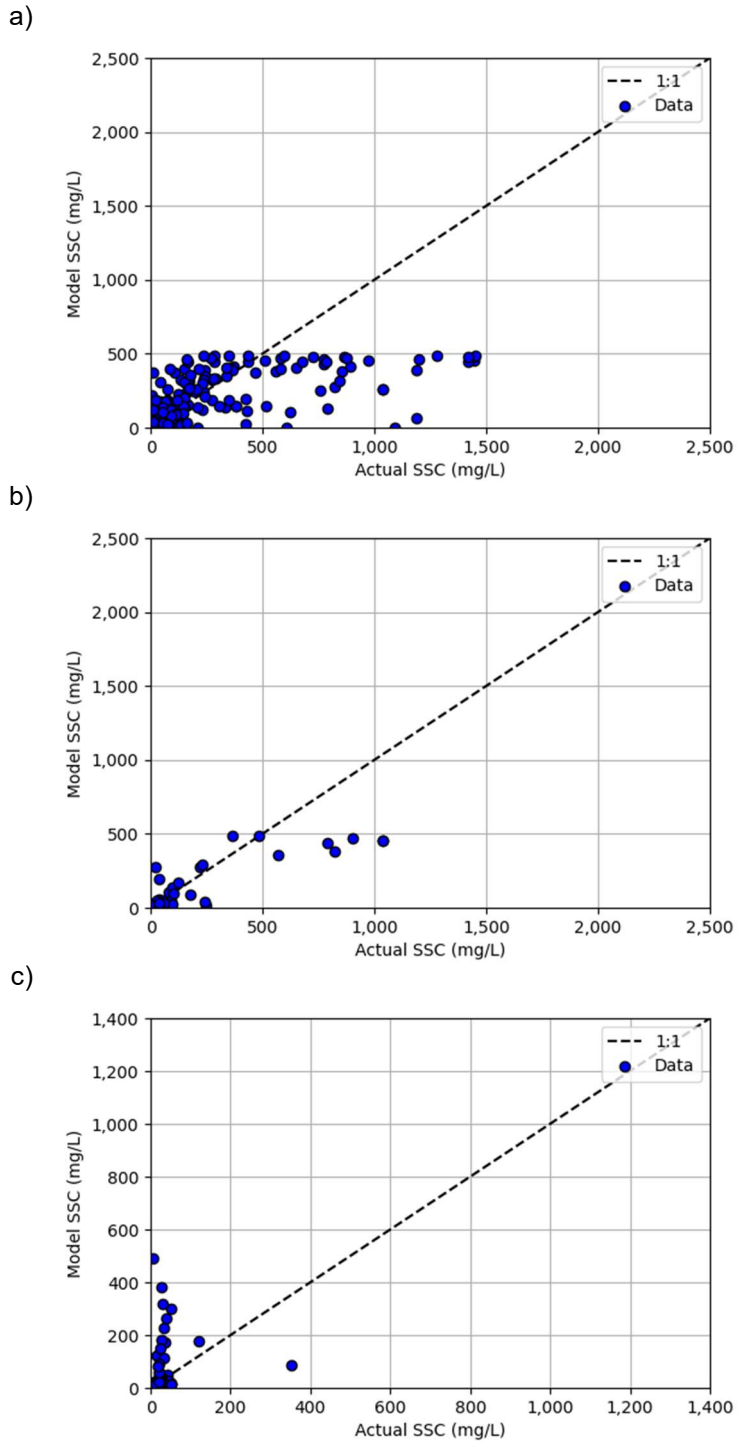


**Figure C-3:** Support Vector Machine Performance with the Red Band for the (a) Training Data Set, (b) Test Data Set, and (c) San Bernard Data
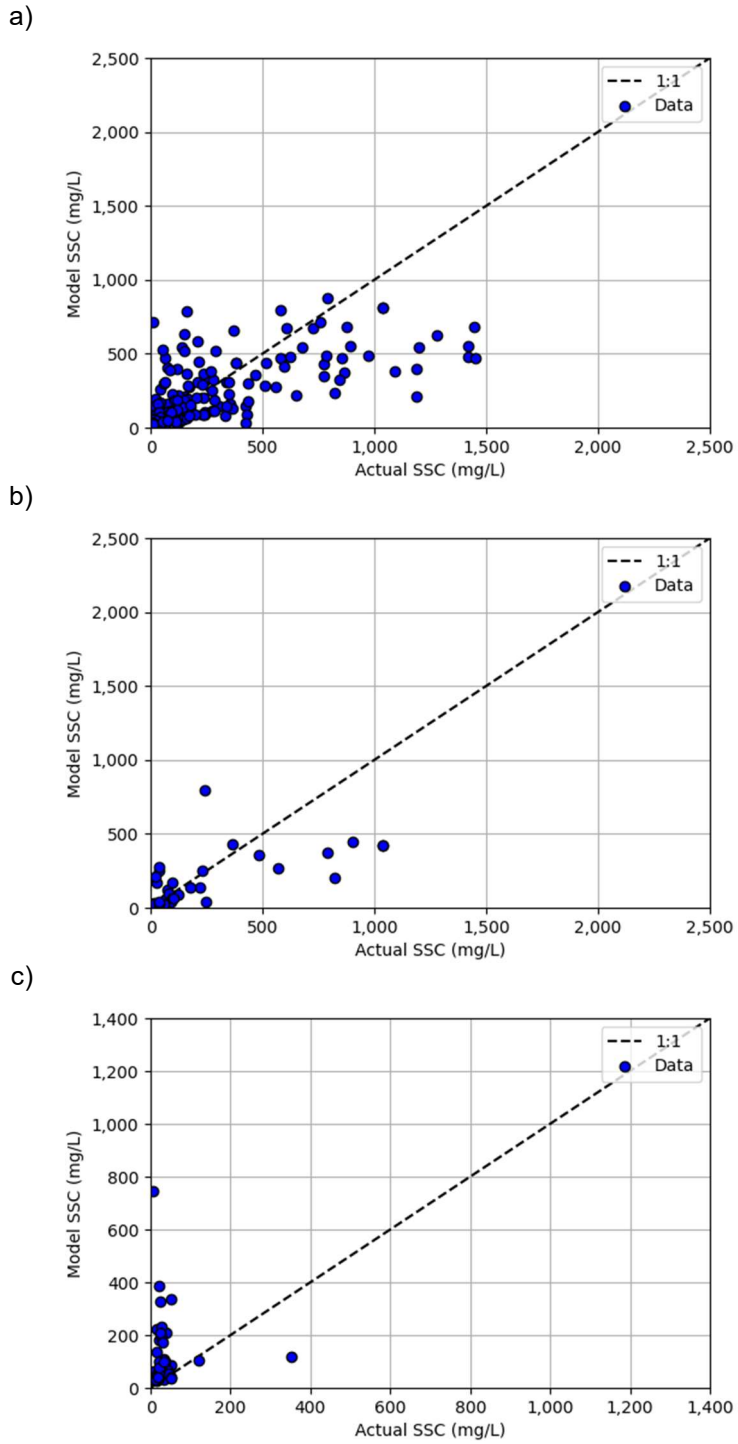
**Figure C-4:** Support Vector Machine Performance with the NIR Band for the (a) Training Data Set, (b) Test Data Set, and (c) San Bernard Data

a)



b)



c)
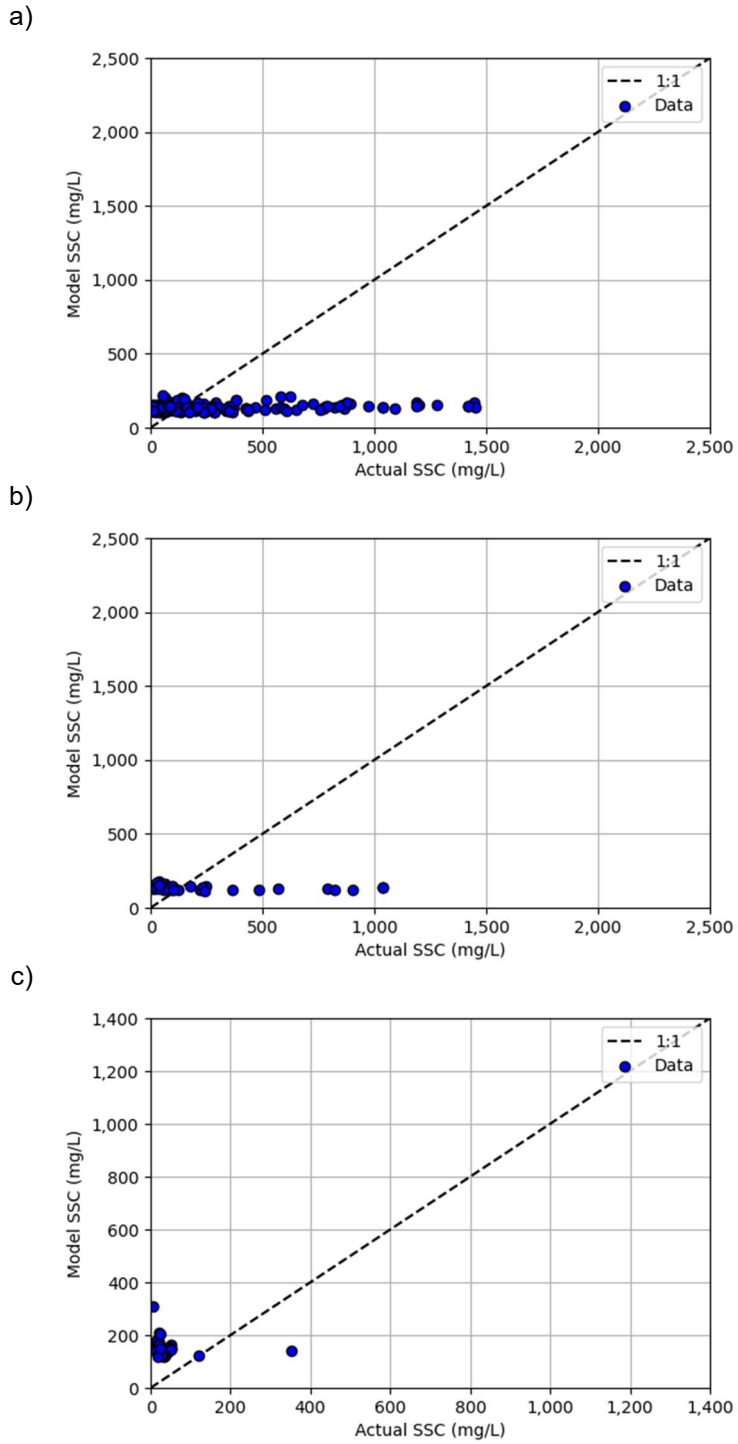


**Figure C-5:** Support Vector Machine Performance with the Red Difference for the (a) Training Data Set, (b) Test Data Set, and (c) San Bernard Data

a)



b)



c)
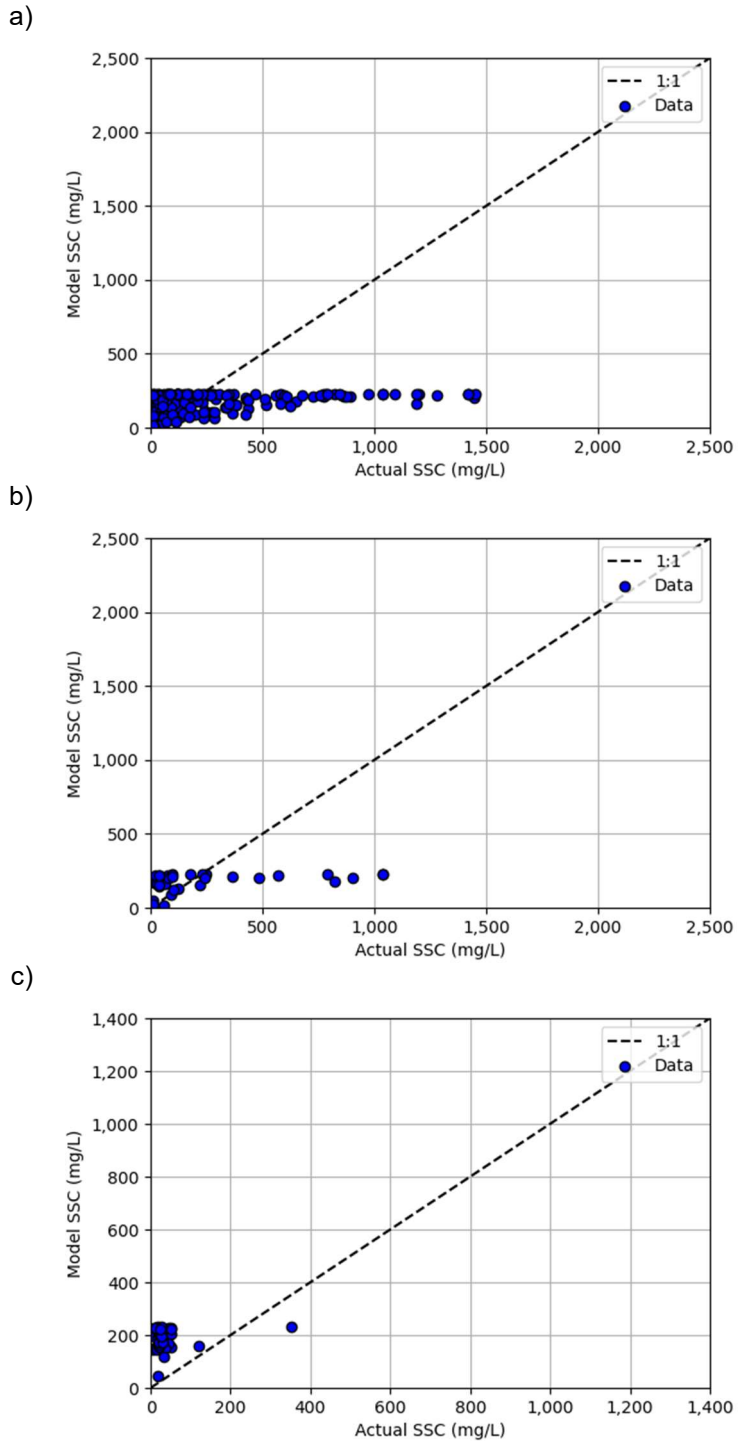


**Figure C-6:** Support Vector Machine Performance with the Sediment Index for the (a) Training Data Set, (b) Test Data Set, and (c) San Bernard Data

a)



b)



c)
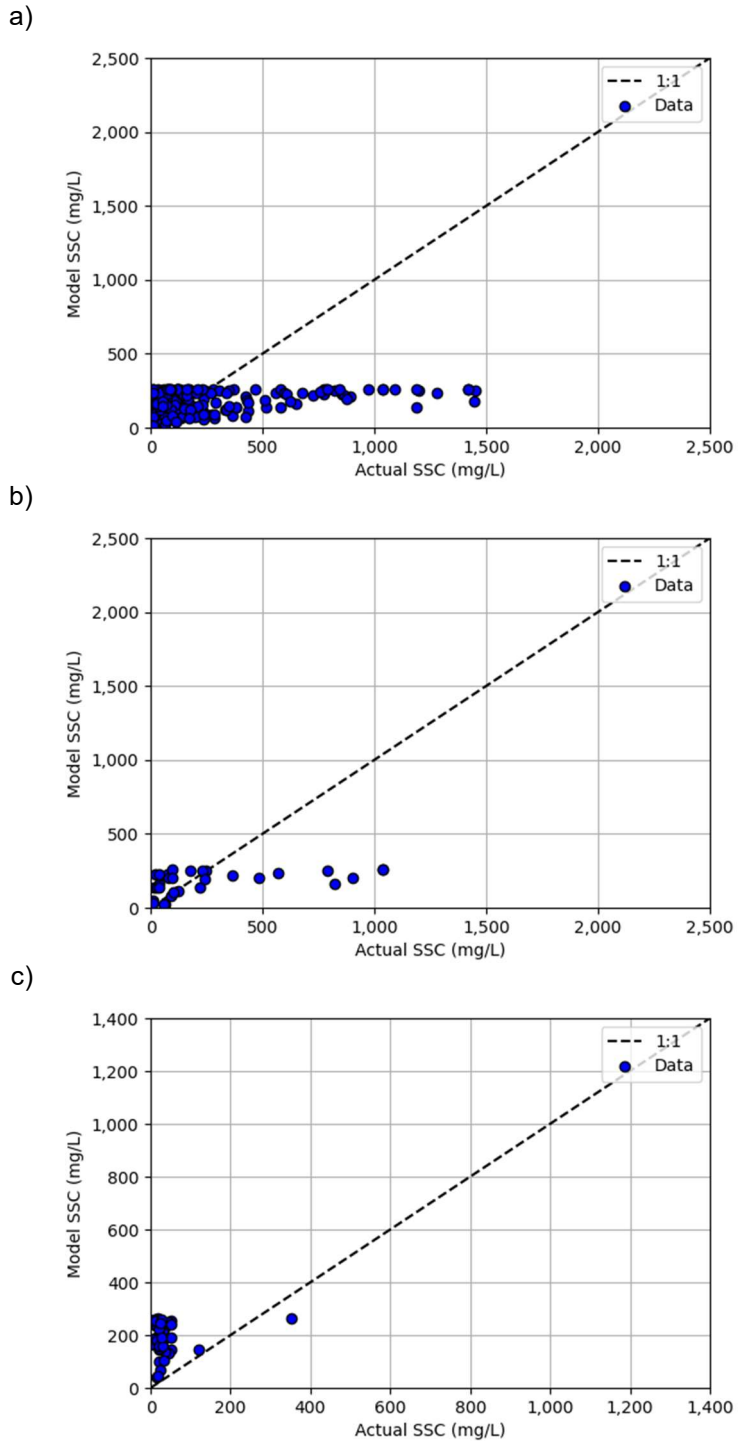


**Figure C-7:** Support Vector Machine Performance with the NIR-Red Ratio for the (a) Training Data Set, (b) Test Data Set, and (c) San Bernard Data

a)



b)



c)
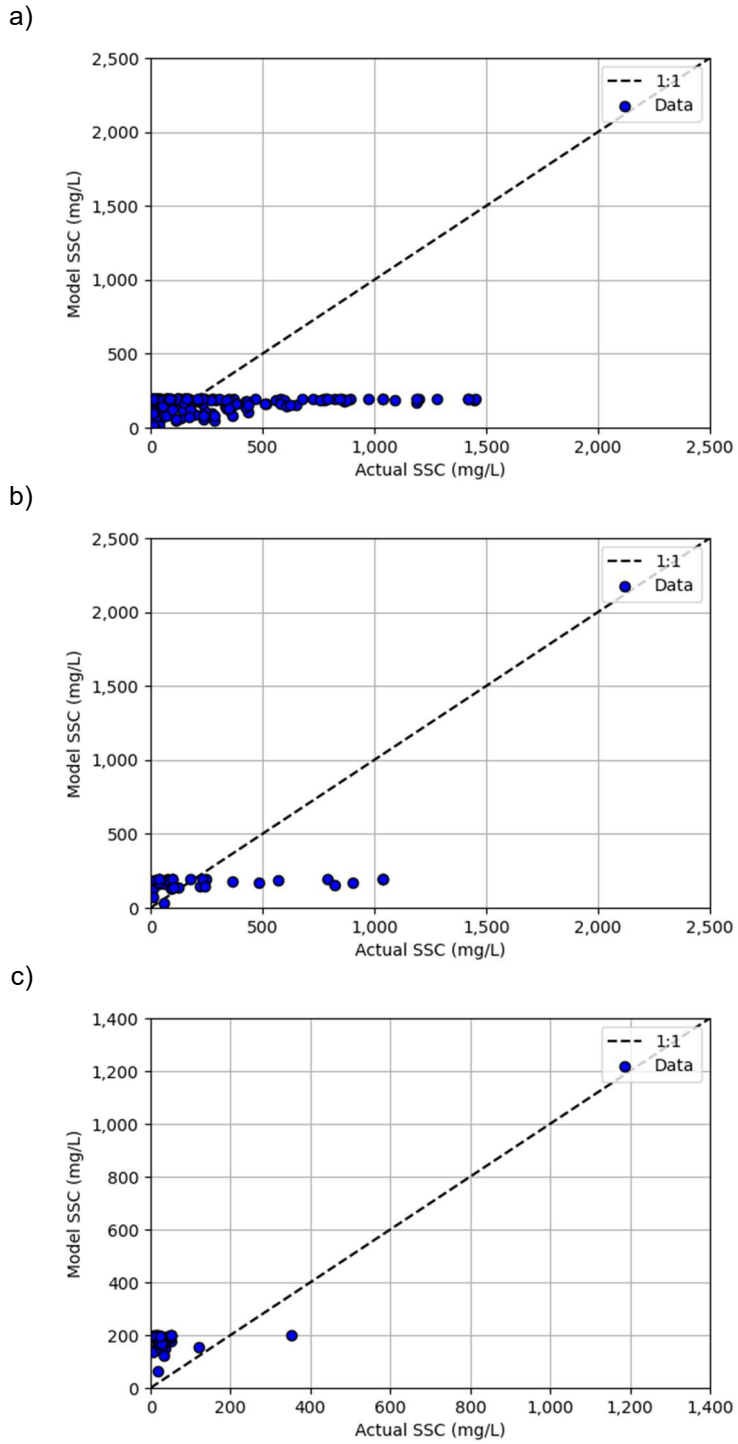


**Figure C-8:** Support Vector Machine Performance with the NIR-Red log-Ratio for the (a) Training Data Set, (b) Test Data Set, and (c) San Bernard Data

a)



b)



c)
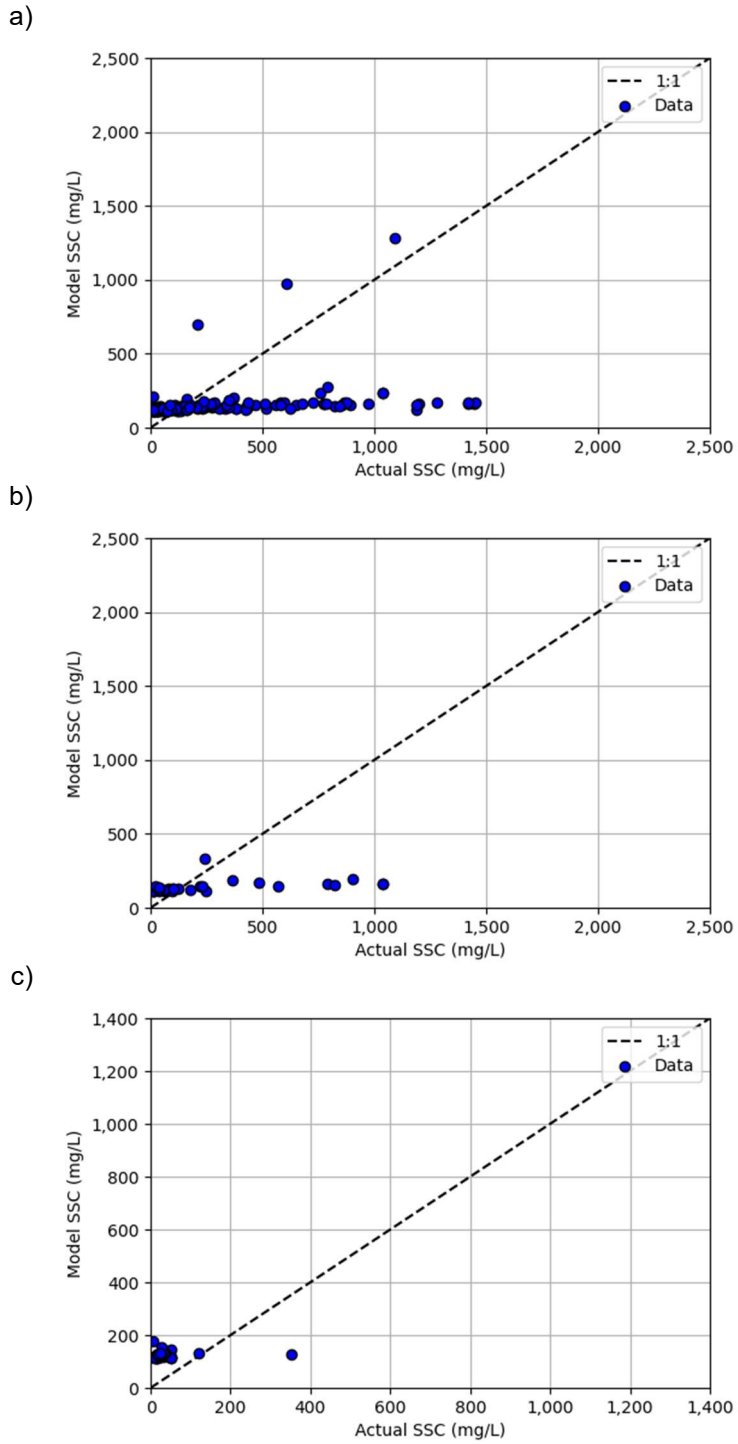


**Figure C-9:** Support Vector Machine Performance with the Red Band Squared for the (a) Training Data Set, (b) Test Data Set, and (c) San Bernard Data

a)



b)



c)
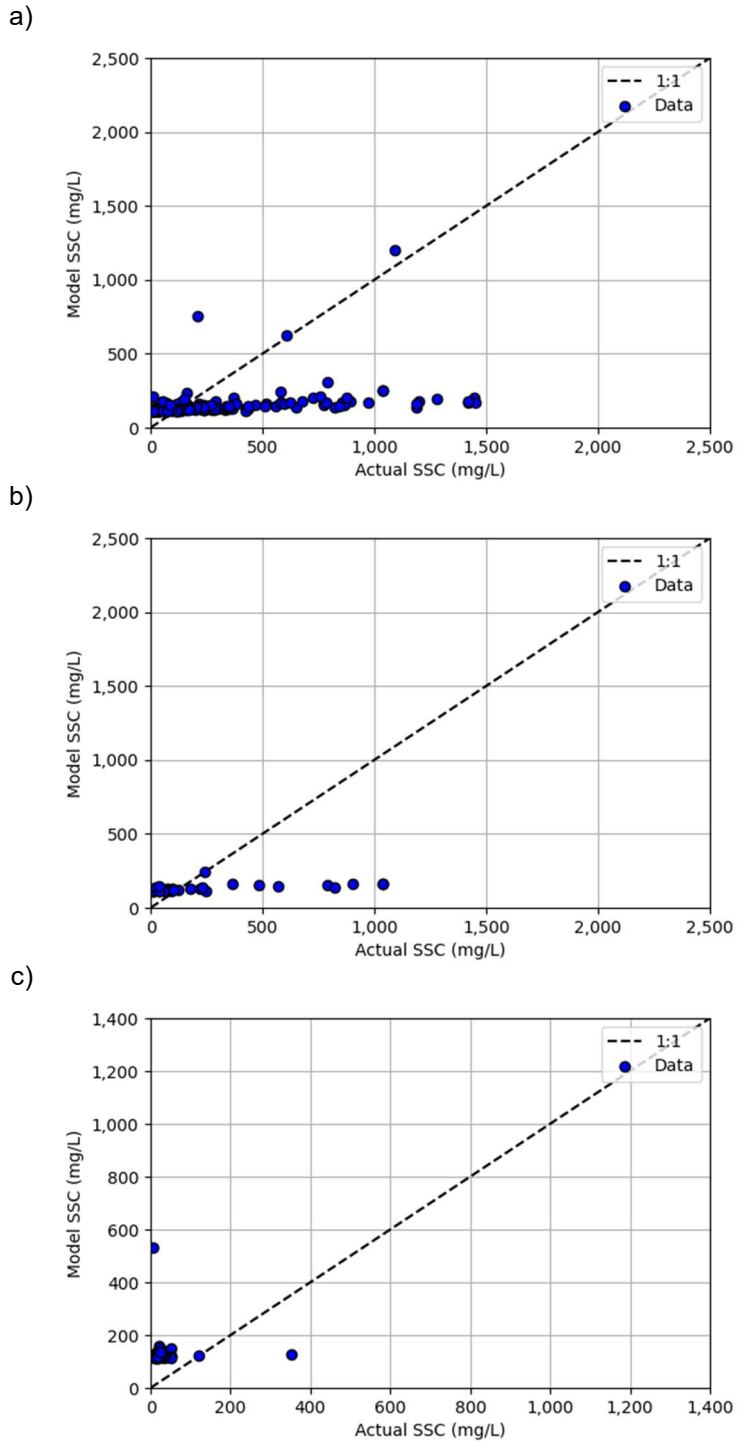


**Figure C-10:** Support Vector Machine Performance with the NIR Band Squared for the (a) Training Data Set, (b) Test Data Set, and (c) San Bernard Data

a)
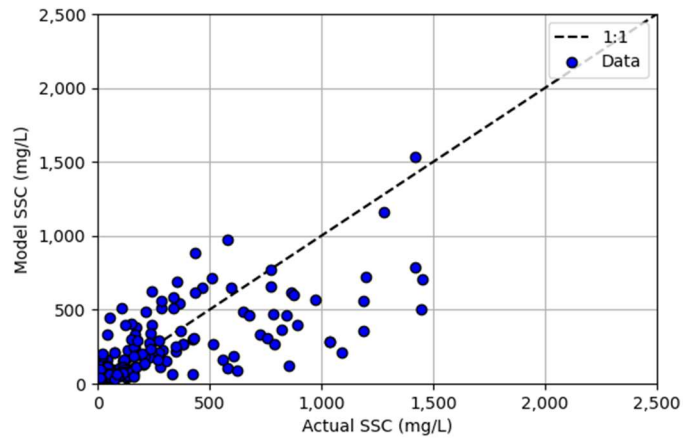


b)
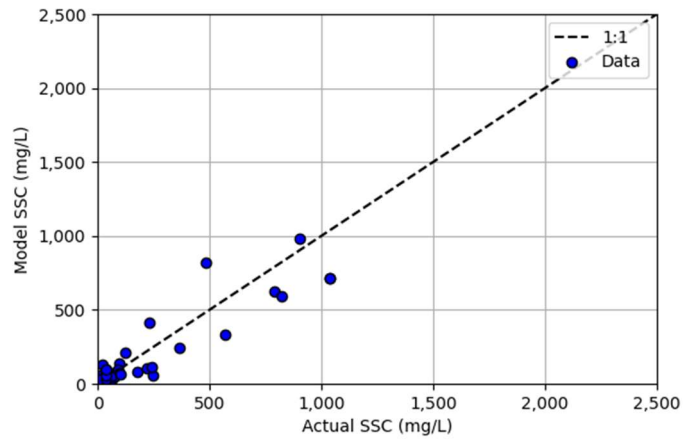


c)
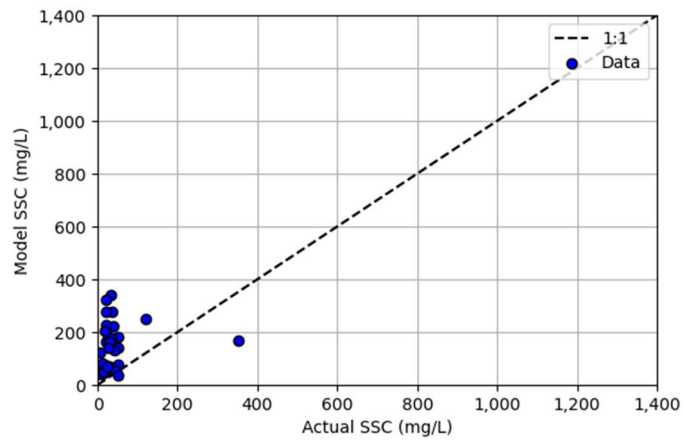


**Figure C-11:** Support Vector Machine Performance with the Red-Green Ratio for the (a) Training Data Set, (b) Test Data Set, and (c) San Bernard Data

a)



b)



c)
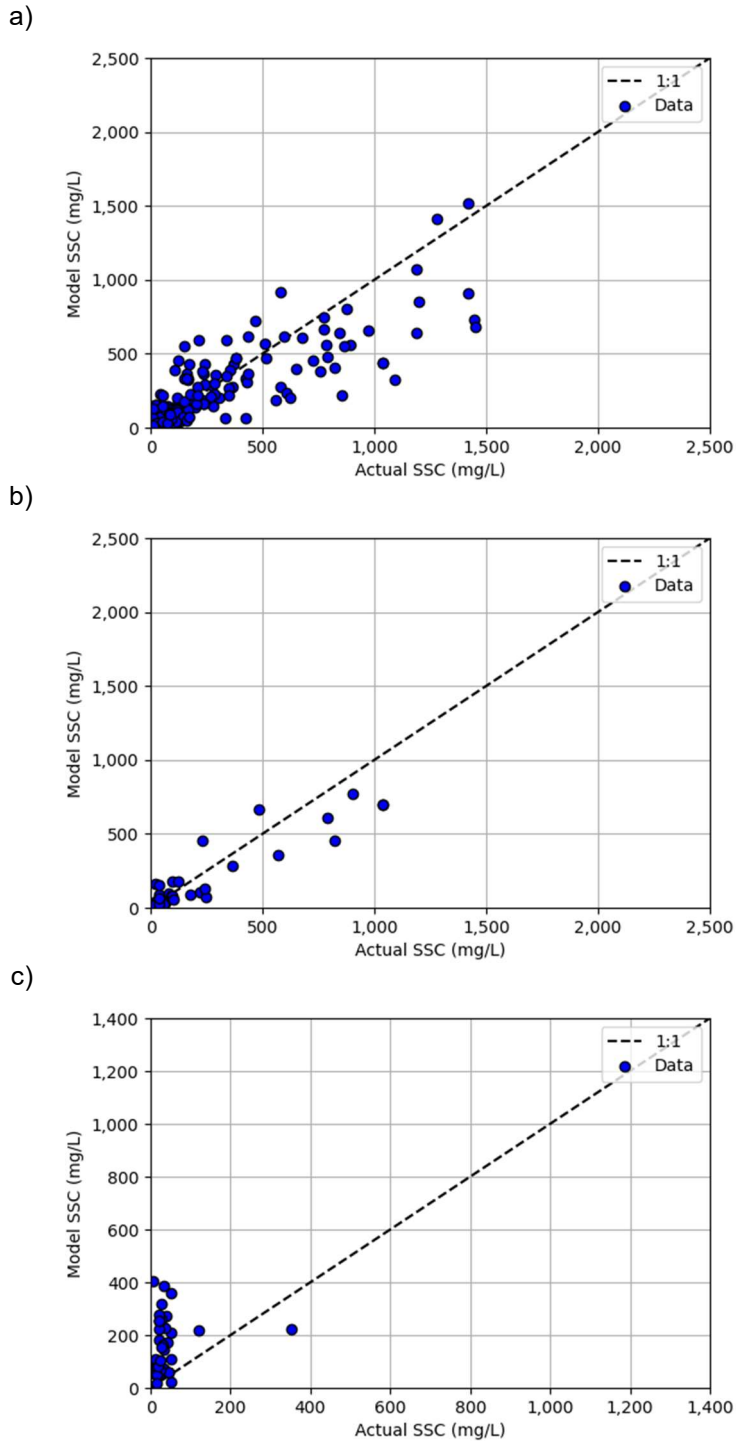


**Figure C-12:** Support Vector Machine Performance with the NIR Ratios for the (a) Training Data Set, (b) Test Data Set, and (c) San Bernard Data

a)



b)



c)
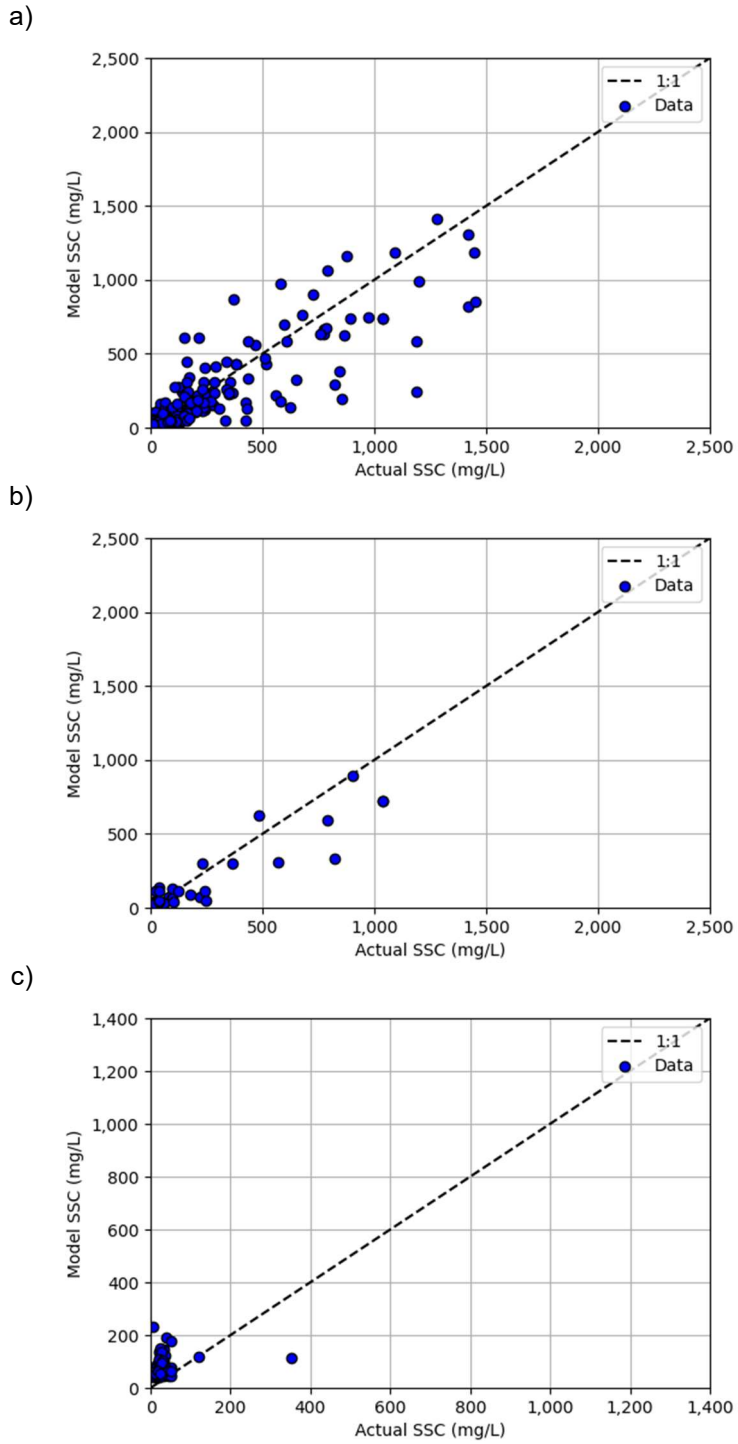


**Figure C-13:** Extreme Learning Machine Performance with All Six Bands for the (a) Training Data Set, (b) Test Data Set, and (c) San Bernard Data

a)



b)



c)
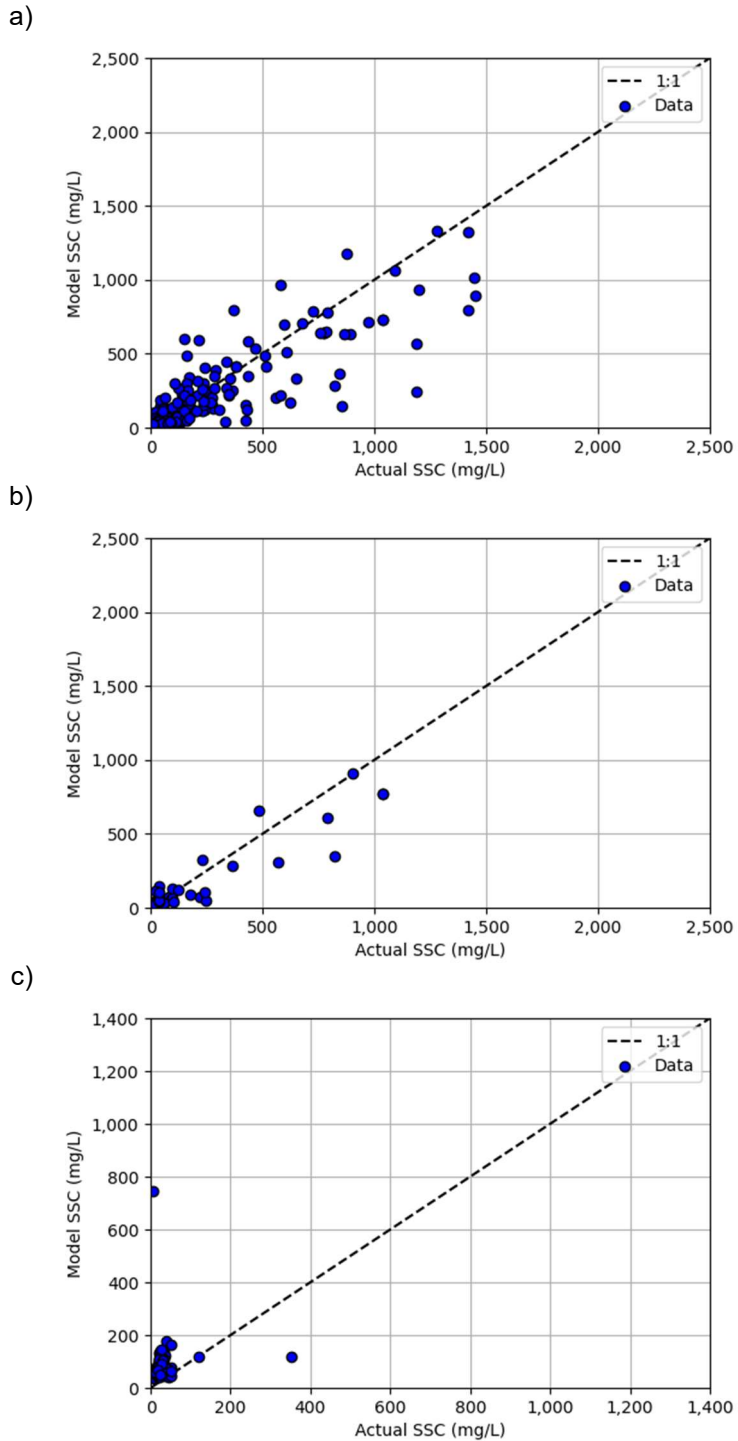


**Figure C-14:** Extreme Learning Machine Performance with Four Major Bands for the (a) Training Data Set, (b) Test Data Set, and (c) San Bernard Data

a)



b)



c)
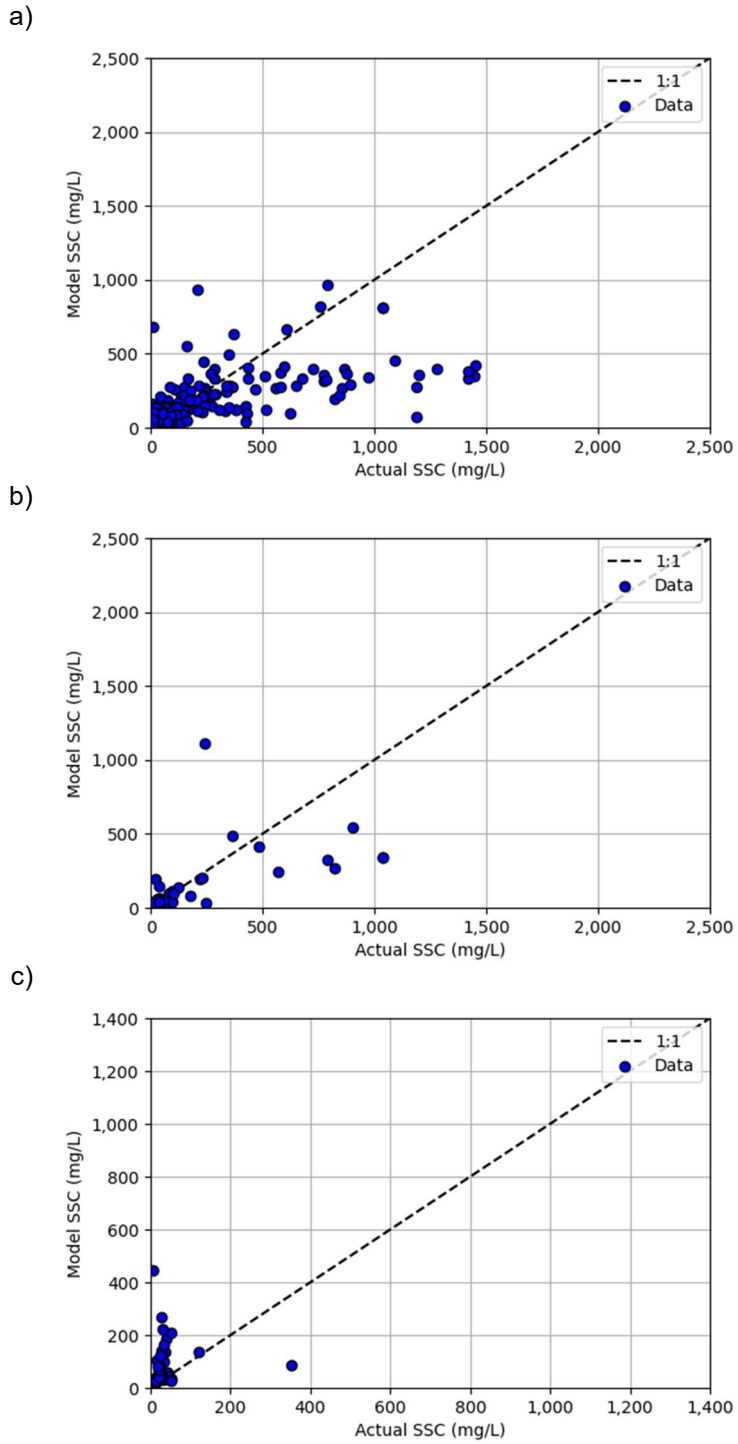


**Figure C-15:** Extreme Learning Machine Performance with the Red Band for the (a) Training Data Set, (b) Test Data Set, and (c) San Bernard Data

a)



b)

c)
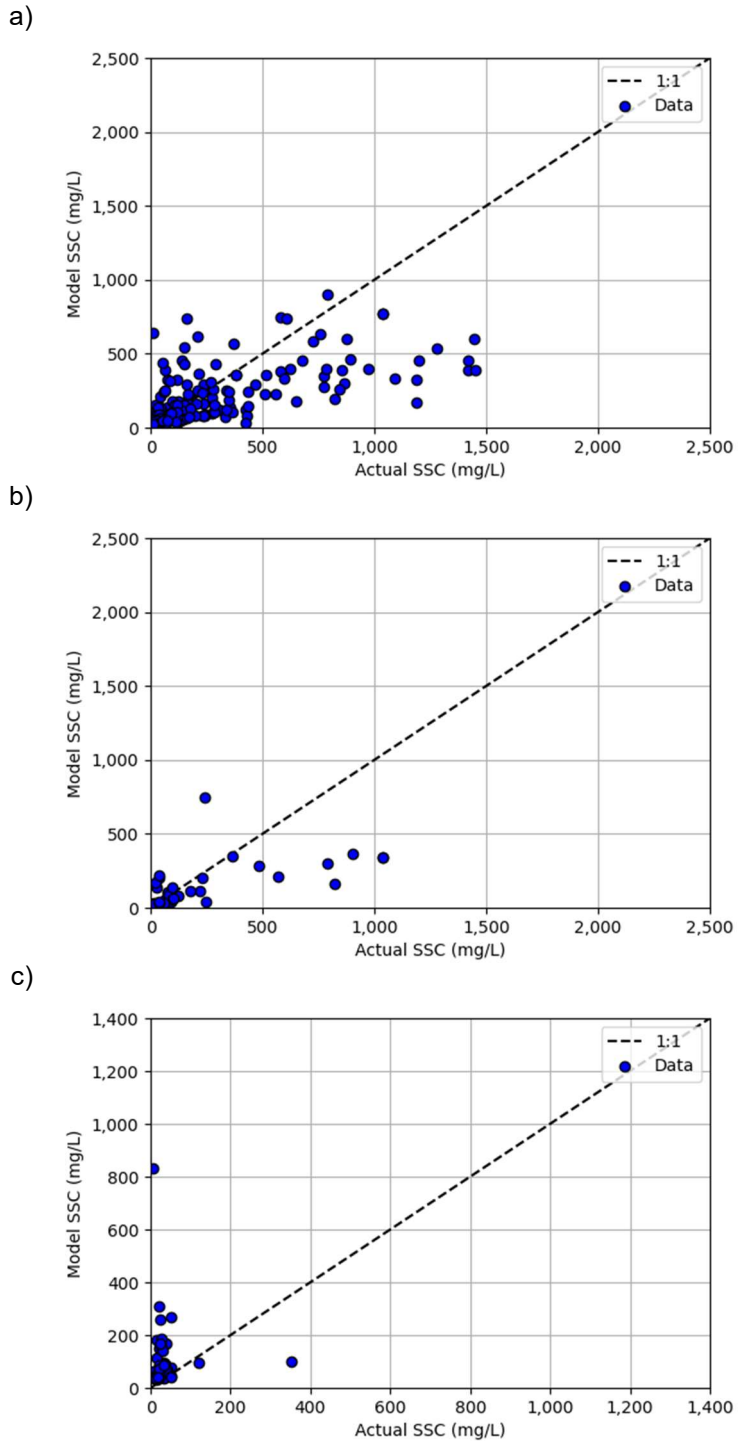
**Figure C-16:** Extreme Learning Machine Performance with the NIR Band for the (a) Training Data Set, (b) Test Data Set, and (c) San Bernard Data

a)



b)



c)
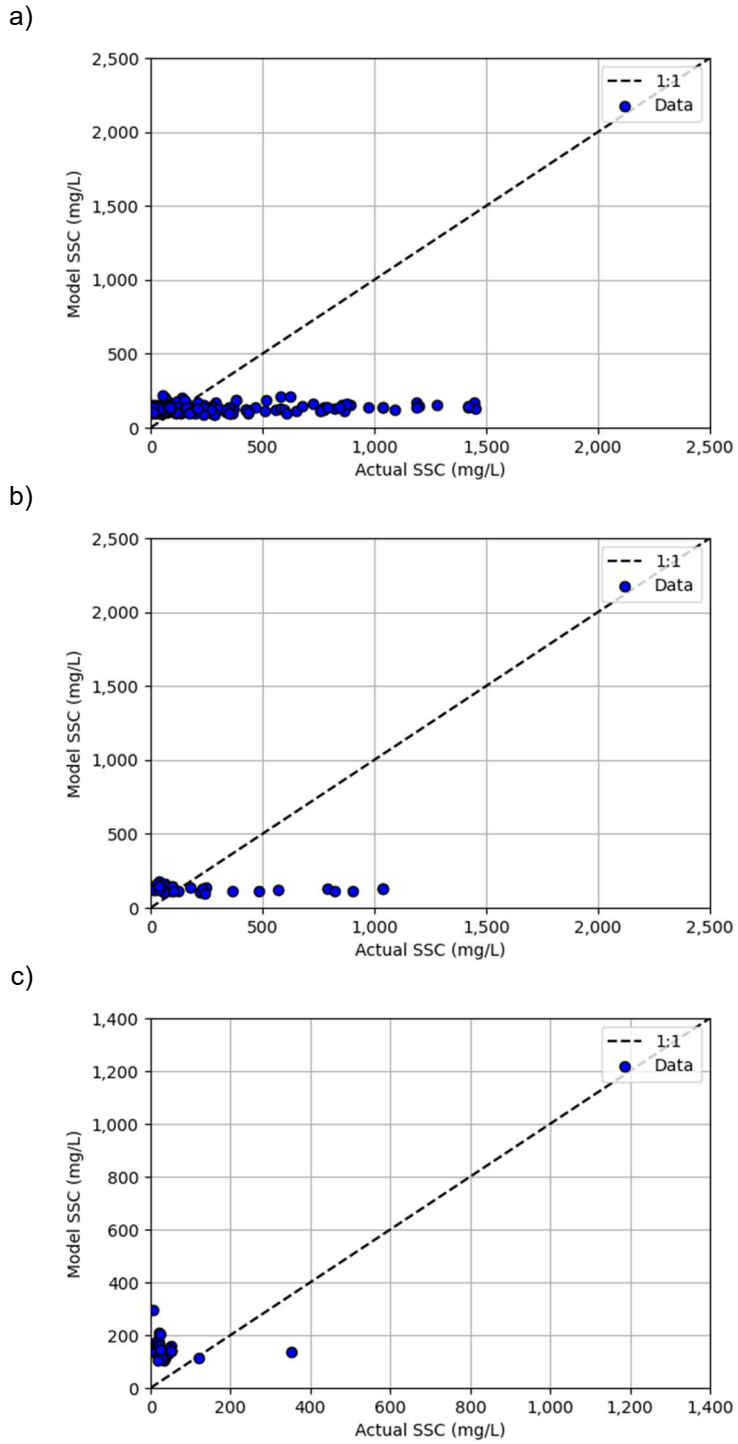


**Figure C-17:** Extreme Learning Machine Performance with the Red Difference for the (a) Training Data Set, (b) Test Data Set, and (c) San Bernard Data

a)



b)



c)
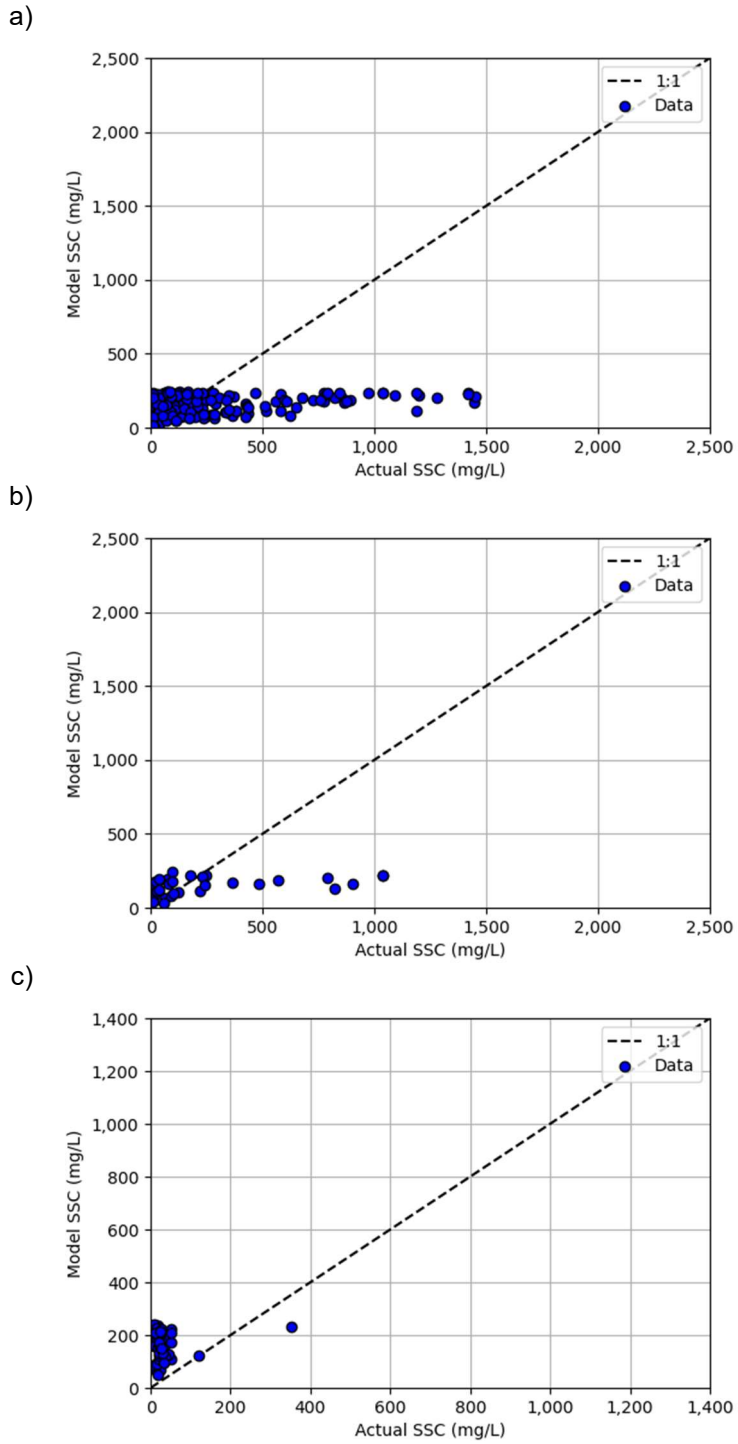


**Figure C-18:** Extreme Learning Machine Performance with the Sediment Index for the (a) Training Data Set, (b) Test Data Set, and (c) San Bernard Data

a)



b)



c)
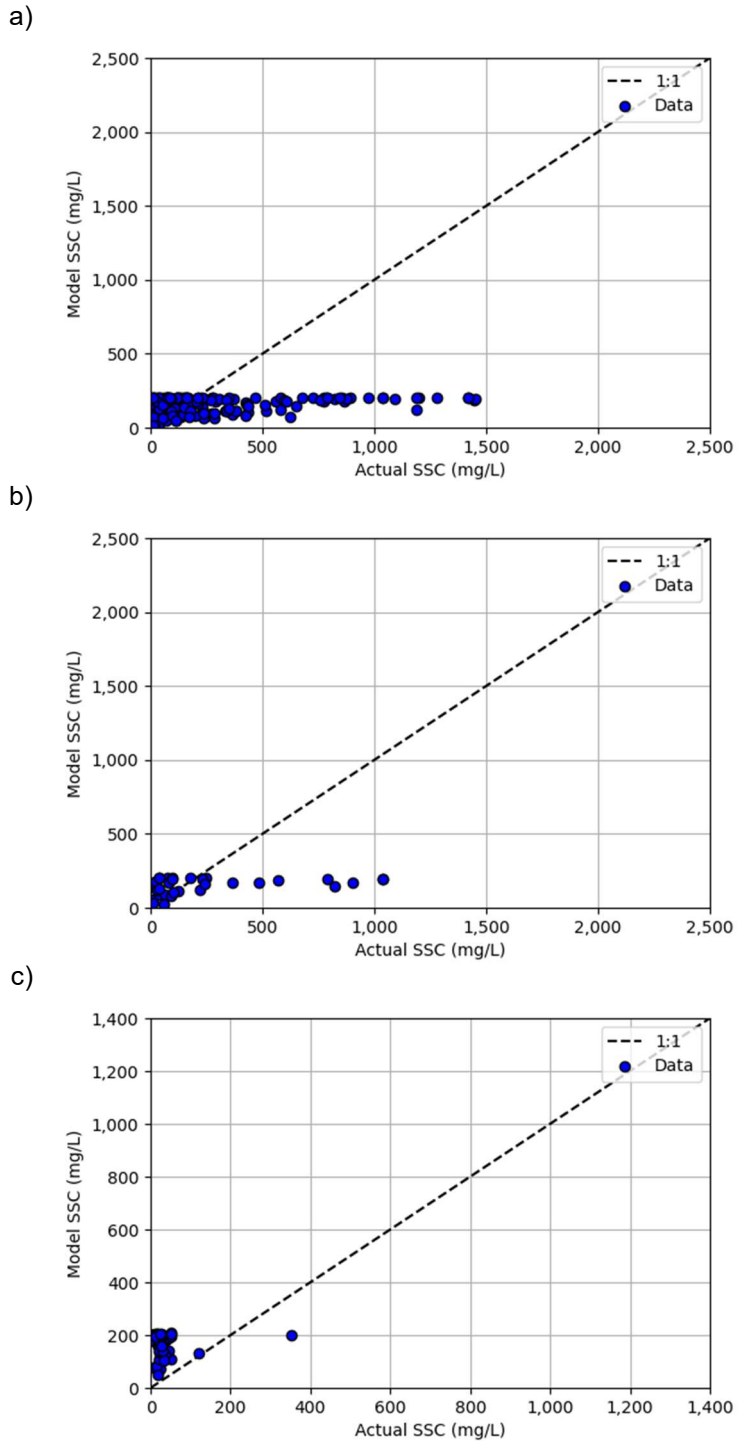


**Figure C-19:** Extreme Learning Machine Performance with the NIR-Red Ratio for the (a) Training Data Set, (b) Test Data Set, and (c) San Bernard Data

a)
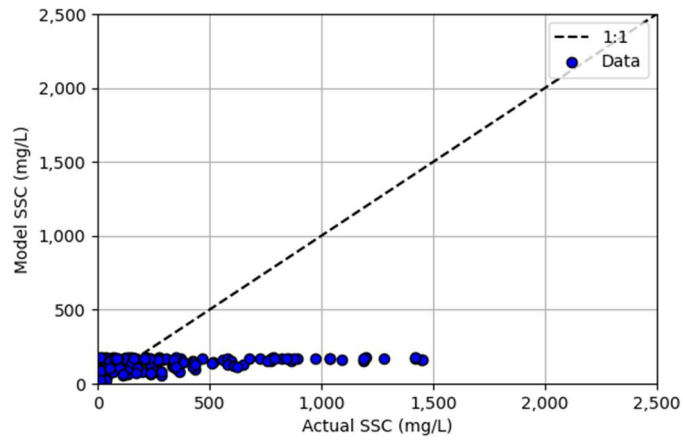


b)
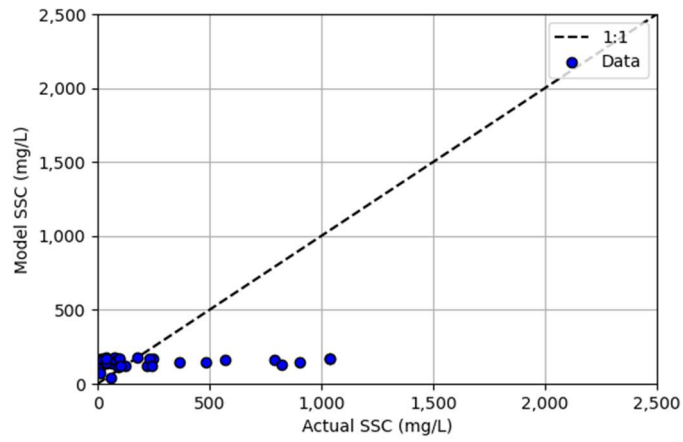


c)
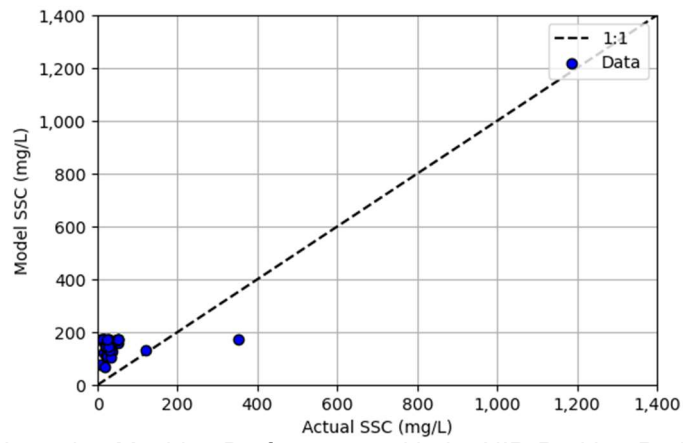


**Figure C-20:** Extreme Learning Machine Performance with the NIR-Red log-Ratio for the (a) Training Data Set, (b) Test Data Set, and (c) San Bernard Data

a)



b)



c)
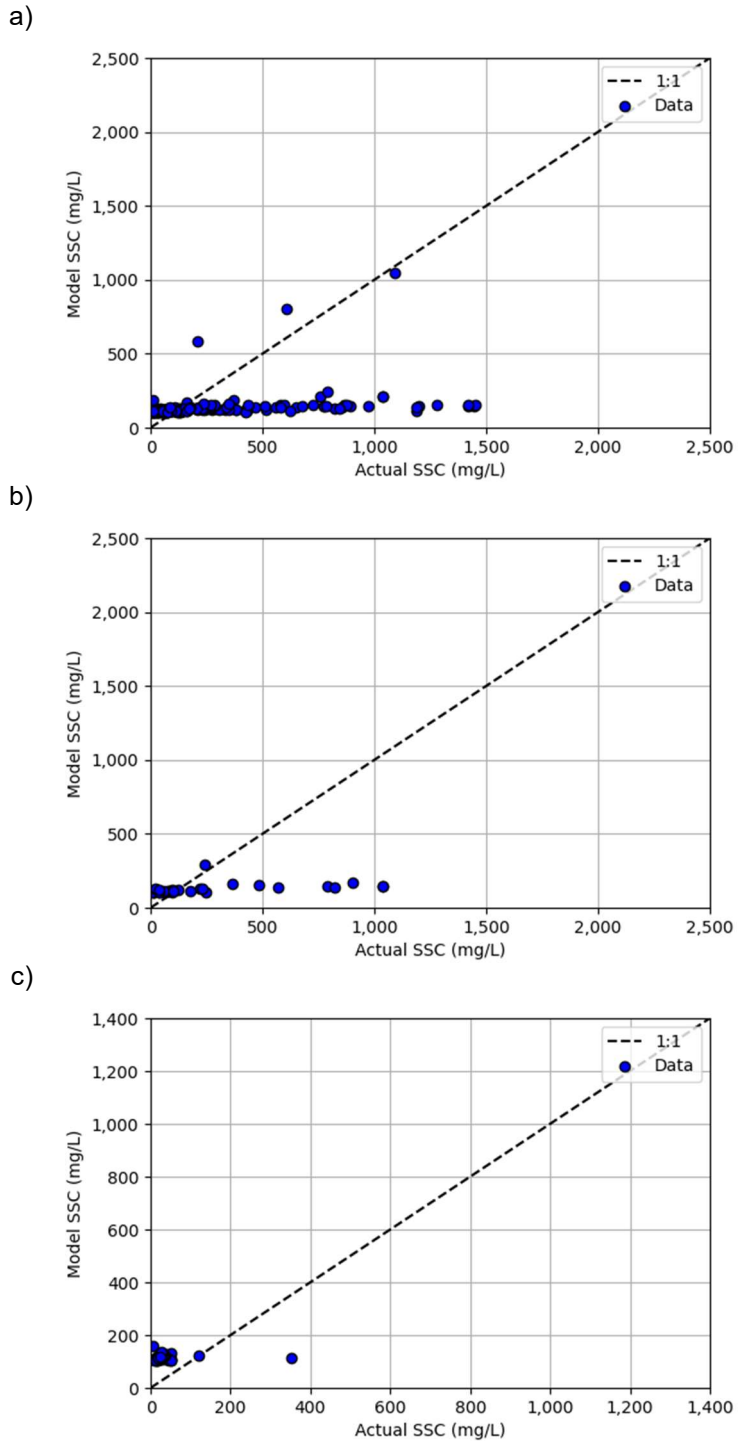


**Figure C-21:** Extreme Learning Machine Performance with the Red Band Squared for the (a) Training Data Set, (b) Test Data Set, and (c) San Bernard Data

a)



b)



c)
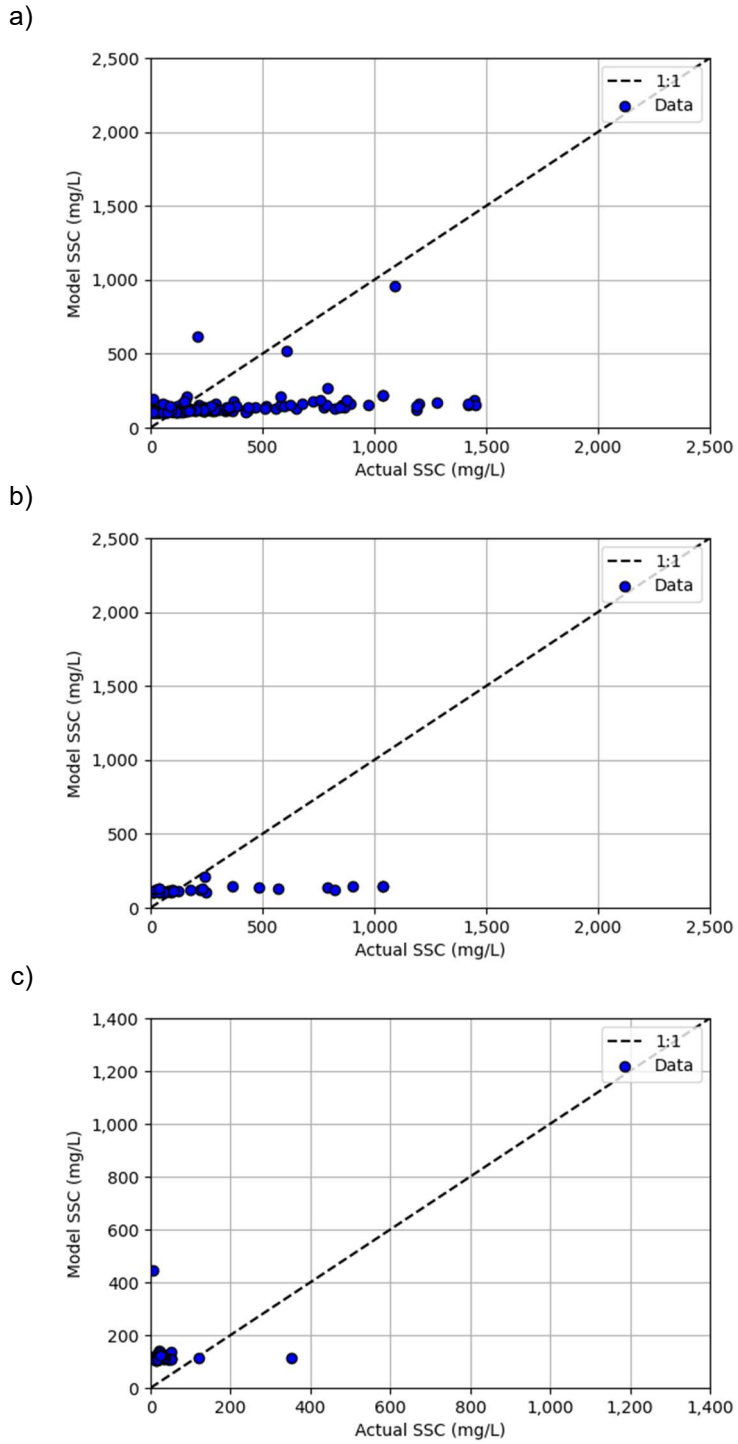


**Figure C-22:** Extreme Learning Machine Performance with the NIR Band Squared for the (a) Training Data Set, (b) Test Data Set, and (c) San Bernard Data

a)



b)



c)
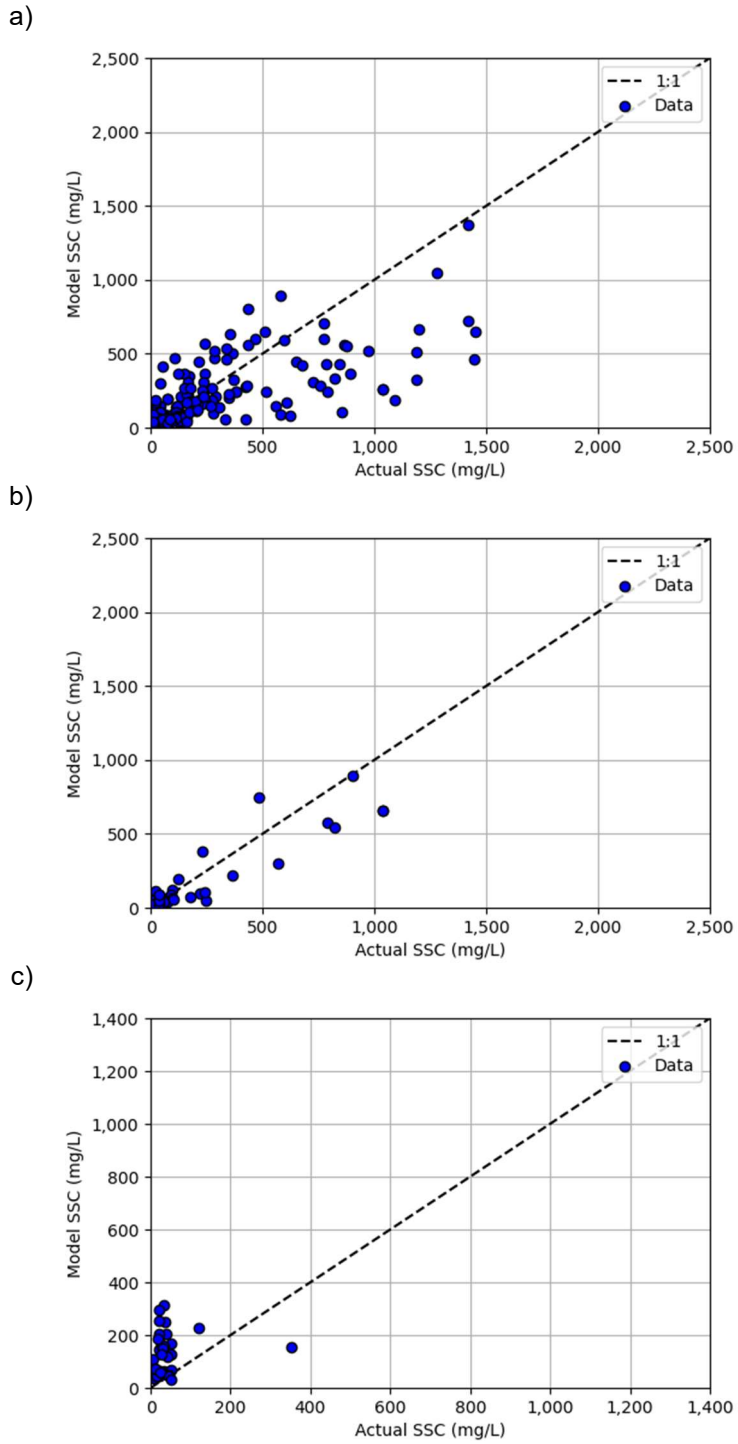


**Figure C-23:** Extreme Learning Machine Performance with the Red-Green Ratio for the (a) Training Data Set, (b) Test Data Set, and (c) San Bernard Data

a)



b)



c)
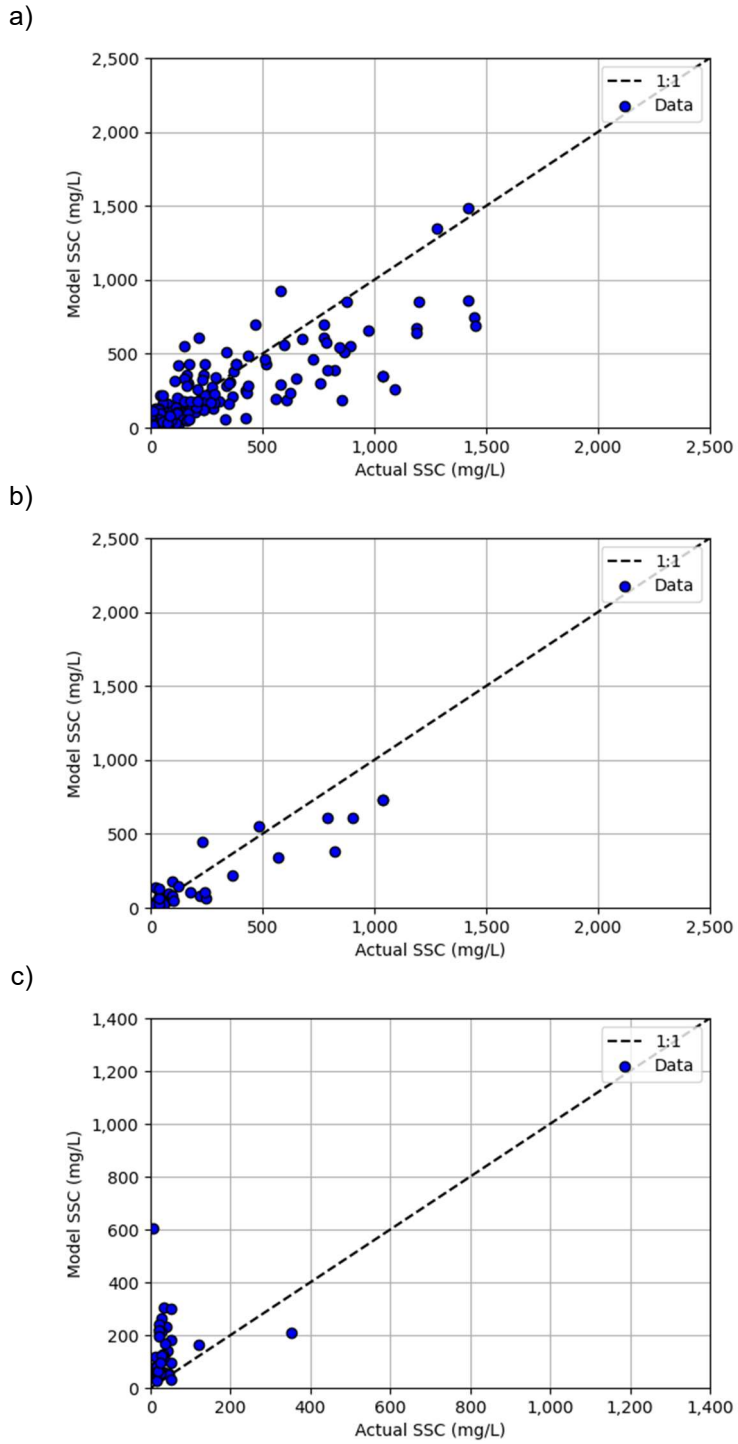


**Figure C-24:** Extreme Learning Machine Performance with the NIR Ratios for the (a) Training Data Set, (b) Test Data Set, and (c) San Bernard Data
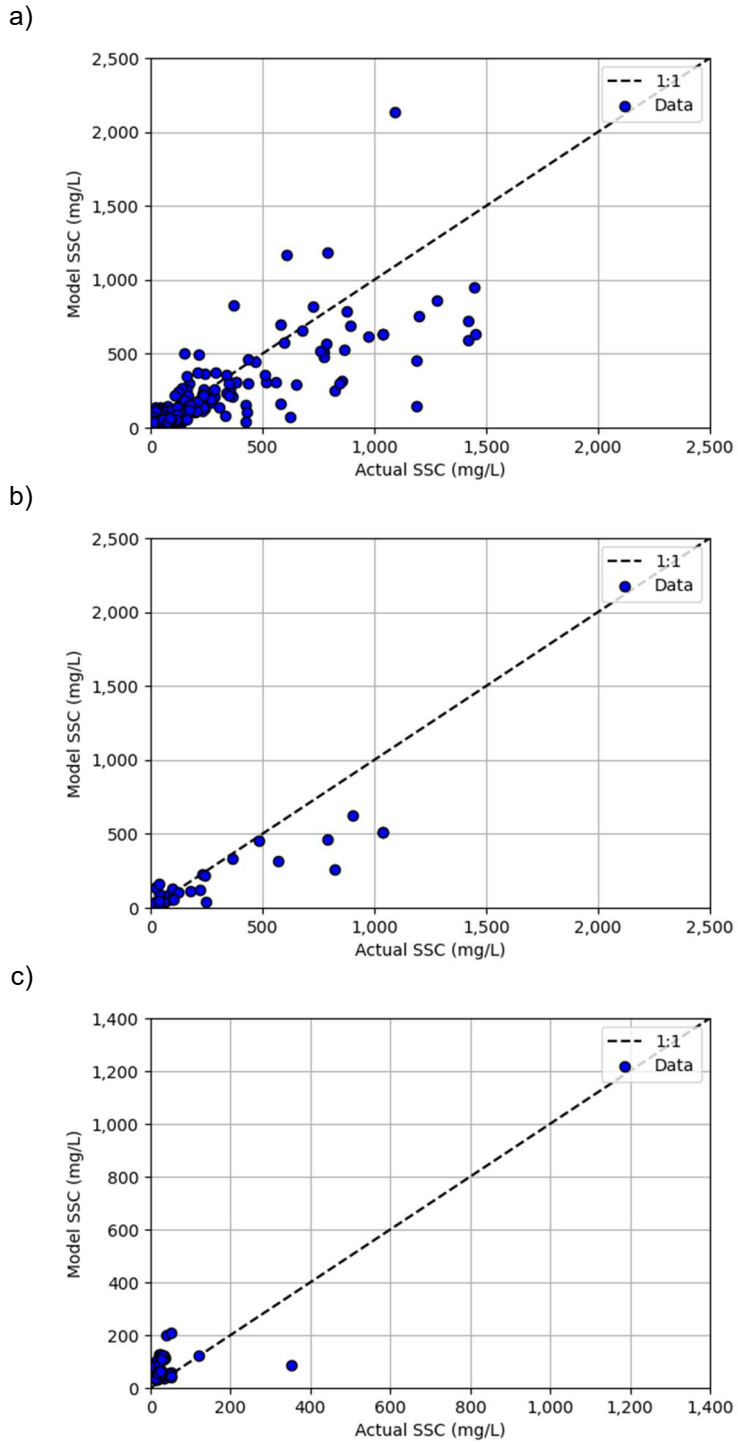
**Figure C-25:** Artificial Neural Network Performance with All Six Bands for the (a) Training Data Set, (b) Test Data Set, and (c) San Bernard Data

a)



b)



c)
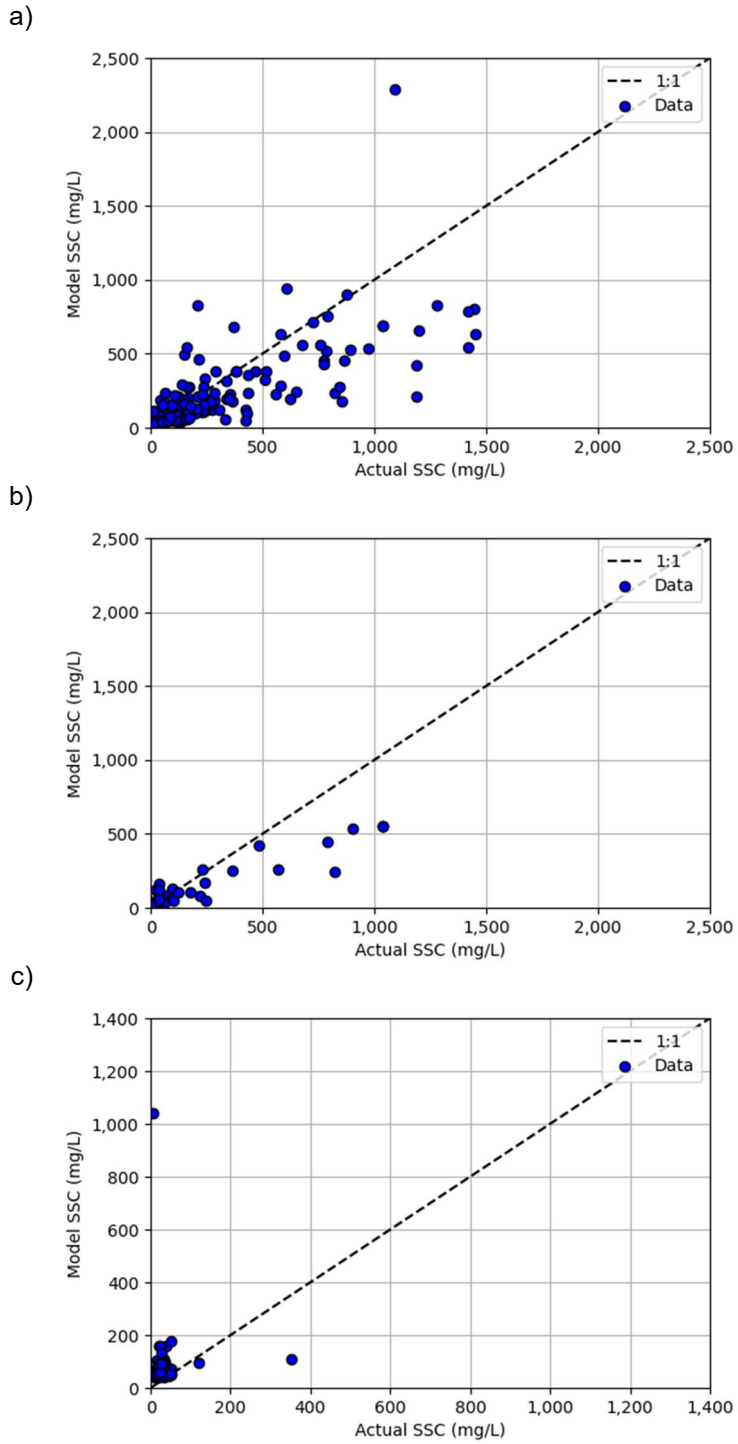


**Figure C-26:** Artificial Neural Network Performance with Four Major Bands for the (a) Training Data Set, (b) Test Data Set, and (c) San Bernard Data
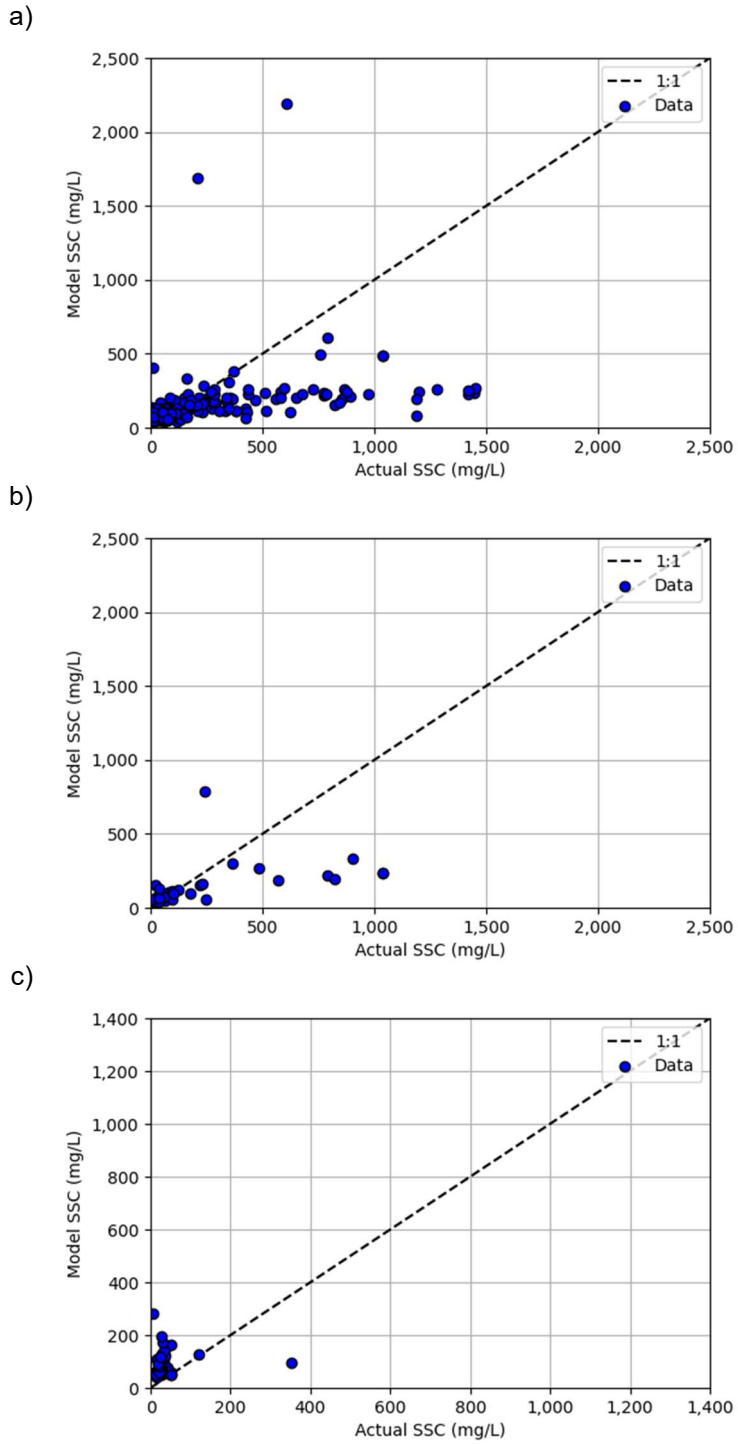
**Figure C-27:** Artificial Neural Network Performance with the Red Band for the (a) Training Data Set, (b) Test Data Set, and (c) San Bernard Data

a)
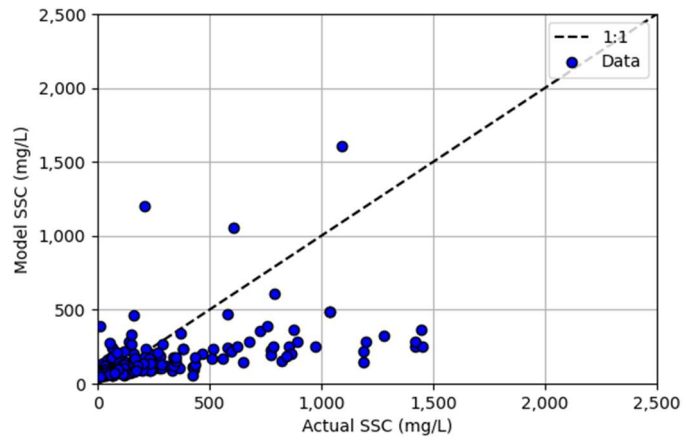


b)
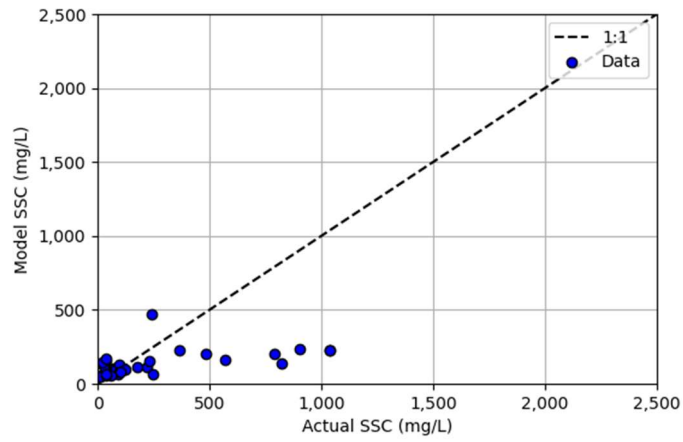


c)
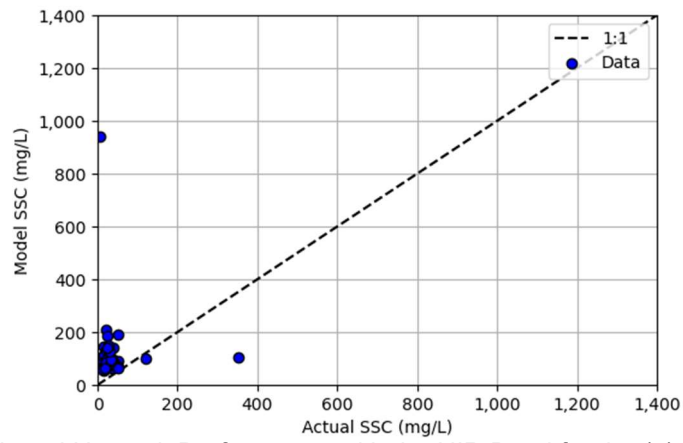


**Figure C-28:** Artificial Neural Network Performance with the NIR Band for the (a) Training Data Set, (b) Test Data Set, and (c) San Bernard Data

a)



b)



c)
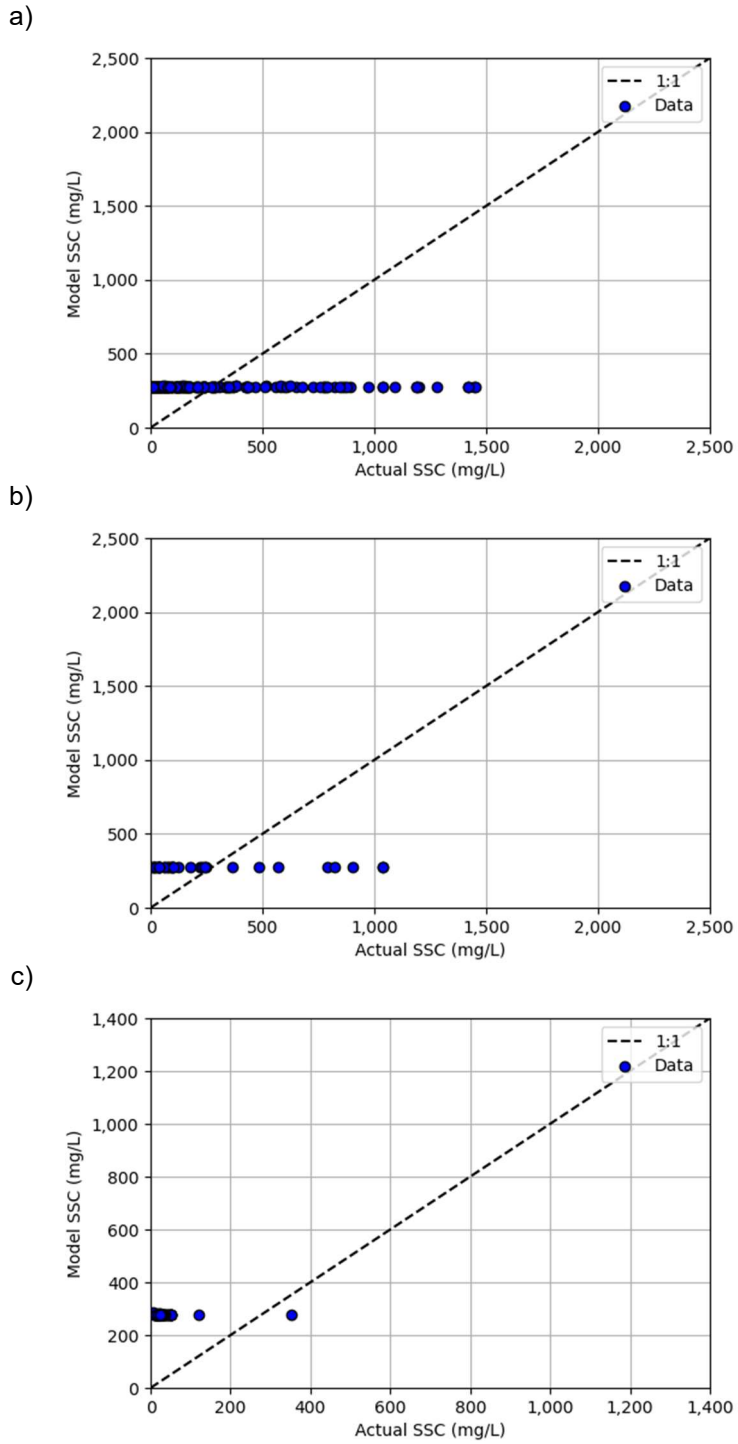


**Figure C-29:** Artificial Neural Network Performance with the Red Difference for the (a) Training Data Set, (b) Test Data Set, and (c) San Bernard Data

a)



b)



c)
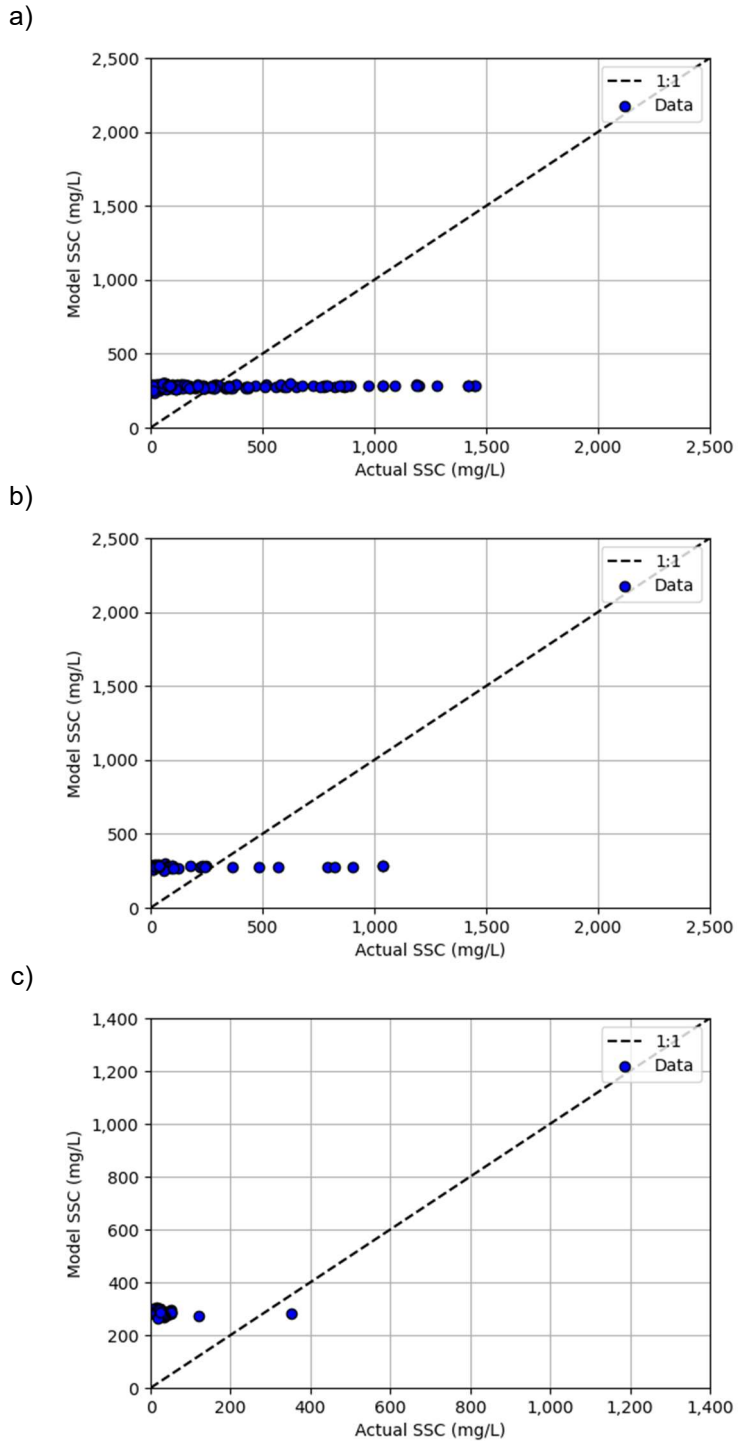


**Figure C-30:** Artificial Neural Network Performance with the Sediment Index for the (a) Training Data Set, (b) Test Data Set, and (c) San Bernard Data

a)



b)



c)
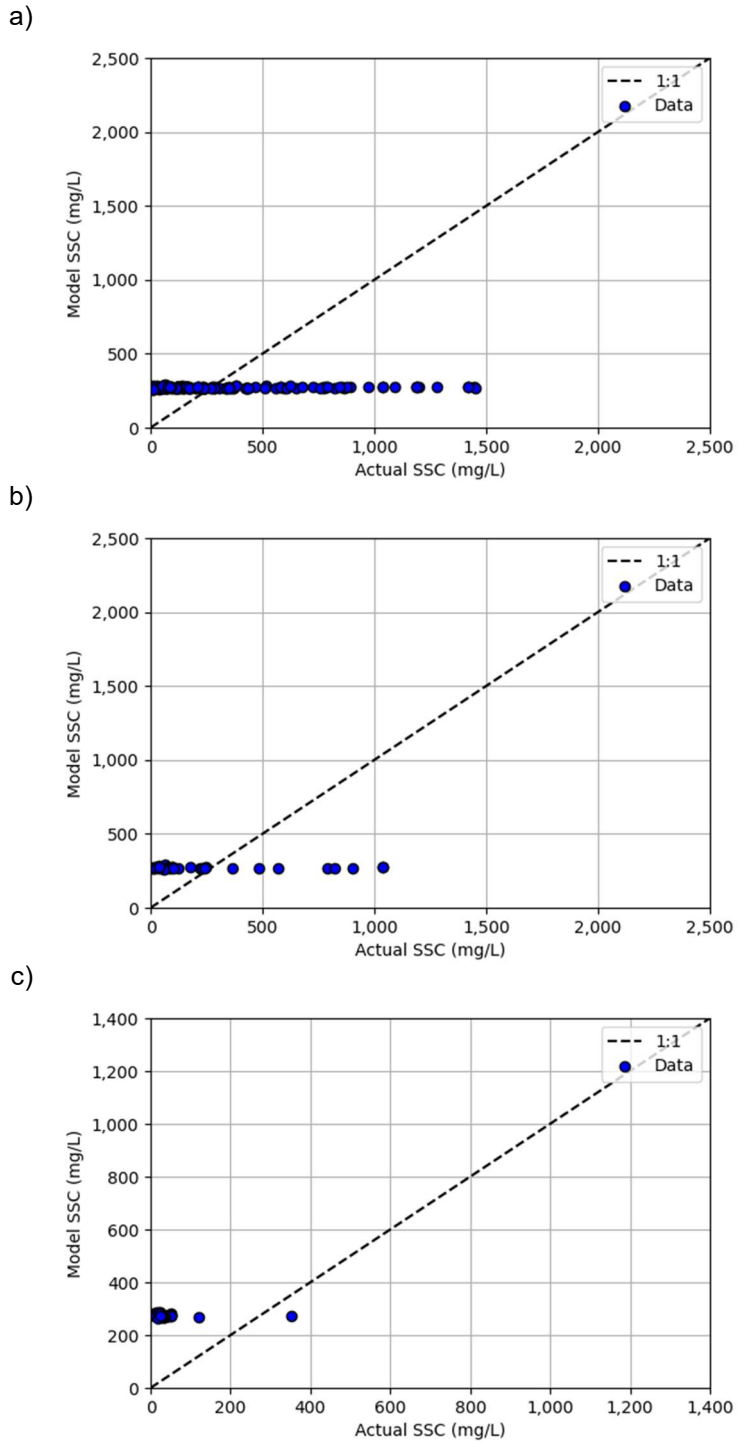


**Figure C-31:** Artificial Neural Network Performance with the NIR-Red Ratio for the (a) Training Data Set, (b) Test Data Set, and (c) San Bernard Data

a)



b)



c)
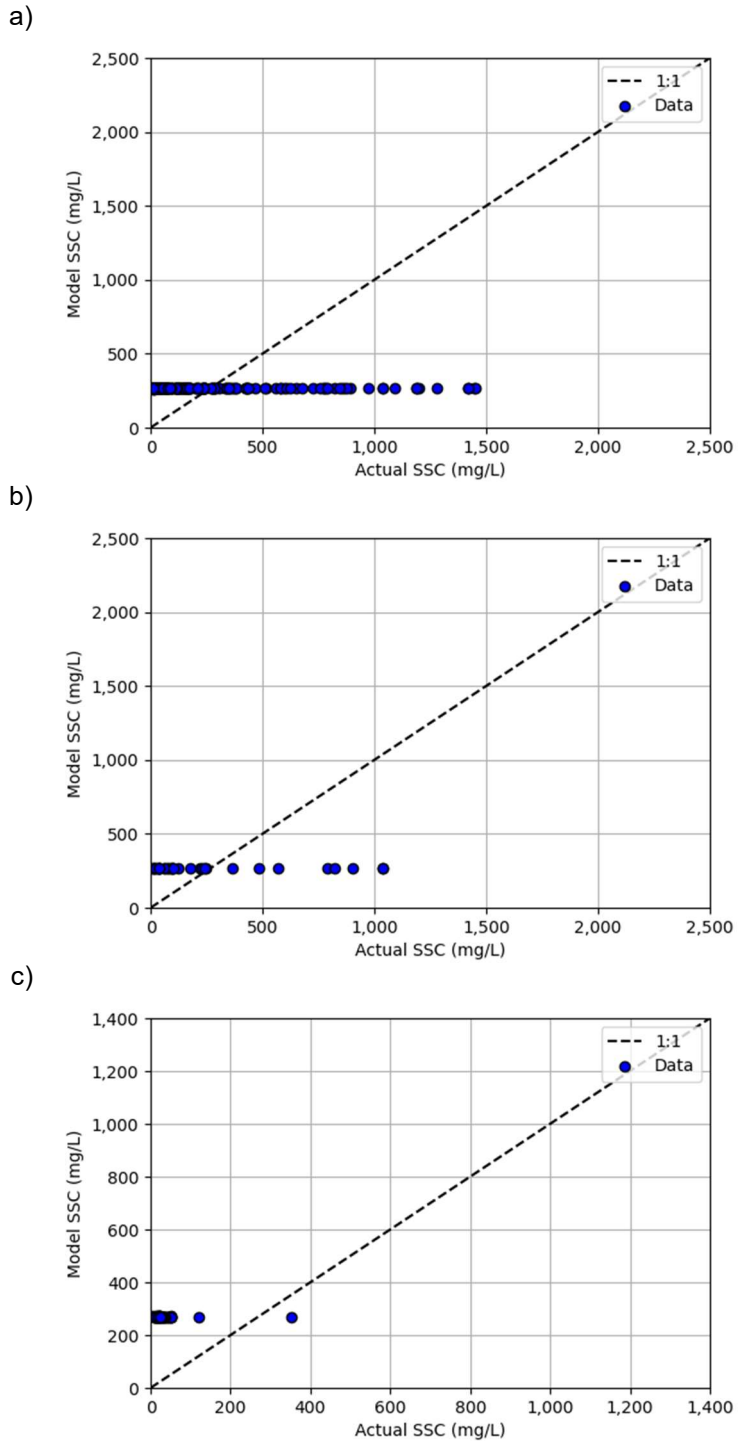


**Figure C-32:** Artificial Neural Network Performance with the NIR-Red log-Ratio for the (a) Training Data Set, (b) Test Data Set, and (c) San Bernard Data

a)



b)



c)
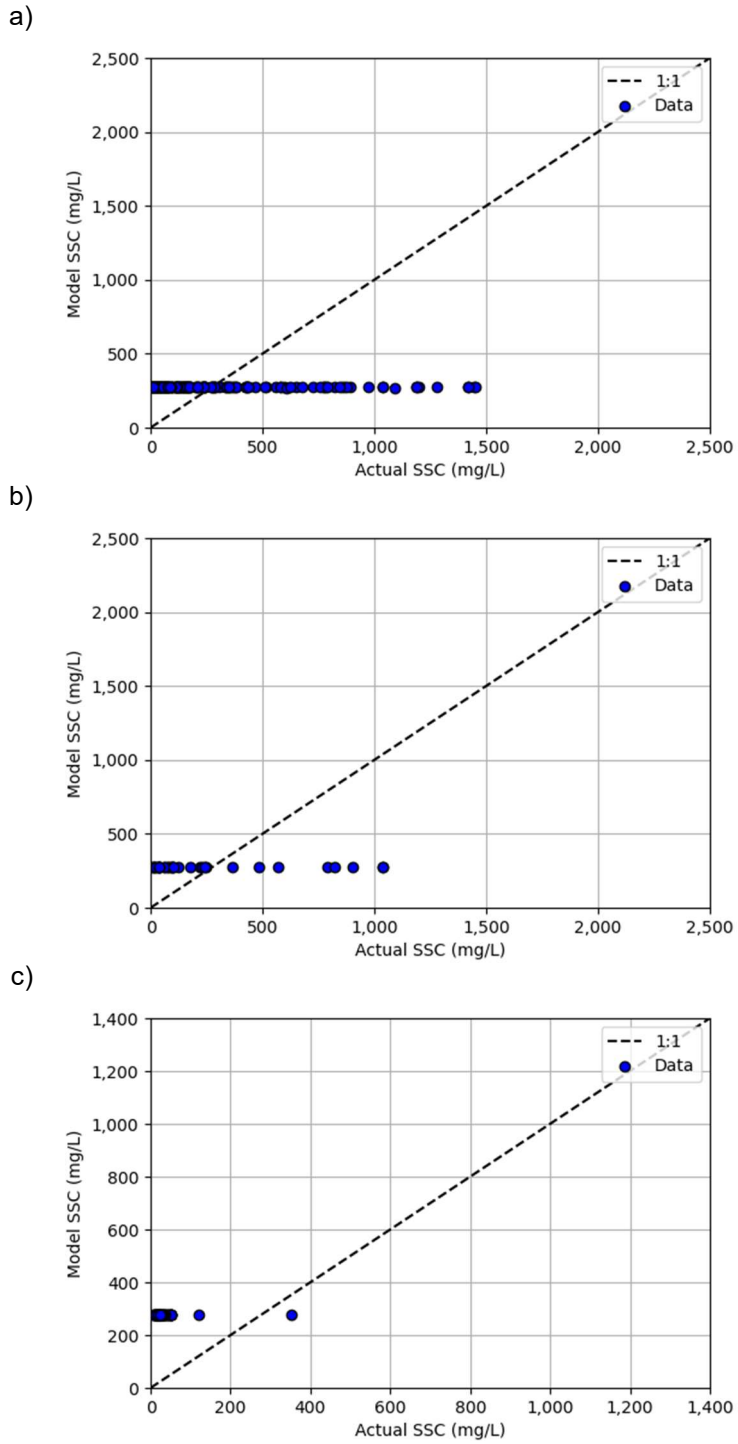


**Figure C-33:** Artificial Neural Network Performance with the Red Band Squared for the (a) Training Data Set, (b) Test Data Set, and (c) San Bernard Data

a)



b)



c)
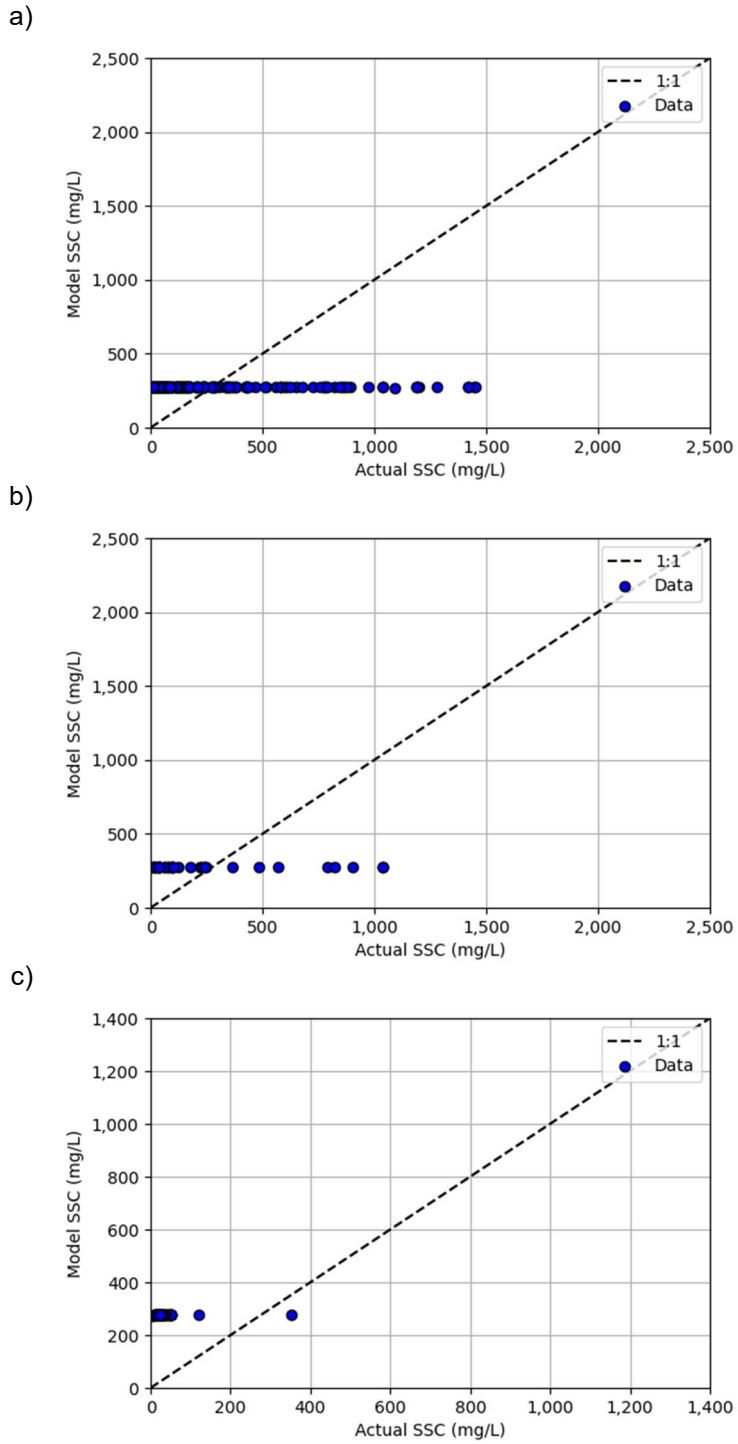


**Figure C-34:** Artificial Neural Network Performance with the NIR Band Squared for the (a) Training Data Set, (b) Test Data Set, and (c) San Bernard Data

a)



b)



c)
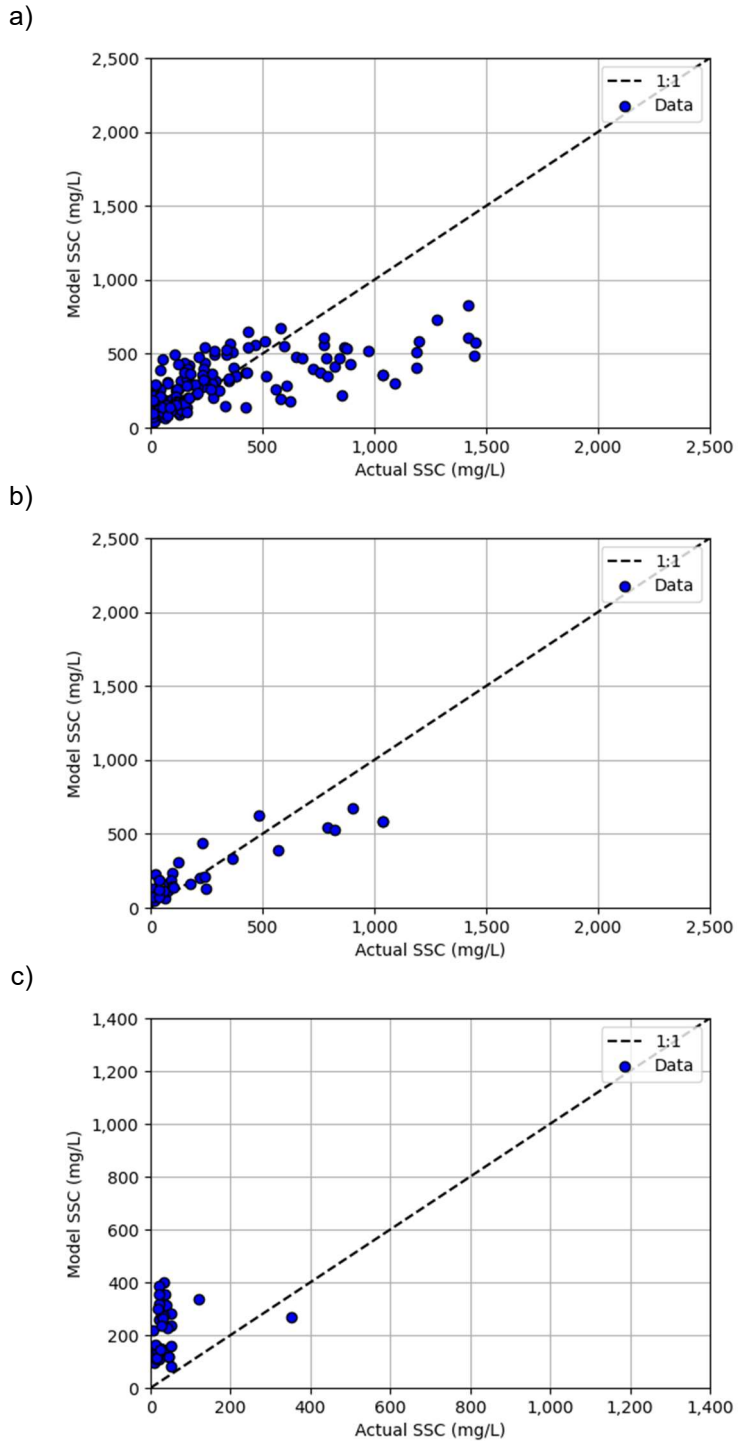


**Figure C-35:** Artificial Neural Network Performance with the Red-Green Ratio for the (a) Training Data Set, (b) Test Data Set, and (c) San Bernard Data

a)



b)



c)
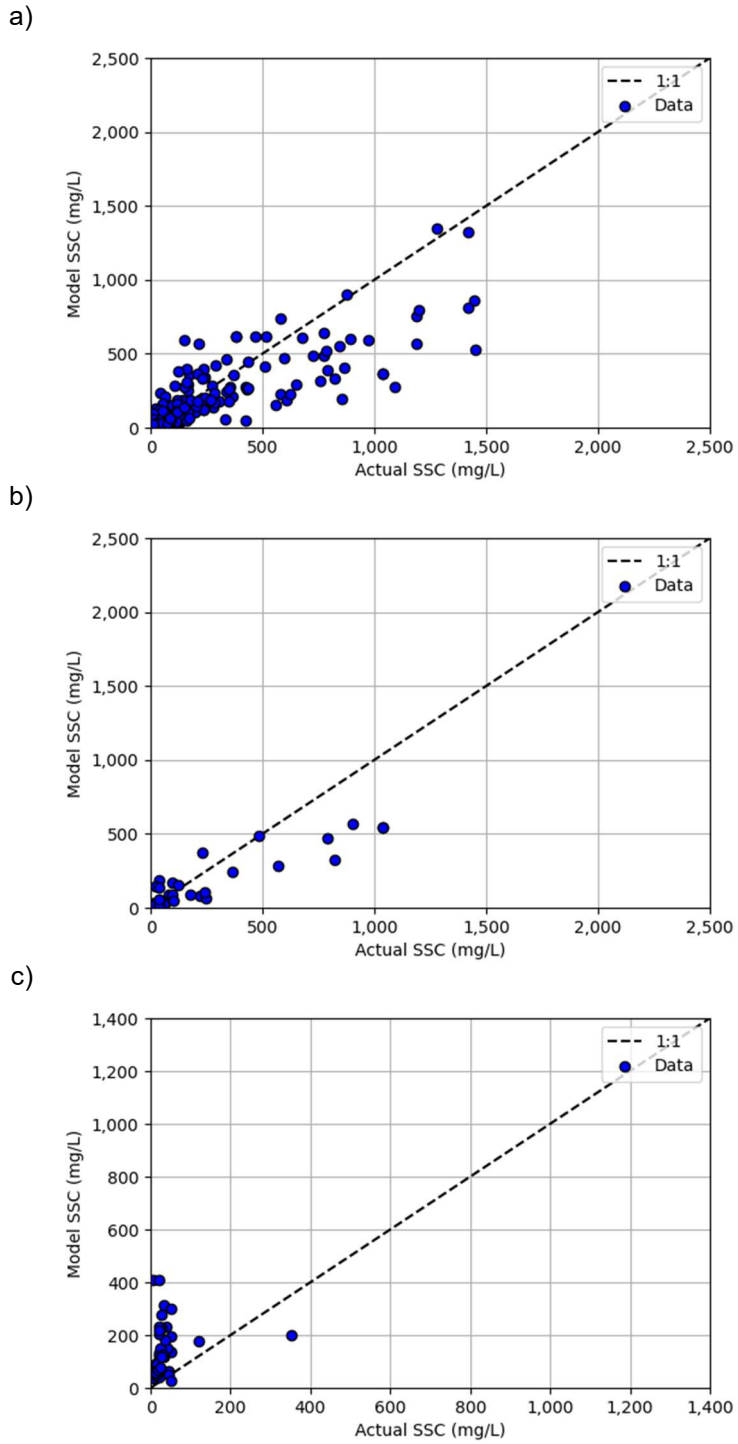


**Figure C-36:** Artificial Neural Network Performance with the NIR Ratios for the (a) Training Data Set, (b) Test Data Set, and (c) San Bernard Data

a)



b)



c)
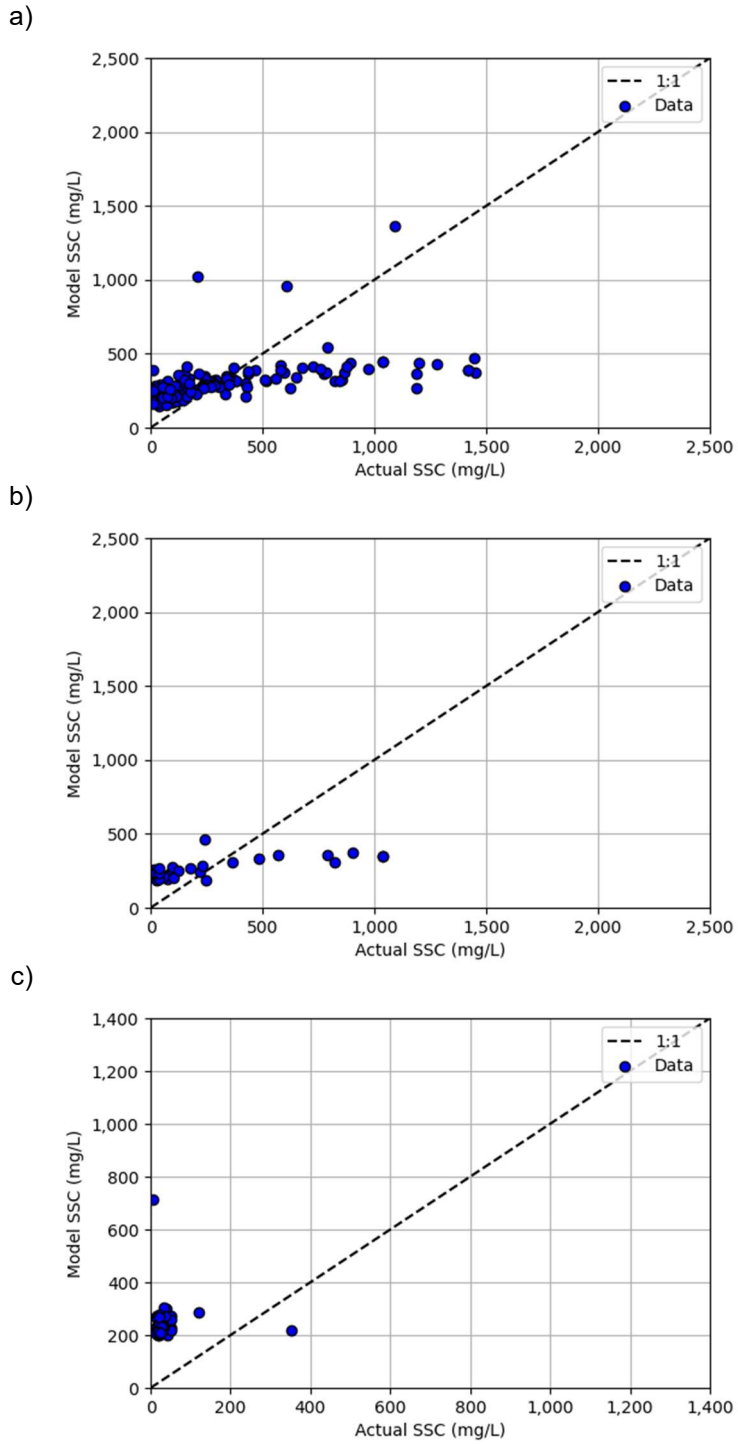


**Figure C-37:** Exponential Relationship Performance with All Six Bands for the (a) Training Data Set, (b) Test Data Set, and (c) San Bernard Data

a)



b)



c)
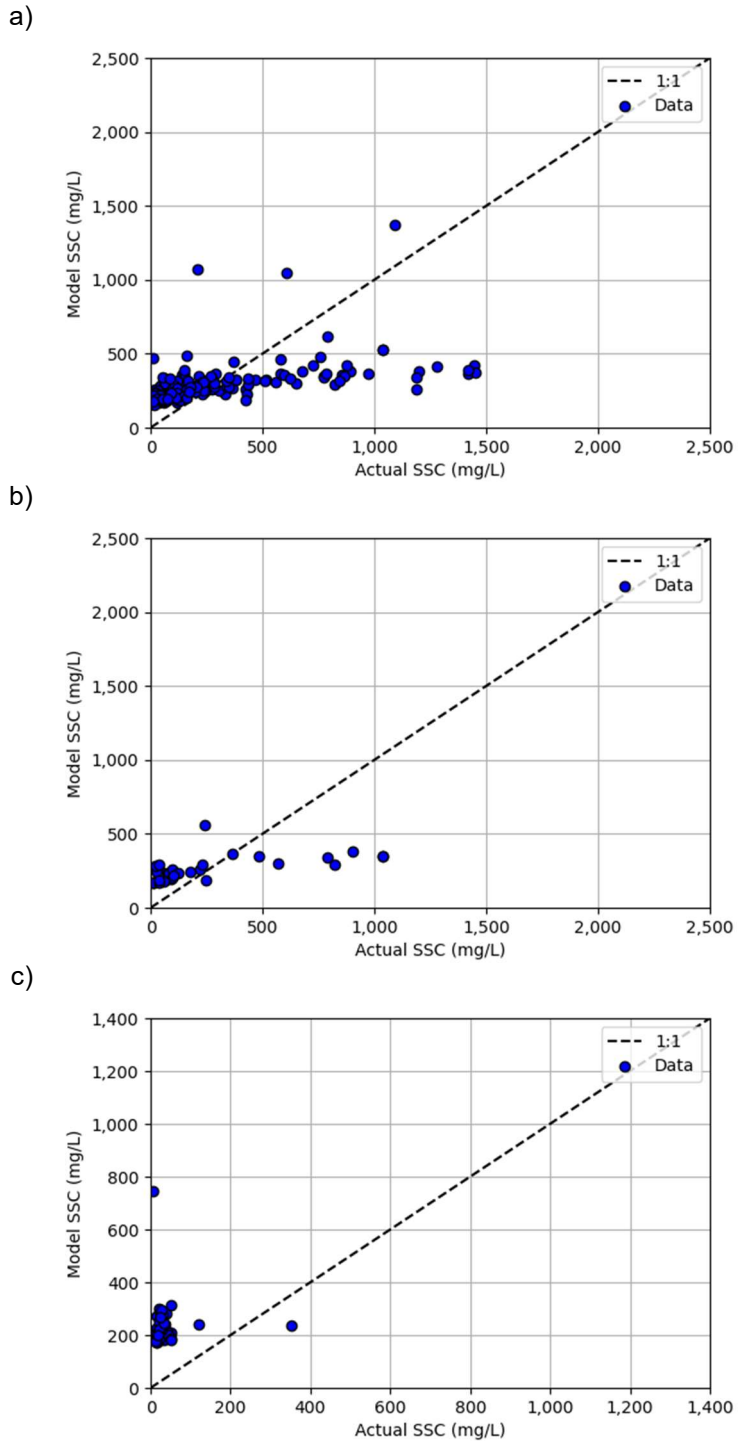


**Figure C-38:** Exponential Relationship Performance with Four Major Bands for the (a) Training Data Set, (b) Test Data Set, and (c) San Bernard Data

a)



b)



c)
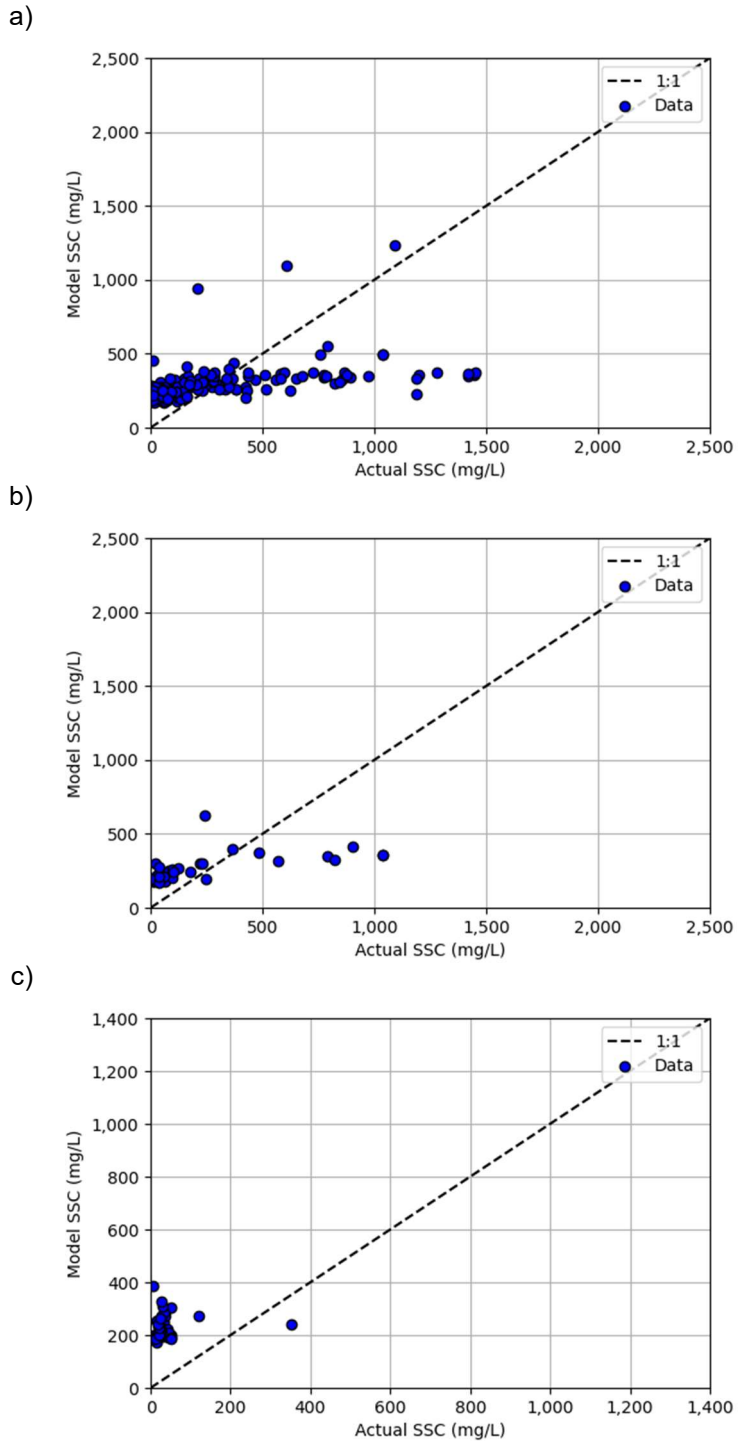


**Figure C-39:** Exponential Relationship Performance with the Red Band for the (a) Training Data Set, (b) Test Data Set, and (c) San Bernard Data
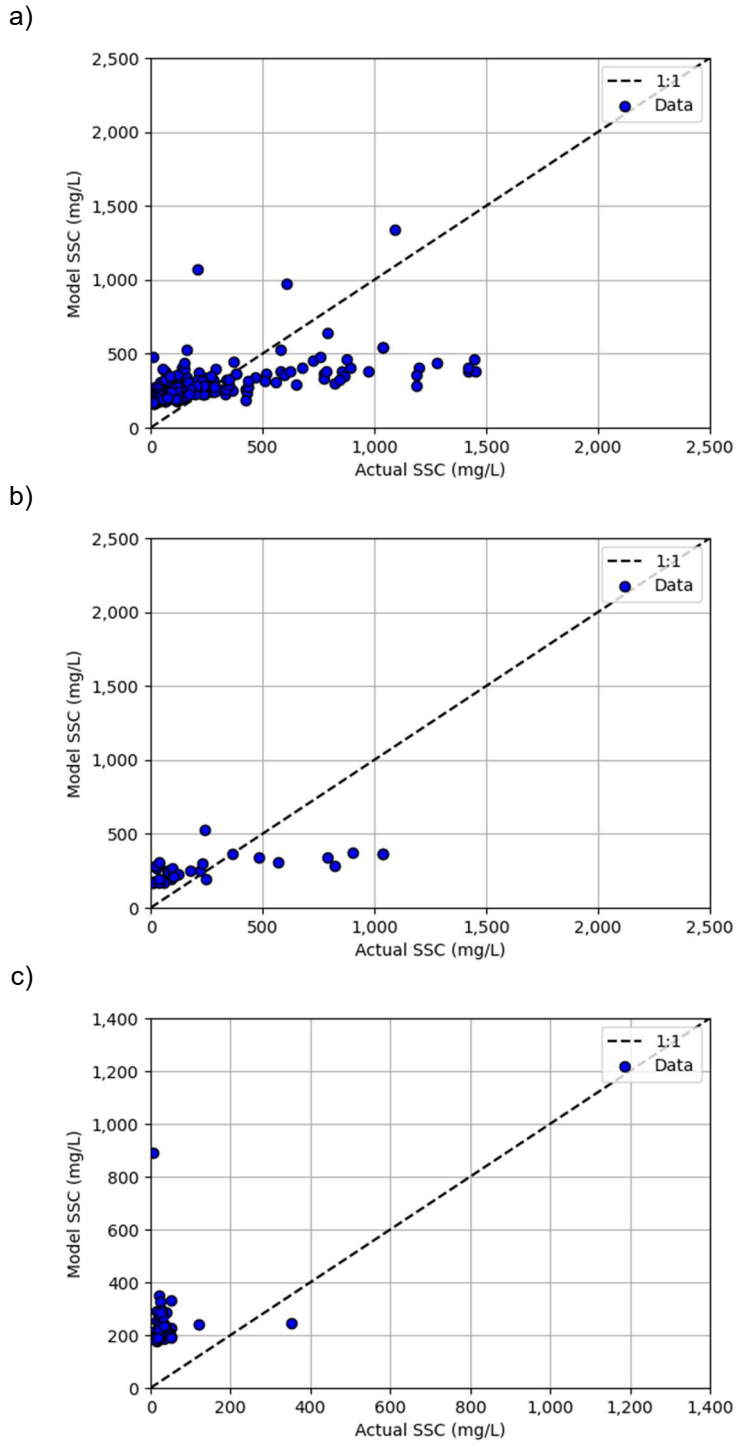
**Figure C-40:** Exponential Relationship Performance with the NIR Band for the (a) Training Data Set, (b) Test Data Set, and (c) San Bernard Data

a)



b)



c)
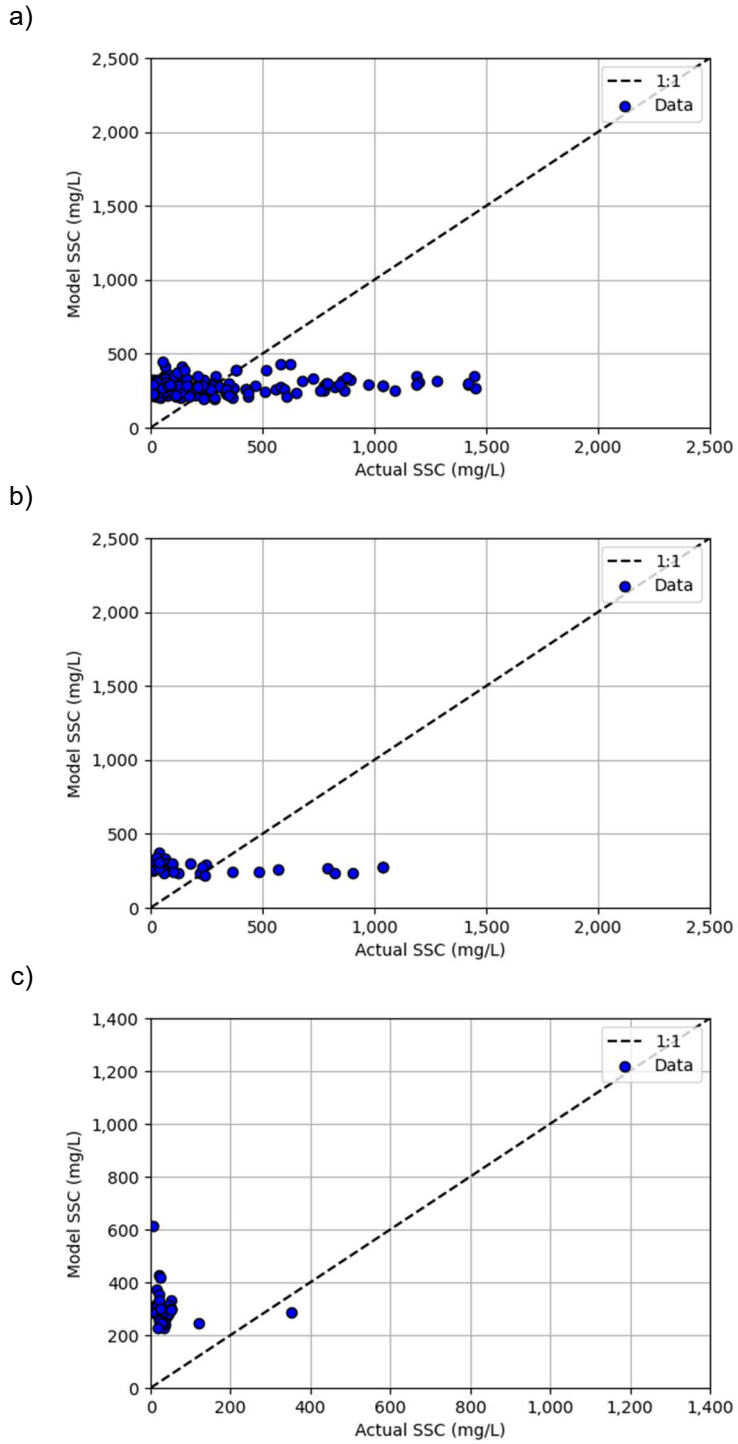


**Figure C-41:** Exponential Relationship Performance with the Red Difference for the (a) Training Data Set, (b) Test Data Set, and (c) San Bernard Data

a)



b)



c)
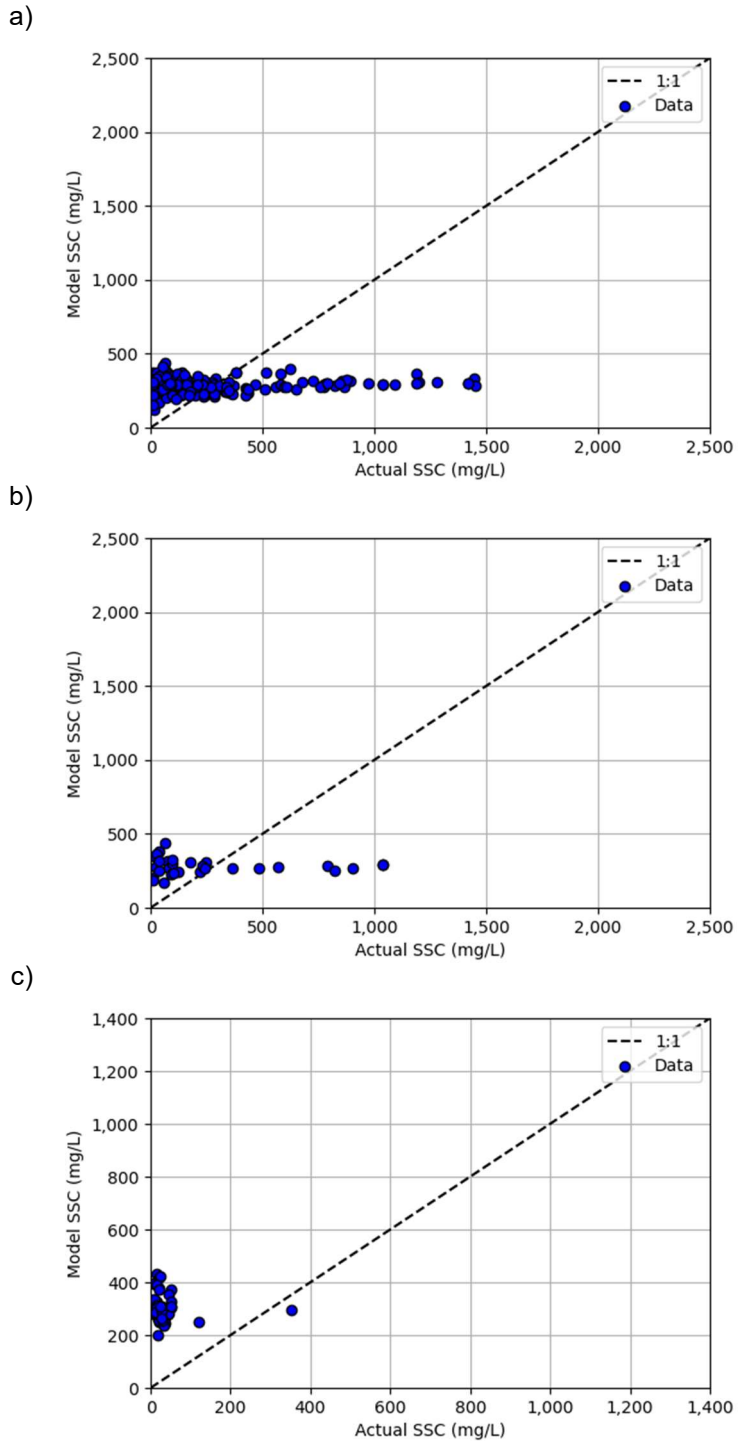


**Figure C-42:** Exponential Relationship Performance with the Sediment Index for the (a) Training Data Set, (b) Test Data Set, and (c) San Bernard Data

a)



b)



c)
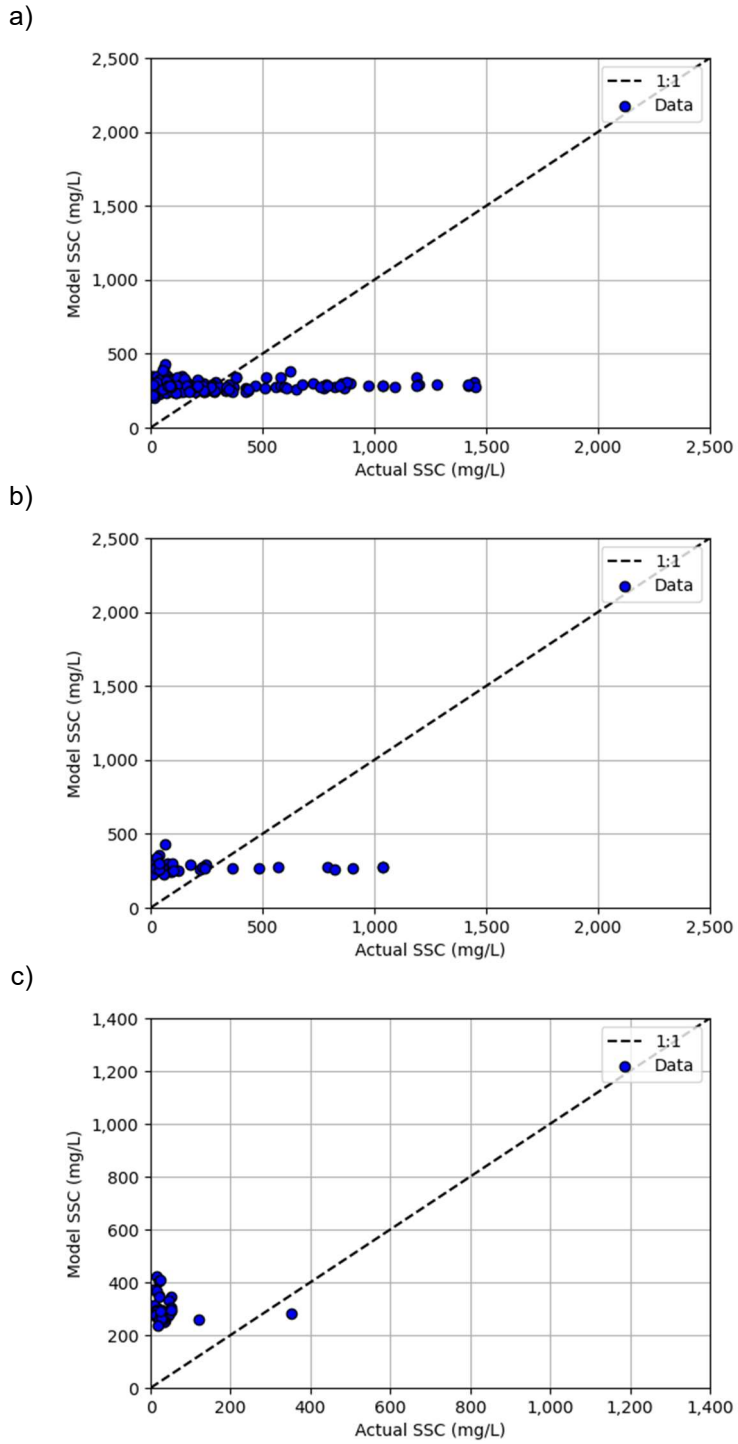


**Figure C-43:** Exponential Relationship Performance with the NIR-Red Ratio for the (a) Training Data Set, (b) Test Data Set, and (c) San Bernard Data

a)



b)



c)
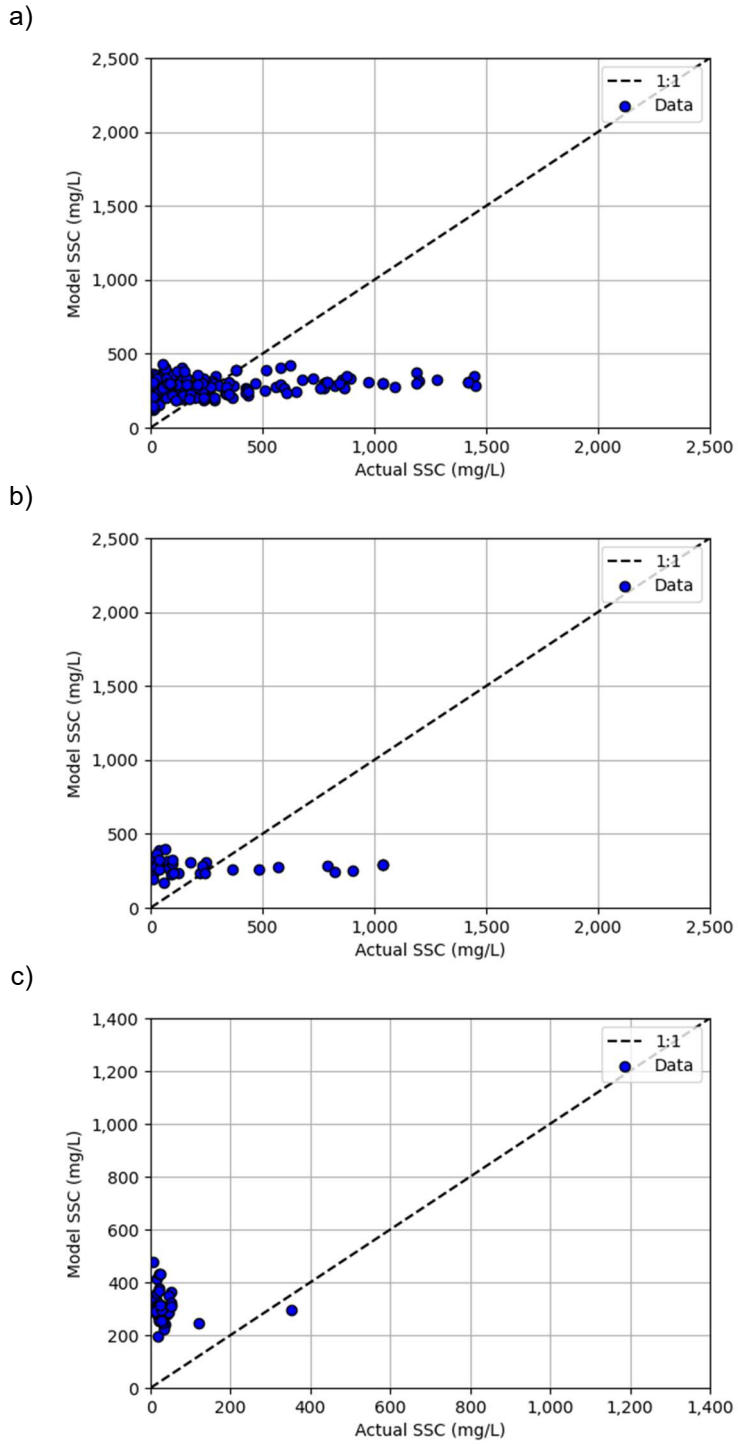


**Figure C-44:** Exponential Relationship Performance with the NIR-Red log-Ratio for the (a) Training Data Set, (b) Test Data Set, and (c) San Bernard Data

a)



b)



c)
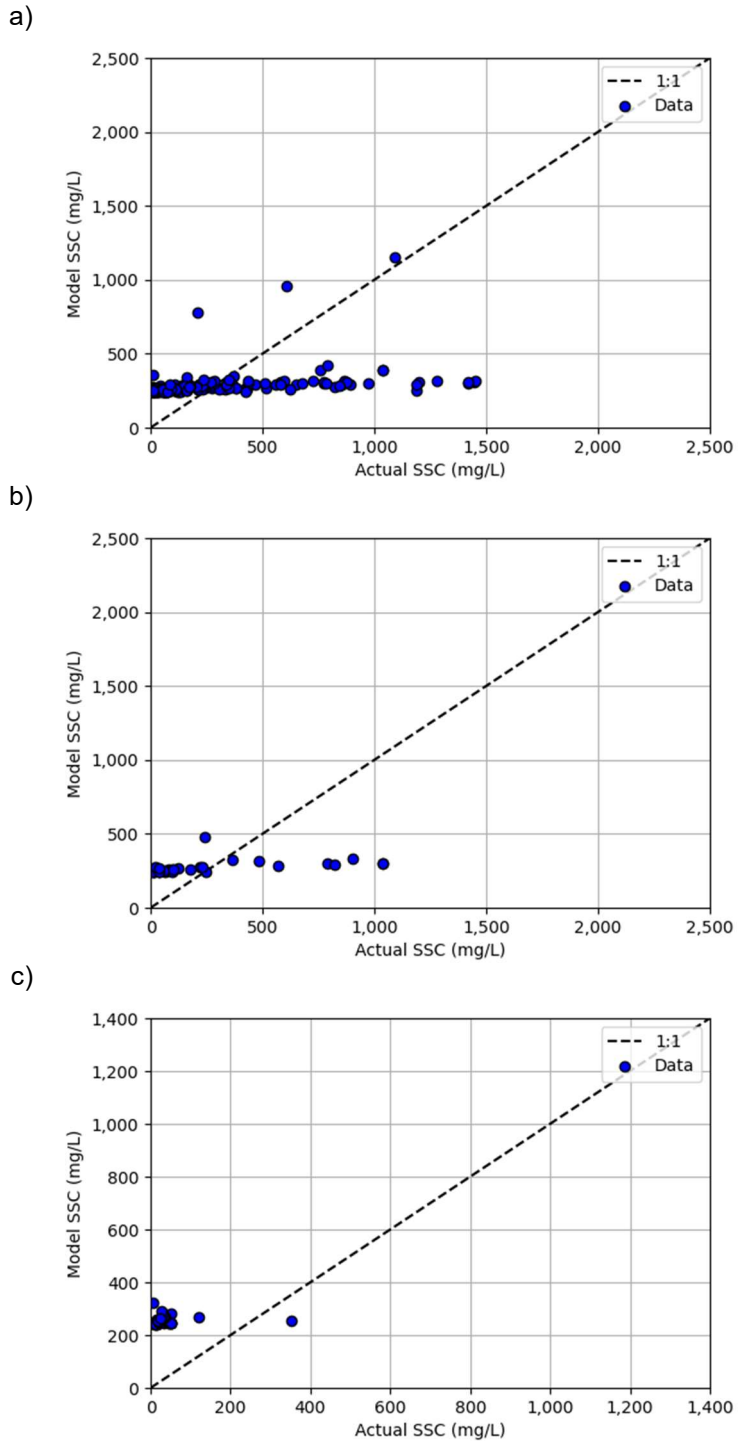


**Figure C-45:** Exponential Relationship Performance with the Red Band Squared for the (a) Training Data Set, (b) Test Data Set, and (c) San Bernard Data

a)



b)



c)
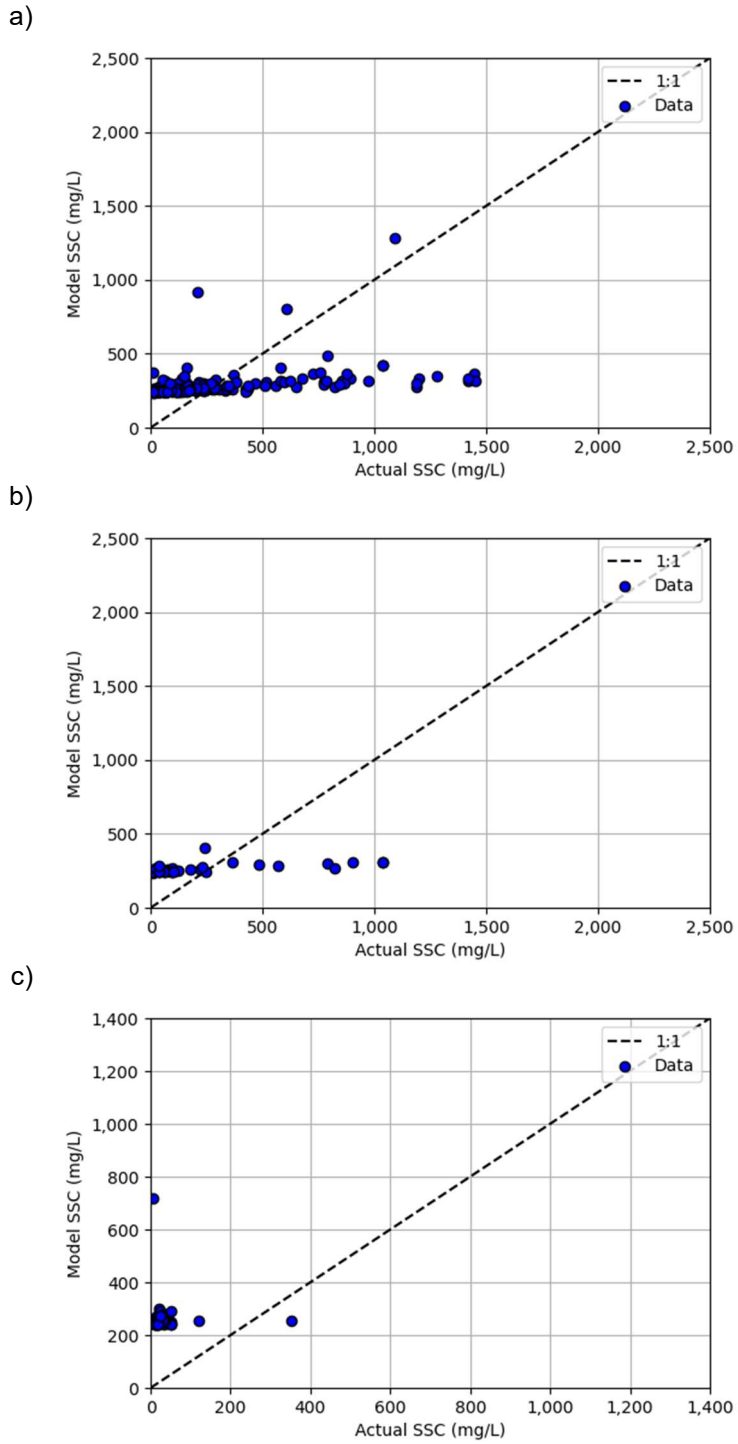


**Figure C-46:** Exponential Relationship Performance with the NIR Band Squared for the (a) Training Data Set, (b) Test Data Set, and (c) San Bernard Data

a)
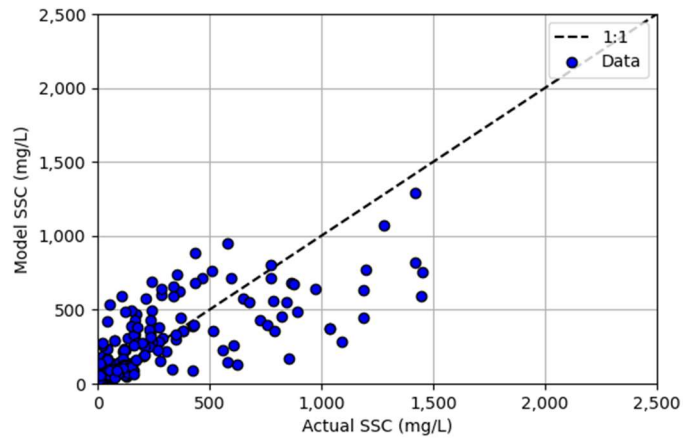


b)
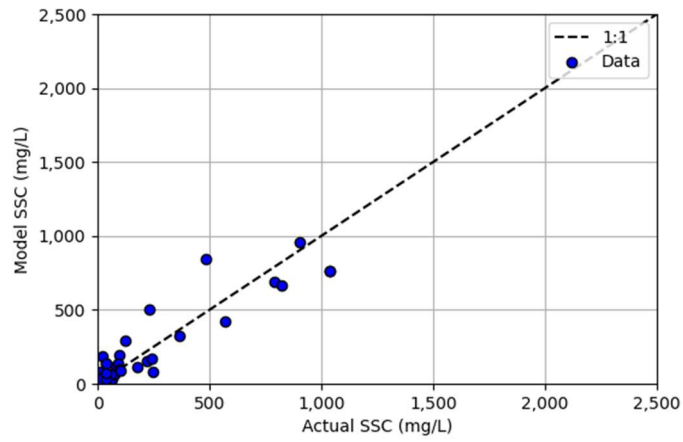


c)
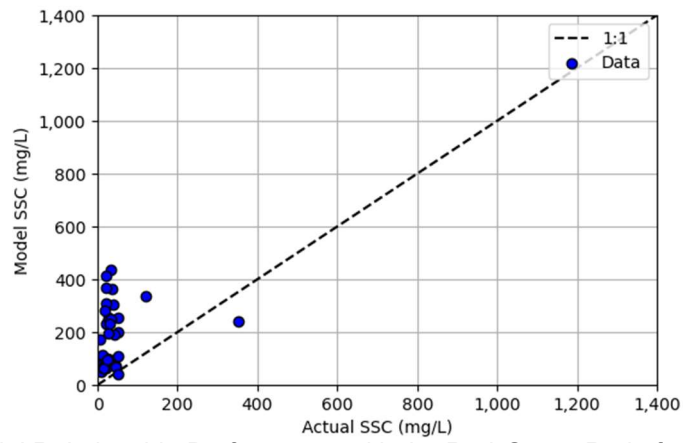


**Figure C-47:** Exponential Relationship Performance with the Red-Green Ratio for the (a) Training Data Set, (b) Test Data Set, and (c) San Bernard Data

a)



b)



c)
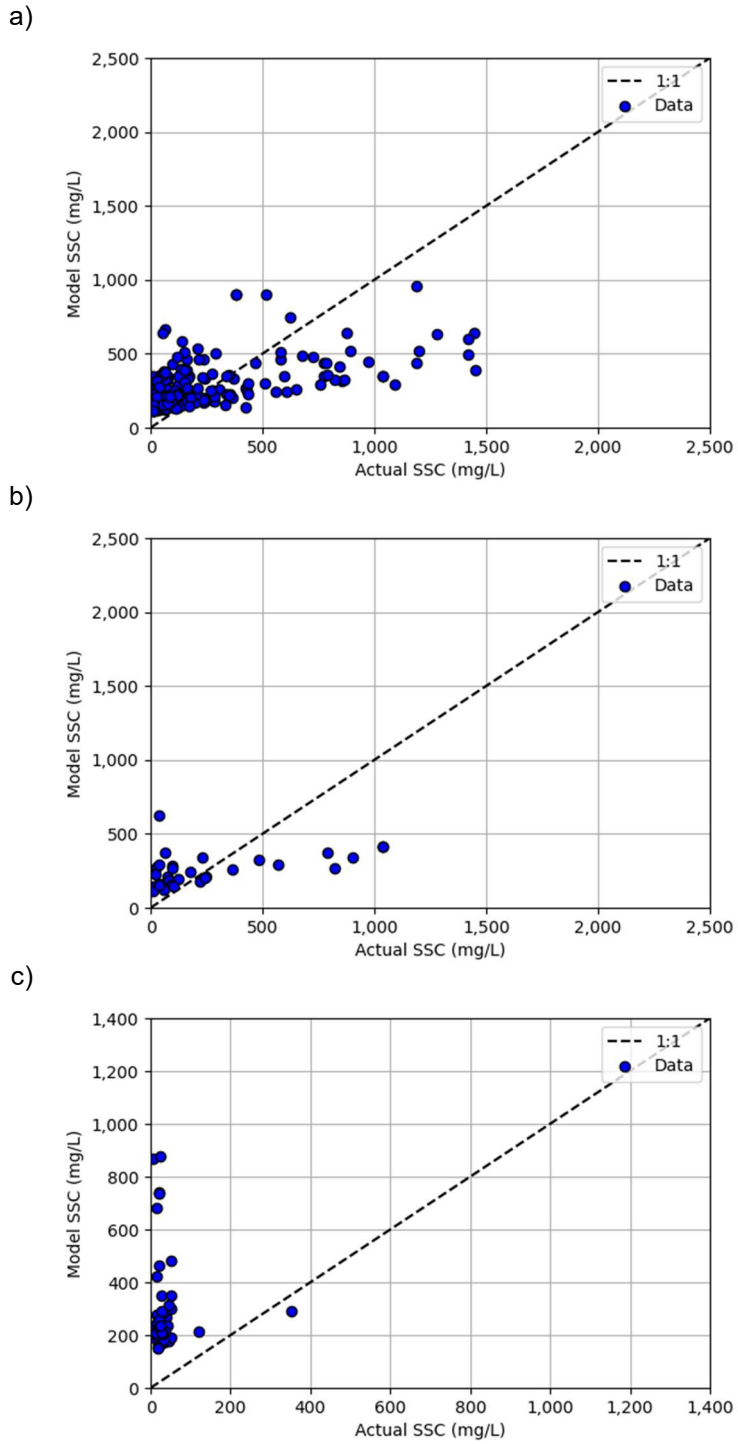


**Figure C-48:** Exponential Relationship Performance with the NIR Ratios for the (a) Training Data Set, (b) Test Data Set, and (c) San Bernard Data

a)
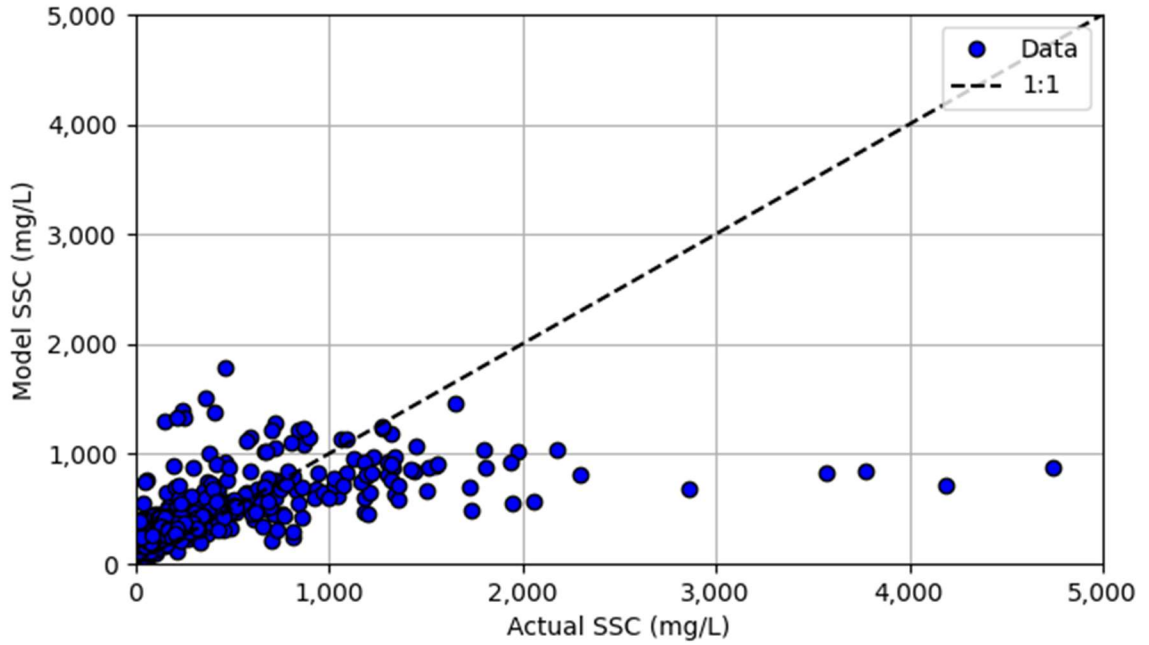


b)
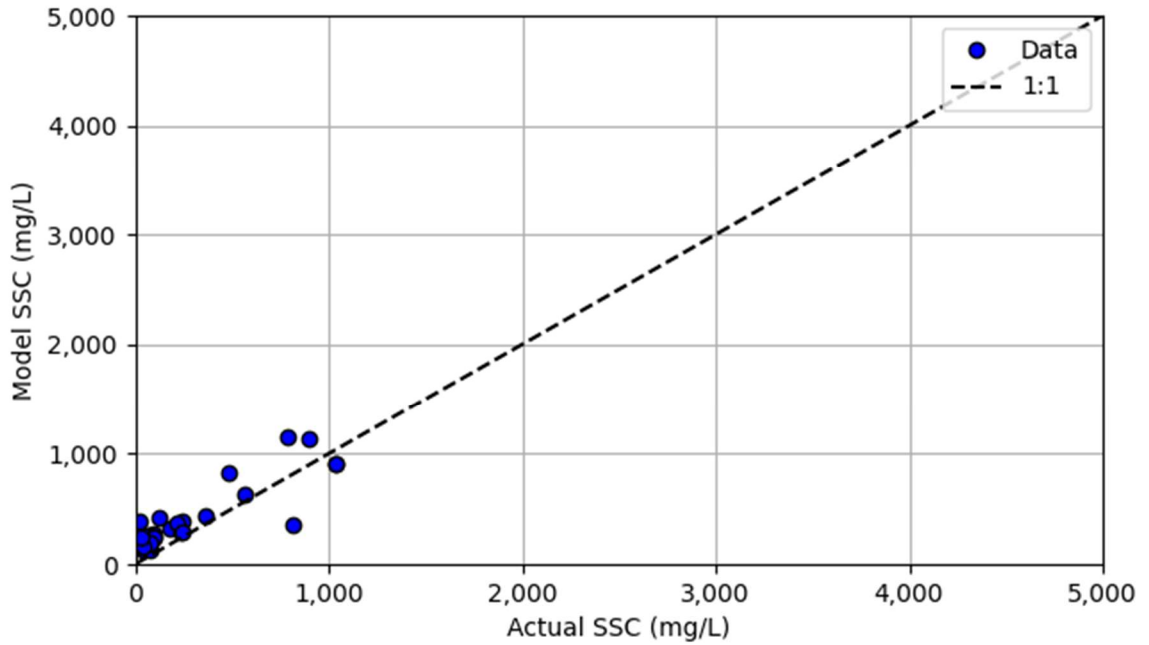


**Figure C-49:** Rating Curve for SSC vs. Flow Performance for the (a) Training Data Set and (b) Test Data Set

a)
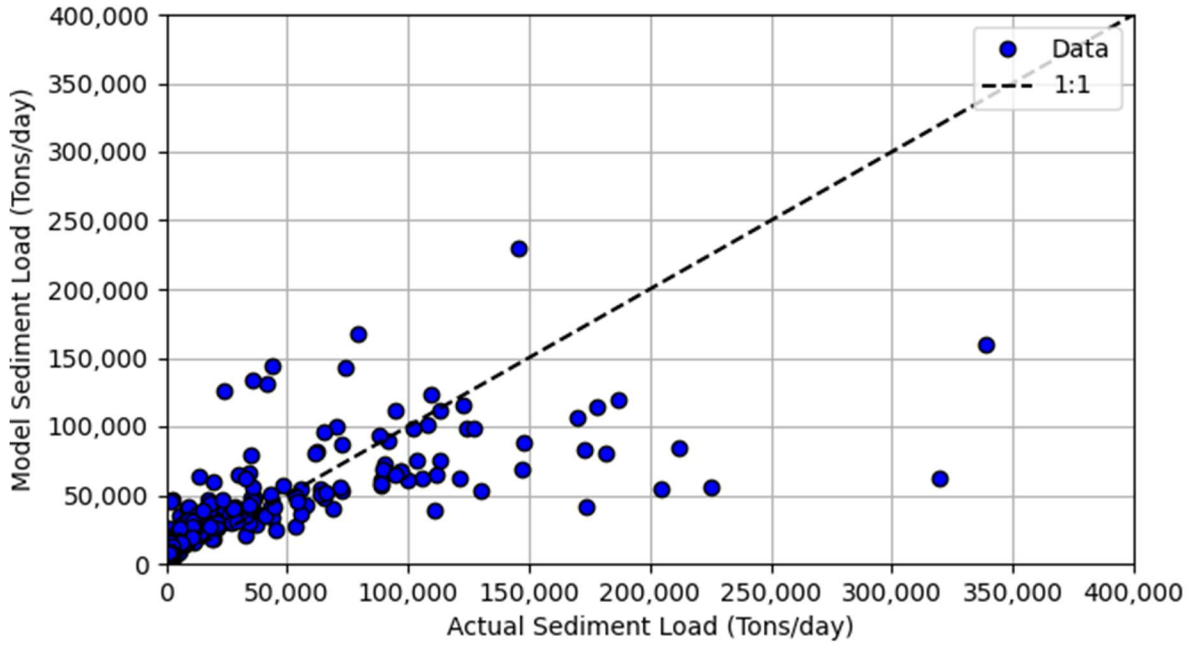


b)
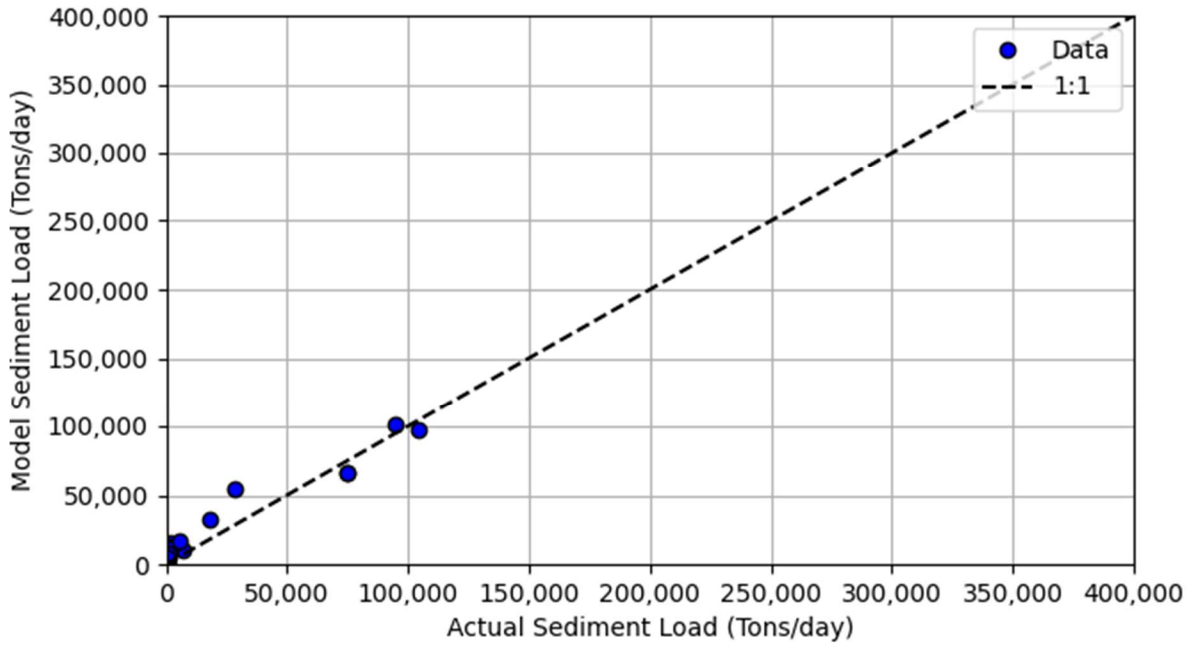


**Figure C-50:** Rating Curve for Sediment Load vs. Flow Performance for the (a) Training Data Set and (b) Test Data Set

a)
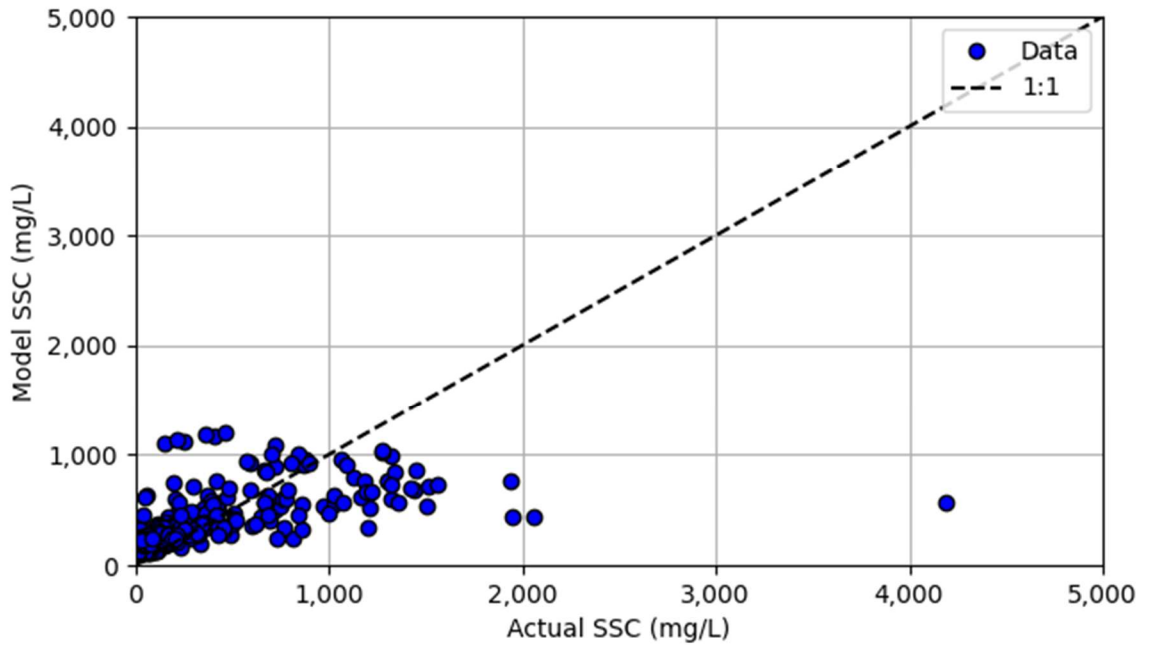


b)
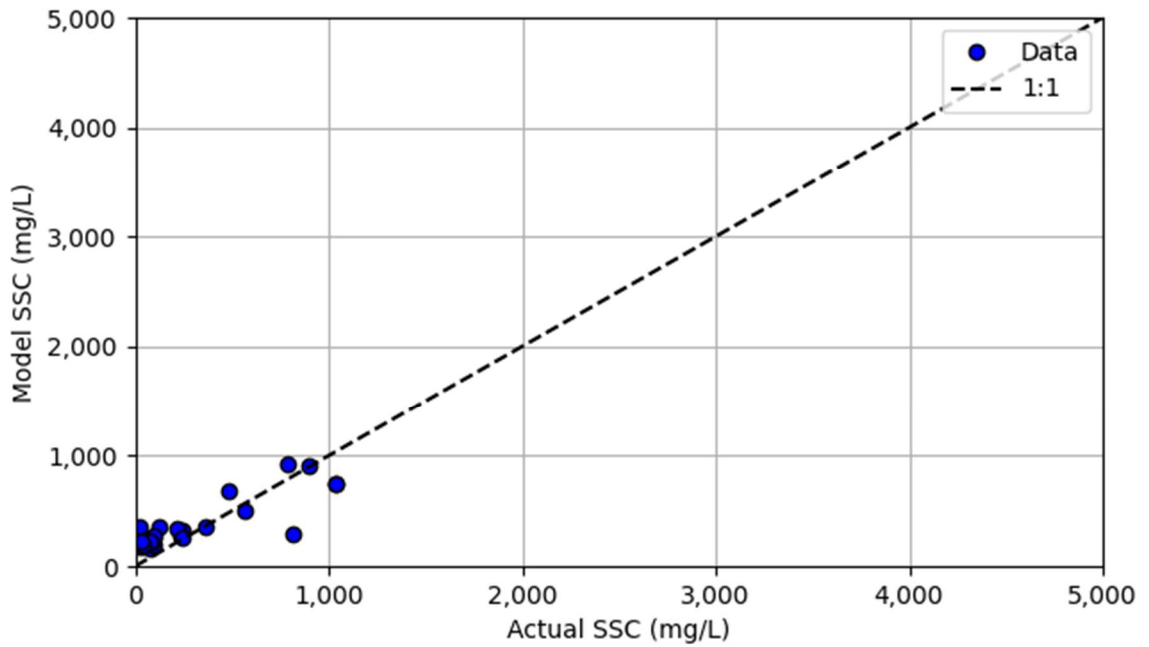


**Figure C-51:** Rating Curve for SSC vs. Depth Performance for the (a) Training Data Set and (b) Test Data Set

a)
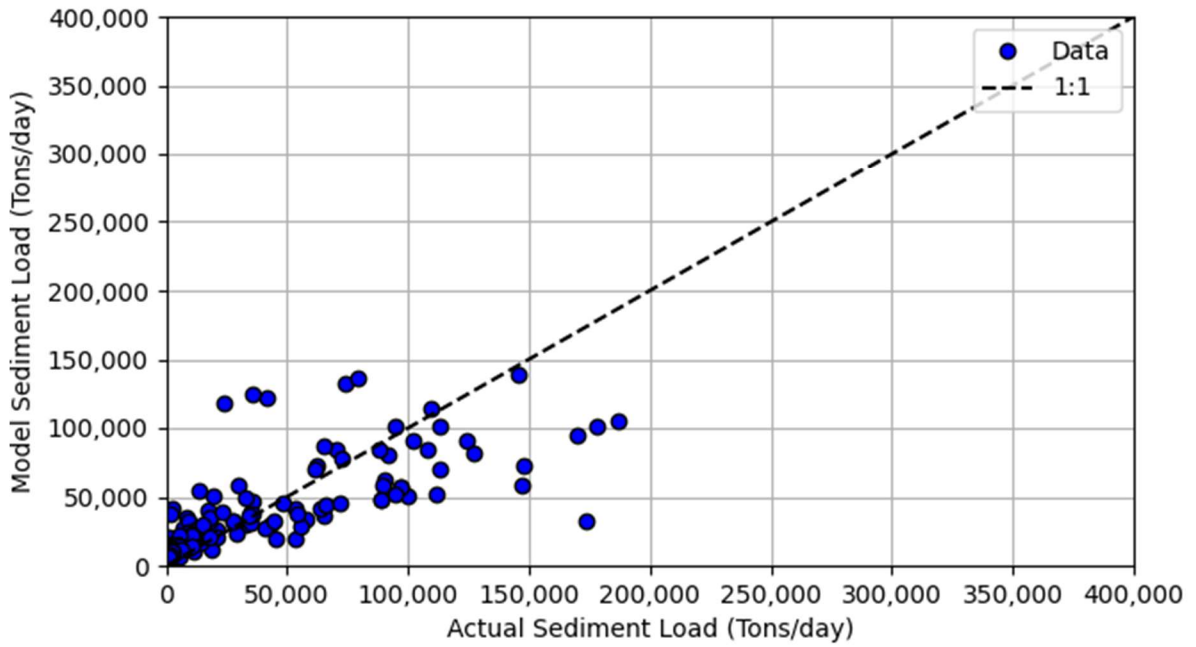


b)
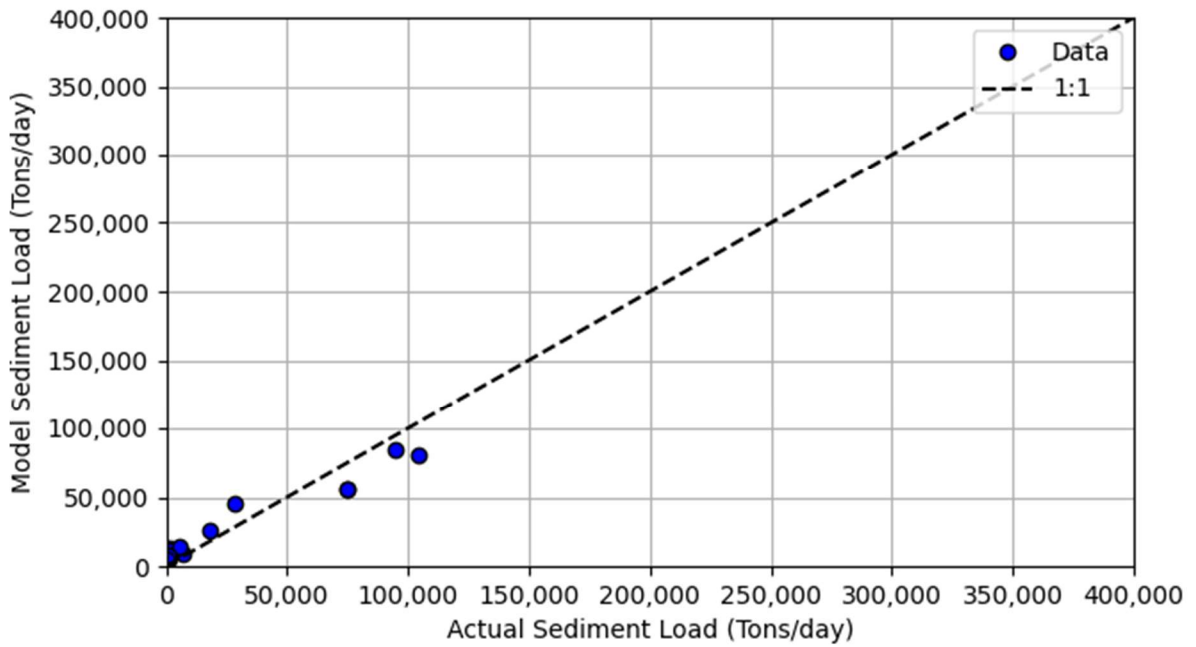


**Figure C-52:** Rating Curve for Sediment Load vs. Depth Performance for the (a) Training Data Set and (b) Test Data Set

# Appendix D – Data Used for Thesis

**Table D-1:** Brazos River SSC and Satellite Image Pairs

| Date of SSC | SSC Site | SSC (mg/l) | Date of Satellite Image | Satellite | Blue | Green | Red | NIR | ~1500 nm | ~2100 nm | Use? | Date Lag |
|---|---|---|---|---|---|---|---|---|---|---|---|---|
| 4/29/1985 | TCEQMAIN-11843 | 12 | 4/30/1985 | LT05 | 0.0717 | 0.1076 | 0.0971 | 0.0962 | 0.0345 | 0.0204 | Y | -1 |
| 12/16/1987 | TCEQMAIN-11843 | 7 | 12/16/1987 | LT05 | 0.0573 | 0.0874 | 0.0672 | 0.0203 | 0.0097 | 0.0038 | Y | 0 |
| 12/15/1988 | TCEQMAIN-11843 | 10 | 12/18/1988 | LT05 | 0.0490 | 0.0628 | 0.0412 | 0.0148 | 0.0110 | 0.0083 | Y | -3 |
| 6/18/1991 | TCEQMAIN-11843 | 240 | 6/18/1991 | LT05 | 0.0592 | 0.1130 | 0.1540 | 0.1400 | 0.0181 | 0.0090 | Y | 0 |
| 6/18/1992 | TCEQMAIN-11843 | 855 | 6/20/1992 | LT05 | 0.1128 | 0.1410 | 0.1533 | 0.1708 | 0.0416 | 0.0302 | Y | -2 |
| 12/20/1994 | TCEQMAIN-11843 | 890 | 12/19/1994 | LT05 | 0.0702 | 0.1176 | 0.1601 | 0.1849 | 0.0089 | 0.0049 | Y | 1 |
| 10/21/1996 | TCEQMAIN-11843 | 21 | 10/21/1996 | LT05 | 0.0504 | 0.0822 | 0.0600 | 0.0464 | 0.0212 | 0.0110 | Y | 0 |
| 2/26/1998 | TCEQMAIN-11843 | 430 | 3/1/1998 | LT05 | 0.0694 | 0.1211 | 0.1643 | 0.1750 | 0.0100 | 0.0072 | N | -3 |
| 3/19/1998 | TCEQMAIN-11843 | 133 | 3/17/1998 | LT05 | 0.0634 | 0.1149 | 0.1425 | 0.0747 | 0.0111 | 0.0050 | Y | 2 |
| 1/28/1999 | TCEQMAIN-11843 | 27 | 1/31/1999 | LT05 | 0.0359 | 0.0633 | 0.0474 | 0.0218 | 0.0141 | 0.0078 | Y | -3 |
| 6/23/1999 | TCEQMAIN-11843 | 42 | 6/24/1999 | LT05 | 0.0703 | 0.1055 | 0.1070 | 0.0765 | 0.0438 | 0.0291 | Y | -1 |
| 10/25/1999 | TCEQMAIN-11843 | 36 | 10/22/1999 | LE07 | 0.0321 | 0.0495 | 0.0324 | 0.0187 | 0.0094 | 0.0050 | Y | 3 |
| 3/29/2000 | TCEQMAIN-11843 | 18 | 3/30/2000 | LE07 | 0.0380 | 0.0659 | 0.0471 | 0.0387 | 0.0173 | 0.0123 | Y | -1 |
| 4/17/2000 | TCEQMAIN-11843 | 25 | 4/15/2000 | LE07 | 0.0514 | 0.0769 | 0.0612 | 0.0512 | 0.0274 | 0.0195 | Y | 2 |
| 8/22/2000 | TCEQMAIN-16355 | 38 | 8/21/2000 | LE07 | 0.0825 | 0.1139 | 0.1165 | 0.1315 | 0.0453 | 0.0240 | Y | 1 |
| 10/23/2000 | TCEQMAIN-16355 | 42 | 10/24/2000 | LE07 | 0.1630 | 0.1888 | 0.1831 | 0.2718 | 0.2071 | 0.1418 | N | -1 |
| 10/26/2000 | TCEQMAIN-11843 | 13 | 10/24/2000 | LE07 | 0.0616 | 0.0804 | 0.0553 | 0.0669 | 0.0332 | 0.0214 | Y | 2 |
| 4/16/2001 | TCEQMAIN-16355 | 172 | 4/18/2001 | LE07 | 0.0564 | 0.1038 | 0.1404 | 0.1320 | 0.0170 | 0.0110 | Y | -2 |
| 5/21/2001 | TCEQMAIN-16355 | 290 | 5/20/2001 | LE07 | 0.0730 | 0.1155 | 0.1431 | 0.1799 | 0.0494 | 0.0285 | Y | 1 |
| 6/18/2001 | TCEQMAIN-16355 | 975 | 6/21/2001 | LE07 | 0.0667 | 0.1178 | 0.1688 | 0.1727 | 0.0171 | 0.0086 | Y | -3 |
| 6/27/2001 | TCEQMAIN-11843 | 8 | 6/29/2001 | LT05 | 0.0659 | 0.1131 | 0.1226 | 0.0644 | 0.0259 | 0.0159 | Y | -2 |
| 8/13/2001 | TCEQMAIN-16355 | 73 | 8/16/2001 | LT05 | 0.0548 | 0.1046 | 0.1018 | 0.1021 | 0.0581 | 0.0416 | Y | -3 |
| 9/18/2001 | TCEQMAIN-16355 | 274 | 9/17/2001 | LT05 | 0.0558 | 0.0949 | 0.1158 | 0.1248 | 0.0143 | 0.0107 | Y | 1 |
| 12/17/2001 | TCEQMAIN-16355 | 204 | 12/14/2001 | LE07 | 0.0744 | 0.1110 | 0.1558 | 0.1700 | 0.0109 | 0.0050 | N | 3 |
| 1/9/2002 | TCEQMAIN-11843 | 74 | 1/7/2002 | LT05 | 0.0632 | 0.1063 | 0.1303 | 0.0758 | 0.0085 | 0.0042 | Y | 2 |
| 1/14/2002 | TCEQMAIN-16355 | 272 | 1/15/2002 | LE07 | 0.0679 | 0.1099 | 0.1422 | 0.0847 | 0.0127 | 0.0077 | Y | -1 |
| 6/11/2002 | TCEQMAIN-16355 | 166 | 6/8/2002 | LE07 | 0.0513 | 0.0855 | 0.1073 | 0.1073 | 0.0151 | 0.0101 | Y | 3 |
| 6/13/2002 | TCEQMAIN-11843 | 11 | 6/16/2002 | LT05 | 0.0243 | 0.0439 | 0.0361 | 0.0573 | 0.0380 | 0.0264 | Y | -3 |
| 7/17/2002 | TCEQMAIN-16355 | 724 | 7/18/2002 | LT05 | 0.0782 | 0.1361 | 0.1804 | 0.2071 | 0.0242 | 0.0201 | Y | -1 |
| 10/8/2002 | TCEQMAIN-11843 | 12 | 10/6/2002 | LT05 | 0.0416 | 0.0445 | 0.0351 | 0.0225 | 0.0133 | 0.0092 | Y | 2 |
| 10/30/2002 | TCEQMAIN-16355 | 466 | 10/30/2002 | LE07 | 0.0596 | 0.1035 | 0.1512 | 0.1492 | 0.0077 | 0.0040 | Y | 0 |
| 12/17/2002 | TCEQMAIN-16355 | 423 | 12/17/2002 | LE07 | 0.0645 | 0.0903 | 0.1177 | 0.0960 | 0.0112 | 0.0096 | Y | 0 |
| 3/26/2003 | TCEQMAIN-11843 | 24 | 3/23/2003 | LE07 | 0.0639 | 0.1033 | 0.1139 | 0.0502 | 0.0140 | 0.0071 | Y | 3 |
| 6/17/2003 | TCEQMAIN-16355 | 280 | 6/19/2003 | LT05 | 0.0863 | 0.1358 | 0.1438 | 0.1414 | 0.0324 | 0.0264 | Y | -2 |

| 7/28/2003 | TCEQMAIN-16355 | 20 | 7/29/2003 | LE07 | 0.0592 | 0.1004 | 0.1015 | 0.1099 | 0.0328 | 0.0165 | Y | -1 |
| 9/10/2003 | TCEQMAIN-11843 | 19 | 9/7/2003 | LT05 | 0.0426 | 0.0792 | 0.0783 | 0.0288 | 0.0079 | 0.0053 | Y | 3 |
| 10/14/2003 | TCEQMAIN-16355 | 195 | 10/17/2003 | LE07 | 0.0848 | 0.1323 | 0.1899 | 0.2004 | 0.0159 | 0.0102 | N | -3 |
| 12/2/2003 | TCEQMAIN-11843 | 73 | 12/4/2003 | LE07 | 0.0644 | 0.0948 | 0.1157 | 0.0639 | 0.0313 | 0.0217 | Y | -2 |
| 3/30/2004 | TCEQMAIN-11843 | 32 | 4/2/2004 | LT05 | 0.0567 | 0.0944 | 0.0803 | 0.0372 | 0.0226 | 0.0106 | Y | -3 |
| 6/22/2004 | TCEQMAIN-11843 | 372 | 6/21/2004 | LT05 | 0.0992 | 0.1632 | 0.2182 | 0.2039 | 0.0376 | 0.0276 | Y | 1 |
| 3/31/2005 | TCEQMAIN-11843 | 44 | 3/28/2005 | LE07 | 0.0590 | 0.1050 | 0.1389 | 0.0686 | 0.0121 | 0.0078 | Y | 3 |
| 5/25/2005 | TCEQMAIN-16355 | 74 | 5/23/2005 | LT05 | 0.0279 | 0.0407 | 0.0335 | 0.0531 | 0.0237 | 0.0138 | Y | 2 |
| 10/4/2005 | TCEQMAIN-11843 | 14 | 10/6/2005 | LE07 | 0.0245 | 0.0397 | 0.0192 | 0.0269 | 0.0077 | 0.0041 | Y | -2 |
| 2/1/2006 | TCEQMAIN-16355 | 57 | 2/3/2006 | LT05 | 0.0386 | 0.0576 | 0.0492 | 0.0496 | 0.0316 | 0.0300 | Y | -2 |
| 3/20/2007 | TCEQMAIN-11843 | 744 | 3/18/2007 | LE07 | 0.0781 | 0.1190 | 0.1532 | 0.1839 | 0.0235 | 0.0123 | N | 2 |
| 1/29/2008 | TCEQMAIN-11843 | 18 | 2/1/2008 | LE07 | 0.0431 | 0.0659 | 0.0649 | 0.0272 | 0.0100 | 0.0095 | Y | -3 |
| 3/11/2008 | TCEQMAIN-11843 | 39 | 3/12/2008 | LT05 | 0.0457 | 0.0801 | 0.0698 | 0.0364 | 0.0132 | 0.0072 | Y | -1 |
| 4/28/2008 | USGS-08116650 | 178 | 4/29/2008 | LT05 | 0.0426 | 0.0896 | 0.0871 | 0.0923 | 0.0219 | 0.0122 | Y | -1 |
| 5/28/2008 | USGS-08116650 | 557 | 5/31/2008 | LT05 | 0.0659 | 0.1320 | 0.1527 | 0.1322 | 0.0182 | 0.0107 | Y | -3 |
| 6/17/2008 | USGS-08116650 | 100 | 6/16/2008 | LT05 | 0.0665 | 0.1013 | 0.0928 | 0.0588 | 0.0420 | 0.0259 | Y | 1 |
| 11/17/2008 | USGS-08116650 | 818 | 11/15/2008 | LE07 | 0.0701 | 0.1149 | 0.1772 | 0.2131 | 0.0133 | 0.0058 | N | 2 |
| 2/25/2009 | USGS-08116650 | 44 | 2/27/2009 | LT05 | 0.0695 | 0.1005 | 0.0871 | 0.1032 | 0.0699 | 0.0480 | Y | -2 |
| 5/19/2009 | USGS-08116650 | 126 | 5/18/2009 | LT05 | 0.0444 | 0.0896 | 0.1034 | 0.0924 | 0.0117 | 0.0099 | Y | 1 |
| 6/24/2009 | USGS-08116650 | 41 | 6/27/2009 | LE07 | 0.0586 | 0.0982 | 0.1143 | 0.1281 | 0.0784 | 0.0572 | Y | -3 |
| 7/28/2009 | USGS-08116650 | 57 | 7/29/2009 | LE07 | 0.0698 | 0.1012 | 0.0996 | 0.1367 | 0.0747 | 0.0437 | Y | -1 |
| 8/25/2009 | USGS-08116650 | 82 | 8/22/2009 | LT05 | 0.0463 | 0.0965 | 0.0953 | 0.0774 | 0.0315 | 0.0218 | Y | 3 |
| 9/10/2009 | USGS-08116650 | 334 | 9/7/2009 | LT05 | 0.0660 | 0.1120 | 0.1037 | 0.0691 | 0.0352 | 0.0206 | Y | 3 |
| 10/8/2009 | TCEQMAIN-11843 | 24 | 10/9/2009 | LT05 | 0.2096 | 0.2584 | 0.2485 | 0.3510 | 0.2812 | 0.2007 | N | -1 |
| 11/19/2009 | USGS-08116650 | 653 | 11/18/2009 | LE07 | 0.0632 | 0.1121 | 0.1574 | 0.1170 | 0.0120 | 0.0067 | Y | 1 |
| 1/12/2010 | TCEQMAIN-11843 | 22 | 1/13/2010 | LT05 | 0.0542 | 0.0955 | 0.0790 | 0.0331 | 0.0100 | 0.0079 | Y | -1 |
| 6/8/2010 | TCEQMAIN-11843 | 31 | 6/6/2010 | LT05 | 0.0685 | 0.1096 | 0.1046 | 0.0625 | 0.0265 | 0.0201 | Y | 2 |
| 11/18/2010 | USGS-08116650 | 131 | 11/21/2010 | LE07 | 0.0465 | 0.0735 | 0.0545 | 0.0548 | 0.0254 | 0.0155 | Y | -3 |
| 3/23/2011 | USGS-08116650 | 85 | 3/21/2011 | LT05 | 0.0739 | 0.1018 | 0.0855 | 0.0832 | 0.0480 | 0.0314 | Y | 2 |
| 4/13/2011 | USGS-08116650 | 74 | 4/14/2011 | LE07 | 0.1337 | 0.1275 | 0.1127 | 0.1581 | 0.0848 | 0.0594 | Y | -1 |
| 6/1/2011 | USGS-08116650 | 65 | 6/1/2011 | LE07 | 0.0655 | 0.0969 | 0.0996 | 0.1706 | 0.1228 | 0.0824 | Y | 0 |
| 6/22/2011 | USGS-08116650 | 66 | 6/25/2011 | LT05 | 0.0643 | 0.1123 | 0.1135 | 0.1394 | 0.1287 | 0.0845 | Y | -3 |
| 8/17/2011 | USGS-08116650 | 56 | 8/20/2011 | LE07 | 0.0417 | 0.0470 | 0.0365 | 0.0625 | 0.0251 | 0.0147 | Y | -3 |
| 1/10/2012 | USGS-08116650 | 2062 | 1/11/2012 | LE07 | 0.0675 | 0.1122 | 0.1640 | 0.1622 | 0.0170 | 0.0111 | N | -1 |
| 1/11/2012 | USGS-08116650 | 773 | 1/11/2012 | LE07 | 0.0675 | 0.1122 | 0.1640 | 0.1622 | 0.0170 | 0.0111 | Y | 0 |
| 1/28/2012 | USGS-08116650 | 863 | 1/27/2012 | LE07 | 0.0623 | 0.1141 | 0.1642 | 0.1625 | 0.0168 | 0.0114 | N | 1 |
| 1/30/2012 | USGS-08116650 | 4185 | 1/27/2012 | LE07 | 0.0623 | 0.1141 | 0.1642 | 0.1625 | 0.0168 | 0.0114 | N | 3 |
| 8/21/2012 | USGS-08116650 | 151 | 8/22/2012 | LE07 | 0.0683 | 0.1047 | 0.1033 | 0.1151 | 0.0392 | 0.0228 | Y | -1 |

| | | | | | | | | | | | | | |
|---|---|---|---|---|---|---|---|---|---|---|---|---|---|
| 12/12/2012 | USGS-08116650 | 117 | 12/12/2012 | LE07 | 0.0603 | 0.0888 | 0.1033 | 0.0727 | 0.0359 | 0.0258 | Y | 0 |
| 2/13/2013 | USGS-08116650 | 45 | 2/14/2013 | LE07 | 0.0520 | 0.0879 | 0.0949 | 0.0553 | 0.0305 | 0.0201 | Y | -1 |
| 3/20/2013 | TCEQMAIN-16355 | 74 | 3/18/2013 | LE07 | 0.0466 | 0.0738 | 0.0678 | 0.0787 | 0.0407 | 0.0298 | Y | 2 |
| 5/20/2013 | USGS-08116650 | 236 | 5/21/2013 | LE07 | 0.0609 | 0.1008 | 0.1270 | 0.1506 | 0.0407 | 0.0282 | Y | -1 |
| 5/22/2013 | TCEQMAIN-16355 | 162 | 5/21/2013 | LE07 | 0.0609 | 0.1008 | 0.1270 | 0.1506 | 0.0407 | 0.0282 | Y | 1 |
| 8/7/2013 | USGS-08116650 | 32 | 8/9/2013 | LE07 | 0.0564 | 0.0956 | 0.0979 | 0.1014 | 0.0457 | 0.0258 | Y | -2 |
| 3/19/2014 | TCEQMAIN-11843 | 7 | 3/21/2014 | LE07 | 0.0424 | 0.0633 | 0.0605 | 0.0409 | 0.0210 | 0.0175 | Y | -2 |
| 5/14/2014 | TCEQMAIN-16355 | 247 | 5/16/2014 | LC08 | 0.0706 | 0.1155 | 0.1633 | 0.1633 | 0.0294 | 0.0220 | N | -2 |
| 7/9/2014 | USGS-08116650 | 142 | 7/11/2014 | LE07 | 0.0683 | 0.1102 | 0.1138 | 0.1834 | 0.0638 | 0.0343 | Y | -2 |
| 11/25/2014 | TCEQMAIN-16355 | 53 | 11/24/2014 | LC08 | 0.0408 | 0.0746 | 0.1034 | 0.0552 | 0.0178 | 0.0109 | Y | 1 |
| 1/28/2015 | TCEQMAIN-16355 | 1445 | 1/27/2015 | LC08 | 0.0713 | 0.1211 | 0.1708 | 0.2094 | 0.0097 | 0.0073 | Y | 1 |
| 2/10/2015 | USGS-08116650 | 115 | 2/12/2015 | LC08 | 0.0458 | 0.0909 | 0.1046 | 0.0452 | 0.0145 | 0.0102 | Y | -2 |
| 3/25/2015 | TCEQMAIN-16355 | 300 | 3/24/2015 | LE07 | 0.0871 | 0.1437 | 0.2084 | 0.1975 | 0.0263 | 0.0206 | N | 1 |
| 4/30/2015 | TCEQMAIN-16355 | 356 | 5/3/2015 | LC08 | 0.0576 | 0.1076 | 0.1583 | 0.1010 | 0.0111 | 0.0068 | Y | -3 |
| 5/27/2015 | TCEQMAIN-16355 | 153 | 5/27/2015 | LE07 | 0.0667 | 0.1142 | 0.1557 | 0.1789 | 0.0360 | 0.0150 | Y | 0 |
| 6/5/2015 | USGS-08116650 | 240 | 6/4/2015 | LC08 | 0.0497 | 0.1013 | 0.1470 | 0.0796 | 0.0065 | 0.0037 | Y | 1 |
| 7/9/2015 | TCEQMAIN-11843 | 538 | 7/6/2015 | LC08 | 0.0897 | 0.1497 | 0.1870 | 0.2175 | 0.0968 | 0.0649 | N | 3 |
| 8/12/2015 | USGS-08116650 | 306 | 8/15/2015 | LE07 | 0.0561 | 0.0917 | 0.1053 | 0.0969 | 0.0196 | 0.0124 | Y | -3 |
| 9/29/2015 | TCEQMAIN-16355 | 99 | 10/2/2015 | LE07 | 0.0289 | 0.0504 | 0.0472 | 0.0557 | 0.0102 | 0.0041 | Y | -3 |
| 10/21/2015 | USGS-08116650 | 26 | 10/18/2015 | LE07 | 0.0276 | 0.0458 | 0.0363 | 0.0569 | 0.0145 | 0.0089 | Y | 3 |
| 10/28/2015 | TCEQMAIN-16355 | 1520 | 10/26/2015 | LC08 | 0.0550 | 0.0994 | 0.1426 | 0.1030 | 0.0087 | 0.0062 | N | 2 |
| 1/20/2016 | USGS-08116650 | 432 | 1/22/2016 | LE07 | 0.0499 | 0.0732 | 0.0957 | 0.0741 | 0.0110 | 0.0112 | Y | -2 |
| 1/27/2016 | TCEQMAIN-16355 | 287 | 1/30/2016 | LC08 | 0.0583 | 0.1184 | 0.1674 | 0.0850 | 0.0158 | 0.0132 | Y | -3 |
| 4/5/2016 | USGS-08116650 | 364 | 4/3/2016 | LC08 | 0.0595 | 0.1087 | 0.1550 | 0.0884 | 0.0072 | 0.0058 | Y | 2 |
| 4/26/2016 | USGS-08116650 | 411 | 4/27/2016 | LE07 | 0.0627 | 0.1119 | 0.1570 | 0.1665 | 0.0228 | 0.0120 | N | -1 |
| 4/27/2016 | TCEQMAIN-16355 | 213 | 4/27/2016 | LE07 | 0.0627 | 0.1119 | 0.1570 | 0.1665 | 0.0228 | 0.0120 | Y | 0 |
| 5/5/2016 | TCEQMAIN-11843 | 773 | 5/5/2016 | LC08 | 0.0638 | 0.1158 | 0.1729 | 0.1470 | 0.0134 | 0.0106 | Y | 0 |
| 5/12/2016 | USGS-08116650 | 676 | 5/13/2016 | LE07 | 0.0710 | 0.1204 | 0.1677 | 0.1837 | 0.0193 | 0.0080 | Y | -1 |
| 6/28/2016 | TCEQMAIN-16355 | 578 | 6/30/2016 | LE07 | 0.0611 | 0.1146 | 0.1761 | 0.1696 | 0.0095 | 0.0055 | Y | -2 |
| 7/11/2016 | TCEQMAIN-16355 | 1040 | 7/8/2016 | LC08 | 0.0574 | 0.1151 | 0.1703 | 0.1612 | 0.0277 | 0.0148 | Y | 3 |
| 7/11/2016 | USGS-08116650 | 1040 | 7/8/2016 | LC08 | 0.0574 | 0.1151 | 0.1703 | 0.1612 | 0.0277 | 0.0148 | Y | 3 |
| 7/26/2016 | USGS-08116650 | 866 | 7/24/2016 | LC08 | 0.0672 | 0.1247 | 0.1806 | 0.1519 | 0.0168 | 0.0102 | Y | 2 |
| 7/27/2016 | TCEQMAIN-16355 | 1357 | 7/24/2016 | LC08 | 0.0672 | 0.1247 | 0.1806 | 0.1519 | 0.0168 | 0.0102 | N | 3 |
| 8/24/2016 | TCEQMAIN-16355 | 1188 | 8/25/2016 | LC08 | 0.0256 | 0.0574 | 0.0769 | 0.1156 | 0.0240 | 0.0176 | Y | -1 |
| 10/18/2016 | USGS-08116650 | 69 | 10/20/2016 | LE07 | 0.0461 | 0.0722 | 0.0613 | 0.0690 | 0.0117 | 0.0090 | Y | -2 |
| 10/26/2016 | TCEQMAIN-16355 | 65 | 10/28/2016 | LC08 | 0.0206 | 0.0496 | 0.0384 | 0.0249 | 0.0185 | 0.0117 | Y | -2 |
| 10/31/2016 | TCEQMAIN-16355 | 65 | 10/28/2016 | LC08 | 0.0206 | 0.0496 | 0.0384 | 0.0249 | 0.0185 | 0.0117 | N | 3 |
| 10/31/2016 | USGS-08116650 | 65 | 10/28/2016 | LC08 | 0.0206 | 0.0496 | 0.0384 | 0.0249 | 0.0185 | 0.0117 | N | 3 |

| | | | | | | | | | | | | |
|---|---|---|---|---|---|---|---|---|---|---|---|---|
| 11/29/2016 | TCEQMAIN-16355 | 137 | 11/29/2016 | LC08 | 0.0240 | 0.0610 | 0.0595 | 0.0853 | 0.0706 | 0.0483 | Y | 0 |
| 1/25/2017 | TCEQMAIN-16355 | 1197 | 1/24/2017 | LE07 | 0.0673 | 0.1172 | 0.1735 | 0.1839 | 0.0119 | 0.0040 | Y | 1 |
| 2/22/2017 | TCEQMAIN-16355 | 1420 | 2/25/2017 | LE07 | 0.0676 | 0.1120 | 0.1677 | 0.1720 | 0.0184 | 0.0103 | Y | -3 |
| 3/21/2017 | TCEQMAIN-11843 | 40 | 3/21/2017 | LC08 | 0.0519 | 0.0955 | 0.0914 | 0.0268 | 0.0140 | 0.0106 | Y | 0 |
| 4/5/2017 | USGS-08116650 | 338 | 4/6/2017 | LC08 | 0.0537 | 0.1040 | 0.1468 | 0.0968 | 0.0046 | 0.0045 | Y | -1 |
| 5/23/2017 | TCEQMAIN-16355 | 820 | 5/24/2017 | LC08 | 0.0554 | 0.0996 | 0.1336 | 0.1221 | 0.0151 | 0.0115 | Y | -1 |
| 6/6/2017 | USGS-08116650 | 517 | 6/9/2017 | LC08 | 0.0405 | 0.0834 | 0.1064 | 0.1643 | 0.0299 | 0.0213 | Y | -3 |
| 6/12/2017 | TCEQMAIN-16355 | 380 | 6/9/2017 | LC08 | 0.0405 | 0.0834 | 0.1064 | 0.1643 | 0.0299 | 0.0213 | Y | 3 |
| 6/12/2017 | USGS-08116650 | 380 | 6/9/2017 | LC08 | 0.0405 | 0.0834 | 0.1064 | 0.1643 | 0.0299 | 0.0213 | Y | 3 |
| 7/10/2017 | TCEQMAIN-16355 | 259 | 7/11/2017 | LC08 | 0.0497 | 0.0994 | 0.1209 | 0.0736 | 0.0124 | 0.0071 | N | -1 |
| 7/10/2017 | USGS-08116650 | 259 | 7/11/2017 | LC08 | 0.0497 | 0.0994 | 0.1209 | 0.0736 | 0.0124 | 0.0071 | N | -1 |
| 7/11/2017 | USGS-08116650 | 243 | 7/11/2017 | LC08 | 0.0497 | 0.0994 | 0.1209 | 0.0736 | 0.0124 | 0.0071 | Y | 0 |
| 7/25/2017 | USGS-08116650 | 102 | 7/27/2017 | LC08 | 0.0338 | 0.0679 | 0.0698 | 0.0396 | 0.0208 | 0.0133 | N | -2 |
| 7/26/2017 | TCEQMAIN-16355 | 90 | 7/27/2017 | LC08 | 0.0338 | 0.0679 | 0.0698 | 0.0396 | 0.0208 | 0.0133 | Y | -1 |
| 8/15/2017 | USGS-08116650 | 165 | 8/12/2017 | LC08 | 0.0558 | 0.1047 | 0.1388 | 0.1108 | 0.0202 | 0.0113 | Y | 3 |
| 8/22/2017 | TCEQMAIN-16355 | 58 | 8/20/2017 | LE07 | 0.0139 | 0.0219 | 0.0149 | 0.0302 | 0.0132 | 0.0068 | Y | 2 |
| 9/8/2017 | USGS-08116650 | 1940 | 9/5/2017 | LE07 | 0.0955 | 0.1335 | 0.1634 | 0.1668 | 0.0679 | 0.0458 | N | 3 |
| 9/27/2017 | TCEQMAIN-16355 | 116 | 9/29/2017 | LC08 | 0.0520 | 0.0952 | 0.1099 | 0.1083 | 0.0561 | 0.0358 | Y | -2 |
| 10/18/2017 | USGS-08116650 | 118 | 10/15/2017 | LC08 | 0.0119 | 0.0218 | 0.0192 | 0.0201 | 0.0123 | 0.0089 | Y | 3 |
| 10/25/2017 | TCEQMAIN-16355 | 126 | 10/23/2017 | LE07 | 0.0533 | 0.0917 | 0.1248 | 0.1168 | 0.0061 | 0.0022 | Y | 2 |
| 11/29/2017 | TCEQMAIN-16355 | 35 | 12/2/2017 | LC08 | 0.0367 | 0.0720 | 0.0754 | 0.0679 | 0.0550 | 0.0371 | Y | -3 |
| 12/12/2017 | USGS-08116650 | 99 | 12/10/2017 | LE07 | 0.0522 | 0.0918 | 0.1029 | 0.1035 | 0.0331 | 0.0187 | Y | 2 |
| 4/25/2018 | TCEQMAIN-16355 | 231 | 4/25/2018 | LC08 | 0.0413 | 0.0842 | 0.0998 | 0.0722 | 0.0119 | 0.0075 | Y | 0 |
| 7/24/2018 | USGS-08116650 | 40 | 7/22/2018 | LE07 | 0.0424 | 0.0730 | 0.0753 | 0.1253 | 0.0724 | 0.0385 | Y | 2 |
| 8/7/2018 | USGS-08116650 | 96 | 8/7/2018 | LE07 | 0.0435 | 0.0825 | 0.0859 | 0.1192 | 0.0523 | 0.0298 | Y | 0 |
| 8/22/2018 | TCEQMAIN-16355 | 120 | 8/23/2018 | LE07 | 0.0649 | 0.1030 | 0.1054 | 0.1572 | 0.0912 | 0.0591 | Y | -1 |
| 9/19/2018 | TCEQMAIN-11843 | 13 | 9/16/2018 | LC08 | 0.0181 | 0.0289 | 0.0253 | 0.0116 | 0.0075 | 0.0051 | Y | 3 |
| 10/9/2018 | USGS-08116650 | 232 | 10/10/2018 | LE07 | 0.0537 | 0.0993 | 0.1359 | 0.1257 | 0.0356 | 0.0192 | Y | -1 |
| 12/20/2018 | TCEQMAIN-11843 | 433 | 12/21/2018 | LC08 | 0.0654 | 0.1159 | 0.1680 | 0.1072 | 0.0053 | 0.0041 | Y | -1 |
| 3/27/2019 | TCEQMAIN-16355 | 239 | 3/27/2019 | LC08 | 0.0582 | 0.1068 | 0.1417 | 0.0707 | 0.0176 | 0.0130 | Y | 0 |
| 4/23/2019 | USGS-08116650 | 1190 | 4/20/2019 | LE07 | 0.0609 | 0.1087 | 0.1554 | 0.1570 | 0.0169 | 0.0114 | Y | 3 |
| 5/28/2019 | USGS-08116650 | 902 | 5/30/2019 | LC08 | 0.0601 | 0.1144 | 0.1662 | 0.1516 | 0.0197 | 0.0113 | N | -2 |
| 5/29/2019 | TCEQMAIN-16355 | 792 | 5/30/2019 | LC08 | 0.0601 | 0.1144 | 0.1662 | 0.1516 | 0.0197 | 0.0113 | Y | -1 |
| 6/18/2019 | USGS-08116650 | 1450 | 6/15/2019 | LC08 | 0.0649 | 0.1250 | 0.1846 | 0.1708 | 0.0253 | 0.0149 | Y | 3 |
| 7/23/2019 | USGS-08116650 | 352 | 7/25/2019 | LE07 | 0.0481 | 0.0931 | 0.1149 | 0.1205 | 0.0183 | 0.0067 | Y | -2 |
| 7/30/2019 | TCEQMAIN-16355 | 22 | 8/2/2019 | LC08 | 0.0514 | 0.0963 | 0.1147 | 0.0705 | 0.0136 | 0.0093 | Y | -3 |
| 10/8/2019 | USGS-08116650 | 27 | 10/5/2019 | LC08 | 0.0211 | 0.0552 | 0.0455 | 0.0564 | 0.0225 | 0.0125 | Y | 3 |
| 8/6/2020 | USGS-08116650 | 114 | 8/4/2020 | LC08 | 0.0365 | 0.0774 | 0.0833 | 0.0651 | 0.0226 | 0.0135 | Y | 2 |

| | | | | | | | | | | | | |
|---|---|---|---|---|---|---|---|---|---|---|---|---|
| 8/19/2020 | USGS-08116650 | 55 | 8/20/2020 | LC08 | 0.0253 | 0.0626 | 0.0540 | 0.0376 | 0.0170 | 0.0118 | N | -1 |
| 8/20/2020 | TCEQMAIN-16355 | 39 | 8/20/2020 | LC08 | 0.0253 | 0.0626 | 0.0540 | 0.0376 | 0.0170 | 0.0118 | Y | 0 |
| 9/29/2020 | TCEQMAIN-16355 | 152 | 9/29/2020 | LE07 | 0.0488 | 0.0920 | 0.1196 | 0.1083 | 0.0221 | 0.0091 | Y | 0 |
| 10/6/2020 | USGS-08116650 | 124 | 10/7/2020 | LC08 | 0.0211 | 0.0619 | 0.0496 | 0.0325 | 0.0120 | 0.0078 | Y | -1 |
| 10/26/2020 | TCEQMAIN-16355 | 36 | 10/23/2020 | LC08 | 0.0095 | 0.0393 | 0.0295 | 0.0405 | 0.0274 | 0.0158 | Y | 3 |
| 12/8/2020 | USGS-08116650 | 73 | 12/10/2020 | LC08 | 0.0213 | 0.0516 | 0.0377 | 0.0380 | 0.0267 | 0.0175 | Y | -2 |
| 12/16/2020 | TCEQMAIN-16355 | 159 | 12/18/2020 | LE07 | 0.0434 | 0.0665 | 0.0606 | 0.0733 | 0.0360 | 0.0181 | Y | -2 |
| 3/8/2021 | USGS-08116650 | 175 | 3/8/2021 | LE07 | 0.0635 | 0.1073 | 0.1294 | 0.0931 | 0.0250 | 0.0195 | Y | 0 |
| 6/9/2021 | USGS-08116650 | 875 | 6/12/2021 | LE07 | 0.0672 | 0.1210 | 0.1748 | 0.2091 | 0.0375 | 0.0164 | Y | -3 |
| 7/13/2021 | USGS-08116650 | 786 | 7/14/2021 | LE07 | 0.0657 | 0.1193 | 0.1666 | 0.1726 | 0.0220 | 0.0132 | Y | -1 |
| 7/27/2021 | USGS-08116650 | 570 | 7/30/2021 | LE07 | 0.0605 | 0.1121 | 0.1482 | 0.1288 | 0.0160 | 0.0040 | Y | -3 |
| 1/13/2022 | TCEQMAIN-11843 | 9 | 1/14/2022 | LC08 | 0.0461 | 0.0819 | 0.0683 | 0.0354 | 0.0309 | 0.0241 | Y | -1 |
| 2/1/2022 | USGS-08116650 | 424 | 1/30/2022 | LC08 | 0.0224 | 0.0581 | 0.0532 | 0.0295 | 0.0220 | 0.0166 | Y | 2 |
| 5/17/2022 | USGS-08116650 | 209 | 5/18/2022 | LE07 | 0.0543 | 0.0871 | 0.1035 | 0.1393 | 0.0485 | 0.0308 | Y | -1 |
| 9/24/2015 | TCEQMAIN-11843 | 10.9 | 9/22/2015 | S2A | 0.0269 | 0.0492 | 0.0289 | 0.0026 | 0.0060 | 0.0063 | Y | 2 |
| 10/21/2015 | USGS-08116650 | 26 | 10/22/2015 | S2A | 0.0811 | 0.0913 | 0.0680 | 0.1025 | 0.0976 | 0.0634 | Y | -1 |
| 11/24/2015 | TCEQMAIN-16355 | 598 | 11/24/2015 | S2A | 0.0714 | 0.1257 | 0.1835 | 0.1600 | 0.0188 | 0.0110 | Y | 0 |
| 1/27/2016 | TCEQMAIN-16355 | 287 | 1/30/2016 | S2A | 0.0732 | 0.1265 | 0.1810 | 0.1082 | 0.0275 | 0.0222 | Y | -3 |
| 2/17/2016 | USGS-08116650 | 201 | 2/19/2016 | S2A | 0.0576 | 0.1054 | 0.1276 | 0.0707 | 0.0292 | 0.0213 | Y | -2 |
| 3/16/2016 | USGS-08116650 | 722 | 3/13/2016 | S2A | 0.0875 | 0.1366 | 0.2043 | 0.2218 | 0.0303 | 0.0250 | N | 3 |
| 3/30/2016 | TCEQMAIN-16355 | 396 | 4/2/2016 | S2A | 0.0843 | 0.1328 | 0.1838 | 0.1397 | 0.0411 | 0.0311 | N | -3 |
| 4/5/2016 | USGS-08116650 | 364 | 4/2/2016 | S2A | 0.0843 | 0.1328 | 0.1838 | 0.1397 | 0.0411 | 0.0311 | N | 3 |
| 4/26/2016 | USGS-08116650 | 411 | 4/29/2016 | S2A | 0.0781 | 0.1309 | 0.2017 | 0.1605 | 0.0241 | 0.0186 | N | -3 |
| 4/27/2016 | TCEQMAIN-16355 | 213 | 4/29/2016 | S2A | 0.0781 | 0.1309 | 0.2017 | 0.1605 | 0.0241 | 0.0186 | N | -2 |
| 6/28/2016 | TCEQMAIN-16355 | 578 | 6/28/2016 | S2A | 0.1332 | 0.1498 | 0.1559 | 0.2352 | 0.1782 | 0.1095 | Y | 0 |
| 7/11/2016 | TCEQMAIN-16355 | 1040 | 7/11/2016 | S2A | 0.1407 | 0.1887 | 0.2430 | 0.2407 | 0.0998 | 0.0714 | Y | 0 |
| 7/11/2016 | USGS-08116650 | 1040 | 7/11/2016 | S2A | 0.1407 | 0.1887 | 0.2430 | 0.2407 | 0.0998 | 0.0714 | Y | 0 |
| 9/28/2016 | TCEQMAIN-16355 | 24 | 9/29/2016 | S2A | 0.0533 | 0.0951 | 0.1153 | 0.0706 | 0.0190 | 0.0110 | Y | -1 |
| 10/26/2016 | TCEQMAIN-16355 | 65 | 10/26/2016 | S2A | 0.0249 | 0.0581 | 0.0364 | 0.0252 | 0.0269 | 0.0217 | Y | 0 |
| 10/31/2016 | TCEQMAIN-16355 | 65 | 10/29/2016 | S2A | 0.0389 | 0.0370 | 0.0227 | 0.0505 | 0.0292 | 0.0157 | Y | 2 |
| 10/31/2016 | USGS-08116650 | 65 | 10/29/2016 | S2A | 0.0389 | 0.0370 | 0.0227 | 0.0505 | 0.0292 | 0.0157 | Y | 2 |
| 11/29/2016 | TCEQMAIN-16355 | 137 | 11/28/2016 | S2A | 0.0465 | 0.0457 | 0.0390 | 0.0434 | 0.0336 | 0.0207 | Y | 1 |
| 1/10/2017 | USGS-08116650 | 107 | 1/7/2017 | S2A | 0.0609 | 0.1073 | 0.1514 | 0.1087 | 0.0279 | 0.0180 | Y | 3 |
| 2/22/2017 | TCEQMAIN-16355 | 1420 | 2/23/2017 | S2A | 0.0637 | 0.1099 | 0.1779 | 0.1844 | 0.0193 | 0.0169 | Y | -1 |
| 3/28/2017 | TCEQMAIN-16355 | 144 | 3/28/2017 | S2A | 0.0704 | 0.1103 | 0.1066 | 0.0918 | 0.0429 | 0.0289 | Y | 0 |
| 4/5/2017 | USGS-08116650 | 338 | 4/7/2017 | S2A | 0.0669 | 0.1097 | 0.1579 | 0.1389 | 0.0206 | 0.0121 | Y | -2 |
| 4/26/2017 | TCEQMAIN-16355 | 756 | 4/27/2017 | S2A | 0.1355 | 0.1872 | 0.2445 | 0.2155 | 0.0919 | 0.0794 | Y | -1 |
| 5/3/2017 | USGS-08116650 | 513 | 5/4/2017 | S2A | 0.0691 | 0.1153 | 0.1705 | 0.1335 | 0.0211 | 0.0147 | Y | -1 |

| 5/23/2017 | TCEQMAIN-16355 | 820 | 5/24/2017 | S2A | 0.0599 | 0.1066 | 0.1537 | 0.1136 | 0.0179 | 0.0149 | Y | -1 |
|---|---|---|---|---|---|---|---|---|---|---|---|---|
| 6/27/2017 | TCEQMAIN-16355 | 448 | 6/26/2017 | S2A | 0.2965 | 0.3499 | 0.4163 | 0.3546 | 0.1931 | 0.1682 | N | 1 |
| 6/27/2017 | USGS-08116650 | 608 | 6/26/2017 | S2A | 0.2965 | 0.3499 | 0.4163 | 0.3546 | 0.1931 | 0.1682 | Y | 1 |
| 7/10/2017 | TCEQMAIN-16355 | 259 | 7/11/2017 | S2B | 0.2313 | 0.2726 | 0.2935 | 0.2350 | 0.1719 | 0.1621 | N | -1 |
| 7/10/2017 | USGS-08116650 | 259 | 7/11/2017 | S2B | 0.2313 | 0.2726 | 0.2935 | 0.2350 | 0.1719 | 0.1621 | N | -1 |
| 7/11/2017 | USGS-08116650 | 243 | 7/11/2017 | S2B | 0.2313 | 0.2726 | 0.2935 | 0.2350 | 0.1719 | 0.1621 | Y | 0 |
| 7/25/2017 | USGS-08116650 | 102 | 7/26/2017 | S2A | 0.0665 | 0.1037 | 0.0988 | 0.0647 | 0.0422 | 0.0343 | N | -1 |
| 7/26/2017 | TCEQMAIN-16355 | 90 | 7/26/2017 | S2A | 0.0665 | 0.1037 | 0.0988 | 0.0647 | 0.0422 | 0.0343 | Y | 0 |
| 8/15/2017 | USGS-08116650 | 165 | 8/15/2017 | S2A | 0.1139 | 0.1577 | 0.1675 | 0.1325 | 0.0818 | 0.0651 | Y | 0 |
| 8/22/2017 | TCEQMAIN-16355 | 58 | 8/22/2017 | S2A | 0.0349 | 0.0730 | 0.0601 | 0.0184 | 0.0223 | 0.0151 | Y | 0 |
| 9/8/2017 | USGS-08116650 | 1940 | 9/9/2017 | S2B | 0.0883 | 0.1267 | 0.1872 | 0.1747 | 0.0412 | 0.0346 | N | -1 |
| 10/18/2017 | USGS-08116650 | 118 | 10/19/2017 | S2B | 0.0800 | 0.1131 | 0.1150 | 0.1077 | 0.0677 | 0.0520 | Y | -1 |
| 10/25/2017 | TCEQMAIN-16355 | 126 | 10/24/2017 | S2A | 0.0506 | 0.0917 | 0.1125 | 0.0732 | 0.0248 | 0.0153 | Y | 1 |
| 11/29/2017 | TCEQMAIN-16355 | 35 | 11/28/2017 | S2B | 0.0402 | 0.0705 | 0.0718 | 0.0791 | 0.0962 | 0.0652 | Y | 1 |
| 12/20/2017 | TCEQMAIN-11843 | 16 | 12/20/2017 | S2A | 0.0092 | 0.0267 | 0.0114 | 0.0006 | 0.0072 | 0.0057 | Y | 0 |
| 1/31/2018 | TCEQMAIN-16355 | 45 | 1/29/2018 | S2A | 0.0482 | 0.0862 | 0.0927 | 0.0615 | 0.0528 | 0.0394 | Y | 2 |
| 2/27/2018 | TCEQMAIN-16355 | 1212 | 2/26/2018 | S2B | 0.1462 | 0.1532 | 0.1899 | 0.2100 | 0.2714 | 0.2725 | N | 1 |
| 4/3/2018 | USGS-08116650 | 1340 | 4/2/2018 | S2A | 0.1162 | 0.1591 | 0.2140 | 0.2422 | 0.0412 | 0.0302 | N | 1 |
| 4/16/2018 | USGS-08116650 | 267 | 4/17/2018 | S2B | 0.1107 | 0.1504 | 0.1745 | 0.1537 | 0.0813 | 0.0705 | Y | -1 |
| 4/25/2018 | TCEQMAIN-16355 | 231 | 4/24/2018 | S2B | 0.0691 | 0.1076 | 0.1382 | 0.1353 | 0.0411 | 0.0284 | Y | 1 |
| 5/9/2018 | USGS-08116650 | 69 | 5/9/2018 | S2A | 0.0371 | 0.0692 | 0.0653 | 0.0287 | 0.0485 | 0.0366 | Y | 0 |
| 5/21/2018 | USGS-08116650 | 161 | 5/22/2018 | S2A | 0.1234 | 0.1715 | 0.2052 | 0.2336 | 0.1272 | 0.1037 | Y | -1 |
| 7/24/2018 | USGS-08116650 | 40 | 7/23/2018 | S2B | 0.0380 | 0.0617 | 0.0578 | 0.0408 | 0.0899 | 0.0641 | Y | 1 |
| 7/26/2018 | TCEQMAIN-11843 | 12 | 7/26/2018 | S2B | 0.2058 | 0.2237 | 0.2246 | 0.2166 | 0.2227 | 0.1994 | Y | 0 |
| 8/7/2018 | USGS-08116650 | 96 | 8/7/2018 | S2A | 0.0524 | 0.0877 | 0.0790 | 0.0440 | 0.0530 | 0.0375 | Y | 0 |
| 8/22/2018 | TCEQMAIN-16355 | 120 | 8/22/2018 | S2B | 0.0576 | 0.0913 | 0.0901 | 0.0860 | 0.0961 | 0.0674 | Y | 0 |
| 9/19/2018 | TCEQMAIN-11843 | 13 | 9/19/2018 | S2A | 0.0730 | 0.0958 | 0.0987 | 0.0530 | 0.0521 | 0.0482 | Y | 0 |
| 12/11/2018 | USGS-08116650 | 1280 | 12/10/2018 | S2B | 0.0724 | 0.1155 | 0.1812 | 0.1981 | 0.0159 | 0.0110 | Y | 1 |
| 12/20/2018 | TCEQMAIN-11843 | 433 | 12/20/2018 | S2B | 0.0736 | 0.1194 | 0.1813 | 0.1373 | 0.0084 | 0.0069 | Y | 0 |
| 1/30/2019 | TCEQMAIN-16355 | 484 | 1/29/2019 | S2B | 0.0740 | 0.1217 | 0.1832 | 0.1489 | 0.0269 | 0.0179 | Y | 1 |
| 3/27/2019 | TCEQMAIN-16355 | 239 | 3/28/2019 | S2A | 0.0998 | 0.1517 | 0.1893 | 0.1131 | 0.0448 | 0.0329 | Y | -1 |
| 4/9/2019 | USGS-08116650 | 146 | 4/9/2019 | S2B | 0.0541 | 0.0907 | 0.0908 | 0.0523 | 0.0469 | 0.0349 | Y | 0 |
| 5/21/2019 | USGS-08116650 | 1090 | 5/22/2019 | S2B | 0.3088 | 0.3633 | 0.4427 | 0.4172 | 0.2065 | 0.1903 | Y | -1 |
| 5/29/2019 | TCEQMAIN-16355 | 792 | 5/29/2019 | S2B | 0.1733 | 0.2084 | 0.2662 | 0.2721 | 0.0727 | 0.0476 | Y | 0 |
| 6/4/2019 | USGS-08116650 | 903 | 6/3/2019 | S2A | 0.0867 | 0.1329 | 0.2044 | 0.1661 | 0.0250 | 0.0169 | Y | 1 |
| 7/30/2019 | TCEQMAIN-16355 | 22 | 7/31/2019 | S2B | 0.0809 | 0.1209 | 0.1334 | 0.1150 | 0.0523 | 0.0420 | Y | -1 |
| 8/6/2019 | USGS-08116650 | 219 | 8/5/2019 | S2A | 0.0848 | 0.1270 | 0.1340 | 0.0923 | 0.0382 | 0.0255 | Y | 1 |
| 9/24/2019 | TCEQMAIN-16355 | 205 | 9/24/2019 | S2A | 0.0744 | 0.1185 | 0.1307 | 0.1131 | 0.0713 | 0.0509 | Y | 0 |

| | | | | | | | | | | | | |
|---|---|---|---|---|---|---|---|---|---|---|---|---|
| 12/3/2019 | USGS-08116650 | 28 | 12/3/2019 | S2A | 0.0327 | 0.0517 | 0.0383 | 0.0484 | 0.0597 | 0.0417 | Y | 0 |
| 12/18/2019 | TCEQMAIN-16355 | 10 | 12/18/2019 | S2B | 0.0204 | 0.0443 | 0.0275 | 0.0303 | 0.0434 | 0.0321 | Y | 0 |
| 1/7/2020 | USGS-08116650 | 70 | 1/7/2020 | S2B | 0.0269 | 0.0572 | 0.0410 | 0.0534 | 0.0705 | 0.0521 | Y | 0 |
| 1/29/2020 | TCEQMAIN-16355 | 148 | 1/29/2020 | S2A | 0.1301 | 0.1444 | 0.1400 | 0.1998 | 0.2197 | 0.1777 | Y | 0 |
| 2/26/2020 | TCEQMAIN-16355 | 842 | 2/26/2020 | S2B | 0.0677 | 0.1008 | 0.1404 | 0.1420 | 0.0242 | 0.0187 | Y | 0 |
| 3/17/2020 | USGS-08116650 | 348 | 3/17/2020 | S2B | 0.1115 | 0.1558 | 0.1965 | 0.1388 | 0.0472 | 0.0337 | Y | 0 |
| 7/7/2020 | USGS-08116650 | 75 | 7/7/2020 | S2A | 0.0598 | 0.0949 | 0.0779 | 0.0873 | 0.0701 | 0.0440 | Y | 0 |
| 8/6/2020 | USGS-08116650 | 114 | 8/6/2020 | S2A | 0.0533 | 0.0948 | 0.0897 | 0.0382 | 0.0273 | 0.0194 | Y | 0 |
| 8/19/2020 | USGS-08116650 | 55 | 8/19/2020 | S2A | 0.0401 | 0.0688 | 0.0546 | 0.0419 | 0.0294 | 0.0177 | Y | 0 |
| 8/20/2020 | TCEQMAIN-16355 | 39 | 8/19/2020 | S2A | 0.0401 | 0.0688 | 0.0546 | 0.0419 | 0.0294 | 0.0177 | N | 1 |
| 9/1/2020 | USGS-08116650 | 89 | 8/31/2020 | S2B | 0.0733 | 0.1040 | 0.0862 | 0.0810 | 0.0571 | 0.0336 | Y | 1 |
| 9/15/2020 | USGS-08116650 | 626 | 9/15/2020 | S2A | 0.0775 | 0.0935 | 0.0944 | 0.1723 | 0.1516 | 0.1072 | Y | 0 |
| 11/23/2020 | TCEQMAIN-16355 | 54 | 11/22/2020 | S2B | 0.0950 | 0.1038 | 0.0938 | 0.1806 | 0.1758 | 0.1317 | Y | 1 |
| 12/8/2020 | USGS-08116650 | 73 | 12/7/2020 | S2A | 0.0290 | 0.0645 | 0.0452 | 0.0442 | 0.0259 | 0.0151 | Y | 1 |
| 12/16/2020 | TCEQMAIN-16355 | 159 | 12/17/2020 | S2A | 0.0377 | 0.0735 | 0.0598 | 0.0575 | 0.0294 | 0.0182 | Y | -1 |
| 3/8/2021 | USGS-08116650 | 175 | 3/7/2021 | S2A | 0.0698 | 0.1150 | 0.1491 | 0.0978 | 0.0432 | 0.0306 | Y | 1 |
| 4/20/2021 | USGS-08116650 | 76 | 4/21/2021 | S2B | 0.0604 | 0.0844 | 0.0685 | 0.0808 | 0.0669 | 0.0546 | N | -1 |
| 5/25/2021 | TCEQMAIN-16355 | 488 | 5/26/2021 | S2A | 0.1665 | 0.2064 | 0.2616 | 0.2502 | 0.1097 | 0.0903 | N | -1 |
| 6/9/2021 | USGS-08116650 | 875 | 6/10/2021 | S2B | 0.2260 | 0.2373 | 0.2364 | 0.3589 | 0.2920 | 0.2750 | N | -1 |
| 8/10/2021 | USGS-08116650 | 367 | 8/9/2021 | S2B | 0.1123 | 0.1559 | 0.1954 | 0.1624 | 0.0607 | 0.0469 | Y | 1 |
| 10/6/2021 | TCEQMAIN-11843 | 174 | 10/5/2021 | S2B | 0.0763 | 0.1233 | 0.1319 | 0.0682 | 0.0086 | 0.0065 | Y | 1 |
| 10/12/2021 | USGS-08116650 | 246 | 10/13/2021 | S2A | 0.0310 | 0.0437 | 0.0384 | 0.0404 | 0.0317 | 0.0235 | Y | -1 |
| 12/7/2021 | USGS-08116650 | 35 | 12/7/2021 | S2B | 0.0146 | 0.0239 | 0.0154 | 0.0176 | 0.0236 | 0.0160 | Y | 0 |
| 1/13/2022 | TCEQMAIN-11843 | 9 | 1/13/2022 | S2B | 0.0508 | 0.0833 | 0.0645 | 0.0145 | 0.0082 | 0.0066 | Y | 0 |
| 4/19/2022 | USGS-08116650 | 87 | 4/18/2022 | S2A | 0.1422 | 0.1699 | 0.1556 | 0.1550 | 0.1488 | 0.1326 | Y | 1 |
| 5/17/2022 | USGS-08116650 | 209 | 5/16/2022 | S2B | 0.2938 | 0.3422 | 0.3830 | 0.3737 | 0.2890 | 0.2719 | Y | 1 |

**Table D-2:** San Bernard River SSC and Satellite Image Pairs

| Date of SSC | SSC Site | SSC (mg/l) | Date of Satellite Image | Satellite | Blue | Green | Red | NIR | ~1500 nm | ~2100 nm | Date Lag |
|---|---|---|---|---|---|---|---|---|---|---|---|
| 8/6/1986 | TCEQMAIN-12146 | 18 | 8/7/1986 | LT05 | 0.0331 | 0.0521 | 0.0434 | 0.0426 | 0.0239 | 0.0176 | -1 |
| 10/14/1987 | TCEQMAIN-12146 | 12 | 10/13/1987 | LT05 | 0.0308 | 0.0499 | 0.0458 | 0.0401 | 0.0169 | 0.0132 | 1 |
| 10/13/1988 | TCEQMAIN-12146 | 8 | 10/15/1988 | LT05 | 0.0261 | 0.0349 | 0.0310 | 0.0313 | 0.0218 | 0.0137 | -2 |
| 10/31/1989 | TCEQMAIN-12146 | 34 | 11/3/1989 | LT05 | 0.0316 | 0.0429 | 0.0399 | 0.0312 | 0.0209 | 0.0105 | -3 |
| 7/22/1991 | TCEQMAIN-12146 | 15 | 7/20/1991 | LT05 | 0.0698 | 0.1052 | 0.0991 | 0.1186 | 0.0600 | 0.0372 | 2 |
| 9/13/1994 | TCEQMAIN-12146 | 38 | 9/14/1994 | LT05 | 0.0669 | 0.1058 | 0.1307 | 0.1143 | 0.0208 | 0.0124 | -1 |
| 10/14/1999 | TCEQMAIN-12146 | 9 | 10/14/1999 | LT05 | 0.0557 | 0.0594 | 0.0456 | 0.0580 | 0.0249 | 0.0151 | 0 |
| 7/19/2000 | TCEQMAIN-12146 | 52 | 7/20/2000 | LE07 | 0.0326 | 0.0459 | 0.0445 | 0.0702 | 0.0298 | 0.0137 | -1 |
| 4/25/2001 | TCEQMAIN-12146 | 52 | 4/26/2001 | LT05 | 0.0834 | 0.1229 | 0.1378 | 0.1447 | 0.0537 | 0.0342 | -1 |
| 12/11/2001 | TCEQMAIN-12146 | 32 | 12/14/2001 | LE07 | 0.0495 | 0.0727 | 0.0967 | 0.0818 | 0.0094 | 0.0055 | -3 |
| 1/15/2002 | TCEQMAIN-12146 | 121 | 1/15/2002 | LE07 | 0.0656 | 0.0902 | 0.1138 | 0.0802 | 0.0171 | 0.0070 | 0 |
| 6/27/2002 | TCEQMAIN-12146 | 14 | 6/24/2002 | LE07 | 0.0410 | 0.0517 | 0.0427 | 0.0920 | 0.0152 | 0.0096 | 3 |
| 7/2/2003 | TCEQMAIN-12146 | 21 | 7/5/2003 | LT05 | 0.0624 | 0.0840 | 0.0765 | 0.1541 | 0.0733 | 0.0446 | -3 |
| 7/19/2005 | TCEQMAIN-12146 | 22 | 7/18/2005 | LE07 | 0.0676 | 0.0712 | 0.0668 | 0.1070 | 0.0553 | 0.0331 | 1 |
| 10/20/2005 | TCEQMAIN-12146 | 14 | 10/22/2005 | LE07 | 0.0302 | 0.0460 | 0.0431 | 0.0473 | 0.0124 | 0.0052 | -2 |
| 1/19/2006 | TCEQMAIN-12146 | 17 | 1/18/2006 | LT05 | 0.0251 | 0.0420 | 0.0349 | 0.0274 | 0.0255 | 0.0158 | 1 |
| 4/6/2009 | TCEQMAIN-12146 | 44 | 4/8/2009 | LE07 | 0.0283 | 0.0424 | 0.0362 | 0.0520 | 0.0259 | 0.0169 | -2 |
| 1/5/2011 | TCEQMAIN-12146 | 41 | 1/8/2011 | LE07 | 0.0469 | 0.0630 | 0.0699 | 0.0616 | 0.0391 | 0.0242 | -3 |
| 4/6/2011 | TCEQMAIN-12146 | 21 | 4/6/2011 | LT05 | 0.0325 | 0.0487 | 0.0402 | 0.0327 | 0.0253 | 0.0186 | 0 |
| 8/7/2013 | TCEQMAIN-12146 | 44 | 8/9/2013 | LE07 | 0.0442 | 0.0649 | 0.0549 | 0.0498 | 0.0128 | 0.0092 | -2 |
| 11/12/2013 | TCEQMAIN-12146 | 28 | 11/13/2013 | LE07 | 0.0427 | 0.0552 | 0.0651 | 0.0710 | 0.0339 | 0.0216 | -1 |
| 1/29/2014 | TCEQMAIN-12146 | 7 | 2/1/2014 | LE07 | 0.1539 | 0.1735 | 0.1889 | 0.3374 | 0.3477 | 0.2694 | -3 |
| 5/29/2014 | TCEQMAIN-12146 | 352 | 6/1/2014 | LC08 | 0.0435 | 0.0743 | 0.0870 | 0.0847 | 0.0376 | 0.0294 | -3 |
| 7/9/2014 | TCEQMAIN-12146 | 25 | 7/11/2014 | LE07 | 0.0510 | 0.0728 | 0.0686 | 0.1422 | 0.0552 | 0.0358 | -2 |
| 8/7/2014 | TCEQMAIN-12146 | 52 | 8/4/2014 | LC08 | 0.0201 | 0.0487 | 0.0341 | 0.0409 | 0.0204 | 0.0149 | 3 |
| 10/8/2014 | TCEQMAIN-12146 | 14 | 10/7/2014 | LC08 | 0.0123 | 0.0246 | 0.0205 | 0.0214 | 0.0171 | 0.0113 | 1 |
| 8/10/2015 | TCEQMAIN-12146 | 16.2 | 8/7/2015 | LC08 | 0.0080 | 0.0188 | 0.0156 | 0.0272 | 0.0216 | 0.0147 | 3 |
| 11/5/2015 | TCEQMAIN-12146 | 51.2 | 11/3/2015 | LE07 | 0.0231 | 0.0275 | 0.0327 | 0.0354 | 0.0117 | 0.0045 | 2 |
| 1/20/2016 | TCEQMAIN-12146 | 36.8 | 1/22/2016 | LE07 | 0.0626 | 0.0877 | 0.1125 | 0.0776 | 0.0161 | 0.0122 | -2 |
| 5/3/2016 | TCEQMAIN-12146 | 22 | 5/5/2016 | LC08 | 0.0295 | 0.0555 | 0.0688 | 0.0580 | 0.0336 | 0.0240 | -2 |
| 10/13/2016 | TCEQMAIN-12146 | 11 | 10/12/2016 | LC08 | 0.0088 | 0.0303 | 0.0296 | 0.0273 | 0.0214 | 0.0149 | 1 |
| 7/18/2017 | TCEQMAIN-12146 | 20 | 7/19/2017 | LE07 | 0.0259 | 0.0420 | 0.0488 | 0.0769 | 0.0256 | 0.0103 | -1 |
| 4/17/2018 | TCEQMAIN-12146 | 28 | 4/17/2018 | LE07 | 0.0650 | 0.0963 | 0.1143 | 0.1098 | 0.0545 | 0.0354 | 0 |
| 10/25/2018 | TCEQMAIN-12146 | 21 | 10/26/2018 | LE07 | 0.0356 | 0.0565 | 0.0745 | 0.0532 | 0.0061 | 0.0077 | -1 |
| 2/4/2020 | TCEQMAIN-12146 | 21 | 2/2/2020 | LE07 | 0.0472 | 0.0694 | 0.0892 | 0.0654 | 0.0125 | 0.0101 | 2 |
| 8/5/2021 | TCEQMAIN-12146 | 34 | 8/7/2021 | LC08 | 0.0595 | 0.1049 | 0.1239 | 0.0772 | 0.0345 | 0.0233 | -2 |

| 3/30/2017 | TCEQMAIN-12146 | 29 | 3/28/2017 | S2A | 0.0941 | 0.1217 | 0.1415 | 0.1041 | 0.0541 | 0.0374 | 2 |
| 4/17/2018 | TCEQMAIN-12146 | 28 | 4/17/2018 | S2B | 0.1170 | 0.1367 | 0.1532 | 0.1204 | 0.0797 | 0.0629 | 0 |
| 2/3/2021 | TCEQMAIN-12146 | 18 | 2/2/2021 | S2A | 0.0481 | 0.0707 | 0.0860 | 0.0376 | 0.0264 | 0.0176 | 1 |
| 4/21/2021 | TCEQMAIN-12146 | 23 | 4/21/2021 | S2B | 0.1055 | 0.1150 | 0.1065 | 0.1146 | 0.0925 | 0.0759 | 0 |

**Table D-3:** USGS-08116650 and TCEQMAIN-16355 Flow, Depth, and Sediment Data

| Date | Daily Mean Flow (cfs) | Sediment Load (Tons/day) | SSC (mg/L) | Gauge Depth (ft) |
|---|---|---|---|---|
| 10/9/1969 | 939 | 76 | 30 | None |
| 11/20/1969 | 1,900 | 686 | 134 | None |
| 12/11/1969 | 14,400 | 111,004 | 2,860 | None |
| 1/15/1970 | 6,530 | 8,800 | 500 | None |
| 2/13/1970 | 7,020 | 32,923 | 1,740 | None |
| 5/6/1970 | 9,650 | 12,901 | 496 | None |
| 6/11/1970 | 7,270 | 13,089 | 668 | None |
| 7/9/1970 | 1,330 | 244 | 68 | None |
| 8/5/1970 | 1,300 | 641 | 183 | None |
| 9/15/1970 | 1,830 | 661 | 134 | None |
| 10/14/1970 | 21,800 | 64,046 | 1,090 | None |
| 12/3/1970 | 1,240 | 107 | 32 | None |
| 12/18/1970 | 880 | 66 | 28 | None |
| 1/28/1971 | 707 | 4 | 2 | None |
| 2/18/1971 | 481 | 19 | 15 | None |
| 3/19/1971 | 90 | 3 | 14 | None |
| 4/6/1971 | 128 | 12 | 36 | None |
| 5/20/1971 | 1,540 | 3,404 | 820 | None |
| 6/16/1971 | 152 | 21 | 52 | None |
| 7/29/1971 | 277 | 34 | 46 | None |
| 8/19/1971 | 1,690 | 984 | 216 | None |
| 9/30/1971 | 1,190 | 346 | 108 | None |
| 10/22/1971 | 3,420 | 4,314 | 468 | None |
| 11/30/1971 | 4,210 | 5,367 | 473 | None |
| 12/22/1971 | 14,000 | 27,395 | 726 | None |
| 1/27/1972 | 3,290 | 2,146 | 242 | None |
| 2/9/1972 | 4,700 | 3,560 | 281 | None |
| 3/30/1972 | 727 | 129 | 66 | None |
| 4/18/1972 | 507 | 57 | 42 | None |
| 5/25/1972 | 3,310 | 3,265 | 366 | None |
| 7/27/1972 | 1,180 | 378 | 119 | None |
| 8/10/1972 | 1,560 | 509 | 121 | None |
| 8/22/1972 | 743 | 152 | 76 | None |
| 9/28/1972 | 1,030 | 366 | 132 | None |
| 10/26/1972 | 669 | 126 | 70 | None |
| 11/28/1972 | 3,170 | 2,427 | 284 | None |
| 12/20/1972 | 6,480 | 9,082 | 520 | None |
| 1/29/1973 | 21,300 | 204,954 | 3,570 | None |
| 1/30/1973 | 22,200 | 225,582 | 3,770 | None |
| 2/21/1973 | 7,840 | 10,523 | 498 | None |
| 3/30/1973 | 24,900 | 121,475 | 1,810 | None |
| 4/30/1973 | 36,100 | 212,116 | 2,180 | None |
| 5/29/1973 | 2,760 | 1,770 | 238 | None |
| 6/28/1973 | 14,200 | 35,824 | 936 | None |
| 7/24/1973 | 6,110 | 19,433 | 1,180 | None |
| 9/12/1973 | 5,840 | 11,979 | 761 | None |
| 10/12/1973 | 14,800 | 69,011 | 1,730 | None |
| 11/7/1973 | 12,600 | 5,604 | 165 | None |
| 12/27/1973 | 11,400 | 32,263 | 1,050 | None |
| 1/7/1974 | 5,020 | 2,936 | 217 | None |

| | | | | |
|---|---|---|---|---|
| 2/5/1974 | 15,600 | 28,424 | 676 | None |
| 3/18/1974 | 2,860 | 2,089 | 271 | None |
| 4/2/1974 | 2,740 | 1,543 | 209 | None |
| 5/9/1974 | 4,610 | 7,604 | 612 | None |
| 6/20/1974 | 1,090 | 256 | 87 | None |
| 7/12/1974 | 286 | 166 | 215 | None |
| 8/30/1974 | 1,650 | 302 | 68 | None |
| 9/19/1974 | 31,200 | 103,435 | 1,230 | None |
| 10/16/1974 | 6,060 | 11,597 | 710 | None |
| 11/15/1974 | 35,600 | 172,716 | 1,800 | None |
| 1/14/1975 | 12,600 | 19,595 | 577 | None |
| 2/18/1975 | 18,600 | 36,196 | 722 | None |
| 3/10/1975 | 11,200 | 17,660 | 585 | None |
| 4/2/1975 | 4,550 | 2,342 | 191 | None |
| 5/19/1975 | 14,200 | 24,265 | 634 | None |
| 6/23/1975 | 11,500 | 20,457 | 660 | None |
| 7/2/1975 | 21,000 | 130,184 | 2,300 | None |
| 8/27/1975 | 3,320 | 1,539 | 172 | None |
| 9/3/1975 | 2,770 | 1,172 | 157 | None |
| 10/14/1975 | 1,200 | 71 | 22 | None |
| 11/4/1975 | 3,230 | 5,772 | 663 | None |
| 12/8/1975 | 1,200 | 49 | 15 | None |
| 1/5/1976 | 2,460 | 404 | 61 | None |
| 2/18/1976 | 1,300 | 154 | 44 | None |
| 3/10/1976 | 2,070 | 240 | 43 | None |
| 4/6/1976 | 1,660 | 438 | 98 | None |
| 5/10/1976 | 33,600 | 34,685 | 383 | None |
| 7/7/1976 | 13,200 | 29,672 | 834 | None |
| 8/24/1976 | 1,550 | 447 | 107 | None |
| 10/6/1976 | 3,420 | 2,627 | 285 | None |
| 11/3/1976 | 13,500 | 26,417 | 726 | None |
| 12/8/1976 | 25,000 | 319,395 | 4,740 | None |
| 1/12/1977 | 5,670 | 1,605 | 105 | None |
| 2/22/1977 | 21,800 | 55,585 | 946 | None |
| 3/9/1977 | 12,400 | 18,817 | 563 | None |
| 4/6/1977 | 24,800 | 88,902 | 1,330 | None |
| 5/4/1977 | 34,000 | 181,449 | 1,980 | None |
| 6/6/1977 | 9,390 | 9,238 | 365 | None |
| 7/20/1977 | 1,020 | 1,935 | 704 | None |
| 8/3/1977 | 1,400 | 215 | 57 | None |
| 9/12/1977 | 1,780 | 235 | 49 | None |
| 10/25/1977 | 932 | 83 | 33 | None |
| 11/30/1977 | 654 | 60 | 34 | None |
| 12/28/1977 | 627 | 257 | 152 | None |
| 1/16/1978 | 1,620 | 681 | 156 | None |
| 2/8/1978 | 2,050 | 2,050 | 371 | None |
| 3/21/1978 | 2,970 | 3,018 | 377 | None |
| 4/11/1978 | 256 | 28 | 41 | None |
| 5/16/1978 | 114 | 18 | 57 | None |
| 6/15/1978 | 1,380 | 1,019 | 274 | None |
| 7/18/1978 | 114 | 9 | 30 | None |
| 8/9/1978 | 754 | 87 | 43 | None |
| 9/27/1978 | 1,420 | 1,206 | 315 | None |
| 10/25/1978 | 573 | 39 | 25 | None |

| | | | | |
|---|---|---|---|---|
| 11/16/1978 | 740 | 94 | 47 | None |
| 12/21/1978 | 682 | 79 | 43 | None |
| 1/30/1979 | 3,260 | 2,153 | 245 | None |
| 2/14/1979 | 10,800 | 26,955 | 926 | None |
| 3/28/1979 | 25,300 | 105,697 | 1,550 | None |
| 4/26/1979 | 12,200 | 44,063 | 1,340 | None |
| 5/9/1979 | 20,800 | 72,881 | 1,300 | None |
| 6/9/1979 | 76,100 | 338,437 | 1,650 | None |
| 7/11/1979 | 5,200 | 1,233 | 88 | None |
| 8/8/1979 | 7,370 | 13,329 | 671 | None |
| 9/12/1979 | 2,100 | 849 | 150 | None |
| 10/30/1979 | 1,650 | 98 | 22 | None |
| 12/4/1979 | 1,680 | 398 | 88 | None |
| 12/19/1979 | 3,730 | 3,861 | 384 | None |
| 1/30/1980 | 10,200 | 37,389 | 1,360 | None |
| 2/13/1980 | 10,800 | 34,349 | 1,180 | None |
| 3/11/1980 | 1,860 | 241 | 48 | None |
| 4/16/1980 | 2,550 | 1,031 | 150 | None |
| 5/13/1980 | 2,090 | 1,369 | 243 | None |
| 6/4/1980 | 6,890 | 11,551 | 622 | None |
| 7/22/1980 | 376 | 36 | 36 | None |
| 8/6/1980 | 683 | 156 | 85 | None |
| 9/9/1980 | 2,010 | 1,474 | 272 | None |
| 3/20/2000 | 794 | 150 | 70 | 5.84 |
| 6/27/2000 | 2,330 | 88 | 14 | 8.54 |
| 8/22/2000 | 371 | 38 | 38 | 4.71 |
| 9/12/2000 | 403 | 75 | 69 | 4.66 |
| 10/23/2000 | 407 | 46 | 42 | 4.56 |
| 11/20/2000 | 17,700 | 17,652 | 370 | 23.15 |
| 12/11/2000 | 3,640 | 1,089 | 111 | 9.86 |
| 1/22/2001 | 29,900 | 90,664 | 1,125 | 31.08 |
| 2/20/2001 | 7,190 | 4,574 | 236 | 13.83 |
| 3/19/2001 | 44,200 | 70,646 | 593 | 37.95 |
| 4/16/2001 | 7,920 | 3,672 | 172 | 14.61 |
| 5/21/2001 | 6,340 | 4,956 | 290 | 12.95 |
| 6/18/2001 | 12,500 | 32,849 | 975 | 18.97 |
| 7/16/2001 | 1,350 | 335 | 92 | 6.47 |
| 8/13/2001 | 676 | 133 | 73 | 5.18 |
| 9/18/2001 | 6,780 | 5,007 | 274 | 13.42 |
| 10/8/2001 | 3,530 | 1,694 | 178 | 8.79 |
| 12/17/2001 | 15,200 | 8,358 | 204 | 21.44 |
| 1/14/2002 | 5,830 | 4,274 | 272 | 11.60 |
| 2/19/2002 | 6,720 | 3,804 | 210 | 12.65 |
| 3/20/2002 | 2,130 | 121 | 21 | 6.93 |
| 4/16/2002 | 8,830 | 1,000 | 42 | 15.07 |
| 5/13/2002 | 1,230 | 278 | 84 | 5.58 |
| 6/11/2002 | 1,750 | 783 | 166 | 6.37 |
| 7/17/2002 | 10,800 | 21,075 | 724 | 17.18 |
| 8/27/2002 | 2,340 | 612 | 97 | 7.22 |
| 10/30/2002 | 27,300 | 34,289 | 466 | 7.22 |
| 12/17/2002 | 26,200 | 29,871 | 423 | 29.63 |
| 1/28/2003 | 6,830 | 3,001 | 163 | 12.78 |
| 2/19/2003 | 4,630 | 636 | 51 | 10.16 |
| 3/11/2003 | 17,800 | 2,831 | 59 | 23.63 |

| | | | |
|---|---|---|---|
| 6/17/2003 | 2,620 | 1,977 | 280 | 7.58 |
| 7/28/2003 | 1,170 | 63 | 20 | 5.48 |
| 8/18/2003 | 717 | 8 | 4 | 5.48 |
| 10/14/2003 | 25,700 | 13,508 | 195 | 28.40 |
| 2/18/2004 | 17,300 | 2,192 | 47 | 22.50 |
| 8/18/2004 | 4,250 | 653 | 57 | 8.69 |
| 11/17/2004 | 5,650 | 3,457 | 227 | 11.67 |
| 2/23/2005 | 10,800 | 6,637 | 228 | 17.77 |
| 5/25/2005 | 2,210 | 441 | 74 | 8.05 |
| 8/3/2005 | 834 | 146 | 65 | 5.63 |
| 11/9/2005 | 1,270 | 284 | 83 | 6.07 |
| 2/1/2006 | 1,150 | 177 | 57 | 5.60 |
| 5/30/2006 | 1,720 | 459 | 99 | 6.06 |
| 4/28/2008 | 2,900 | 1,391 | 178 | 6.06 |
| 5/28/2008 | 8,400 | 12,611 | 557 | 6.06 |
| 6/17/2008 | 1,860 | 501 | 100 | 7.30 |
| 7/1/2008 | 1,360 | 268 | 73 | 6.45 |
| 7/15/2008 | 362 | 51 | 52 | 4.90 |
| 7/29/2008 | 269 | 20 | 28 | 4.70 |
| 8/15/2008 | 464 | 29 | 23 | 5.10 |
| 8/29/2008 | 2,920 | 3,872 | 492 | 8.32 |
| 11/17/2008 | 2,100 | 4,630 | 818 | 7.14 |
| 1/14/2009 | 592 | 59 | 37 | 4.66 |
| 2/25/2009 | 550 | 65 | 44 | 4.56 |
| 5/6/2009 | 18,400 | 65,464 | 1,320 | 21.80 |
| 5/19/2009 | 1,630 | 554 | 126 | 7.00 |
| 6/3/2009 | 663 | 145 | 81 | 5.02 |
| 6/24/2009 | 40 | 4 | 41 | 2.86 |
| 7/1/2009 | 302 | 48 | 59 | 3.84 |
| 7/28/2009 | 529 | 81 | 57 | 4.50 |
| 8/12/2009 | 329 | 54 | 61 | 3.93 |
| 8/25/2009 | 422 | 93 | 82 | 4.21 |
| 9/10/2009 | 944 | 850 | 334 | 5.39 |
| 11/19/2009 | 9,050 | 15,928 | 653 | 14.50 |
| 3/11/2010 | 15,500 | 9,358 | 224 | 20.24 |
| 5/26/2010 | 5,450 | 5,318 | 362 | 10.87 |
| 6/16/2010 | 14,000 | 28,301 | 750 | 18.95 |
| 7/13/2010 | 2,460 | 583 | 88 | 18.95 |
| 8/4/2010 | 2,030 | 383 | 70 | 7.05 |
| 8/17/2010 | 910 | 88 | 36 | 7.05 |
| 9/1/2010 | 1,030 | 283 | 102 | 5.55 |
| 9/1/2010 | 1,030 | 28 | 10 | 5.55 |
| 11/18/2010 | 1,730 | 611 | 131 | 6.65 |
| 12/14/2010 | 925 | 309 | 124 | 5.16 |
| 2/15/2011 | 1,150 | 387 | 125 | 5.22 |
| 3/23/2011 | 491 | 112 | 85 | 3.89 |
| 4/13/2011 | 138 | 28 | 74 | 2.61 |
| 4/26/2011 | 309 | 90 | 108 | 3.63 |
| 5/12/2011 | 212 | 59 | 103 | 3.21 |
| 6/1/2011 | 401 | 70 | 65 | 3.54 |
| 6/22/2011 | 200 | 36 | 66 | 2.72 |
| 7/7/2011 | 94 | 11 | 45 | 2.55 |
| 7/28/2011 | 411 | 47 | 42 | 3.57 |
| 8/17/2011 | 300 | 45 | 56 | 3.30 |

| | | | |
|---|---|---|---|
| 10/6/2011 | 380 | 42 | 41 | 3.58 |
| 1/10/2012 | 9,620 | 53,465 | 2,062 | 14.67 |
| 1/11/2012 | 5,580 | 11,626 | 773 | 10.45 |
| 1/28/2012 | 4,840 | 11,258 | 863 | 9.62 |
| 1/30/2012 | 15,400 | 173,710 | 4,185 | 19.99 |
| 2/16/2012 | 4,530 | 3,797 | 311 | 8.98 |
| 3/22/2012 | 15,600 | 43,308 | 1,030 | 19.34 |
| 3/26/2012 | 47,500 | 169,636 | 1,325 | 40.95 |
| 4/11/2012 | 10,400 | 14,296 | 510 | 15.78 |
| 4/25/2012 | 4,700 | 2,508 | 198 | 10.06 |
| 5/16/2012 | 2,980 | 1,703 | 212 | 7.80 |
| 5/17/2012 | 2,410 | 526 | 81 | 7.12 |
| 5/30/2012 | 467 | 33 | 26 | 3.84 |
| 6/12/2012 | 304 | 60 | 73 | 3.62 |
| 6/27/2012 | 287 | 32 | 42 | 3.83 |
| 7/12/2012 | 2,050 | 1,558 | 282 | 6.74 |
| 7/18/2012 | 4,590 | 2,450 | 198 | 9.42 |
| 8/21/2012 | 1,020 | 415 | 151 | 4.85 |
| 10/17/2012 | 1,020 | 187 | 68 | 4.91 |
| 11/27/2012 | 405 | 19 | 17 | 3.35 |
| 12/12/2012 | 388 | 122 | 117 | 3.06 |
| 1/17/2013 | 5,770 | 18,662 | 1,200 | 10.45 |
| 2/13/2013 | 698 | 85 | 45 | 3.68 |
| 3/13/2013 | 376 | 24 | 24 | 2.77 |
| 3/20/2013 | 925 | 184 | 74 | 4.42 |
| 4/16/2013 | 472 | 88 | 69 | 4.42 |
| 4/30/2013 | 1,400 | 457 | 121 | 5.00 |
| 5/9/2013 | 171 | 12 | 25 | 2.40 |
| 5/20/2013 | 1,130 | 719 | 236 | 4.34 |
| 5/22/2013 | 1,560 | 681 | 162 | 5.22 |
| 6/6/2013 | 575 | 167 | 108 | 3.79 |
| 6/20/2013 | 201 | 14 | 25 | 2.21 |
| 7/1/2013 | 174 | 30 | 63 | 2.36 |
| 7/16/2013 | 406 | 117 | 107 | 3.16 |
| 8/7/2013 | 419 | 36 | 32 | 2.62 |
| 11/12/2013 | 12,400 | 13,469 | 403 | 17.41 |
| 11/13/2013 | 10,800 | 9,519 | 327 | 15.90 |
| 12/10/2013 | 5,210 | 1,966 | 140 | 10.51 |
| 1/22/2014 | 1,290 | 191 | 55 | 4.72 |
| 2/12/2014 | 1,030 | 86 | 31 | 4.34 |
| 3/5/2014 | 1,500 | 675 | 167 | 5.24 |
| 4/3/2014 | 491 | 57 | 43 | 3.79 |
| 4/16/2014 | 1,240 | 304 | 91 | 4.76 |
| 5/7/2014 | 289 | 64 | 82 | 3.13 |
| 5/14/2014 | 4,630 | 3,082 | 247 | 9.64 |
| 5/20/2014 | 7,700 | 14,424 | 695 | 13.19 |
| 6/12/2014 | 2,990 | 999 | 124 | 7.54 |
| 6/25/2014 | 1,900 | 845 | 165 | 5.93 |
| 7/9/2014 | 1,620 | 620 | 142 | 5.43 |
| 7/22/2014 | 1,910 | 1,097 | 213 | 5.82 |
| 8/12/2014 | 745 | 127 | 63 | 3.41 |
| 8/13/2014 | 640 | 102 | 59 | 3.27 |
| 9/24/2014 | 1,870 | 988 | 196 | 6.13 |
| 10/28/2014 | 405 | 22 | 20 | 3.06 |

| | | | |
|---|---|---|---|
| 10/29/2014 | 280 | 20 | 27 | 2.88 |
| 11/25/2014 | 2,500 | 357 | 53 | 6.62 |
| 12/2/2014 | 2,620 | 5,169 | 732 | 6.85 |
| 12/29/2014 | 3,070 | 1,506 | 182 | 7.47 |
| 1/13/2015 | 4,650 | 3,597 | 287 | 9.56 |
| 1/28/2015 | 22,900 | 89,189 | 1,445 | 25.93 |
| 2/10/2015 | 3,310 | 1,026 | 115 | 7.79 |
| 2/25/2015 | 1,330 | 143 | 40 | 4.94 |
| 3/3/2015 | 1,070 | 110 | 38 | 4.53 |
| 3/25/2015 | 24,200 | 19,568 | 300 | 26.98 |
| 4/7/2015 | 5,080 | 1,848 | 135 | 10.04 |
| 4/22/2015 | 12,500 | 14,319 | 425 | 17.62 |
| 4/30/2015 | 13,200 | 12,666 | 356 | 18.20 |
| 5/20/2015 | 43,400 | 123,995 | 1,060 | 39.64 |
| 5/27/2015 | 58,000 | 23,918 | 153 | 47.11 |
| 6/5/2015 | 67,600 | 43,729 | 240 | 47.11 |
| 6/18/2015 | 43,300 | 102,469 | 878 | 39.60 |
| 6/23/2015 | 60,600 | 41,977 | 257 | 48.28 |
| 6/30/2015 | 38,900 | 91,742 | 875 | 36.86 |
| 7/14/2015 | 18,800 | 34,812 | 687 | 22.93 |
| 7/28/2015 | 10,100 | 11,379 | 418 | 15.39 |
| 7/29/2015 | 9,650 | 8,843 | 340 | 14.92 |
| 8/12/2015 | 6,120 | 5,048 | 306 | 11.24 |
| 8/27/2015 | 3,780 | 1,895 | 186 | 8.38 |
| 9/29/2015 | 1,540 | 411 | 99 | 5.13 |
| 10/21/2015 | 640 | 45 | 26 | 4.61 |
| 10/28/2015 | 24,300 | 99,554 | 1,520 | 27.05 |
| 11/24/2015 | 22,400 | 36,104 | 598 | 25.63 |
| 12/9/2015 | 37,100 | 72,697 | 727 | 35.76 |
| 12/22/2015 | 34,900 | 62,554 | 665 | 34.32 |
| 1/20/2016 | 15,300 | 17,815 | 432 | 20.07 |
| 1/27/2016 | 11,700 | 9,051 | 287 | 16.84 |
| 2/17/2016 | 6,400 | 3,467 | 201 | 11.54 |
| 2/24/2016 | 6,650 | 9,069 | 506 | 11.82 |
| 3/7/2016 | 7,690 | 4,539 | 219 | 12.94 |
| 3/7/2016 | 7,690 | 4,539 | 219 | 12.94 |
| 3/16/2016 | 56,300 | 109,561 | 722 | 46.31 |
| 3/30/2016 | 16,600 | 17,718 | 396 | 21.09 |
| 4/5/2016 | 11,000 | 10,792 | 364 | 16.23 |
| 4/26/2016 | 67,000 | 74,221 | 411 | 50.71 |
| 4/27/2016 | 62,200 | 35,709 | 213 | 48.80 |
| 5/12/2016 | 33,900 | 61,767 | 676 | 33.68 |
| 5/25/2016 | 49,900 | 95,089 | 707 | 42.55 |
| 5/25/2016 | 49,900 | 113,380 | 843 | 42.55 |
| 6/8/2016 | 80,700 | 78,957 | 363 | 51.74 |
| 6/22/2016 | 40,600 | 87,872 | 803 | 37.95 |
| 6/28/2016 | 41,900 | 65,276 | 578 | 38.73 |
| 7/11/2016 | 26,800 | 75,124 | 1,040 | 28.86 |
| 7/11/2016 | 26,800 | 75,124 | 1,040 | 28.86 |
| 7/26/2016 | 14,900 | 34,779 | 866 | 19.71 |
| 7/27/2016 | 15,900 | 58,155 | 1,357 | 20.58 |
| 8/18/2016 | 10,900 | 29,379 | 1,000 | 16.10 |
| 8/24/2016 | 28,000 | 89,657 | 1,188 | 29.71 |
| 8/29/2016 | 15,300 | 27,382 | 664 | 20.06 |

| | | | |
|---|---|---|---|
| 8/29/2016 | 15,300 | 27,382 | 664 | 20.06 |
| 9/28/2016 | 4,380 | 283 | 24 | 9.85 |
| 10/3/2016 | 3,730 | 1,267 | 126 | 9.24 |
| 10/3/2016 | 3,730 | 1,267 | 126 | 9.24 |
| 10/18/2016 | 2,580 | 480 | 69 | 8.13 |
| 10/26/2016 | 2,400 | 420 | 65 | 7.88 |
| 10/31/2016 | 1,800 | 315 | 65 | 6.97 |
| 10/31/2016 | 1,800 | 315 | 65 | 6.97 |
| 11/29/2016 | 3,240 | 1,196 | 137 | 8.66 |
| 12/6/2016 | 13,600 | 55,351 | 1,510 | 18.55 |
| 12/28/2016 | 2,900 | 508 | 65 | 8.26 |
| 1/10/2017 | 2,590 | 747 | 107 | 7.85 |
| 1/16/2017 | 2,550 | 584 | 85 | 7.85 |
| 1/16/2017 | 2,550 | 584 | 85 | 7.85 |
| 1/25/2017 | 19,800 | 63,881 | 1,197 | 23.76 |
| 2/6/2017 | 5,100 | 2,598 | 189 | 10.90 |
| 2/6/2017 | 5,100 | 2,598 | 189 | 10.90 |
| 2/7/2017 | 4,630 | 2,421 | 194 | 10.48 |
| 2/22/2017 | 23,200 | 88,794 | 1,420 | 26.35 |
| 3/7/2017 | 14,300 | 15,417 | 400 | 19.33 |
| 3/28/2017 | 4,580 | 1,778 | 144 | 10.16 |
| 4/5/2017 | 5,040 | 4,592 | 338 | 10.60 |
| 4/20/2017 | 27,600 | 96,708 | 1,300 | 29.45 |
| 4/20/2017 | 27,600 | 96,708 | 1,300 | 29.45 |
| 4/25/2017 | 19,500 | 43,098 | 820 | 29.45 |
| 4/26/2017 | 17,500 | 35,659 | 756 | 22.03 |
| 5/3/2017 | 8,190 | 11,324 | 513 | 13.87 |
| 5/16/2017 | 1,860 | 802 | 160 | 7.37 |
| 5/18/2017 | 1,860 | 476 | 95 | 7.37 |
| 5/18/2017 | 1,860 | 476 | 95 | 7.37 |
| 5/23/2017 | 3,260 | 7,205 | 820 | 8.89 |
| 6/6/2017 | 7,680 | 10,702 | 517 | 13.37 |
| 6/12/2017 | 6,710 | 6,873 | 380 | 12.39 |
| 6/12/2017 | 6,710 | 6,873 | 380 | 12.39 |
| 6/27/2017 | 5,720 | 6,907 | 448 | 11.34 |
| 6/27/2017 | 5,720 | 9,374 | 608 | 11.34 |
| 7/10/2017 | 4,350 | 3,037 | 259 | 9.83 |
| 7/10/2017 | 4,350 | 3,037 | 259 | 9.83 |
| 7/11/2017 | 4,240 | 2,777 | 243 | 9.71 |
| 7/25/2017 | 1,560 | 429 | 102 | 6.39 |
| 7/26/2017 | 1,470 | 357 | 90 | 6.28 |
| 8/15/2017 | 1,800 | 801 | 165 | 6.76 |
| 8/22/2017 | 984 | 154 | 58 | 5.58 |
| 8/30/2017 | 117,000 | 145,377 | 461 | 52.51 |
| 9/8/2017 | 28,200 | 147,455 | 1,940 | 29.87 |
| 9/27/2017 | 4,960 | 1,551 | 116 | 12.17 |
| 10/18/2017 | 3,490 | 1,110 | 118 | 10.95 |
| 10/25/2017 | 4,790 | 1,627 | 126 | 11.40 |
| 11/29/2017 | 1,080 | 102 | 35 | 7.19 |
| 12/12/2017 | 1,580 | 422 | 99 | 7.92 |
| 12/27/2017 | 4,120 | 3,220 | 290 | 10.67 |
| 1/9/2018 | 1,750 | 495 | 105 | 7.99 |
| 1/31/2018 | 1,440 | 175 | 45 | 7.58 |
| 2/13/2018 | 2,590 | 3,162 | 453 | 9.37 |

| | | | |
|---|---|---|---|
| 2/27/2018 | 12,600 | 41,161 | 1,212 | 18.14 |
| 3/6/2018 | 3,900 | 2,144 | 204 | 10.95 |
| 3/27/2018 | 1,270 | 226 | 66 | 7.83 |
| 4/3/2018 | 31,300 | 113,047 | 1,340 | 33.43 |
| 4/16/2018 | 4,580 | 3,296 | 267 | 11.61 |
| 4/25/2018 | 5,290 | 3,294 | 231 | 11.53 |
| 5/9/2018 | 1,080 | 201 | 69 | 6.72 |
| 5/21/2018 | 760 | 330 | 161 | 5.98 |
| 5/30/2018 | 1,640 | 575 | 130 | 7.25 |
| 6/5/2018 | 711 | 176 | 92 | 5.80 |
| 6/19/2018 | 858 | 271 | 117 | 5.96 |
| 6/20/2018 | 2,620 | 2,302 | 326 | 8.30 |
| 7/10/2018 | 1,510 | 627 | 154 | 7.13 |
| 7/24/2018 | 546 | 59 | 40 | 5.25 |
| 7/31/2018 | 724 | 133 | 68 | 5.53 |
| 8/7/2018 | 622 | 161 | 96 | 5.34 |
| 8/22/2018 | 880 | 285 | 120 | 5.81 |
| 9/25/2018 | 1,260 | 489 | 144 | 6.43 |
| 10/9/2018 | 2,220 | 1,388 | 232 | 8.26 |
| 10/16/2018 | 5,140 | 4,378 | 316 | 11.31 |
| 12/11/2018 | 51,700 | 178,365 | 1,280 | 42.57 |
| 12/27/2018 | 19,300 | 53,372 | 1,026 | 23.62 |
| 1/30/2019 | 21,500 | 28,047 | 484 | 25.32 |
| 2/5/2019 | 17,900 | 22,965 | 476 | 22.91 |
| 2/27/2019 | 17,200 | 53,870 | 1,162 | 22.19 |
| 3/5/2019 | 9,440 | 10,559 | 415 | 15.53 |
| 3/27/2019 | 9,010 | 5,804 | 239 | 15.44 |
| 4/9/2019 | 4,180 | 1,645 | 146 | 10.73 |
| 4/23/2019 | 20,500 | 65,752 | 1,190 | 24.85 |
| 4/24/2019 | 16,300 | 34,136 | 777 | 21.93 |
| 5/7/2019 | 54,100 | 186,645 | 1,280 | 43.78 |
| 5/21/2019 | 43,200 | 126,917 | 1,090 | 37.03 |
| 5/28/2019 | 44,300 | 107,701 | 902 | 37.85 |
| 5/29/2019 | 44,500 | 94,994 | 792 | 37.95 |
| 6/4/2019 | 42,800 | 104,170 | 903 | 36.81 |
| 6/18/2019 | 37,800 | 147,730 | 1,450 | 34.13 |
| 6/26/2019 | 21,900 | 72,190 | 1,223 | 25.21 |
| 7/23/2019 | 5,440 | 5,161 | 352 | 12.27 |
| 7/30/2019 | 4,100 | 243 | 22 | 10.91 |
| 8/6/2019 | 3,640 | 2,149 | 219 | 10.41 |
| 8/21/2019 | 3,800 | 1,260 | 123 | 10.61 |
| 9/24/2019 | 1,920 | 1,061 | 205 | 8.07 |
| 10/8/2019 | 841 | 61 | 27 | 6.15 |
| 10/30/2019 | 1,250 | 209 | 62 | 6.84 |
| 11/21/2019 | 1,430 | 181 | 47 | 7.16 |
| 12/3/2019 | 862 | 65 | 28 | 6.06 |
| 12/18/2019 | 929 | 25 | 10 | 6.19 |
| 1/7/2020 | 876 | 165 | 70 | 6.04 |
| 1/29/2020 | 1,630 | 650 | 148 | 7.45 |
| 2/18/2020 | 8,690 | 45,673 | 1,950 | 14.62 |
| 2/26/2020 | 9,160 | 20,788 | 842 | 15.05 |
| 3/17/2020 | 5,580 | 5,234 | 348 | 11.57 |
| 6/9/2020 | 3,910 | 3,172 | 301 | 10.12 |
| 6/24/2020 | 2,280 | 1,745 | 284 | 8.33 |

| | | | |
|---|---|---|---|
| 6/25/2020 | 4,320 | 4,984 | 428 | 10.43 |
| 7/7/2020 | 953 | 193 | 75 | 6.01 |
| 7/21/2020 | 2,660 | 2,273 | 317 | 8.63 |
| 7/28/2020 | 1,780 | 835 | 174 | 7.33 |
| 8/6/2020 | 1,820 | 559 | 114 | 7.39 |
| 8/19/2020 | 675 | 100 | 55 | 5.31 |
| 8/20/2020 | 653 | 69 | 39 | 5.26 |
| 9/1/2020 | 749 | 180 | 89 | 5.49 |
| 9/15/2020 | 6,290 | 10,613 | 626 | 11.97 |
| 9/29/2020 | 4,840 | 1,983 | 152 | 10.67 |
| 10/6/2020 | 3,200 | 1,070 | 124 | 9.10 |
| 10/26/2020 | 980 | 95 | 36 | 6.02 |
| 11/23/2020 | 592 | 86 | 54 | 5.13 |
| 12/8/2020 | 1,200 | 236 | 73 | 6.10 |
| 12/16/2020 | 1,720 | 737 | 159 | 6.98 |
| 1/25/2021 | 3,080 | 1,137 | 137 | 8.77 |
| 1/26/2021 | 2,750 | 1,290 | 174 | 8.37 |
| 2/9/2021 | 1,370 | 174 | 47 | 6.42 |
| 3/8/2021 | 2,470 | 1,165 | 175 | 7.87 |
| 3/22/2021 | 1,360 | 121 | 33 | 6.22 |
| 4/6/2021 | 966 | 182 | 70 | 5.46 |
| 4/20/2021 | 874 | 179 | 76 | 5.26 |
| 4/27/2021 | 4,940 | 6,072 | 456 | 10.65 |
| 5/4/2021 | 15,500 | 44,702 | 1,070 | 20.01 |
| 5/18/2021 | 9,720 | 18,077 | 690 | 15.36 |
| 5/25/2021 | 25,100 | 33,014 | 488 | 26.76 |
| 6/9/2021 | 52,200 | 123,108 | 875 | 26.76 |
| 6/29/2021 | 26,500 | 111,424 | 1,560 | 27.60 |
| 6/29/2021 | 26,500 | 94,425 | 1,322 | 27.60 |
| 7/13/2021 | 22,800 | 48,302 | 786 | 25.30 |
| 7/27/2021 | 11,900 | 18,282 | 570 | 17.20 |
| 8/10/2021 | 5,220 | 5,164 | 367 | 11.45 |
| 8/18/2021 | 3,190 | 2,218 | 258 | 9.18 |
| 10/12/2021 | 2,170 | 1,439 | 246 | 7.74 |
| 12/7/2021 | 1,400 | 132 | 35 | 6.54 |
| 1/4/2022 | 1,450 | 723 | 185 | 6.63 |
| 2/1/2022 | 2,440 | 2,788 | 424 | 8.13 |
| 3/8/2022 | 1,390 | 124 | 33 | 6.45 |
| 4/5/2022 | 3,960 | 2,700 | 253 | 9.62 |
| 4/19/2022 | 1,740 | 408 | 87 | 6.96 |
| 5/3/2022 | 2,790 | 1,602 | 213 | 8.15 |
| 5/17/2022 | 1,980 | 1,115 | 209 | 7.00 |